SEISMIC BEHAVIOUR OF CONNECTIONS BETWEEN PRECAST CONCRETE ELEMENTS

A thesis
submitted in partial fulfilment
of the requirements for the Degree
of
Doctor of Philosophy in Civil Engineering
at the
University of Canterbury

by

José I. Restrepo-Posada

University of Canterbury
Christchurch
New Zealand

1992

To Clemencia

CONTENTS

ABSTRACT

Several precast concrete systems have been in use in New Zealand in the construction of moment resisting frames designed for earthquake resistance, despite the lack of code design guidelines. The two design codes for buildings, NZS 4203 (1984) and NZS 3101 (1982), deal only with the design of monolithic concrete construction.

The use of precast concrete in moment resisting frames in New Zealand assumes that this method of construction behaves the same as monolithic reinforced concrete structures. A test programme was devised to provided experimental evidence on the seismic behaviour of the most commonly used precast concrete arrangements. Six full-scale subassemblages were quasi-statically tested under reverse load conditions with increasing displacements to failure. Four tests were conducted in H-shaped specimens connected at the beam midspan. The remaining two specimens were cruciform-shaped and had the connection detail in the critical region at the beam-column joint. It was found that neither of the connection detail nor the construction joints have a detrimental effect on the seismic performance. Hence, the assumption of designing these systems as if monolithic is adequate.

Theoretical work was undertaken to give simple design recommendations for the design of different connecting details, including the design of interior beam-column joints. Truss models and the concept of shear friction were extensively used.

This report also discusses in some detail the stress-strain behaviour of the two grades of New Zealand manufactured reinforcing steel. Test results on the effects of bar deformations, strain ageing and strain rate on the cyclic behaviour of reinforcing steel are presented. An analytical model based on test results is postulated.

ACKNOWLEDGEMENTS

The research work reported in this thesis was carried out in the Department of Civil Engineering, University of Canterbury, New Zealand under the guidance of Professor R. Park.

I express my deepest gratitude to Professor R. Park and Dr. A.H. Buchanan, supervisors of this project, for their invaluable advice and permanent encouragement.

This investigation was funded under the sponsorship of the New Zealand Concrete Society. The encouragement of its Council and the financial assistance of the following members is gratefully acknowledged:

Beca Carter Hollings and Ferner Ltd.
Cement and Concrete Association
Downer and Co. Ltd.
Firth Stresscrete
KRTA Ltd.
Mainzeal Construction
McConnell Dowell Corporation Ltd.
Murray North Ltd.
Precision Precast (Wgtn) Ltd.
Structon Group Ltd.
Wilco Concrete Products Ltd.
Wilkins and Davies Ltd.
Works Consultancy Services

The financial support and the scholarship provided by the Earthquake and War Damage Commission and the donation of the reinforcing steel by Pacific Steel Ltd. are also gratefully acknowledged.

Special thanks are given to Emeritus Professor T. Paulay for his permanent interest and fruitful discussions; to Professor R. Fenwick, at Auckland University, for showing a great deal of interest in this project and for supplying the information regarding the construction of the clip gauges.

Sincere thanks are given to Mrs. V.J. Grey for putting up with the amount of work and pressure while still keeping her sense of humour, ah!, and obviously for her superb quality drawings. The superior job of Mrs. D.L. Forbes for typing the manuscript is also thanked. The excellent assistance of the technical staff of the Department of Civil Engineering under the management of Mr. G.E. Hill is acknowledged. In particular to Mr. G. Sim, now retired, who made the experimental work a most enjoyable blend of technicalities and philosophy. Mr. F. Greenslade and Mr. M. Stuart-Jones who spent a great deal of time in the logistics for testing the reinforcing steel coupons. Mr. R.N. Allen for his precise work in manufacturing the test frames. Mr. H.H. Crowther for his assistance with the purchase of the materials. Messrs. G.H. Clarke, G. Grey, D.J. MacPherson, J.H. Maley, P.A. Murphy are also thanked for their assistance in the construction and testing of the precast concrete specimens. Thanks are also given to Mr. N.H. Hickey for his advice and friendship, to Messrs. P.J. Coursey and

B. Hutchinson for their support with the computer facilities and to Messrs. L.H. Gardner (retired) and M. Roestenburg for their photographic assistance.

I owe a great deal to all my fellow post-graduate students and visitors for their constructive discussions. In particular I like to mention Drs. P.C. Cheung and L.L. Dodd. Mr. E. Thomson who assisted in the testing of the fourth specimen. Miss V. Bienvenu, Drs. G. MacRae, M. Rodriguez, H. Tanaka and N.D. Vitharana; Messrs. M. Ellis, Li Bing, S. Hakuto, Y. Sato, J. Tjondro and S. Wijanto for their friendiship during the lapse of this research.

The helpful advice received from Messrs. F. MacKenzie of Firth Industries Ltd., Christchurch and G. Wilkinson of Holmes Consulting Group, Christchurch is very much appreciated.

Thanks are given to Dr. S. Wood of the University of Illinois for providing the digitized data for the cyclic behaviour of reinforcing steel and to the Department of Mechanical Engineering at the University of Canterbury for facilitating the use of their electron microscope.

I am also indebted to my fellow structural engineers in Colombia, in particular to Messrs. J.H. Arango, C. Blodek, L.E. García, E. Germanetti, E. Isaza, J.H. Londoño, J. Muñoz, F.J. Pérez, L. Restrepo and B. Villegas for their encouragement and wisdom.

Finally, I express my deepest gratitude to my wife for her continuous support, encouragement and forbearance during all the hours spent in setting up the experiments, data processing and writing. She also contributed in editing all the final draft of this thesis.

NOTATION

CHAPTER 2

A = instantaneous cross sectional area

A_o = initial cross-sectional area

b = strain magnitude of the work hardening region

e = natural base of logarithms

E_1', E_2' = true slopes of the bi-linear envelope describing the Bauschinger effect

E_m = slope of first asymptote in the Menegotto-Pinto expression

E_s = initial elastic modulus in engineering coordinate system

E_s' = initial elastic modulus in natural coordinate system

E_{sh} = strain hardening modulus as required by the model proposed by Mander et al

E_u = engineering unloading modulus

E_u' = true unloading modulus

f' = true stress

f_a' = true stress at the initiation of the Bauschinger effect

f_b' = true stress at the end of the Bauschinger effect

f_b'' = true normalized stress at the end of the Bauschinger effect

f_{ch} = characteristic stress required by Ramberg-Osgood and Menegotto-Pinto expressions

f_N'' = normalized-transformed true stress

f_o = steel stress at a reversal of stress in Mander et al model

f_{or}, $f_{0.06}$ = stresses required by the model proposed by Tjokrodimuljo-Fenwick

f_p' = stress magnitude between the inclined envelope to the point at the initiation of the Bauschinger effect in the natural coordinate system

$f_{r,major}'$ = true stress at a major reversal point

$f_{r,minor}'$ = true stress at a minor reversal point

f_s = engineering steel stress

f_s' = true steel stress

$f_{s,rejoin}'$ = stress at the rejoining of Bauschinger curve with skeleton curve

f_s'' = transformed true stress

$f_{sh,1}$ = engineering stress at a strain $\epsilon_{sh,1}$

f_t' = stress magnitude between the top and bottom inclined envelopes in the natural coordinate system

f_y = yield stress in engineering coordinate system

f_r' = true stress at a reversal point

f_{su} = ultimate stress in engineering coordinate system

f_{su}' = "ultimate stress" and slope in natural coordinate system

h_d = "hardness" ratio of an Universal Testing Machine

k = directional factor: 1 if tensioning, 2 if compressing

ℓ = instantaneous gauge length

ℓ_o = initial gauge length

m = directional factor: 2 if tensioning, 1 if compressing

N = axial load

P = exponential factor to define the work hardening region of the skeleton curve and the shape of the Bauschinger effect

Q = ratio between slopes in Menegotto-Pinto expression

R, r = exponential factors used in Ramberg-Osgood and Menegotto-Pinto expressions

s = directional factor: 1 if tensioning, -1 if compressing

W_a, W_n = constants required by Kent and Park model

$\Delta\ell$ = change in gauge length

ϵ = general engineering strain

ϵ' = general natural strain

ϵ'_a = natural strain at the initiation of the Bauschinger effect

ϵ'_b = natural strain at the end of the Bauschinger effect

ϵ''_b = transformed natural strain at the end of the Bauschinger effect

ϵ_{ch} = characteristic strain required by Ramberg-Osgood and Menegotto-Pinto expressions

ϵ^o = engineering compressive strain

$\epsilon^{o\prime}$ = true compressive strain

ϵ_o = steel strain at a reversal of stress in Mander et al model

ϵ'_o = shifted origin strain

ϵ_{or}, $\epsilon_{0.06}$ = strains required by the model proposed by Tjokrodimuljo-Fenwick

ϵ_r = strain at reversal point used by Spurr-Paulay model and by Stanton-McNiven model

ϵ'_r = natural strain at a reversal point

$\epsilon'_{r,major}$ = natural strain at a major reversal point

$\epsilon'_{r,minor}$ = natural strain at a minor reversal point

ϵ_s = steel strain in engineering coordinate system

ϵ'_s = steel strain in natural coordinate system

$\epsilon'_{s,rejoin}$ = strain at the rejoining of Bauschinger curve with skeleton curve

ϵ''_s = transformed natural strain

ϵ_{sh} = engineering strain at the initiation of work hardening region

$\epsilon_{sh,1}$ = strain in the work hardening region of the tension monotonic curve

ϵ'_{sh} = natural strain at the initiation of work hardening

ϵ_{su} = ultimate strain in engineering coordinated system

ϵ'_{su} = "ultimate" strain in natural coordinate system

$\epsilon'_{su,shift}$ = natural strain associated with the "ultimate" true stress

ϵ''_N = transformed-normalized natural strain

ϵ_y = yield strain in engineering coordinate system

ν = Poisson's ratio

σ = general engineering stress

σ' = general true stress

σ^o = engineering compression steel

$\sigma^{o\prime}$ = true compression stress

Ω = partial area under the normalized Bauschinger curve

CHAPTER 3

A_{st} = area of transverse steel

b = beam width

d = effective depth of a beam

d' = distance from the extreme fibre in compression to the centroid of the compression steel

d_b = nominal diameter of reinforcing bar

d_p = distance from the compression steel in the beam to the linear potentiometer in the tensile chord of the beam

E_g = Young's modulus of grout

E_s = Young's modulus of steel

f'_c = concrete cylinder compressive strength

f'_{cc} = confined compressive strength of concrete

f'_g = grout cylinder compressive strength

f_ℓ = lateral confining stress

$f_{sh,1}$ = steel stress at a strain $\epsilon_{sh,1}$

f_{su} = ultimate (maximum) strength of steel in the tensile test

f'_t = concrete split-cylinder tensile strength

f'_{tg} = grout split-cylinder tensile strength

f_y = yield strength of steel

f_{yt} = measured yield strength of transverse steel

h_c = column depth

h_p = distance between top and bottom linear potentiometers in the span of the beam

H_a = theoretical lateral load capacity of a test unit based on the measured material properties

K_e = "elastic" stiffness measured at $0.75H_a$

ℓ_b = horizontal distance between column centrelines in Units 1 to 4 and horizontal distance between beam pins in Units 5 and 6

ℓ_c = vertical distance between column pins

ℓ_g = gauge length of a segment in the beam span

ℓ_j = diagonal gauge length at the beam-column joint

ℓ_h = horizontal distance between linear potentiometers used to monitor the rigid body rotation

ℓ_{st}, ℓ'_{st} = length of the diagonal strut in the beam, radiating from the column face

s = spacing between set of transverse beam reinforcement

x = distance at which a flexural displacement is determined

x_{cr} = distance from the column at which the diagonal strut develops

x_p = distance from the column face to the centre of a segment in the beam

V_a = beam shear associated with H_a

V^o = beam shear at overstrength

$\alpha_1..\alpha_3$ = angle of rotation of slaved column

β = angle between the horizontal at the level of the compression steel and a line radiating from the column face at the level of the compression steel and passing through the centre of a segment in the beam

γ = angular shear distortion

δ_A = measured gross top horizontal column displacement

$\delta_{b,f\ell}$ = beam flexural displacement

$\delta_{b,fe}$ = beam displacement due to fixed-end rotation

$\delta_{b,sf}$ = beam displacement due to shear-flexure

$\delta_{b,ss}$ = beam displacement due to sliding shear

δ_B = measured horizontal rigid body displacement

δ_{co} = total horizontal column displacement calculated from internal deformations

$\delta_{c,c}$ = column displacement caused by internal deformations within the column

$\delta_{c,fe}$ = column displacement due to fixed-end rotation in the beams

$\delta_{c,f\ell}$ = column displacement due to flexural deformations in the beams

$\delta_{c,j}$ = column displacement due to distortion of the beam-column joints

$\delta_{c,s}$ = column displacement due to shear displacement in the beams

δ_C , $\delta_{C'}$ = measured displacement to estimate the rigid body rotation

δ_f = beam displacement at a distance x from the column face including fixed-end and flexural components

δ_H = net measured top horizontal column displacement

δ_s, $\delta_{s'}$ = measured interior displacements

δ_r = calculated displacement at the longitudinal beam bars centroid

δ_θ = estimated discrete rotation

Δ = applied horizontal column displacement

Δ_y = first yield displacement

Δ_{75} = horizontal displacement associated to $0.75H_a$

ϵ_{avg} = average strain at the level of the beam longitudinal reinforcement, calculated from linear potentiometer readings

ϵ_{sh} = steel strain at the commencement of strain hardening

$\epsilon_{sh,1}$ = steel strain used to define the strain hardening region

ϵ_{su} = strain at ultimate (maximum) load in the tensile steel test

η = angle of a diagonal gauged length to the horizontal

$\theta_{f\ell}$ = rotation of beam caused by flexure

θ_{fe} = fixed-end rotation

ρ = area ratio of top beam reinforcement

ρ' = area ratio of bottom beam reinforcement

v^o = beam nominal shear stress at overstrength

μ_Δ = displacement ductility factor

μ_f = coefficient of friction

CHAPTER 4

b = beam width

d = effective depth of a beam

f'_c = concrete cylinder compressive strength

f_s = steel stress
f_y = yield strength of steel
H = storey shear
H_a = theoretical load capacity of a test unit based on the measured material properties
H_N, H_S = column shear
K_{test} = measured initial "elastic" stiffness of a test unit
K_{th} = theoretical initial "elastic" stiffness of a test unit
T_y = tension force of beam chord at yield of reinforcement
V^o = shear force at overstrength
u = bond stress

Δ = column lateral displacement
Δ_y = first yield displacement
ϵ = local bar strain
$\bar{\epsilon}$ = average bar strain
θ = beam rotation
θ_y = beam rotation at first yield
μ_a = available displacement ductility factor
μ_Δ = displacement ductility factor
μ_θ = rotational ductility factor
μ_ϕ = curvature ductility factor
v^o = nominal shear stress at overstrength
ϕ = beam curvature
ϕ_y = beam curvature at first yield

CHAPTER 5

A_T = effective friction surface
b = beam width
d = effective depth of a beam
d_b = diameter of bar
f_b = bearing stress
f'_c = concrete cylinder compressive strength
f'_{cr} = diagonal tensile strength of concrete
f_s = steel stress
f'_t = concrete cylinder splitting strength
f_y = yield strength of steel
H = storey shear
H_a = theoretical load capacity of a test unit based on the measured material properties
H_N, H_S = column shear
S_T = axial force in steel straps
T = axial force in the diagonal bars

T_H = horizontal force component of diagonal bars
T_V = vertical force component of diagonal bars
T_y = tension force of beam chord at yield of reinforcement
V_a = shear force in the beam associated with H_a
V^o = shear force at overstrength

Δ = column lateral displacement
Δ_y = first yield displacement
ϵ = local bar strain
μ_a = available displacement ductility factor
μ_Δ = displacement ductility factor
v^o = nominal shear stress at overstrength
ϕ = beam curvature

CHAPTER 6

b = beam width
d = effective depth of a beam
f'_c = concrete cylinder compressive strength
f_s = steel stress
f_y = yield strength of steel
H = storey shear
H_a = theoretical load capacity of a test unit based on the measured material properties
H_f = bar force at the beginning of the hook
K_{test} = measured initial "elastic" stiffness of a test unit
K_{th} = theoretical initial "elastic" stiffness of a test unit
U = bond stress
V^o = shear force at overstrength
V_f = bar force at the end of the hook
u = bond stress

Δ = column lateral displacement
Δ_y = first yield displacement
ϵ = local bar strain
$\bar{\epsilon}$ = average bar strain
θ = beam rotation
θ_y = beam rotation at first yield
μ_a = available displacement ductility factor
μ_Δ = displacement ductility factor
μ_θ = rotational ductility factor
μ_ϕ = curvature ductility factor
τ_f = average shear stress

v^o = nominal shear stress at overstrength

ϕ = beam curvature

ϕ_y = beam curvature at first yield

CHAPTER 7

A_b = the largest reinforcement area between beam top or bottom reinforcement

A_g = gross area of column section

A_{sh} = area of joint horizontal reinforcing steel

A_{st} = area of transverse reinforcing steel

A_{SB} = area of beam bottom reinforcing steel

A_{SS} = area of effective tension reinforcement in a slab

A_{ST} = area of beam top reinforcing steel

A_v = area of reinforcing steel required by shear

A_T = effective friction surface

b_j = effective joint width

b_w = beam width

c_o = concrete cover to the main reinforcement

C = compression force in the beam reinforcement

C_{CB} = concrete compressive force at the bottom of the beam

C_{CT} = concrete compressive force at the top of the beam

C_j = joint shear participation factor

C_{SB} = compressive force carried by the bottom beam reinforcement

C_{ST} = compressive force carried by the top beam reinforcement

d = effective beam depth

d_b = bar diameter

d′ = distance from extreme compression fibre to centroid of compression reinforcement in the beam

D° = inclined force carrying the beam shear at the flexural overstrength

e_v = tension shift

f'_c = unconfined concrete cylinder strength

f'_s = compressive steel stress

f_b = bearing stress

f'_{cr} = diagonal tensile strength of concrete

f_y = yield strength of reinforcement

f_{yh} = yield strength of horizontal joint reinforcement

f_{yt} = yield strength of transverse reinforcement

g = distance between outer layers of column reinforcement as a proportion of the overall column depth

h_b = overall beam depth

h_c = overall column depth in the direction of loading being considered

j = internal beam lever arm in proportion of its effective depth, d

k = column neutral axis depth as a proportion of the overall column depth
k_3 = bond strength factor required by Xin's bar anchorage equation
l_b = distance between column centrelines
l_b' = beam clear span
l_c = distance between the point of contraflexure and the critical region
l_d = code required development length
l_e = beam clear span
l_{pf} = length of the beam where the shear is transferred through the stirrups
l_{ph} = distance between positive and negative beam plastic hinges
l_s = splice length
$m_1 \ldots m_4$ = modification factors to evaluate the code required development length
n = factor to relate the maximum force being transferred by lapping action
n_s = number of transverse ties around a straight lap
P_u = minimum design axial load in the column
T, T', T'' = tension force in a the beam reinforcement
T° = tension force of the reinforcement at overstrength
T_B = tension force in the beam bottom reinforcement
T_{c2} = vertical force in the column intermediate bars caused by column flexure only
T_S = tension force due to slab effective reinforcement
T_T = tension force in the beam top reinforcement
U_a = average bond stress
V_{ch} = horizontal contribution of concrete strut in the traditional joint strut and truss model
V_{col} = column shear force
V_{cv} = vertical contribution of concrete strut in the traditional joint strut and truss model
V_{jx}, V_{jz} = joint shear forces in perpendicular directions
V_{sh} = horizontal contribution of concrete strut in the traditional joint strut and truss model
V_{sv} = vertical contribution of concrete strut in the traditional joint strut and truss model
$V_{tr,v}$ = vertical force caused by the combined column flexural and beam-column joint shear actions
$V_{t,v}'$ = vertical force caused by the joint shear action only
V° = beam shear at the flexural overstrength

α = bond strength factor to account for the frictional mechanism
β = ratio between amounts of beam bottom and top reinforcement
δ_{el} = beam elongation
ΔV° = fraction of the beam shear at the flexural overstrength
ζ = ratio between diameter of bend and bar diameter
η = ratio between the overlapping of hooks and the bar diameter
θ, θ', θ'' = angle of inclination of the compression field in a beam
θ_f = interstorey drift
θ_T = inclination of the resultant diagonal force carrying the beam shear in the plastic hinge region of a beam
κ = ratio between amounts of compression and tension reinforcement

λ_o = reinforcement steel overstrength factor

ρ = area ratio of top beam reinforcement

ρ' = area ratio of bottom beam reinforcement

μ_Δ = displacement ductility factor

μ_a = available displacement ductility factor

μ_f = coefficient of friction in the shear-friction mechanism

ξ_c = factor that recognizes the combined column flexure and joint actions in the vertical directions in proportion of the joint action

ξ_f = bond strength factor allowing for bi-directional effects

ξ_m = bond strength factor allowing for input bar forces into the joint

ξ_p = bond strength factor allowing for column axial load

ξ_t = bond strength factor allowing for "top bar" effect

ξ_u = factor allowing for the effects of ductility on the strength of the joint diagonal compression field

ξ_v = factor that considers the influence of the horizontal joint reinforcement provided on the joint vertical force required

τ_f = average shear stress

v_j = joint shear stress

v_{jcr} = joint shear stress at first cracking

ϕ = strength reduction factor

CHAPTER 1

INTRODUCTION

1.1 BACKGROUND

The construction industry has long recognized the benefits of using precast concrete members in the construction of simple and complex structures. Precast concrete construction can be a very competitive alternative to cast in place construction, especially when speed of construction is a prime concern. Cost-Benefit analyses can demonstrate that not always the cheapest structure but the fastest method of construction is the best choice. This is because the need of early rent-flow is often decisive in selecting the most suitable option.

Besides construction speed, precast concrete construction possesses many other advantages. One of them is the high quality product that can be obtained as prefabrication is done in almost ideal labour conditions. High quality comprises accuracy with tolerances, excellent durability and good aesthetics. Another advantage of precast concrete is the reduction in the use of site formwork.

The use of precast concrete members in the construction of multistorey buildings in New Zealand commenced in 1959-1960 when shell beams were developed for a project [Wood (1988)]. However its use as an earthquake resistant system remained shunned for many years [Park (1990)]. Since the early 1980's moment resisting frames incorporating precast concrete members designed to be ductile and providing the primary earthquake resistance have become widely used in New Zealand, [for example, O'Leary et al (1988), Poole and Clendon (1988), Silvester and Dickson (1988), O'Grady (1988)].

No provisions exist for the design with precast concrete in New Zealand. The two design codes for design of buildings, the Code of Practice for General Structural Design and Design Loadings for Buildings [NZS 4203 (1984)] and the Code of Practice for the Design of Concrete Structures [NZS 3101 (1982)], deal only with the design of monolithic concrete construction.

1.2 CRITICAL ASPECTS IN THE DESIGN OF DUCTILE PRECAST CONCRETE MOMENT RESISTING FRAMES

The main problem in the design and construction of ductile moment resisting frames incorporating precast concrete elements to provide seismic resistance is in finding economical and practical methods of connecting the elements together. Perhaps because of numerous connection failures and general poor performance during the Alaska earthquake of 1964 [Berg and Stratta (1964), Steinbrugge (1965)] the use of precast concrete as an alternative for seismic resistance remained shunned

in New Zealand for many years. However, in recent years many innovative ideas involving construction using precast concrete have been developed and successfully used in practice based on the thorough understanding of the capacity design philosophy. In general the New Zealand practice has favoured the use of precast concrete systems with cast in place joints which can be designed as if monolithic structures.

1.3 SEISMIC DESIGN PHILOSOPHY

1.3.1 The Basic Assumption in the Design of Precast Concrete Frames for Earthquake Resistance in New Zealand

Experience in recent earthquakes and extensive development based on experimental research work have shown that well designed cast in place structures perform very satisfactorily in major earthquakes [Park (1990)].

The basic assumption in the design of moment resisting frames incorporating precast concrete members for earthquake resistance in New Zealand is that they can be designed to be equivalent to a cast in place concrete system. This requires demonstration that the precast concrete system shows at least equal levels of strength, stiffness, ductility and energy dissipation characteristics as those expected from the equivalent cast in place concrete system.

1.3.2 Basic Design Principles

When some members of a reinforced concrete structure respond plastically during a seismic event the lateral inertial forces induced in the structure are significantly smaller than those if it was to respond elastically to the same input motion [Housner (1956, 1959)]. Period shift, increased damping, mechanism capacity and plastic energy absorption, among several factors, are used to explain the above phenomena. The design adopting smaller inertial forces than those required by the structure responding elastically results in smaller member sizes and overall economy.

Based on accepting some degree of damage and aiming to protect, as far as possible, loss of life during the largest earthquake that can be expected to occur during the useful life of the building, many seismic codes have explicitly or implicitly adopted the following performance criteria on its design recommendations:

a) ***Resist minor earthquakes with no damage.***

b) ***Resist moderate earthquakes without structural damage, but with some non-structural damage.***

c) ***Resist major earthquakes with structural and non-structural damage, even beyond repair, but without collapse.***

The New Zealand Loadings Code [NZS 4203 (1984)] bases its provisions on the assumption that a building located in a high seismic risk region is susceptible to experience one or more earthquakes of high intensity and duration and several earthquakes of low intensity and duration during its useful life. The probabilities of these events to occur in lower seismic risk regions are smaller.

To satisfy the above performance criteria any structure will have to possess sufficient strength, stiffness, ductility and energy dissipation characteristics.

A minimum level of strength is required to reduce structural damage during minor events and to restrict excessive member ductility demands to those readily available in a major earthquake. Codes recommend to distribute the strength in the members of the structure following the results of an equivalent elastic or a elastic dynamic analysis. In New Zealand it is always encouraged to exploit the benefits of moment redistribution where the negative moments in the beams are allowed to deviate up to 30% of the maximum value obtained from any combination of loads [Paulay (1976)]. The aims of moment redistribution are to reduce the absolute negative design moment, to equalize the critical moment demands in the beams at each side of the columns and to use the potential flexural strength of the beams due to at least the minimum reinforcing steel provided in the bottom at the faces of the columns. According to the Draft Revision of the Loadings Code [Hutchison et al (1986)] the minimum strength required of a structure should be determined from a 1/150 annum risk spectrum.

Any structure requires a minimum level of protection against premature non-structural damage. Thus a minimum level of stiffness needs to be provided throughout the height of the building. In the past few years there has been an increasing awareness of the importance of direct and indirect costs resulting from the halt caused by disruption of operations because of non-structural damage occurring in minor events [Arnold (1991)]. Codes contain provisions to limit the maximum inter storey drift of the structure based on the horizontal displacements obtained from an elastic analysis using a set of equivalent lateral forces.

The survival of a structure against collapse during a major earthquake relies on its ability to respond in a ductile manner [Park and Paulay (1975)]. The member ductility demand in multistorey buildings is largely controlled by the characteristics of the ground motion, the distribution of strengths in the structure, the magnitude of these strengths, the damping and to some extent to the plastic energy dissipation characteristics. Instability of the structure, which is also linked to lack of strength, will also increase the ductility demand in certain members [Paulay et al (1978), Thomson et al (1991)]. The envelope of several inelastic time history analyses using records to represent the site conditions may gave an estimate of these demands. An approximate elasto-plastic collapse mechanism analysis assuming that a reference displacement ductility factor is known can also give an indication of the ductility demands in the members. Ductility demands are often expressed in terms of system ductility or member ductility factors which need to be compared with the available ductilities. However, as Mahin and Bertero (1976) and Bertero (1988) point out there are difficulties in matching these demands.

The available ductilities are obtained from laboratory tests and theoretical analyses on members similar to those used in the design. However, there is lack of agreement in the definitions of

"ductility" among several research institutions, which in some cases lead to the misuse of the term [Park (1988)].

The Schools of Engineering at the Universities of Canterbury and Auckland have carried out much research in the past twenty years to find methods for detailing reinforced concrete members so as to achieve reliable ductile response and to select modes of plastic deformation which minimize concentrations of ductility demand in a few members. These recommendations have been compiled and presented in the Loadings and the Concrete Design Codes.

A design strategy termed "Capacity Design" is the basis of the seismic design of ductile multistorey reinforced concrete buildings in New Zealand. This design procedure was initially proposed by Hollings (1969, 1969a) and subsequently furthered by the engineering community and the University of Canterbury.

Capacity Design is a deterministic approach in which the most suitable mode of plastic deformation is chosen and the regions where inelastic deformation takes place are designed for ductility. Other regions of the structure which are to remain elastic are deliberately made overstrong to ensure that the chosen mode of plastic deformation can be maintained.

Fig. 1.1 shows three possible mode of plastic deformation. The column sidesway mechanism of Fig. 1.1 (a), with plastic hinges only in the columns of one storey, requires large curvature ductility demands in the plastic hinges in the case of multistorey frames which can not be readily supplied, especially in tall multistorey buildings [Park and Paulay (1975)]. The combined mechanism of Fig. 1.1 (b) appears to be more suitable than the column sidesway mechanism. However, it requires careful design considerations to preclude plastic hinges forming in the corner columns to avoid a "soft storey". Two additional considerations need to be counted as plastic hinges form in the interior columns: (a) the spliced region in the column needs to be displaced away from the beam face at the beginning of each storey to avoid a large curvature ductility demand in that region, and (b) full column confinement is required at each end of the columns to ensure that the available curvature ductilities are satisfactory. The most desirable mechanism for tall multistorey buildings is the beam sidesway mechanism is illustrated in Fig. 1.1 (c). Design achieving a beam sidesway mechanism is known as "strong column-weak beam" design. For the same displacement, the curvature demands in beams and columns are more moderate for beam sidesway mechanisms than for the column sidesway mechanism [Park and Paulay (1975)]. To ensure that this mechanism can form, plastic hinges in the columns need to be avoided, except at the column bases where special detailing is required and at the top floor where it is allowed and even recommended because of the poor anchorage conditions of the beam bars in the interior joint regions [Paulay and Priestley (1992)]. The protection of the columns against the formation of plastic hinges requires consideration of the probable flexural capacity of the beam, including contribution from the slab as designed plus overstrength factors in the reinforcing steel, considerations of concurrent earthquake loading and variations in the bending moment diagram of the columns owing to dynamic effects.

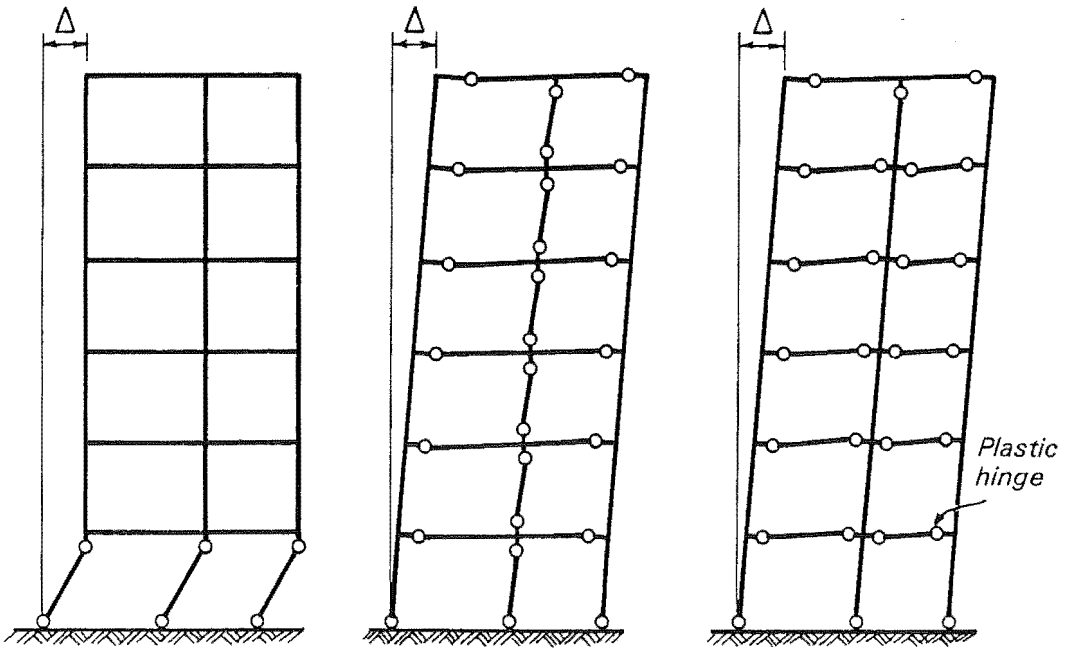

(a) Column Sideway Mechanism (b) Combined Mechanism (c) Beam Sideway Mechanism

Fig. 1.1 - Sway Mechanisms in Multistorey Frame Buildings.

1.4 LITERATURE REVIEW

The literature review in this section is intended to cover the state of the practice of different systems incorporating precast concrete elements in moment resisting frames designed for earthquake resistance. When applicable, test results of research projects on the topic will also be presented.

1.4.1 New Zealand

The main design trend for buildings between 9 and 25 storeys high, when using precast concrete frames is to allocate the whole of the earthquake resistance to stiff and strong ductile moment resisting perimeter frames, because the depth of the beams, being outside the services and ceiling areas, may be large without compromising the storey height. The interior frames are less stiff and carry mainly gravity loading. Another alternative is to combine structural walls in the core of the building with precast concrete perimeter frames to provide the necessary torsional strength and stiffness.

New Zealand favours the use of concrete systems which are connected in a cast in place joint and are designed to behave as monolithic concrete structures.

A number of possible arrangements of precast concrete members for ductile moment resisting frames have been used in New Zealand. Park (1990) has identified three main systems of wide use which are outlined below.

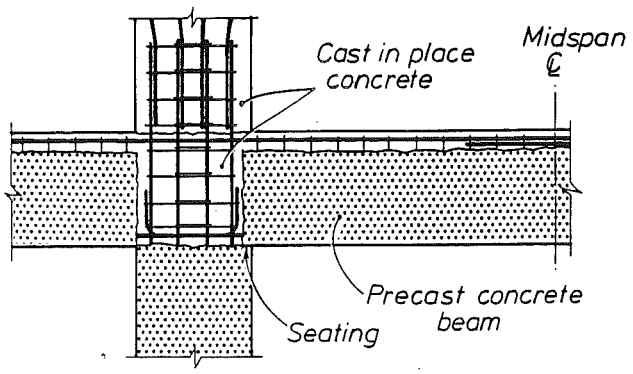

(a) System 1 - Precast Beam Units between Columns

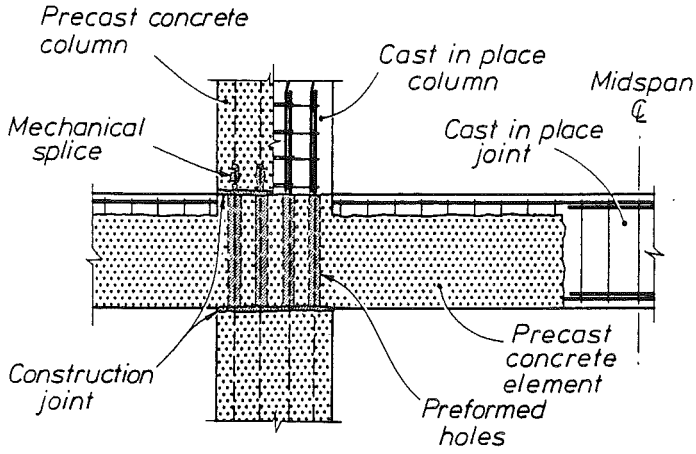

(b) System 2 - Precast Beam Units through Columns

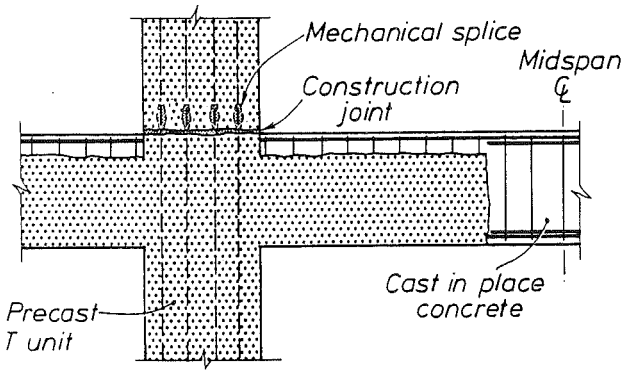

(c) System 3 - Precast T or Cruciform Units

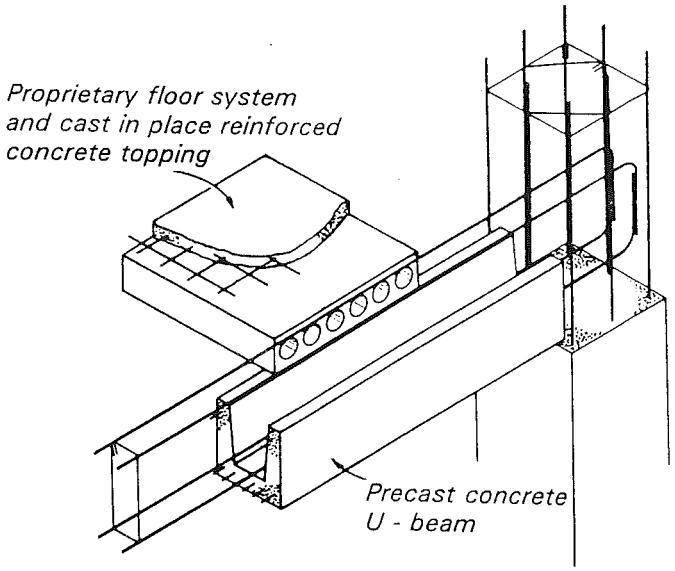

(d) Precast Concrete System Involving Shell Beams

Fig. 1.2 - Commonly Used Arrangements of Precast Members and Cast in Place Concrete for Constructing Moment Resisting Reinforced Concrete Frames in New Zealand.

System 1

In the first arrangement, illustrated in Fig. 1.2 (a) the lower portion of the beams is precast. The beams span from column to column and can be either seated on the concrete cover of the column below or be temporarily propped at the ends. The reinforcing steel in the beam-column joint region is then placed, then top beam longitudinal steel and the proprietary precast concrete floor system. Cast in place concrete is used in the columns, in the beam-column region, and in the top part of the beam and the topping of the proprietary slab. According to the current Code of Practice for the Design of Concrete Structures [NZS 3101 (1982)] the hooked ends of the bars shall be outside the beam-column region. Fig. 1.3 shows a construction detail using precast concrete beams typical of System 1.

Stevenson and Beattie (1988) (see also Beattie (1989)) reported a full scale test on a cruciform sub-assemblage incorporating relatively short precast concrete beams typical of this system. The vertical end face of the beams at the joint region was scrubbed. The top surface of one precast beam was scrubbed while the other beam had a smooth surface. The beams were seated on 10mm of cover concrete of the bottom column. The bent up bottom bars protruding from the precast beams overlapped inside the joint core. The remainder of the sub-assemblage complied with the specifications of the Concrete Design Code. Test results indicated a good cyclic lateral load versus lateral deflection hysteretic performance with little strength degradation up to interstorey drifts of 2.3%, equivalent to a displacement ductility factor of 10. Pinching of the loops occurred at the end of the test as a result of some sliding shear across the cold joint between the precast beams and the cast in place beam-column joint. It was concluded that anchoring the hooked beam bottom bars inside the beam-column joint region did not affect the seismic performance of the test unit. The condition of the horizontal joint between the precast beam and the top cast in place concrete did not influence the test results. It was recommended that shear keys or castellations be introduced in the vertical joint of the beams at the column face to reduce the effects of sliding shear.

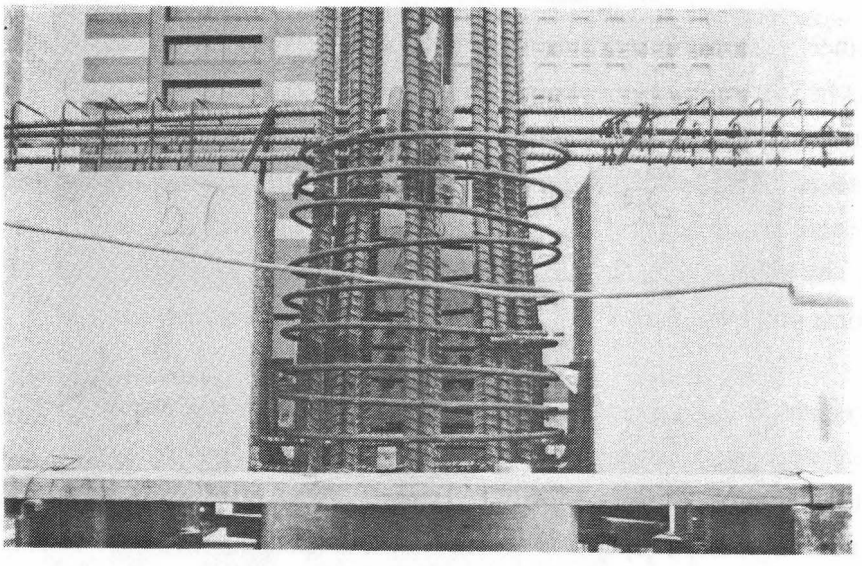

Fig. 1.3 - Typical Construction Example Using System 1.

System 2

Another arrangement making extensive use of precast concrete is shown in Fig. 1.2 (b). This system incorporates the congested beam-column joint region in the precast member. Plastic hinges can be detailed to occur in the beams at or away from the column faces. The precast beams are seated on steel shims creating a construction joint 10 to 25mm thick. Protruding column longitudinal bars pass through precast preformed vertical holes in the member and protrude above the top surface. The holes in the precast element are formed by corrugated steel ducting, similar to that used for post-tensioned tendons of concrete structures. The vertical ducts and the horizontal construction joint at the bottom of the precast member are grouted in one operation. A precast concrete column is then positioned above the precast element using grouted vertical laps or grouted steel sleeves to connect the vertical column bars. Alternatively, vertical laps or mechanical connectors are used to splice the longitudinal bars if the columns are cast in place. Fig. 1.4 shows several aspects of the construction of a building making use of this system.

Stevenson and Beattie (1989) (see also Beattie (1989)) tested a full scale specimen using System 2. The reinforcing details were based on construction details of a real structure built in Wellington. The horizontal construction joint between the precast member and the lower column was sealed around the periphery and then all empty spaces were grouted from a corner duct using a commercially available grout, Embecon LL897. The compressive strength of the grout of 49.7MPa was comparatively similar to the compressive strength of the concrete in the precast member of 47.5MPa. The cyclic lateral load versus lateral deflection behaviour of the sub-assemblage was very satisfactory up to interstorey drifts of 3.2%, equivalent to a displacement ductility factor of 10. The corrugated ducting, the grout and the construction joint between the bottom column and the precast beam performed very well.

System 3

Another possible arrangement incorporating precast T-shaped elements is shown in Fig. 1.2 (c). As in System 2, potential plastic hinge regions can be detailed to form in the beams away from the column faces if necessary. The vertical column bars in the precast T-units are connected using grouted steel sleeves. An alternative to the T-shaped units is to use cruciform-shaped precast concrete units or even double cruciform precast concrete elements if the crane capacity does not limit the size of the elements. An advantage of System 3 is the extensive use of precast concrete. Fig. 1.5 illustrates a double cruciform precast concrete unit being position in a construction site.

In systems 2 and 3 the protruding beam bars of the precast element are lapped in a joint to be cast at or near midspan. The lap region needs to be located away from the critical regions of the beams to comply with the requirements of the concrete code. Thus conventional straight laps are used when there are not limitations of space. Fig. 1.6 illustrates the construction of a straight lap connection detail at midspan. Short and non-conventional connection details are used when there are restrictions of space. One short connecting detail consists in overlapping the 90°or 180° hooked bars protruding from the precast beams, as shown in Fig. 1.5. One disadvantage of this system is the difficulty

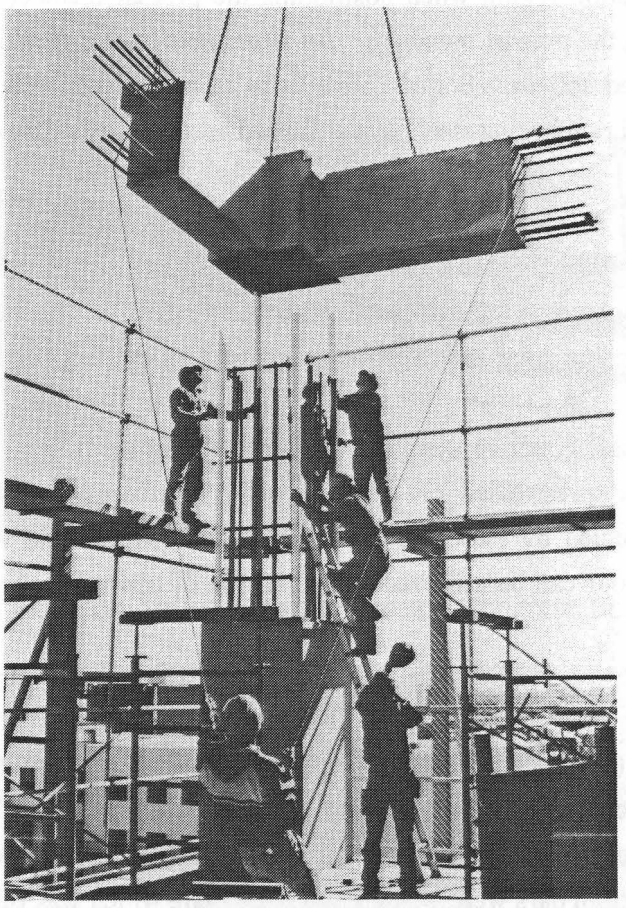

Fig. 1.4 - Construction Details Using System 2.

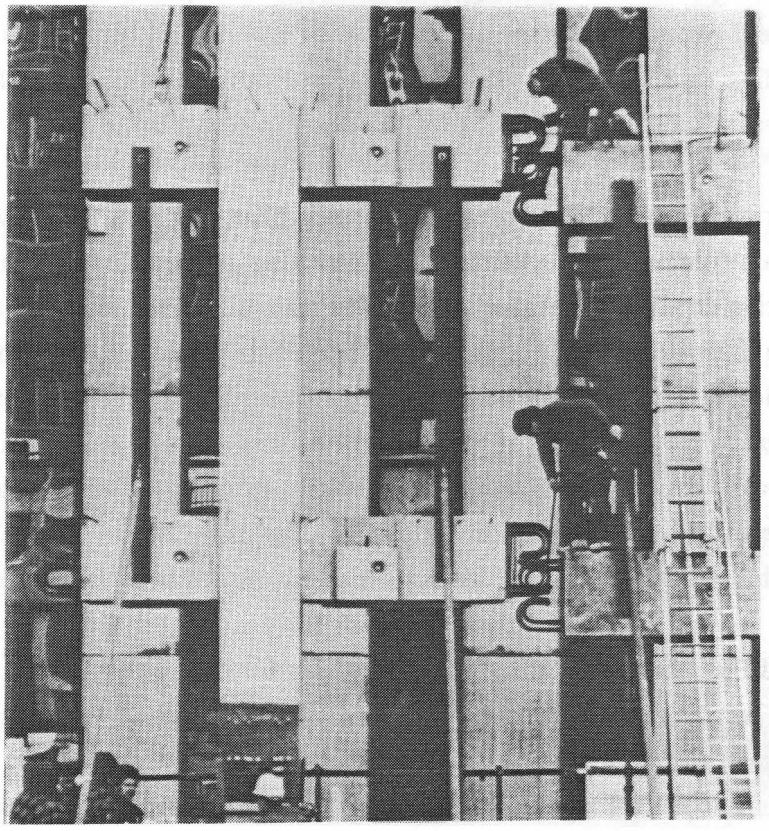

Fig. 1.5 - Double Cruciform Precast Unit Typical of System 3.

encountered in the connection region when positioning the precast member because of the precision required when positioning the precast members. An alternative to this method, illustrated in Fig. 1.7, is to use "drop in" hooked splices. Bolted connections in precast concrete members with relocated plastic hinges and diagonal reinforcing steel have also been used. An example of this connecting method is shown in Fig. 1.8.

Beattie (1989) has conducted four cyclic load tests on several midspan connection details. Satisfactory results were obtained but test results cannot be relied on since the beams were subjected to significant axial load arising from the constraints imposed by the test set-up.

A further precast concrete system for moment resisting frames involves the use of shell beams that can be either prestressed or conventionally reinforced such as the one depicted in Fig. 1.2 (d). Tests conducted by Park and Bull (1986) have shown that with appropriate detailing satisfactory ductile behaviour can be achieved with this type of construction.

1.4.2 Canada

Pilai and Kirk (1981) conducted nine exterior beam-column joint tests under reversed cyclic loading. The precast concrete beams had a rebate to expose the top bar at the column face as shown in Fig. 1.9. These bars were welded to a steel plate and butt welded to reinforcing bars protruding from the column. The beam bottom bars were welded to a steel angle which was fillet welded to an anchored plate in the columns. The main variable in this programme was the aspect ratio of the beams, which varied from 4 to 8. All specimens were designed to form plastic hinges in the beams. Fracture of the bottom bars in the weld region was the cause of failure of all units except one. This system makes extensive use of welding that demands a very high quality control. Also, this method requires strict tolerances when the precast members are designed to span between columns.

In an improved version of the previous research Bhatt and Kirk (1985) tested two exterior and two interior beam-column joint specimens incorporating precast concrete beams. Fig. 1.10 illustrates the connection detail used in these series. The main difference from the tests conducted by Pillai and Kirk was in the welding detail of the bottom beam bars where fillet welding was used. Also it was intended to relocate the beam plastic hinges away from the column faces by welding two U-shaped reinforcing bars at the mid-depth of the beam to the steel plate at the column face. The main variables in the tests were the performance of the connection detail in the exterior and interior beam-column joints and the influence of the aspect ratio of the beams. The test results presented appear inconclusive despite the authors' claim that this system can withstand high ductility demands.

Seckin and Fu (1990) tested three interior beam-column units with precast beams welded to the precast column. Top and bottom beam longitudinal bars were welded to steel plates at the beam ends. These plates were also welded to plates protruding from the precast column. A shear transfer mechanism detailed in the precast units consisted in web plates welded to horizontal bars extending through the plastic hinge region. These plates were also welded to plates protruding from the column. Fig. 1.11 shows the connection detail. The main variable in the tests was the aspect ratio of the beams.

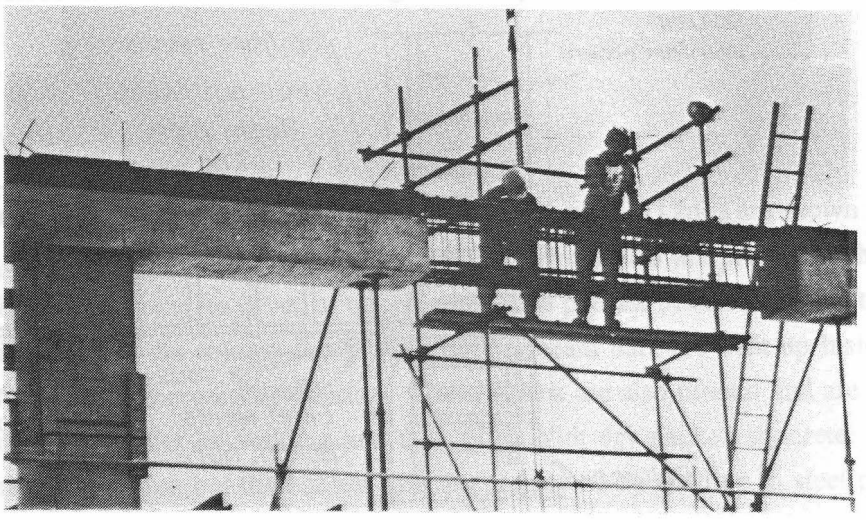

Fig. 1.6 - Straight Midspan Splice Between Precast Concrete Beams of System 3.

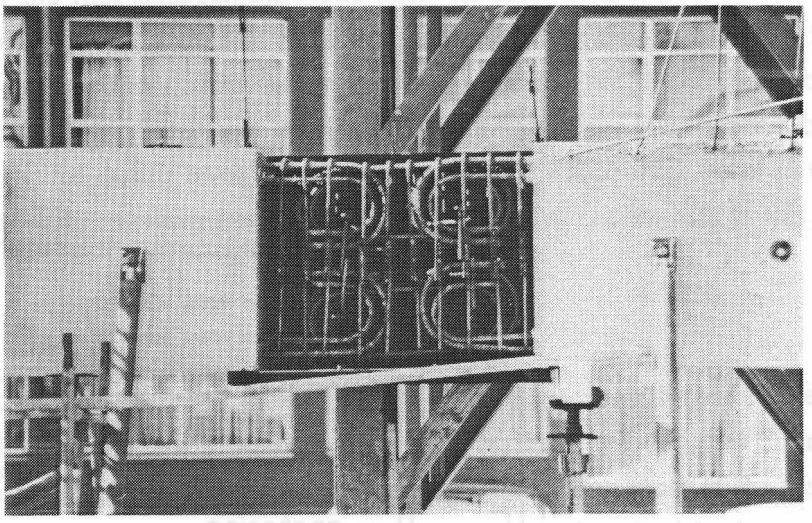

Fig. 1.7 - "Drop in" Midspan Splice in Use Between Precast Concrete Double Cruciform Members of System 3.

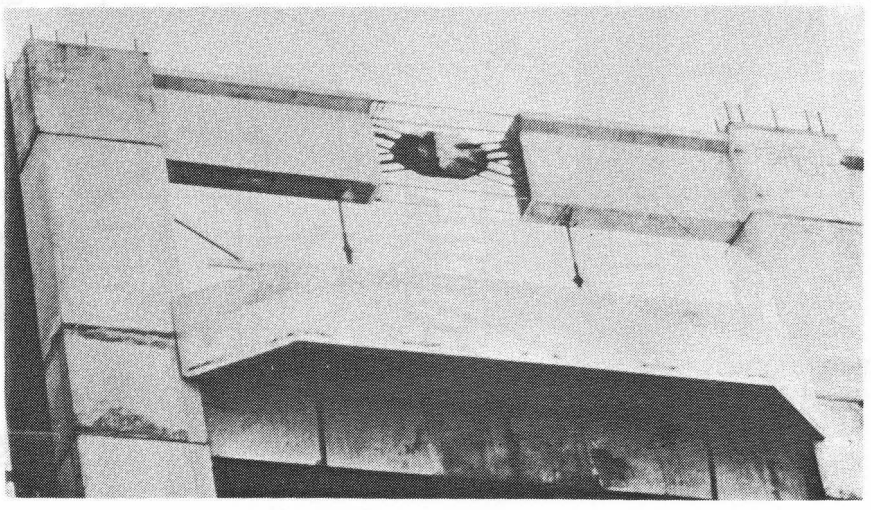

Fig. 1.8 - Bolted Midspan Connections Between Precast Concrete Diagonally Reinforced Beams with Relocated Plastic Hinges.

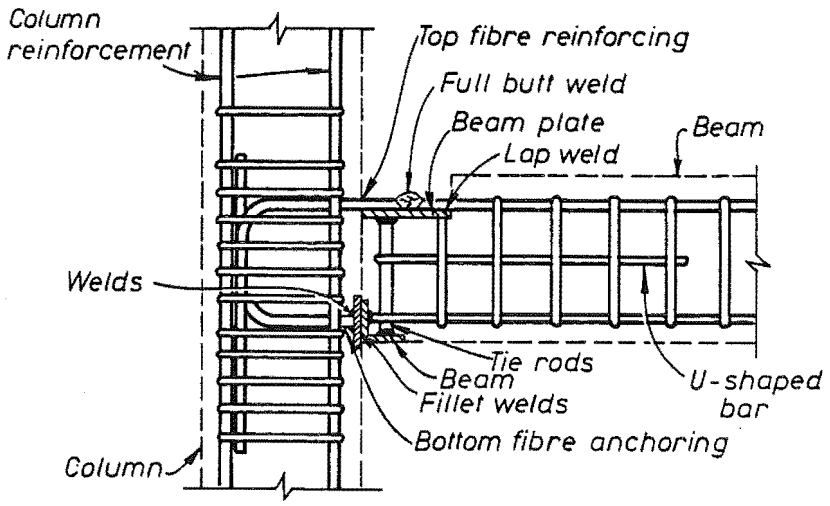

Fig. 1.9 - Connection Detail Tested by Pillai and Kirk (1981).

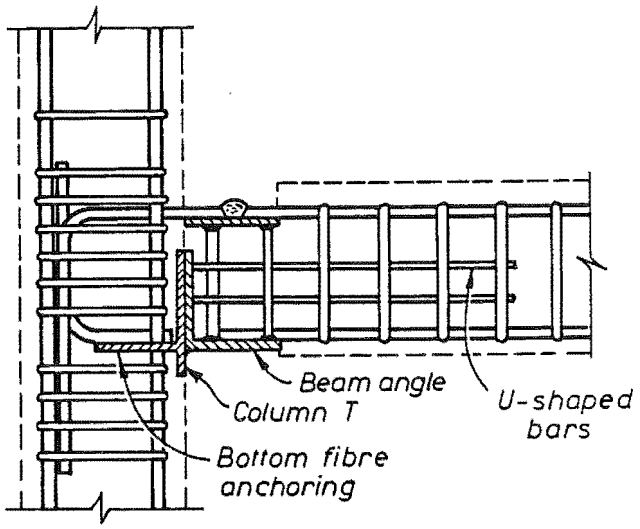

Fig. 1.10 - Connection Detail Tested by Bhatt and Kirk (1985).

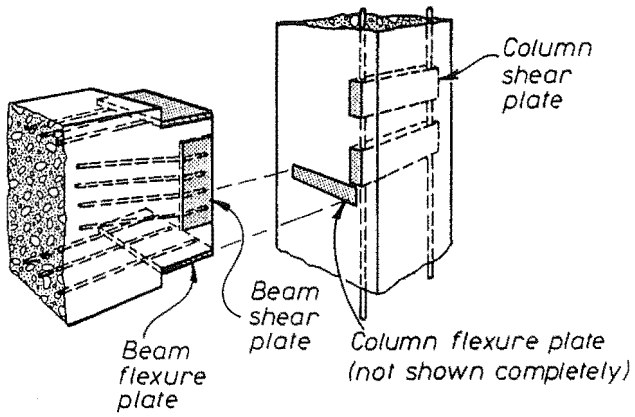

Fig. 1.11 - Connection Detail Tested by Seckin and Fu (1990).

Brittle failures occurred in all tests in the weld region. Only a limited ductile response was attained before failure.

1.4.3 China

Two arrangements of precast moment resisting frames used in China are shown in Fig. 1.12. The first arrangement is similar to System 1 of Fig. 1.2 (a). The beams are precast in the lower part and are seated resting on the concrete cover of the column. The precast beams incorporate large shear keys at in the vertical joint at the column faces. The bottom beam bars are bent up inside the beam-column joint region but do not necessarily overlap. The columns are also precast and are connected to the top of the beam-column joint by welding and then filled with dry packed concrete. The second arrangement is similar to the first but the bottom bars are connected by welding to steel plates.

The Beijing Institute of Architectural Design (undated) has conducted two tests into the seismic behaviour of the first arrangement. The main variables of the experimental work were the anchorage of the hooked bottom beam bars and the shear resistance of the joint. Fig. 1.13 (a) illustrates the anchorage detail of the bottom beam bars in the first test unit. The bottom beam bars are bent up inside the beam-column region but do not overlap. Bond failure of the bottom beam bars occurred in the joint region at a limited ductile level. Fig. 1.13 (b) shows the anchorage detail in the second unit. A better response was obtained from the overlapping anchorage of bottom bars in this test.

1.4.4 Japan

Kanoh (1986) has presented the state of the practice report on the use of precast concrete in Japan. Generally precast concrete structures constructed in Japan are designed as monolithic ones. Limited information regarding test results is available largely because most of the research has been conducted by private corporations. The four main arrangements described in the report are outlined below.

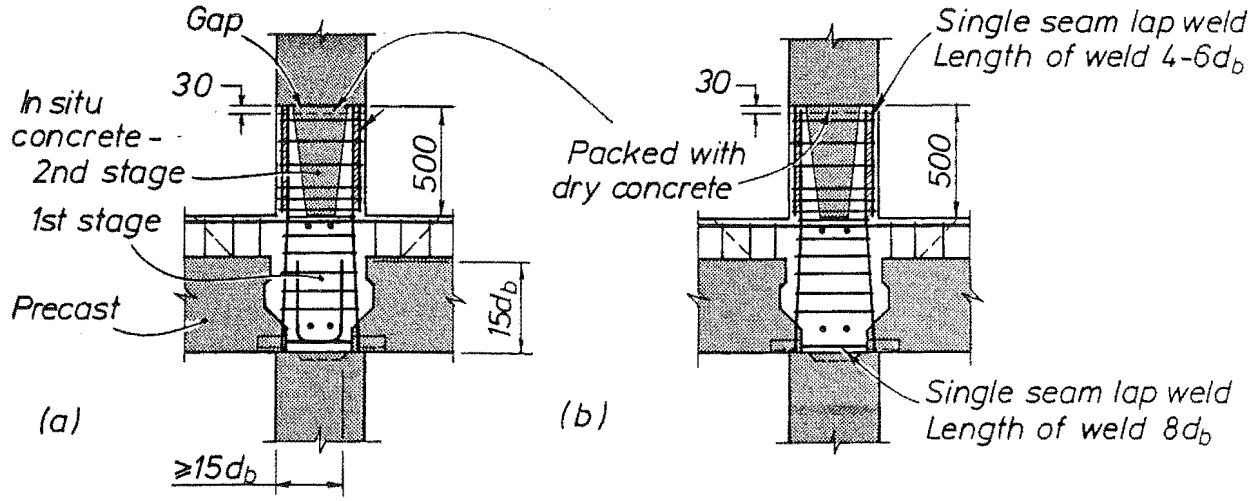

Fig. 1.12 - Typical Arrangements of Precast Concrete Frame Systems Used in China.

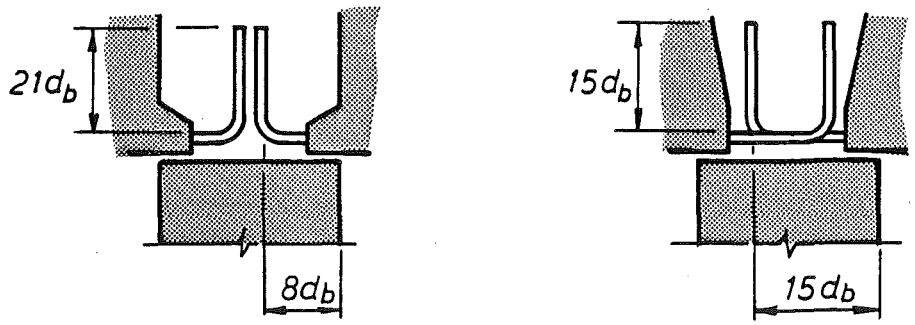

Fig. 1.13 - Anchorage Details Tested at the Beijing Institute for Architectural Design.

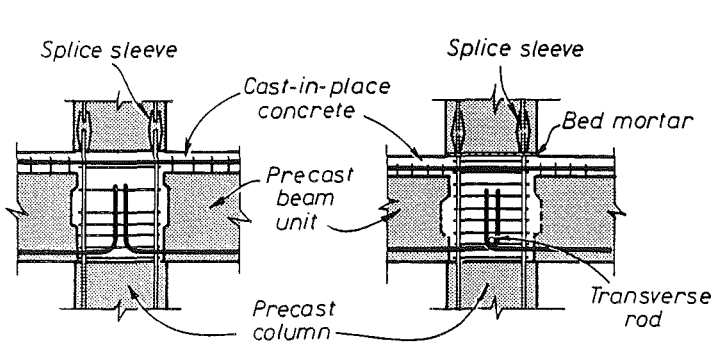

(a) and (b) FRPC System

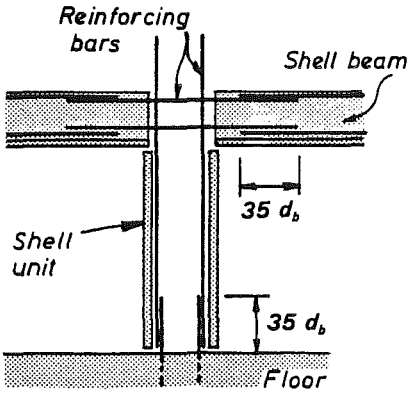

(c) TO-RPC System

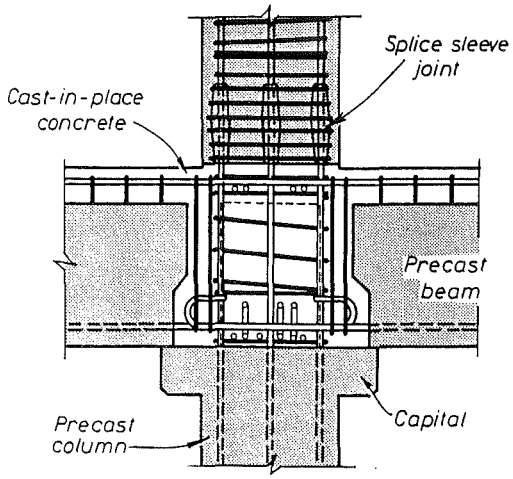

(d) PREBIC Method

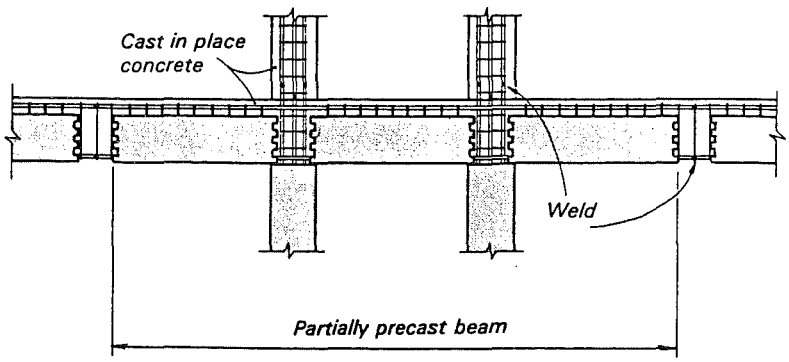

(e) R.C. Layered Construction System

Fig. 1.14 - Commonly Used Arrangements of Moment Resisting Frames Incorporating Precast Concrete Members in Japan [Kanoh (1986)].

FRPC System

This system, shown in Figs. 1.14 (a) and (b), has been used in buildings up to 25m high. Structural concrete walls, cast in place or precast, share the seismic resistance with the precast concrete frames. As in System 1 of Fig. 1.2 (a) the lower part of the beams is precast and the bottom bars are bent up inside the joint region. The hooked bars do not necessarily overlap in the construction of buildings up to four storeys high.

TO-RPC System

As in previous system, the precast concrete beams are connected at the beam-column joint. A detail of the connection is shown in Fig. 1.14 (c). The beams rest seated on the columns with the bottom bars anchored in the joint using 180 degree hooks. This system has often been used in the construction of space frames.

PREBIC Method

The method, shown in Fig. 1.14 (d), uses precast concrete shells for beams and columns and is used for construction of low rise buildings up to 3 storeys high. Hoops and stirrups are included in the precast elements and the longitudinal reinforcement is placed in site.

R.C. Layered Construction System

This system has been utilized for medium and high-rise buildings. It uses concrete beams, precast in their lower part, that rest seated on top of the cast in place column concrete. The precast beams do not include the beam-column joint region and are connected at every other span by butt welding the longitudinal bars as indicated in Fig. 1.14 (e).

Japan has commenced a large cooperative research project with United States on the use of precast concrete as a primary earthquake resisting system. A brief review of this project is given in Section 1.4.7.

1.4.5 Portugal

Santos (1987) has outlined a method of construction used in Portugal and has carried out an experimental programme on three series of four specimens each to assess their seismic resistance. The system is illustrated in Fig. 1.15. Concrete shells are combined with cast in place concrete to form the columns. The main longitudinal column reinforcing steel is placed at the corners of the precast shells. Extra bars are added in the column core to provide continuity in the beam-column joint region. The lower part of the beams are precast and are connected similarly to System 1 of Fig. 1.2 (a). The top column shell is lowered and seated on mortar after concreting the beam-column joint and the top of the beam with the slab.

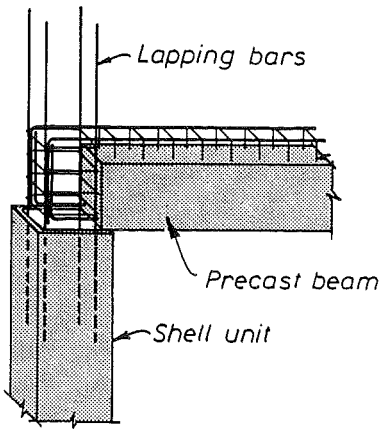

Fig. 1.15 - Typical Precast Concrete System Used in Portugal and Tested by Santos (1987).

The experimental work was designed to investigate the monotonic and cyclic load behaviour of the shelled columns and precast beams tested individually, and the behaviour of exterior beam-column joint specimens.

Santos concluded that columns possess only limited ductility capacity because of concentration of rotation at the beginning of the lap between the bars required for continuity and those in the shell. The beam components behaved like monolithic ones providing that sliding shear is prevented. Full ductile behaviour of the structural system can be anticipated if a joint failure is restricted.

1.4.6 Romania

The current Romanian practice of precast concrete frames designed for earthquake resistance has been reviewed by Constantinescu (1985). Fig. 1.16 shows that this method is rather similar to System 1 of Fig. 1.2 (a). However horizontal and vertical castellations are provided at the construction joints.

No structural damage in multistorey building using this system was reported after the Bucharest earthquake of 1977 [Fattal (1977)].

1.4.7 United States

The construction of ductile moment resisting frames in seismic areas of United States to provide the lateral load resistance to earthquakes is uncommon. Lum (1981) developed grouted steel sleeves to connect precast concrete H-shaped components in a 38 storey building although the primary earthquake resistance was provided by structural walls. The beams were connected at midspan using

straight laps surrounded by coil spirals. Sorensen (1981) used beam shells and precast concrete columns spliced with grouted steel sleeves in the construction of a 14 storey building.

Englekirk (1979, 1989) has discussed the need to establish general criteria for the seismic design of ductile moment resisting frames incorporating precast concrete members.

Martin and Korkosz (1982) and Stanton et al (1986) have published two reports for the Prestressed/Precast Concrete Institute on connections between precast concrete members including some for earthquake resistance.

French et al (1989, 1990) conducted experimental work on different connecting systems between precast partially prestressed beams and precast columns including three specimens similar to those sketched in the PCI reports. Six exterior beam-column joints and one interior beam-column joint units were tested under reversed cyclic load conditions. The main variable was the connection detail between the precast members. Post-tensioning, composite construction, welded bolted and mechanically spliced connection details were studied.

They concluded that all tests displayed good energy dissipation characteristics and performed in a ductile manner. After comparing the energy dissipation characteristics, available ductility and easy fabrication, they favoured the systems using mechanically spliced tapered-threaded reinforcing bars, one of which is depicted in Fig. 1.17.

Priestley (1989, 1991) has outlined the objectives of a coordinated research programme, Precast Seismic Structural Systems (PRESSS), between United States and Japan. The ultimate goal of this research programme is to provide recommendations for the design of precast concrete construction for earthquake resistance. Analytical and experimental work is envisaged including the construction and testing of a least one full scale five storey super-assemblage representing the lower part of a ten storey building. It is of note that Japan, like New Zealand, favours the use of systems incorporating precast members designed to behave as if of monolithic construction. This has been referred to as an equivalent monolithic system. The United States will be investigating mainly systems where yielding may occur in the joints between precast members, and the precast members are designed to remain elastic.

1.4.8 U.S.S.R

Bychencov (1978) has discussed several systems in standard use in the Soviet Union. Moment resisting frames alone are used to provide the lateral load resistance in industrial installations and buildings up to 16 storeys high. Taller buildings combine precast concrete walls and precast concrete frames.

One system used for the construction of buildings is illustrated in Fig. 1.18. Precast concrete columns are connected at mid-height by welding the longitudinal bars. Precast concrete inverted T-beams rest seated on steel angles. Beam top and bottom longitudinal bars are welded to steel angles

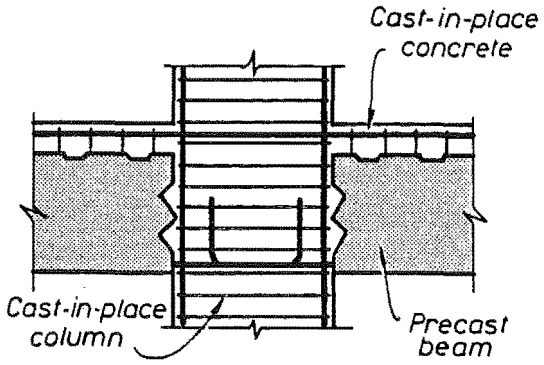

Fig. 1.16 - Common Arrangement for the Construction of Framed Multistorey Buildings in Romania [Constantinescu (1985)].

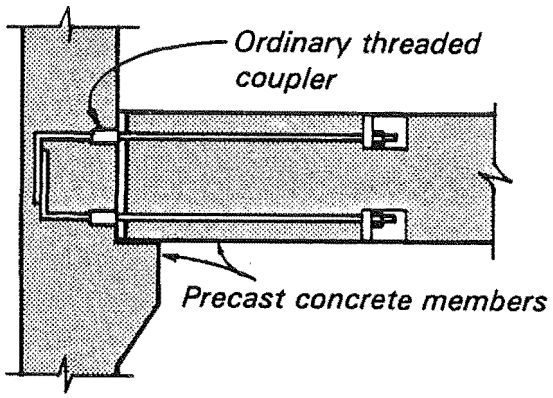

Fig. 1.17 - Connection Using Threaded-Tapered Bars and Steel Couplers Tested by French et al (1990).

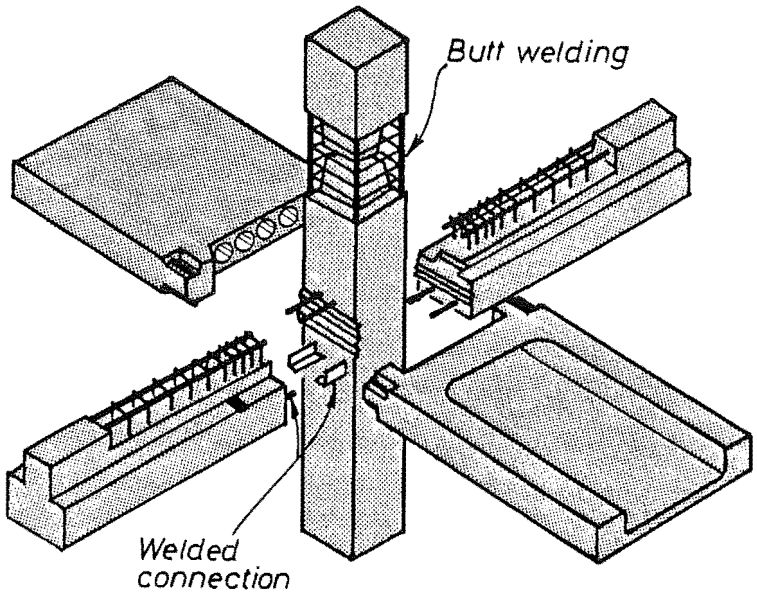

Fig. 1.18 - Typical Arrangement of Precast Concrete Framed Construction Used in the U.S.S.R. [Bychenkov (1978)].

protruding from the precast column. A proprietary precast concrete floor system is placed seated on top of the beam flanges.

The survey presented in the Armenia Earthquake Reconnaissance Report (1989) indicates that the performance of precast concrete buildings during the earthquake of 1988 was extremely poor. 54% of all buildings collapsed and 41% were heavily damaged and were demolished .

1.5 AIMS OF THE RESEARCH WORK

The objectives of this research work are based on the outcome of a workshop held a the University of Canterbury in early 1988. In the Seminar Report (1988) several problem areas were identified, among them:

a) Connections between precast concrete elements in frames designed for earthquake resistance.
b) Grouting of bars and joints.
c) Floor unit support.
d) Floor unit continuity.
e) Tolerances.
f) General bibliography.

This research was also supported in this seminar with the basic aim to provide knowledge on the seismic behaviour of moment resisting frames incorporating precast concrete components designed to perform as if of monolithic construction when acting as the primary earthquake resistant system. It is also intended to give guidelines for the design of different connection details. In addition, a Joint Study Group was jointly funded by the New Zealand Concrete Society and the New Zealand National Society for Earthquake Engineering to present a report on guidelines for the use of structural precast concrete in buildings. This report has been recently published [Guidelines for the Use of Structural Precast Concrete in Buildings (1991)].

1.6 SCOPE

This study is basically divided in three independent parts:

The first part of the study, presented in Chapter 2, investigates the cyclic stress-strain behaviour of the two grades of reinforcing steel currently manufactured in New Zealand. Based on test results an analytical model for the stress-strain behaviour is obtained. This section also includes a literature review of previous research work and a brief discussion on the effects of strain rate and strain ageing.

The second part of the study comprises experimental work on full scale precast concrete frame sub-components typical of perimeter frames. Experimental work was conducted for connection

details at the midspan and the beam-column joint regions. All units were quasi-statically tested and subjected to reversed cyclic loading. Recommendations for the design of different connection details are also given in this part. It comprises five chapters.

Chapter 3 describes details of the test programme on the connections between precast concrete elements including the test history, reaction frames, and data acquisition system. The method used to determine the various sources of displacement is also discussed.

Chapter 4 reports test results obtained from three different connection details at the midspan of the beam when plastic hinges form at column faces.

Chapter 5 presents test results of one unit with relocated plastic hinges and connected at midspan using bolted plates welded to diagonal reinforcing steel bars. This unit was tested, repaired and strengthened and re-tested. Results of both the original and repaired unit are also discussed.

Chapter 6 presents test results obtained from of two interior beam-column joint units representing systems 1 and 2.

Chapter 7 contains theoretical work on the design of connections between precast members in moment resisting frames. A summary of design recommendations, that can be used as a basis for a code of practice on connections between precast concrete elements, is also included in this chapter. Also, the effects of cumulative beam elongation during lateral reverse loading on the normal design procedures are briefly discussed.

Chapter 8 compiles a summary of the research project and presents the main conclusions and the recommendations for future research work.

CHAPTER 2

CYCLIC BEHAVIOUR OF REINFORCING STEEL

2.1 INTRODUCTION

For more than 100 years, researchers have been observing the uniaxial stress-strain behaviour of steel. Much of this behaviour is still not understood even at the microscopic level and so analytical stress-strain models must be based on observations of the macroscopic behaviour. The behaviour of steel is greatly affected by its chemical composition and the method of its manufacture.

The most common type of steel test is the monotonic tensile test. Some researchers have investigated the monotonic compression behaviour but such tests are often hampered by post-elastic buckling. Some research has been conducted on the cyclic stress-strain behaviour of steel but much of the experimental data has been taken within a limited strain range. Analytical models have been proposed based on the observed behaviour. Very limited research has been carried out on the effects of strain rate and strain ageing on reinforcing steel under cyclic conditions.

Recently Pacific Steel Ltd, the only mill in New Zealand which manufactures reinforcing bars, has introduced two new grades of steel, namely Grade 300 and Grade 430 which supersede the Grade 275 and Grade 380, respectively. Grades 275 and 380 steel were specified by NZS 3402R (1973) which has been superseded by NZS 3402 (1989) for Grades 300 and 430 steel.

The research conducted for this chapter was jointly proposed, designed, and carried out by Dr. L. Dodd, a former Ph.D student, and the author. This chapter is therefore included in Dr. Dodd's Ph.D. thesis (1992).

2.2 OBJECTIVES

The research work reported in this chapter endeavours to study, experimentally and analytically, the main variables affecting the cyclic stress-strain behaviour of the two current New Zealand grades of reinforcing steel under a small number of large amplitude cycles. A detailed analysis of buckling, however, is outside of the scope of this research as it was intentionally decided to isolate the material behaviour from the combined material and geometrical behaviour. Nevertheless, some observations of its effect, especially regarding deformed bars, are given.

The chief aim at the initiation of this work was to investigate the calibration of the model by Mander et al (1984) and to complement it with results from the experimental work. However, it was found that some of the Mander et al model rules are not compatible with the findings, as will be

discussed later in this chapter. Another purpose for this work was to investigate the behaviour of the new Grade 430 reinforcing steel which has recently been adopted by the construction industry in New Zealand.

The main points of interest covered in this study are:

a) The cyclic stress-strain behaviour of the New Zealand Grades 300 and 430 steel under a random strain history within and beyond the Lüders (yield plateau) strain region.

b) The effects on the cyclic stress-strain behaviour of rolled deformations present on reinforcing steel bars.

c) The influence of the strain rate on the monotonic and reverse cyclic stress-strain curves.

d) The effect of natural strain ageing on the cyclic stress-strain behaviour on the two grades of steel.

2.3 REVIEW OF PREVIOUS RESEARCH WORK

2.3.1 The Cyclic Stress-Strain Behaviour of Steel

In 1886, Johann Bauschinger published a paper which noted that upon reversal from loads above the elastic limit of a Bessemer steel rod, a reduction in the elastic limit in the opposite direction is found [Mughrabi (1987), Bauschinger (1886, 1887)]. This reduction has since been called the "Bauschinger effect" and has been the subject of much research at the microscopic and macroscopic levels. Jago (1987) notes in the editorial of an edition of Materials Forum which honoured the centennial of Bauschinger's paper "***that even after 100 years it*** [the Bauschinger effect] ***is by no means fully understood***".

In the early 1960's Burns and Siess (1962) and Singh et al (1965) noted that the Bauschinger effect in reinforcing steel would affect the behaviour of reinforced concrete members subjected to load reversals beyond the elastic range.

Since then many researches have reported several macroscopic models to represent the cyclic stress-strain behaviour of different reinforcing steels. A comprehensive literature review of this type of models has been given by Kato (1979) and the Comité Euro-International du Béton (1983). Microscopic models, on the other hand, have been developed in other disciplines. These models have had limited applications and are unable of accurately predict the complex behaviour of a material with several load reversals because of the lack of a complete understanding of the mechanisms involved in the Bauschinger effect. Bate and Wilson (1986) as well as Abel (1987) present a literature review of these models.

Table 2.1
Research Work on the Cyclic Behaviour of the Manufactured New Zealand Steel

Researcher	Analytical Model	Model for Bauschinger Effect	Cyclic Load Tests		
			Grade of Steel (MPa)	Cycles in Lüders Region	Cycles in Work Hardened Region
Kent-Park (1969,1973)	●	Ramberg-Osgood	275	●	●*
Leslie (1974)			380		●
Thompson-Park (1975, 1978)	●	Ramberg-Osgood			
Spurr-Paulay (1984)	●	Ramberg-Osgood			
Mander et al (1984)	●	Menegotto-Pinto			
Tjokrodimuljo-Fenwick (1985)	●	Menegotto-Pinto	275	●	●

* Limited number of cycles.

Several investigators have looked at the stress-strain behaviour of New Zealand reinforcing steel. Table 2.1 summarizes the research conducted in New Zealand which will be briefly discussed below.

Kent and Park (1969, 1973) conducted experimental work on coupons made from Grade 275 steel. Test specimens were machined from different reinforcing bars. The cyclic tests were mainly confined to the Lüders strain region. They proposed a model which uses the monotonic curve as an envelope while the stress has the same sign, see Fig. 2.1. When the stress sign changes, the monotonic curve is abandoned. The unloading branch is described as a straight line with a slope equal to the elastic modulus up to the point of zero stress. Beyond this point, the Bauschinger effect is represented by a modified Ramberg-Osgood relationship as illustrated in Fig. 2.1.

Leslie (1974) did experimental work on the cyclic behaviour of Grade 380 steel. Unlike the work carried out by Kent and Park, the first reversal in all tests commenced beyond the Lüders strain region. Based on the test results, Leslie proposed that the monotonic tensile skeleton curve forms the envelope of curves with stress reversals as long as the strain history remains within the tensile direction. He also assumed that the tension and compression monotonic curves are the same.

Thompson and Park (1975, 1978) proposed a refined analytical model based on the experimental results presented by Kent and Park. The cyclic stress-strain response is assumed to lie within sliding tension and compression monotonic curves as shown in Fig. 2.2. The Bauschinger effect is considered to begin immediately upon reversal and is modelled by a modified Ramberg-Osgood

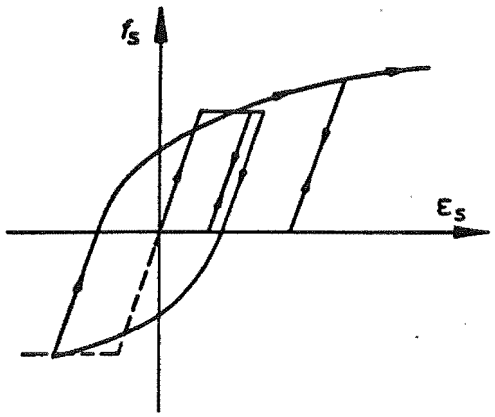

Fig. 2.1 - Cyclic Stress-Strain Model by Kent and Park (1969).

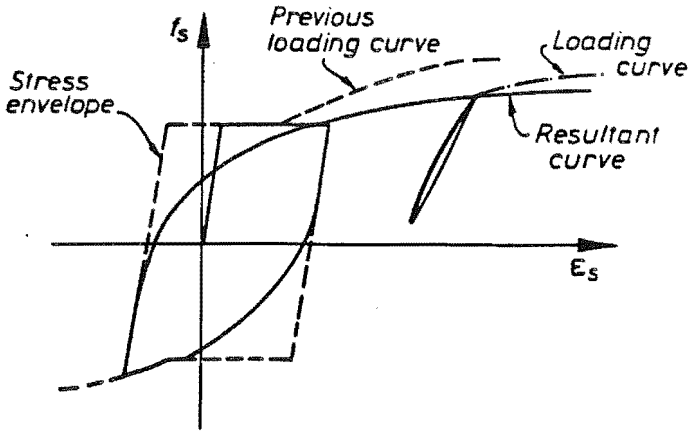

Fig. 2.2 - Cyclic Stress-Strain Model Proposed by Thompson and Park for Grade 275 Steel (1975).

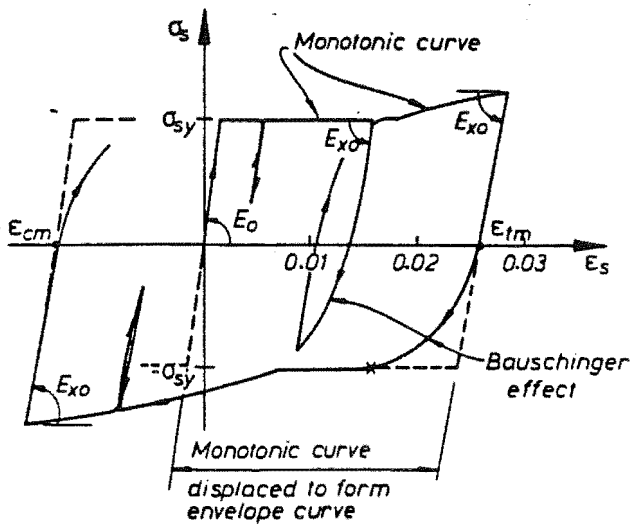

Fig. 2.3 - Cyclic Stress-Strain Model Proposed by Spurr and Paulay (1985).

relationship. A retained stress-strain history scheme allows small reversal cycles with a plastic strain less than 0.0005 to rejoin the previous loading curve in that direction. The use of the model is limited to mild steel with a strain history similar to the tests used in the calibration.

In reformulating the Thompson and Park analytical model, Spurr and Paulay (1984) recognized that the monotonic compression curve could not be identical to the tension curve since the change in diameter due to the Poisson effect had to be taken into account. In their model, the Bauschinger effect begins immediately after a stress reversal. A different modified Ramberg-Osgood relationship represents the Bauschinger effect. The model takes into account the softening of the unloading modulus with the plastic strain. Also, the retained stress-strain memory scheme presented by Thompson and Park is substantially modified and formulated to accurately predict the behaviour of loop cycles nesting inside a larger cycle. The calibration of the model was carried out with the experimental data compiled by Kent and Park and Aktan et al (1973). Fig. 2.3 depicts the main features of this model.

Mander et al (1984) gave an empirical correlation between the tension and compression skeleton curves based on a series of monotonic tests. They proposed a new model that was calibrated with data reported by Kent and Park, Aktan et al, Leslie and Ma et al (1976) and which they claimed could be universally used for all grades of reinforcing steel. In this model the monotonic curves are similarly displaced as in Thompson and Park model but an additional shift term accounts for cycle reversals in the work hardened region and strain short falls. Rules are given to determine the point and slope where a function due to Menegotto and Pinto function (1973), (see also Comité Euro-International du Béton 1983), representing the Bauschinger effect, merges with the skeleton curve. It is assumed that the Bauschinger effect commences immediately after a stress reversal. Both the unloading modulus and the shape of the curve are calculated through an iterative process. In general, the calculated unloading modulus is greater than the elastic modulus. Fig. 2.4 illustrates several aspects of this model.

Tjokrodimuljo and Fenwick (1985) conducted 12 cyclic tests on deformed 10 and 16mm diameter (D10 and D16) bars Grade 275 reinforcing steel. The test history comprised cycles within and beyond the Lüders strain region. The information was used in a comparative analysis with different models. A model based on the basic model postulated by Menegotto and Pinto was proposed. Fig. 2.5 shows the main parameters required by this model. The yield stress in compression for deformed reinforcing steel bars is taken to be 10% higher than that in tension. The Bauschinger effect lies between an initial asymptote with slope equal to the initial elastic modulus and a final asymptote calculate from the points (ϵ_{or}, f_{or}) and $(\epsilon_{0.06}, f_{0.06})$ at 6% strain in the monotonic tension curve. The Bauschinger effect is represented by the Menegotto and Pinto function and was calibrated with the results on the D16 bars. The test results of D10 bars as well as tests reported by Kent and Park, Leslie, and Ma et al were compared with the model predictions.

All of the above stress-strain models have correlated the shape of the Bauschinger effect with the plastic strain in the previous half cycle, following the discussion presented by Singh et al (1965), except for the model proposed by Mander et al.

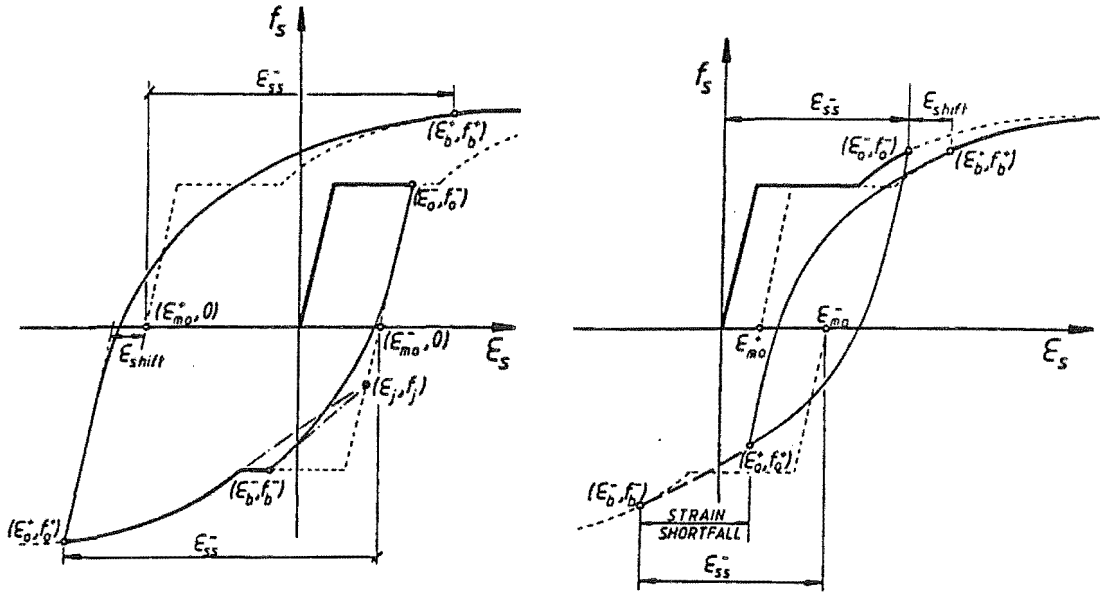

(a) Reversal from Skeleton Branch (b) Reversal from Softened Branch

Fig. 2.4 - Cyclic Stress-Strain Model Proposed by Mander et al (1984).

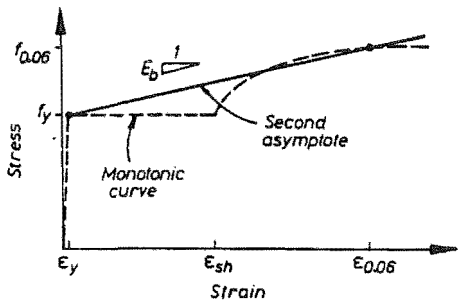

(a) Location of the Second Asymptote on the Monotonic Curve

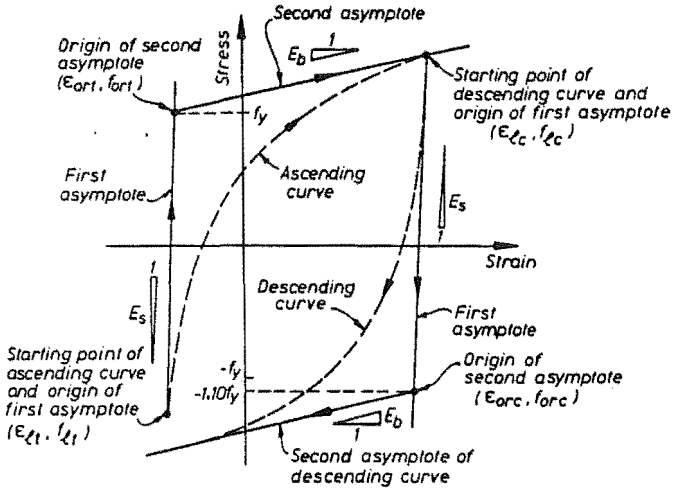

(b) Location of the Second Asymptotes on Ascending and Descending Curves

Fig. 2.5 - Modified Menegotto-Pinto Model Proposed by Tjokrodimuljo and Fenwick (1985).

2.3.2 Research Work on the Strain Rate Effects

Davis (1938) and Nádai (1950) agree that Ludwik was perhaps the first researcher to observe the effects of varying the strain rate on the behaviour of metals in 1909.

Manjoine (1944) conducted a thorough investigation on the influence of the strain rate on mild steel rods tested monotonically in tension. Tests conducted at room temperature covered strain rates from 0.00084/sec to 300/sec, with testing durations between 24 hours and a fraction of a second. Test results reproduced in Figs. 2.6 (a) and 2.6 (b) indicate an increase of the yield stress with an increase in the strain rate and a decrease of the ratio between the ultimate stress and the yield stress, with the exception of the slowest test where strain ageing influenced the test result.

Nowadays, there is a general agreement on the effects of the strain rate on the yield stress of reinforcing steel bars.

Based on test results, the ACI Committee 439 (1969) indicates that the yield stress increases with increasing strain rate, but to a lesser extent in higher strength steels.

Mander et al (1984) conducted monotonic compression tests on deformed reinforcing steel bars of Grades 275 and 380. The strain rate ranged between 0.00001 and 0.013/sec. Test results show similar trends to those presented earlier by Manjoine and the ACI Committee 439. The increase in the overall monotonic strength was found to be approximately the same as the increase in the initial modulus. Thus, it was assumed that the strength and stiffness of the monotonic and cyclic stress-strain curves are amplified by a unique dynamic magnification factor, a function dependent only of the strain rate.

The Comité Euro-International du Béton, CEB, (1988) has reported the strain rate effects on the monotonic behaviour of different steel types. The report includes several expressions for each steel type showing a general trend on the yield stress, the ultimate stress and ultimate strain to increase with an increase in the strain rate. It is reported that the initial elastic modulus is not affected by the strain rate.

Mahin and Bertero (1972) have dealt with the effects of strain rate on the cyclic stress-strain behaviour of reinforcing steel. Test results, in which the strain rates were 0.00005, 0.005 and 0.05/sec, indicate a significant increase in stress for cycles within the Lüders strain region. However, for cycles in the work hardened region, this effect was less pronounced. Fig. 2.7 reproduces test results in the Lüders strain region.

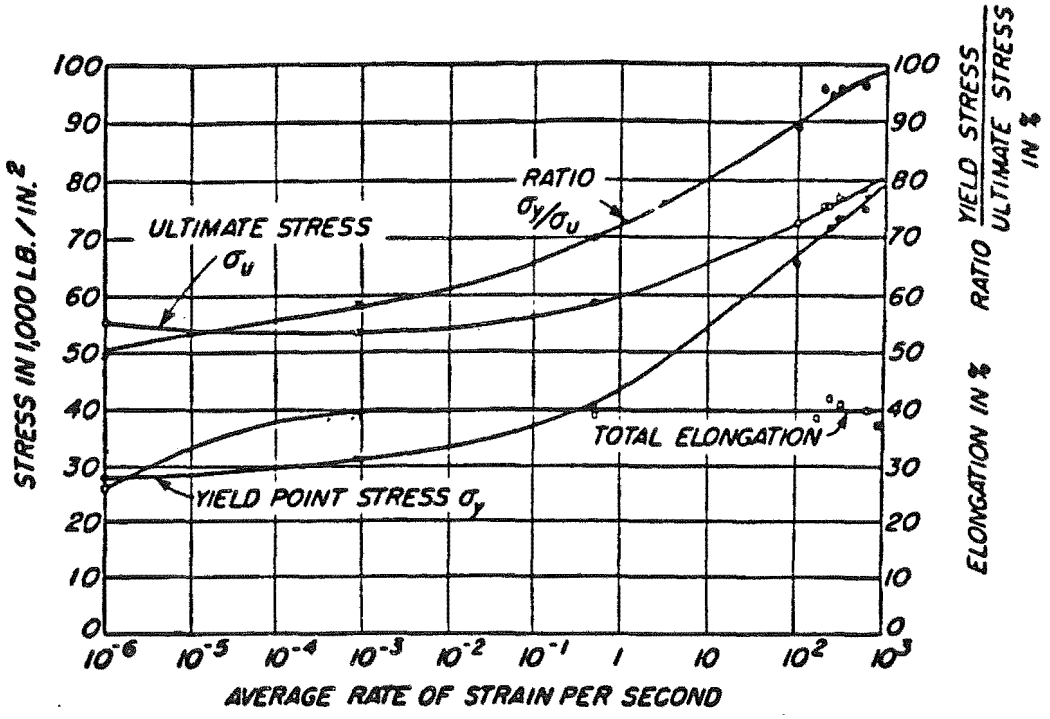

(a) Dependence of the Tensile Properties on Rate of Straining

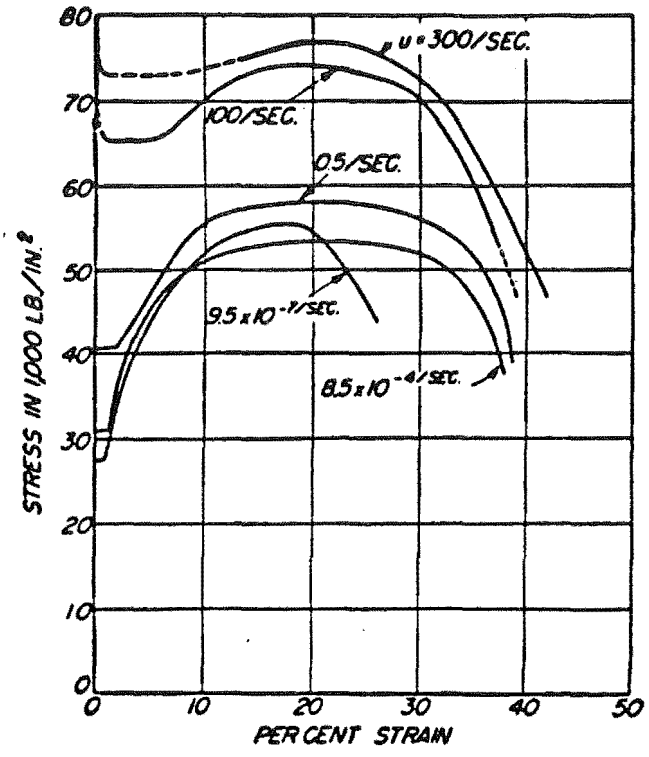

(b) Stress-Strain Curves at Various Rates of Strain

Fig. 2.6 - Test Results by Manjoine (1944) Showing the Effects of Strain-Rate on the Monotonic Behaviour of Mild Steel Tested at Room Temperature.

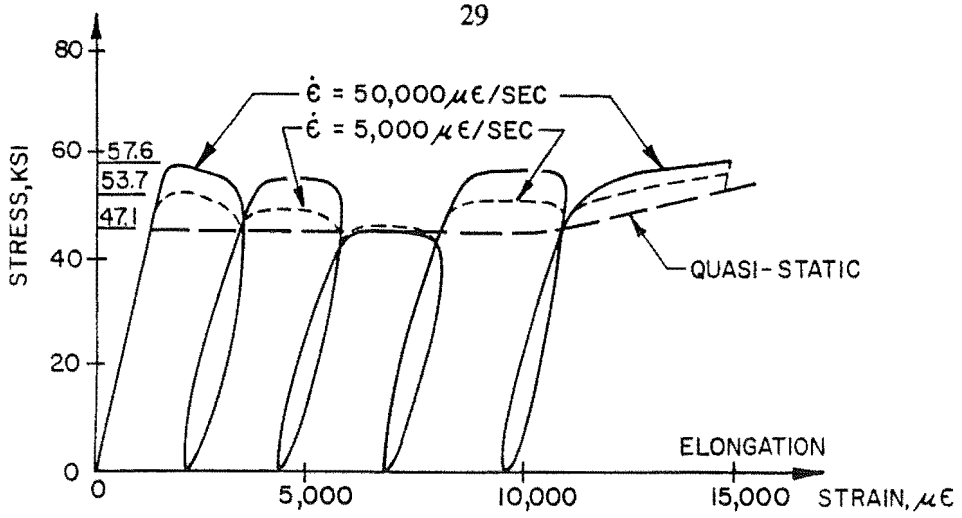

Fig. 2.7 - Test Results by Mahin and Bertero (1972) Showing the Effect of Strain Rate on the Cyclic Behaviour of Reinforcing Steel in the Yield Plateau Region.

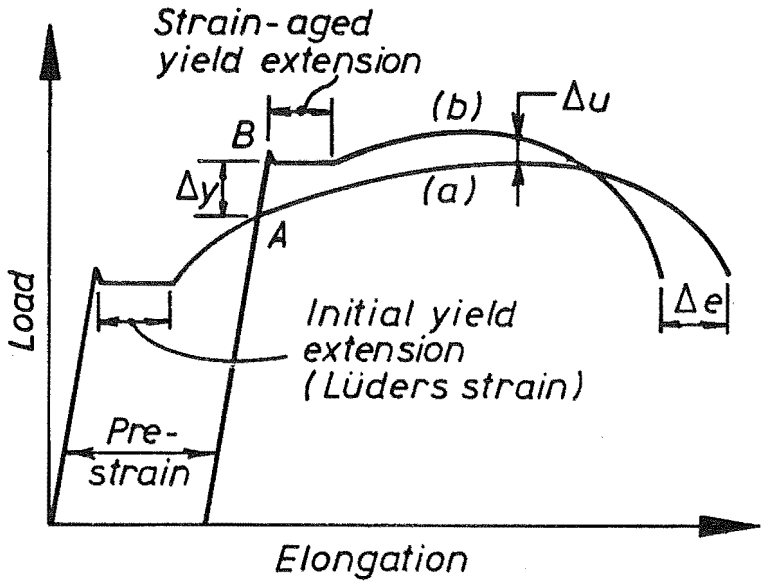

Fig. 2.8 - Main Features of Strain Ageing on the Tensile Test [Erasmus and Pussegoda (1977)].

2.3.3 Research Work on the Strain Ageing of the Reinforcing Steel

Bauschinger also observed an increase in the maximum load capacity of a test piece of steel after it was tested in the inelastic range, left resting for some period of time and then retested [Bauschinger (1886, 1887)]. This phenomenon is known today as strain ageing.

For certain combinations of chemical composition, level of pre-straining, temperature and elapsed ageing, the behaviour of the steel may even show a new distinct yield plateau as illustrated in Fig. 2.8. Cottrell and Bilby (1949) explained how carbon and nitrogen atoms diffuse through the lattice of the pre-strained steel towards the position of the free dislocations, pinning them as before. Erasmus (1987) found nitrogen to be the only factor responsible for strain ageing of reinforcing steels at temperatures below 150°C.

The effects of strain ageing in reinforcing steel has been extensively studied using monotonic tests. Amongst others, Erasmus and Pussegoda (1978) and Erasmus (1987) discussed the effects of strain ageing on the failure mode of bent reinforcing steel bars. Beckingsale et al (1980) and Spurr and Paulay (1984) carried out monotonic tests on reinforcing steel bars to assess the magnitude of the increase in strength of reinforced concrete assemblages due to natural strain ageing.

The effects of strain ageing on the cyclic stress-strain behaviour of steel has not been so extensively studied. Singh et al (1965) found that reversed curves showed a recovery in stiffness and strength towards the virgin elastic properties. In a study of retrofitting of beams, Tasai et al (1988) concluded that strain ageing in the longitudinal bars of a beam caused an increase in strength of the repaired member when tested monotonically but the strength was not enhanced in the test units with cyclic load reversals.

2.4 TEST PROGRAMME

2.4.1 Test Coupons

Fig. 2.9 shows the dimensions of the coupons tested in this experimental programme. The aspect ratio of the test region was 2.5 for machined coupons H and M and 4 for deformed test coupons MJ, HV and HX. These small aspect ratios were chosen to eliminate, as far as possible, any source of geometrical non-linearity (buckling) so the behaviour of the material itself could be studied. The larger aspect ratio selected for coupons made of deformed bars was to avoid any influence of the welded region in the gauged length.

Approximately 120 test Coupons were tested for this project. Test coupons H, HV and HX were of Grade 430 steel while coupons M and MJ were of Grade 300 steel. Table 2.2 gives the chemical analysis of the test specimens.

All H and M coupons were machined from 12 m long commercial 40mm diameter deformed reinforcing steel bars. This procedure ensured that all test specimens belonged to the same heat. An automated machining process was selected for convenience as well as for the uniformity in the dimensions of the end product. Fig. 2.10 illustrates an original 40mm deformed bar alongside several tested and untested machined specimens.

Test coupons MJ, HV and HX were made from 16mm and 24mm diameter reinforcing steel deformed bars. Emphasis was placed on keeping any eccentricity to a minimum. Fig. 2.11 displays the stages in the fabrication of the specimens. Bar lengths approximately 80mm in excess of the specified test length were cut from bars used in other research projects. Each end was machined down to form a 5mm diameter region. At the same time a transition "V" cut was lathed for posterior welding. 40mm diameter mild steel rods were inserted through the machined ends of the reinforcing steel bars, and then the end pieces were butt welded together. The last operation consisted of threading the 40mm diameter end rods. Deformed test specimens can be seen in Fig. 2.12.

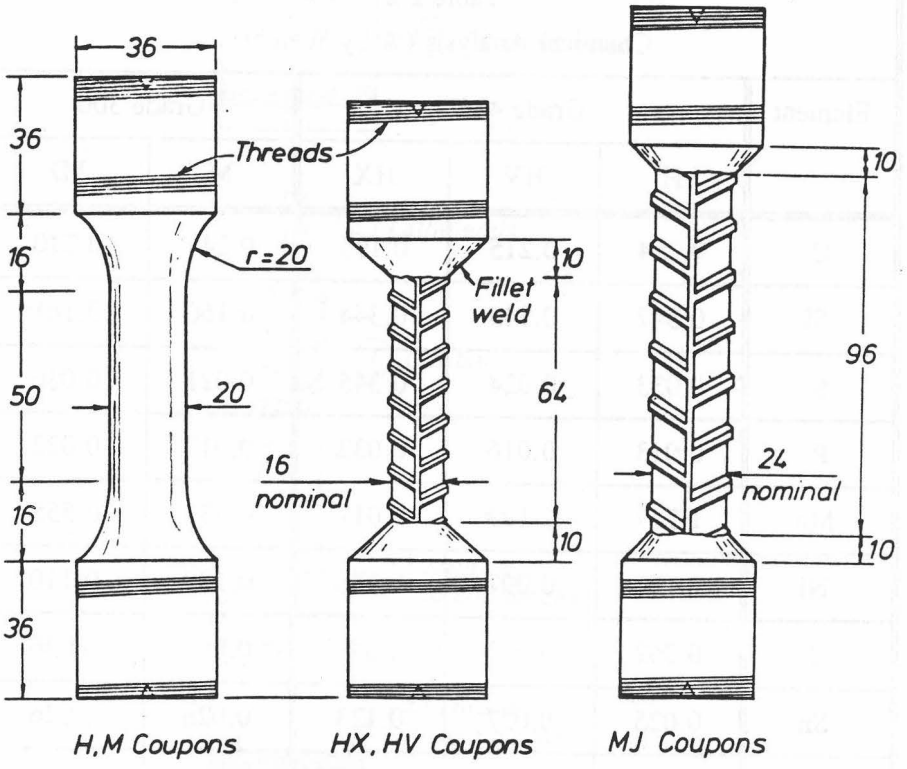

Fig. 2.9 - Dimensions of Test Coupons Tested.

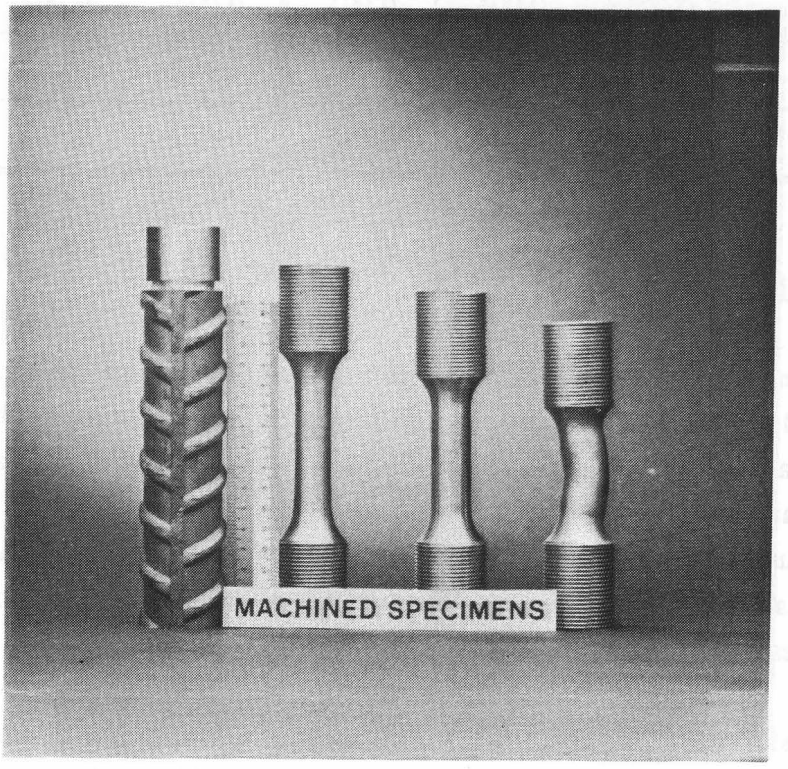

Fig. 2.10 - Machined Test Coupons and Virgin Bar.

Table 2.2
Chemical Analysis (% by Weight)

Element	Grade 430			Grade 300	
	H	HV	HX	M	MJ
C	0.254	0.215	0.195	0.244	0.210
Si	0.347	0.345	0.344	0.160	0.161
S	0.033	0.024	0.345	0.021	0.036
P	0.013	0.016	0.032	0.012	0.022
Mn	1.267	1.199	0.017	0.531	0.555
Ni	0.137	0.097	1.136	0.100	0.110
Cr	0.062	0.093	0.051	0.060	0.036
Sn	0.025	0.027	0.123	0.026	0.026
Cu	0.286	0.245	0.339	0.263	0.340
Mo	0.031	0.021	0.032	0.021	0.025
V	0.040	0.035	0.034	-	-
Ti	0.004	0.004	0.003	0.003	0.003
Al	0.007	0.008	0.007	0.007	0.007
W	0.027	0.031	0.018	0.020	0.028

2.4.2 The Loading System

The loading frame used for testing the steel coupons is illustrated in Fig. 2.13. The test programme was conducted in a 250 kN mechanical Instron Universal Testing Machine model 1116 which was driven by a stepping motor control unit. Fixed to the base of the Instron Machine was a stiff device designed to guide the test coupon and prevent double curvature buckling that was observed in trial tests and was caused by the lack of stiffness in the frame of the Universal Machine. Teflon pads were placed on the walls of the anti-buckling device to minimize friction from the contact with the top bracket holding the test specimen.

The two slotted brackets seen in Fig. 2.13 were designed to transfer the load to the test coupons. Wide dimensions were chosen to provide a fixed-end condition at the top and the bottom of the specimen.

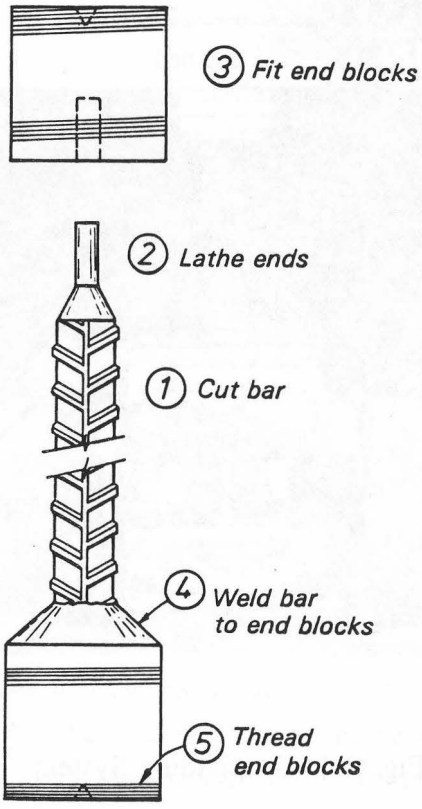

Fig. 2.11 - Manufacture Process of Deformed Steel Coupons.

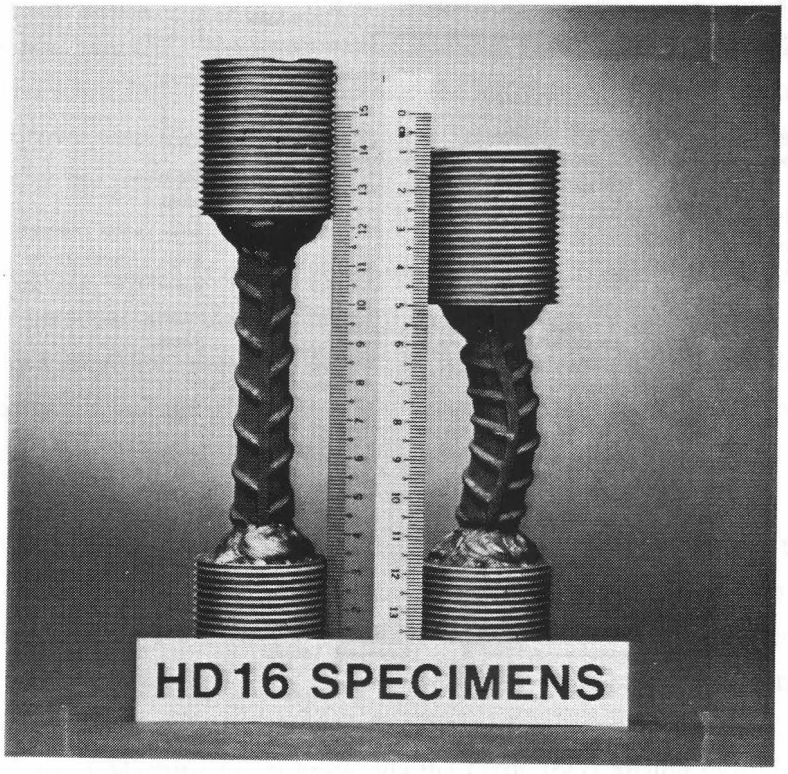

Fig. 2.12 - Deformed Steel Coupons After Testing.

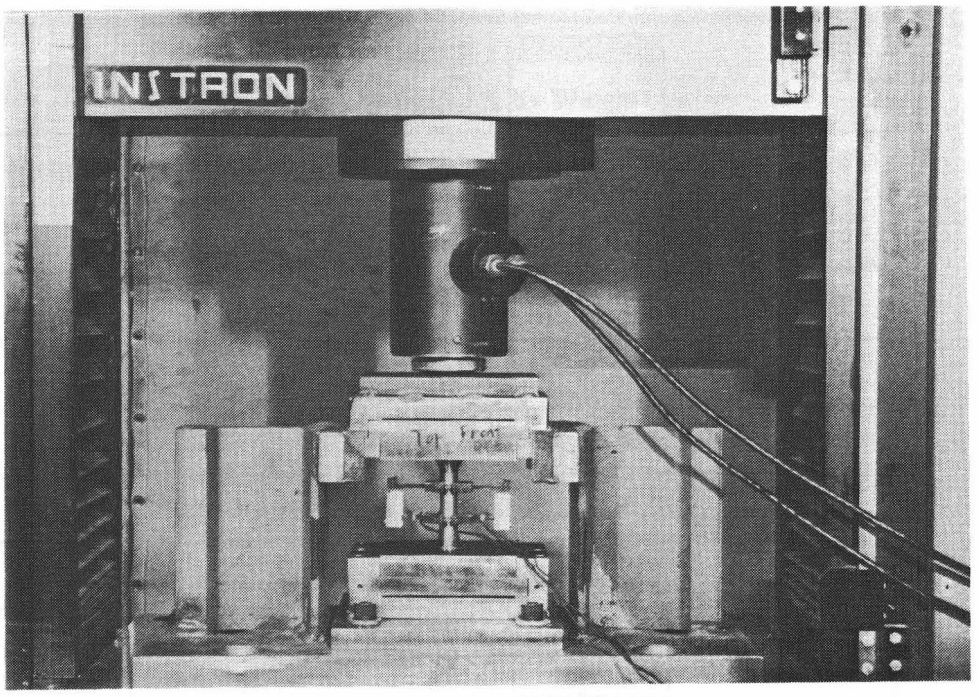

Fig. 2.13 - Loading System.

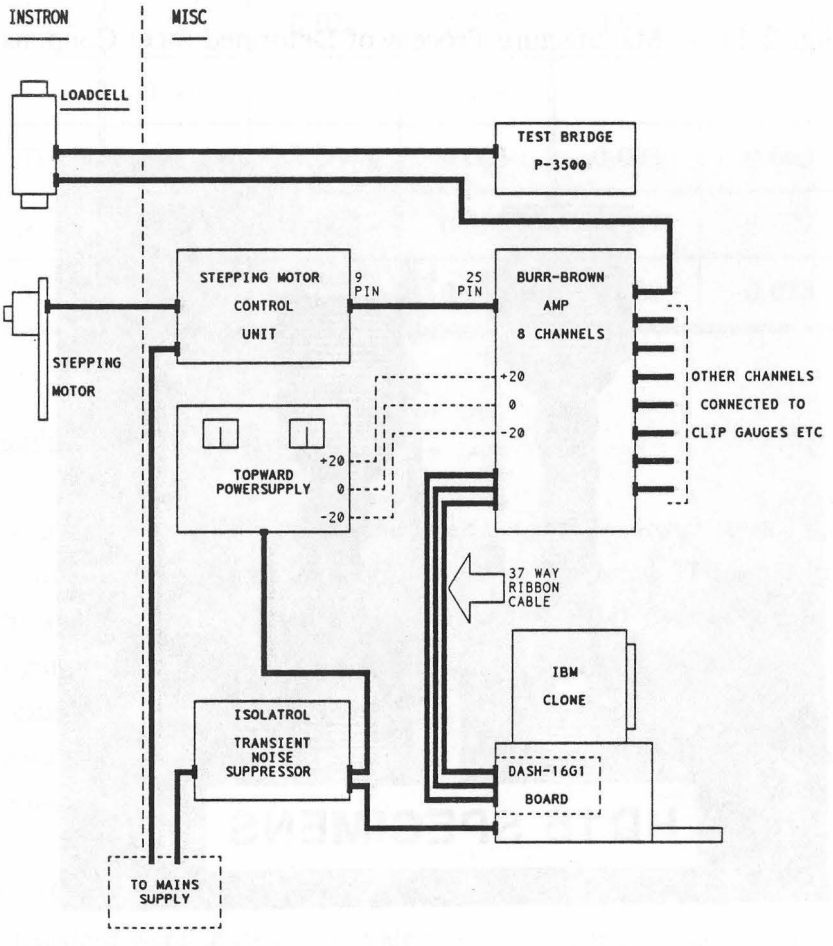

Fig. 2.14 - Schematic Representation of the Test Set-up.

Table 2.3
Summary of Transducers Set Up

Transducer	Input Voltage (v)	Gain	Bridge Configuration	Nominal Resolution
Load Cell	4.0	1000	Full (Poisson)	0.25 kN/dlu*
Extensometer	6.0	1000	Full (Bending)	100$\mu\epsilon$/dlu

* dlu = data logger units

2.4.3 Data Acquisition System

2.4.3.1 Test Set-Up

A schematic representation of the test set-up is shown in Fig. 2.14. Fig. 2.15 illustrates a view of the overall set-up including the loading frame in the background. The core of the system resided in a computer program written to automatically drive each test with minimum supervision. The sections below detail the different aspects of the system.

2.4.3.2 Transducers

Three transducers were used in the test programme, namely a load cell installed in the mobile head of the Instron Machine and two extensometers attached to the test specimen. The transducers were connected to a Burr-Brown amplifier which supplied the individual input voltages and pre-amplified the signal. The Burr-Brown amplifier was powered by a Topward TPS 4000 power supply with $\pm$20.0v. Table 2.3 summarizes the principal parameters of the transducers.

A Dash 16G1 analog to digital board was connected to one of the expansion slots of an AT 16 IBM compatible personal computer to convert the signals from the Burr-Brown amplifier. The gains set in the Burr-Brown amplifier, shown in Table 2.3, were calculated to obtain a desired resolution and based on the characteristic voltage of the Dash 16G1 analog to digit board of -10.0v to 10.0v equivalent to -2047 to 2048 data logger units.

The load cell consisted of a high strength steel hollow cylinder with two independent full bridge (Poisson) circuits, each with 2-350Ω 5mm strain gauges per arm. One of the circuits was connected to the Burr-Brown amplifier and the other was connected to a Measurements Group P-3500 Digital Strain Indicator. The load cell was calibrated in tension and compression in an Avery Universal Testing Machine using the circuit connected to the Digital Strain Indicator. This calibration was later reproduced in the Instron Machine to calibrate, via the Dash 16G1 analog to digital board, the second circuit of the load cell.

The extensometers utilised for measuring the strain in the test coupons were specifically designed for the present study. They were designed to read strains of up to 20% in tension and compression with acceptable resolution, without being affected by the change in diameter of the test coupon at large post-elastic strains. It was felt that two diametrically opposite transducers would provide information on the initiation of buckling and also allow average section strain to be determined.

Fig. 2.16 shows complete details of the extensometers. They were self-supported by attaching four springs at the level of the hardened steel knife edges in contact with the test coupon. The gauge length of 30mm was set by two removable aluminium jigs. The thickness of the feeler gauge steel plate was 0.15mm and was chosen so that the plate would remain well within the elastic range at test specimen strains of $\pm 20\%$. Several prototypes were built and tested to determine the best configuration for high output voltage, low hysteresis and minimum zero shift. The best results were obtained with 4-350Ω 5mm strain gauges forming a full bridge (bending). The strain gauges were glued with 401 Loctite Cyanoacrylate Adhesive. Waterproofing was kept to a minimum to reduce hysteresis. The maximum input voltage of 6.0v was chosen to avoid problems with heat dissipation and zero shift.

In addition, the transverse strain at the specimen mid-height was manually measured in some tests with a Mitutoyo digital vernier with a resolution of 0.01mm.

2.4.3.3 Software

The computer program written to test the steel coupons enabled any test to be controlled by a succession of reversals at predetermined strains and/or stresses. The program was structured in three main blocks:

a) An initial block read the input batch file containing the details of the test to be carried out. Then a theoretical estimation was calculated using the model proposed by Mander et al (1984). This prediction was plotted on the computer screen prior the initiation of the test.

b) The second block emitted a series of square wave signals to drive the stepping motor forward or backwards at a specified rate.

c) The last block continuously scanned the load and transducers extension. The reversal conditions were checked at each scan. Information regarding stress, strain and time were collected at certain intervals of stress or average strain as well as at each reversal point. This data was updated on the screen and a plot of the measured behaviour was superimposed over the theoretical prediction. An ASCII file containing the test results was created at the end of the test.

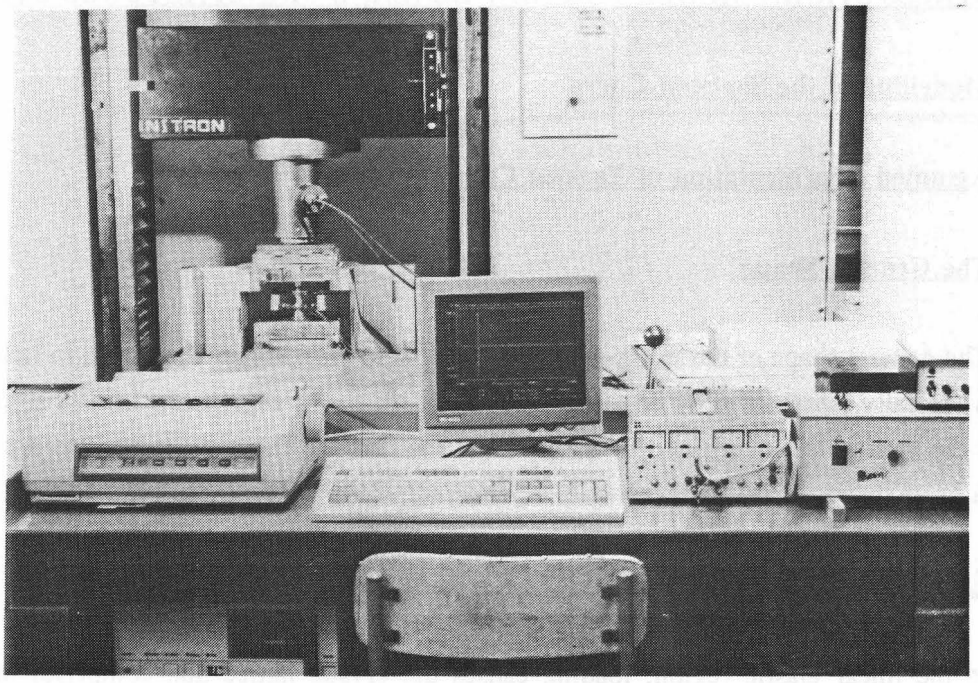

Fig. 2.15 - General View of the Test Set-up.

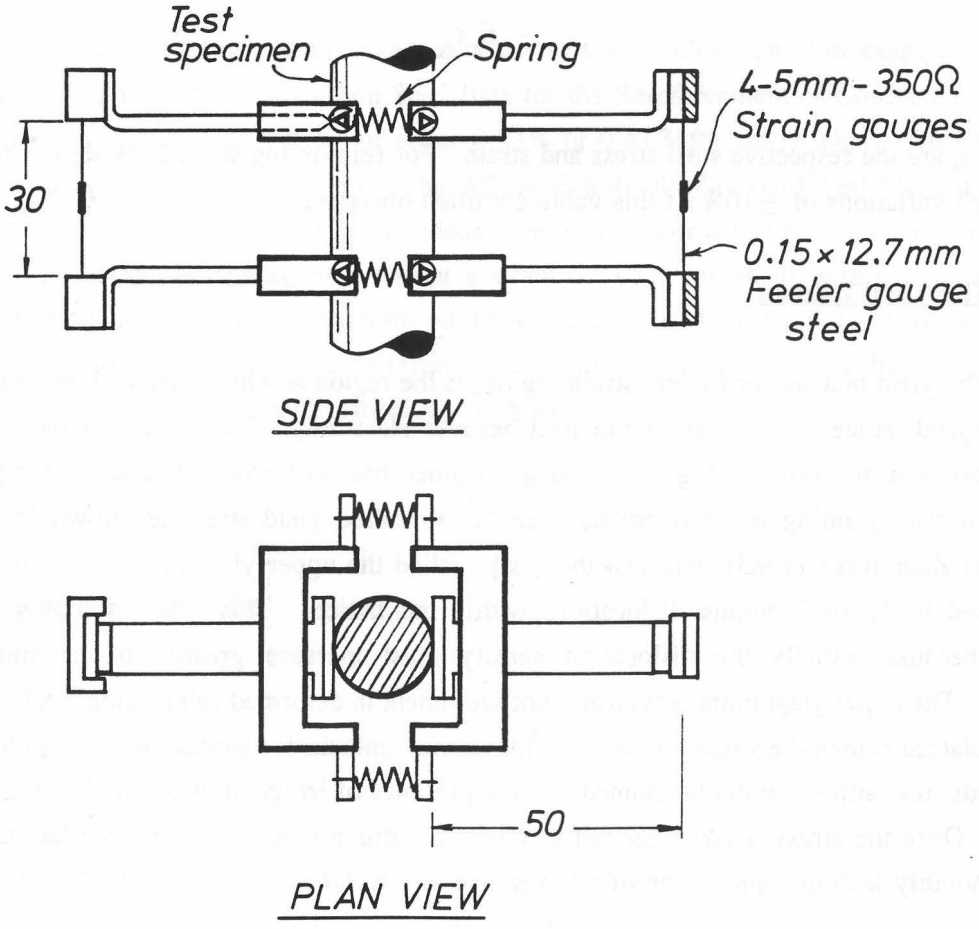

Fig. 2.16 - General Details of Extensometers Used.

2.5 STRESS-STRAIN MODEL FOR NEW ZEALAND MANUFACTURED STEEL

2.5.1 Modelling of the Skeleton Curve

2.5.1.1 Assumed Representation of Tension Curve

(a) The General Shape

The general shape of the stress-strain curve for mild steel loaded in tension to failure is well known. It is typically represented by three regions, the linear elastic region, the Lüders strain or yield plateau, and the strain-hardening region, as shown in Fig. 2.17. These three regions are described below with a brief statement of the accepted understanding of the microscopic behaviour.

(b) Linear Elastic Region

In the linear elastic region, loading causes the crystal lattice that comprises the steel to distort, but upon release of the load the lattice returns to its original configuration releasing all of the strain energy. This region of the stress-strain relation is linear and the slope is referred to as Young's Modulus or the elastic modulus, E_s. The stress-strain relationship in this region is

$$f_s = E_s \epsilon_s \tag{2.1}$$

where f_s and ϵ_s are the respective steel stress and strain. For reinforcing steel, E_s is approximately 200 GPa, although variations of $\pm 10\%$ of this value are often observed.

(c) The Yield Plateau

The yield plateau, or Lüders strain region, is the region at which dislocations begin to form within the crystal lattice. At this stage the steel behaves plastically. This region of the stress-strain relation is shown in the inset of Fig. 2.17. If a specimen has no history of cold working, the load required to initiate yielding is often greater than the so called yield stress as shown in Fig. 2.17. Bernstein and Zaimovsky (1983) state that this peak, called the upper yield point, corresponds to the stress required to "unpin" mobile dislocations within the lattice. This value is highly strain-rate dependent, because initially the dislocation density must increase greatly to accommodate the deformation. The upper yield point is typically not prominent in deformed reinforcing steel. The stress of the yield plateau is then the stress required to "move free (unlocked) dislocations through the lattice". In other words, the lattice is initially "pinned" by the presence of irregular atoms in the lattice or grain boundaries. Once the stress is large enough to overcome this pinned condition, the lattice can slide relatively smoothly with the application of a lower stress.

The yield plateau region of the stress-strain relation is typically assumed to be perfectly horizontal, but as Fig. 2.17 shows this is not actually the case. Fahy et al (1980) point out that although

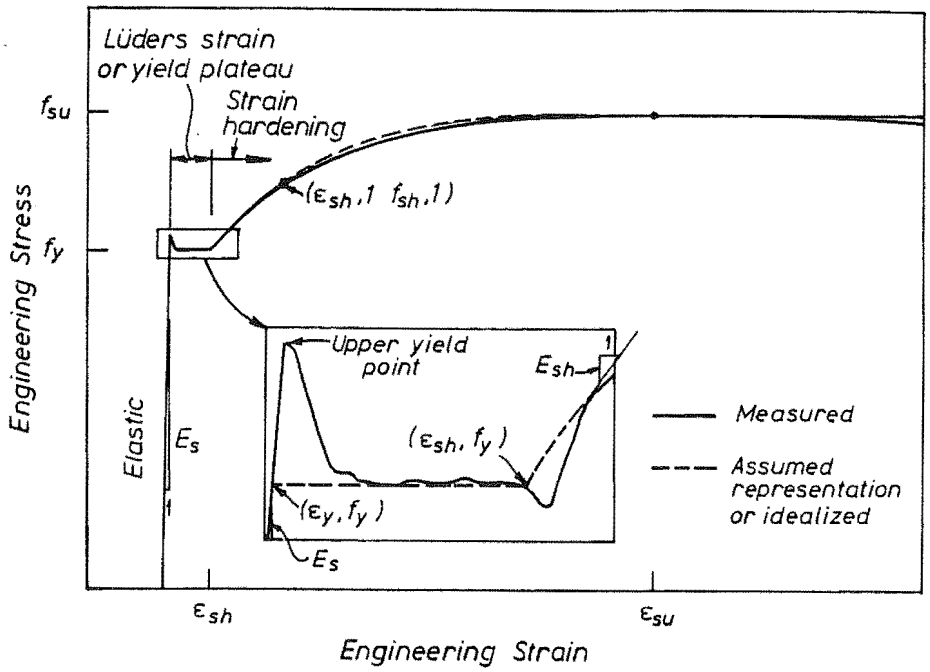

Fig. 2.17 - Monotonic Tensile Curve for Mild Steel.

the yield stress is a main design factor, no agreement exists in its definition. For example, the BS 4449 British Standard Specification for Carbon Steel Bars for the Reinforcement of Concrete (1988) defines the yield stress as the stress at a strain of either 0.33% or 0.43% for steels with a characteristic yield stress of 250 and 460MPa, respectively. The ASTM E 8M -90a Standard Test Method for Tension Testing of Metallic Materials (1991) recommends several procedures to find the yield stress, the most appropriate one being perhaps as the stress at a strain of 0.5% for steels with a yield stress below 550MPa. Both standards impose restrictions on the test rate. The yield stress, f_y, corresponding to the idealized yield plateau must therefore be taken as an arbitrary average value within the range of this plateau. The idealized stress-strain relationship in this region is therefore

$$f_s = f_y \tag{2.2}$$

which begins at the yield strain, ϵ_y, given by

$$\epsilon_y = \frac{f_y}{E_s} \tag{2.3}$$

(d) <u>The Strain-Hardening Region</u>

The point where the yield plateau ends and strain-hardening begins is not clearly obvious. Before strain hardening initiates, a dip generally occurs in the yield plateau followed by a steep increase which suddenly changes slope into the relatively smooth strain hardening region. The strain at which

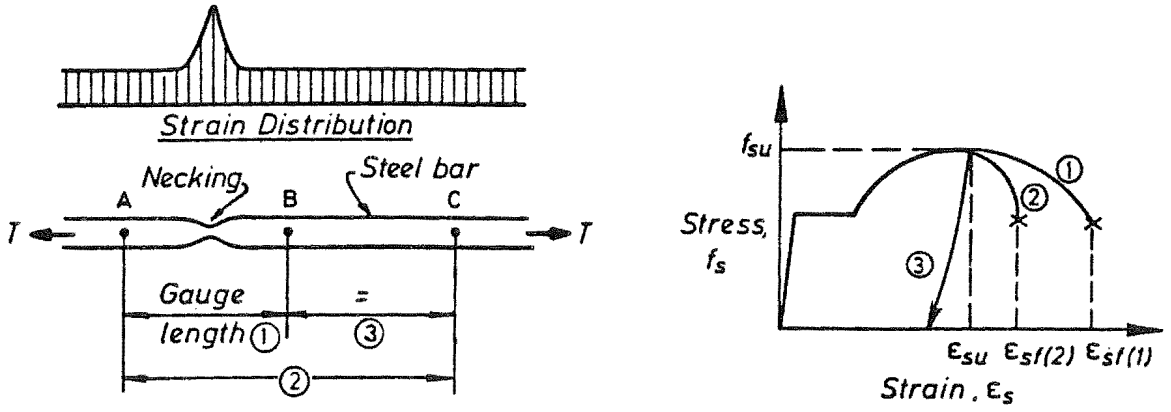

(a) Gauged Region

(b) Stress-Strain Curves

Fig. 2.18 - Effect of the Location and Length of the Gauged Region on the Tensile Curve Beyond Ultimate Load [Tanaka and Park (1990)].

the idealized strain hardening region begins is therefore greatly affected by the assumptions of the yield stress and the strain hardening model, as shown in Fig. 2.17. The strain-hardening region ranges from the idealized coordinates at which strain-hardening begins, (ϵ_{sh},f_y), to the ultimate coordinates, (ϵ_{su},f_{su}). The ultimate coordinates correspond to the point where the maximum load is resisted and the stress-strain curve has a slope of zero.

The shape of the tension stress-strain curve beyond the ultimate load is related to the location and gauge length over which data is collected as shown in Fig. 2.18. Once necking begins within the test specimen, strain is no longer evenly distributed along its length but rather is as shown in Fig. 2.18 (a). If the measured gauge length includes the necking region, a large amount of post-ultimate strain may be implied as shown in Fig. 2.18 (b). This strain decreases with increasing gauge length as demonstrated by curves "1" and "2". If the gauge length does not include the failure region, then the implied strain never exceeds the strain ϵ_{su} but rather decreases as the stress drops to zero as demonstrated by curve "3". Therefore, it is assumed that the ultimate coordinates mark the end of the useful region of stress-strain curve and that the measured stress-strain curve beyond ϵ_{su} has little meaning in design.

Several equations have been proposed for modelling the strain-hardening region. Burns and Siess (1962) recommended

$$f_s = f_y\left[\frac{112\left|\epsilon_s - \epsilon_{sh}\right| + 2}{60\left(\epsilon_s - \epsilon_{sh}\right) + 2} + \frac{\left|\epsilon_s - \epsilon_{sh}\right|}{\left(\epsilon_{su} - \epsilon_{sh}\right)}\left(\frac{f_{su}}{f_y} - 1.7\right)\right] \qquad (2.4)$$

where f_s and ϵ_s are the respective steel stress and strain, ϵ_{sh} is the strain where strain-hardening commences, ϵ_{su} is the ultimate strain, f_y is the yield stress, and f_{su} is the ultimate stress.

Kent and Park (1969, 1973) showed that the Burns and Siess equation assumes that $f_{su}/f_y = 1.5654$ and that $\epsilon_{su} = \epsilon_{sh} + 0.14$. Kent and Park modified the Burns and Siess equation such that the ultimate stress and yield stress, and the strain-hardening strain and ultimate strain, can all be considered independently. Thus the Kent and Park equation is

$$f_s = f_y \left[\frac{W_h (\epsilon_s - \epsilon_{sh}) + 2}{60 (\epsilon_s - \epsilon_{sh}) + 2} + \frac{(\epsilon_s - \epsilon_{sh})}{(\epsilon_{su} - \epsilon_{sh})} \left(\frac{f_{su}}{f_y} - W_a \right) \right] \tag{2.5}$$

where

$$W_h = \frac{\frac{f_{su}}{f_y}(30\,b + 1)^2 - 60\,b - 1}{15\,b^2} \tag{2.6}$$

$$W_a = \frac{W_h\,b + 2}{60\,b + 2} \tag{2.7}$$

$$b = \epsilon_{su} - \epsilon_{sh} \tag{2.8}$$

The Kent and Park equation is no more complex than the Burns and Siess equation since b, W_h, and W_a are constants for a given stress-strain curve.

Mander et al (1984) proposed a power curve of the form

$$f_s = f_{su} + (f_y - f_{su}) \left(\frac{\epsilon_{su} - \epsilon_s}{\epsilon_{su} - \epsilon_{sh}} \right)^P \tag{2.9}$$

This equation satisfies the end conditions of passing through the point (ϵ_{su}, f_{su}) at zero slope and through the point (ϵ_{sh}, f_{sh}). The power term, P, can be used to ensure the appropriate slope at the initiation of strain-hardening, the strain-hardening modulus, E_{sh}, and is given by

$$P = E_{sh} \left(\frac{\epsilon_{su} - \epsilon_{sh}}{f_{su} - f_y} \right) \tag{2.10}$$

This equation can give very good correlation with measured data. The problem with using E_{sh} as a measured parameter is that it is difficult to determine from experimental data as shown in Fig. 2.17 and the shape of the analytical curve given by the equation is very sensitive to this value. It is easier and more accurate to measure a point on the strain-hardening curve, $(\epsilon_{sh,1}, f_{sh,1})$, and then to determine P as

$$P = \frac{\log\left(f_{su} - f_{sh,1}\right)}{\log\left(\left(f_{su} - f_y\right)\left(\frac{\epsilon_{su} - \epsilon_{sh,1}}{\epsilon_{su} - \epsilon_{sh}}\right)\right)} \qquad (2.11)$$

2.5.1.2 Previously Proposed Relationships Between Monotonic Tension and Compression Stress-Strain Curves

Many researchers in the civil engineering field have assumed that the monotonic skeleton stress-strain curve of reinforcing steel in compression is equal and opposite to the curve in tension.

Spurr (1984) recommended that the stress of the compression stress-strain curve at a given strain be obtained by multiplying the stress for the corresponding strain on the tension curve by $-(1-2\epsilon_s)$. This factor allows for the theoretical difference between the area of the specimen at equivalent compressive and tensile strains and assumes that Poison's ratio, ν, is 0.5. Because ϵ_s is negative for compression, $(1-2\epsilon_s)$ is always greater than 1.

Mander et al (1984) related the compression skeleton curve parameters to the tension skeleton curve using the following empirical relationships:

$$f_y^- = -0.92\, f_y^+$$

$$E_s^- = 1.04\, E_s^+$$

$$\epsilon_{sh}^- = \epsilon_y^- - 0.5(\epsilon_{sh}^+ - \epsilon_y^+)$$

$$E_{sh}^- = 1.38\, E_{sh}^+$$

where the "-" superscript denotes a value for the compression skeleton curve, the "+" superscript denotes a value for the tension skeleton curve, ϵ_y and f_y are the strain and stress at the initiation of yield, E_s is Young's modulus, and ϵ_{sh} and E_{sh} are the strain and modulus at the commencement of strain hardening. They suggested that the ultimate compressive strain and stress (ϵ_{su}^-,f_{su}^-) can be determined by considering inelastic buckling. No values were suggested for the case in which buckling is not critical. Therefore, their model does not provide a strain-hardening curve from which a tangent modulus can be calculated to determine when buckling is likely to occur.

The experimental data for monotonic loading collected in this study does not agree with any of these relationships. However, it was found that the tension and compression curves are essentially the same if the stress and strain are changed to the natural coordinate system which takes into account the instantaneous geometry of the specimen.

2.5.1.3 The Natural Coordinate System

(a) Engineering and Natural Strains and Stresses

Engineering stress and engineering strain are typically used in the analysis of the behaviour of materials for engineering purposes.

Engineering strain, ϵ, is defined as

$$\epsilon = \frac{1}{\ell_o}\int_{\ell_o}^{\ell} d\ell = \frac{\ell - \ell_o}{\ell_o} = \frac{\Delta\ell}{\ell_o} \tag{2.12}$$

where ℓ_o is the initial length of an element, ℓ is the instantaneous length of the element, and $\Delta\ell$ is the change in length of the element from its initial length.

Engineering stress, σ, is defined as

$$\sigma = \frac{N}{A_o} \tag{2.13}$$

where N is an axial force acting on an element and A_o is the initial cross-sectional area of the section.

The notation σ is used for stress instead of f_s because these coordinate systems are valid for any material. The engineering coordinates are used because they are conveniently based on only the initial geometry of an element and they are therefore linearly related to the applied load and the material elongation. Strain energy can also be readily calculated based on initial volume.

In 1909, Ludwik and Leon proposed the concept of natural or logarithmic strain, ϵ' [Nádai (1950)]. Natural Strain is defined as

$$\epsilon' = \int_{\ell_o}^{\ell} \frac{d\ell}{\ell} = \ln\left(\frac{\ell}{\ell_o}\right) \tag{2.14}$$

For an incompressible material, this parameter has the advantage that the sum of the strains in the three principal directions is zero. This is true for the engineering strains only when they are infinitesimal. The natural strain and the engineering strain are related to each other as:

$$\epsilon' = \ln(1 + \epsilon) \tag{2.15}$$

and

$$\epsilon = e^{\epsilon'} - 1 \tag{2.16}$$

A parameter which gives a more correct indication of the actual stress acting on an element is true stress. True stress, σ', is related to the instantaneous cross-sectional area, A, and is defined as

$$\sigma' = \frac{N}{A} \tag{2.17}$$

If the volume is assumed to be constant, i.e. Poisson's ratio, ν, is 0.5, which is quite reasonable for metals in the plastic region, $A_o/A = \ell/\ell_o = \epsilon+1$ since the volume is $A_o\ell_o = A\ell$. For this case,

$$\sigma' = \sigma(1 + \epsilon) = \sigma e^{\epsilon'} \tag{2.18}$$

and

$$\sigma = \frac{\sigma'}{e^{\epsilon'}} = \frac{\sigma'}{(1 + \epsilon)} \tag{2.19}$$

If true stress and natural strain are used in the analysis of an element, instantaneous geometry is always considered and a better description of the material behaviour is given. The greatest advantage is the similarity between compression and tension behaviour of ductile materials such as steel in this coordinate system.

(b) The Relationship Between the Tension and Compression Curves

If the coordinates, (ϵ,σ), of a point on the skeleton tension curve in the engineering coordinates is chosen, the corresponding coordinates, (ϵ',σ') of that point in the natural coordinate system can be found. The corresponding point on the compression curve has the coordinates $(-\epsilon',-\sigma') = (\epsilon^{o\prime},\sigma^{o\prime})$ since the compression and tension curves are equal and opposite in natural coordinate system. From these coordinates, the corresponding coordinates, (ϵ^o,σ^o), on the engineering compression curve can be derived.

Any strain in the engineering coordinate system can be related to the natural coordinate system using Eq. 2.15. If the strain, ϵ, is on the tensile side, then the corresponding natural strain on the compression side is

$$\epsilon^{o'} = -\ln(1+\epsilon) = \ln\left(\frac{1}{1+\epsilon}\right) \tag{2.20}$$

Now this strain in engineering coordinates is

$$\epsilon^{o} = e^{\epsilon^{o'}} - 1 = \frac{1}{1+\epsilon} - 1 \tag{2.21}$$

which simplifies to

$$\epsilon^{o} = \frac{-\epsilon}{1+\epsilon} \tag{2.22}$$

It should be noted that this equation can be used to calculate a corresponding compression strain from a tensile strain in the engineering coordinate system without making use of the natural coordinate system or a corresponding tensile strain from a compression strain. It should also be noted that

$$1 + \epsilon^{o} = (1+\epsilon)^{-1} \tag{2.23}$$

Similarly, Eq. 2.18 relates stress in both coordinate systems. Assuming that σ is a tension stress, the corresponding natural compression stress is

$$\sigma^{o'} = -\sigma(1+\epsilon) \tag{2.24}$$

The stress in engineering coordinates is

$$\sigma^{o} = \frac{\sigma^{o'}}{1+\epsilon^{o}} = \frac{-\sigma(1+\epsilon)}{1+\left(\frac{-\epsilon}{1+\epsilon}\right)} \tag{2.25}$$

which on simplifying yields

$$\sigma^{o} = -\sigma(1+\epsilon)^{2} \tag{2.26}$$

With the use of Eqs. 2.22 and 2.26, any point on the tension branch of the (ϵ,σ) curve can be transformed to the corresponding point on the compression branch and vice versa. Fig. 2.19 (a) shows in the same quadrant a tension and a compression monotonic tests of a deformed bar in the

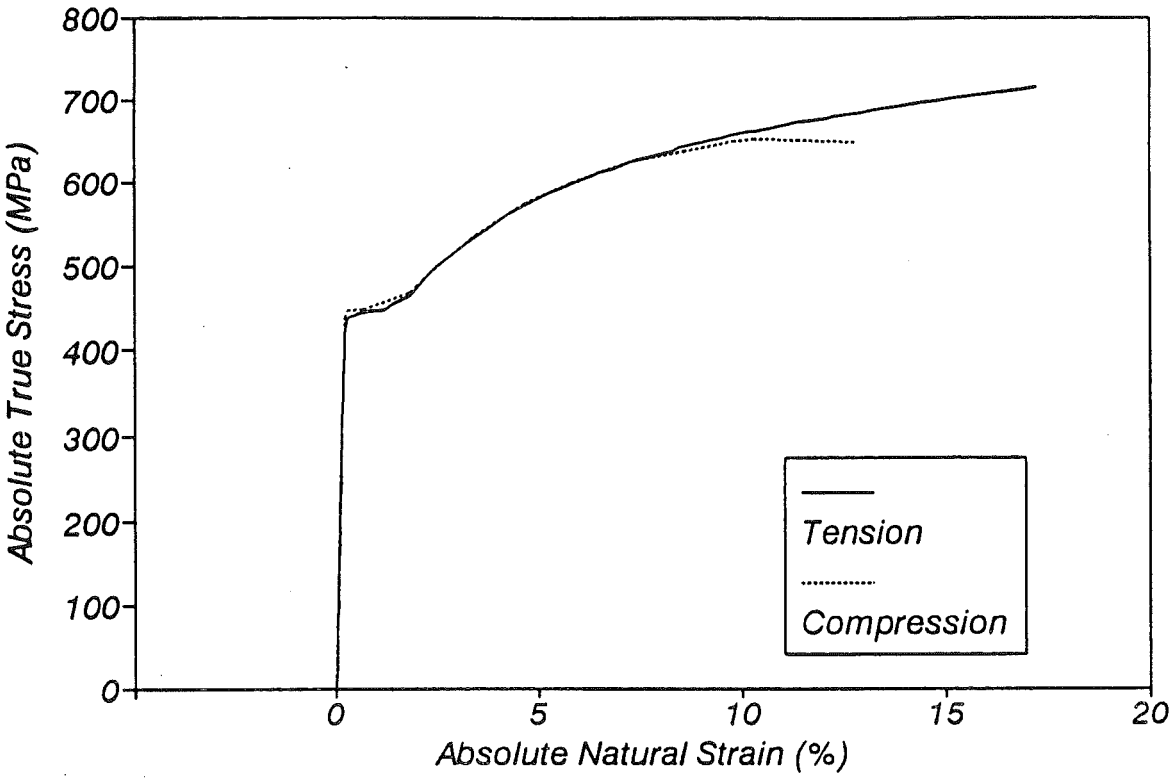

(a) Natural Coordinate System

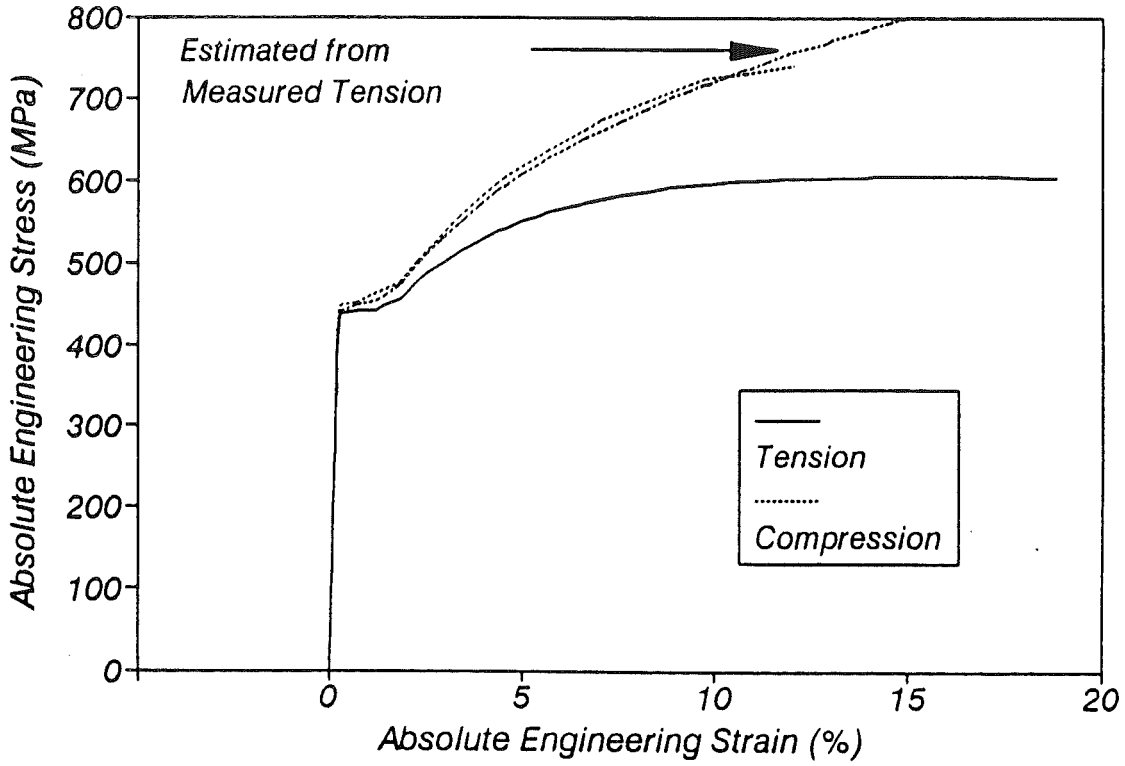

(b) Engineering Coordinate System

Fig. 2.19 - Tension and Compression Monotonic Curves.

natural coordinate system. Both curves are very similar despite buckling developing at an early stage in the compression test. Fig. 2.19 (b) illustrates the same tests in the engineering system. Additionally, a prediction of the compression curve calculated using Eqs. 2.22 and 2.26 and based on the data measured in the tension test shows the same degree of accuracy on the engineering coordinate system.

(c) The Relationship of Slope in the Coordinate Systems

The slope in the two coordinate systems will obviously be different since the abscissa and the ordinate are different. It is important to know how these slopes are related so that information such as unloading stiffness can be readily transferred between the two systems. In the engineering coordinate system, the unloading stiffness is affected by geometric changes as well as material behaviour. The natural coordinate system allows the effects of geometric changes to be removed.

The slope of a curve in the natural coordinate system is

$$\frac{d\sigma'}{d\epsilon'} = \frac{d\sigma(1+\epsilon)}{d\epsilon'} = \frac{d\sigma e^{\epsilon'}}{d\epsilon'} \tag{2.27}$$

Differentiation yields

$$\frac{d\sigma'}{d\epsilon'} = \frac{d\sigma}{d\epsilon'}e^{\epsilon'} + \sigma e^{\epsilon'} = e^{\epsilon'}\left(\frac{d\sigma}{d\epsilon'} + \sigma\right) \tag{2.28}$$

From the chain rule of differentiation,

$$\frac{d\sigma}{d\epsilon'} = \frac{d\sigma}{d\epsilon}\frac{d\epsilon}{d\epsilon'} \tag{2.29}$$

The first term on the right hand side of this equation is the slope in the engineering coordinate system. The second term is simplified as

$$\frac{d\epsilon}{d\epsilon'} = \frac{d(e^{\epsilon'} - 1)}{d\epsilon'} = e^{\epsilon'} \tag{2.30}$$

Rearranging Eq. 2.16 gives

$$e^{\epsilon'} = (\epsilon + 1) \tag{2.31}$$

Substituting Eqs. 2.29, 2.30, and 2.31 into Eq. 2.28 gives

$$\frac{d\sigma'}{d\epsilon'} = \left(\frac{d\sigma}{d\epsilon} + \frac{\sigma}{\epsilon+1}\right)(\epsilon+1)^2 \tag{2.32}$$

If the slope, $d\sigma/d\epsilon$, is zero, the right hand side of Eq. 2.32 simplifies to σ'.

The slope in the engineering coordinate system can be found from the slope in the natural coordinate system as

$$\frac{d\sigma}{d\epsilon} = \frac{d\left(\frac{\sigma'}{1+\epsilon}\right)}{d\epsilon} = \left(\frac{d\sigma'}{d\epsilon}e^{\epsilon'} - \sigma'\right)(1+\epsilon)^{-2} \tag{2.33}$$

From the chain rule,

$$\frac{d\sigma'}{d\epsilon} = \frac{d\sigma'}{d\epsilon'}\frac{d\epsilon'}{d\epsilon} \tag{2.34}$$

The first term on the right hand side of this equation is the slope in the natural coordinate system. The second term is simplified as

$$\frac{d\epsilon'}{d\epsilon} = \frac{d\,\ln(1+\epsilon)}{d\epsilon} = \frac{1}{1+\epsilon} \tag{2.35}$$

Substituting Eqs. 2.31, 2.34, and 2.35 into Eq. 2.33 yields

$$\frac{d\sigma}{d\epsilon} = \left(\frac{d\sigma'}{d\epsilon'} - \sigma'\right)e^{-2\epsilon'} \tag{2.36}$$

Eqs. 2.32 and 2.36 are the transfer equations for the slope of the curve in the two coordinate systems. These two equations can be used to relate the slope of the tension branch to corresponding points of the compression branch of the engineering coordinate system in the same manner in which the points themselves were related using the natural coordinate system by using the relationship,

$$\frac{d\sigma^o}{d\epsilon^o} = \frac{d\left[-\sigma(1+\epsilon)^2\right]}{d\epsilon^o} = \frac{-d\left[\frac{\sigma}{(1+\epsilon^o)^2}\right]}{d\epsilon^o} \tag{2.37}$$

Carrying out the differentiation on the right-hand-side of Eq. 2.37 gives

$$\frac{d\sigma^o}{d\epsilon^o} = \left(\frac{-d\sigma}{d\epsilon^o} + \frac{2\sigma}{1+\epsilon^o}\right)(1+\epsilon^o)^{-2} \tag{2.38}$$

From the chain rule,

$$\frac{d\sigma}{d\epsilon^o} = \frac{d\sigma}{d\epsilon}\frac{d\epsilon}{d\epsilon^o} \tag{2.39}$$

The second term on the right hand side of the equation can be simplified as

$$\frac{d\epsilon}{d\epsilon^o} = \frac{d\left(\frac{-\epsilon^o}{1+\epsilon^o}\right)}{d\epsilon^o} = -(1+\epsilon^o)^{-2} \tag{2.40}$$

Substituting Eqs. 2.23, 2.39, and 2.40 into Eq. 2.38 yields

$$\frac{d\sigma^o}{d\epsilon^o} = (1+\epsilon)^4\left[\frac{d\sigma}{d\epsilon} + \frac{2\sigma}{1+\epsilon}\right] \tag{2.41}$$

2.5.1.4 Idealized Skeleton Stress-Strain Curve in Natural Coordinates

The typical idealized monotonic stress-strain behaviour of reinforcing steel is described in Section 2.5.1.1. The relationships are given in the engineering coordinate system. Similar relationships are required in the natural coordinate system to take advantage of the symmetric behaviour of the steel in tension and compression. Experimental data will normally be in engineering coordinates and the values for the elastic modulus, E_s, the yield stress, f_y, the strain at initiation of strain hardening, ϵ_{sh}, the strain and stress at the ultimate load, ϵ_{su} and f_{su}, and an additional point on the strain hardening curve, $(\epsilon_{sh,1}, f_{sh,1})$ will be known (see Fig. 2.17). The strain and stress values at (ϵ_{sh}, f_y), (ϵ_{su}, f_{su}), and $(\epsilon_{sh,1}, f_{sh,1})$ can be used to calculate the corresponding points in the natural coordinate system, $(\epsilon'_{sh}, f'_{sh})$, $(\epsilon'_{su}, f'_{su})$, and $(\epsilon'_{sh,1}, f'_{sh,1})$ using Eqs. 2.15 and 2.18. From these values, the skeleton curve in the natural coordinate system can be defined.

The linear elastic region can be described by the relationship

$$f'_s = E_s \epsilon'_s \tag{2.42}$$

This equation is similar to Eq. 2.1 and will yield almost identical results for small pre-yield strains.

The relationship in the yield plateau or Lüders strain region is given by

$$f'_s = sf_y(1+\epsilon_s) = sf_y e^{\epsilon'_s} \tag{2.43}$$

where s is a factor indicating straining direction and is 1 for the tension curve, -1 for the compression curve. For the tension curve, this equation transforms into Eq. 2.2. The slope in this region is assumed to be

$$\frac{df_s'}{d\epsilon_s'} = f_y \tag{2.44}$$

This does not transform to zero slope as in the engineering coordinate system but will be within 2% for most cases.

The proposed equation for the strain hardening region is based on the power curve given by Eq. 2.9. However, because the slope of the skeleton is not zero at the point at ultimate load but f'_{su} (see Eq. 2.32 where $\sigma' = f'_{su}$), the relationship is slightly more complex. Solving for the conditions of passing through the points $(\epsilon'_{sh}, f'_{sh})$ and $(\epsilon'_{sh,1}, f'_{sh,1})$ and through the point $(\epsilon'_{su}, f'_{su})$ at a slope of f'_{su} gives

$$f_s' = s\,c_1\left[\frac{\epsilon_{su}' - s\,(\epsilon_s' - \epsilon_o'(k))}{\epsilon_{su}' - \epsilon_{sh}'}\right]^P - f_{su}'\left(s\epsilon_{su}' - \left(\epsilon_s' - \epsilon_o'(k)\right)\right) + sf_{su}' \tag{2.45}$$

where

$$P = \frac{\log\left(\dfrac{f_{sh,1}' + f_{su}'(\epsilon_{su}' - \epsilon_{sh,1}') - f_{su}'}{c_1}\right)}{\log\left(\dfrac{\epsilon_{su}' - \epsilon_{sh,1}}{\epsilon_{su}' - \epsilon_{sh}'}\right)} \tag{2.46}$$

and

$$c_1 = f_{sh}' + f_{su}'(\epsilon_{su}' - \epsilon_{sh}') - f_{su}' \tag{2.47}$$

The term $\epsilon_o'(k)$ in Eq. 2.45 is zero for monotonic loading. When a load reversal takes place, it is used to take into account a shift in the skeleton curve which will be discussed in Section 2.5.2. The term s is 1 for the tension curve and -1 for the compression curve.

It should be noted that the slope of the strain hardening curve is

$$\frac{df_s'}{d\epsilon_s'} = \frac{-P\,c_1}{\epsilon_{su}' - \epsilon_{sh}'}\left[\frac{\epsilon_{su}' - s(\epsilon_s' - \epsilon_o'(k))}{\epsilon_{su}' - \epsilon_{sh}'}\right]^{P-1} + f_{su}' \tag{2.48}$$

2.5.2 Stress-Strain Behaviour of Reinforcing Steel After a Load Reversal

2.5.2.1 General

Several rules for the behaviour of reinforcing steel after load reversals are proposed in this section. These rules were developed from data collected in this project and then were used to predict the behaviour of specimens given in the literature. The natural coordinate system is used because of the symmetric behaviour in tension and compression.

2.5.2.2 Unloading Branch

Fig. 2.20 illustrates the typical stress-strain behaviour of reinforcing steel after a load reversal from the coordinates (ϵ_r',f_r'). The first part of the unloading branch to the point (ϵ_a',f_a'), where yielding commences, can be approximated by a straight line with slope E_u'. An analysis of the digitized data recorded in the tests indicated that the extent of the linear portion ranges between $0.85f_y$ and $1.35f_y$. No correlation between the plastic strain and the magnitude of the linear portion was found to occur. For simplicity, a value of $1.0f_y$ was chosen for this study. The coordinates (ϵ_a',f_a') can then be calculated as

$$f_a' = f_r' + sf_y$$

$$\epsilon_a' = \epsilon_r' + \frac{sf_y}{E_u'} \qquad (2.49)$$

where f_y is the yield stress in the engineering coordinate system, s is a factor indicating straining direction of the unloading branch and is equal to 1 for the tensile direction and -1 for the compressive direction, and E_u' is the unloading modulus.

These assumptions are different from those made by previous research studies. For instance, Kent and Park (1969, 1973) assumed that softening begins at zero stress while Spurr and Paulay (1984), Thompson and Park (1975, 1978), Mander et al (1984), and Tjokrodimuljo and Fenwick (1985) assumed that softening begins immediately after the load reversal.

2.5.2.3 Determination of Unloading Modulus, E_u'

As noted in the previous section, a straight line for a stress change of $1.0f_y$ upon reversal was found to describe the first part of the unloading branch. The analysis of the test data showed the unloading modulus, E_u', decreases very rapidly after yielding, but stabilizes at larger strains. Hence, a close relation between the maximum absolute plastic strain and the unloading modulus appears to exist. Furthermore, the unloading modulus shows a small increase for reversals with a plastic strain smaller than the maximum absolute plastic strain. It is assumed in this study that the unloading modulus varies only with the absolute maximum plastic strain, ϵ_o', according with the following expression:

$$\frac{E_u'}{E_s'} = 0.82 + \frac{1}{5.55 + 1000\left|\epsilon_o'\right|} \tag{2.50}$$

Fig. 2.21 (a) shows all the unloading modulus values with a coefficient of correlation greater than 0.997 versus the maximum absolute plastic strain. Unloading moduli with a lower coefficient of correlation were not used for the calibration of Eq.2.50. Fig. 2.21 (b) illustrates the interpretation of the unloading modulus varying only with the maximum plastic strain.

As early as 1886 Bauschinger reported this variation [Bauschinger (1886, 1887)]. Stanton and McNiven (1979) have proposed the following relation for reinforcing steel:

$$\frac{E_u}{E_s} = 1 - 3.6\epsilon_r - \frac{1 - e^{-390\,\epsilon_r}}{15.56}, \quad \textit{and} \quad \frac{E_u}{E_s} > 0.733 \tag{2.51}$$

Spurr and Paulay (1984), based on an expression obtained for prestressing steel by Thompson and Park (1975), postulated:

$$\frac{E_u}{E_s} = 58.27\epsilon_r^2 - 6.946\epsilon_r + 1.008$$

$$\textit{and} \quad 0 \le \epsilon_r \le 0.03 \tag{2.52}$$

$$\frac{E_u}{E_s} \le 1$$

Eqs. 2.51 and 2.52 are given in the engineering coordinate system. Assuming σ equal to 400MPa and using Eq. 2.32 it is possible to transform these two equations to the natural coordinate system. For comparison with Eq. 2.51, the transformed equations are also plotted in Fig. 2.21 (a) assuming that ϵ_o' is equal to (ϵ_r' - 0.002).

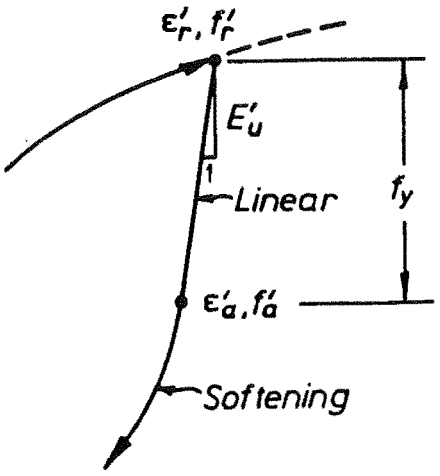

Fig. 2.20 - Stress Strain Behaviour of Reinforcing Steel upon Reversal of Load.

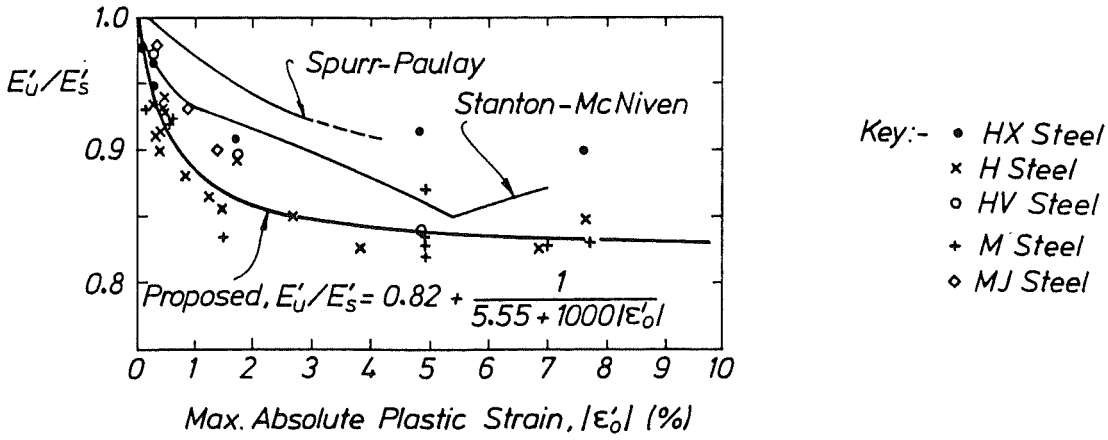

(a) All Unloading Modulus Values with a Coefficient of Correlation Greater than 0.997 versus Maximum Absolute Plastic Strain

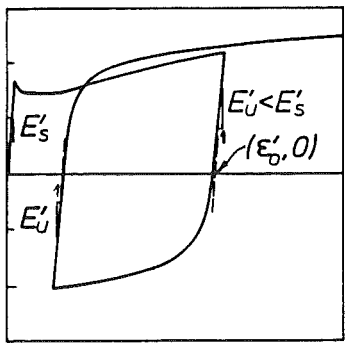

(b) Interpretation of Unloading Modulus Varying Only with Maximum Plastic Strain

Fig. 2.21 - Variation of Unloading Modulus with Plastic Strain.

2.5.2.4 Reversals within the Lüders Strain or Yield Plateau Region

When a reversal takes place from the Lüders strain or yield plateau of the skeleton curve, the stress-strain curve approaches a shifted skeleton curve in the opposite direction as shown in Fig. 2.22. The origin of the shifted skeleton curve is $(\epsilon'_o(k),0)$, where $\epsilon'_o(k)$ is termed the "shift strain" and k is 1 for the tension skeleton curve and 2 for the compression skeleton curve. The shift strain is in line with the linear portion of the unloading curve and is defined as

$$\epsilon'_o(k) = \epsilon'_r + \frac{sf_y}{E'_u} \qquad (2.53)$$

which corresponds to ϵ'_a in Eq. 2.49, but only when the reversal takes place from the yield plateau. In Fig. 2.22, when load reversal occurs at point "b", the shift strain $\epsilon'_o(2)$ moves from the origin, point "O", to point "c". When load reversal occurs at point "f", the shift strain, $\epsilon'_o(1)$ moves from the origin, point "O", to point "g". It should be noted that the tension skeleton curve can only shift along the

compressive strain direction while the compression skeleton curve can only shift along the tensile strain direction.

The point at which the stress-strain curve rejoins the skeleton curve in the opposite direction, $(\epsilon'_{s,rejoin}, f'_{s,rejoin})$ is assumed to be

$$f'_{s,rejoin} \approx sf_y$$

$$\epsilon'_{s,rejoin} = \epsilon'_o(m) + \frac{sf_y}{E'_u} \approx \epsilon'_r + s\left(\epsilon'_o(2) - \epsilon'_o(1) + \frac{2f_y}{E'_u}\right) \qquad (2.54)$$

where m is 1 for the branch rejoining the compression skeleton curve and 2 for the branch rejoining the tension skeleton curve. This expression compares reasonably well with data for New Zealand manufactured steel but data for steels with other carbon contents is not available and hence Eq. 2.54 cannot be generalised. The reversal curve rejoins the skeleton curve with the slope of the yield plateau, f_y. The approximations in Eq. 2.54 represent the facts that the Lüders strain or yield plateau region has

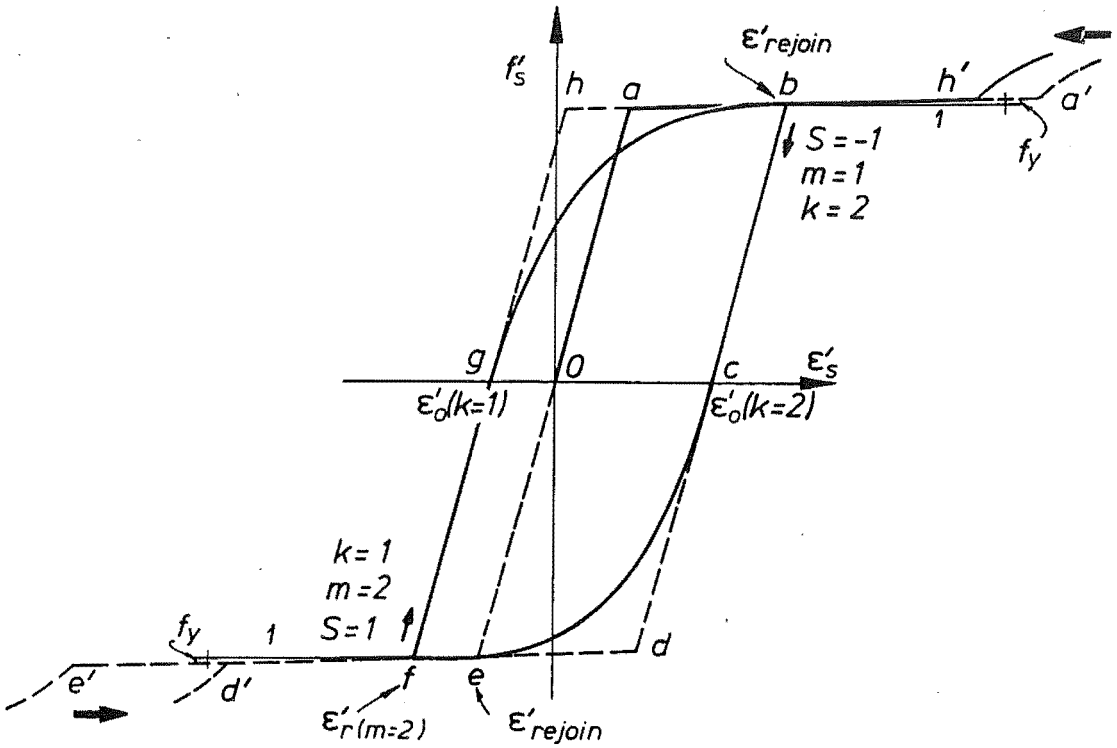

Fig. 2.22 - Stress-Strain Behaviour in Yield Plateau Region.

a non-zero slope in the natural coordinate system and decreases in the unloading modulus, E'_u, with increased plastic strain has a minor effect on the values of the shift strains, $\epsilon'_o(1)$ and $\epsilon'_o(2)$. Both of these effects are negligible. It is to be noted that in this section the yield stress in the engineering coordinate system has been used instead of the transformed yield stress in the natural coordinate system. The main reason for this approximation is that in the engineering system the idealized yield stress is a constant while in the natural system it varies, but the difference between both yield stresses is of the order of 1-2% at the end of the yield plateau which is smaller than the real fluctuation of the stresses observed in a test.

The total Lüders strain is assumed to be a constant, independent of the number of reversals, i.e. from Fig. 2.22,

$$\overline{ab} + \overline{ef} + \overline{bh'} = \overline{ab} + \overline{ed'} = \overline{aa'} = \overline{ee'} \qquad (2.55)$$

The measured data showed that this assumption is not actually true. Under cyclic conditions, the Lüders strain decreases and the magnitude of this reduction seems to be related to the accumulated complementary energy during reversals. Ma et al (1983) have proposed an empirical relation based on the amplitude of the loop to account for this reduction. Raske and Morrow (1969) noted that during low cycle fatigue tests, tests with increasing strain show a complete vanishing of the Lüders strain region. A definite relationship was not found and hence the proposed model will exhibit a delay in the initiation of strain-hardening relative to actual behaviour.

The shifting of the skeleton curve and the location of the rejoining point are similar to those which were proposed by Thompson and Park (1975, 1978) and Mander et al (1984). However, the actual shape of the reversal curve is substantially different.

2.5.2.5 Reversal from the Strain Hardening Curve

When the natural coordinate system is used, the slope of the stress-strain curve at the "ultimate" condition is not zero as it is in the engineering coordinate system. The natural coordinate system is therefore better suited for determining if the reversal curve rejoins the shifted skeleton curve, as proposed by Mander et al (1984), and if so, what the magnitude of this shift is. It was found that once strain hardening commences, the shape of the reversal curve is independent of the skeleton curve, which is in direct contrast to the findings of Spurr and Paulay (1984) and Mander et al (1984). However, it was found that the reversal curve becomes parallel to the original skeleton curve at large strains as shown in Fig. 2.23. It was concluded that the reversal curve approaches the coordinates $(\epsilon'_{su,shift}(k), sf'_{su})$ where f'_{su} is the true stress associated with the ultimate engineering stress and $\epsilon'_{su,shift}(k)$ is the "shifted" ultimate strain which is defined as

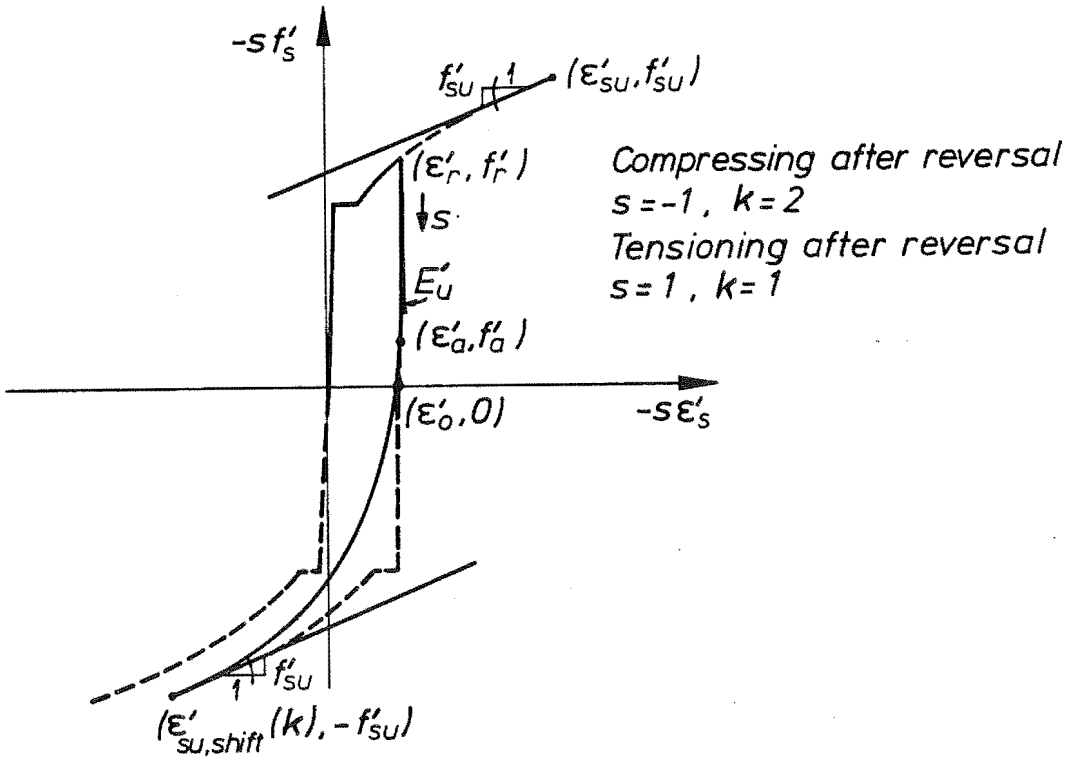

Fig. 2.23 - Boundary Conditions at Ultimate Load.

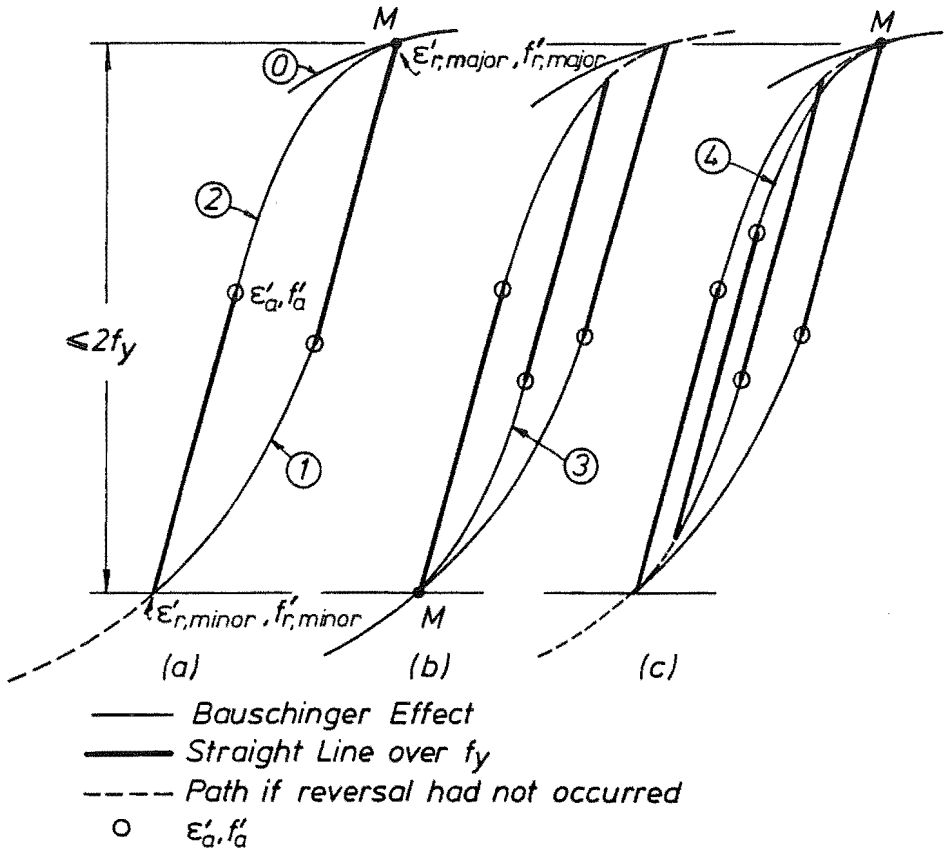

Fig. 2.24 - Stress-Strain Behaviour for Stress Reversals

$$\epsilon'_{su,shift}(k) = s\,\epsilon'_{su} + \epsilon'_o(k) \tag{2.56}$$

where

$$\epsilon'_o(k) = \epsilon'_r + \frac{sf'_r}{E'_u} \tag{2.57}$$

The direction of this shift follows the same rules as the reversals within the yield plateau region. The reversal curve begins with a linear portion with the length and modulus as described above. The Bauschinger curve goes from the point (ϵ'_a,f'_a), at a slope E'_u, to the point ($\epsilon'_{su,shift}$(k),sf'_{su}), at a slope f'_{su}.

2.5.2.6 Reversal from a Reversal Curve

(a) General

When a reversal takes place from another reversal curve, three types of behaviour are observed. If the change in stress between the two reversal points is sufficiently large, the new curve is independent of the previous reversal points and is termed a "major reversal curve". Otherwise, the new reversal curve will return to a previous reversal point. In the latter condition, the point to which the curve returns is determined by the preceding strain-history and can be a "minor reversal curve" or a "simple reversal curve". These curves are explained in the following sections.

(b) Major Reversal Curve

A curve which is independent of the previous reversal points is termed a "major reversal curve" which begins at the major reversal point, ($\epsilon'_{r,major}$,$f'_{r,major}$). Any reversal from the skeleton curve is a major reversal curve. The behaviour for such curves has already been discussed. It was also found that when a reversal takes place from a previous major reversal curve, if the difference between the new reversal stress, f'_r, and the previous major reversal stress, $f'_{r,major}$, exceeds a certain value, the new curve is a major reversal curve. The critical change in stress was found to be approximately $2f_y$ and this value was adopted. Therefore

$$If \left| f'_r - f'_{r,major} \right| > 2f_y \; then \; new \; f'_{r,major} = f'_r \tag{2.58}$$

It is then necessary to check if the shift strain, ϵ'_o(k), must be updated by testing

$$If \left(s\,\epsilon_o'(k)\right) > s\left(\epsilon_r' - \frac{f_r'}{E_u'}\right) \qquad (2.59)$$

$$then\ new\ \epsilon_o'(k) = \epsilon_r' - \frac{f_r'}{E_u'}$$

At this point, it is necessary to check if the unloading modulus value must be updated using Eq. 2.50. Then as is the case for a reversal from the strain hardening branch of the skeleton curve, the reversal curve is linear from (ϵ_r',f_r'), to (ϵ_a',f_a') and then a softening curve approaches the coordinates ($\epsilon_{su,shift}'(k)$,sf_{su}') as shown in Fig. 2.23.

(c) Minor Reversal Curve

A minor reversal is a reversal from a major reversal curve in which the reversal stress, f_r', is less than $2f_y$ from $f_{r,major}'$ as shown in Fig. 2.24 (a). The minor reversal curve (curve "2" in Fig. 2.24 (a)) approaches the major reversal point, ($\epsilon_{r,major}'$,$f_{r,major}'$) at which it rejoins the curve from which the previous major reversal had occurred (curve "O") as shown in Fig. 2.24 (a) at point "M". If the minor reversal point, ($\epsilon_{r,minor}'$,$f_{r,minor}'$), occurs from the softened portion of the major reversal curve (curve "1"), the minor reversal curve returns along the typical linear portion to (ϵ_a',f_a') and then to ($\epsilon_{r,major}'$,$f_{r,major}'$) along a softening curve which merges with the same slope as the original curve, curve O. If the minor reversal point occurs in the linear portion of the major reversal curve, the minor reversal curve simply returns along the same linear curve to ($\epsilon_{r,major}'$,$f_{r,major}'$) at which it rejoins the curve from which the previous major reversal had occurred.

(d) Simple Reversal Curve

A simple reversal curve is a reversal from either a minor reversal curve or another simple reversal curve as shown in Figs. 2.24 (b) and 2.24 (c) respectively. The point at which a simple reversal curve occurs is never considered for future reversal curves. The general behaviour of a simple reversal curve is similar to that for a minor reversal curve. Depending on the direction of the reversal, the curve can approach ($\epsilon_{r,minor}'$,$f_{r,minor}'$) and rejoin the major reversal curve at point "M" as shown by curve "3" in Fig. 2.24 (b), or it can rejoin the original curve at point "M" as shown by curve "4" in Fig. 2.24 (c). The slope of the simple reversal curve matches that of the curve that is joined at the junction point.

2.5.3 Numerical Modelling of Bauschinger Effect

Each of the reversal curves discussed has a region in which softening of the Bauschinger effect must be considered, except for the case of a reversal on the linear portion of a preceding curve. In each case, the initial and final point of the curve, as well as the slope at these points, is known. An appropriate relationship is required which will satisfy these boundary conditions.

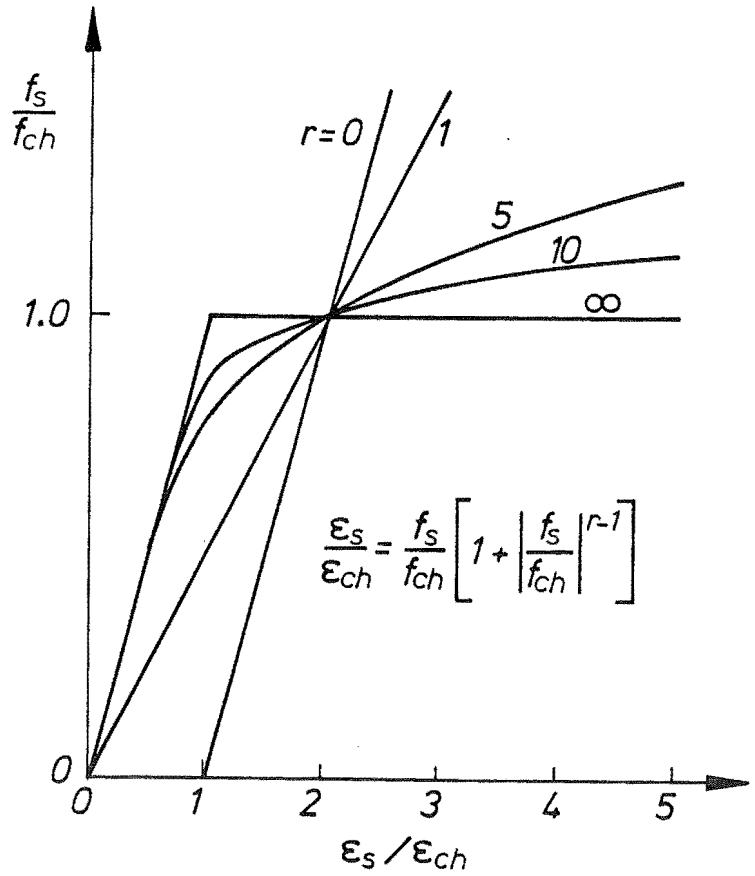

Fig. 2.25 - Ramberg-Osgood Relationship.

In the past, several equations have been used to model the Bauschinger effect. Models at the University of Canterbury have typically used either the Ramberg-Osgood relationship or the Menegotto-Pinto function. The Ramberg-Osgood relationship is of the form

$$\frac{\epsilon_s}{\epsilon_{ch}} = \frac{f_s}{f_{ch}} + \left(\frac{f_s}{f_{ch}}\right)^r \qquad \textbf{(2.60)}$$

and is shown in Fig. 2.25. There are several difficulties when using the Ramberg-Osgood relationship. First, it is used to find strain in terms of stress. Analyses of reinforced-concrete members typically assume that plain sections remain plain and for a given curvature, a moment is calculated. The Ramberg-Osgood relationship cannot be used in a closed form for such an analysis. Another problem is that for finite values of "r", the relationship does not approach any limit. Finding a set of values for the characteristic stress, f_{ch}, and strain, ϵ_{ch}, and the exponent, r, for which the relationship will pass through a desired point at a desired slope is very complex.

The Menegotto-Pinto function as used by Mander et al (1984) is of the form

$$f_s = f_o + (\epsilon_s - \epsilon_o)\left[Q + \frac{1-Q}{\left(1 + \left|E_m \frac{\epsilon_s - \epsilon_o}{f_{ch} - f_o}\right|^R\right)^{1/R}}\right] \tag{2.61}$$

and approaches an asymptote as shown in Fig. 2.26. This function has been frequently used by other investigators. However, it is difficult to determine a set of variables, f_{ch}, Q, and R, for which the relationship will pass through a desired point at a desired slope. Also, there is no single solution but rather a set of solutions which will satisfy the boundary conditions. It was also found in the tests that the shape of this relationship is not suitable to describe the full extent of the Bauschinger curve to the ultimate load.

A new approach was considered in this project. An equation was needed for which a closed form solution could be found for any set of end conditions and it needed to have a simple parameter which would allow the "softness" of the curve, as determined by the area under the curve relative to the enclosing parallelogram, to be controlled. It was found that such an equation could be more readily found if the curve was transformed from the natural coordinate system to a normalised perfectly-rigid-perfectly-plastic coordinate system as shown in Fig. 2.27. Fig. 2.27 (a) shows the desired curve in the natural coordinate system. This curve first needed to be transformed into a perfectly-rigid-perfectly-plastic coordinate system with the same area, as shown in Fig. 2.27 (b). This transformation is carried out as shown in Fig. 2.28. Both the transformed stress, f''_s, and the transformed strain, ϵ''_s, are a function of f'_s, and ϵ'_s. If the stress is transformed first, then from Fig. 2.28 (a),

$$f''_s = \left(f'_s - f'_a\right) - E'_2\left(\epsilon'_s - \epsilon'_a\right) \tag{2.62}$$

The strain is determined by the intersection of the two lines

$$f' = f'_s + E'_1(\epsilon' - \epsilon'_s) \tag{2.63}$$

and

$$f' = f_a + E'_2\left(\epsilon' - \epsilon'_s\right) \tag{2.64}$$

at point "A" in Fig. 2.28 (a). If the intersection point is (ϵ'_A, f'_A) then

$$\epsilon'_A = \frac{f'_a - f'_s + E'_1\epsilon'_s - E'_2\epsilon'_a}{E'_1 - E'_2} \tag{2.65}$$

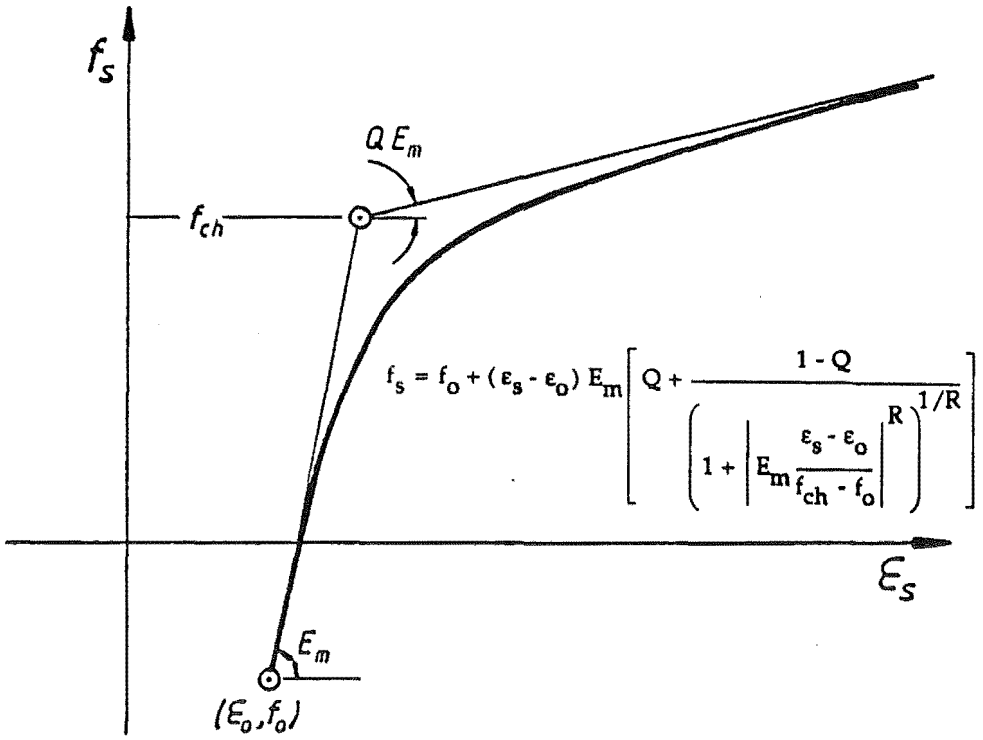

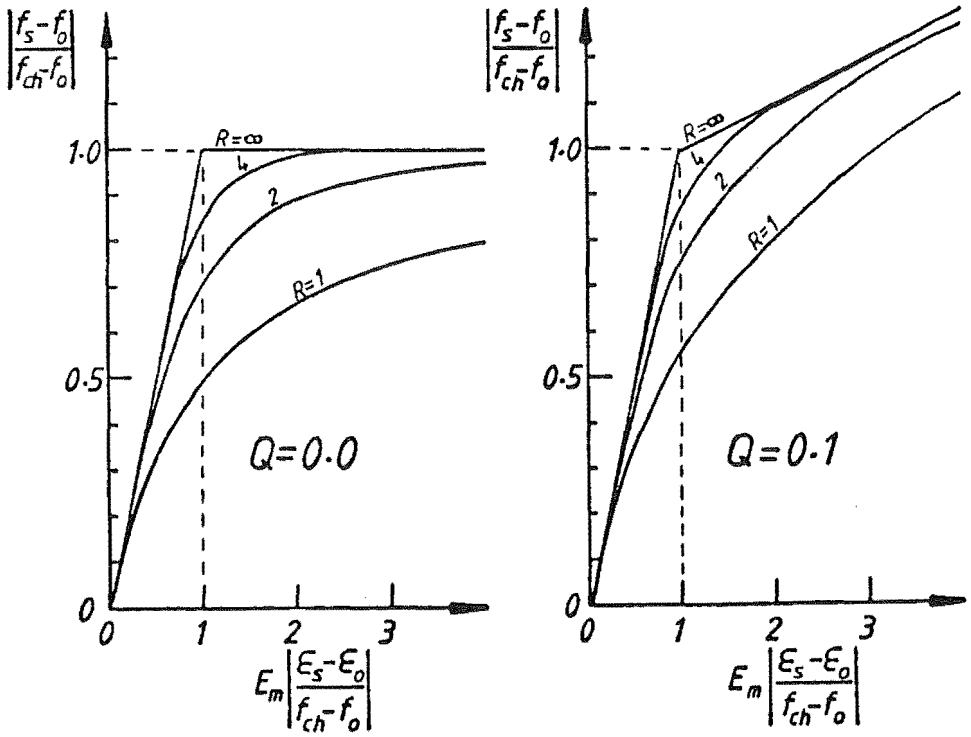

Fig. 2.26 - Menegotto-Pinto Function after Mander et al (1984).

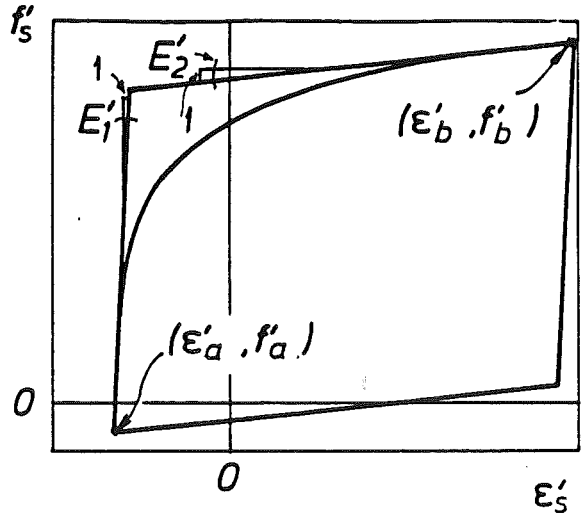

(a) Natural Coordinates

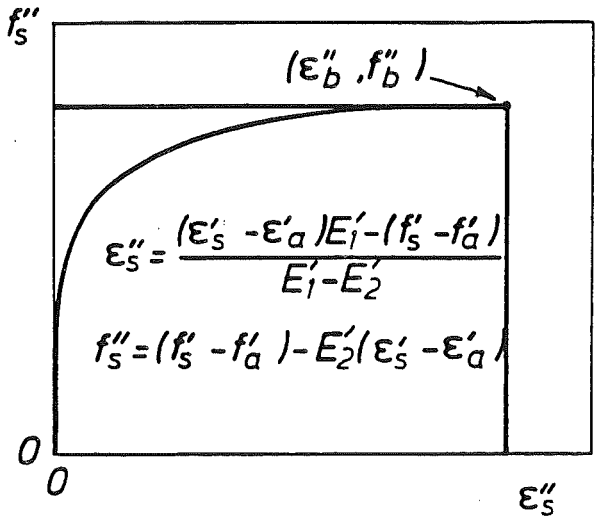

(b) Transformed Coordinates

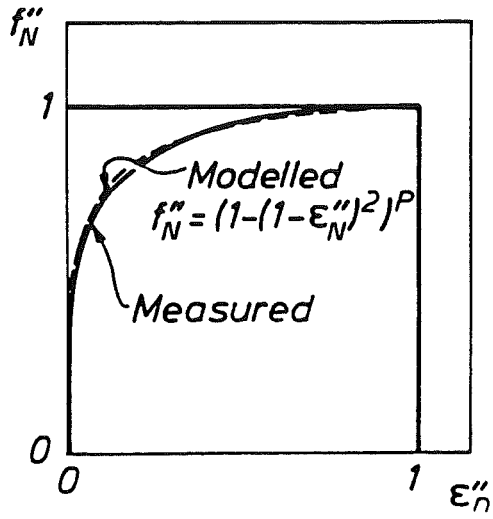

(c) Normalized Transformed Coordinates

Fig. 2.27 - Normalization of Bauschinger Effect.

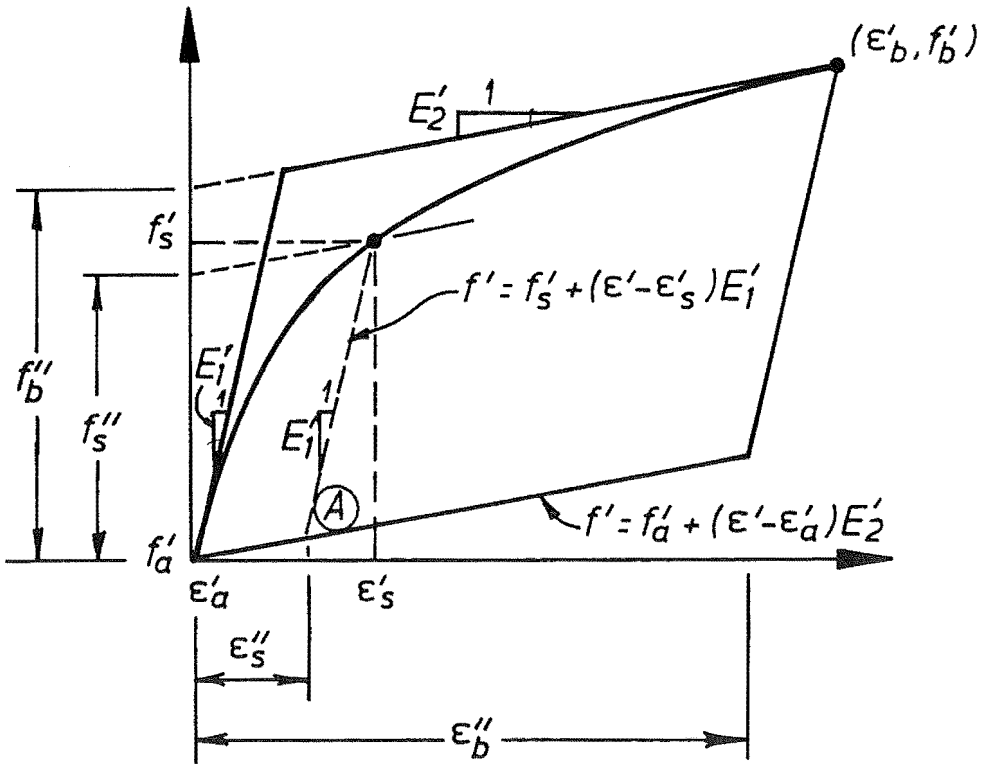

(a) Natural Coordinates

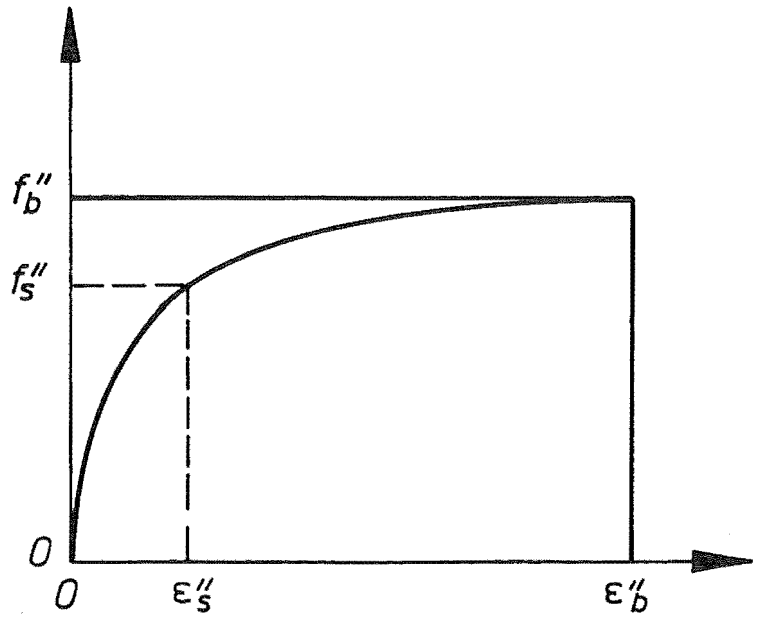

(b) Transformed Coordinates

Fig. 2.28 - Transformation of the Bauschinger Curve from the Natural to a Perfect-Rigid-Perfect-Plastic Coordinate System.

and therefore

$$\epsilon_s'' = \epsilon_A' - \epsilon_a' = \frac{E_1'\left(\epsilon_s' - \epsilon_a'\right) - \left(f_s' - f_a'\right)}{E_1' - E_2'} \tag{2.66}$$

The coordinates at the end of the curve, (ϵ_b',f_b'), transform to the coordinates (ϵ_b'',f_b''), as shown in Fig. 2.28 (b). These values can be calculated by substituting f_b' and ϵ_b' into Eqs. 2.62 and 2.66 respectively which yields

$$f_b'' = \left(f_b' - f_a'\right) - E_2'\left(\epsilon_b' - \epsilon_a'\right) \tag{2.67}$$

and

$$\epsilon_b'' = \frac{E_1'\left(\epsilon_b' - \epsilon_a'\right) - \left(f_b' - f_a'\right)}{E_1' - E_2'} \tag{2.68}$$

The normalized transformed coordinates, (ϵ_N'',f_N''), are calculated by dividing the transformed coordinates by the coordinates (ϵ_b'',f_b''), as shown in Fig. 2.27 (c). Therefore, the normalized transformed stress, f_N'', is

$$f_N'' = \frac{f_s''}{f_b''} = \frac{\left(f_s' - f_a'\right) - E_2'\left(\epsilon_s' - \epsilon_a'\right)}{\left(f_b' - f_a'\right) - E_2'\left(\epsilon_b' - \epsilon_a'\right)} \tag{2.69}$$

and the normalized transformed strain, ϵ_N'', is

$$\epsilon_N'' = \frac{\epsilon_s''}{\epsilon_b''} = \frac{\left(f_s' - f_a'\right) - E_1'\left(\epsilon_s' - \epsilon_a'\right)}{\left(f_b' - f_a'\right) - E_1'\left(\epsilon_b' - \epsilon_a'\right)} \tag{2.70}$$

If (ϵ_a',f_a'), (ϵ_b',f_b'), E_1', and E_2' are known, then for a given set of coordinates (ϵ_s',f_s'), the corresponding coordinates (ϵ_N'',f_N'') can be found using Eqs. 2.69 and 2.70.

The curvature at the beginning and the end of the normalized Bauschinger curves were found to be different. A family of curves that exhibits a similar behaviour is

$$f_N'' = \left(1 - \left(1 - \epsilon_N''\right)^2\right)^P \tag{2.71}$$

where the exponent "P" is empirically determined.

If (ϵ'_a,f'_a), (ϵ'_b,f'_b), E'_1, E'_2, and P are known, then for a given natural strain ϵ'_s, the corresponding coordinates (ϵ''_N,f''_N) can be found as follows. Rearranging Eqs. 2.69 and 2.70 in terms of f'_s and equating them yields

$$f''_N\left[\left(f'_b - f'_a\right) - E'_2\left(\epsilon'_b - \epsilon'_a\right)\right] + E'_2\left(\epsilon'_s - \epsilon'_a\right) + f'_a = \epsilon''_N\left[\left(f'_b - f'_a\right) - E'_1\left(\epsilon'_b - \epsilon'_a\right)\right] + E'_1\left(\epsilon'_s - \epsilon'_a\right) + f'_a \tag{2.72}$$

Solving Eq. 2.72 in terms of f''_N gives

$$f''_N = \frac{\epsilon''_N\left[\left(f'_b - f'_a\right) - E'_1\left(\epsilon'_b - \epsilon'_a\right)\right] + (E'_1 - E'_2)\left(\epsilon'_s - \epsilon'_a\right)}{\left(f'_b - f'_a\right) - E'_2\left(\epsilon'_b - \epsilon'_a\right)} \tag{2.73}$$

Combining Eqs. 2.71 and 2.73 gives

$$\left(1 - \left(1 - \epsilon''_N\right)^2\right)^P = \frac{\epsilon''_N\left[\left(f'_b - f'_a\right) - E'_1\left(\epsilon'_b - \epsilon'_a\right)\right] + (E'_1 - E'_2)\left(\epsilon'_s - \epsilon'_a\right)}{\left(f'_b - f'_a\right) - E'_2\left(\epsilon'_b - \epsilon'_a\right)} \tag{2.74}$$

in which the only unknown value is ϵ''_N.

Eq. 2.74 can be solved by using a Newton-Raphson algorithm on the function

$$f(\epsilon''_N) = (1 - (1 - \epsilon''_N)^2)^P - c_1\epsilon''_N - c_2 = 0 \tag{2.75}$$

where

$$c_1 = \frac{f'_b - f'_a - E'_1(\epsilon'_b - \epsilon'_a)}{f'_b - f'_a - E'_2(\epsilon'_b - \epsilon'_a)} \tag{2.76}$$

and

$$c_2 = \frac{(E'_1 - E'_2)(\epsilon'_s - \epsilon'_a)}{f'_b - f'_a - E'_2(\epsilon'_b - \epsilon'_a)} \tag{2.77}$$

The derivative of Eq. 2.75 is

$$\frac{df(\epsilon''_N)}{d\epsilon''_N} = 2P(1 - (1 - \epsilon''_N)^2)^{P-1}(1 - \epsilon''_N) - c_1 \tag{2.78}$$

An initial approximation for ϵ_N'' can be

$$\epsilon_N'' \approx \frac{\epsilon_s' - \epsilon_a'}{\epsilon_b' - \epsilon_a'} \tag{2.79}$$

Then using the Newton-Raphson algorithm, improved approximations can be made as

$$(\epsilon_N'')_{new} = (\epsilon_N'')_{old} - \frac{(1-(1-(\epsilon_N'')_{old})^2)^P - c_1(\epsilon_N'')_{old} - c_2}{2P(1-(1-(\epsilon_N'')_{old})^2)^{P-1}(1-(\epsilon_N'')_{old}) - c_1} \tag{2.80}$$

The algorithm converges very rapidly and sufficient accuracy can normally be obtained in three iterations. For very small values of ϵ_N'' (say $\epsilon_N'' < 0.001$), the algorithm can give a negative value which makes the numerator and denominator of Eq. 2.80 undefined. For such a case, a bi-sectional algorithm can be performed. A Fortran computer code was written for a 16 bit computer. Eq. 2.80 is executed for five iterations or until $f(\epsilon_N'')$ in Eq. 2.75 is less than 0.001, whichever occurs first. If at any time an estimated value for ϵ_N'' is less than 0.02, then a bi-sectional analysis is begun in which the initial upper estimated value is the previous estimate for ϵ_N'' and the initial lower estimated value is nil. Bi-sectional iterations are conducted for five iterations or until $f(\epsilon_N'')$ in Eq. 2.75 is less than 0.03. The single-precision accuracy of the computer made tighter restraint on the convergence impossible.

Once ϵ_N'' is known, f_s' can be found by rearranging Eq. 2.70 to give

$$f_s' = \epsilon_N''\left[(f_b' - f_a') - E_1'(\epsilon_b' - \epsilon_a')\right] + E_1'(\epsilon_s' - \epsilon_a') + f_a' \tag{2.81}$$

In summary, when the Bauschinger curve is required, this approach is used as follows. The values for E_1', ϵ_a', and f_a', are known from Eqs. 2.50 and 2.49; E_2', ϵ_b', f_b' are also known. The calculation of P will be discussed in Section 2.5.4. For a given value of ϵ_s', ϵ_s'' can be calculated using Eqs. 2.79 and 2.80. Then f_s' can be found using Eq. 2.81.

The proposed algorithm has the disadvantage of requiring an iterative solution for every point on the Bauschinger curve. However, the values which define the curve and are required at each load-reversal are obtained directly unlike algorithms using the Ramberg-Osgood relationship (Eq. 2.60) or the Menegotto-Pinto function (Eq. 2.61) which require laborious trial-and-error procedures to obtain a curve which satisfies the desired boundary conditions. No tests were done to determine the required computational effort of this algorithm but it seems that the required effort is comparable to other Bauschinger curve algorithms. For a single stress-strain history with many points on each curve, the proposed algorithm may require slightly more computational effort. However, for a reinforced-concrete sectional analysis with many layers of reinforcing steel, the proposed algorithm probably requires less effort because such an analysis requires an iterative solution of the section centroid axial strain and curvature. Each trial combination of strain and curvature typically assumes that at least one layer of steel is subjected to a strain reversal.

It is also important to know the tangential slope of the stress-strain relationship because minor and simple reversals must rejoin the previously departed from curves at the appropriate slope. The slope of the normalized transformed curve is the first derivative of Eq. 2.71, which is

$$\frac{df_N''}{d\epsilon_N''} = 2P\left(1 - \left(1 - \epsilon_N''\right)^2\right)^{P-1}\left(1 - \epsilon_N''\right) \tag{2.82}$$

The transformation of the slope from the normalized coordinate system to the transformed coordinate system is

$$\frac{df_s''}{d\epsilon_s''} = \frac{df_N''}{d\epsilon_N''}\frac{f_b''}{\epsilon_b''} \tag{2.83}$$

where f_b'' comes from Eq. 2.67 and ϵ_b'' from Eq. 2.68.

Difficulty was encountered in transforming slope from the transformed coordinate system to the natural coordinate system and so some simplifying assumptions were made. Initially, the transformation was done with the assumption that the second slope, E_2', is zero. For this case,

$$\epsilon_s'' = \epsilon_s' - \frac{f_s'}{E_1'} \Rightarrow \epsilon_s' = \epsilon_s'' + \frac{f_s'}{E_1'} \tag{2.84}$$

and

$$f_s'' = f_s' \tag{2.85}$$

from the chain rule for differentiation,

$$\frac{df_s''}{d\epsilon_s''} = \frac{df_s'}{d\epsilon_s'}\frac{df_s''}{df_s'}\frac{d\epsilon_s'}{d\epsilon_s''} \tag{2.86}$$

since

$$\frac{df_s''}{df_s'} = 1 \tag{2.87}$$

and

$$\frac{d\epsilon_s'}{d\epsilon_s''} = 1 + \frac{df_s'}{d\epsilon_s''}\frac{1}{E_1'} = 1 + \frac{df_s''}{d\epsilon_s''}\frac{1}{E_1'} \tag{2.88}$$

then

$$\frac{df_s''}{d\epsilon_s''} = \frac{df_s'}{d\epsilon_s'}\left(1 + \frac{df_s''}{d\epsilon_s''}\frac{1}{E_1'}\right) \tag{2.89}$$

Equation 2.89 can be rearranged to

$$\frac{df_s'}{d\epsilon_s'} = \frac{\frac{df_s''}{d\epsilon_s''}}{1 + \frac{df_s''}{d\epsilon_s''}\frac{1}{E_1'}} = \frac{\frac{df_s''}{d\epsilon_s''}E_1'}{\frac{df_s''}{d\epsilon_s''} + E_1'} \tag{2.90}$$

Because E_1' is much greater than E_2', sufficient accuracy for the slope of the curve in natural coordinate system can be obtained by simply adding E_2' to Eq. 2.90. Therefore, it is assumed that

$$\frac{df_s'}{d\epsilon_s'} = \frac{\frac{df_s''}{d\epsilon_s''}E_1'}{\frac{df_s''}{d\epsilon_s''} + E_1'} + E_2' \leq E_u' \tag{2.91}$$

The upper bound shows that it is not possible for the slope to exceed the unloading modulus, E_u'. This slope will typically overestimate the actual slope by less than 1% for a major reversal.

2.5.4 Calibration of the Normalized Bauschinger Effect

2.5.4.1 Major Reversals

(a) Shape of the Bauschinger Effect in the Lüders Strain or Yield Plateau Region

An analysis of the Bauschinger curves of tests H and M indicated that after normalization, a unique curve of the family of curves given by Eq. 2.71 described accurately the non-linear behaviour in this region:

$$f_N'' = \left(1 - (1 - \epsilon_N'')^2\right)^{0.35} \tag{2.92}$$

where for simplicity the exponent term "P" in Eq. 2.71 is considered constant and equal to 0.35.

(b) Shape of the Bauschinger Effect in the Work Hardened Region

Unlike the unique relationship adopted for modelling the Bauschinger effect in the Lüders strain or yield plateau region, it was found that in the work hardened region the exponent term "P" is not constant. The shape of the normalized Bauschinger curve is softer at the beginning of the work hardened region. In other words, the area under the normalized Bauschinger curve increases as the material is work hardened.

The shape of the normalized Bauschinger curves was quantified by evaluating the area under the curve between 0 and 0.1 as shown in Fig. 2.29 (a). This second limit is realistic in terms of the amplitude of reversals often encountered in seismic tests of reinforced concrete members. Besides, it permitted the evaluation of a large number of reversal cycles from the conducted tests. Thus, all reversals from tests H and M which could be normalized to the second limit were analyzed. The area under the normalized curve, Ω, is given by:

$$\Omega = \int_0^{0.1} f_N'' \, d\epsilon_N'' \tag{2.93}$$

these Ω values were correlated with the variables f_p'/f_t' and $\epsilon_p'/\epsilon_{su}'$ as seen in Fig. 2.29 (b), where

$$\begin{aligned} f_p' &= f_{su}'\left(s - \epsilon_{su,shift}'(k) + \epsilon_a'(m)\right) - f_a'(m) \\ f_t' &= f_{su}'\left(2 - \epsilon_{su,shift}'(1) + \epsilon_{su,shift}'(2)\right) \\ \epsilon_p' &= \left|\epsilon_{su,shift}'(k) - \epsilon_a'(m)\right| \end{aligned} \tag{2.94}$$

and the following empirical relation was obtained:

$$\Omega = \left(\frac{f_p'}{f_t'} - 0.69\right)\left(0.001 + \frac{0.00108}{1.043 - \dfrac{\epsilon_p'}{\epsilon_{su}'}}\right)\frac{1}{0.18} + 0.085 \tag{2.95}$$

Eq. 2.95 is shown in Fig. 2.30 for clarity.

The exponent term "P" of Eq. 2.71 can be calculated if the area of the measured curve, Ω, is equated to the area of the model curve, that is:

$$\Omega = \int_0^{0.1}\left(1 - (1 - \epsilon_N'')^2\right)^P d\epsilon_N'' \tag{2.96}$$

The above expression requires an explicit form of the indefinite integral of the model curve which in this case is not available. Thus a numerical approach was adopted. The integral of the model

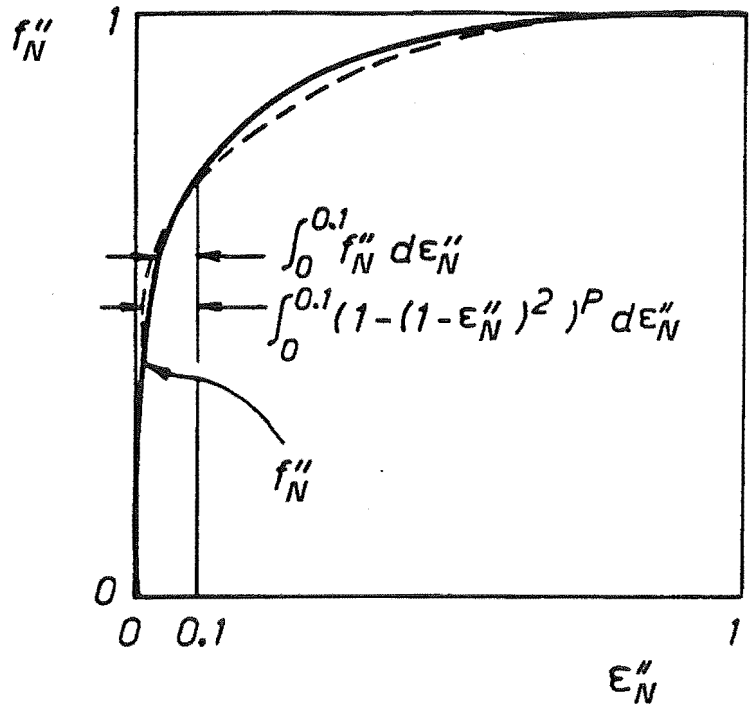

(a) Evaluation of Bauschinger Effect

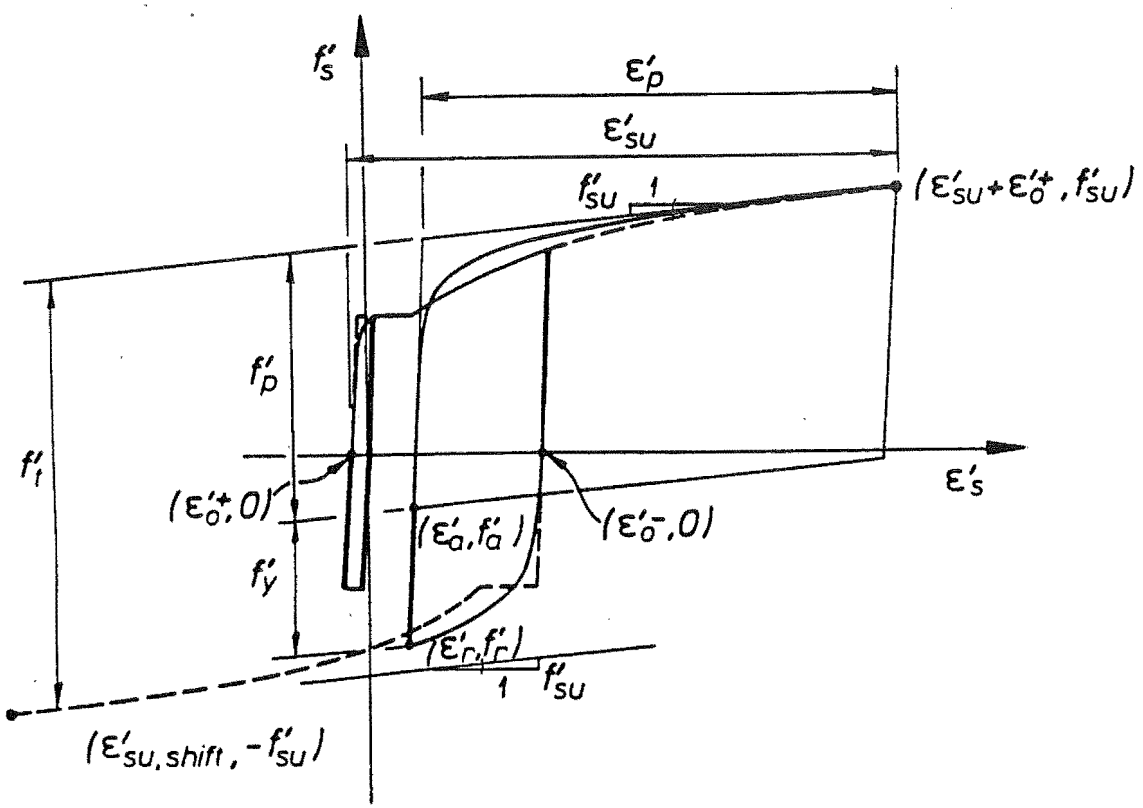

(b) Calibration of Bauschinger Curve

Fig. 2.29 - Calibration of the Shape of the Bauschinger Effect.

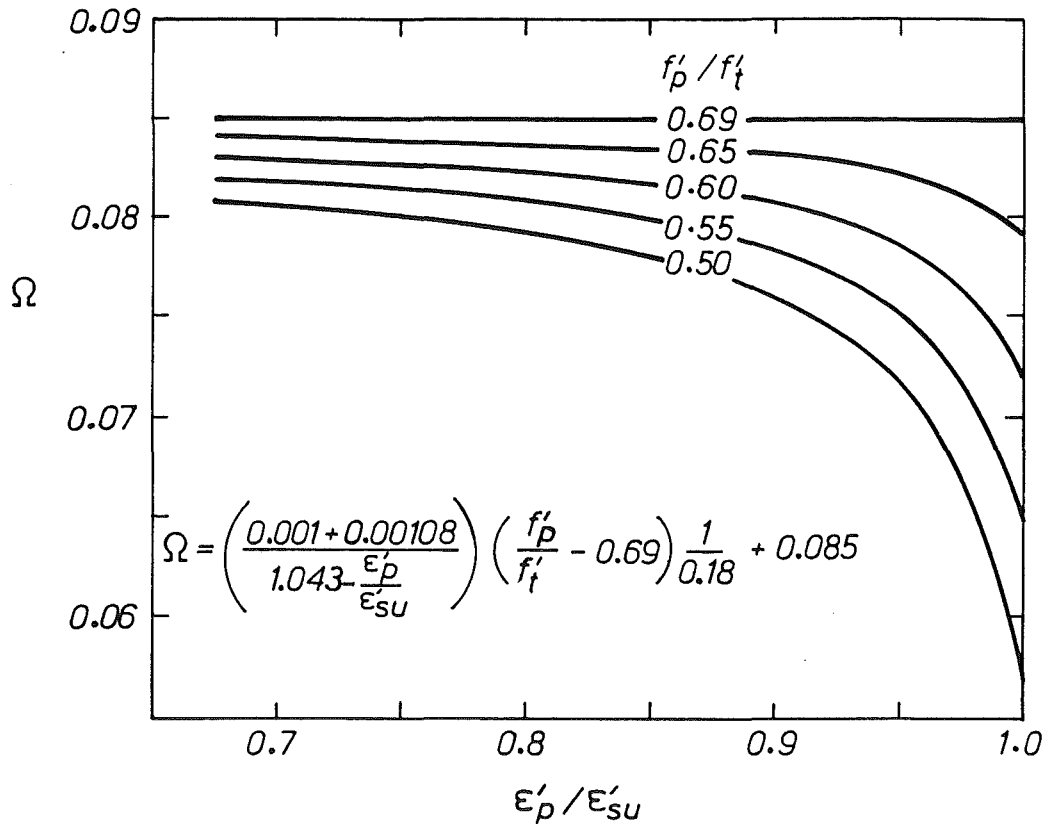

Fig. 2.30 - Empirical Relation to Estimate the Shape of Bauschinger Effect.

curve was numerically evaluated for a range of values of "P" between 0.06 and 0.30. Then, a parabolic relationship was fitted to obtain an approximate form of the indefinite integral within this range. The following expression was found:

$$\int_0^{0.1}\left(1-(1-\epsilon''_N)^2\right)^P d\epsilon''_N \approx 0.12 - \sqrt{\frac{1}{530.84} - \frac{(0.1-P)}{56.689}} \qquad (2.97)$$

for $0.06 \le P \le 0.30$

Substituting Eq. 2.96 into Eq. 2.97 and rearranging for P gives

$$P = 56.689(\Omega - 0.077)^2 - 4.921(\Omega - 0.077) + 0.1 \qquad (2.98)$$

In summary, at each reversal f'_p, f'_t and ϵ'_p are calculated using Eq. 2.94. Then Ω is solved using Eq. 2.95 and finally P is calculated using Eq. 2.98.

2.5.4.2 Minor and Simple Reversals

Minor and simple reversals are more relevant to cycles within the Lüders strain region, it was decided to use Eq. 2.92. The modelled Bauschinger effect of minor reversals in the strain hardening region shows an acceptable fitting.

2.6 TEST RESULTS

2.6.1 Measured and Predicted Stress-Strain Behaviour

2.6.1.1 General

The analytical model discussed in the previous section was calibrated with data from machined coupon tests H and M. The following assumptions were made and therefore it would be expected that results from tests carried out under other conditions may differ.

a) The number of cycles, even if of large strain amplitude, is too small for considering low-cycle fatigue as having an important influence in the ultimate conditions of the tests.

b) Buckling has no effect on the test results.

c) The change in ambient temperature is small enough to be considered constant throughout the experimental period.

d) Strain ageing effects do not develop in any of the test that were carried out continuously.

The first assumption has been made because, in the present work the maximum number of reversals was 28, including strain reversals of up to 7%. The measured strain at ultimate load in the natural coordinate system was 0.90-1.07 of the predicted one accounting for the shift of origin using Eqs. 2.53 or 2.56 and ignoring the number of cycles. The effects of "low cycle fatigue" will be addressed in Section 2.7.

Test results indicate that buckling in test coupons H and M only occurred at large compressive strains in the monotonic compression tests so the second assumption can largely be held true. In cyclic tests the maximum difference between the two side extensometers was of the order of 0.3%, which is negligible. As explained before, one of the aims of this study was to separate the material behaviour from the combined material and geometrical behaviour and minimise buckling effects.

Table 2.4
Parameters to Describe the Monotonic Tensile Curve for Use in the Analytical Model

Test Type	f_y (MPa)	f_{su} (Mpa)	ϵ_{sh} (%)	ϵ_{su} (%)	E_s (MPa)	$\epsilon_{sh,1}$ (%)	$f_{sh,1}$ (MPa)
M	295.4	479.5	1.600	20.7	210000	5.300	420.0
H	467.0	660.0	1.280	14.5	216000	4.500	600.0
MJ	319.0	476.0	2.200	22.5	197000	3.930	380.0
HV	482.0	641.0	1.780	14.6	199000	5.100	591.6
HX	447.0	605.0	1.700	15.8	196000	5.100	552.3
Leslie	384.6	690.3	0.625	12.0	200000	2.000	499.0
T-F[1]	320.0	460.0	2.250	18.9	192000	5.000	400.0
Test Type	f_y (ksi)	f_{su} (ksi)	ϵ_{sh} (%)	ϵ_{su} (%)	E_s (ksi)	$\epsilon_{sh,1}$ (%)	$f_{sh,1}$ (ksi)
K-P[2] (B25)	42.7	64.1	(1.500)	(18.0)	31300	(2.500)	(46.0)
K-P[2] (B29)	42.7	67.2	[1.600]	[18.0]	25600	[4.000]	[54.0]
Aktan et al	68.0	108.2	1.050	18.77	29305	2.568	86.9

1) T-F = Tjokrodimuljo-Fenwick
2) K-P = Kent-Park
( ) = values estimated by authors
[ ] = dummy values not required in analysis

The third assumption is almost true. All tests were conducted at ambient temperature which was kept approximately constant.

It can be said that strain ageing commences immediately after the test specimen undergoes a plastic state. However, these effects are minimum given the temperature conditions and the duration of the tests and hence will be ignored. The maximum duration of a test was approximately 6 hours yet the ultimate load was comparatively similar to the one recorded in monotonic tests. Strain ageing effects were therefore insignificant.

The prediction of the test results was obtained from the computer program STEELTEST which calls the subroutine STEEL. STEELTEST and STEEL are given in Appendix A. The input parameters required by STEEL are those of the monotonic tensile test. Table 2.4 shows the parameters input to the program which was reported in the literature or estimated by the authors when such information was not reported.

2.6.1.2 Machined H and M Coupons

A series of tests were conducted on H and M steel coupons varying from simple monotonic tension and compression tests to tests with several reversals.

Fig. 2.31 shows the measured and modelled monotonic tension curves of an H coupon of Grade 430 steel. There is a very close agreement between the measured and predicted compression curves as seen in Fig. 2.32. The compression H steel coupons were machined to 18mm diameter because of the limitations on the capacity of the Instron Universal Testing Machine. Similar results were obtained for test coupons M for Grade 300 steel as shown in Figs. 2.38 and 2.39. A barrelling effect caused by the confinement provided by the tapered ends was characteristic of test coupons subjected to large compressive strains. Also, these specimens showed a buckling mode at the end of the test. Both effects can be clearly seen in Fig. 2.10.

Results of cyclic tests on H steel coupons are illustrated in Figs. 2.33 to 2.37 and Figs. 2.40 to 2.46 for tests on M steel coupons. The prediction of these results is expected to be accurate as they were used in the calibration of the model.

2.6.1.3 Tests on Deformed Bar Coupons

The two main points of interest in the tests performed on deformed bar coupons are the effect of deformations and the predictions of the model on specimens of the same type of steel of a different heat and bar diameter.

Figs. 2.47 and 2.48 shows monotonic test results on HV coupons. It can be seen that the predicted monotonic compression curve accurately matches the measured behaviour to strains up to 6% in spite of the early buckling which commenced at a strain of 2%. Similar results were obtained for test coupons HX, seen in Fig. 2.19 (b), and MJ, which are not presented in this report. It can be concluded that the overall behaviour is not affected by the deformations in the reinforcing steel bars.

Figs. 2.49 to 2.51 show cyclic tests on test coupons HX, HV and MJ respectively. The measured and predicted behaviour of the model are in close agreement which appears to validate the calibration of the model for use on the two current Grades 300 and 430 reinforcing steels manufactured in New Zealand.

2.6.1.4 Prediction of Tests by Other Researchers

(a) Tests on Grade 275 Steel

Grade 275 steel has been superseded in New Zealand by the new Grade 300 steel. The new Grade 300 steel shows similar characteristics to the old Grade 275 steel [NZS 3402 (1989)].

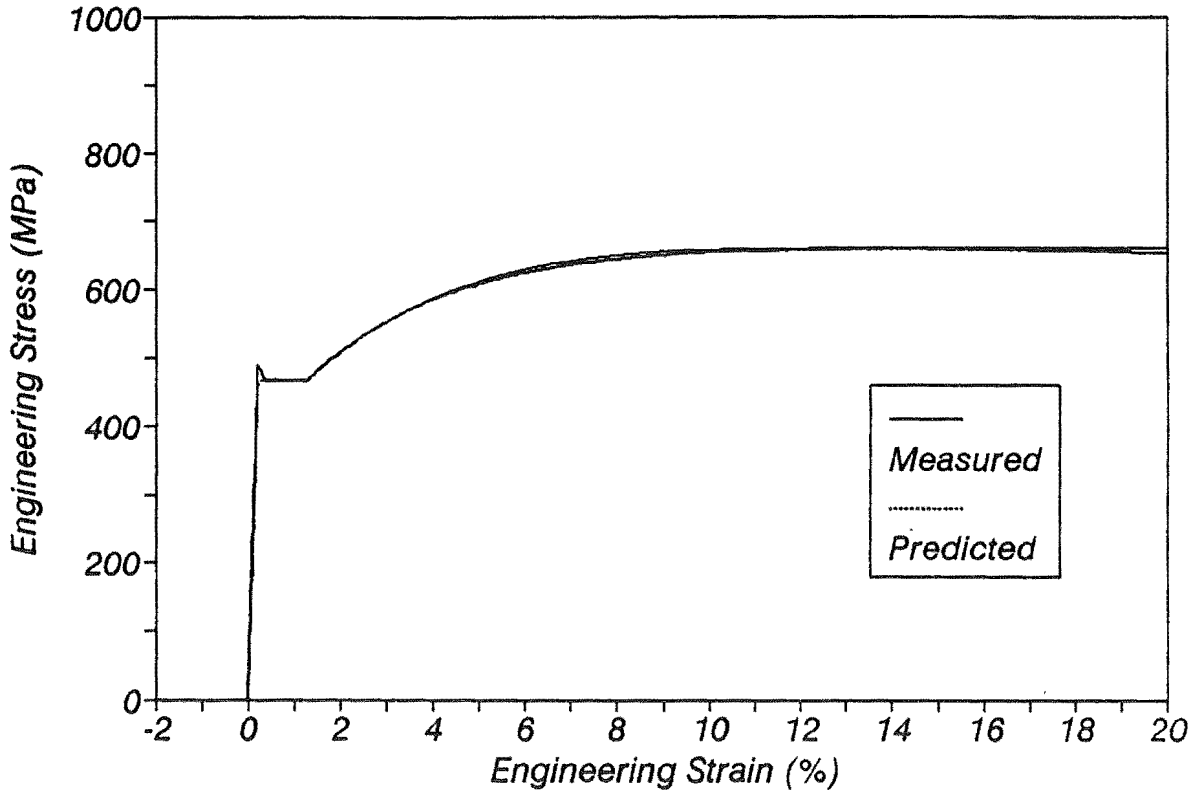

Fig. 2.31 - Measured and Modelled Stress-Strain Behaviour for Test HST03.

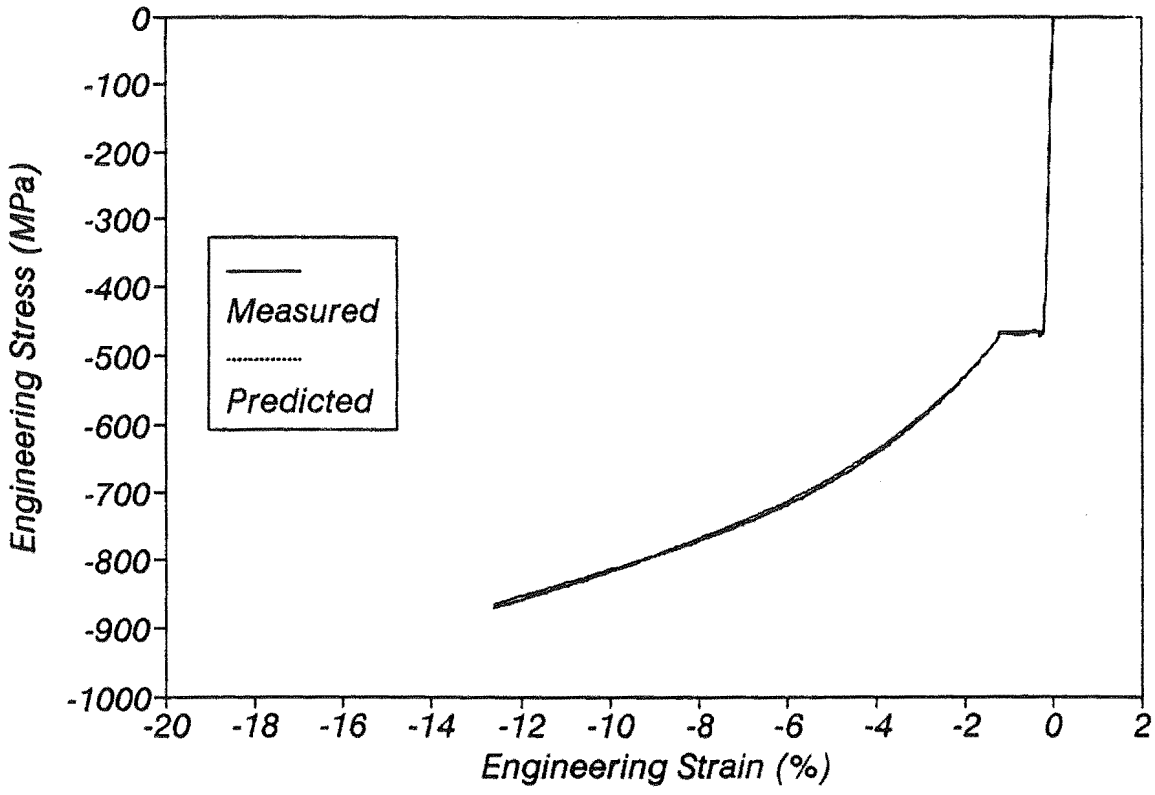

Fig. 2.32 - Measured and Modelled Stress-Strain Behaviour for Test HSC04.

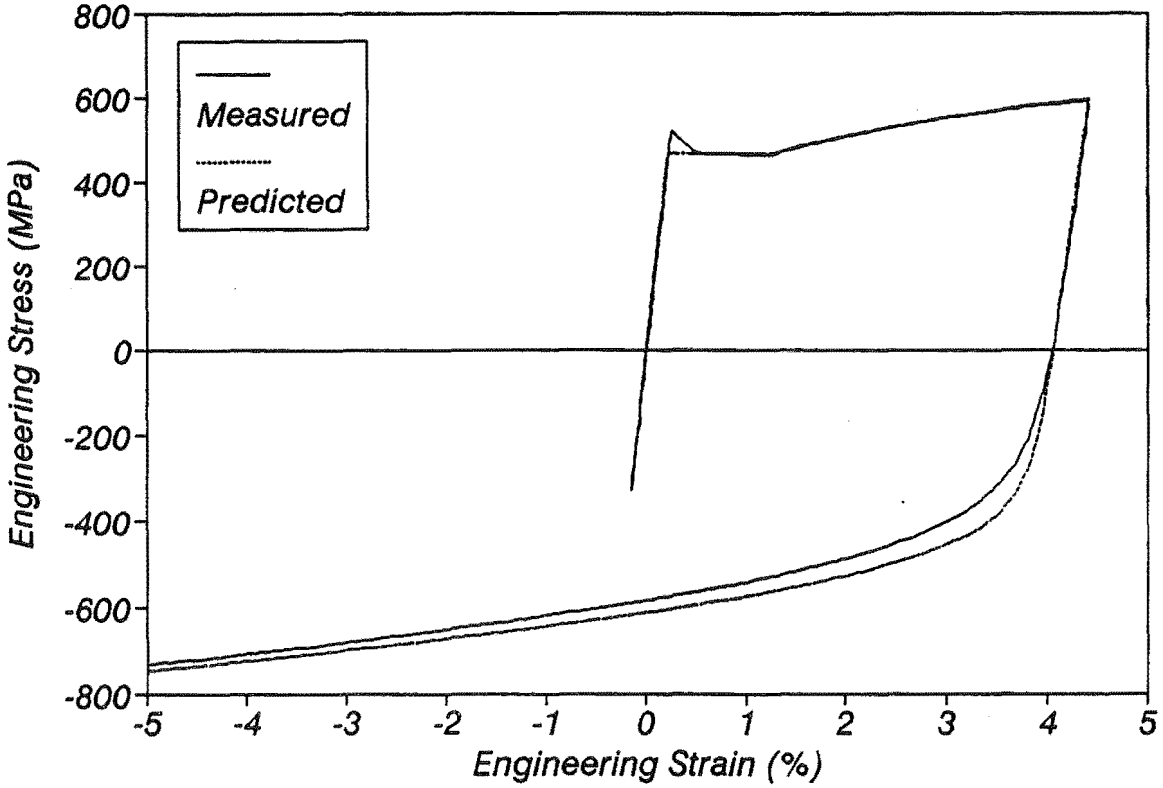

Fig. 2.33 - Measured and Modelled Stress-Strain Behaviour for Test H1CS1.

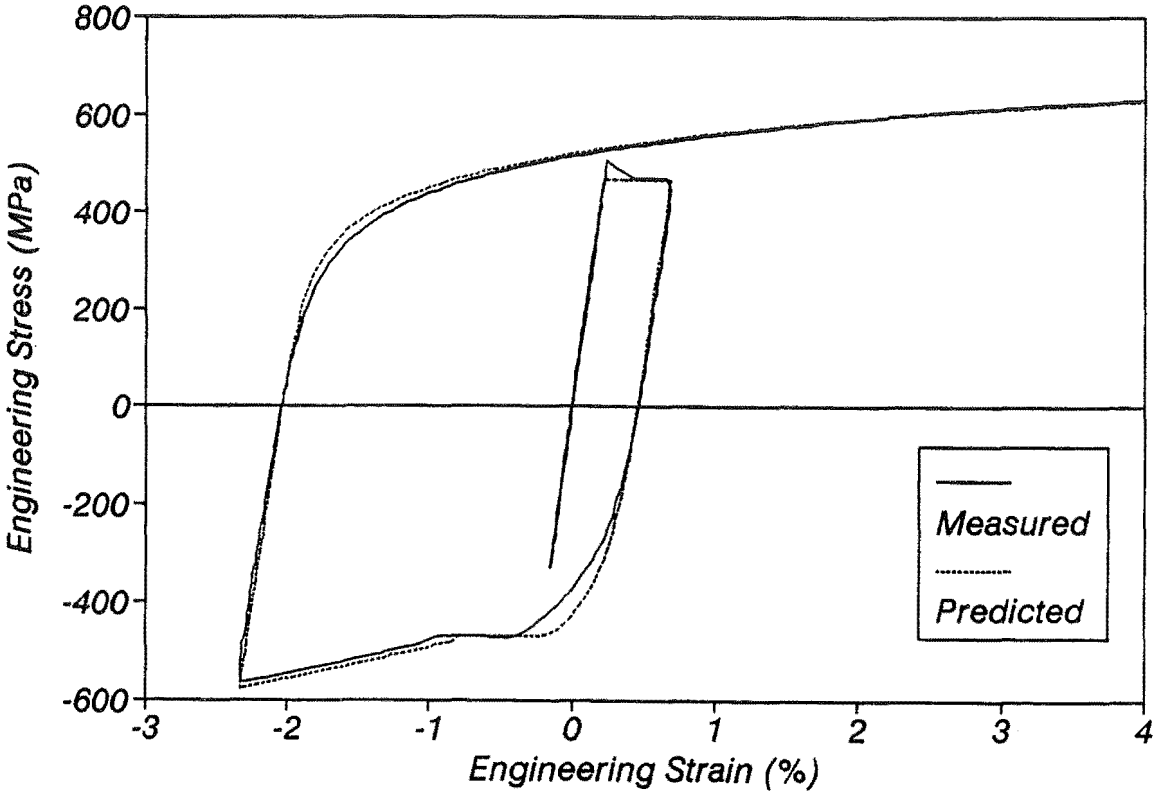

Fig. 2.34 - Measured and Modelled Stress-Strain Behaviour for Test H2TY11.

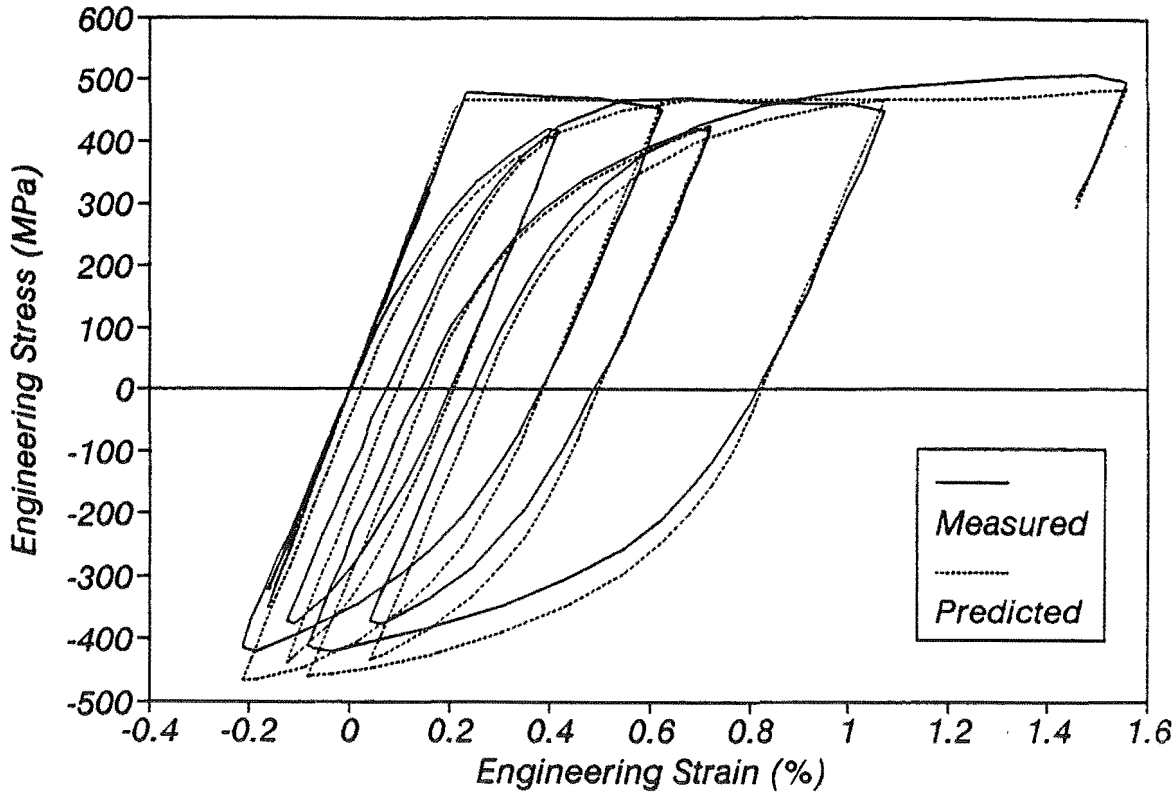

Fig. 2.35 - Measured and Modelled Stress-Strain Behaviour for Test HSG1.

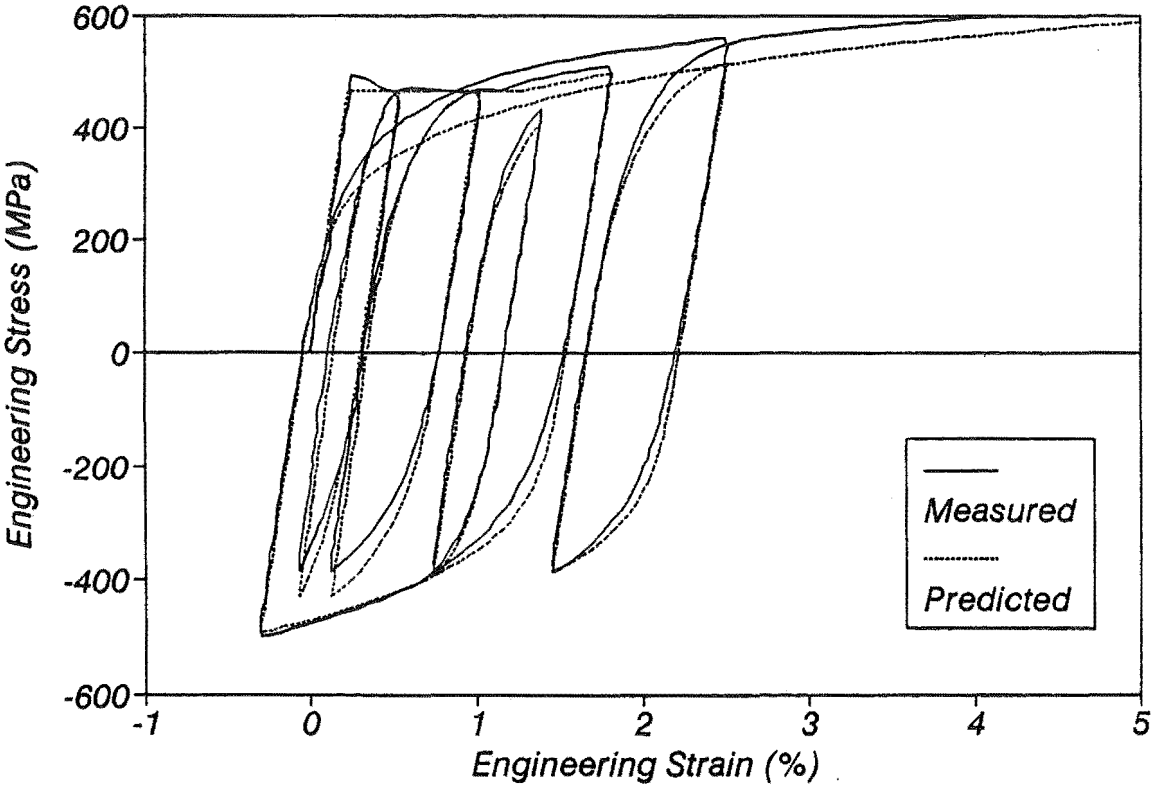

Fig. 2.36 - Measured and Modelled Stress-Strain Behaviour for Test H10TS1.

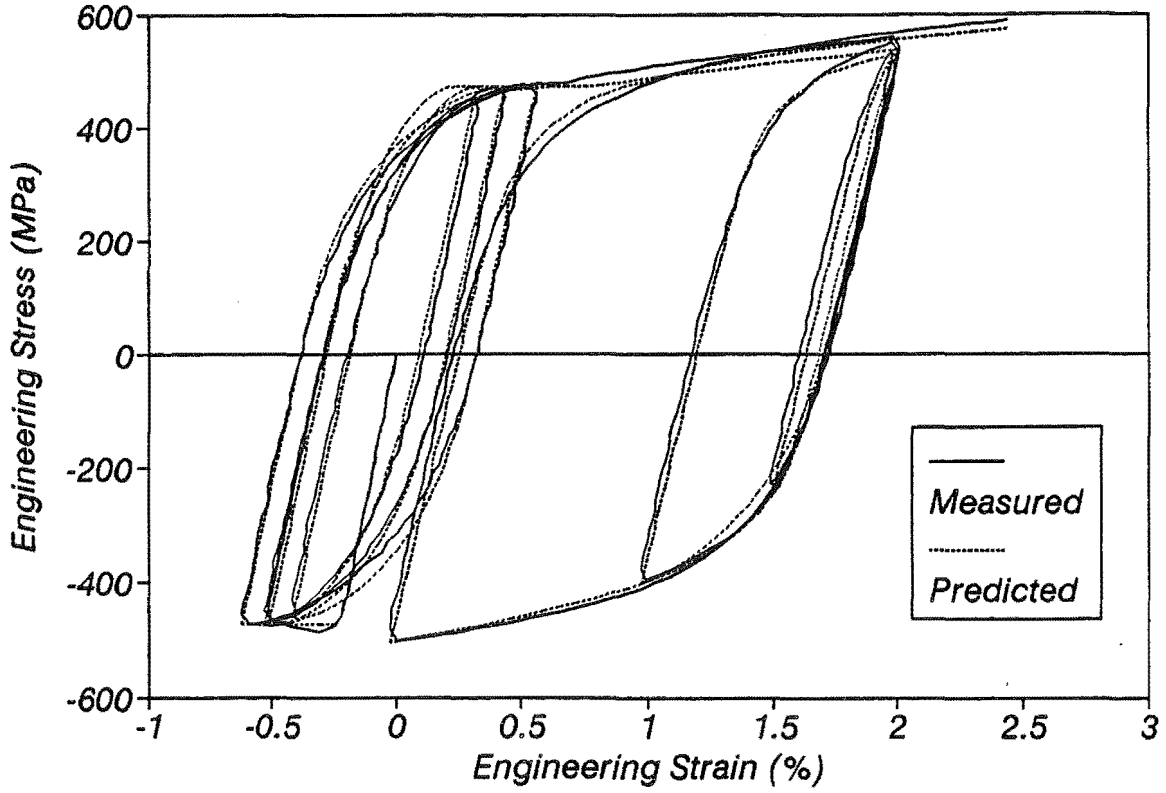

(a) Initial Cycles

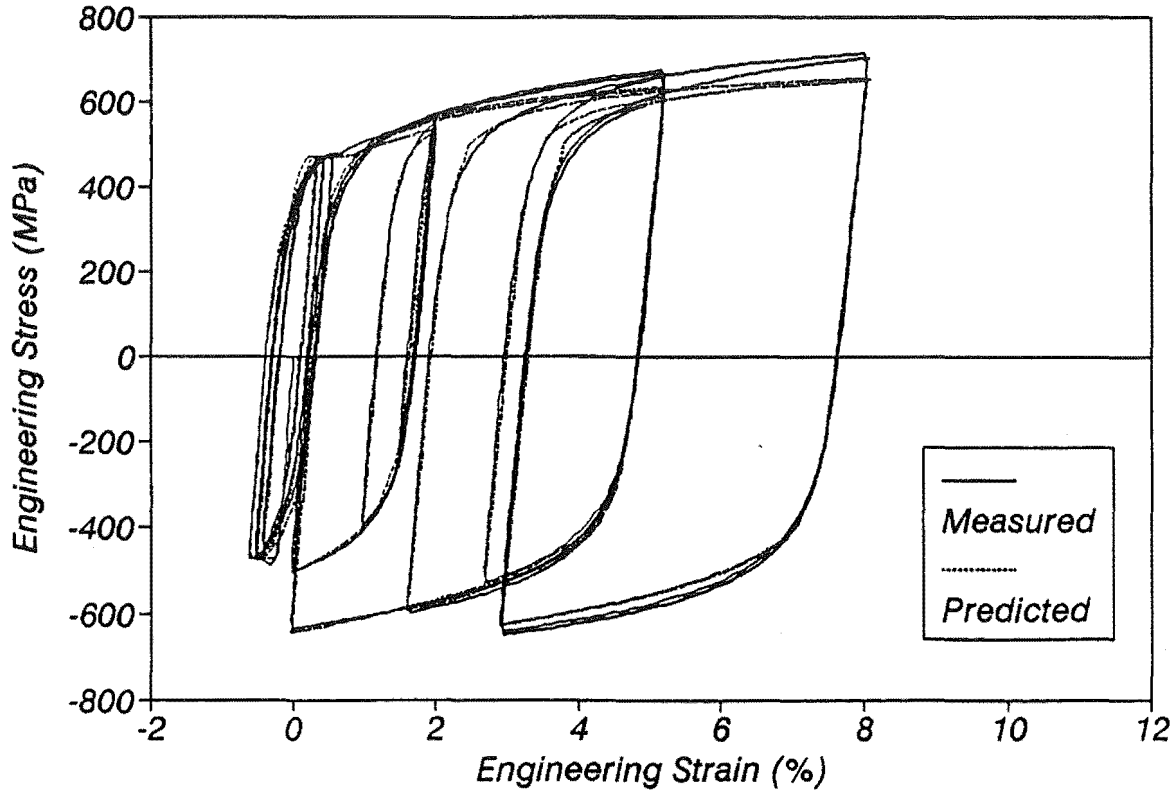

(b) Complete Test

Fig. 2.37 - Measured and Modelled Stress-Strain Behaviour for Test HD28.

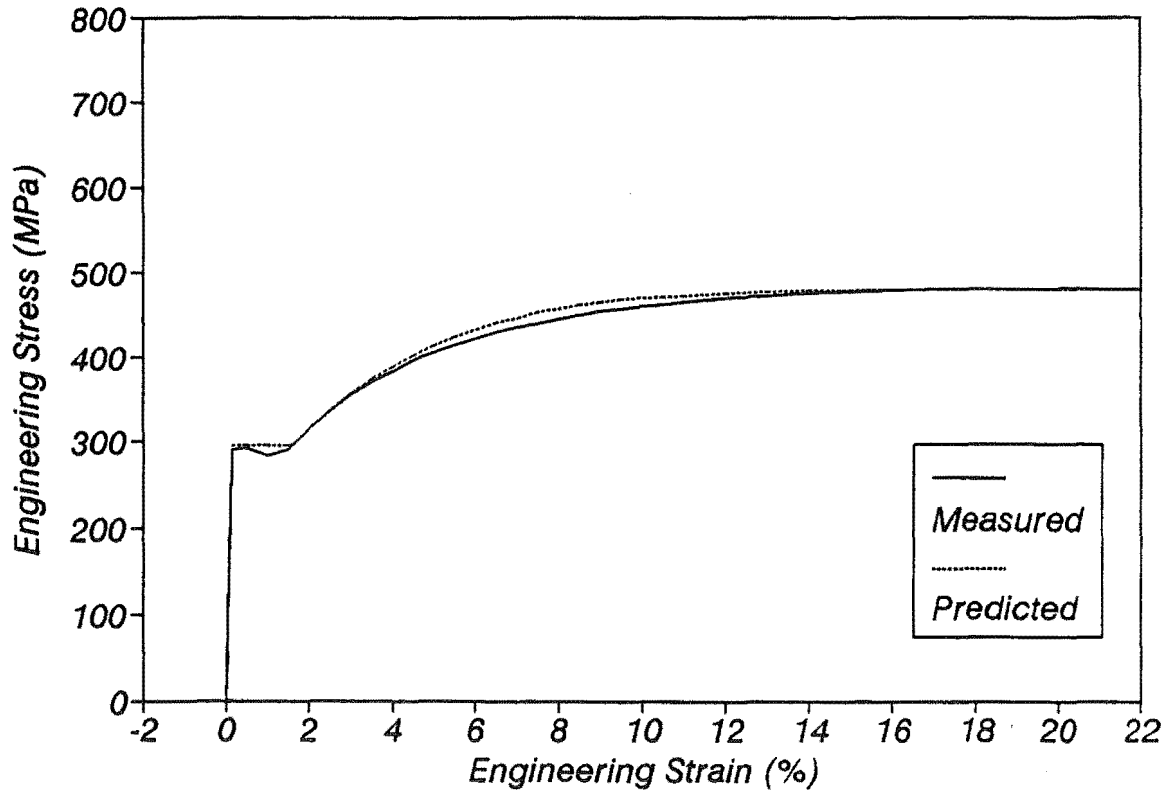

Fig. 3.38 - Measured and Modelled Stress-Strain Behaviour for Test MST02.

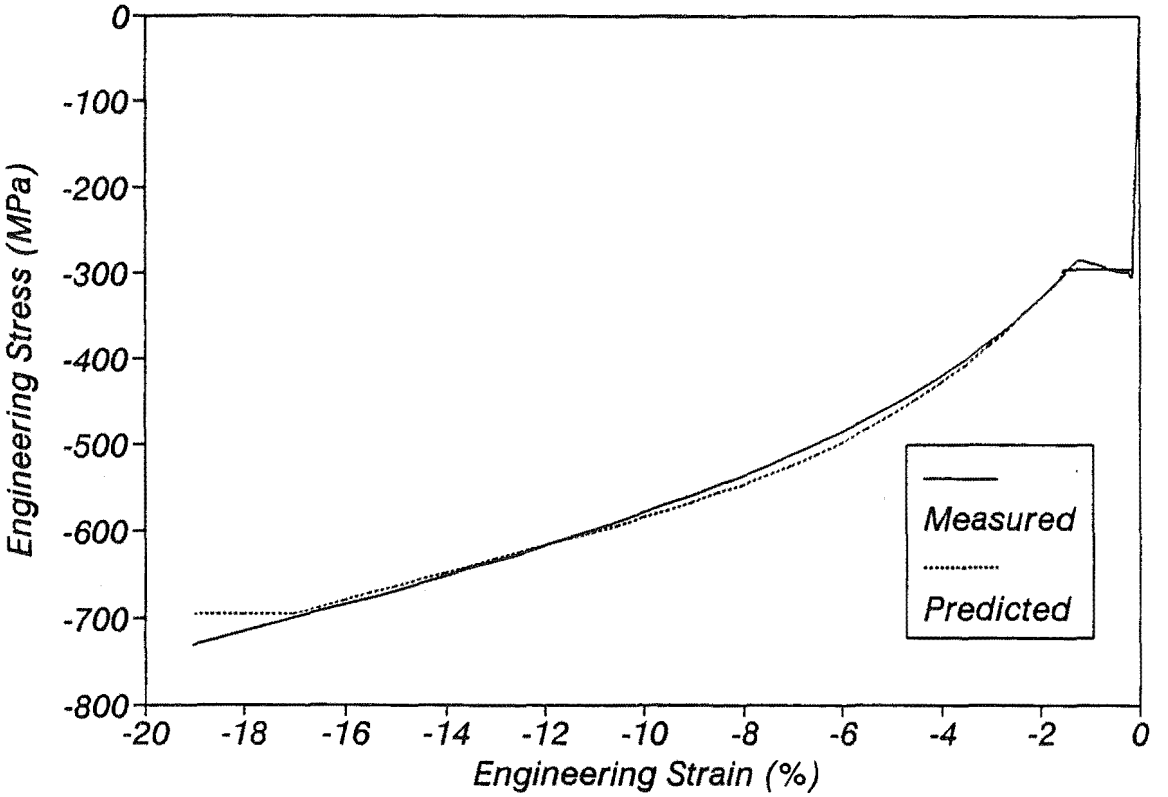

Fig. 2.39 - Measured and Modelled Stress-Strain Behaviour for Test MSC03.

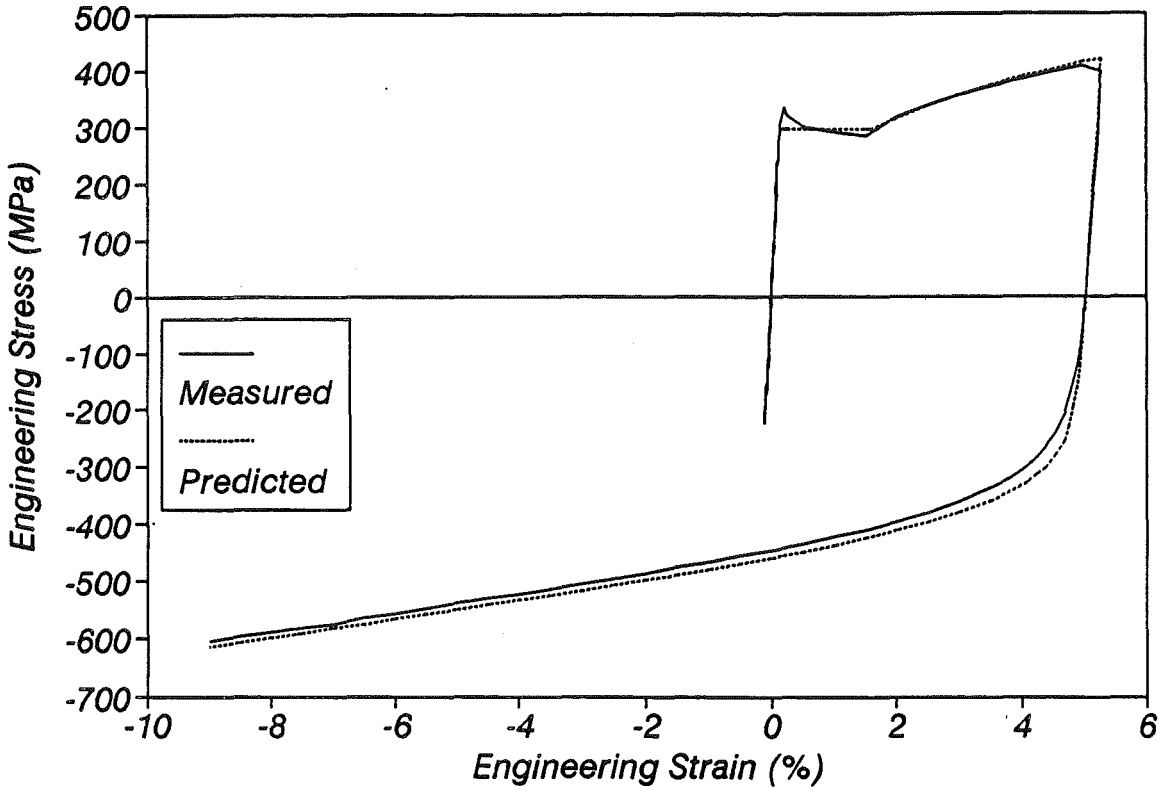

Fig. 2.40 - Measured and Modelled Stress-Strain Behaviour for Test M1CS1.

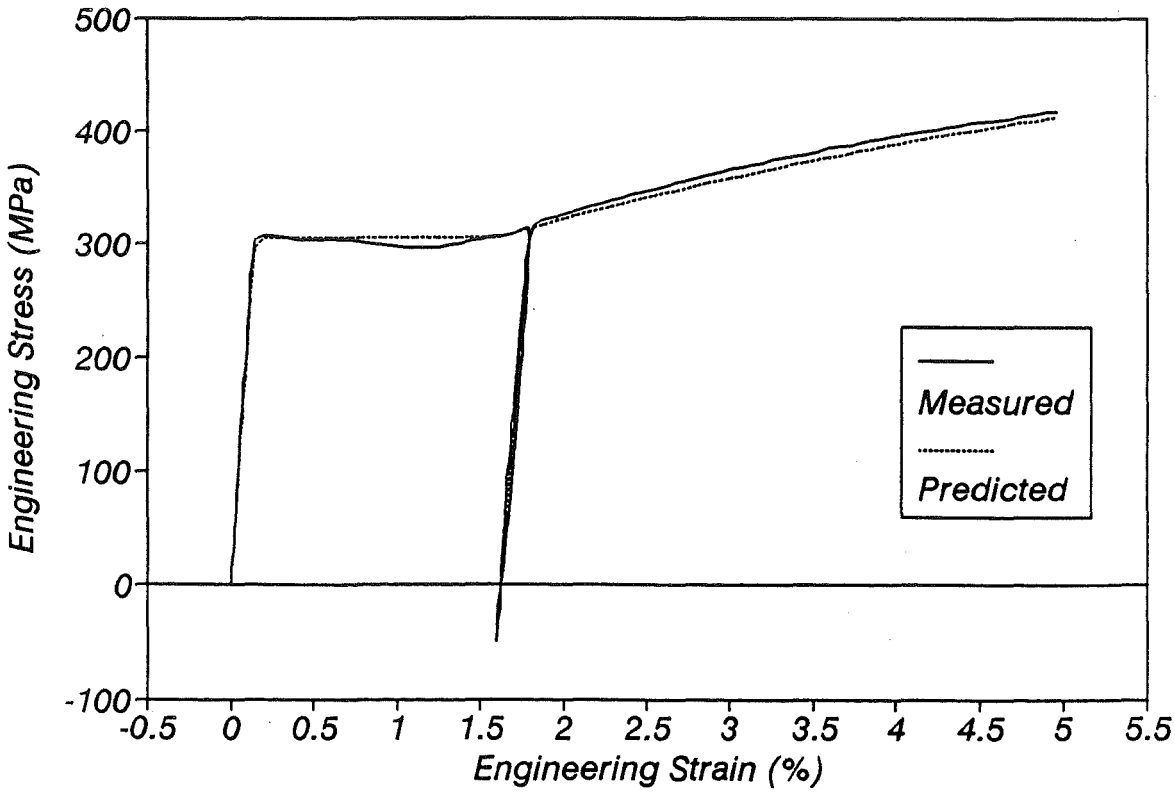

Fig. 2.41 - Measured and Modelled Stress-Strain Behaviour for Test M2TS14.

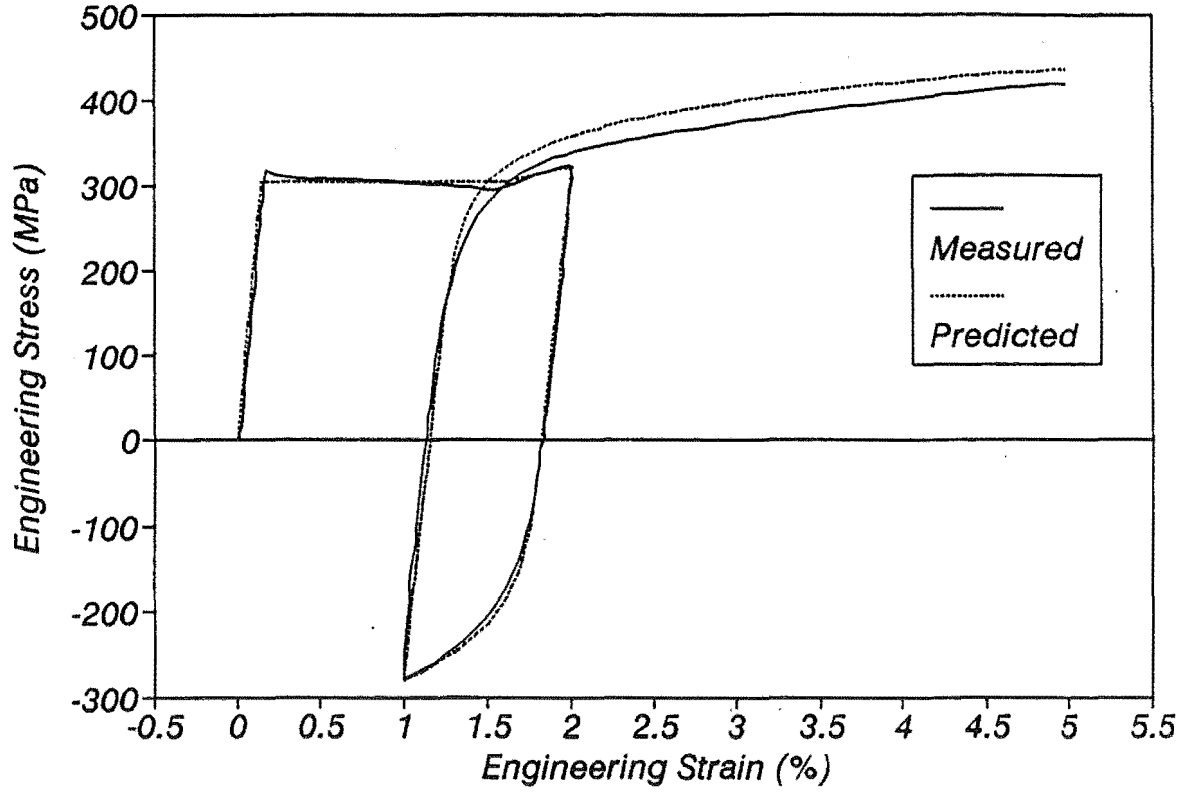

Fig. 2.42 - Measured and Modelled Stress-Strain Behaviour for Test M2TS15.

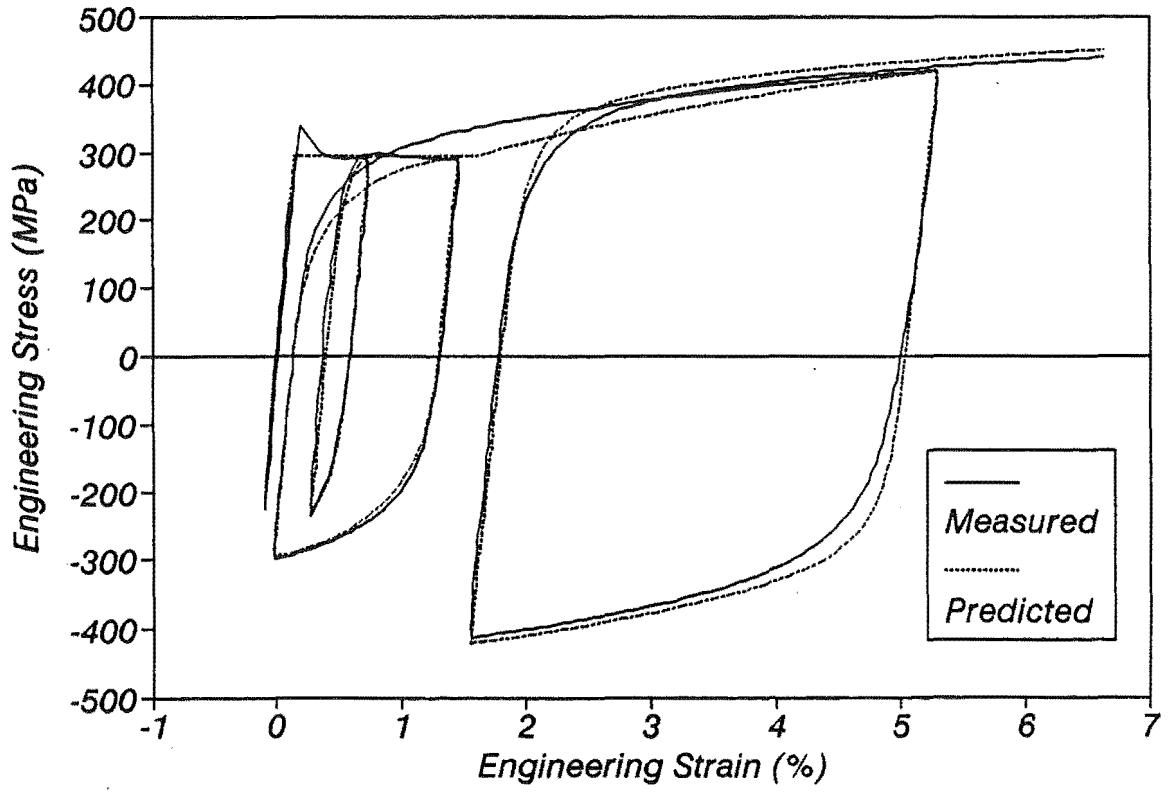

Fig. 2.43 - Measured and Modelled Stress-Strain Behaviour for Test M6TG01.

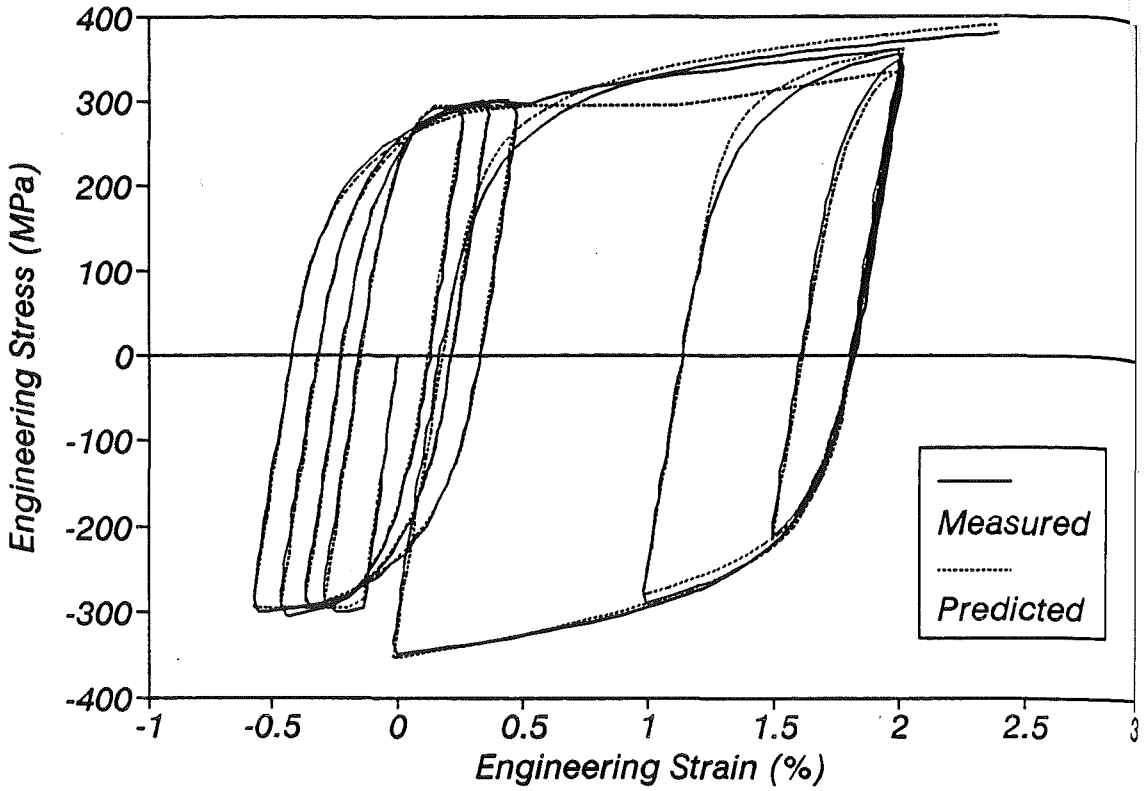

(a) Initial Cycles

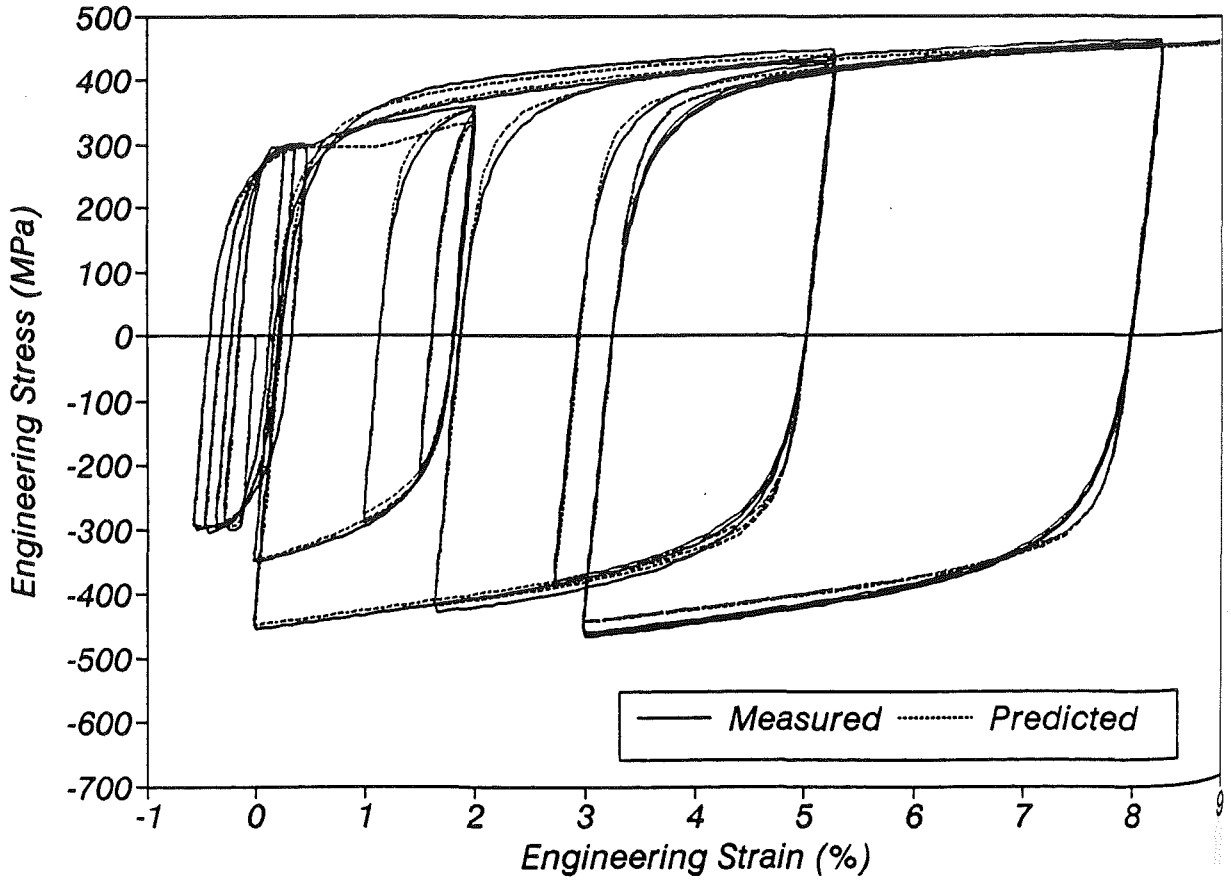

(b) Complete Test

Fig. 2.46 - Measured and Modelled Stress-Strain Behaviour for Test M28TS1.

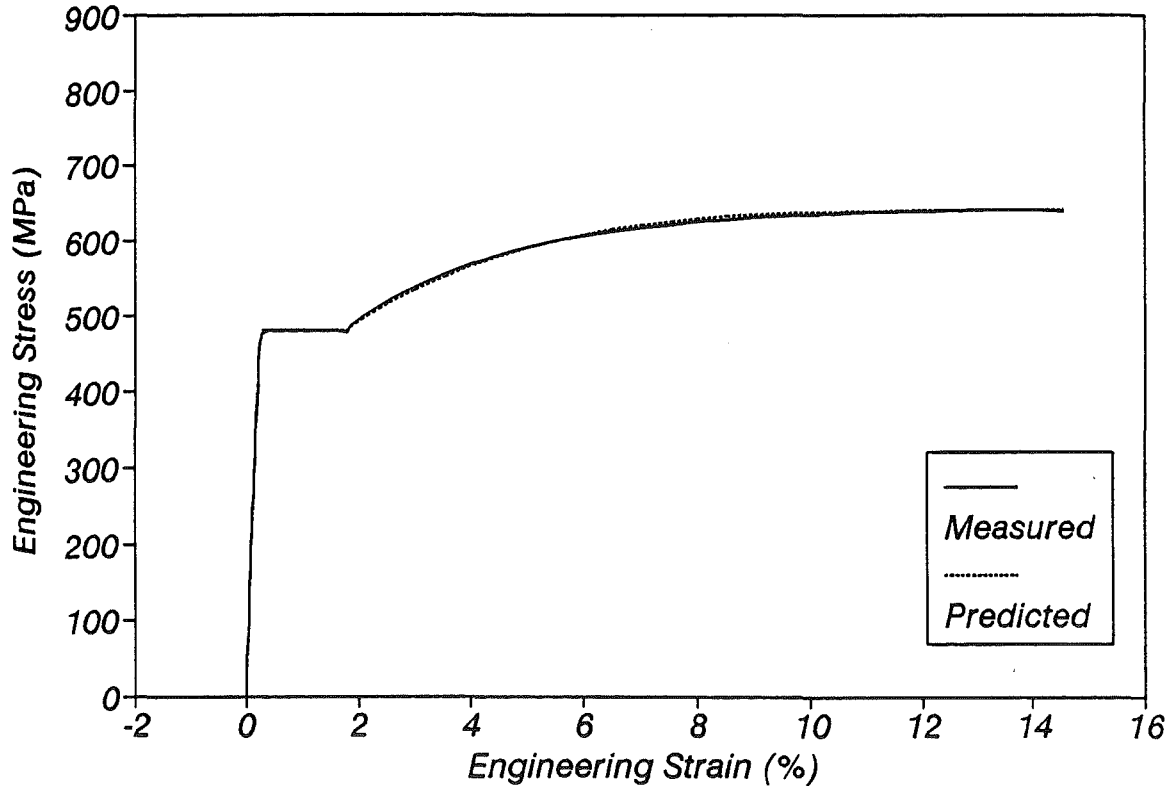

Fig. 2.47 - Measured and Modelled Stress-Strain Behaviour for Test HVTS1.

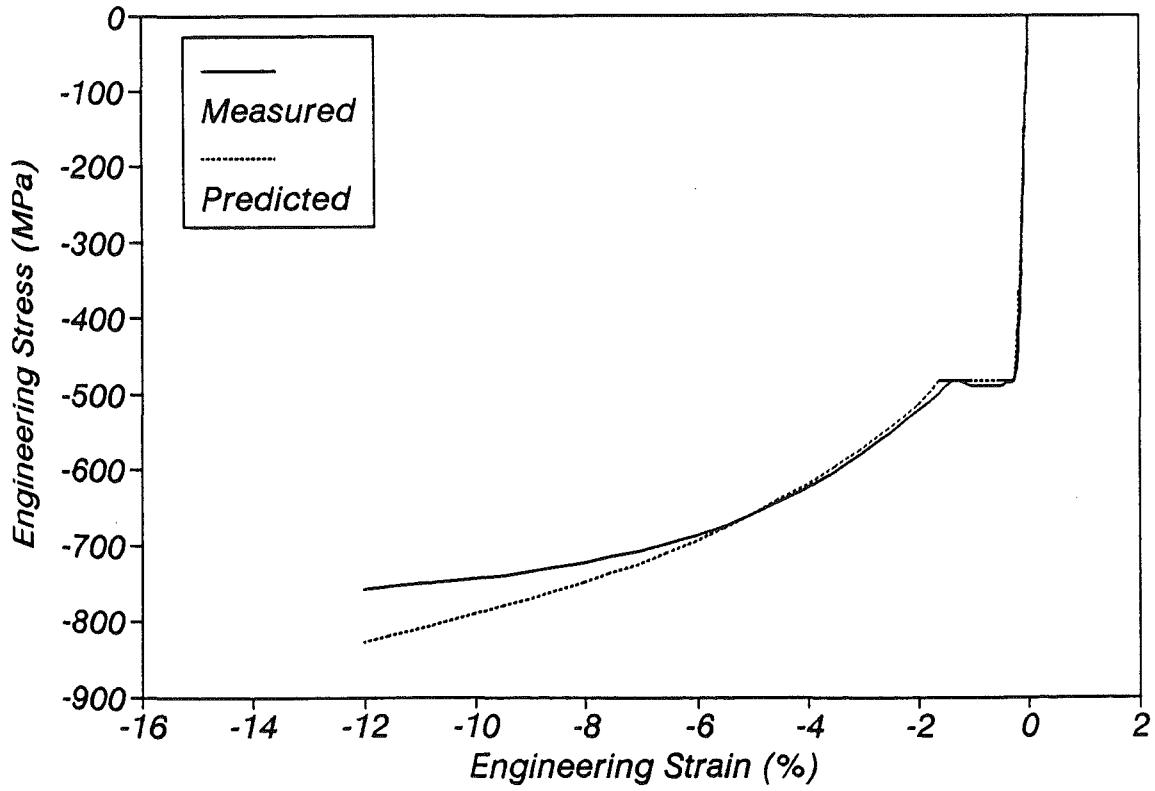

Fig. 2.48 - Measured and Modelled Stress-Strain Behaviour for Test HVCS1.

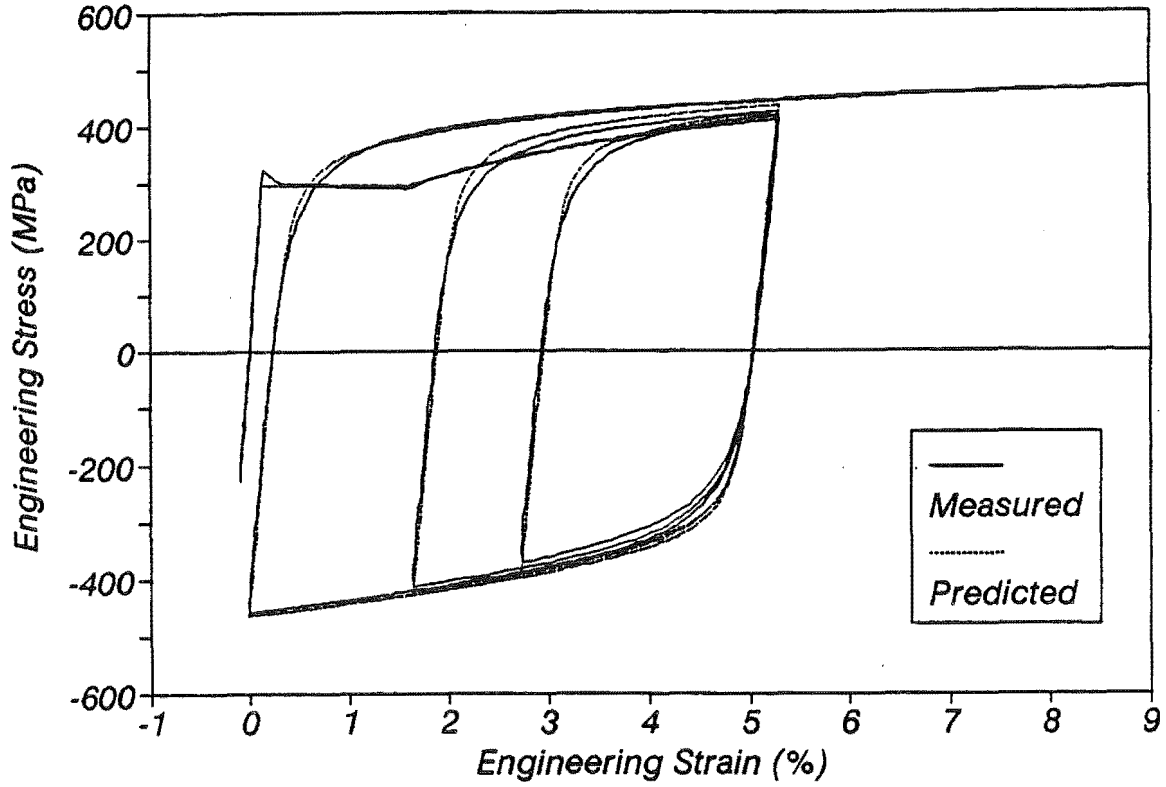

Fig. 2.44 - Measured and Modelled Stress-Strain Behaviour for Test M7TS1.

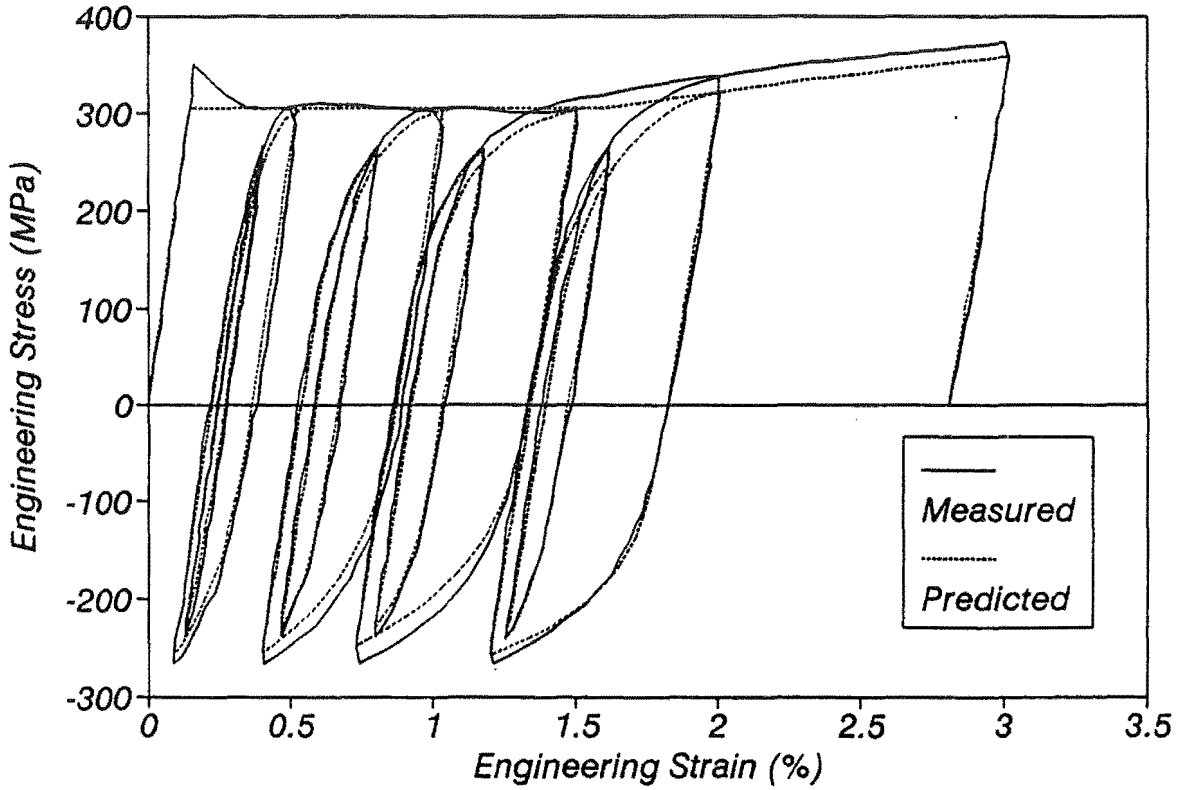

Fig. 2.45 - Measured and Modelled Stress-Strain Behaviour for Test M17TS1.

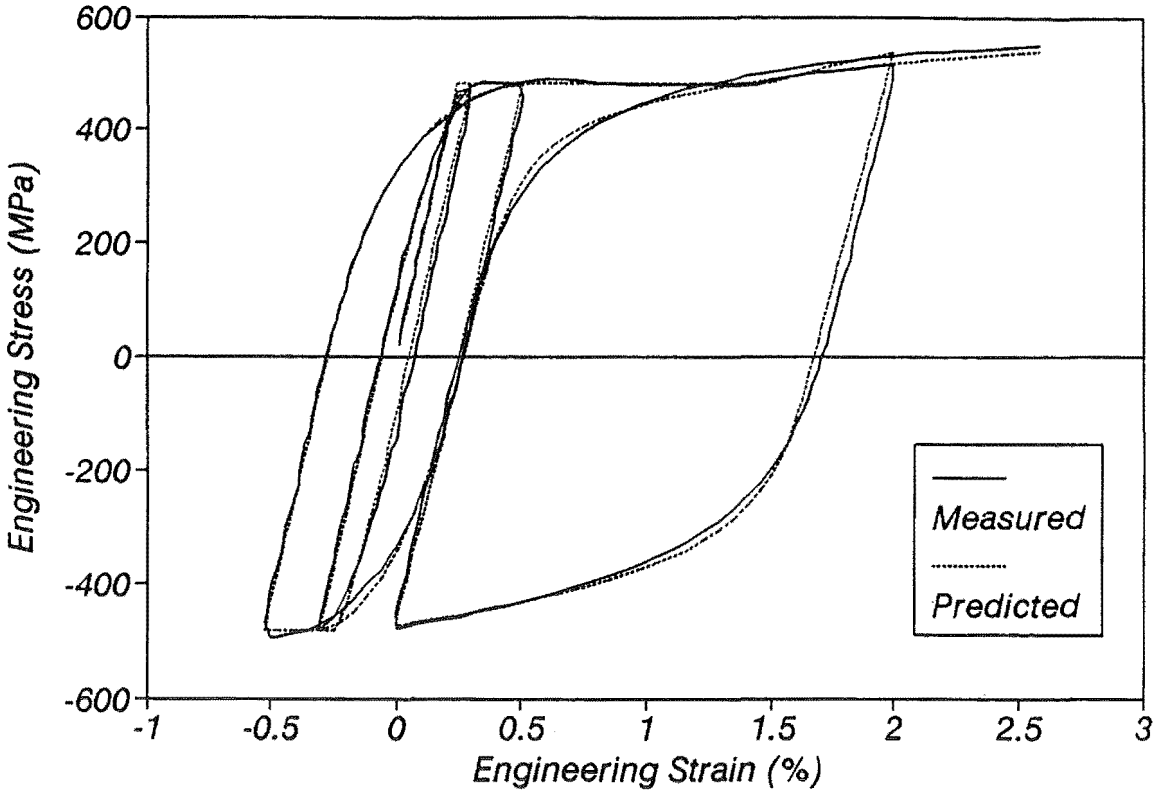

Fig. 2.49 - Measured and Modelled Stress-Strain Behaviour for Test HV15.

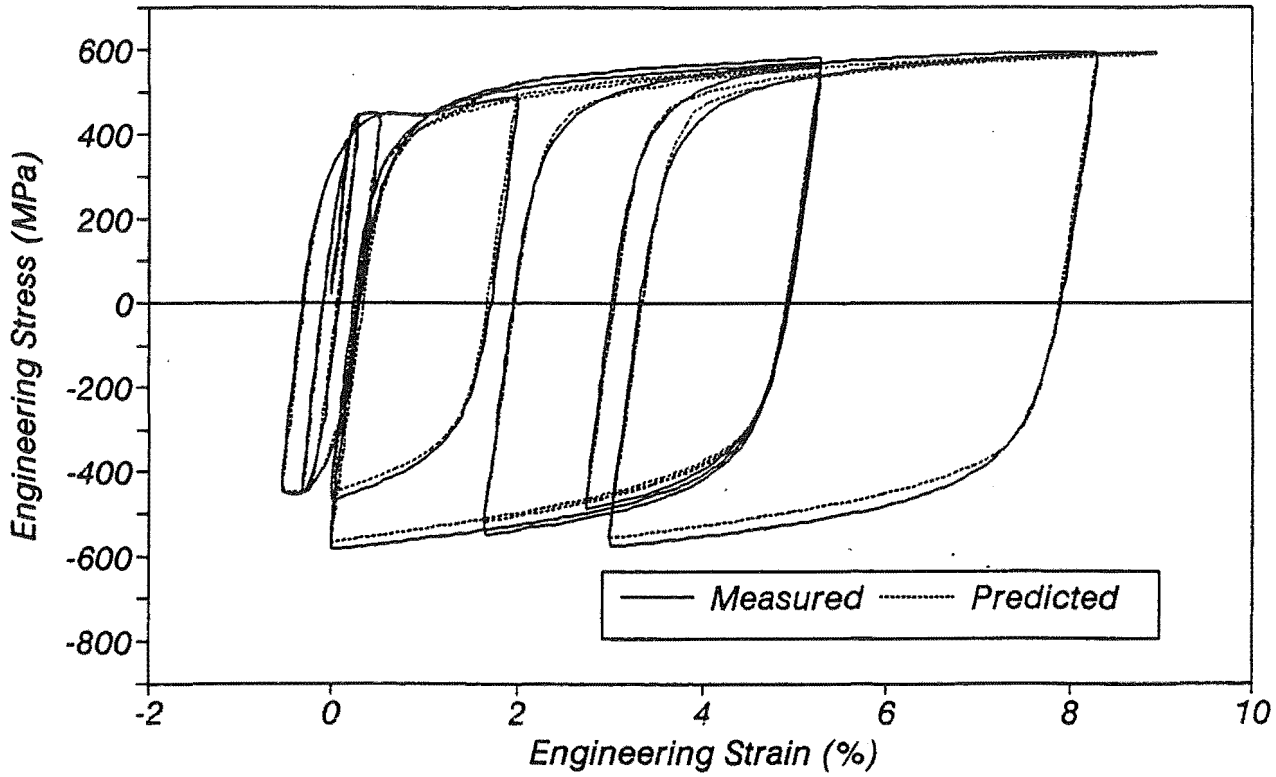

Fig. 2.50 - Measured and Modelled Stress-Strain Behaviour for Test HX15.

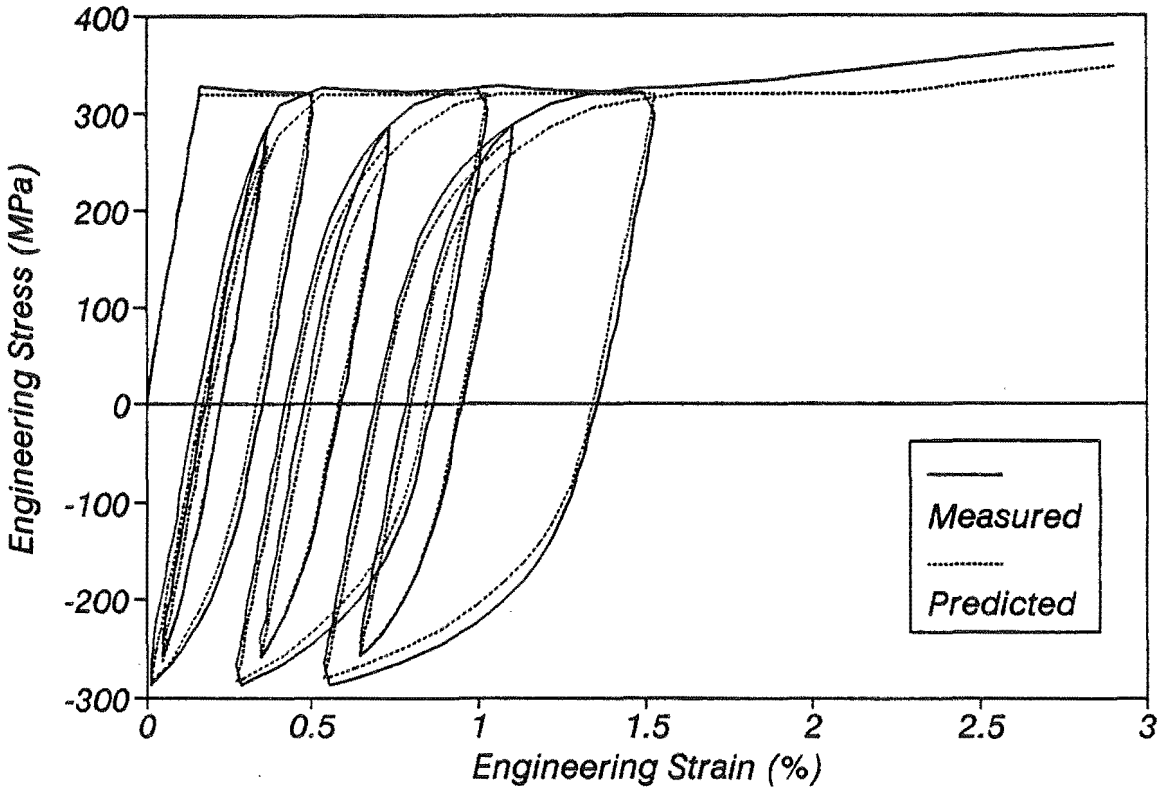

Fig. 2.51 - Measured and Modelled Stress-Strain Behaviour for Test MJSG2.

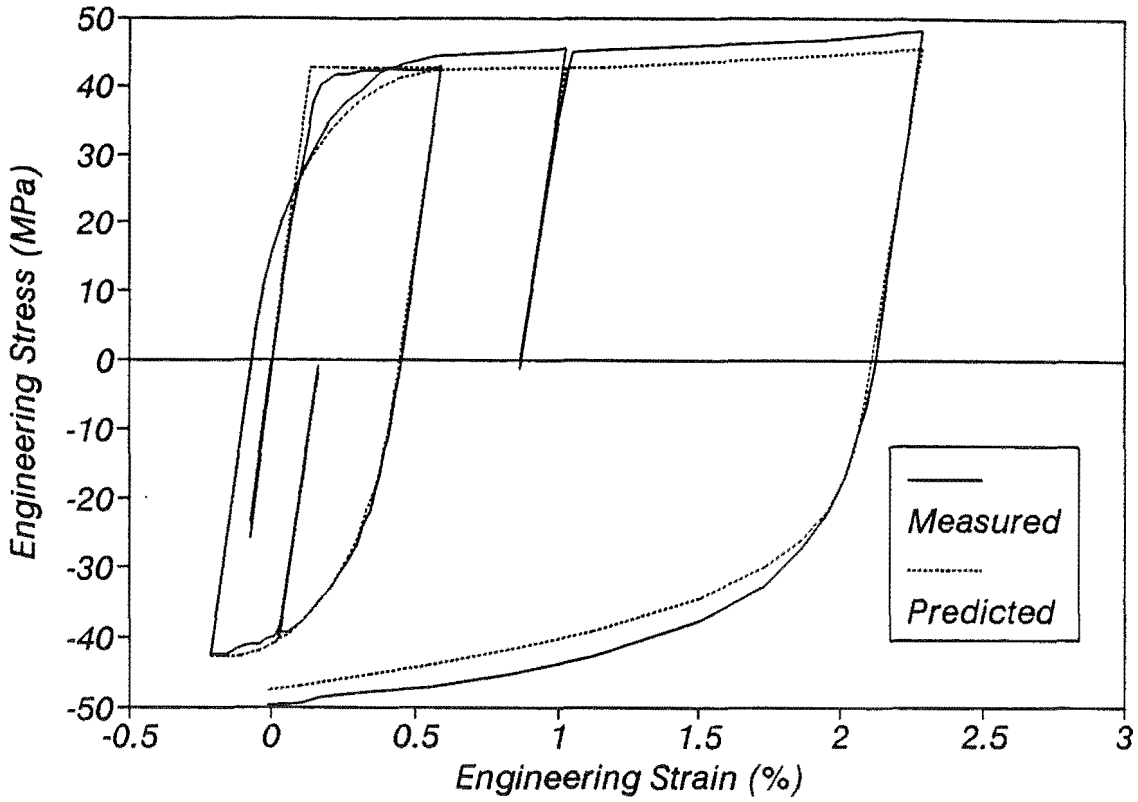

Fig. 2.52 - Measured and Modelled Stress-Strain Behaviour for Kent (1969), Test B25 on Grade 275 Steel.

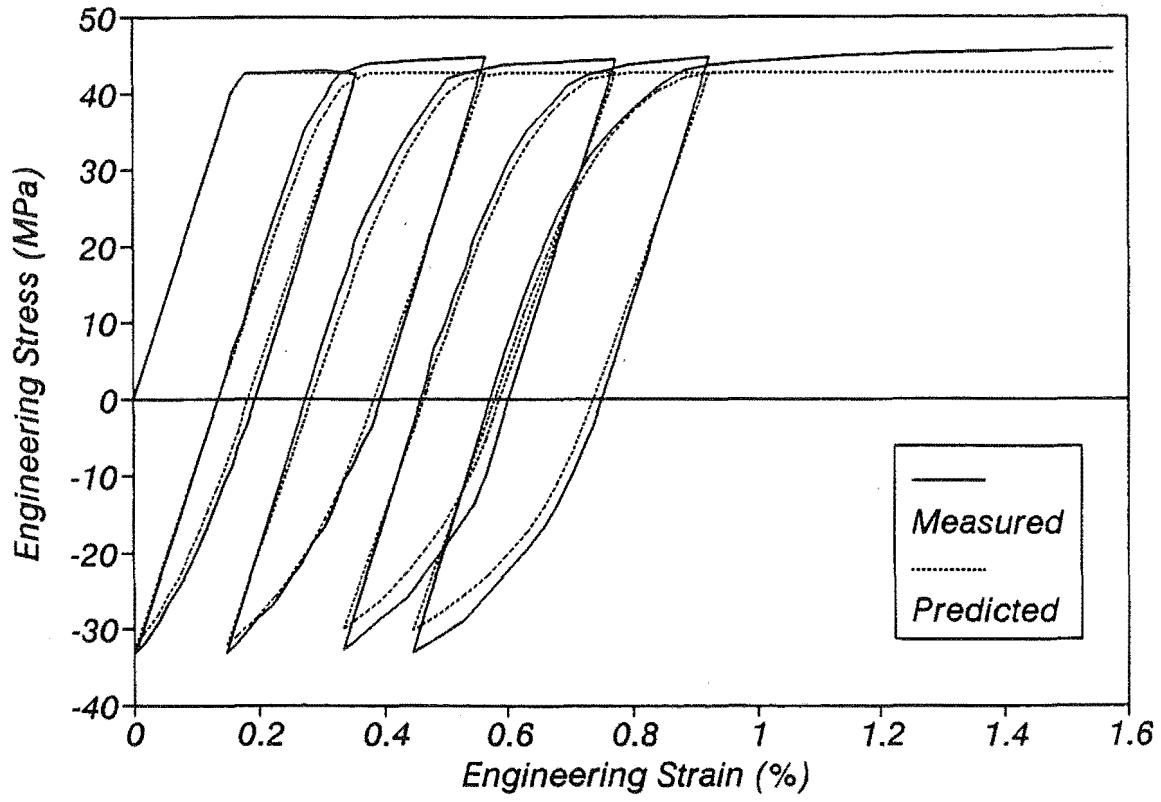

Fig. 2.53 - Measured and Modelled Stress-Strain Behaviour for Kent (1969), Test B29 on Grade 275 Steel.

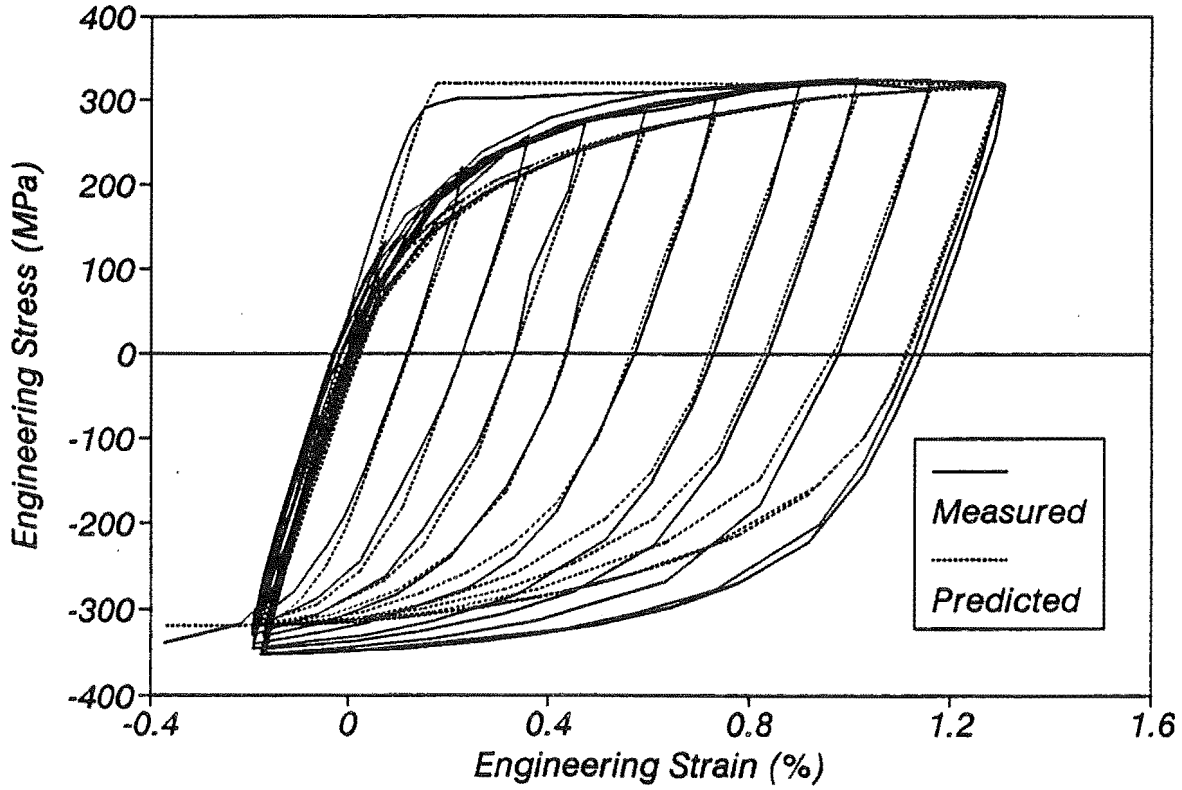

Fig. 2.54 - Measured and Modelled Stress-Strain Behaviour for Tjokrodimuljo and Fenwick (1985), Test 16 on Grade 275 Steel.

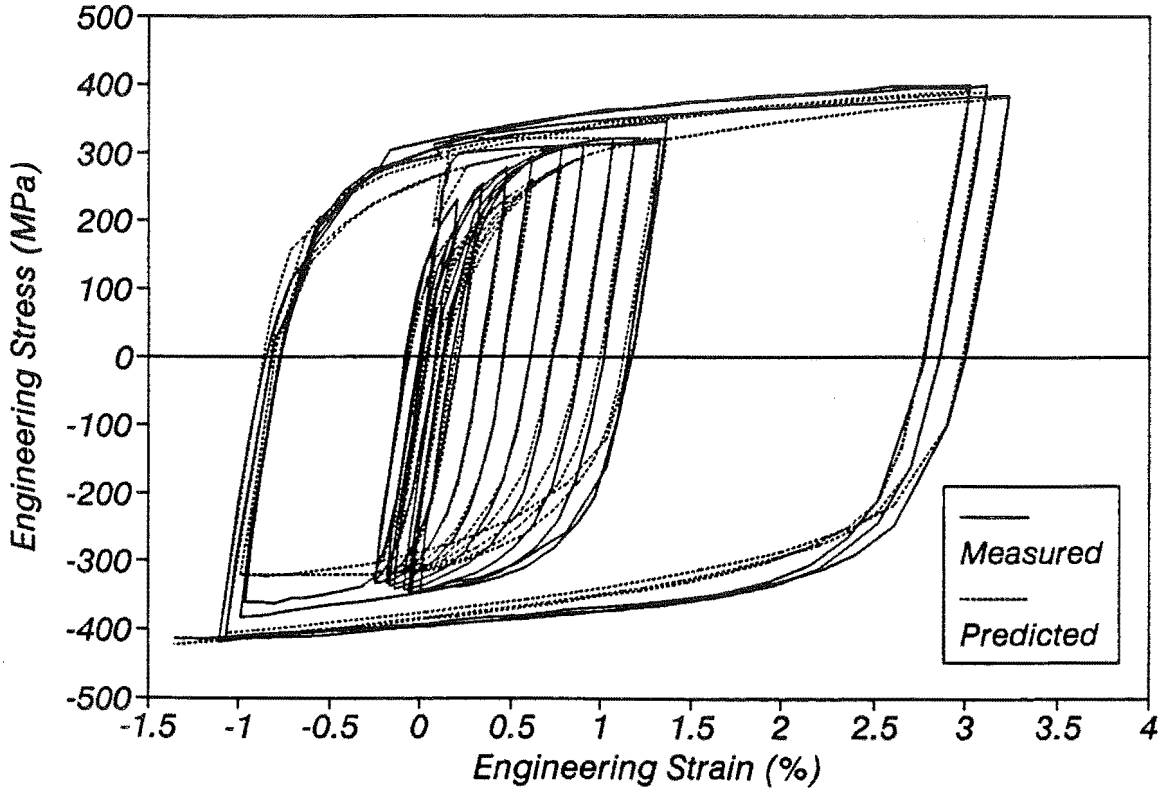

Fig. 2.55 - Measured and Modelled Stress-Strain Behaviour for Tjokrodimuljo and Fenwick (1985), Test 17 on Grade 275 Steel.

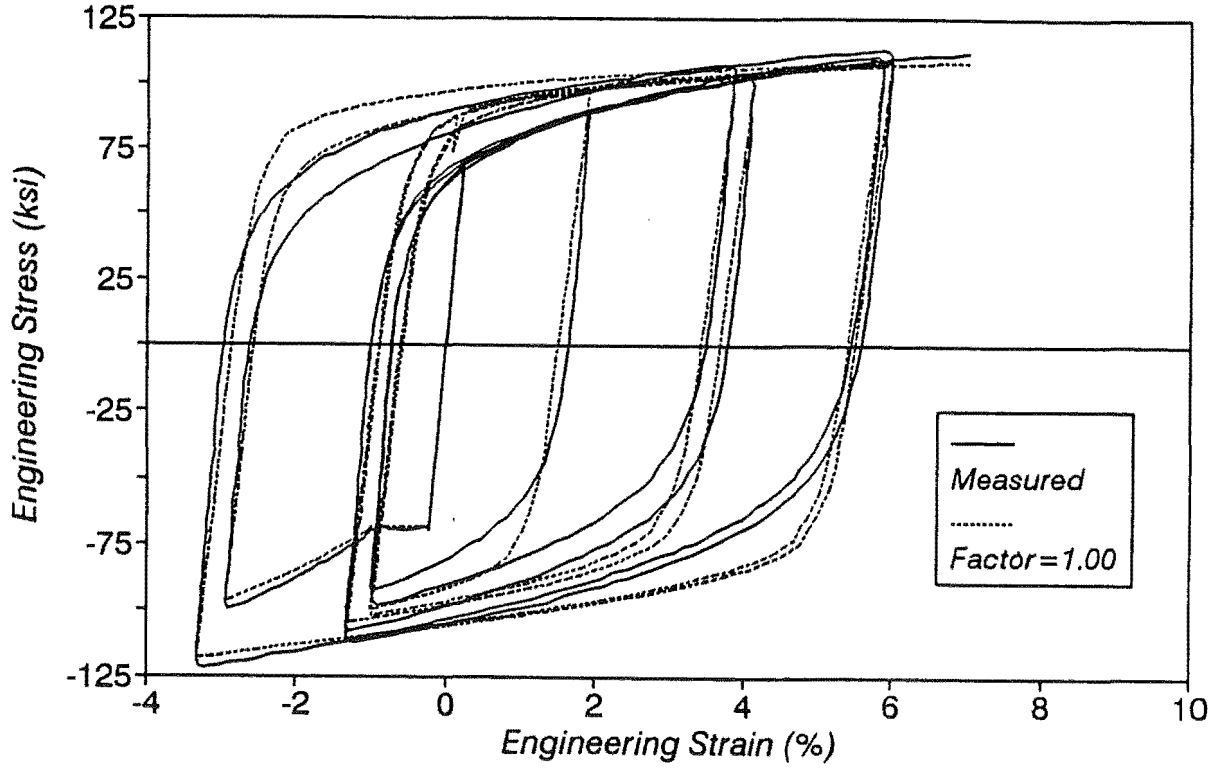

(a) Predicted Using 1.00Ω

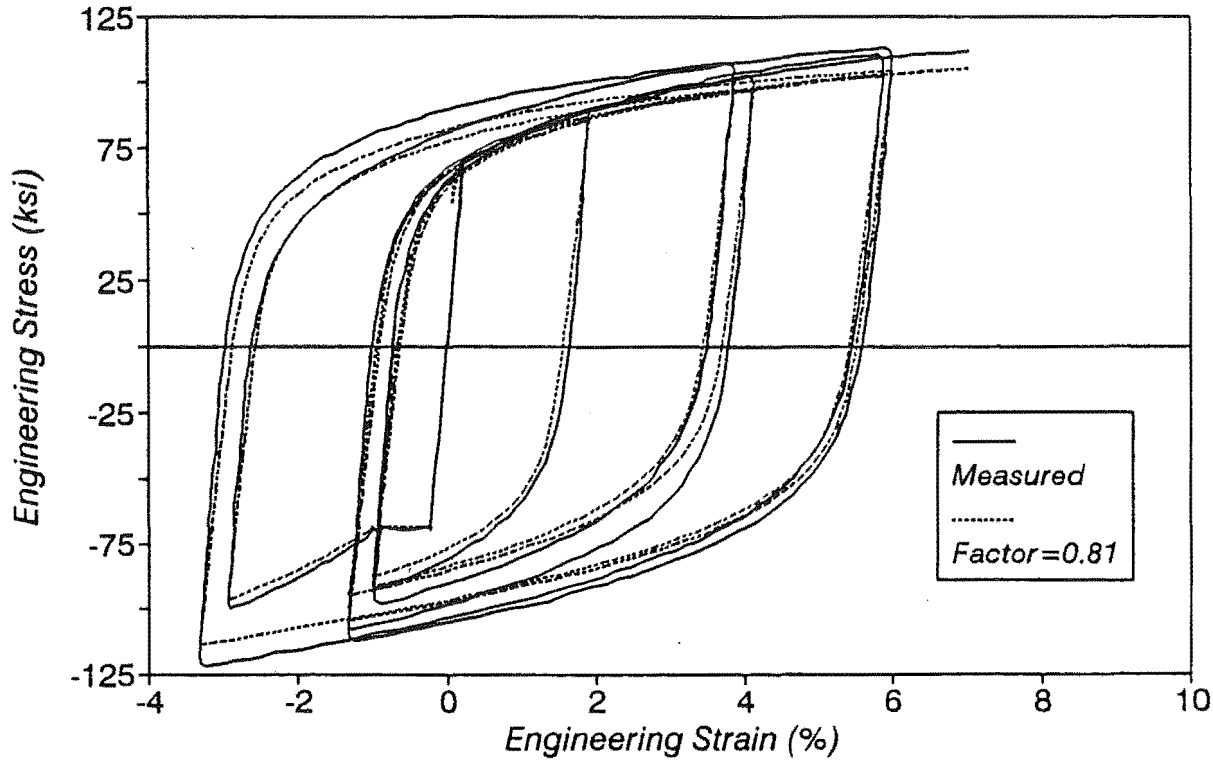

(b) Predicted Using 0.81Ω

Fig. 2.56 - Measured and Modelled Stress-Strain Behaviour for Aktan et al (1972), Test 5.

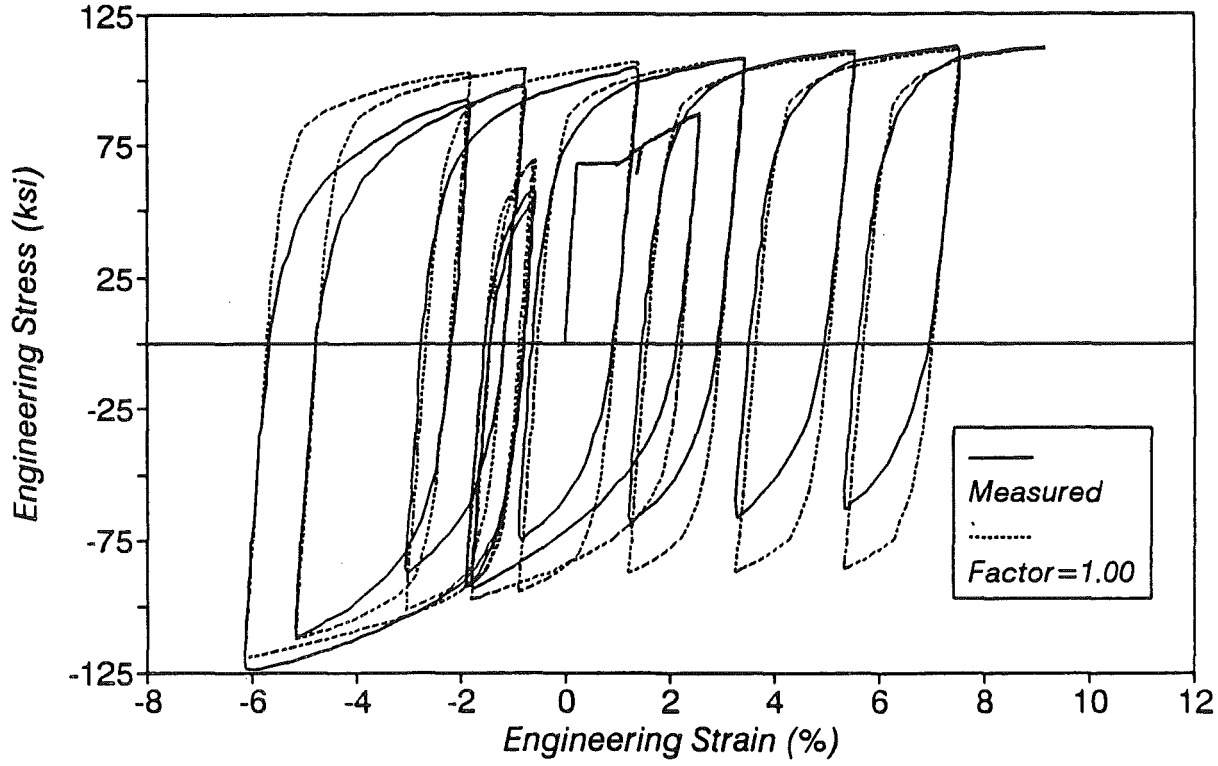

(a) Predicted Using 1.00Ω

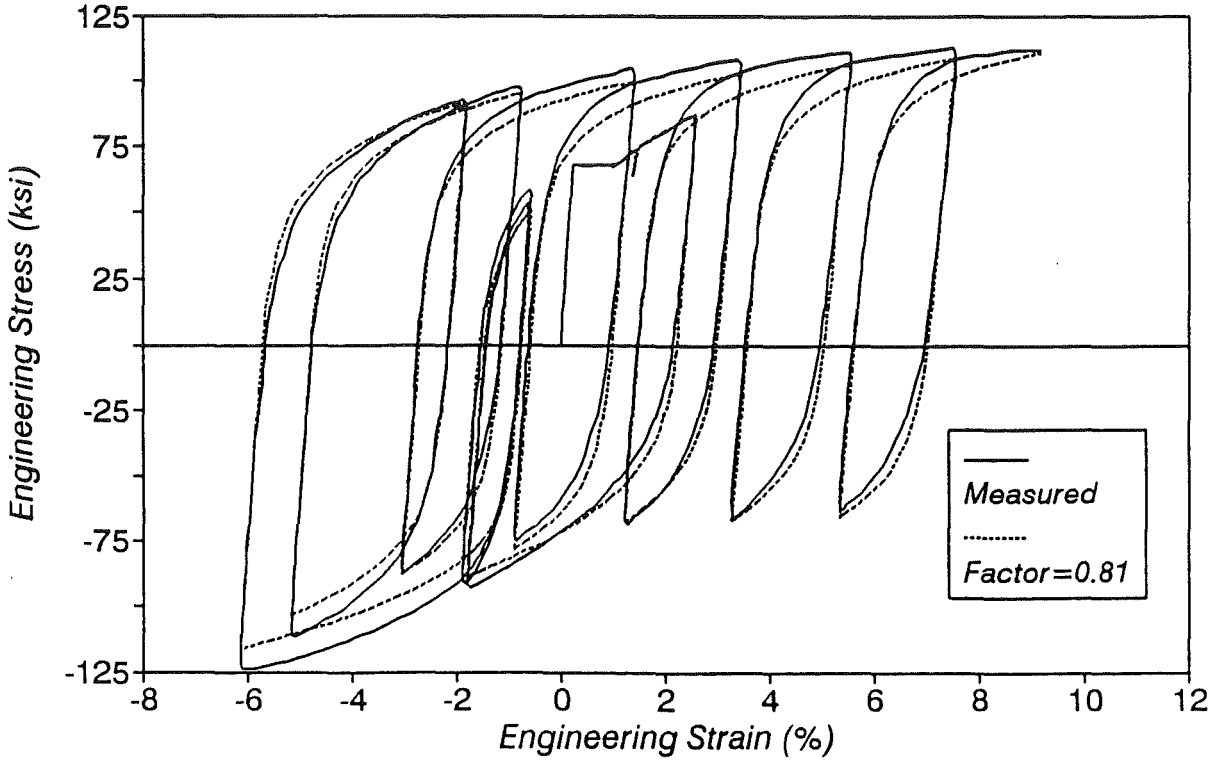

(b) Predicted Using 0.81Ω

Fig. 2.57 - Measured and Modelled Stress-Strain Behaviour for Aktan et al (1972), Test 6.

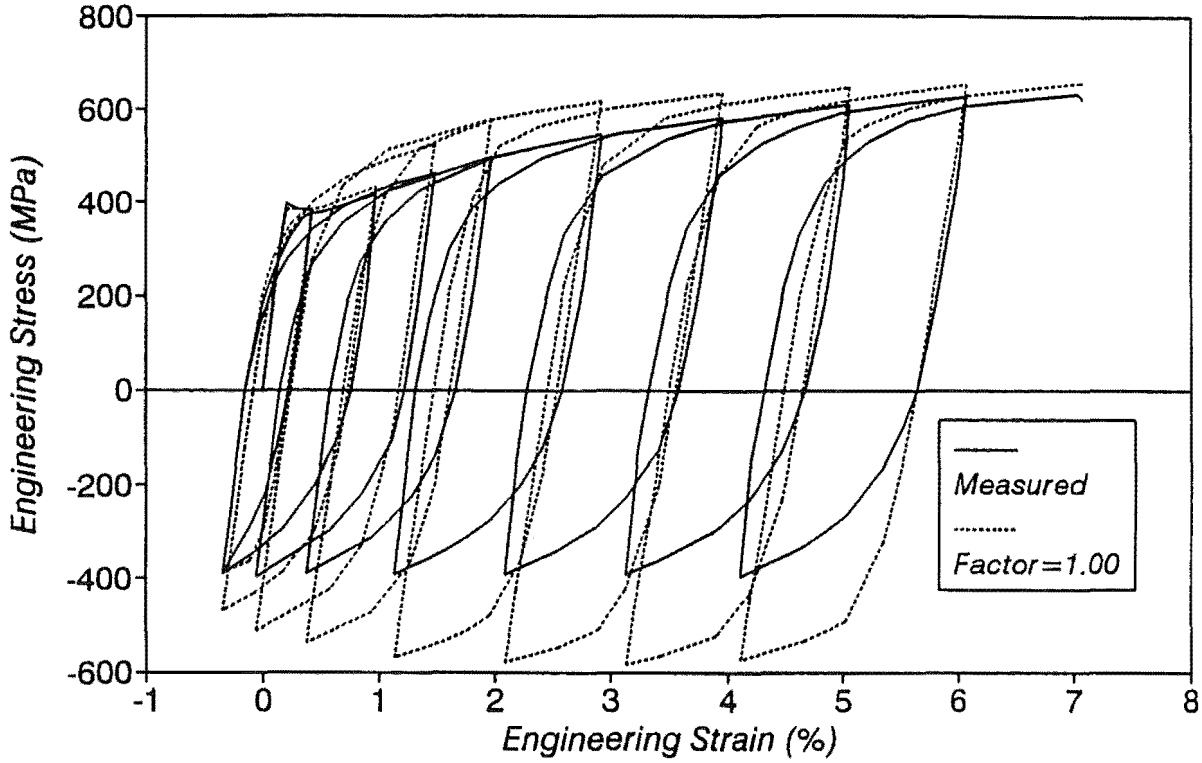

(a) Predicted Using 1.00Ω

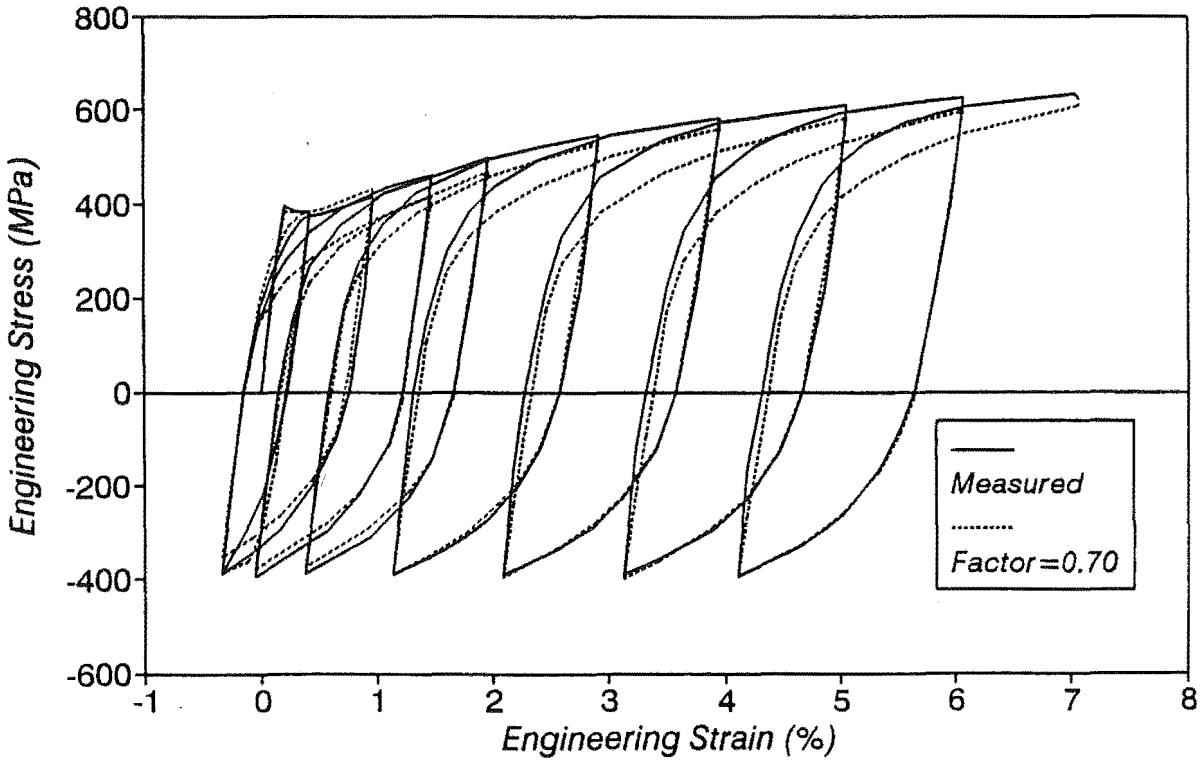

(b) Predicted Using 0.70Ω

Fig. 2.58 - Measured and Modelled Stress-Strain Behaviour for Leslie (1973), Test B7.

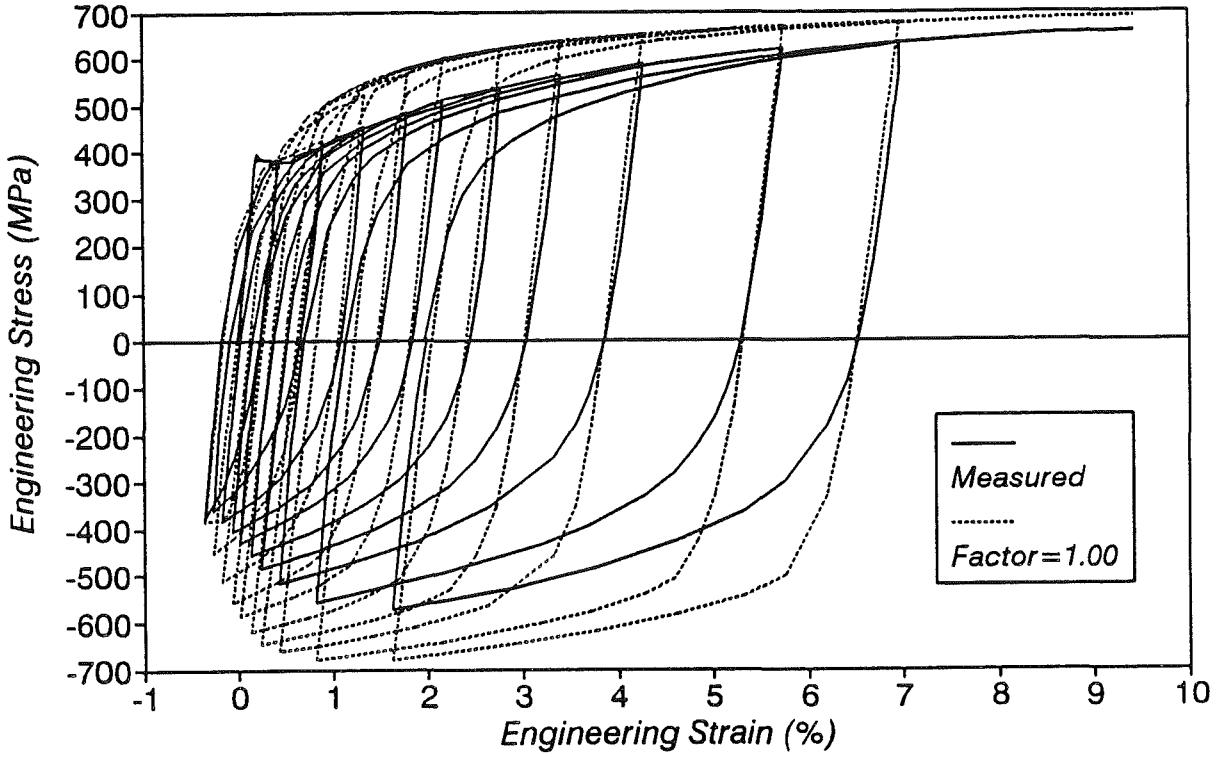

(a) Predicted Using 1.00Ω

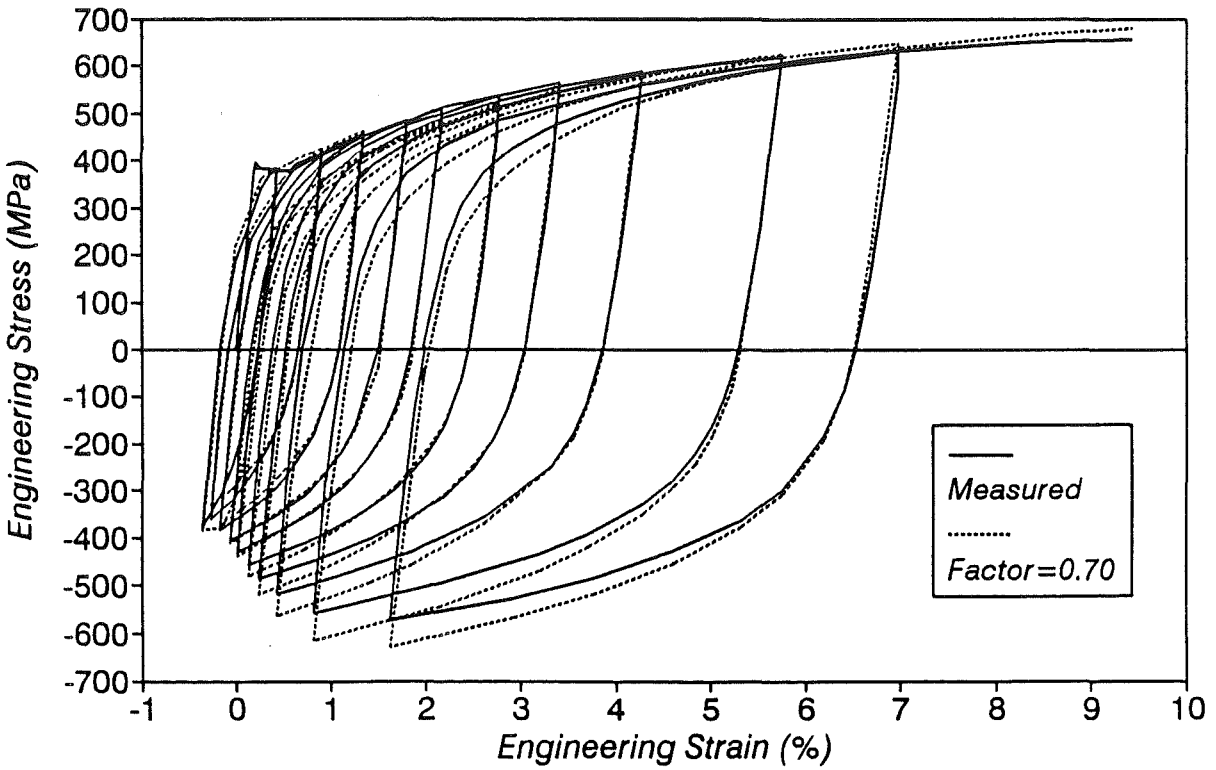

(b) Predicted Using 0.70Ω

Fig. 2.59 - Measured and Modelled Stress-Strain Behaviour for Leslie (1973), Test B8.

Kent (1969) tested Grade 275 steel coupons machined from deformed bars of different diameters. All tests were cycled in the Lüders strain range. Figs. 2.52 and 2.53 shows a close agreement between the observed response and the prediction of the model proposed in the present study.

Two tests conducted by Tjokrodimuljo and Fenwick (1985) on deformed 10mm diameter bars are reproduced in Figs. 2.54 and 2.55 together with the response predicted by the model proposed in the present study. The measured behaviour is stiffer than the predicted one. In addition, the yield stress in compression is higher than the one in tension which disagrees with the findings and assumptions made in this study.

(b) Tests on Other Types of Reinforcing Steels

Aktan et al (1973) carried out a series of tests on coupons of Grade 60 steel (ksi). Figs. 2.56 and 2.57 depict the measured and predicted behaviour of two tests. It is evident that the Bauschinger effect in this type of steel is softer and therefore the behaviour predicted by the model proposed in the present study is inaccurate. The predicted behaviour is closer when the Ω factor is multiplied by 0.81.

A similar behaviour occurs with the prediction of the measured behaviour of the tests carried out by Leslie (1974) on Grade 380 steel coupons manufactured to NZS 3402 (1973). The predicted cyclic behaviour shows a closer agreement when the Ω factor is multiplied by 0.70 as seen in Figs. 2.58 and 2.59.

These reduced Ω factors indicate that the Bauschinger effect in different steels does not have the same shape but appears to follow a similar trend. The main reason for the difference in shape is the influence of the carbon content in the steel as discussed in the section below.

2.6.2 The Influence of Carbon Content

The discrepancy between the observed and predicted response of the tests of Aktan et al and Leslie can be attributed to the carbon content of the steel tested. Polakowski (1951) associated the shape of the Bauschinger effect with the carbon content, based on test results on different carbon steels. Lower carbon steels were found to have a stiffer Bauschinger effect than higher carbon steels. Bate and Wilson (1986) and Wilson and Bate (1986) also showed that for spheroidised steels with low and high carbon content the Bauschinger effect showed a similar trend to that observed by Polakowski. This effect is demonstrated by tests results obtained by Wilson and Bate and reproduced in Fig. 2.60. Unfortunately the carbon content of the steel coupons tested by Aktan et al is unknown. This steel was probably manufactured to either A615-68, A616-68 or A617-68 [ASTM (1972)] which do not specify limitations on the carbon content. The steel used by Leslie had a measured carbon content of 0.39 wt%.

Mander et al (1984) and Spurr and Paulay (1984) did not recognize the influence of the carbon content on the shape of the Bauschinger effect. Their models were calibrated from test results in only the Lüders strain region or only the work hardening region using steels with different chemical compositions. In the specific case of the model proposed by Mander et al, the concepts of additional

shift and of a rejoining point in the work hardening region yield results that follow the measured behaviour only for the test results used for their calibration. Their model for additional shift is discontinuous at the beginning of the work hardening region and it seems to present computational errors for reversals from the softened branch. Many of the parameters required to describe the monotonic curves, which are so important in the Mander et al and Spurr and Paulay models, were assumed because of the lack of complete information. Furthermore, Mander et al and Spurr and Paulay did not attempt to predict the cyclic response of tests which were not included in the calibration of their analytical models. Figs. 2.61 and 2.62 illustrate the measured versus predicted response for two tests using the model postulated by Mander et al. Test results in this study indicate that neither grade of New Zealand steel has the tendency for the Bauschinger curve to rejoin a shifted skeleton curve. It is apparent that no universal macroscopic models can be developed unless a correlation is made with the carbon content in different reinforcing steels.

In this study, emphasis has been given to modelling the behaviour of the two current New Zealand grades of steel. These two grades are manufactured under the NZS 3402 (1989) where the carbon content is limited to a maximum of 0.22 wt%.

Table 2.5 illustrates the results of a statistical analysis on the carbon content of the two grades of steels for several bar diameters as manufactured [Pacific Steel (1991)]. It can be seen that for Grade 300 steel there is a trend for the carbon content to increase with the increase in the bar diameter. Grade 430 steel does not show this trend. Because the variation in carbon content shown in Table 2.5 is not large, it could be expected that the Bauschinger effect would be similar for all bar diameters of both grades of steel.

2.6.3 Tests Using Various Strain Rates

2.6.3.1 Tests Conducted

Two different tests were carried out to observe the strain rate effects on both grades of New Zealand reinforcing steels. In the first type of test, the load was applied monotonically in tension while in the second type of test, the load was cycled.

The monotonic load tests were carried out at three different nominal strain rates, starting with a quasi-static strain rate of 0.000015/sec and two faster rates of 0.000150/sec and 0.001500/sec. The maximum strain rate was controlled by the capacity of the Instron Universal Testing Machine. The cyclic load tests were only conducted at the quasi-static strain rate of 0.000015/sec and at the maximum rate of 0.001500/sec. Real strain rates calculated from measured time and strain in the elastic range were 1.5 times the nominal strain rates.

It is well known that the actual strain rate applied to a test specimen is dependent on the specimen stiffness and increases when the stiffness decreases [Fahy et al (1980)]. Hence, the strain rate

Table 2.5 Mean Carbon Distribution of New Zealand Manufactured Reinforcing Steel		
Nominal Bar Diameter (mm)	Grade 300 Steel (% W)	Grade 430 Steel (% W)
10	0.159	0.206
12	0.161	0.191
16	0.170	0.189
20	0.179	0.191
24	0.183	0.194
28	0.191	0.199
32	0.200	0.204

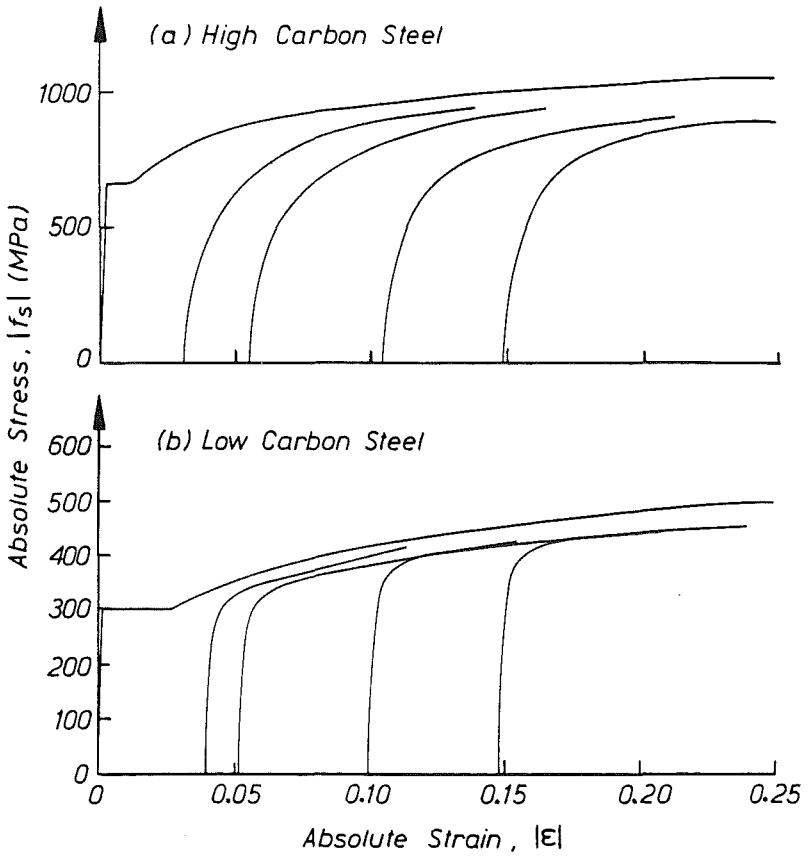

Fig. 2.60 - Bauschinger Test Results Plotted in Terms of Absolute Values of Stress and Strain [Wilson and Bate (1989)].

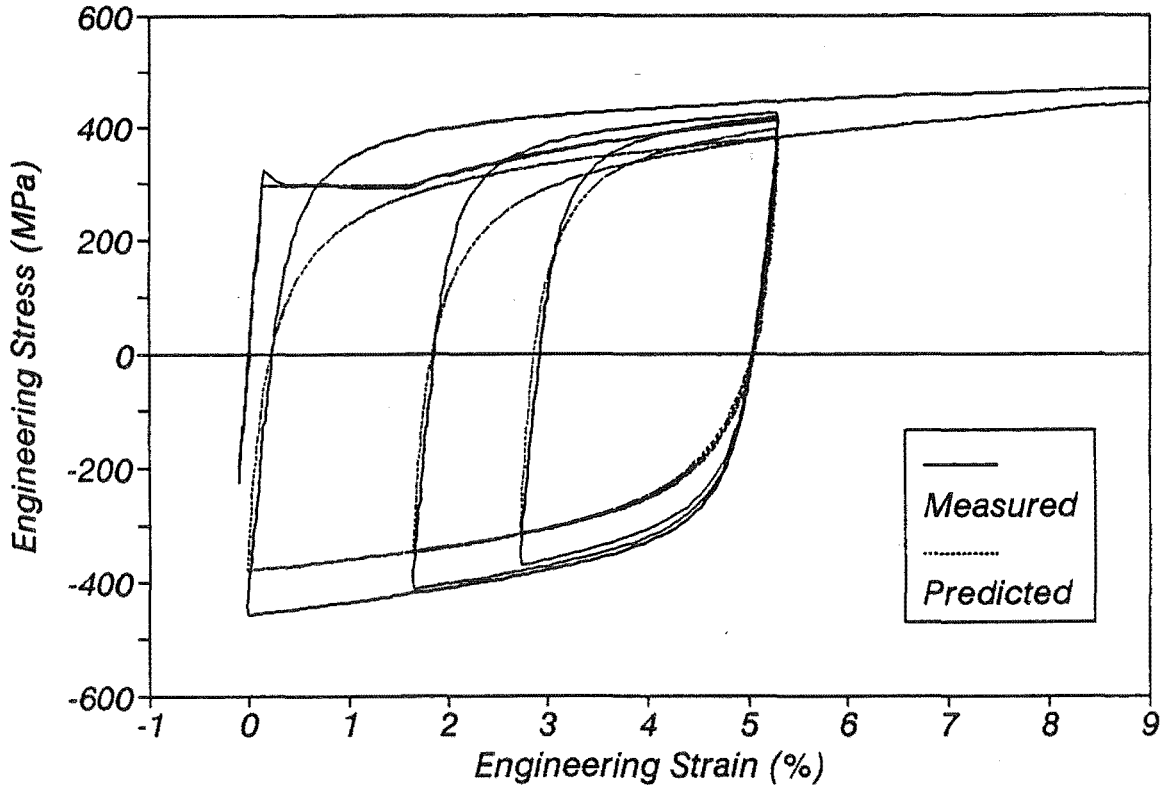

Fig. 2.61 - Test M7TS1 as Predicted by Mander et al Model (1984).

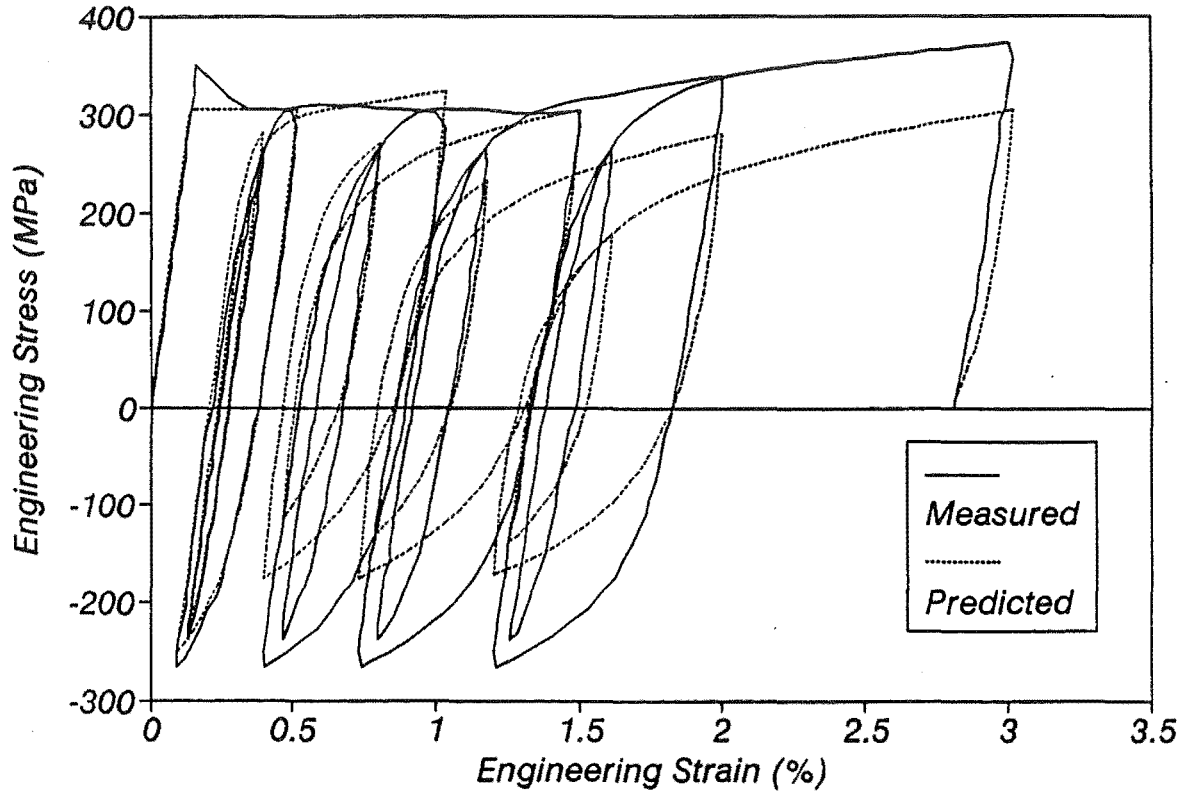

Fig. 2.62 - Test M17TS1 as Predicted by Mander et al Model (1984).

is greatest during yielding of the specimen and in the region of the maximum tensile load. The ratio between the maximum strain rate and the strain rate in the elastic region is a constant for each universal testing machine and is termed the "hardness" ratio. The hardness ratio, h_d, is given by

$$h_d = \frac{strain\ rate\ during\ yielding}{strain\ rate\ in\ the\ elastic\ range} \qquad (2.99)$$

The average hardness ratio of the Instron machine was found to be equal to 19.8. That is, the strain rate increased by 19.8 times in the Lüders strain region and near the ultimate tension load, and was therefore 30 times the nominal strain rate. In this study the strain rates reported are based on the nominal strain rates.

2.6.3.2 Monotonic Load Tests

Figs. 2.63 and 2.64 show monotonic test results of both grades of steel. Some trends can be obtained from these figures. The upper and lower yield stress, the ultimate stress and the strain at strain hardening increase with an increase in the strain rate. On the other hand, there is a trend for the ultimate strain to decrease with an increase of the strain rate. These observations are in agreement with those presented by Manjoine (1944).

Fig. 2.65 allows a comparison to be made of the test results for the two grades of reinforcing steel. All properties have been normalized using the quasi-static tests as a base. In general, Grade 430 steel is less sensitive to any change of rate than Grade 300 steel. The strain rate has a larger effect on the yield stress than on the ultimate stress for both grades of steel. Also, it can be seen that the strain at strain hardening is influenced by the strain rate. The modulus of elasticity does not seem to be affected.

2.6.3.3 Cyclic Load Tests

Results of the effect of the strain rate on the cyclic load behaviour are shown in Figs. 2.66 and 2.67. The strain rate effects appear to diminish once the material enters the work hardened range. The maximum increase in the strength was 3.7% and 3.0% for grades 300 and 430 steel respectively. These results agree with early observations by Mahin and Bertero (1972).

2.6.4 Strain Ageing Effects

2.6.4.1 Tests Conducted

This test programme was designed to observe the effect of natural strain ageing at low and moderate levels of tensile plastic pre-straining such as those that could normally be encountered in reinforced concrete members to be repaired after an earthquake.

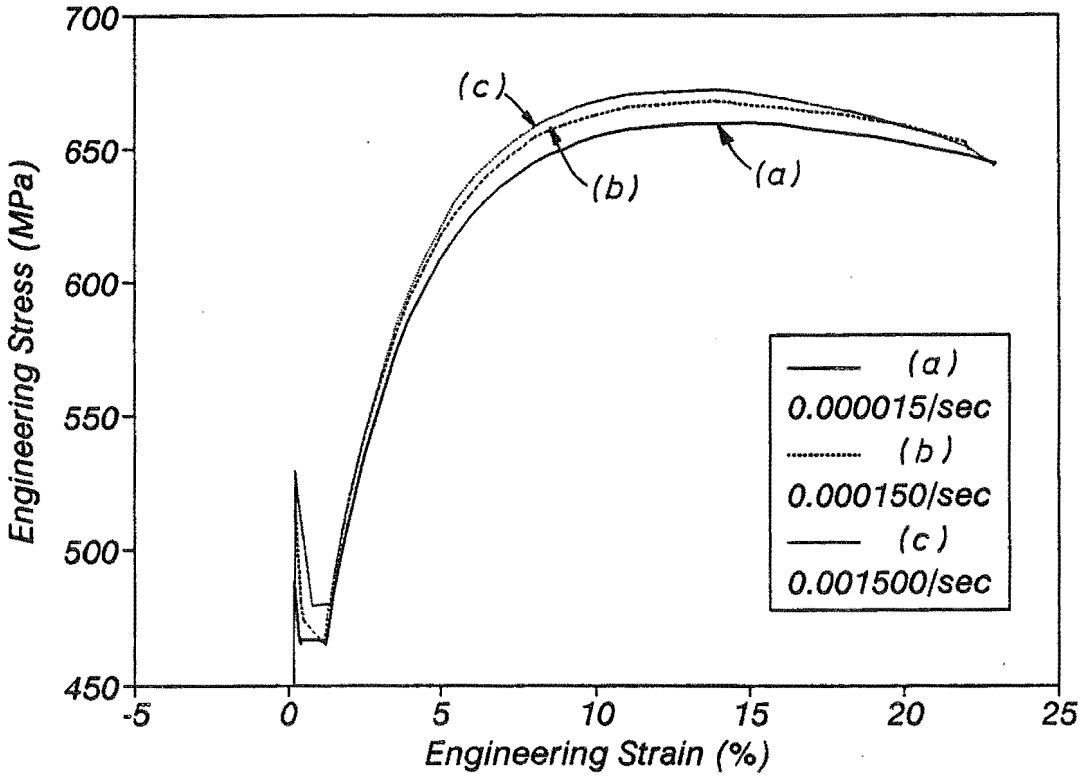

(a) Complete Test

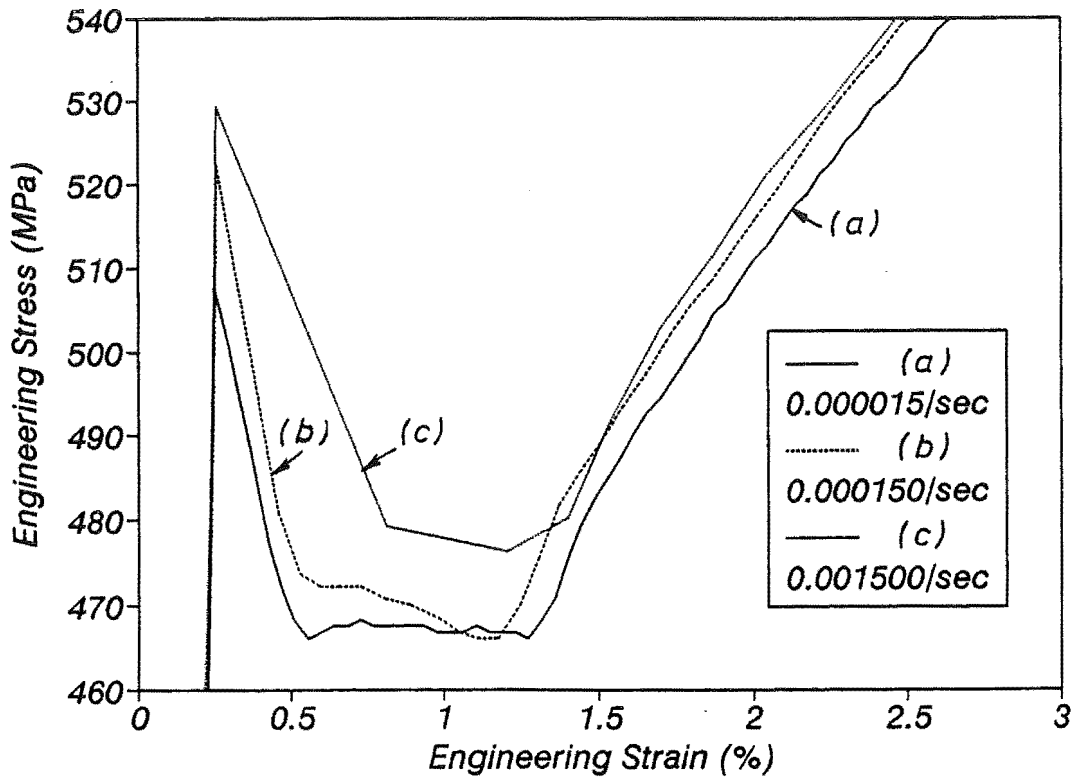

(b) Close up of Yield Plateau Region

Fig. 2.63 - Strain Rate Effects on the Monotonic Behaviour of Grade 430 Steel.

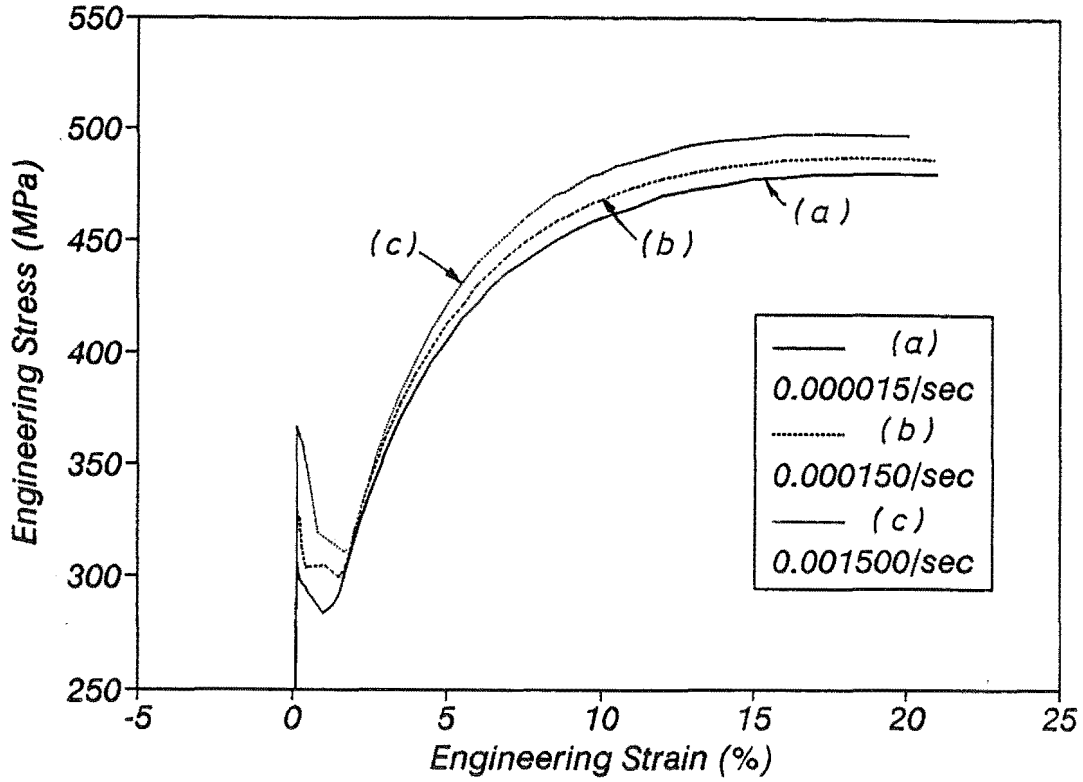

(a) Complete Test

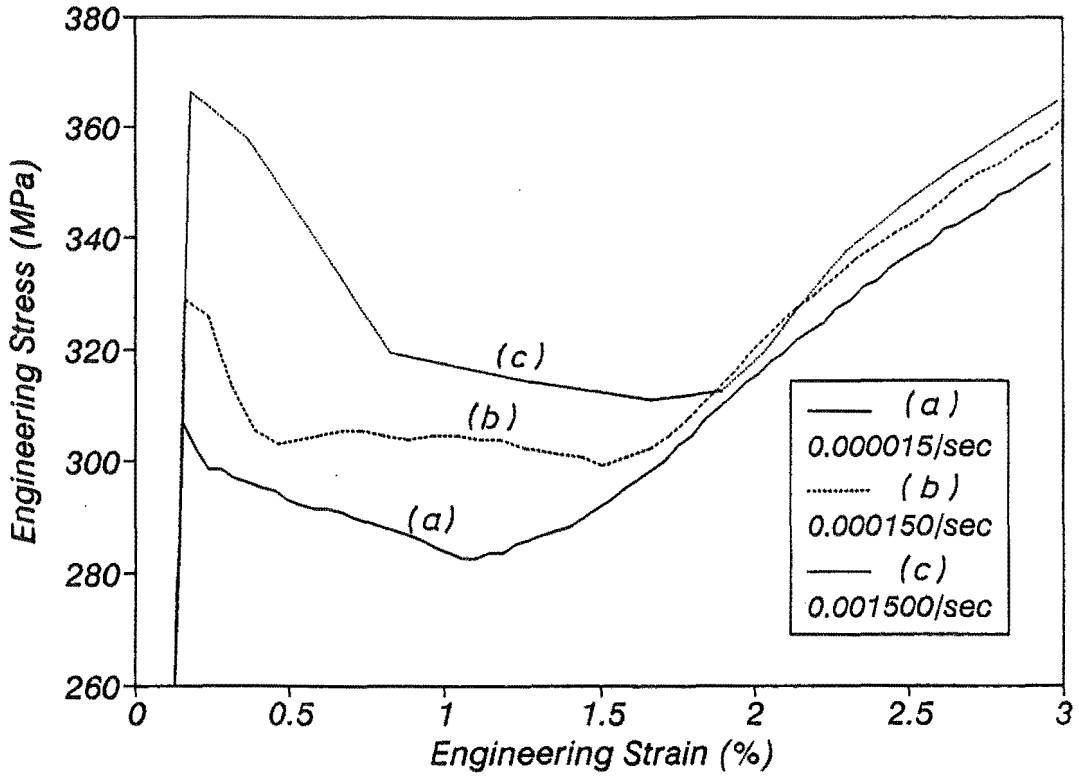

(b) Close up of Yield Plateau Region

Fig. 2.64 - Strain Rate Effects on the Monotonic Behaviour of Grade 300 Steel.

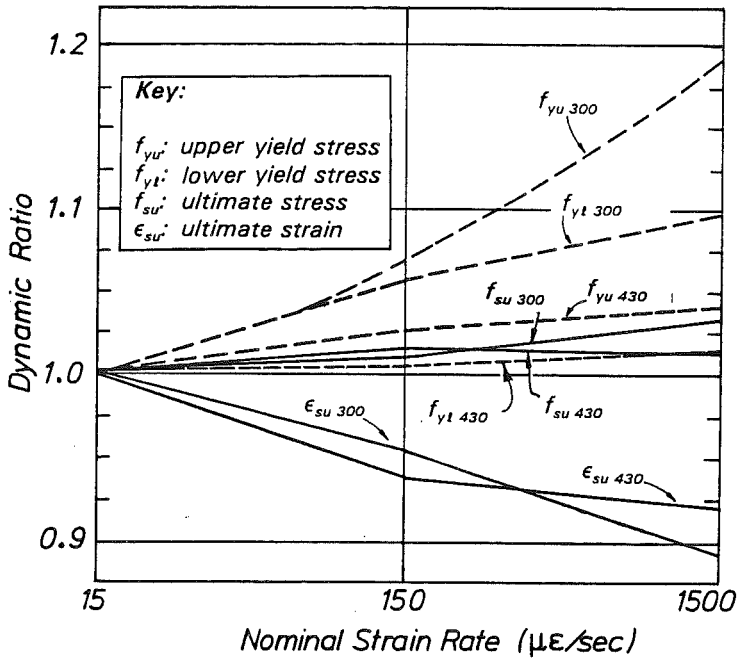

Fig. 2.65 - Comparison Between the Strain Rate Effects on Grades 430 and 300 Steel.

Four tests were carried out for each steel grade to examine the effects of natural strain ageing. Two tests were carried out in the Lüders strain region and the other two at the initiation of the work hardening region. In each case, one of the tests was pre-strained, unloaded and then restrained while the second test included a reverse cycle to compare the effects of strain ageing with the previous strain-stress history.

For each test type a control test, where the test history was continuously applied at a quasi-static rate, was carried out so that natural strain ageing would be insignificant. Two other tests were partially tested and then re-tested after 37 and 147 days. The pre-tested coupons were left in an incubator at 20°C during this period. It is assumed that most of the strain ageing would occur within 147 days, although according to Erasmus (1987), for a constant temperature below 150°C, strain ageing develops over a period of time which depends on the manganese content, the "active" nitrogen and the grain diameter.

2.6.4.2 Test Results on Grade 430 Steel

Figs. 2.68 to 2.71 show test results for the Grade 430 steel. No strain ageing was observed to occur in this steel. The main reason for this behaviour is the addition of vanadium in the chemical structure. Pussegoda (1978) has demonstrated that traces of vanadium of 0.018-0.06% practically eliminate the effects of strain ageing. Vanadium is a strong nitride forming element which precipitates the "active" nitrogen that otherwise would cause natural strain ageing to occur. The vanadium content of the Grade 430 steel coupons H, HV and HX tested in this programme was within this range as can

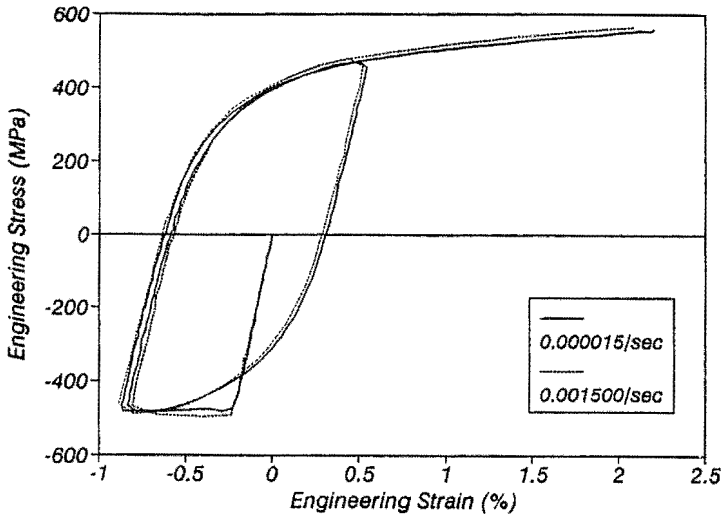

(a) Cycles in the Yield Plateau Region at Initiation of Strain Hardening

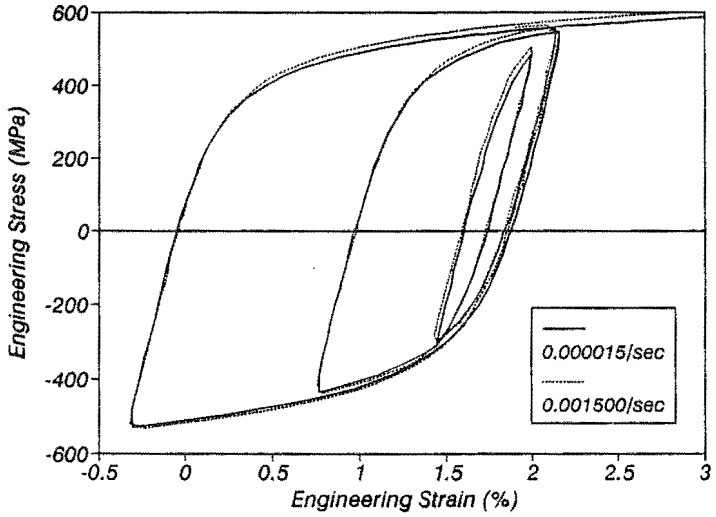

(b) Cycles in the Strain Hardening Region up to 2.2% of Strain

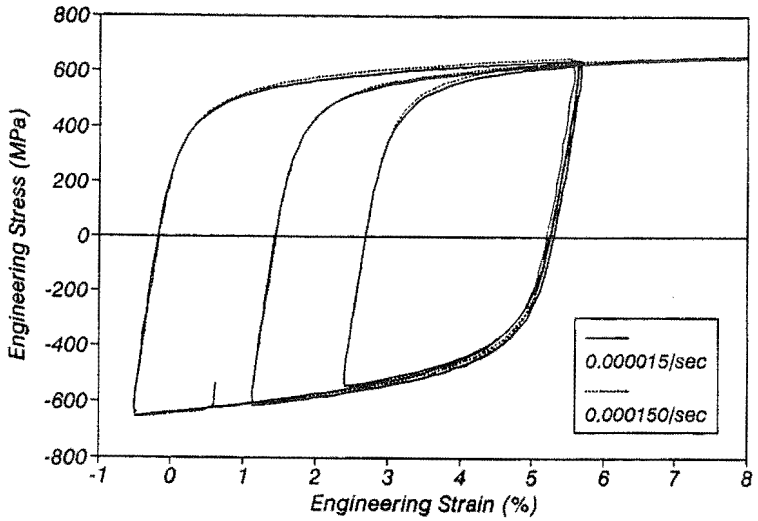

(c) Cycles in the Strain Hardening Region up to 5.6% of Strain

Fig. 2.66 - Strain Rate Effects on the Cyclic Behaviour of Grade 430 Steel.

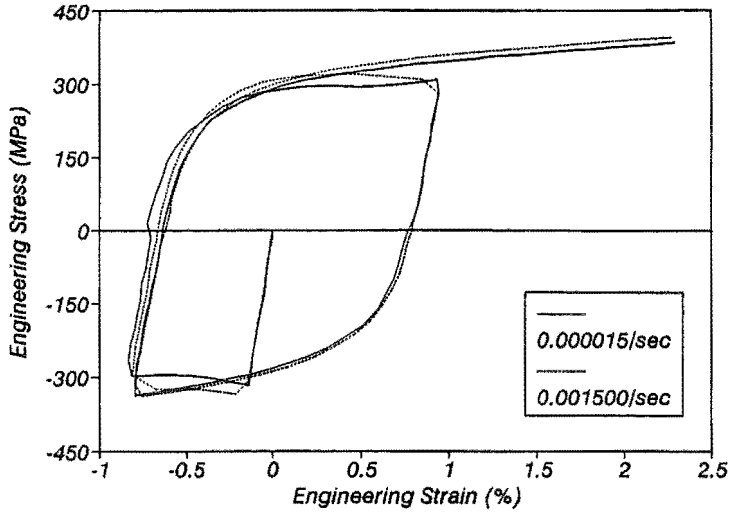

(a) Cycles in the Yield Plateau Region at Initiation of Strain Hardening

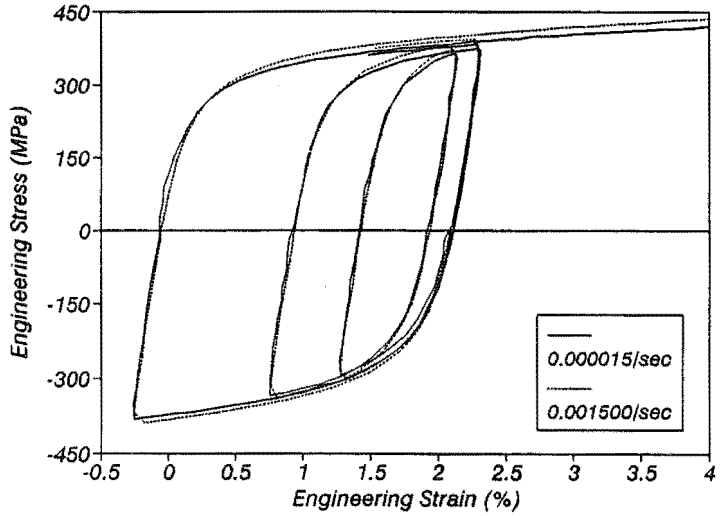

(b) Cycles in the Strain Hardening Region up to 2.4% of Strain

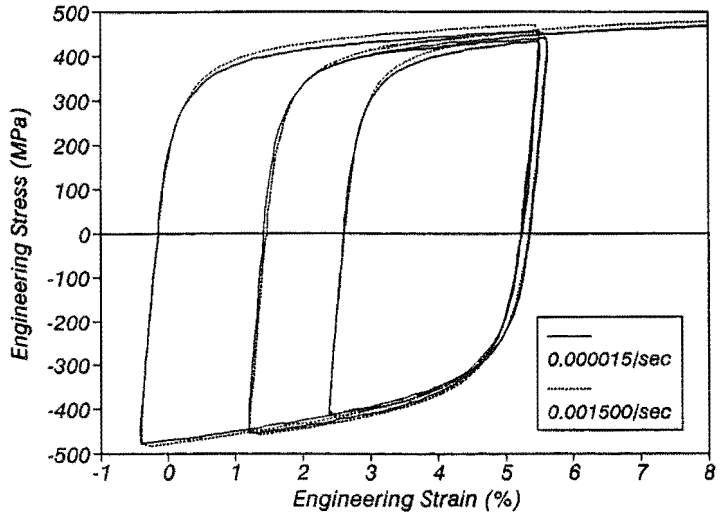

(c) Cycles in the Strain Hardening Region up to 5.5% of Strain

Fig. 2.67 - Strain Rate Effects on the Cyclic Behaviour of Grade 300 Steel.

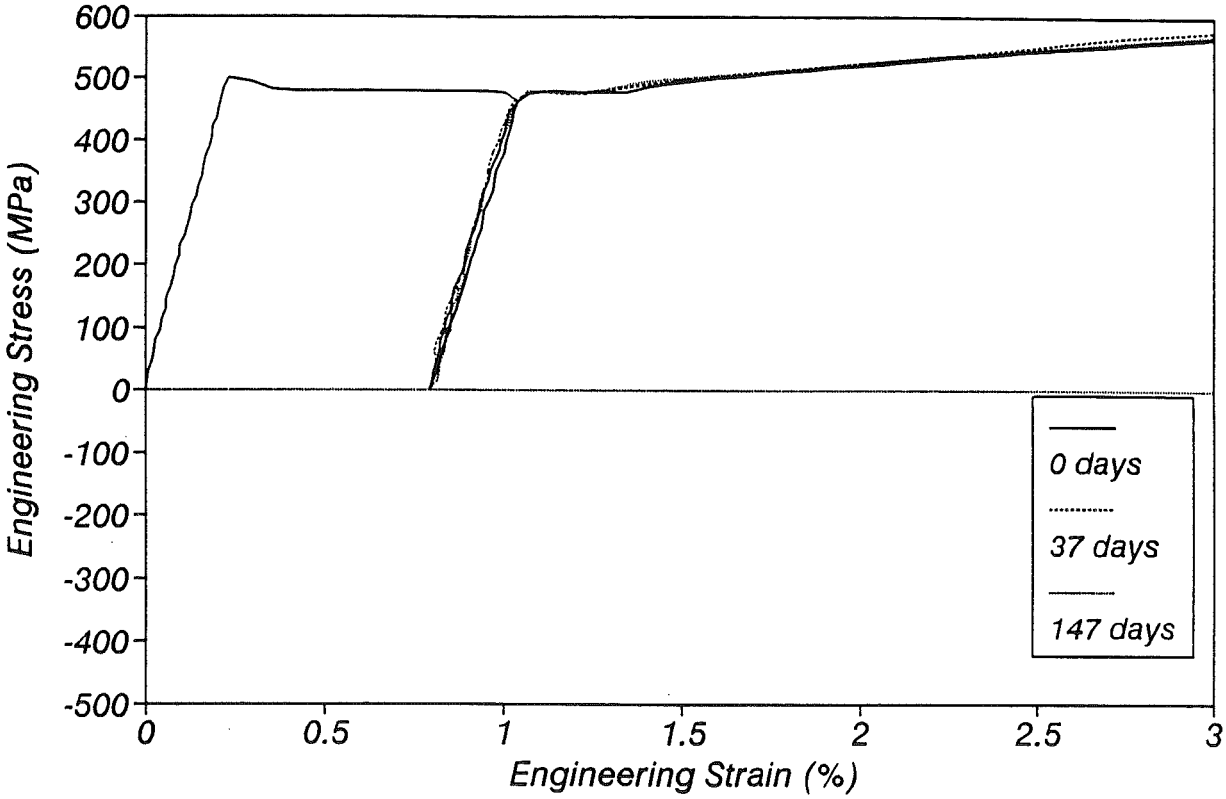

Fig. 2.68 - Strain Ageing Test H1T.

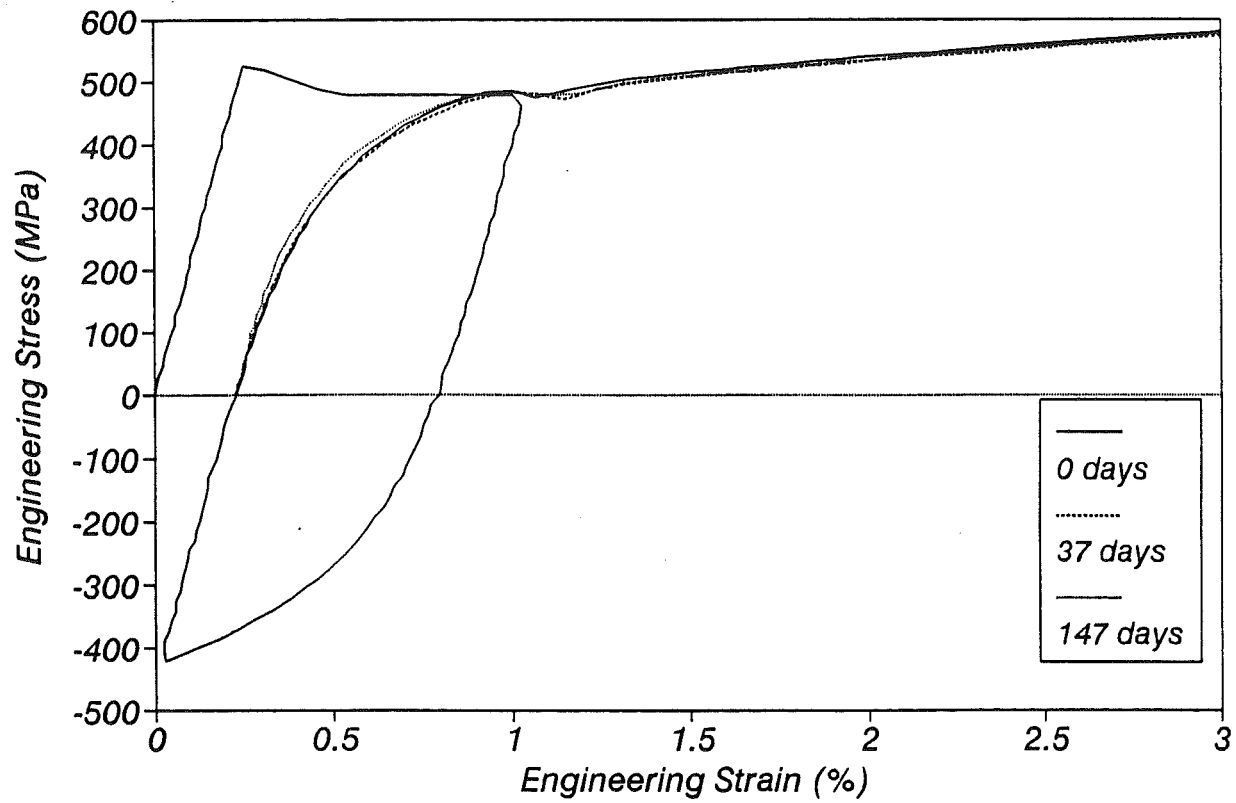

Fig. 2.69 - Strain Ageing Test H1C.

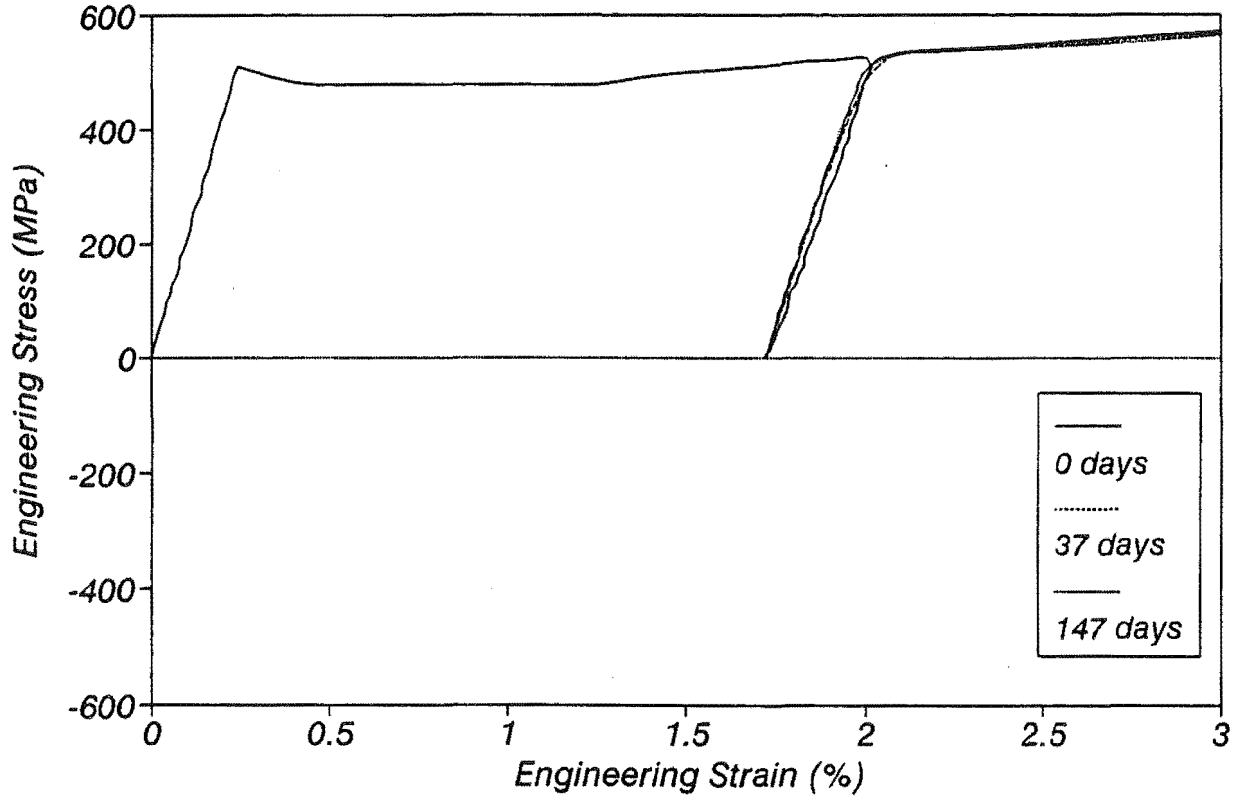

Fig. 2.70 Strain Ageing Test H2T.

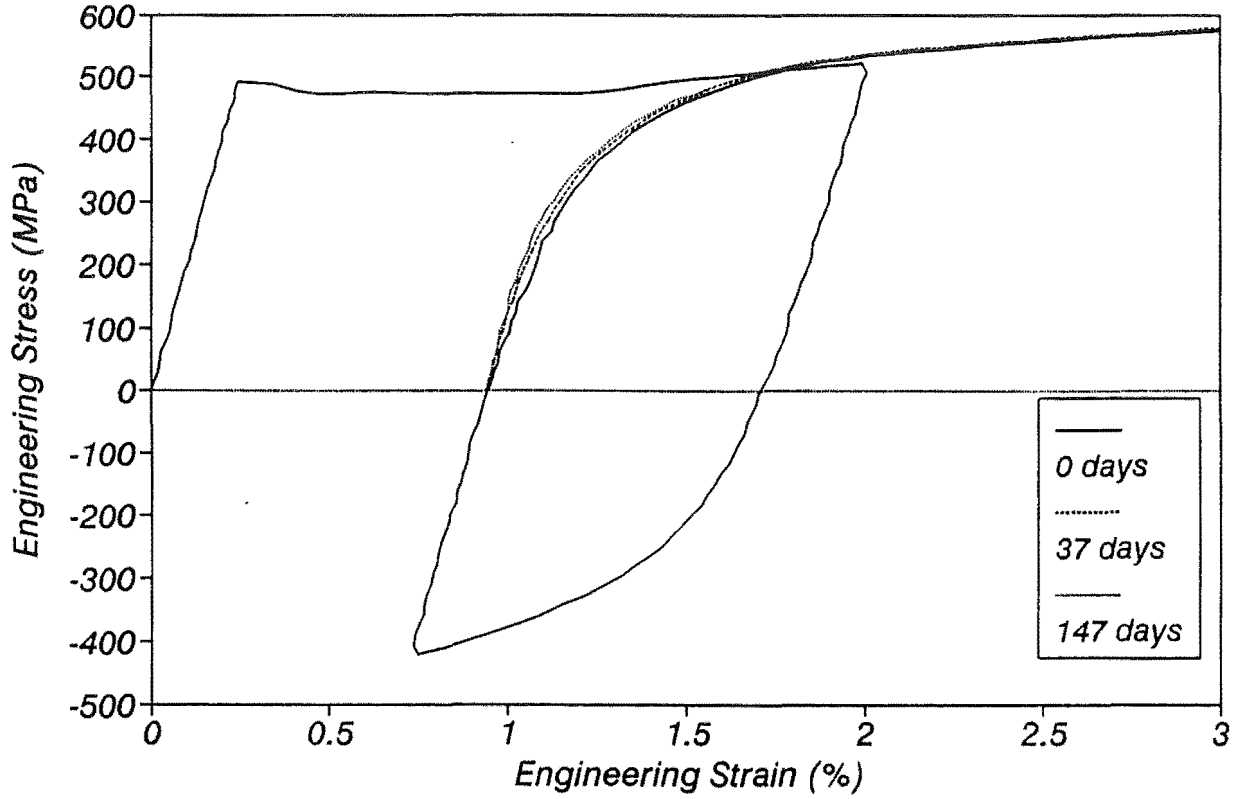

Fig. 2.71 - Strain Ageing Test H2C.

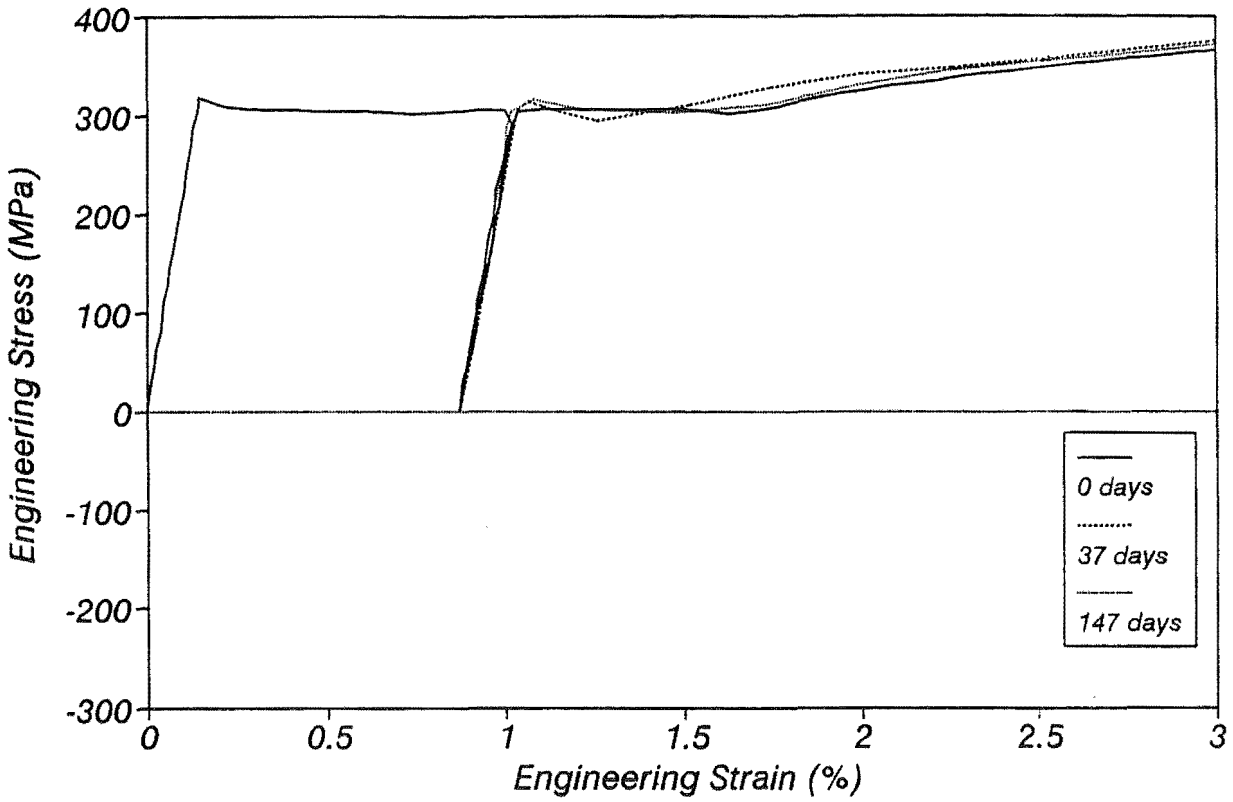

Fig. 2.72 - Strain Ageing Test M1T.

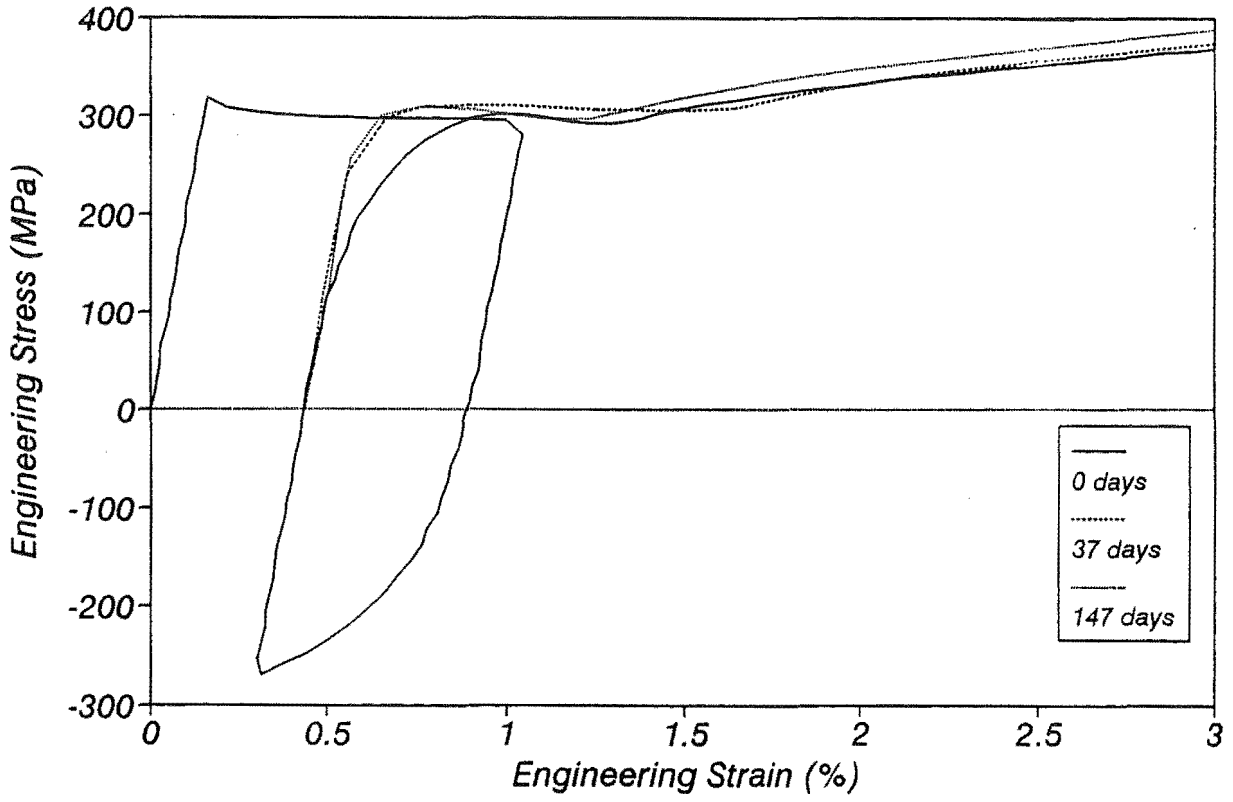

Fig. 2.73 - Strain Ageing Test M1C.

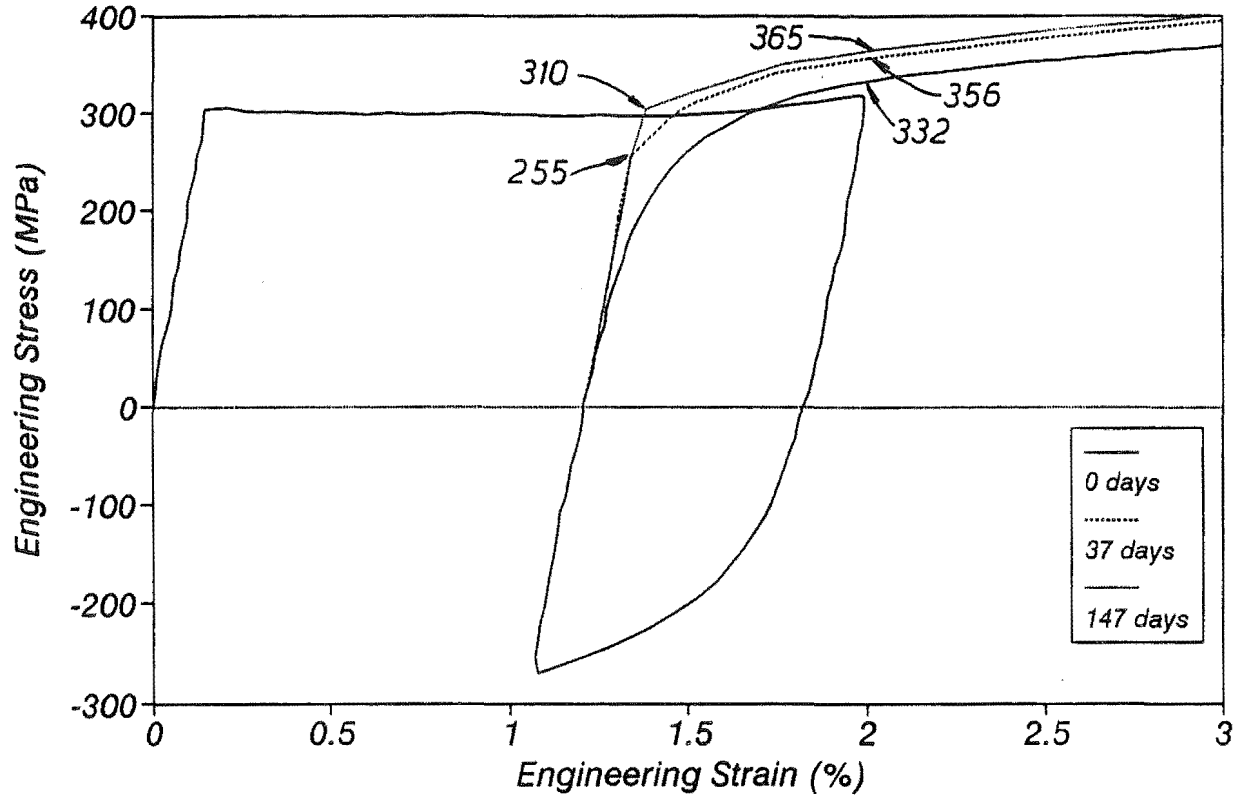

Fig. 2.74 - Strain Ageing Test M2T.

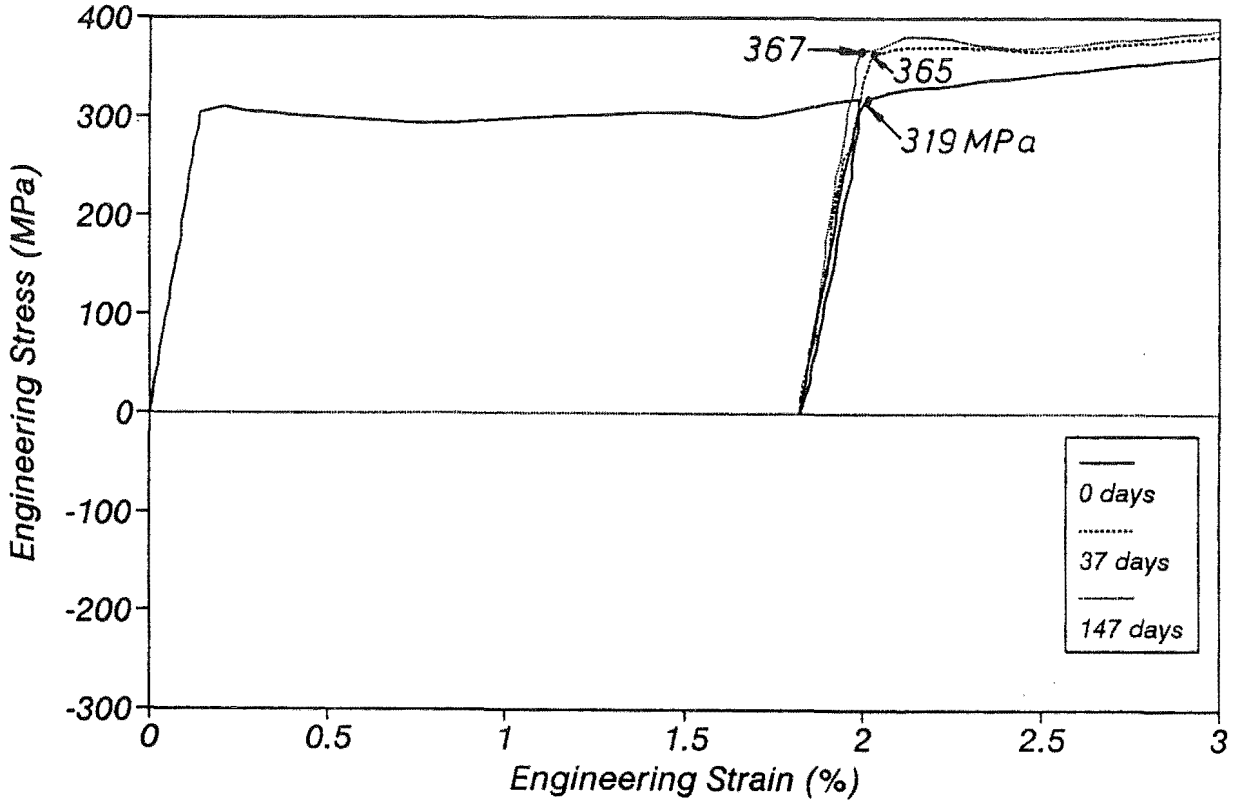

Fig. 2.75 - Strain Ageing Test M2C.

be seen in Table 2.2. It can therefore be concluded that strain ageing effects can be ignored for this type of steel at moderate levels of pre-straining.

2.6.4.3 Test Results on Grade 300 Steel

The Grade 300 steel was susceptible to some natural strain ageing as shown in Figs. 2.72 to 2.75. Figs. 2.72 and 2.73 show the test results in the Lüders strain region. Most of the strain ageing occurred in the first 37 days. It can be seen that the Bauschinger effect gradually vanishes and the initial elastic behaviour appears instead, showing a new upper and lower yield point. The increase in stiffness is not accompanied by an increase in strength. This behaviour can be explained as strain ageing developing in discrete bands or Lüders bands where the plastic deformation has previously taken place leaving the elastic bands to act as a fuse which controls any increase in strength.

The tests in the work hardening region also showed a recovery of the initial elastic modulus and a significant increase in strength was also observed. In test M2T, depicted in Fig. 2.74, a new yield plateau reappeared at a stress level 1.25 times larger than the yield stress of the virgin material. In test M2C, shown in Fig. 2.75, the material behaved linearly to a stress level comparatively similar to the yield stress of the virgin material but the work hardening region had a shift of similar magnitude to the one observed in test M2T. Thus, it appears that the previous stress-strain history only influences the magnitude of the effects of strain ageing on the yield stress and any increase of strength in an aged reinforcing steel bar is coupled with the increase in strength caused by strain hardening.

It is difficult to evaluate the increase in strength caused by the combined actions of strain ageing and strain hardening in a reinforced concrete member reinforced with Grade 300 steel which is repaired after a seismic event. Two main factors are very relevant for any assessment:

a) The previous strain-stress history of the longitudinal bars in the plastic hinge region to be repaired.

b) The extent of the damage of the plastic hinge region.

The first point has already been discussed. With regard to the second point it is important to note that tension-stiffening may have a beneficial effect. Reinforcing steel bars in a region with little damage may still have good bond with the surrounding concrete. Strains in the strain hardening region are likely to be found adjacent to the main cracks. In between main cracks, bar strains may not reach the strain hardening strain and therefore this region may not show any increase in strength. Hence, the strength of the repaired member is not expected to increase in this case.

The longitudinal strain distribution in reinforcing bars is more uniform in the plastic hinge region of a reinforced concrete member where spalling or splitting of the concrete around the bars is observed. In this case the combined effects of strain ageing and strain hardening will increase the capacity of the member and the consequences of the plastic hinge migrating elsewhere in the member or even into an adjacent member need to be carefully evaluated.

Overstrength factors accounting for the combined effects of strain ageing and strain hardening need to be experimentally determined to evaluate the capacity of a repaired member fabricated with either Grade 300 or Grade 380 steel. For example, a factor of the order of 1.40 could be expected for members built with Grade 300 steel while a larger factor would probably be found for Grade 380 steel.

2.7 EFFECT AND MODELLING OF BUCKLING

A detailed analysis of the effect and modelling of buckling in reinforcing steel is beyond the scope of this project. However, buckling of longitudinal reinforcing steel leads to the failure of reinforced concrete members and so it will be discussed briefly in this section.

When longitudinal reinforcement is stretched and then recompressed, it becomes susceptible to buckling. Buckling can cause lateral steel to fracture as the buckled steel bears out against the lateral steel. Buckling can also lead to fracture of the longitudinal steel itself, as well as slightly decreasing the flexural and axial compressive strength of the member from the loss of compression force carrying capacity in the reinforcement. When buckling occurs, the concave surface of the buckled region can reach average compressive strains of 40% or more and larger values can be reached at the root of the deformations. The authors have noted splitting of reinforcing steel parallel to the longitudinal axis and cracking at the root of the deformations in reinforcing steel from reinforced concrete prisms subjected to monotonic compression tests. The splitting cracks were formed at locations which initially had surface blemishes and although the cracks are interesting and indicate the bursting strain in the compression side of the longitudinal steel, they are not critical. However, the cracks that form at the roots of the deformations were perpendicular to the bar axis and are susceptible to stress concentrations as the bar is loaded in tension. Such cracks are shown in Fig. 2.76 in photographs from an electron microscope. Fig. 2.76 illustrates a longitudinal cut through the concave side of a HD12 buckled bar, where two "compression" cracks can be seen. This bar was subjected only to monotonic compression. The radius of buckling was equal to 13mm. A companion probe tested in tension showed the propagation of the cracks at the root of the deformations until the bar fracture prematurely showing a low tensile carrying capacity.

Such fractures are often referred to as "low-cycle fatigue" [e.g. Mander (1984) and Chai et al (1991)]. In the Introduction to an ASTM publication on low cycle fatigue, Coffin (1969) noted that "failure in low cycle fatigue occurs in fewer than 50,000 cycles. It is further characterized by the existence of a stress-strain hysteresis loop and by the measurement of a plastic strain range in the test specimen." Coffin states that the configuration of low cycle fatigue specimens is important since buckling or bending must be avoided.

It is the belief of the authors that the fracture of longitudinal steel in reinforced concrete members is not caused by low cycle fatigue but rather is caused by the capacity of the material compression side of the buckle being used up. It was noted in Section 2.5.2 that the strain which corresponds to the peak tensile load resisted by a reinforcing bar seems to be directly affected by the

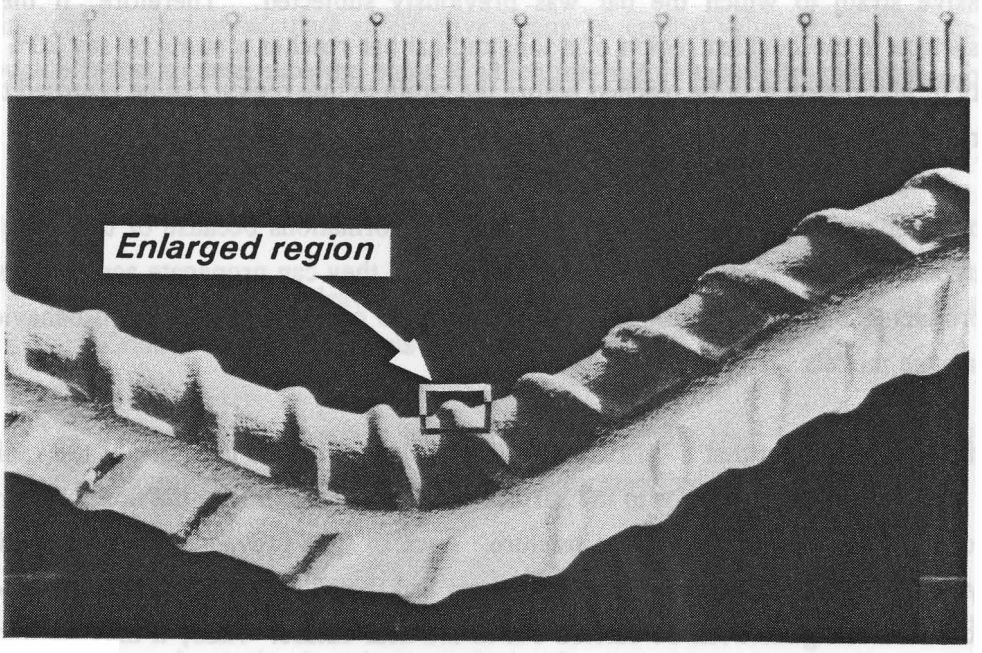

(a) Buckled Longitudinal Bar (Scale is in mm)

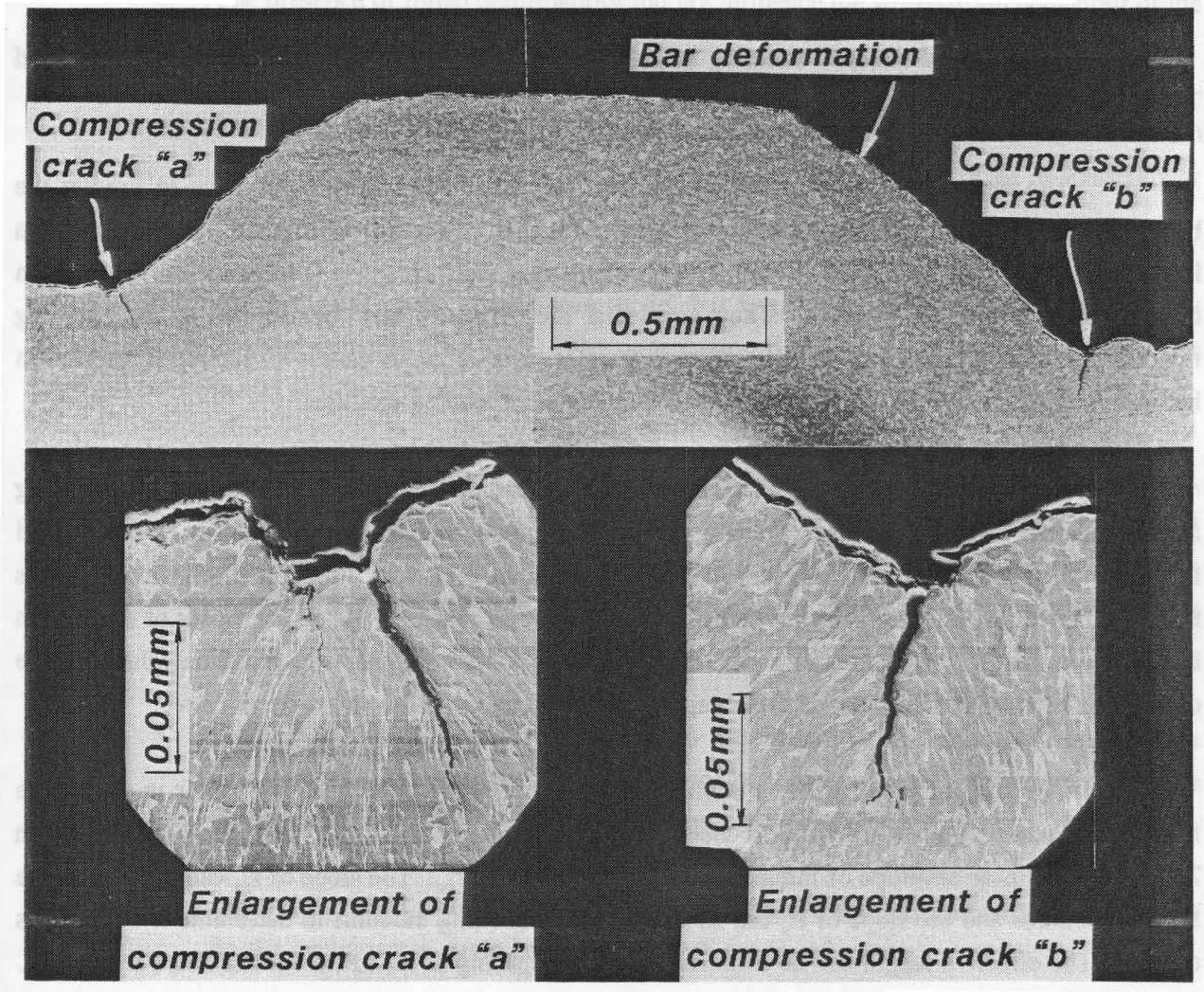

(b) Rib with Compression Cracks at the Roots

Fig. 2.76 - Longitudinal Section Showing Compression Cracks at the Root of a Deformation of the Concave Side of a Buckled HD12 Reinforcing Steel Bar.

peak compressive strain to which the bar was previously subjected. Therefore, if the extreme compression surface in the buckled region of a longitudinal bar reaches a strain of say 20%, then the tensile capacity of that region may be reached before the strain in that region can be returned to nil, i.e. before the bar can be straightened.

This problem is increased by the presence of deformations because of the "compression" cracks that can occur at their roots. Once cracks are formed, they can propagate across the section of the bar thus producing a premature failure. It is important to consider this localised behaviour when considering damage models for reinforcing steel.

The authors suspect that a "critical buckle" can be defined as the ratio of the radius of the buckle (either to the longitudinal axis or to the surface of the deformations) to the nominal bar diameter below which cracks form which will lead to fracture. Lack of time prevented an investigation of the mechanism by which the initial compression cracks form and the existence of a critical buckle but it is hoped that such an investigation can be carried out in the near future. Also, it may be important to address the question, is the critical radius of buckling affected by the previous stress-strain history, especially after large amplitude reversals?

A review of inelastic buckling is given by Mander et al (1984), Zahn et al (1986), and Tanaka and Park (1990) and only the concepts will be discussed here.

The tangent theory uses the tangential modulus of the stress-strain curve to predict the buckling load using the well known Euler equation. Mander et al reported that the peak compression loads resisted in monotonic compression tests on reinforcing steel exceeded the theoretical values even though buckling had commenced. They noted that the curvature that corresponds to the buckling requires that much of the section be subjected to a stress reversal which causes stiffening of the section because the unloading modulus is greater than the tangential loading modulus.

The double modulus theory takes into account the difference in the material that is loading and the material that is unloading. If the two moduli are known, then the neutral axis can be determined for which axial and flexural equilibrium across the section are satisfied. Flexural equilibrium requires that the shape of the buckle or the curvature distribution be estimated so the displacement of the section can be determined. Various methods can be used to determine the appropriate modulus values for the double modulus approach; most of these depend on the location on the stress-strain curve.

The authors propose that a double modulus approach can be used with their model in the following manner. The model for post-yield-plateau Bauschinger effect that was described in Section 2.5.2 has a bi-linear envelope of initial slope E'_u and final slope f'_{su}. The slope of f'_{su} can be used as the loading modulus and the slope of E'_u can be used as the unloading modulus to determine if buckling is critical. The effective length can be estimated by spiral spacing as noted by Tanaka and Park (1990). If unstable buckling is expected to occur, i.e. sufficiently large stiffness cannot be generated to prevent instability, then the compressive stress can be reduced. For a given shape, the distance between two points, the points of contraflexure for example, can be determined. The change in distance between

these points can be used to calculate an effective strain. A critical value can possibly be related to the critical buckle radius to determine the point at which pre-mature tensile fracture might be expected.

2.8 CONCLUSIONS

1. This study has endeavoured to isolate the material behaviour of the two grades of New Zealand reinforcing steels manufactured to NZS 3402 (1989).

2. The cyclic stress-strain behaviour of reinforcing steel is symmetrical in tension and compression up to the point of plastic instability when necking occurs ONLY in the natural coordinate system.

3. The monotonic stress-strain curve in compression can be derived from the monotonic curve in tension based on conclusion 2.

4. The presence of rolled deformations did not influence the stress-strain behaviour of the reinforcing steel.

5. The shape of the Bauschinger effect is not dependent on the monotonic stress-strain curve. The carbon content is an important variable affecting the shape of Bauschinger effect.

6. An analytical cyclic stress-strain model has been proposed and calibrated for New Zealand manufactured steel. The same basic principles can be used to calibrate this model to other types of steels to account for the different chemical composition.

7. The strain ageing effect in Grade 430 steel can be ignored for practical purposes. However, the implications of the strain ageing effects on reinforced concrete members constructed using Grade 300 steel need to be carefully evaluated specially when considering post-earthquake retrofitting. Strain ageing in members constructed with the old Grade 380 steel can have even more severe implications.

8. Strain rate effects are more significant in the Lüders strain region (or yield plateau region) than in the work hardening region for both types of steel. A maximum increase in the yield stress of 10% was observed for a variation of the strain rate of 100 times.

9. Beyond the yield plateau region, a variation of the strain rate has only a small effect on the cyclic stress-strain behaviour of both grades of steel.

10. Grade 300 steel is more susceptible to the strain rate effects than Grade 430 steel.

11. Buckling in deformed reinforcing steel bars can cause large stress concentrations at the root of the deformations in the concave side of the bar which can lead to premature fracture.

2.9 RECOMMENDATIONS FOR FUTURE RESEARCH

1. A complementary buckling model could be integrated with the proposed stress-strain model to consider the geometrical non-linearities. A bi-linear envelope describing the Bauschinger curve could be used as a basis of the buckling model.

2. A detailed look on the effects of buckling on deformed reinforcing steel bars needs to be investigated to address the critical buckling radius at which premature fracture of the bar can be expected to occur. Experimental data is also required to observe on whether the critical radius of buckling is sensitive to the previous stress-strain history.

3. Overstrength factors for the combined effects of strain ageing and strain hardening need to be experimentally evaluated for New Zealand manufactured steel in use in reinforced concrete members.

CHAPTER 3

TEST PROGRAMME ON CONNECTIONS BETWEEN PRECAST CONCRETE ELEMENTS

3.1 INTRODUCTION

The information regarding different connection details to be investigated in the experimental programme for this project was gathered from several consulting engineering firms. This information was used to identify the preferred structural systems in New Zealand for moment resisting frames incorporating precast concrete elements, and to obtain specific details on the arrangements used for connecting the precast elements together. It was found that for buildings between 9 and 21 storeys in height the general trend is to allocate the whole of the earthquake resistance to stiff perimeter frames. Typically, the clear span to overall depth ratio for beams ranges from 3 to 6 while for columns in the upper floors of the building the clear height to overall depth ratio varies between 2.5 and 4. Hence, the emphasis in this experimental programme is on precast concrete components representative of perimeter frames.

3.2 TEST UNITS

3.2.1 Design Considerations

The test programme involved the testing of six subassemblages and the repair work and retesting of one of them. The connection details between the precast concrete elements of the subassemblages were typical of those already described in Section 1.4.1. Fig. 3.1 illustrates the origin of the subassemblages tested. The first four units, Units 1 to 4, were H-shaped subassemblages representing components of Systems 2 or 3 in the lower storeys of a perimeter frame. There, the flexural capacity of the beams may be limited by the maximum level of shear in the potential plastic hinge regions permitted by the Concrete Design Code [NZS 3101 (1982)] if diagonal reinforcement is to be avoided. Units 5 and 6 were cruciform-shaped subassemblages and represented components of Systems 1 and 2 in the upper floors of a perimeter frame where the absence of high axial compression loads in the columns makes the most unfavourable condition for the beam-column joint region.

One feature of perimeter frames is that gravity loading does not have a significant influence on the bending moment diagram of the beams when combined with the full seismic action and therefore both negative and positive moments are of similar magnitude. Also, the point of contraflexure remains near midspan. Fig. 3.2 displays a typical bending moment diagram of a beam of a perimeter frame. Often in practice the designer uses a small moment redistribution to permit equal amounts of top and bottom longitudinal reinforcing steel to be placed in the beams.

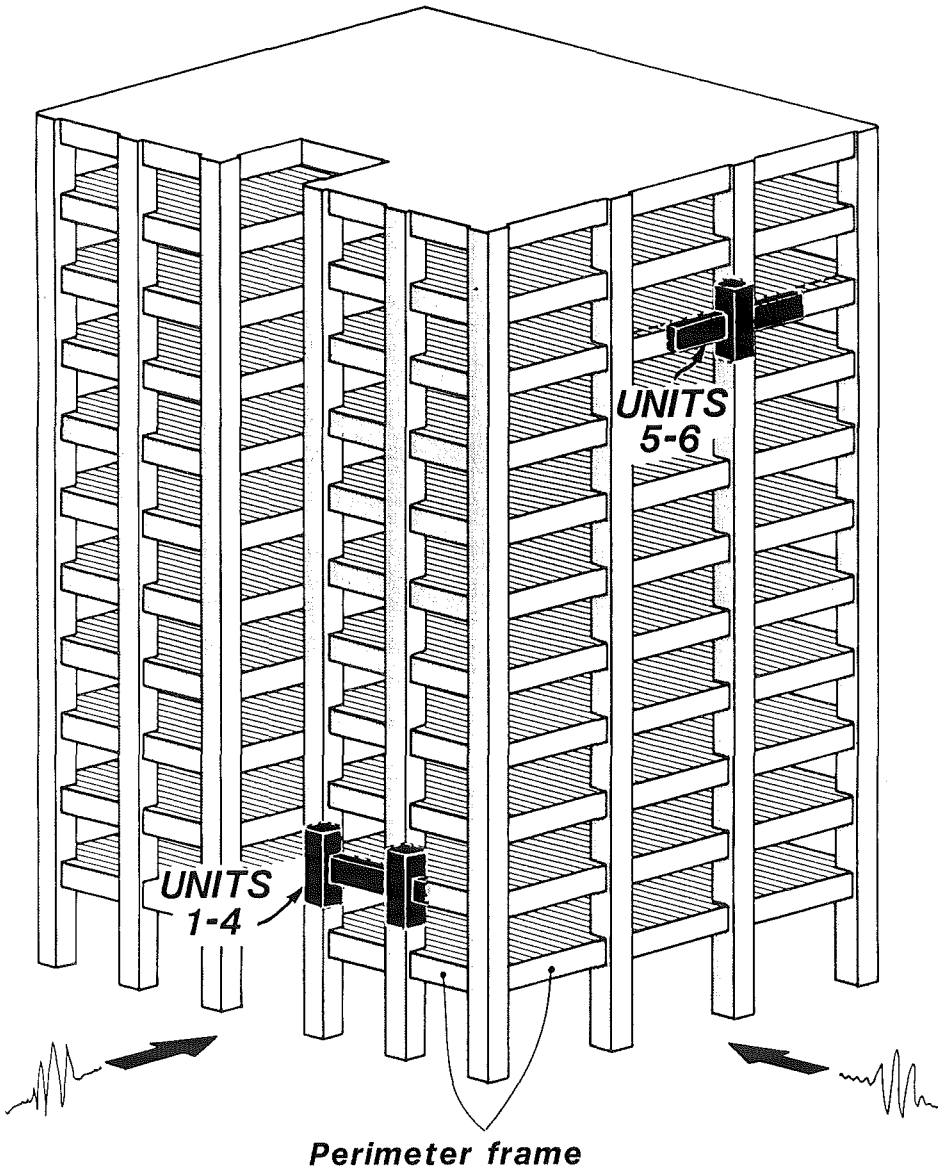

Fig. 3.1 - Origin of Test Units.

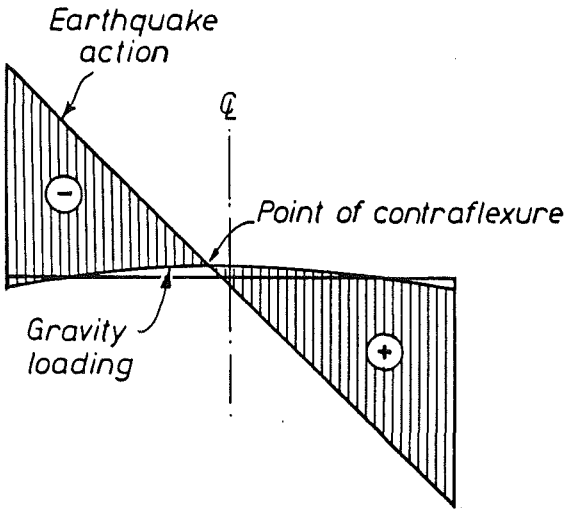

Fig. 3.2 - Typical Bending Moment Diagram of a Beam of a Perimeter Frame.

Table 3.1
Theoretical Stiffness and Drift of Test Units

Unit	Dependable Lateral Load Strength (1) H_D kN	Theoretical Stiffness (2) K_{th} MN/m	Theoretical Drift at H_D %
1	350.2	124.0	0.13
2	350.2	124.0	0.13
3	346.7	124.0	0.12
4	535.0	133.8	0.18
5	254.9	40.6	0.28
6	252.6	40.6	0.28

(1) Based on the specified properties of the materials and assuming a rectangular stress block for the compressed concrete, a bilinear stress-strain relation for the steel and a strength reduction factor $\phi = 0.9$.

(2) Based on one-half of the gross section values for the beams and columns and accounting for flexural and shear deformations only.

The design of the units with regard to interstorey drift complied with the Loadings Code [NZS 4203 (1984)]. This code stipulates that the theoretical interstorey drift for ductile reinforced concrete frames in which all partitions are separated, when acting elastically when subjected to the design seismic loading, shall not exceed 0.33% of the story height. The theoretical interstorey drifts, presented in Table 3.1, were calculated based on the dimensions of the test units following an elastic analysis. To account for cracking in the elements only one half of the gross section properties for flexure and shear of beam and columns was considered. Other sources of flexibility were not included in order to follow normal office procedures. The dependable lateral load strength was used to establish this theoretical interstorey drift.

3.2.2 Description of the Test Units

Figs. 3.3 to 3.8 show complete reinforcing details of all test units. The dimension of the test specimens were near full scale. The effect of a proprietary precast floor system was outside of the scope of this project and therefore the prototypes were slabless.

3.2.2.1 Units 1, 2 and 3

Units 1, 2 and 3 were conventionally reinforced precast concrete units connected at midspan by short lap splices. The two main points of interest to be investigated in the tests on these units were:

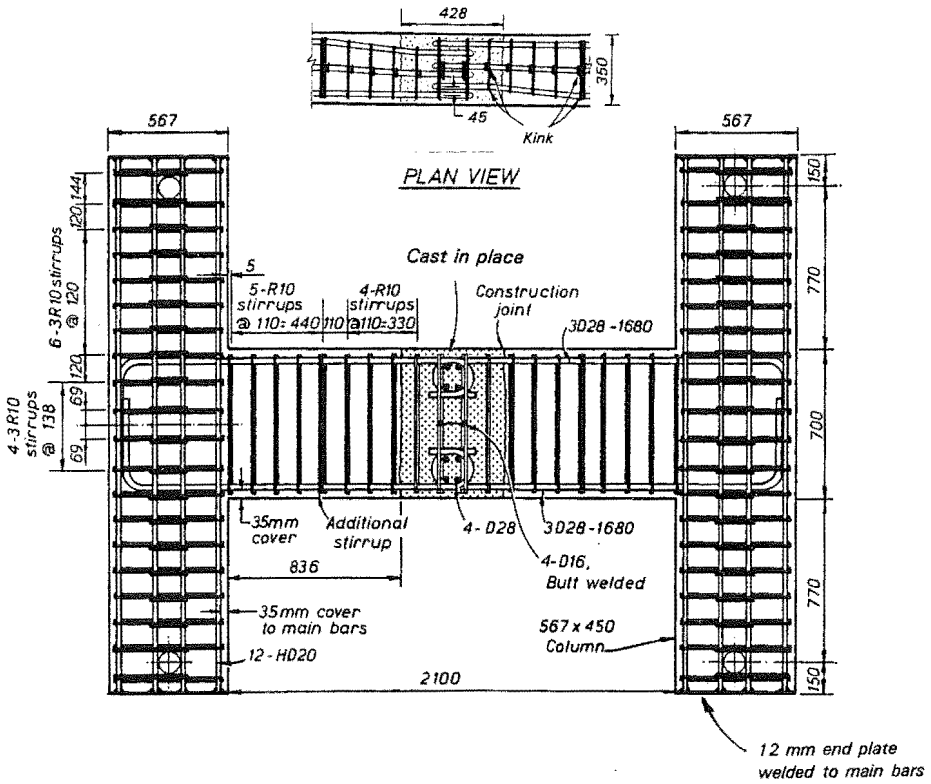

Fig. 3.3 - Reinforcing Details of Unit 1.

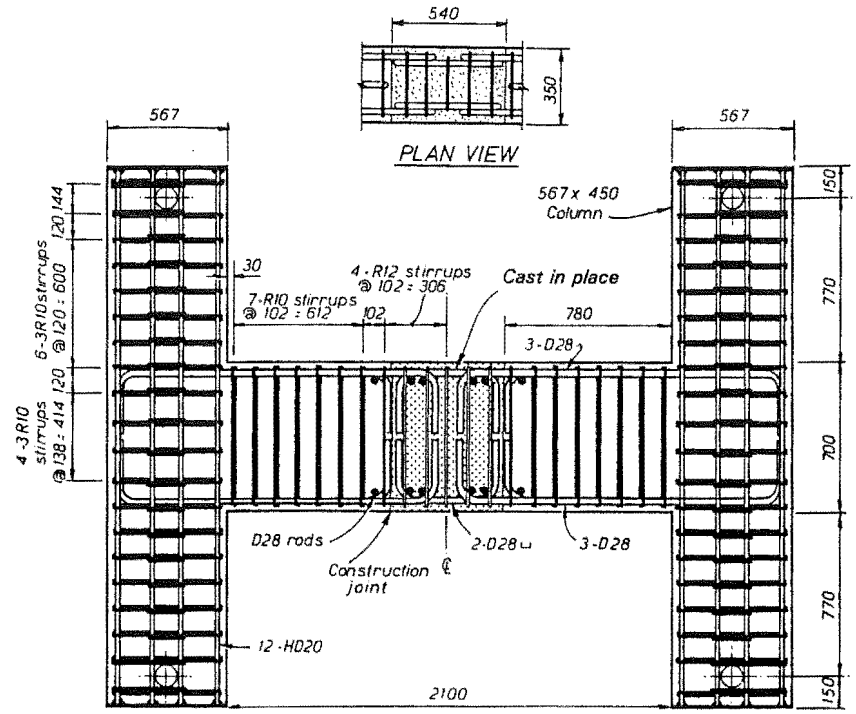

Fig. 3.4 - Reinforcing Details of Unit 2.

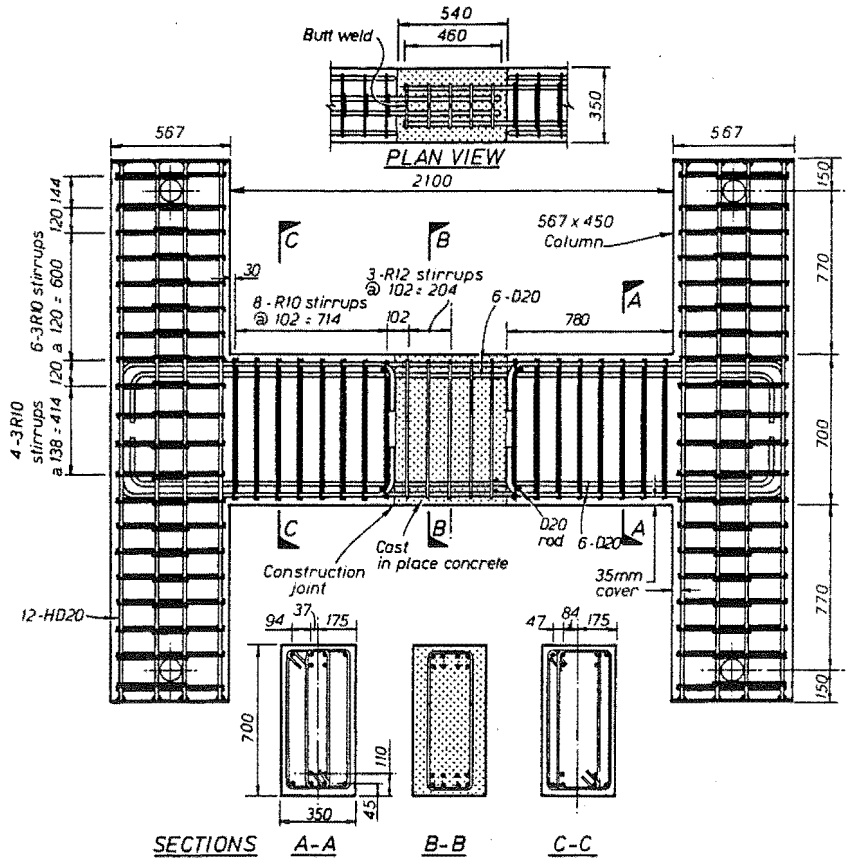

Fig. 3.5 - Reinforcing Details of Unit 3.

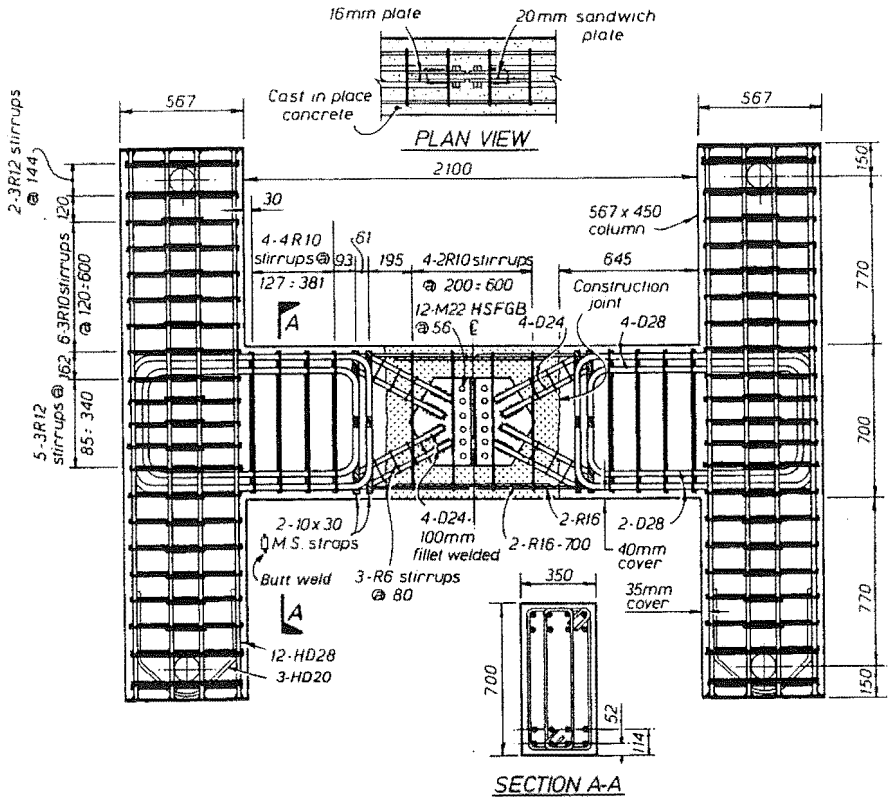

Fig. 3.6 - Reinforcing Details of Unit 4.

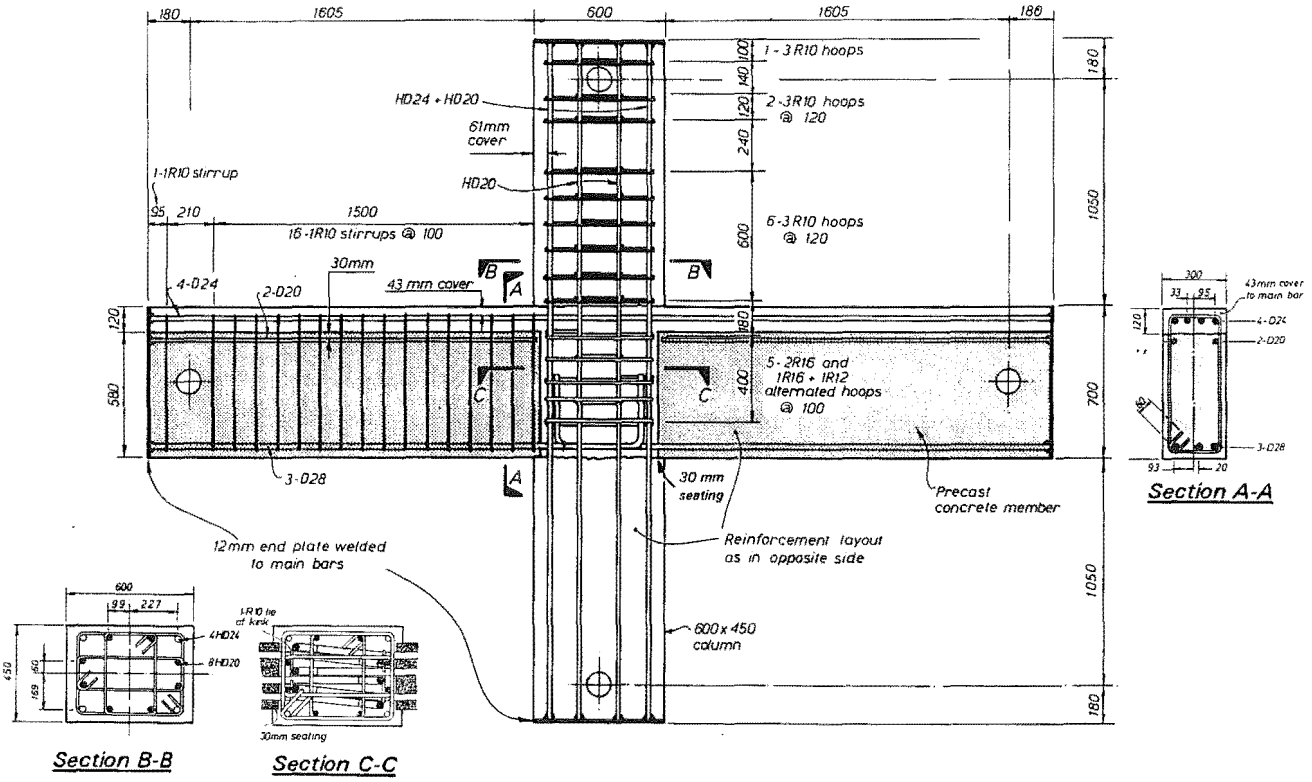

Fig. 3.7 - Reinforcing Details of Unit 5.

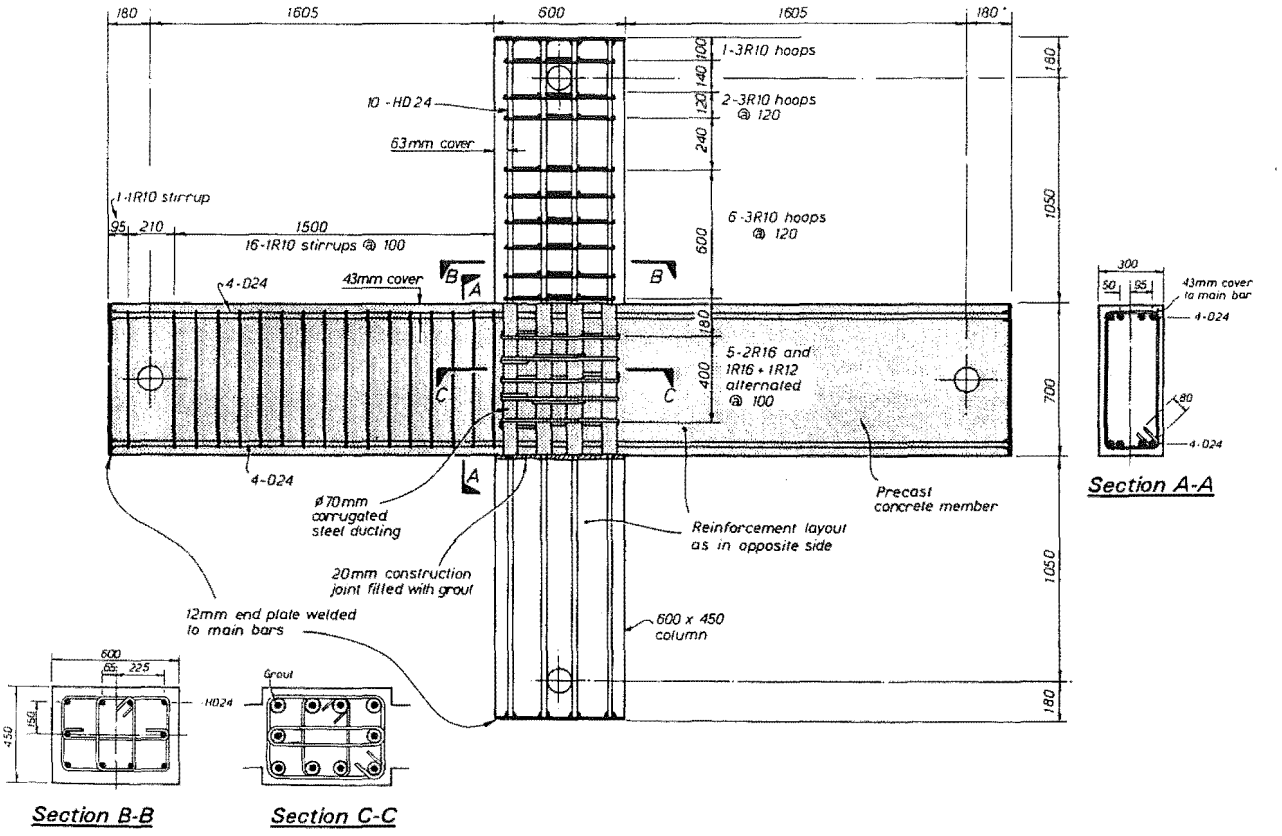

Fig. 3.8 - Reinforcing Details of Unit 6.

a) The behaviour of the connection detail at midspan.

b) The proximity of the lap splice to the critical region in the beams at the column faces.

One difficulty encountered connecting short precast concrete beams in accordance with the Concrete Design Code prior to the recent Amendment No.1 was that when plastic hinges are expected to develop in the beams at the column faces no part of the splice of the longitudinal reinforcement was permitted to occur within a distance of 2d from the column face where d is the effective depth of the beam. Thus, the clear span of the beam had to be at least $4d + \ell_s$ where ℓ_s the splice length. To satisfy this requirement in practice it was necessary to reduce as far as possible the length of the splice and/or to reduce the distance the splice is permitted to commence from the column face without adversely affecting the seismic response of the structure. The alternative of reducing the beam depth to increase the aspect ratio was not often viable since the size of these elements is largely dictated by stiffness needed to satisfy the interstorey drift requirements. A clear span to overall depth ratio of 3 was chosen for the beams tested in Units 1, 2 and 3 to represent the shortest concrete beam normally encountered in practice in such frames. The units were designed to develop plastic hinges in the beams at the column faces. Thus, using capacity design, the columns and beam-column joints were made overstrong. The midspan connections were tested under the maximum shear permitted by the Concrete Design Code when symmetrically reinforced beams are expected to develop plastic hinges and diagonal reinforcing steel in these regions is to be avoided. In terms of nominal shear stresses this limitation is equal to $v^\circ = V^\circ/bd = 0.30\sqrt{f'_c}$ evaluated at a flexural overstrength of 1.25, where V° is the beam shear at overstrength, b is the width of the beam and d is the effective depth of the beam. Hence the longitudinal reinforcement ratio of the beams based on Grade 300 steel was $\rho = \rho' = 0.81\%$ and a nominal concrete compressive strength of 30MPa was specified.

The midspan connection detail of Unit 1, shown in Fig. 3.3, consisted of overlapping 180° hooks commencing at 1.46d from the critical region at the column face. Four D28 transverse rods were placed in contact with the inside of the bends of the hooks. D16 stirrups surrounded the connection in the cast in place concrete joint and was arbitrarily chosen following an existing detail. This reinforcement was, according to the nominal properties of the steel, able of transferring 115% of the beam shear at overstrength. Transverse steel elsewhere in the beam was controlled by the shear demand in the plastic hinge regions. All the longitudinal steel in the beam was spliced using this detail involving overlapping 180° hooks at midspan and kinking of the longitudinal bars was necessary to offset them in the connection. An additional stirrup was placed at the kink.

Unit 2 was connected at midspan using double 90° hooked "drop in" bars as shown in Fig. 3.4. The connection detail commenced at a distance 1.23d from the column face. As in Unit 1, transverse rods were tied in contact with the inside of the hooks of the lapped bars. Two-thirds of the bars were spliced using this detail at midspan and one-third of the beam longitudinal bars were anchored within the precast concrete members. This curtailment was deliberately made to observe the effects of higher stresses in the longitudinal steel, up to yielding, in the connection region. The transverse reinforcement in the connection region was capable of transferring 80% of the beam shear at

overstrength. Elsewhere in the beam the transverse reinforcement provided was governed by the shear requirements in the plastic hinge regions.

Fig. 3.5 depicts the complete reinforcing details of Unit 3. The midspan connection detail consisted of non-contact lap splices commencing at 1.27d from the column faces. The lap length of $23d_b$ used accounted for the direction of concreting or top bar effect and the amount of transverse steel surrounding the lap. As for Unit 2 only two thirds of the longitudinal bars were spliced at midspan. The transverse reinforcing steel in the plastic hinge regions was controlled by the anti-buckling requirements. The transverse reinforcement in the connection region was governed by the need to transfer the forces between the splices by a 45° truss as suggested by Paulay (1982).

3.2.2.2 Unit 4

Unit 4, shown in Fig. 3.6, had a diagonally reinforced midspan connection scaled from a real component. This arrangement has been used when the nominal shear stress at overstrength, $v°$, in the potential plastic hinge regions has exceeded $0.30\sqrt{f'_c}$. For nominal shear stresses $v° = V°/bd > 0.30\sqrt{f'_c}$ the Concrete Design Code requires the use of diagonal reinforcing steel to resist the shear force in that region, so as to avoid loss of energy dissipation and strength degradation caused by an early sliding shear failure. This Code requirement makes it difficult to detail reinforcement for short precast concrete beams falling in this category. However, the beam longitudinal reinforcement can be detailed to preclude the formation of plastic hinges at the column faces and hence to concentrate all plasticity into the beam midspan region where the diagonal reinforcing steel can be easily fitted. This solution has been presented by Buchanan (1979) and tested by Bull (1978) for cast in place construction. It can be modified for precast concrete construction by welding the diagonal bars to steel plates which are bolted at midspan. This arrangement also has the advantage that the beam-column joint region can be designed to be less congested because the Concrete Design Code easies the transverse joint reinforcement requirements if the adjacent portions of the beam remain in the elastic range.

The dimensions of the real diagonally reinforced component were adjusted within the dimensions of Units 1 to 3. The design used the simple truss model illustrated in Fig. 3.9. At the bend

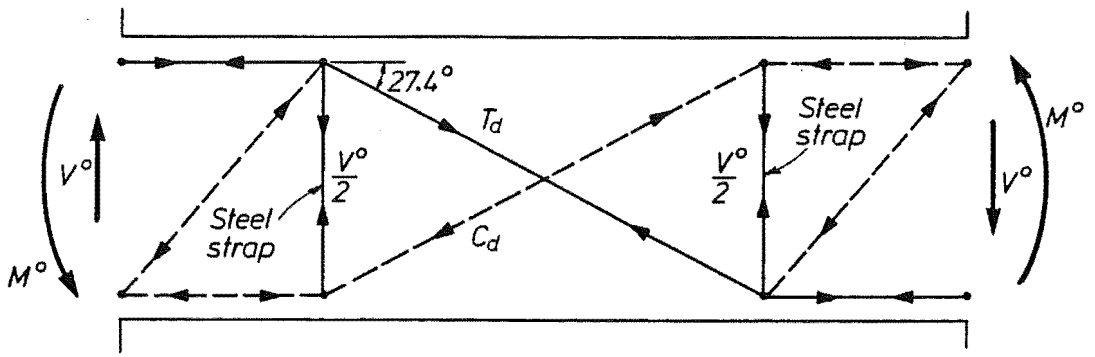

Fig. 3.9 -Simple Truss Model Assumed for the Design of Unit 4.

of the diagonal bars, 30x10 mm vertical steel straps were provided to transfer one half of the total shear force with an overstrength factor of 1.25. These straps were cut from a flat bar, formed to a "C" shape and joined by butt welding the ends. Four extra D28 bars were provided in the strong regions of the beam next to the column faces to preclude the formation of plastic hinges in this region. These bars were anchored with 90° hooks adjacent to the bend in the diagonal bars. The D24 diagonal bars were fillet welded over a length equal to $4d_b$ to 16mm thick mild steel plates at the midspan of the beam. The D24 and D28 were bent using a 140 mm diameter mandril, equivalent to a diameter of bend of $5.8d_b$ and $5d_b$, respectively. A 20mm thick sandwich steel plate was used for interconnecting the steel plates of the precast components at midspan. The holes in this plate were 2mm oversized on one side and slotted on the other side to give ample construction tolerances. M22/TF high strength friction grip bolts passing through the 16mm and the 20mm thick steel plates were used to interconnect the precast concrete units. The bolts were designed to transfer by friction the total shear force at overstrength plus the small moment arising from the eccentricity between the line of action of the bolts and the point of contraflexure at midspan. A coefficient of friction of 0.32 was assumed in the design.

Unit 4 was repaired after testing and retested. Repair details are presented in Chapter 5 together with test results.

3.2.2.3 Units 5 and 6

The cruciform shaped units tested, Units 5 and 6, had beams with an equivalent clear span to overall depth ratio of 4.58. Both units had identical dimensions and were designed to develop plastic hinges in the beams at the column faces.

Unit 5, shown in Fig. 3.7, had a beam-column joint with a cast in place joint core. The bottom bars of the beams were anchored inside the core of the beam-column joint, which contravened the requirements of the Concrete Design Code [NZS 3101 (1982)], which recommends that longitudinal beam bars that are intended to be terminated at an interior column be passed right through the core of the column and terminated with a standard hook immediately outside the far side of the hoops enclosing the beam-column joint.

Some of the potential problems to be investigated in this system were:

a) The effect of the hooked anchorage of the bottom bars of the beams inside the beam-column joint core on the overall behaviour of the joint.

b) The influence of the cold joint between the end of the precast beam and the column face when the plastic hinge develops in that region.

The longitudinal steel reinforcement of the beams, based on Grade 300 steel, was $\rho = 0.93\%$ and $\rho' = 0.95\%$. D24 bars were selected as top reinforcing steel since the code limits the maximum bar diameter to $h_c/25$. D28 bars were chosen as bottom reinforcing steel to reduce congestion and because it was the largest bar diameter that could be anchored in the joint core. Section C-C in Fig. 3.7 shows the positioning of the hooked bars inside the beam-column joint region. The outer D28 bars were

kinked inside the joint core and an additional R10 tie was detailed for the out of plane forces induced in the kink. The inner D28 bars were 20mm offset from the beam vertical centreline. The end of the precast concrete beams were seated on the 30mm of concrete cover of the lower column. If that cover concrete remained intact, it was calculated that the beam shear at overstrength could be transmitted by bearing between the precast member and the concrete cover of the column below, based on a maximum bearing stress at an overstrength of $0.85f'_c$. The transverse reinforcement in the potential plastic hinges of the beams was governed by the antibuckling requirements. The hoops in the beam-column joint were designed to take all the horizontal shear in this region.

Unit 6, depicted in Fig. 3.8, had a precast concrete element which passed through the beam-column joint region. The precast concrete member had vertical ducts in the joint core region to allow the protruding column bars to pass through. The horizontal construction joint between the precast beam and column and the vertical ducts was grouted in one operation. Potential problems to be investigated in this system were:

a) The effectiveness of the grout around the longitudinal column bars, which needs to provide adequate bond and to permit adequate transfer of the transverse forces from the joint hoops to the vertical column bars.

b) The performance of the grouted horizontal construction joints between the precast beam and the columns.

The beams of Unit 6 had 4-D24 bars as top and bottom reinforcing steel; that is $\rho=\rho'=0.93\%$. The vertical ducts in the joint core region of the precast beams were formed using corrugated 70mm overall diameter steel tubes made from 0.4mm thick by 36mm wide galvanized steel sheets. The amount of transverse steel in the beams and in the beam-column joint region was identical to that used in Unit 5. However, the arrangement of the column reinforcement in Unit 6 was slightly changed due to the different positioning of the beam bars and the larger spaces required by the corrugated vertical ducting.

3.3 LOADING FRAMES

Two different loading frames were designed for the experimental programme. They are shown in Fig. 3.10. Appendix B contains construction details of both frames.

The loading frame LF1 designed for the testing of the H-shaped Units 1, 2, 3 and 4 is shown in Fig. 3.10 (a). The main consideration in the design of this frame was to be able to apply equal displacements at each column to induce a bending moment in the beam similar to that normally encountered in the beam of a perimeter frame shown in Fig. 3.2. That is, the interstorey drift applied to each column of the units was identical. Two 1000kN independent hydraulic double-acting actuators were used to apply the predetermined cyclic test sequence. The hydraulic actuators reacted against the testing floor and induced some axial tension and compression loads on the columns, which had to be

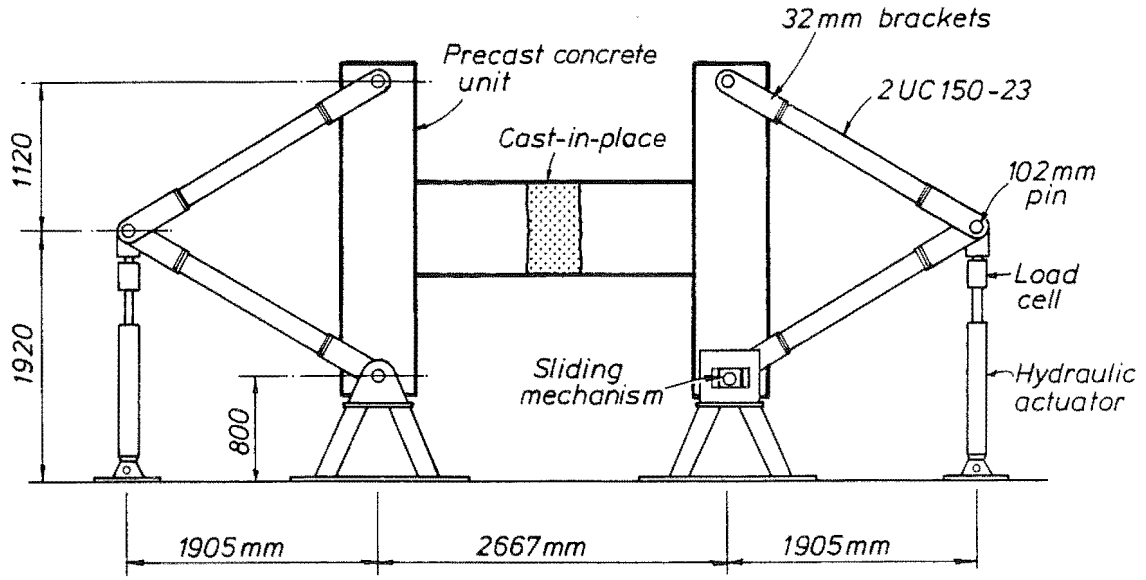

(a) Loading Frame LF1

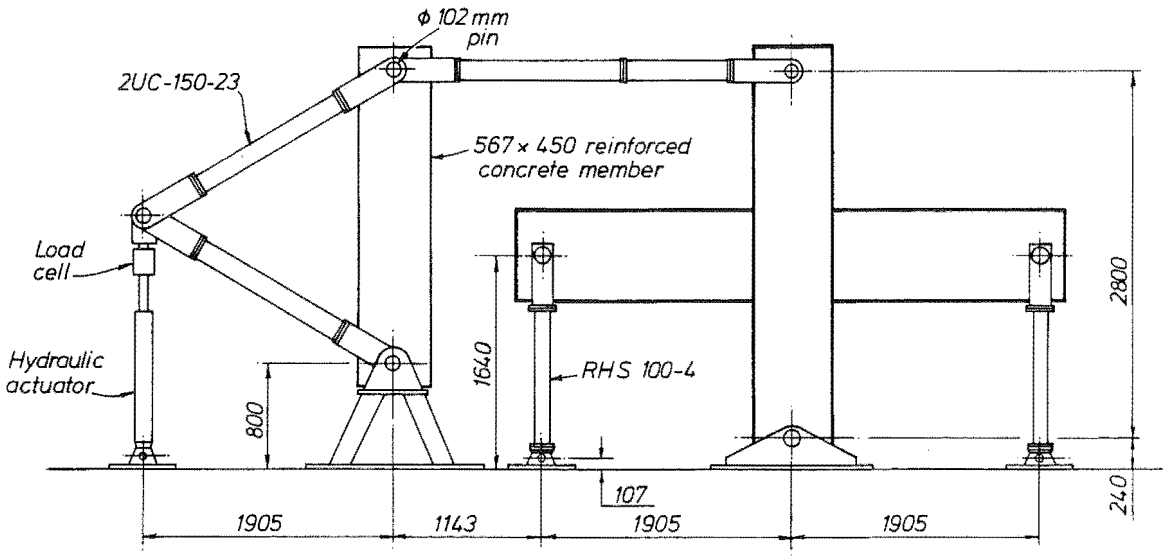

(b) Loading Frame LF2

Fig. 3.10 - Loading Frames Used in the Test Programme.

distributed from the base of the column to the strong floor. In addition, a sliding mechanism was provided at the bottom support of one column to allow for the elongation of the beams during the test.

Friction forces arising from the sliding mechanism caused a redistribution of the applied forces. The effects of the frictional force on the bending moment diagram of the beam can be seen in Fig. 3.11. The frictional force could not be directly monitored but a prediction of it was possible based on equilibrium considerations and the ratio of the measured loads at each jack. Fig. 3.12 depicts the predicted coefficient of friction from the measured loads on the hydraulic actuators. During the test of Unit 1 a moderate level of friction forces developed during the test. The sliding mechanism was modified with Permaglide T20 teflon strips to reduce the friction force in subsequent tests. Following the instructions from the manufacturer, the teflon strips were run in against the sliding steel block to overcome the initial friction of the virgin material. The measured coefficient of friction varied with the level of axial load being 3% at a pressure of 80MPa and larger at smaller pressures.

The loading frame LF2, designed for the test of Units 5 and 6, had only one double acting 1000kN hydraulic actuator as seen in Fig. 3.10 (b). The 567x450mm reinforced concrete column of Unit 4 was used as part of the frame to provide sufficient transverse and torsional stiffness. It was necessary to strain gauge the beam end supports and form a load sensitive device to determine the distribution of the applied lateral forces. These supports were inclined at 12.3° to the perpendicular planes of the beam to provide torsional and lateral restraint to the beams.

3.4 CONSTRUCTION OF THE SPECIMENS

3.4.1 Formwork

The formwork for the specimens was manufactured using 19mm plywood sheets. The moulds were stiffened with timber battens, steel angles and brackets at distances of no more than 400mm apart to minimize any bowing during the concreting of the specimens. In addition, steel rods placed inside a plastic hose passed through the columns of Units 5 and 6. The moulds were painted with undercoat and for each pour they were repainted and oiled. All edges were sealed with parcel tape and silicone to avoid bleeding of the water and segregation of fines from the fresh concrete. A commercial retarder, RUGASOL, was spread to the plywood mould on the vertical construction joints of Units 1 to 5. In addition, the retarder was also spread on to the base of the mould of the beam of Unit 6 in the horizontal construction joint with the lower column.

3.4.2 Reinforcing Cages

Most of the bars selected for instrumentation had either tack welded studs or strain gauges attached before the reinforcing cages were made. Only in one case, the repair of Unit 4, were strain gauges placed on bars when the reinforcement was in the test unit. In another case, Unit 5, tack weld of studs in the beam reinforcing at the beam-column joint region was carried out with the bars in its final position. The procedure for this operation will be discussed later in this chapter.

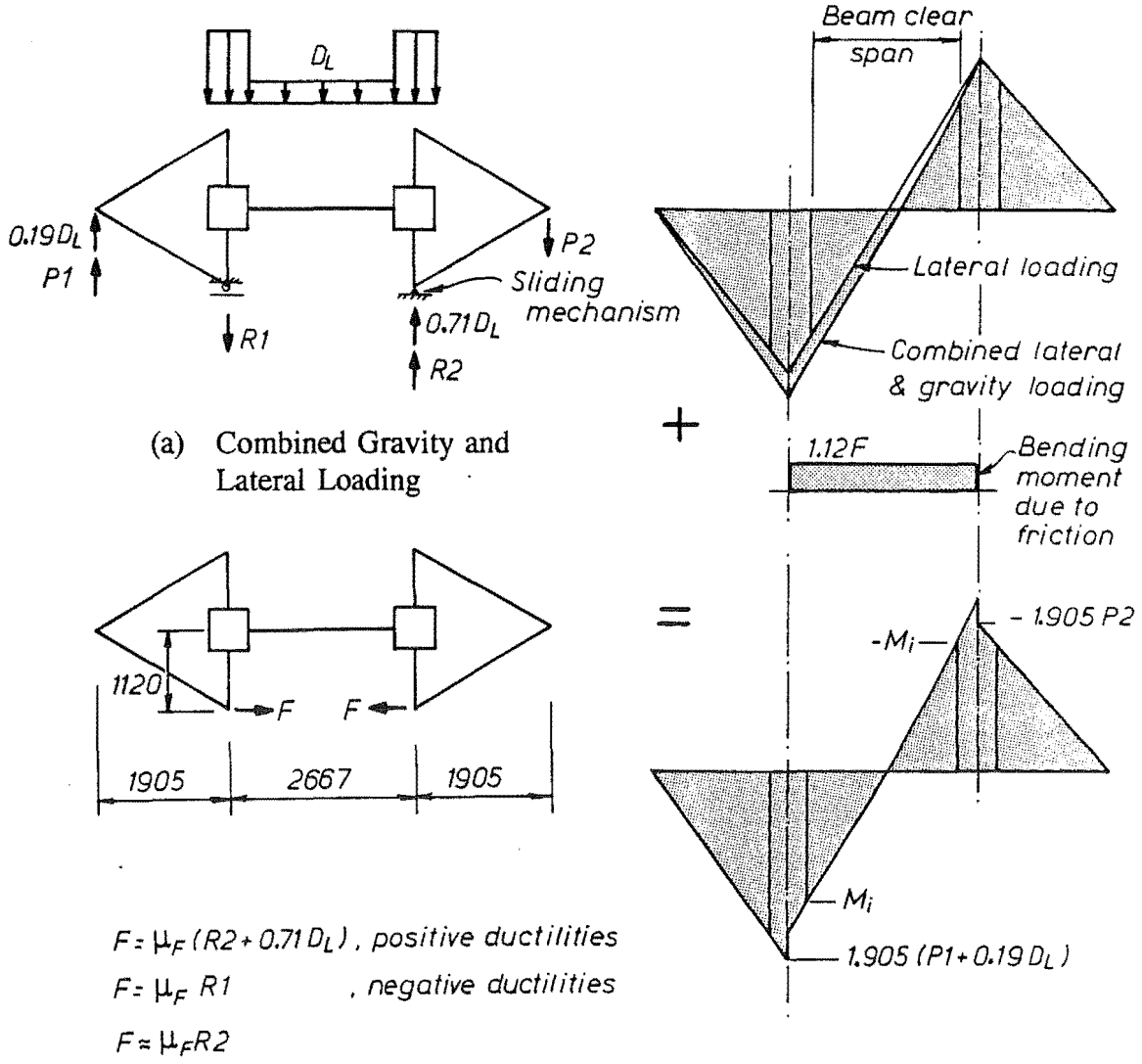

(a) Combined Gravity and Lateral Loading

(b) Friction Forces

Fig. 3.11 - Effect of Friction Forces Arising at the Sliding Mechanism in Loading Frame LF1.

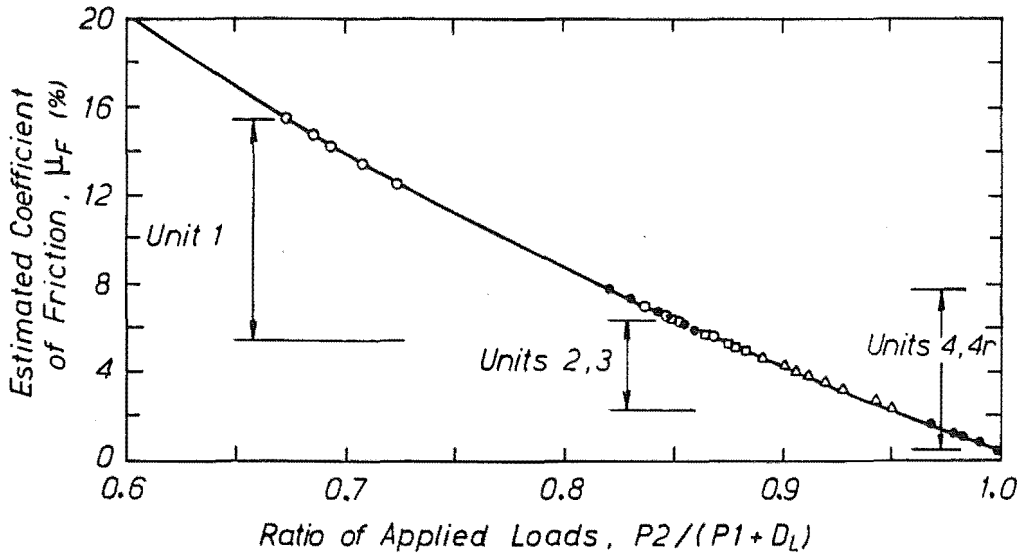

Fig. 3.12 - Coefficient of Friction Estimated to Have Developed in the Sliding Mechanism.

Stirrups, hoops and ties were all cut and bent by a local firm. Despite the accuracy required, it was not possible to shape this reinforcing to within ±5mm. Main bars were all cut and bent in the concrete laboratory where closer tolerances could be attained. It was decided that all extension tails of the 90° anchorage hooks of longitudinal bars would be equal to $8d_b$ instead of the standard $12d_b$. Stirrups and hoops in the test specimens were tied to the longitudinal bars within an accuracy of one-half of their own diameter.

The construction of the reinforcing cages for Unit 4 involved several extra steps. It was decided to incorporate the bent D24 bars in a strain aged condition. The strain ageing at the bent of the D24 diagonal reinforcement was accelerated by placing the bent bars in an oven at 97°C for 12 hours, which is equivalent to a natural strain ageing of 23 months at ambient temperature of 15°C [Erasmus (1987), Hundy (1954)]. This procedure was carried out because there has been some concern regarding strain age embrittlement of bent bars at the critical region of a member designed to respond inelastically during an earthquake [Erasmus (1978, 1981), Yap (1986)]. A quarter of the bars were not artificially strain aged as they had already been instrumented with strain gauges and the glue used for bonding them was susceptible to the oven temperature. The diagonal bars were fixed to a jig in contact with the 16mm end plate and fillet welded. A class S type of welding, in accordance with the Arc Welding Standard for Reinforcing Bars [NZS 4702 (1982)], was specified for the job. MIG welding was chosen because it had the advantage of no leaving slag and enabled uninterrupted welding runs to be carried out. Three probes were made to assess the quality and strength of the weld. One probe was sectioned to examine the penetration and quality of the weld. Fig. 3.13 shows that there is an underfill between the reinforcing bar and the steel plate that can not be relied on for strength purposes. Because of the critical consequences of a weld failure in this region, it was specified that the weld should commence from the bar midheight and with a slope to the horizontal not larger than 60°. Tensile tests on the remaining two trial samples showed fracture of the reinforcing bars at a section away from the weld region. That is, the weld did not affect the ultimate strength nor the ultimate strain characteristics. Details of the welding procedure are presented in Fig. 3.14.

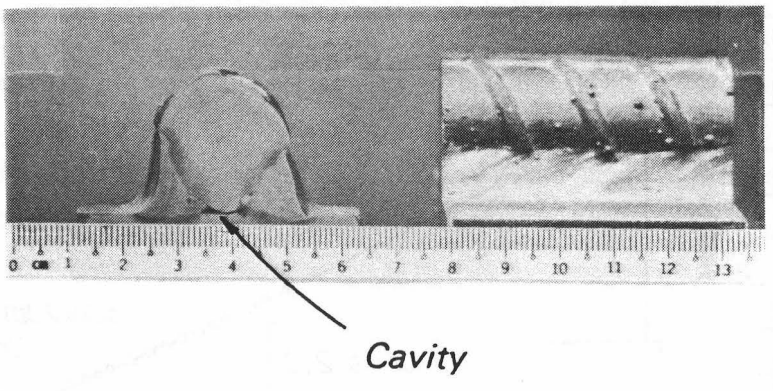

Fig. 3.13 - Close up of a Probe to Examine the Quality of MIG Welding of a D24 Bar to a Steel Plate in Unit 4.

APPENDIX A NZS 4702: 1982

WELDING PROCEDURE QUALIFICATION DETAIL SHEET FOR GRADE 275 REINFORCING STEEL

Contract ..... Welding procedure No. .....
Weld class S

1. Bar diameter (plain/deformed) D24
2. Joint preparation .....
3. Height of reinforcement above main body of bar Full bar contact
4. Welding process MIG
5. Filler metal specification and classification Mild Steel MIG Welding Wire 1.2mm Diameter
6. Shielding gas: Composition ARGOSHIELD 20
   Flow rate 10 l/min
7. Power source characteristics 200 amps, 30 v dc, Gun to + (a.c. and open circuit voltage or d.c. and polarity)
8. Position of welding Horizontal right to left (including direction of vertical welding)
9. Root treatment (back gouging etc.) N/A
10. Preheating and interrun temperature (250 °C max.) No
11. Run details Fillet

Run no.	*Electrode diameter*	*Welding current*	*Welding* voltage*	*Joint detail sketch – include run sequence*
1	1.2	200	30	
2	1.2	200	30	

* For gas-shielded processes only.

This procedure may vary due to fabrication sequence, fit-up, bar diameter, runs and so on, within the changes permitted in Appendix B of NZS 4702.

Welder's name R. Allen ..... Approved by .....
..... Date .....

Fabricator .....

Fig. 3.14 - Specifications of Welding Procedure.

Next, the reinforcing cages of Unit 4 were assembled (see Fig. 3.15). Care was exerted to ensure full contact between the outer D24 diagonal bars and the 30x10mm straps in the bend region. The straps were C-shaped and were connected by being butt welded at the top and bottom sides of the beam.

The cages of all units were placed in the formwork including additional 10mm diameter rods required to hold part of the instrumentation during the test. A length of wire spring and a plastic hose was fitted to the instrumentation rods and welded studs to create an annular void in the concrete cover. Special care was taken with the alignment of the steel sleeves at the column and beam ends since small errors would introduce large misalignments of the units in the loading frame. The sleeves were cut and milled at right angles, the positioned in the formwork using a high precision bubble level and locked in position with interior plywood disks. In addition, the sleeves of the columns of Units 1 to 4 were fixed to the sides of the mould with steel straps. A similar procedure was carried out to lock the corrugated ducts in Unit 6. Finally, lifting hooks were tied to the reinforcing cages of each unit. Fig. 3.15 shows several reinforcing cages prior concreting.

3.4.3 Concreting of the Precast Units

The concreting of Units 1 to 4 was carried out with the frame units in the horizontal plane. On the other hand, Units 5 and 6 were concreted in vertical position. The concrete was placed using a hopper and was mechanically vibrated. The exposed surface of the horizontal top test Units 1 to 4 and 6 was floated a few hours after casting of the concrete to obtain a smooth surface. The horizontal top surface of the beam of Unit 5 was left untouched but the construction joints of the columns of Units 5 and 6 were scrubbed 24 hours after being cast.

All units were cured for seven days with damp hessian fabrics and covered with plastic sheets. Immediately after removing the plywood mould, the paste affected by the retarder in the construction joints of the units was wire brushed. The cold joint showed a rather smooth face, with a total amplitude of about 2mm. It was also found that the coarse aggregate tended to lie flat against the walls of the formwork as shown in Fig. 3.16. No further scrubbing was done because it was considered that this smooth surface could be near the "worst" situation found in practice.

3.4.4 Preparation of the Connection

The connection of all units was assembled with the precast components in the loading frame. The stirrups in the midspan region of Units 1, 2 and 3 were placed temporarily in the one precast unit in the loading frame. The second precast unit was mounted and the midspan connection detail was prepared by sliding the stirrups along. All the stirrups in this region were 5mm oversized to ease the in situ work. Figs. 3.17 to 3.19 illustrate the reinforcement details in the midspan connection regions of these units.

The connection of the precast elements of Unit 4 using the 20mm thick sandwich plate was carried out with both precast sub-components placed in the loading frame. This plate showed some

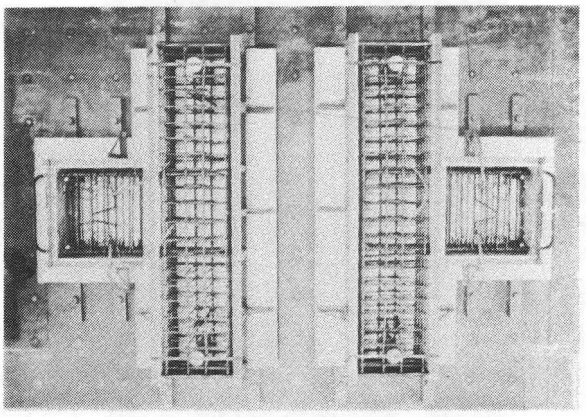

(a) Unit 2 before Casting of the Concrete

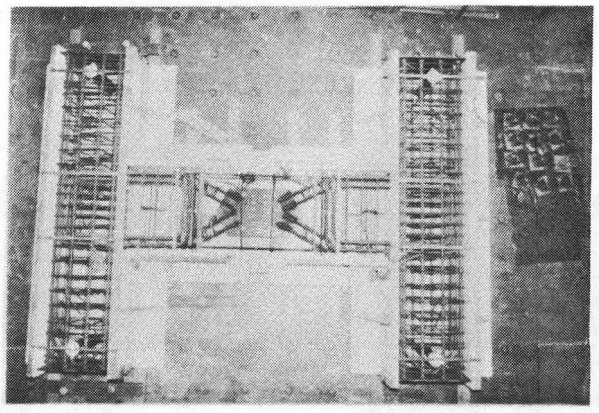

(b) Unit 4 before Casting of the Concrete

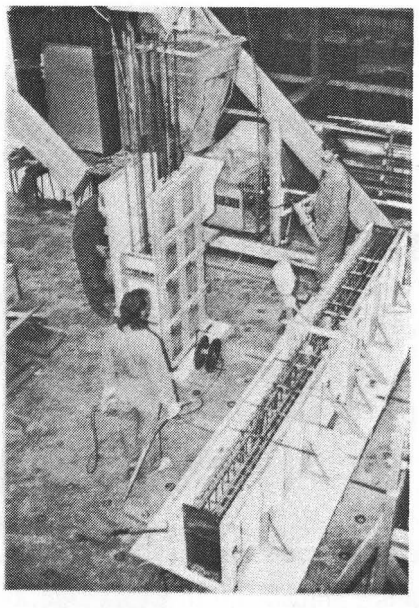

(c) Unit 6 being Cast

Fig. 3.15 - Reinforcing Cages prior Concreting.

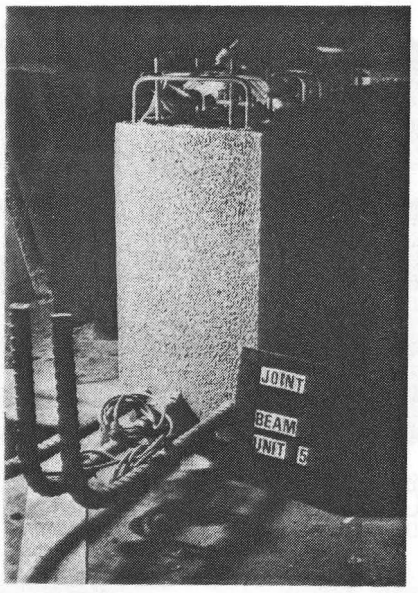

Fig. 3.16 - View of Vertical Cold Joint in a Beam of Unit 5.

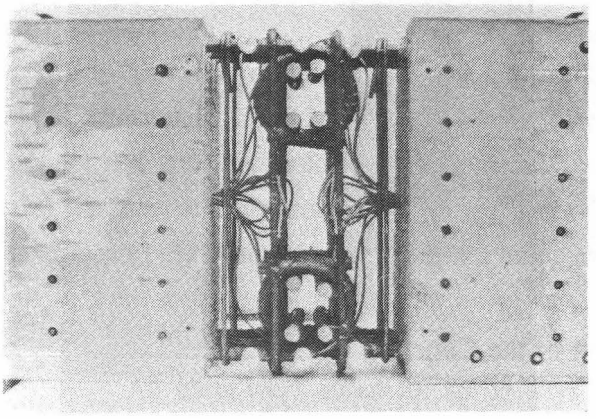

(a) Elevation

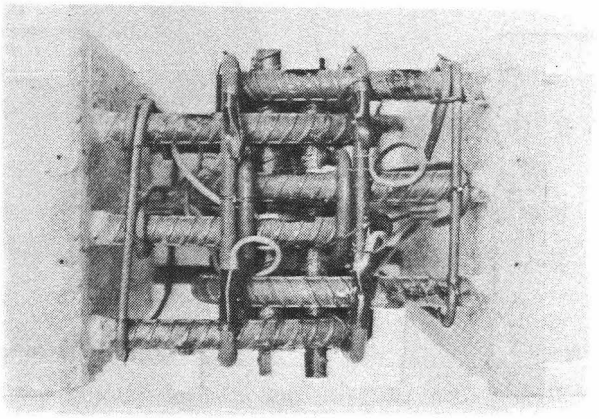

(b) Plan View

Fig. 3.17 - Midspan Connection Detail of Unit 1.

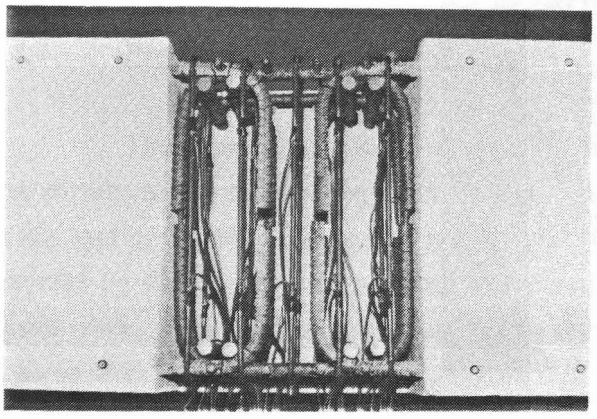

(a) Elevation

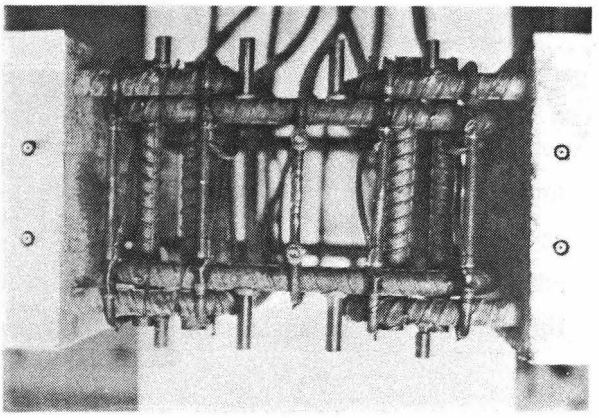

(b) Plan View

Fig. 3.18 - Midspan Connection Detail of Unit 2.

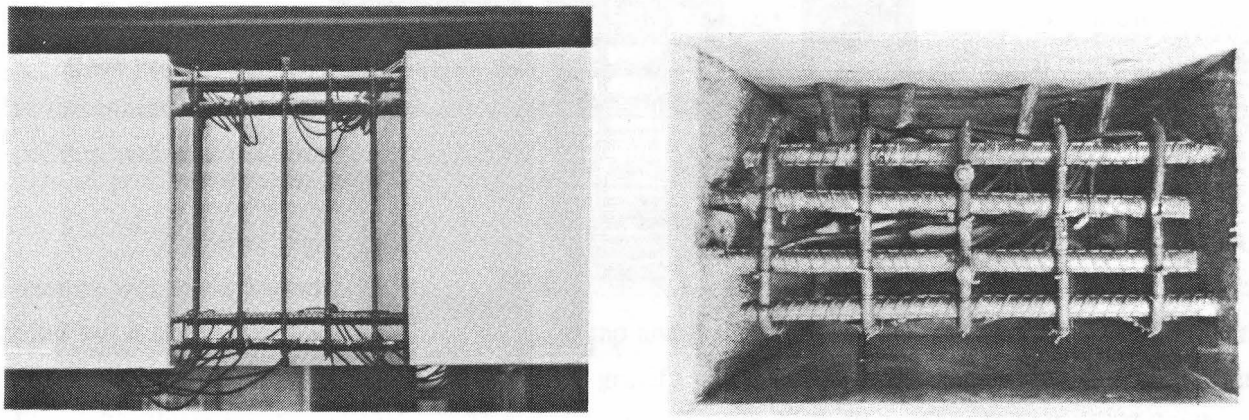

(a) Elevation (b) Plan View

Fig. 3.19 Midspan Connection Detail of Unit 3.

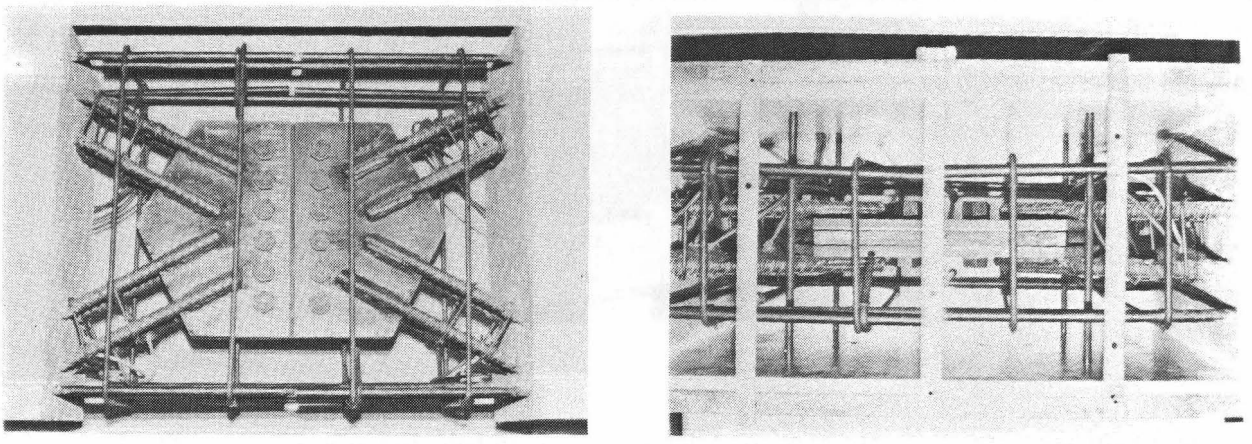

(a) Elevation (b) Plan View

Fig. 3.20 - Midspan Connection Detail of Unit 4.

incipient rust because it had been wetted and dried for about two weeks. High friction grip bolts with coronet load indicator washers were inserted between the plates and manually pre-tightened using a spanner. The final tightening was carried out in a staggering pattern using an impact wrench until the protrusions on the coronet load indicator washers were nearly flattened. When the cage around the connecting plates was completed, the formwork was set-up and the concrete was cast. Fig. 3.20 illustrates the midspan connection of Unit 4.

For Unit 5, the precast concrete beams were seated on the cover of the column below, which had already been pinned on the bottom bracket of the loading frame. The beams were seated in contact with the concrete of the column without any mortar or similar material between. The next step consisted of sliding the joint reinforcement and then top beam reinforcement. Fig. 3.21 shows the arrangement of the reinforcement in the beam-column joint region prior concreting.

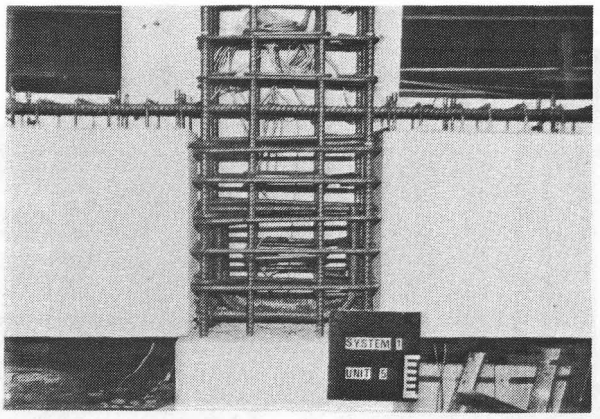

Fig. 3.21 - Arrangement of the Cast in Place Connection of Unit 5.

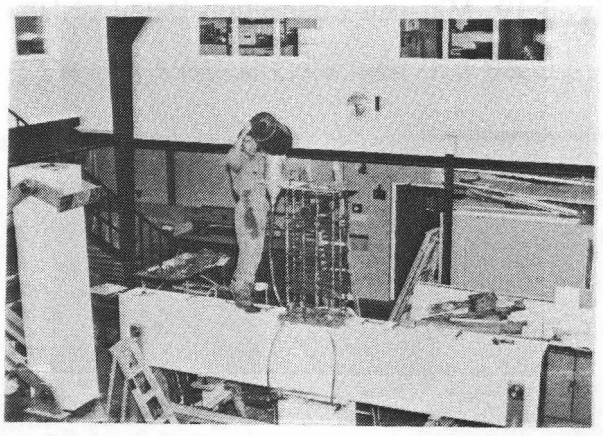

Fig. 3.22 - Grout Being Fed Through Corrugated Ducts in Unit 6.

The labour involved in the preparation of the joint of Unit 6 was minimal since the reinforcement was all included in the precast members. The precast concrete member was seated on shims on the column below so as to leave a 20-30mm gap. This gap was to be grouted in the same operation as the grouting of the vertical column bars in the corrugated ducting in the precast member. Then, the perimeter of the joint between the precast concrete beam and the concrete column below was sealed, leaving 16mm diameter outlets fitted to plastic hose at each corner of the joint.

3.4.5 Concreting of the Cast in Place Connections

In Units 1 to 4, the concrete in the connection at midspan was vertically placed. Unfortunately the compressive strength of the concrete in the midspan connection between the precast concrete elements of Unit 1 was below acceptable strength and had to be removed and recast. For all other units the cast in place concrete was of acceptable strength.

In Unit 5 the concrete had a high slump and the texture of the surface of the top horizontal construction joint indicated that bleeding of the fresh concrete had occurred. Cracks in the concrete along the protruding stirrups of the precast beams were also observed. The horizontal construction joint at the column was wired brushed and water blasted to obtain a rather rough appearance. Then the top column was cast from the top from a hole left in the top steel plate.

The joint region in Unit 6 was saturated with water for at least 6 hours prior grouting. An attempt was made to pump a none-grown described in Section 3.5.2.2 grout through the bottom of the joint but it segregated and packed inside the pump and the hose and it was impossible to carry on with the operation. Instead, the grout was fed by gravity using a tremie hose located in a corner duct. Fig. 3.22 illustrates this operation. The grout was seen to ascend through each duct and through the four corner hoses at the interface between the precast beam and the column below. Topping was required after the operation because of losses on the hydraulic head. It was felt that most of the coarser material remained in the bottom and did not ascend through the corrugated ducts and therefore the topping added would introduce a more homogeneous material. Inspection of the grout in the plastic hoses showed that some channelling had occurred because of the migration of the free water to the top of the hose. This observation was also made for the dummy ducting cast at the same time as the connection. The first 50mm of the grout in the ducts was removed because of the excessive bleeding observed. Then the top column was cast following the same procedure as for Unit 5.

3.5 MATERIALS

3.5.1 Concrete

The concrete was provided by a commercial ready-mix supplier with a specified target 28 day compressive strength of 30MPa for all units except Unit 4 where 35MPa concrete was specified. In general the maximum specified aggregate size was 20mm but in some cases 13mm aggregate was used because of the congestion of the reinforcement cage. Table 3.2 summarizes the main concrete properties. 100mm diameter by 200mm high cylinders were used to determine the mechanical properties of the concrete. The samples were cast over a vibrating table, cured in a fog room at 20°C constant temperature and 100% relative humidity and left to dry for at least four hours before testing. The compression strengths in Table 3.2 are the average of three tests while the tensile strengths are the average of two splitting tests. All tests were quasi-statically conducted in an 2500kN Avery Universal Testing Machine.

3.5.2 Grout

3.5.2.1 General

A study of different properties of fluid high strength grouts needed for joining the precast concrete elements in Unit 6 was undertaken in this project.

Three different cement-based grouts were investigated; one of them was designed in the concrete laboratory at the University of Canterbury while the other two were commercially available preparatory grouts.

The main parameters to be looked at were fluidness, segregation and bleeding of the fresh grout. In addition, the compressive and splitting strength, the elastic modulus, the size effect of the test cylinders and the enhancement of the compressive strength due to the metallic ducting were investigated.

3.5.2.2 Self-Mixed Grout

Several trials were prepared in the concrete laboratory to obtain an ideal grout with a compressive strength at 28 days, measured on 50mm diameter by 100mm high cylinders, of at least 10MPa higher than the nominal compressive strength of 30MPa of the precast concrete unit to be grouted. The fluidness of the grout was measured according to the flow cone method [ASTM Standard C939-87 (1988)]. It was found that the ideal flow should be kept around 40-50 seconds to be able to spread freely through the construction joint of the precast unit while avoiding excessive segregation.

Table 3.3 contains the final proportions per cubic metre of the mix as poured into Unit 6. Kaiapoi fine sand with a fineness modulus of 2.15, a maximum aggregate size of 5mm and a specific gravity of 2.59 was used as aggregate in the grout. Onoda, an expansive agent, was added to compensate for shrinkage caused by the high content of water and cement in the mix. In addition, Daracem 100 was incorporated to reduce as much as possible the water in the mix. This product also had a retardant effect.

3.5.2.3 Preparatory Grout

The preparatory grouts selected for study were SIKA 212 and Monogrout of Grace. The grouts were mixed with the maximum amount of water recommended by the manufacturer of 4.5 and 4.6 lts per 25 kg bag for SIKA 212 and Monogrout respectively.

Two series of tests were conducted for each grout. SIKA 212 showed a low fluidness with a time in the cone test of 62 and 73 seconds. The consistency of the mix was acceptable although some segregation was observed. Monogrout showed a low viscosity. The time in the cone test was 17 and 33 seconds. Segregation, large plastic settlement and bleeding were observed in this grout.

3.5.2.4 Test Results

Table 3.4 shows the grout compressive strength of the slices cut from a 66mm diameter by 700mm high dummy duct that was vertically cast following actual construction practice. The aspect ratio of the slices was kept as close as possible to 2:1.

Table 3.2
Concrete Properties

Pour No.	Location	Maximum Aggregate Size (mm)	Slump (mm)	Age at Test (Days)	Compressive Strength f'_c (MPa)		Split Cylinder Tensile Strength f'_t (MPa)		$f'_t/\sqrt{f'_c}$	
					At 28 Days	At Test	At 28 Days	At Test	At 28 Days	At Test
1	Unit 1, precast concrete member	20	85	116	25	29	-	-	-	-
2	Unit 1, connection	13	100	64	32	41	-	-	-	-
3	Unit 2, precast concrete member	20	90	168	33	33	-	-	-	-
4	Unit 2, connection Unit 3, precast concrete member	20	50	48 96	31	32 38	2.6	2.9	0.47	0.51
5	Unit 3, connection	20	180	21	28	29	3.0	2.6	0.57	0.48
6	Unit 4, precast concrete member	13	80	100	31	35	3.5	3.9	0.62	0.66
7	Unit 4, connection Unit 5, precast beams, bottom column	20	110	21 207	36	36 41	3.5	3.5 3.7	0.58	0.58 0.58
8	Unit 4, repair region	13	75	32	62	62	4.5	4.8	0.57	0.61
9	Unit 6, precast beam, bottom column	20	100	183	36	44	3.2	4.5	0.53	0.68
10	Unit 5, beam-column joint, beam top	20	200	62	20	27	2.3	2.2	0.51	0.42
11	Unit 5, top column	20	90	61	32	43	3.2	3.5	0.57	0.53
12	Unit 6, top column	20	150	20	35	35	2.8	3.0	0.47	0.51

Table 3.3
Mix Proportions of Self-Mixed Grout

COMPONENT	AMOUNT per m^3
Water	290 kgf
Ordinary Portland Cement	547 kgf
Onoda (Expanding Agent)	68 kgf
Sand	1333 kgf
Daracem-100 (Superplastizicer)	4377 ml

Table 3.4
Compressive Strength f'_g (MPa), at 28 Days of Grouted Cylinder Cut from Dummy Ducts

Position	Self-Mixed	SIKA 212 (a)	SIKA 212 (b)	Monogrout (a)	Monogrout (b)
Top	36.0	45.3	56.6	66.1	40.3
	36.6	59.8	67.3	59.8	40.5
	44.8	55.9	65.7	66.1	46.6
	40.3	67.3	55.9	70.7	49.2
Bottom	48.0	65.2	63.8	59.3	52.3
Average	41.1	58.7	61.9	64.4	45.8

Table 3.5
Mean Compressive Strength of Grout, f'_g (MPa)

Nominal Size of Cylinder (mm)	Self-Mixed	SIKA 212 (a)	SIKA 212 (b)	Monogrout (a)	Monogrout (b)
50x100	63.3	62.5	68.3	65.0	60.6
66x132	-	49.9	63.0	61.6	-
100x200	-	51.2	63.4	61.0	55.0

Table 3.6
Splitting Strength of Grout

Nominal Size of Cylinder (mm)	SIKA 212 (a)		SIKA 212 (b)		Monogrout (a)		Monogrout (b)	
	f'_{tg} (MPa)	$\frac{f'_{tg}}{\sqrt{f'_g}}$	f'_{tg} (MPa)	$\frac{f'_{tg}}{\sqrt{f'_g}}$	f'_{tg} (MPa)	$\frac{f'_{tg}}{\sqrt{f'_g}}$	f'_{tg} (MPa)	$\frac{f'_{tg}}{\sqrt{f'_g}}$
50x100	3.8	0.46	4.3	0.52	4.9	0.60	4.1	0.53
100x200	3.3	0.47	3.3	0.41	3.2	0.40	4.5	0.60

Table 3.7
Initial Elasticity Modulus of Grout

Grout	E_g (GPa)	$E_g/\sqrt{f'_g}$
Self-Mixed	26.2	3293
SIKA (b)	29.7	3588
Monogrout (a)	22.5	2790

It can be noted that in all cases in Table 3.4 the compressive strengths trend to increase with the depth of the cylinder except in the series (a) of Monogrout. One reason for this behaviour is believed to be caused by free water ascending through the duct and causing a high water cement ratio in the top segments. Another factor could be the effect of cutting on the edges of the cylinders. Results obtained in this study do not permit to withdraw conclusions regarding the variation of the grout compressive strength throughout the height of the duct.

The compressive strength of the grout was slightly affected by the size of the cylinder test as shown in Table 3.5. Test results, presented are the mean of 5 cylinder tests for 50 and 100mm diameter cylinders and 2 tests for the 66mm diameter probes. It was observed that the larger the cylinder test the smaller its mean compressive strength between 50mm diameter cylinders and 68mm or 100mm diameter test cylinders. No differences were observed between the 68mm and 100mm diameter cylinders. From the results shown in Table 3.5 it can be concluded that size effects can be

ignored for the ratio between the diameter of the ducts normally used in precast concrete construction typical of System 2 and the diameter of the test cylinders used for determining the compressive strength of the grout.

The splitting strength of the grout f'_{tg}, taken as the mean of three tests is shown in Table 3.6. The ratio between the splitting strength and its compressive strength varies similarly to concrete.

Table 3.7 shows the measured modulus of elasticity of different grouts estimated from measurements diametrically taken over a gauge length of 50.8mm on 50mm diameter by 100mm high cylinders. The values presented are the mean of three tests in which the initial modulus was measured as the slope of the secant line passing through the origin and the strain at a stress of 0.5 f'_g. It is evident that the initial modulus is significantly lower than the modulus of $4{,}700\sqrt{f'_c}$ recommended by the Concrete Code [NZS 3101 (1982)] for normal weight concrete.

The final variable to be studied was the enhancement of the compressive strength of the grout caused by the confinement provided by the 0.4mm thick metallic ducting to be used in Unit 6. Fig. 3.23 plots the mean unconfined versus confined compressive strength of different grouts as measured on two 66mm diameter by 132mm high cylinder tests. Also shown in Fig. 3.23 is the predicted enhancement according to the formula postulated for concrete by Richart et al [Park and Paulay (1975)].

$$f'_{cc} = f'_c + 4.1\, f_t \qquad (3.1)$$

where f'_{cc} is the confined compressive strength of concrete and f_t is the lateral confining pressure. It can be seen that Eq. 3.1 fits reasonably well the data obtained in this study and therefore appears to be also applicable for determining the confined strength of grout.

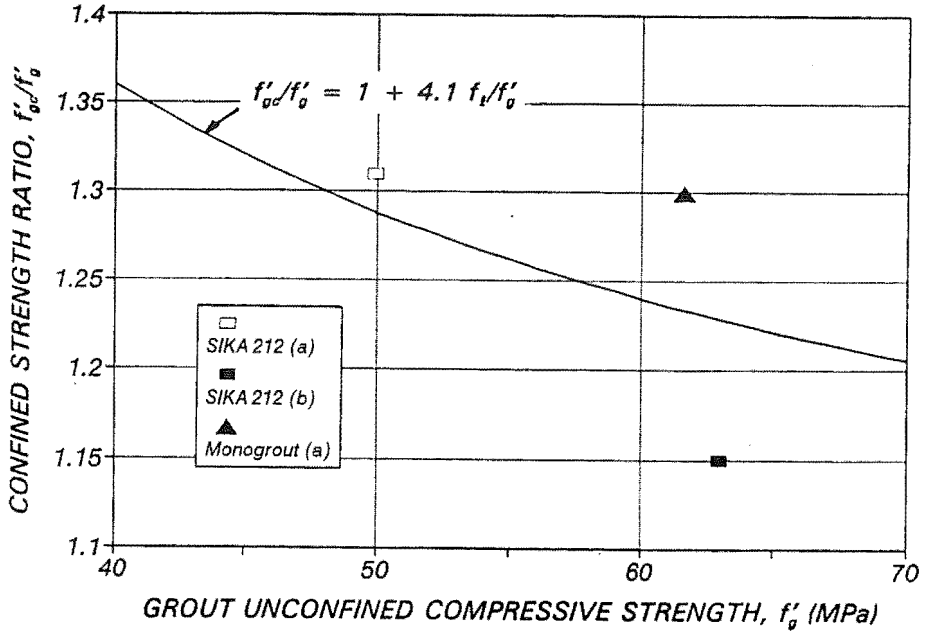

Fig. 3.23 - Confined versus Unconfined Compressive Strength of Grout.

3.5.3 Reinforcing Steel

In conformity with the New Zealand practice, the longitudinal reinforcement was deformed steel bar with a lower characteristic yield strength of 300MPa for the beams and 430MPa for the columns. Plain round steel bar with a lower characteristic yield strength of 300MPa was used for transverse reinforcement.

Table 3.8 presents the mechanical tensile properties of the steel used in the test units. Test results are the average of two tests monotonically conducted at a quasi-static rate in an 1000kN Avery Universal Testing Machine. Strains up to approximately 4% were measured with a Batty Gauge Extensometer with a gauge length of 50.8mm. The resolution of this device was $25\mu\epsilon$. The ultimate strain, ϵ_{su}, could not be directly measured since the Batty Gauge had been previously removed from the test specimen. Instead the apparent ultimate strain, $\epsilon_{su,a}$, was obtained after unloading the test sample upon maximum loading as illustrated in Fig. 3.24. A Mitutoyo Digital Vernier with a resolution of 0.01mm was used to measure the extension between two initial gauge lengths of 100mm in the original specimen. However, it is possible to obtain a reasonable approximation of the ultimate strain by accounting for the unloading slope. All ultimate strains in Table 3.8 have been calculated as $\epsilon_{su} = \epsilon_{su,a} + f_{su} / 0.8E_s$. The coordinates $\epsilon_{sh,1}$, $f_{sh,1}$ are also presented to describe the strain hardening region according to the model discussed in Chapter 2.

All steels showed a well defined yield plateau region, however the yield strength of the D28 bars used in Units 1, 2 and 5, which were supposed to come from the same batch, varied and tended to two different values. Results from eight tests indicate that it is likely that steel from two different heats was delivered to the project.

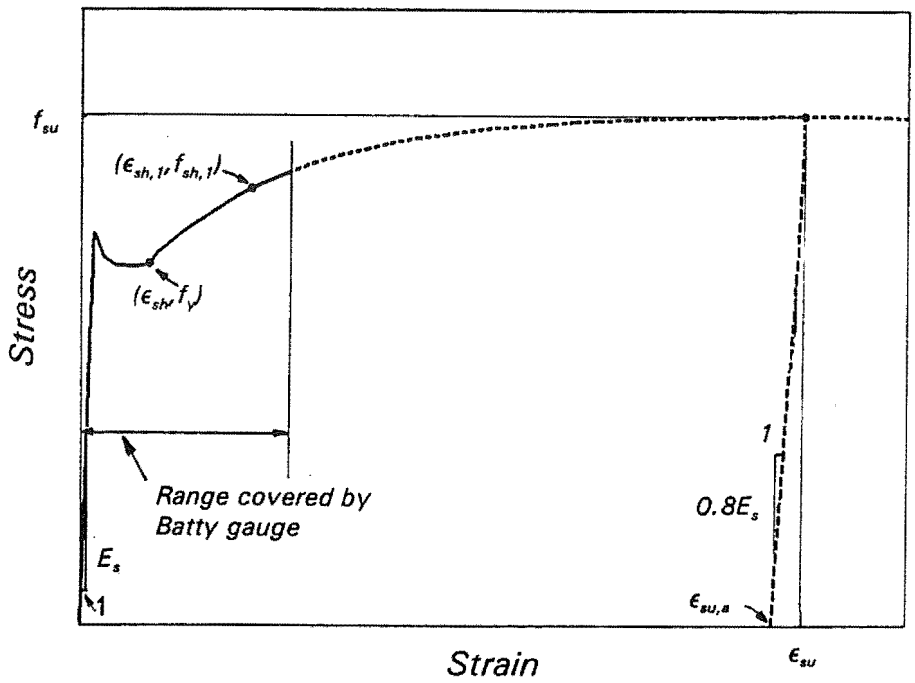

Fig. 3.24 - Typical Stress-strain Diagram for Reinforcing Steel.

3.6 TEST PROCEDURE

The activities before commencing testing included a coat of water based white paint or a combination of white and light blue paint applied to the units to permit better crack observation. Besides, all strain gauges were checked for continuity and resistance to earth; those with a resistance of less than 2MΩ were rejected. All linear potentiometers were calibrated in position in the test unit using steel spacers. Clip gauges that were fabricated from a prototype supplied by the Department of Civil Engineering at the University of Auckland [Fenwick and Thom (1982)] were calibrated with a metric calibrator and then fitted in position in the test specimen. All calibration data was checked with a linear regression program and only data with a coefficient of correlation larger than 0.99998 was accepted. The principle of these gauges is the same as for the clip gauges used for testing the reinforcing steel specimens discussed in Chapter 2. At the fixing points at the bases of the columns of the clip gauges, miniature bearings were inserted to ensure a roller type of boundary condition. At this point 4mm diameter steel rods held the clip gauges.

The test was quasi-statically conducted with load applied in small increments. At each increment a selected set readings was taken with the data logger unit and at the peak of each run a complete set of readings, including manual readings and crack widths, was recorded. At this point photographs of the test specimen were also taken. Prior to unloading, another complete set of readings was taken, to pick up any error in the manual readings and any creep of the strain gauges.

3.7 TEST SEQUENCE

As is common with many other quasi-static seismic tests, the test regime of displacement history imposed on the test units did not attempt to follow the displacement sequence from the response of a structure to a specific earthquake record. Instead, a simple test sequence with increasing symmetrical cyclic displacements was adopted, as is common in tests conducted to evaluate the probable seismic resistance of a sub-component. The rationale behind the simple test sequence is that a specimen that behaves satisfactorily when subjected to appropriately severe symmetrical cyclic displacements is likely to behave satisfactorily during a real seismic event [Park (1989)].

The quasi-static test sequence imposed on the test units is shown in Fig. 3.25. The two first cycles, runs 1 to 4, were load controlled; the rest of the test was displacement controlled.

The load controlled cycles were used to determine the initial yield displacement as well as the initial "elastic" stiffness of the units. The specimens were loaded to 3/4 of the theoretical lateral load capacity, H_a, which was calculated using the measured properties of the materials and assuming a perfect elasto-plastic stress-strain relation for the reinforcing steel and an equivalent rectangular block compressive stress for concrete. The corresponding interstorey horizontal displacements (measured at column tops of units) so measured during these runs were averaged to obtain the displacement Δ_{75} associated with the application of load $0.75H_a$. The first yield displacement, Δ_y, was linearly extrapolated as:

Table 3.8

Mechanical Properties of Reinforcing Steel of Test Units

Description	Location	f_y (MPa)	ε_{sh} (%)	Es (GPa)	$\varepsilon_{sh,1}$ (%)	$f_{sh,1}$ (MPa)	ε_{su} (%)	f_{su} (MPa)
R6	Unit 4	364	1.2	179	3.0	402	5.7	428
R10	All units	356	1.6	202	3.0	394	17.4	469
R12	Unit 3	324	2.2	201	4.0	382	15.3	449
R12	Unit 4	317	2.0	200	3.0	355	15.3	436
R16	Units 1, 4, 5 and 6	298	2.5	206	4.0	349	24.7	444
D20	Unit 3	307	2.3	196	3.8	352	17.5	447
D24	Unit 4	320	2.1	178	4.0	381	23.2	477
D24	Units 5 and 6	285	1.9	180	4.0	352	23.7	444
D28	Units 1, 2 and 4	313	2.1	202	4.1	373	21.1	477
D28	Unit 5	321	2.1	186	3.8	380	21.5	481
HD20	Units 1, 2, 3 and 5	456	1.4	193	3.9	542	15.3	617
HD24	Units 5 and 6	486	1.8	195	4.0	570	14.6	637
HD28	Unit 4	440	1.6	193	4.0	527	18.8	603
30x10 mm straps	Unit 4	315	1.9	201	3.0	358	20.0	479
36x0.4 mm metal sheet	Unit 6	290	2.7	190	-	-	20.0	361

$$\Delta_y = \frac{4}{3}\Delta_{75} \tag{3.2}$$

and the "elastic" stiffness, K_e:

$$K_e = \frac{3}{4}\frac{H_s}{\Delta_{75}} \tag{3.3}$$

The imposed displacement cycles were applied following runs 1 to 4 to the levels of nominal displacement ductility factors, μ_Δ, shown in Fig. 3.25, where

$$\mu_\Delta = \frac{\Delta}{\Delta_y} \tag{3.4}$$

where Δ is the applied interstorey horizontal displacement. A similar procedure was also used in the data reduction to define the curvature and rotational ductility factors.

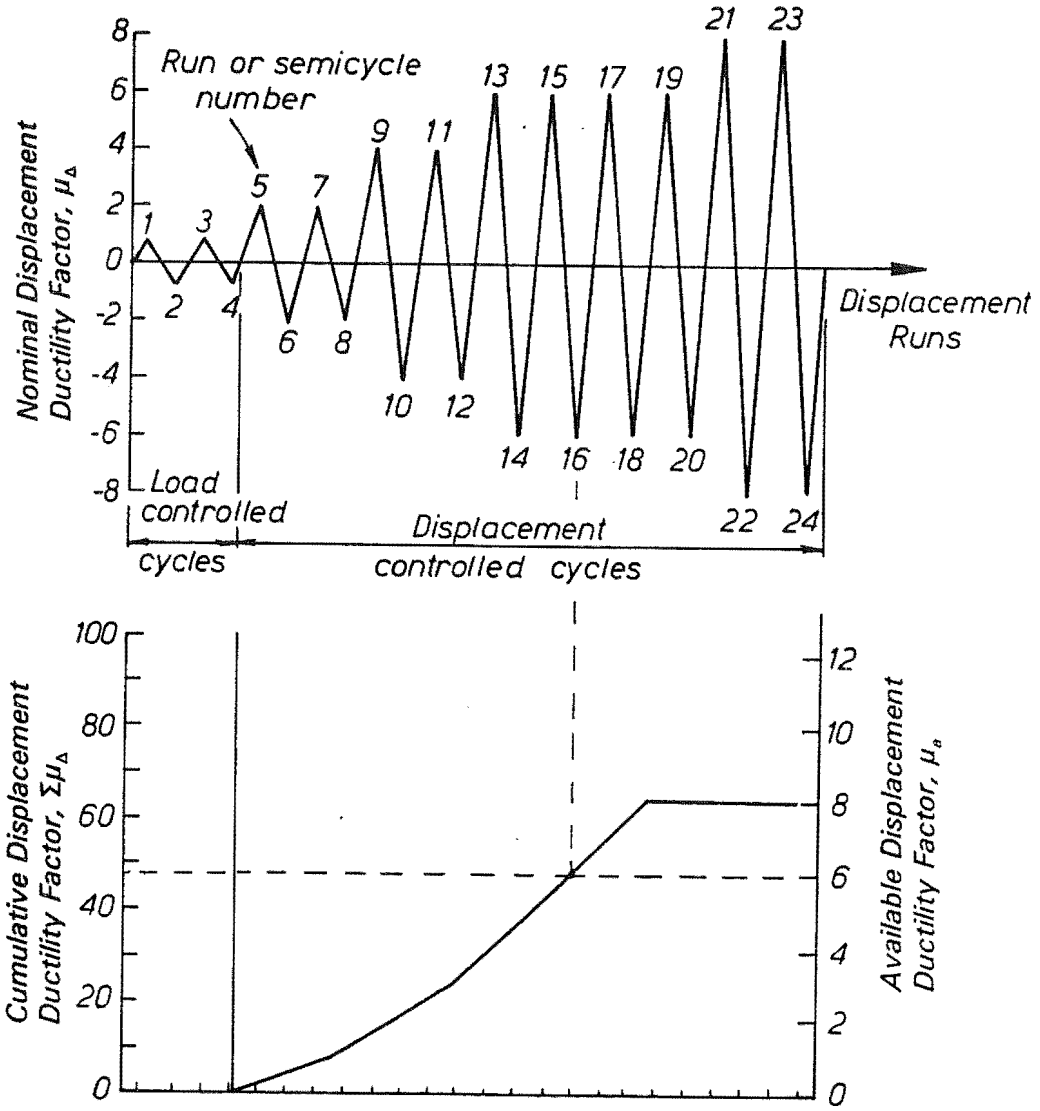

Fig. 3.25 - Test Sequence of Cyclic Load and Displacement Used for Tests.

The smaller ideal lateral capacity of Unit 1 was mistakenly taken instead of the "actual" theoretical lateral capacity and caused a 6.7% error in definition of the first yield displacement and in the displacement ductility factor. However, it is believed that this error does not compromise the results obtained from this test. In order to compare the behaviour Unit 6 was subjected to the same displacement history as Unit 5.

The end of the test was reached when the lateral load in the run dropped to less than 80% of the maximum applied load recorded in the initial runs. The available displacement ductility factor was taken equal to be $\mu_a = \Sigma\mu_\Delta/8$ [Park (1989)] but no larger than 8, where $\Sigma\mu_\Delta$ is the cumulative displacement ductility factor attained in the runs prior to failure.

3.8 INSTRUMENTATION

3.8.1 Measurement of Loads

The loads measured were the forces applied with all the hydraulic actuators to all units, and the reactive forces at the beam ends of Units 5 and 6. Load cells coupled with the hydraulic actuators consisted on a hollow cylinders machined from high strength steel and containing strain gauges. Two independent full bridge (Poisson) circuits were set up for each load cell. Each arm of the circuit had 2-5mm strain gauges of 350Ω of resistance. One circuit was directed to a strain indicator and the other to a data logger unit. The load cells had been calibrated in compression in an Avery Universal Testing Machine. It was assumed that the tensile characteristics of the load cells were equal to those measured in compression.

The RHS sections at the end of the beams of Units 5 and 6 (see loading frame LF2 in Fig. 3.10 (a)) were instrumented with 120Ω 5mm strain gauges forming a full bridge (Poisson) and calibrated in the same Universal Testing Machine as used for the load cells.

3.8.2 Measurement of Displacements and Deformations

3.8.2.1 Measurement of Displacements

The displacements measured during the test programme were the gross horizontal displacement, the rigid body horizontal displacement and the lateral displacement due to rigid body rotation of the test specimen. These sources of displacements were measured with Sakae linear potentiometers of 10kΩ of resistance. Figs. 3.26 and 3.27 show the position of these devices on the test specimen. The two linear potentiometers, with 300mm of travel, marked **A**, measured the gross horizontal displacement of the column top and its twist at the pin height. A steel wire, a pulley and a weight were used to connect the devices from the specimen to a reference point located outside the strong floor area. Linear potentiometers, with 15mm travel, marked **B**, monitored the horizontal rigid body displacement of the units at the pin in the bottom column due to clearances between the sleeve and the pin. The linear potentiometers marked **C** and **C'**, with 15mm of travel, enabled the calculation of

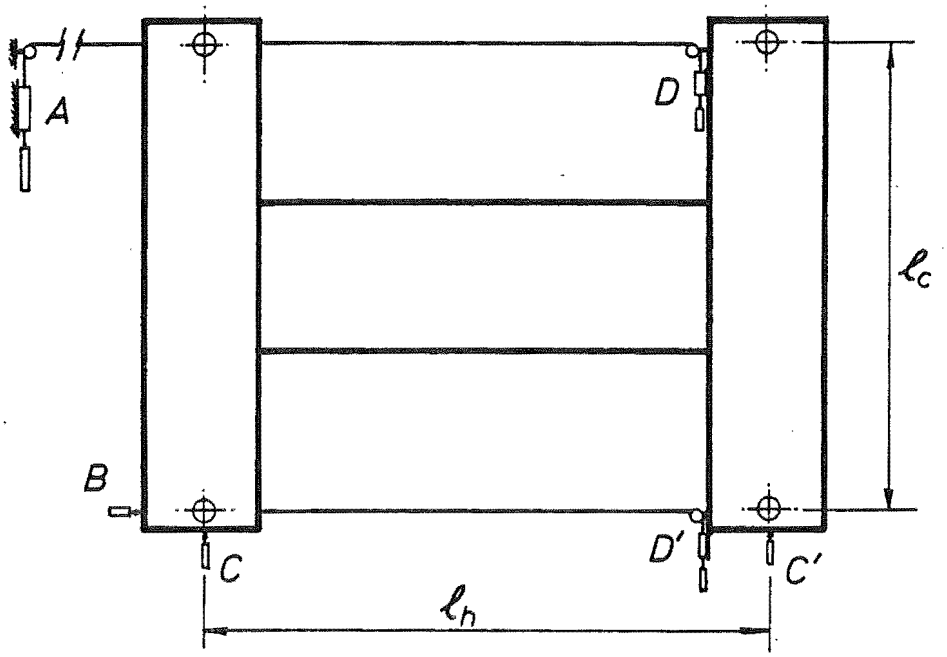

Fig. 3.26 - Lay out of Linear Potentiometers Measuring Displacements of Units 1 to 4.

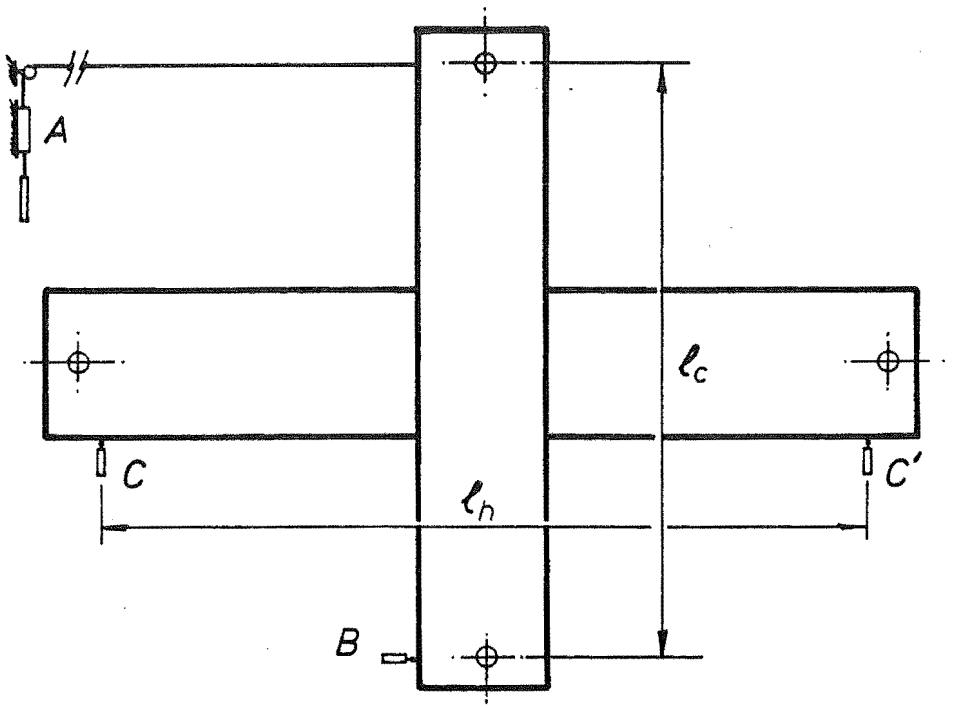

Fig. 3.27 - Lay out of Linear Potentiometers Measuring Displacements of Units 5 and 6.

the rigid body rotation. In the test of Unit 1 linear potentiometers marked **B**, **C** and **C'** were mounted on steel frames attached to the test floor. Measurements taken with a theodolite indicated that displacement readings gathered were affected by deformation within the testing slab floor caused by the axial forces transmitted by the loading system. Hence, in the remainder of the test programme, these linear potentiometers were attached to steel frames placed away from the test floor. Because of space constraints, the linear potentiometers marked **C** and **C'** were not in line with the pins at the ends of the beams of Units 5 and 6.

The net interstorey displacement was determined using the information gathered from these transducers as follows:

$$\delta_H = \delta_A - \delta_B - (\delta_C - \delta_{C'}) \frac{\ell_c}{\ell_h} \tag{3.5}$$

where δ_H is the net horizontal column or interstorey displacement; δ_A, δ_B, δ_C and $\delta_{C'}$ are the displacements measured by the transducers marked **A**, **B**, **C** and **C'** respectively; ℓ_c is the vertical distance between the column pin and ℓ_h is the horizontal distance between the linear potentiometers marked **C** and **C'**. The 50mm travel linear potentiometers marked **D** and **D'** in Fig. 3.26 were used to maintain the same horizontal displacement (interstorey drift) between both columns.

3.8.2.2 Measurement of Internal Deformations

Several devices were utilized in the test programme to monitor the internal deformations in the test specimens. Figs. 3.28 and 3.29 show the location and type. The deformations of the chords of the beams was measured using 30 or 50mm travel Sakae linear potentiometers of 10kΩ of resistance. They were mounted on steel brackets screwed into the 10mm steel rods embedded in the concrete. The readings from the top and bottom linear potentiometers were used to determine the fixed-end rotation in the beams of all units except Unit 4. The remaining transducers were used to determine the rotation of the chord and the average strains. This procedure will be discussed later in this chapter. The accuracy of measurements using this method was satisfactory. However it was always observed that near the end of the tests the steel rods kinked in the diagonal cracks and tilted, inducing false readings on the devices. At this stage it was decided to remove them from the test specimen.

The mid-depth elongation of the beams was directly monitored by 200mm travel linear potentiometers attached to the ends of the test specimens by a steel wire and a pulley. In the beams of Units 5 and 6 it was not possible to attach the steel wire at the mid-depth of the beam. Instead both attachments were located near the bottom chord. In addition, the linear potentiometers located in the chords of the beams were used as an indirect way of determining this elongation.

A partial measure of the rotation of the columns of Unit 5 and 6 was estimated from manual readings using DEMEC (demountable mechanical) gauges. Any displacement was read between drilled steel targets that had been waxed to the surface of the concrete. Similarly, DEMEC gauges were used

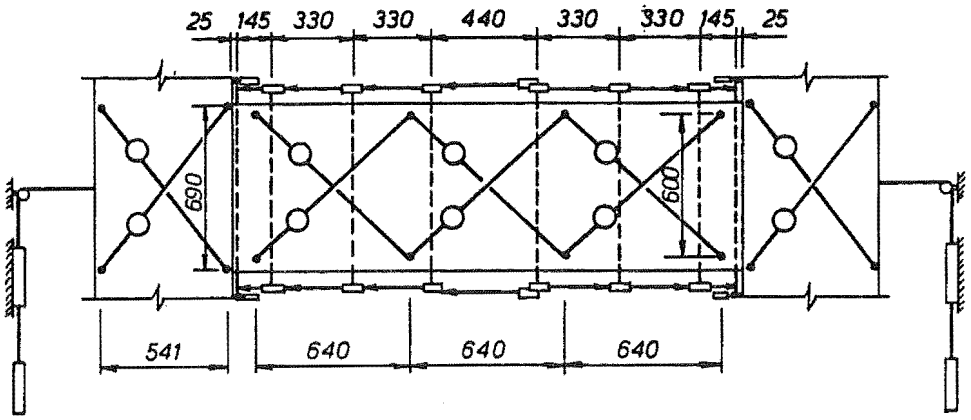

(a) Unit 1

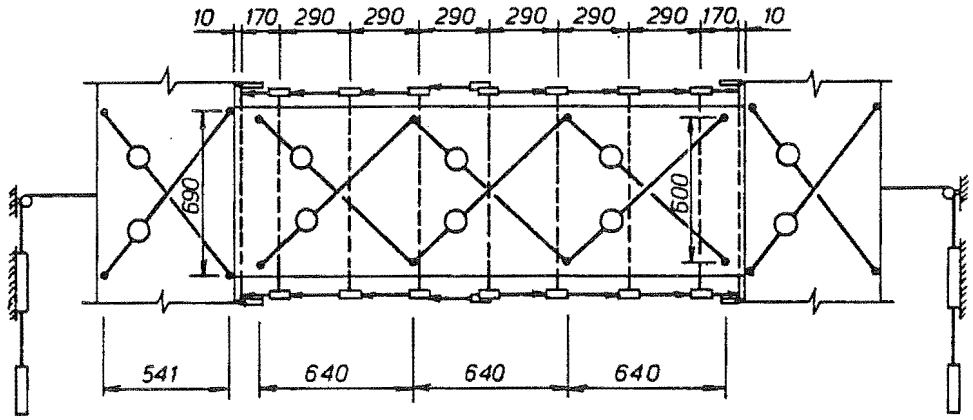

(b) Units 2 and 3

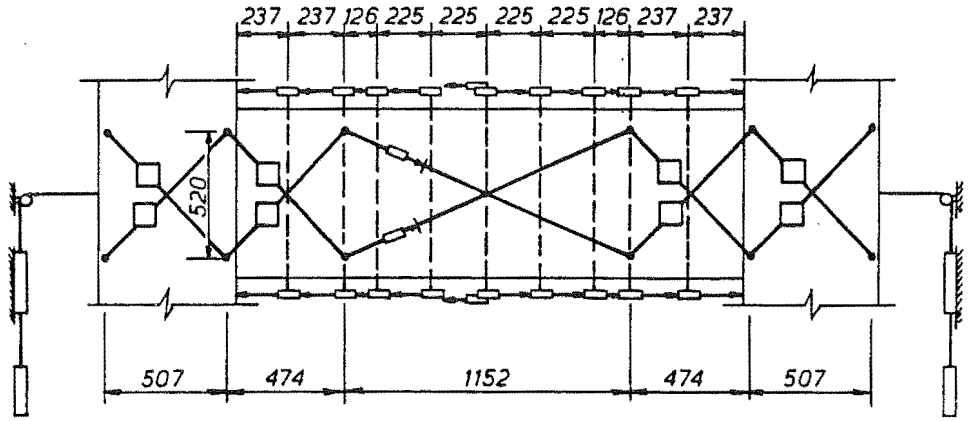

(c) Unit 4

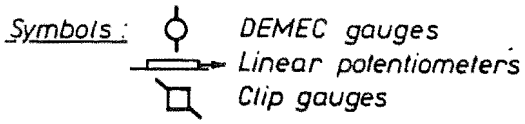

Fig. 3.28 - Lay out of Linear Potentiometers Measuring Internal Deformations of H-shaped Units.

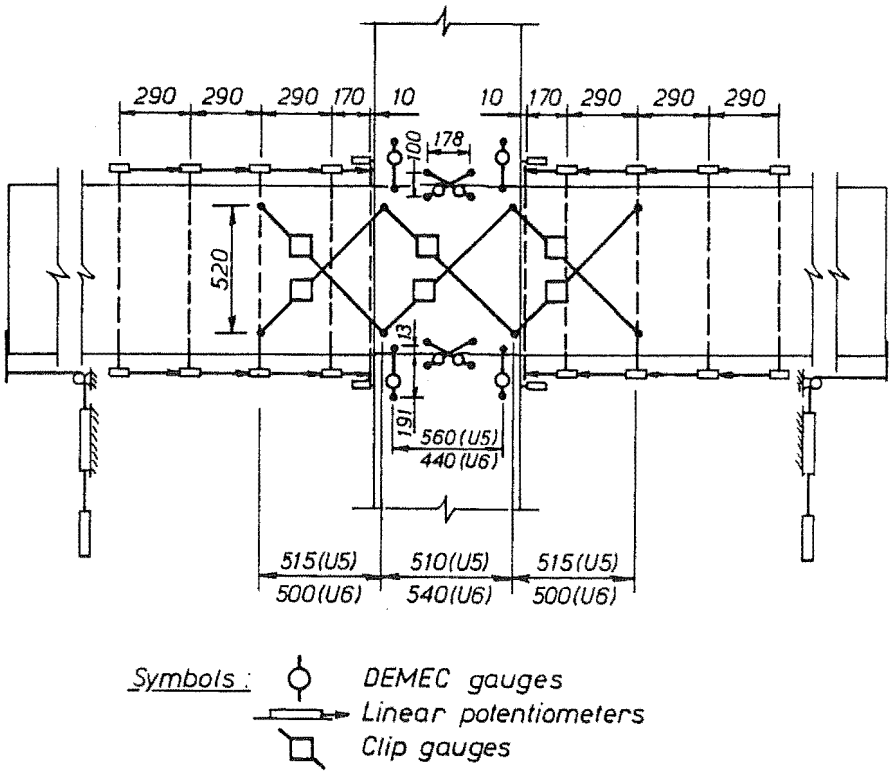

Fig. 3.29 - Lay out of Linear Potentiometers Measuring Internal Deformations of Unit 5 and 6.

to monitor any relative sliding shear between the horizontal construction joints in the columns of these two units. The position of DEMEC gauges is shown in Fig. 3.29.

Diagonal deformations of the beam span and in the beam-column joint region were made with the intention of monitoring the average shear distortions. An extended DEMEC gauge was initially used for this measurement in Units 1 to 3. A further development was the use of clip gauges and linear potentiometers mounted on stiff steel brackets to replace most diagonal readings manually taken. At large shear distortions most of the devices used for reading the diagonal deformations ran out of travel and instead manual measurements were taken using a 1m steel rule, which permitted readings within 0.5mm of accuracy.

3.8.3 Reinforcement Strains

3.8.3.1 Local Strains

Local strains in the reinforcing bars were measured using 120Ω 5mm foil strain gauges type Showa N11-FA-5-120-11 with a nominal gauge factor of 2.1. Details of the position of the strain gauges on the reinforcing bars will be given with the test results.

The surface preparation of the bars before attaching the strain gauges had the following steps:

a) The deformation of the bar where the gauge was to be attached was removed using either a file or a pneumatic belt sander. Care was taken to avoid an excessive reduction of the bar section in this region.

b) The prepared surface of the bar was then abraded by cross hatching at 45° using a 180 grit wet and dry paper.

c) The bar surface was then decontaminated using Methyl-Ethyil-Ketone, (MEK) applied with cotton-tipped applicators. The surface was scrubbed into the surface until the applicator appeared to have removed all contaminants. Caution was taken to avoid any material, such as grease, to recontaminate the surface.

Each strain gauge was stuck to a piece of sellotape with the backing surface exposed. Then, Loctite 401, an ethyl cyanoacrylate adhesive, was spread in a thin layer to cover all the backing surface of the strain gauge and then the gauge was immediately placed on the reinforcing bar. The strain gauge was held with pressure for space of at least one minute and the sellotape was removed several minutes later. Self-adhesive terminals were placed near the strain gauge to complete the circuit. A layer of Shinkoh SN/4, a waterproofing cement, was placed within 24 hours over the strain gauges and terminals. At least two additional layers of the waterproofing compound were added. Finally, 3M VM vynil mastic tape was used to cover the instrumented region and give further insulation and protection against physical damage.

The wires from the terminals were fed through a 4mm diameter PVC flexible sleeve to insulate them from moisture and give mechanical strength in the region near the terminal where the wires had to be tied to the reinforcing bar. They were bundled in groups containing not more than 8 sleeves and directed to a region in the test specimen that would not interfere with the instrumentation.

The reliability of the strain gauge readings was assessed in three cyclic load tests on machined reinforcing steel specimens similar to those used in the test program discussed in Chapter 2. Four strain gauges were arranged longitudinally at the centre of the specimens. The surface preparation followed the steps described above except for one strain gauge in each test where the surface was not abraded. The cyclic load tests stopped for five minutes at each load reversal to simulate the conditions at the peak of each run in tests on precast concrete assemblages in this programme.

Fig. 3.30 shows the test results. The main differences in the strain readings were due to the Lüders bands at the initiation of yielding which do not spread uniformly across the section of the specimen. Creep was always observed before the failure of the strain gauges. This creep occurred usually during the lapse before reversal of load direction. The strain gauges glued on to a smooth unabraded surface performed surprisingly poorly. Although the other strain gauges showed a longer life, it can be said that reliable strain readings beyond 1.2% to 1.8% strain cannot be obtained. Microscopic observations showed that the failure at large strains was due to debonding of the strain gauges at the surface of the specimen. The strain gauges themselves remained in working condition. It appears that creep during the lapse taken at the peak of each loading run for crack observation,

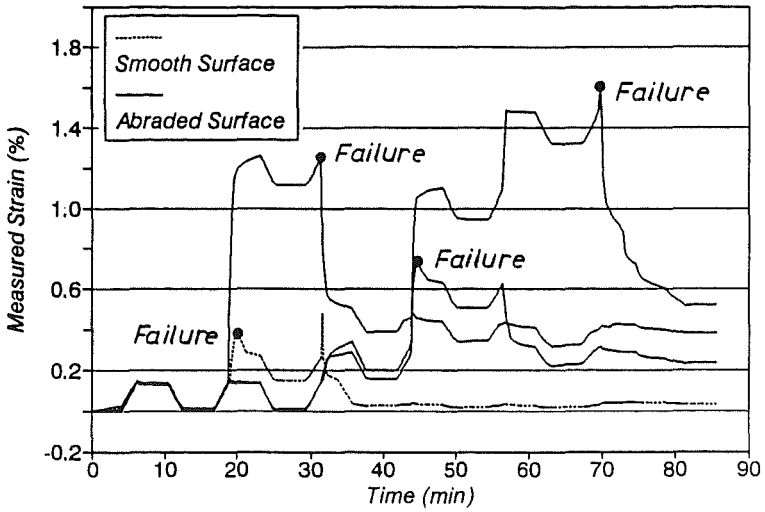

(a) Test 1

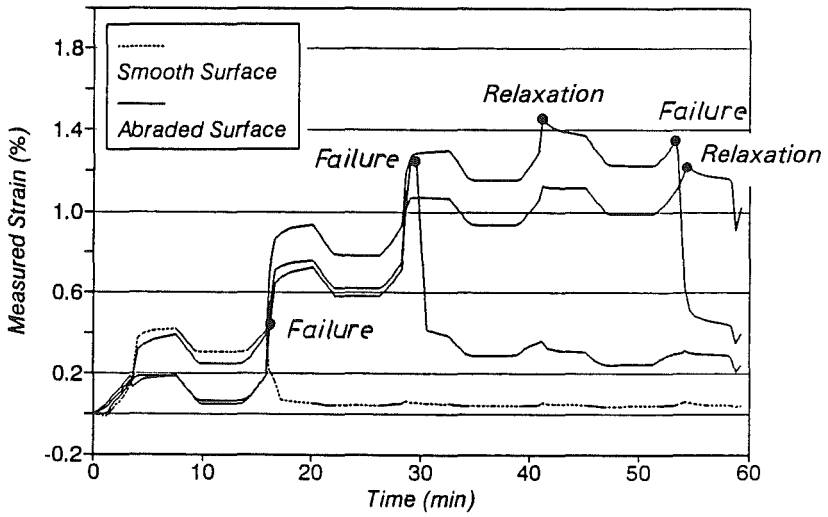

(b) Test 2

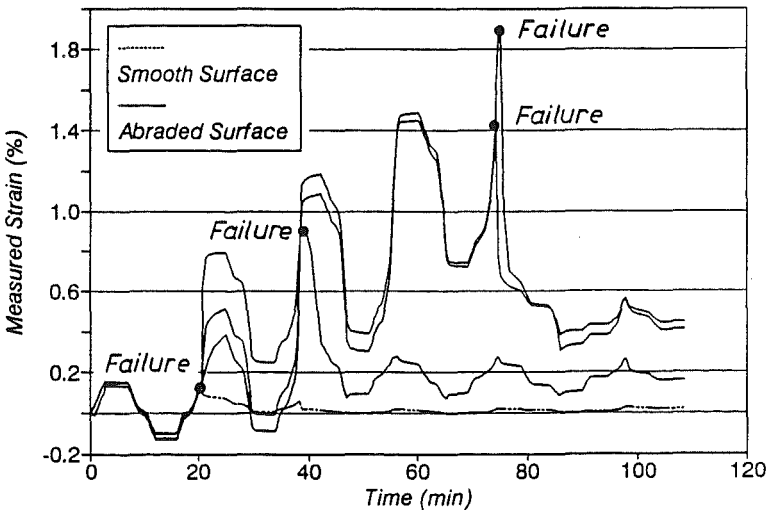

(c) Test 3

Fig. 3.30 - Results of Cyclic Load Tests to Assess the Reliability of Strain Gauges Used.

manual readings, etc. may show a critical condition for the strain gauge, especially if they are located in regions of moderate to high plasticity. It also appears that after the strain gauge debonds, the gauge is still capable of some cyclic response, because of the waterproofing cement which is still firmly adhered to the specimen and the strain gauge. The author has observed that because of this phenomena some researchers in the past have not realized that some strain gauges have failed and have used these false readings as "measured" data. It appears that the best way to identify whether a strain gauge has failed is to compare its reading at the peak of each loading run with that obtained from a scan prior unloading. Also, local bar strains measured by strain gauges can be affected by factors such as tension stiffening and local kinking of the bars near a crack. Hence, some judgement is required when analyzing strain readings obtained from electrical resistance strain gauges.

An additional problem faced in this project was the measurement of strains in the beam bars passing through the beam-column joint region in Units 5 and 6. The wires attached to the strain gauges can be subjected to large strains, which eventually may cause the loss of the circuit, because of the movement of the instrumented bars relative to the surrounding concrete. Hence, the region where the strain gauges were attached to the beam bar was covered with a soft material to give some flexibility to the wire near the terminal. Clip gauges were attached to these bars at the face of the columns since it was expected that the life of the strain gauges would not last beyond the initial stages of the test. The author believes that some other techniques could be successfully implemented to give more reliability to strain measurements in this important region. For instance, the use of spot welded strain gauges could be studied.

3.8.3.2 Average Strains

An alternative to measuring local strains using electrical resistance strain gauges is to measure average reinforcement strains using a mechanical strain gauge. In this study average reinforcement strains were initially measured using DEMEC strain gauges with a resolution of 0.002mm/division. That is, 2 and 1 $\mu\epsilon$ of resolution for gauge lengths of 102 and 204mm, respectively. Drilled steel targets were waxed onto the heads of screws that were locked to the steel studs that had been welded to the reinforcement. DEMEC gauges were later replaced by clip gauges that could be automatically scanned by the data logger unit. Clip gauges hanging from 4mm diameter rods were fixed to the welded studs using T-shaped fasteners.

Average strains at the level of the longitudinal reinforcing steel could also be estimated using the readings obtained from the linear potentiometers placed along the chords of the beams. If a diagonal crack is idealized at the centre of each segment gauged by a linear potentiometer as shown in Fig. 3.31, then the average strain average strain, ϵ_{avg}, at the level of the longitudinal reinforcing steel is given by

$$\epsilon_{avg} = \frac{\delta_r}{\ell_g} \tag{3.6}$$

where

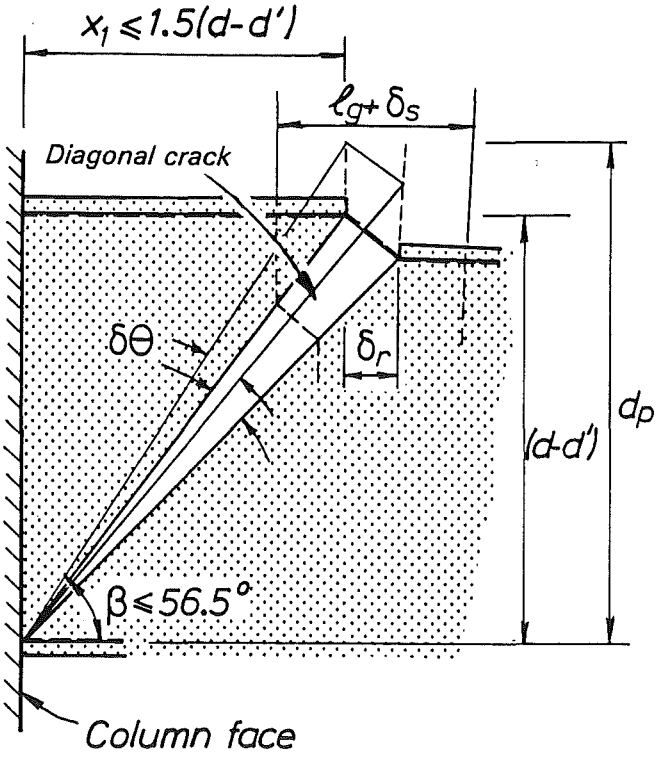

Fig. 3.31 - Average Strain at the Level of the Longitudinal Reinforcement Obtained from Linear Potentiometer Readings.

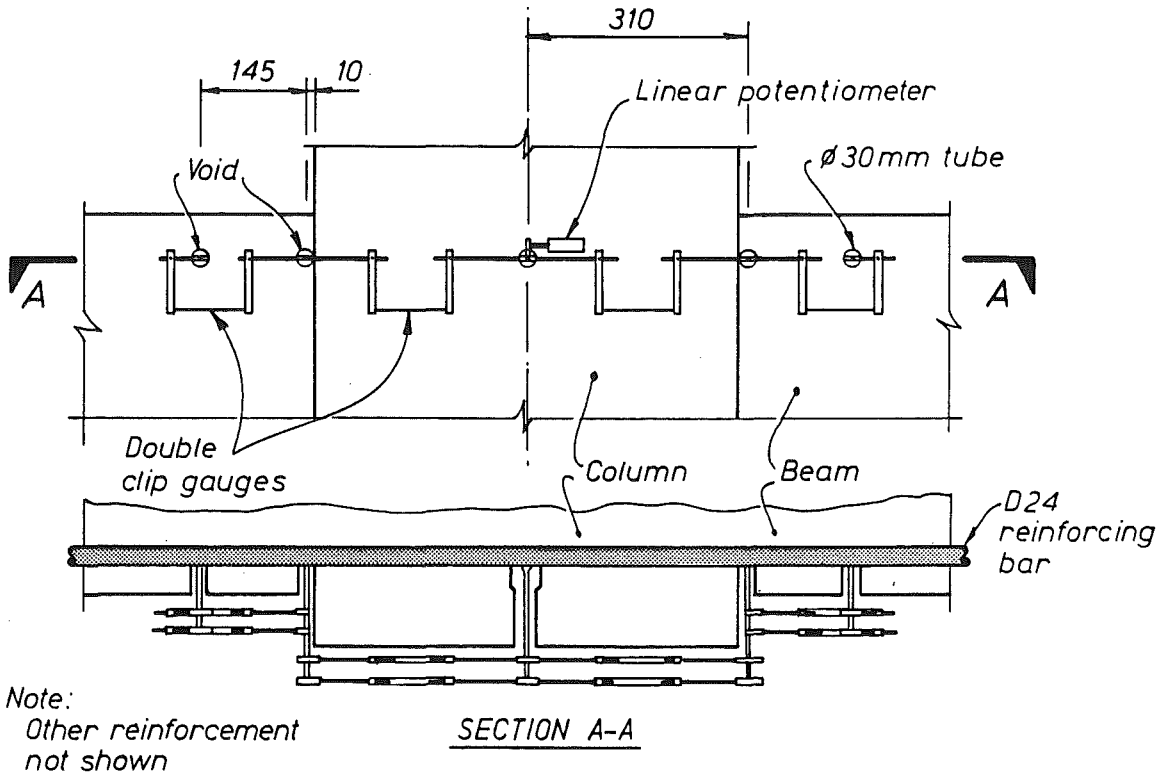

Fig. 3.32 - Set-up of Displacement Transducers to Monitor the Bar Slippage in the Beam-Column Joint Region of Units 5 and 6.

$$\delta_r = (d - d')\frac{\delta_s}{d_p}$$

and ℓ_g is the initial gauge length, d-d' is the distance between top and bottom beam reinforcement, δ_s is extension measured with the linear potentiometer over gauge length δ_g, d_p is the distance between the linear potentiometer and the centroid of the steel in compression.

Note that a small error in the idealization of the cracks is introduced when it is assumed that diagonal cracks will radiate into the beam from the column face up to a distance larger than the critical distance x_{cr} found using Eq. 3.12.

The average strains so found will not, of course, be equal to those in the reinforcing steel itself. However, they will follow the same trends and the error when the reinforcing steel is in tension is not expected to be large. Moreover, average strains at large displacement ductility cycles found using Eq. 3.6 were considered to give more reliable information than those obtained directly from strain gauge measurements. This is of special interest in Units 3, 4, 5 and 6 where average reinforcement strains were not directly measured along the beam span using either DEMEC gauges nor clip gauges.

3.8.4 Bar Slippage

The slippage of the longitudinal bars passing through the beam-column joint region of Units 5 and 6 was monitored as shown in Fig. 3.32. A 30mm travel linear potentiometer was used to measure the relative displacement at the column centreline between the concrete surface and a target stud welded to the D24 reinforcing bars. Clip gauges were used to measure the elongation of the bars between this target and targets welded on the same bars at 10mm away from the column faces. The so called local bar slip at the centreline of the column is based on the assumption that the concrete in this region forms an infinite rigid matrix around the bar. By adding the local bar slip at the column centre line to the elongation of the bars at 310mm from this point it is then possible to determine the movement of the bars relative to the column centre line. For obvious reasons this movement is not a local bar slip, because the concrete in the beam can not be considered as forming an infinity rigid matrix. However, the bar slip at the level of the outer column bars can be approximated by subtracting the elongation of the bar due to the strain to the measured bar movement. For that, it is necessary to assume that the beam bar strain between the outer column bars and the target at 10mm from the column face is constant and is equal to the one measured with the clip gauges over a gauge length of 145mm (see Fig. 3.32). This assumption is reasonably accurate since the bond conditions in this region deteriorate as the test progresses.

3.8.5 Data Acquisition System

All circuits from load cells, linear potentiometers, clip gauges and strain gauges were connected to data logger units with analogue-to-digital converter cards that converted voltage changes into divisions ranging between ± 2048. The output voltage of each transducer was amplified several times to obtain a predetermined sensitivity. Table 3.9 summarizes input voltages, gain factors and

resolution of the transducers used. Two data logger units were used in the test programme. Unit 1 was tested using a Cedacs I unit with a characteristic voltage of 20000mv/4096 divisions. This data logger unit presented problems with electrical noise as well as with wild points. The software to run this data logger was basic and during the test, displacements and load had to be manually reduced. A Burr Brown data logger unit replaced the Cedacs I unit in the remainder tests. Its characteristic voltage was equal to 10000mv/4096 divisions. The tailored software was especially written to give displacements and forces in real time.

The second independent circuit of the load cells was read by a strain indicator. For Unit 1 an analog Showa SI-10 strain indicator connected to a switch box was used. For the other tests Measurements Group P-3500 digital strain indicators were selected.

The voltage change of the linear potentiometers marked **A** and the differential output of linear potentiometers **D** and **D'** in Figs. 3.26 and 3.27 were monitored using a Hewlett-Packard Digital Voltmeter model 3440A.

Table 3.9
Set-up for Transducers on Data Logger Units

Transducer	Input Voltage (v)	Bridge Configuration	Gain Factors		Nominal Resolution	Accuracy
			Cedacs I	Burr Brown		
Load Cells	4	full	250	500	1.05 dlu/kN (1)	2.1 kN
RHS Sections	4	full	-	200	1.35 dlu/kN	2.7 kN
Linear Potentiometers	5	half	1	2	(2)	0.1%
Clip Gauges	4	full	- -	1,000 500	200 dlu/mm 100 dlu/mm	0.5%
Strain Gauges	4	quarter	50	100	0.085 dlu/$\mu\varepsilon$	0.3%

(1) Resolution of Linear Potentiometer depends on its maximum travel
(2) dlu : data logger units

3.9 COMPONENTS OF INTERSTOREY DISPLACEMENT

3.9.1 General

One important aspect of the experimental programme was the determination of the sources of the lateral displacement of the columns of the test units.

The instrumentation to enable the calculation of the different sources of displacement was concentrated in those regions of the test units where large inelastic displacements were expected. For the units tested the instrumentation was concentrated in the beam spans where plastic hinges were expected to develop, and in the beam-column joint regions to measure shear distortions. However, column deformations were only partially measured or not measured at all. The sections below describe the procedures used to find these sources of displacement.

3.9.2 Column Deformations

The column of the units were designed to remain in the elastic range. Hence, no major contributions to the total horizontal displacements of the units were expected to arise from deformations within the columns themselves. Except in the initial elastic load cycles where the flexibility of the columns could make an important contribution to the horizontal displacement imposed.

Several approximate methods can be used to evaluate the deformations due to the columns. One method is to assume an approximate value for the elastic properties of the cracked section of the member. Another method is to estimate the column deflection from a moment curvature analysis [Park and Paulay (1975)]. In the latter method the calculated deflection due to flexure may be larger than the actual deflection measured if the effect of tension stiffening has been disregarded. In both cases, approximations for the shear displacements and the contribution of the fixed-end rotation need to be added.

The moment-curvature approach was selected for the evaluation of the deformation of the columns of Units 1 to 4. The curvature diagram was assumed to be proportional to the bending moment diagram. This assumption is not necessarily exact since the curvature in the columns may be affected by the tension shift effect [Park and Paulay (1975)]. Also, a strain penetration of $15d_b$, where d_b is the nominal diameter of the longitudinal column bar anchored, was assumed to estimate the fixed-end rotation or in other words the additional rotation at the beam ends due to strain penetration in the beam-column joint core. Shear deformations and the effect of tension stiffening were ignored.

In Units 5 and 6, the deformation of the columns was partly determined from measured displacements at the ends of the columns. In addition, a calculated deflection, as for the column of Units 1 to 4, was added to account for the deformations outside the instrumented region.

The instrumentation placed in the columns of Units 5 and 6 at the beam faces was aimed to measure the fixed-end rotation as well as the part of the flexural deformations within the column. Also, DEMEC gauges monitored the shear displacement across the horizontal construction joints. The arrangement of this instrumentation is illustrated in Fig. 3.29.

3.9.3 Beam-Column Joint Shear Distortion

Diagonal readings in the beam-column joint panel enabled the average shear distortion to be estimated. From Fig. 3.33 it can be demonstrated that the joint shear strain, γ, is given by

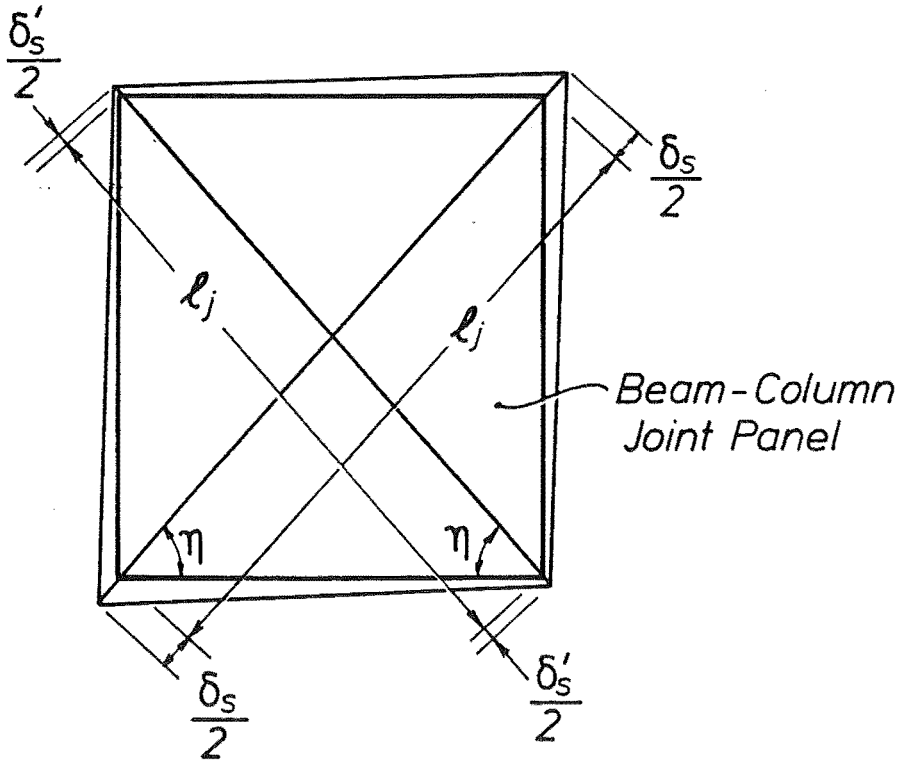

Fig. 3.33 - Shear Distortion in a Beam-Column Joint Panel.

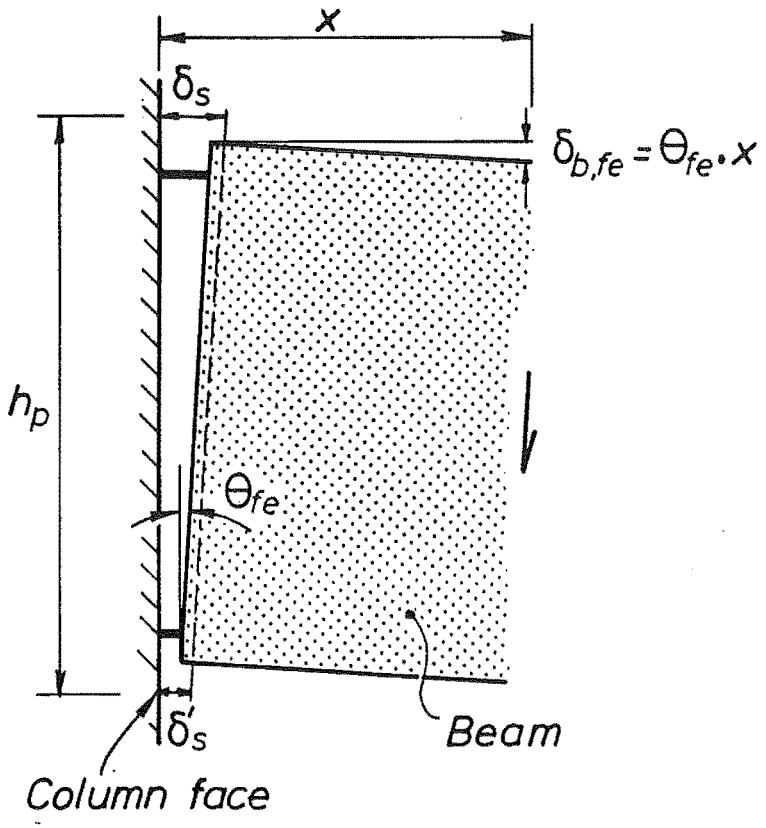

Fig. 3.34 - Evaluation of the Fixed-End Rotation in a Beam at the Column Face.

$$\gamma = \frac{(\delta_s - \delta_s')}{2\ell_j} (\tan\eta + \frac{1}{\tan\eta}) \quad (3.7)$$

where δ_s and δ_s' are the changes in length of the diagonals, ℓ_j is the initial length of the diagonals and η is the angle of the diagonals to the horizontal.

3.9.4 Beam Deformations

3.9.4.1 Fixed-End Rotation

The fixed-end rotation in a beam is caused by the elastic and inelastic deformations of the longitudinal bars anchored in the joint core or by global slippage of these bars or by both. The fixed-end rotation can be directly evalated from the pull out of the longtitudinal bars. An approximate method is to assume that the fixed-end rotation is given by the pair of linear potentiometers located in the beam next to the column faces, as shown in Fig. 3.24. This method has the disadvantage that the fixed-end rotation so obtained is overestimated due to the strain penetration of the longitudinal bars in the beam span. This approximate method was adopted in this study. From Fig. 3.34 the fixed-end rotation, θ_{fe}, and the corresponding vertical beam displacement, $\delta_{b,fe}$, evaluated at a distance x from the column face can be obtained as

$$\theta_{fe} = \frac{\delta_s - \delta_s'}{h_p} \quad (3.8)$$

$$\delta_{b,fe} = \theta_{fe}\, x \quad (3.9)$$

where h_p is the distance between the linear potentiometers.

3.9.4.2 Flexural Deformations

In this study, flexural deformations, $\delta_{b,f\ell}$, are defined as those estimated from the discrete rotations of each segment of the beam span, obtained from a pair of linear potentiometers located at the top and bottom chords. From Fig. 3.35

$$\delta_{b,f\ell} = \Sigma \frac{(\delta_s - \delta_s')}{h_p} (x - x_p) \quad (3.10)$$

Eq. 3.10 assumes the Navier-Bernoulli hypothesis of plane sections remain plane after deformation to calculate the flexural component. Other component of the beam deformation is allocated to shear, as discussed in the following section.

3.9.4.3 Beam Shear Deformations

Celebi and Penzien (1973) and Ma et al (1976) and have pointed out that shear deformations in the span of a short beam are coupled with flexural deformations. Hiraishi (1984) has also shown that in structural walls a similar effect occurs. Shear deformations obtained using Eq. 3.7 lead to errors because the change in length of the diagonals is also affected by the extension of the tension chord due to flexure in the beam. Fig. 3.36 shows a case of an apparent shear deformation due to the effect of

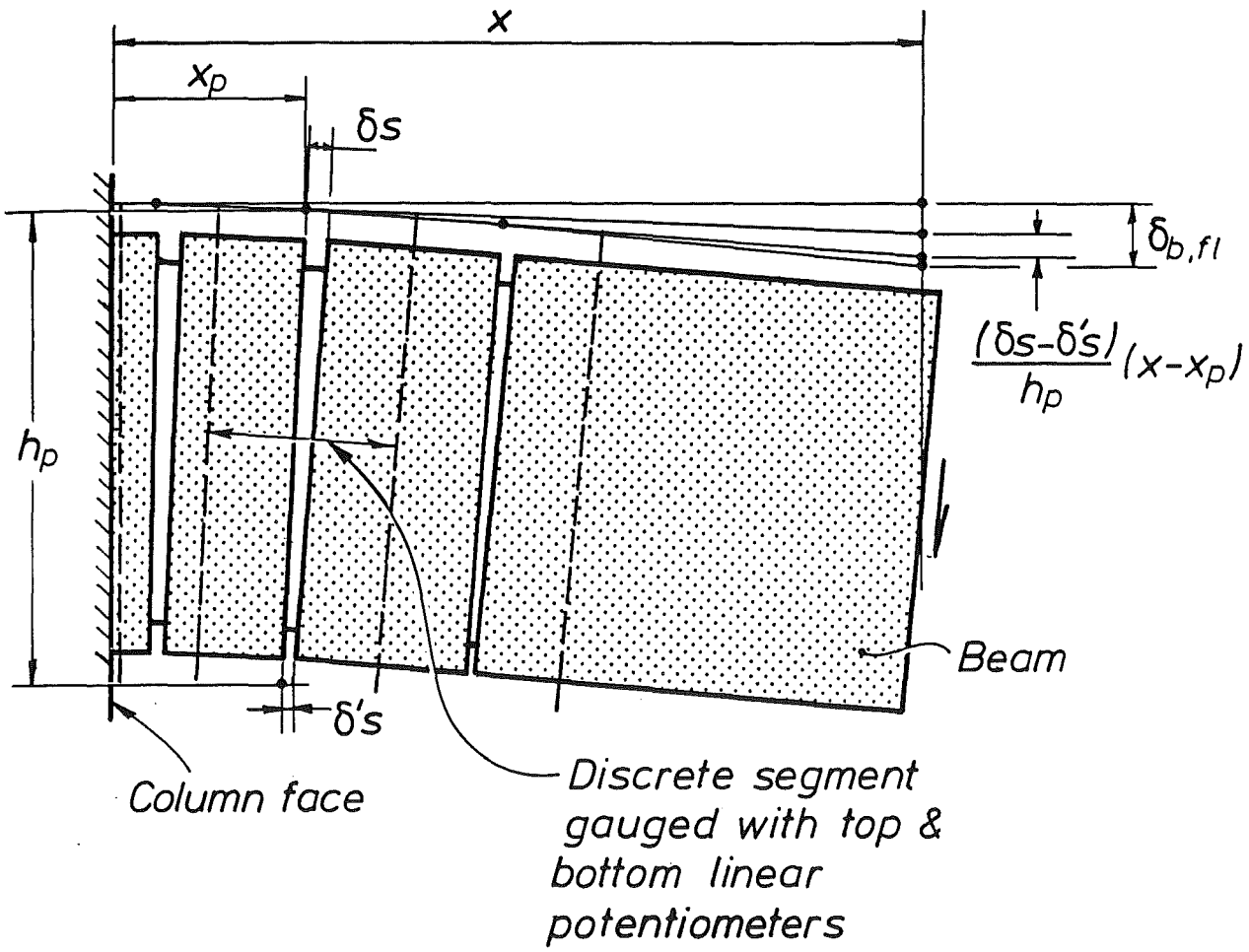

Fig. 3.35 - Evaluation of the Beam Flexural Displacements.

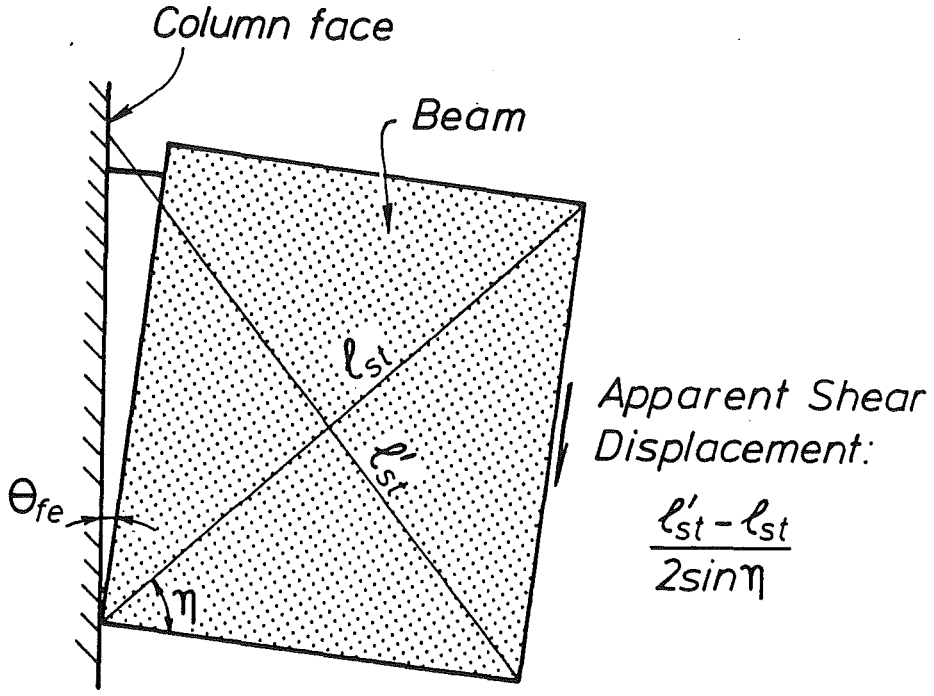

Fig. 3.36 - Apparent Shear Displacement Due to Elongation of a Diagonal Gauge.

the fixed-end rotation. In this study another methodology was developed to assess the shear deformations in the plastic hinge regions of the beams. Shear deformations elsewhere in the span of the beam were disregarded in spite of diagonal measurements taken. The different approach is discussed in the paragraphs below.

(a) Shear-flexure Action

Fig. 3.37 shows the kinematics of the plastic hinge of a beam where the flexure shear cracks have been lumped in an equivalent crack radiating from the centroid of the compression steel at the column face. At a distance x from the column face, the extension of the chords and the beam displacement due to flexure and fixed-end rotation, δ_f, are all known.

The shear component due to the diagonal shear-flexure cracking can be determined by assuming that the length of the compression strut, ℓ_{st}, remains unchanged. From geometry this shear deformation, $\delta_{b,sf}$, is given by

$$\delta_{b,sf} = \frac{\delta_s}{\tan\eta} - \delta_f \tag{3.11}$$

The critical distance, x_{cr} at which the diagonal strut develops can be approximated by

$$x_{cr} = \frac{V_a}{\frac{A_{st}}{s} f_{yt}} \tag{3.12}$$

where V_a is the theoretical shear in the beam associated with the lateral capacity H_a, A_{st} is the area of transverse steel spaced at a distance s and f_{yt} is the measured yield strength of the transverse reinforcement. This expression assumes that the critical crack will cross the necessary amount of transverse reinforcement that is required to transfer the whole shear in the beam.

For practical purposes the value of x_{cr} taken to evaluate the shear deformation due to flexure can be approximated as to the nearest end of the segment covered by linear potentiometers.

(b) Sliding Shear

Fig. 3.38 illustrates another mode of shear displacement, termed here as sliding shear. Because of yielding of the stirrups, disintegration of the diagonal strut or because of relative sliding between cracks in the plastic hinge region, the length of the strut, ℓ_{st}, will decrease and induce an additional vertical displacement, $\delta_{b,sa}$, due to the sliding action. If the new length, ℓ'_{st}, is known then the sliding shear displacement can be estimated as

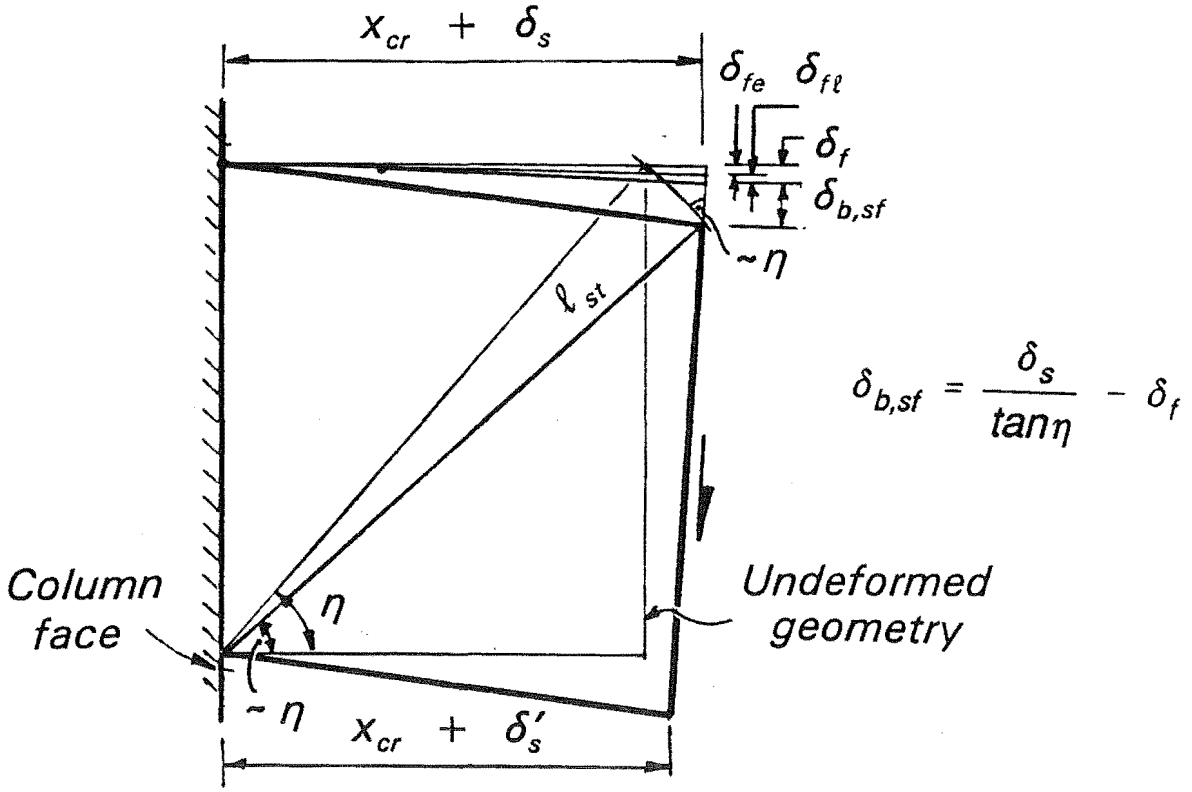

Fig. 3.37 - Shear Displacement Due to Shear-Flexure.

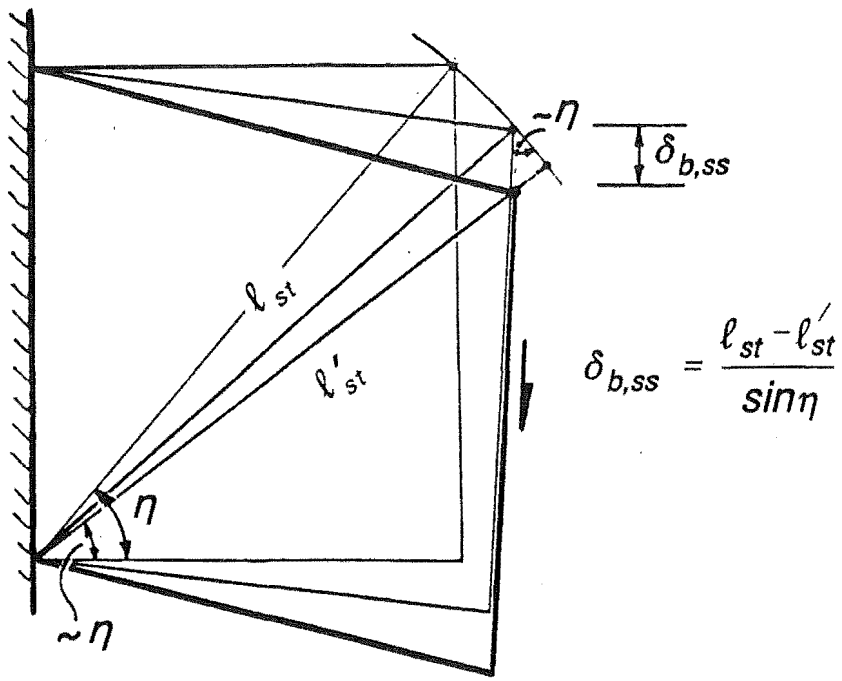

Fig. 3.38 - Shear Displacement Due to Sliding Shear.

$$\delta_{b,ss} = \frac{\ell_{st} - \ell_{st}'}{\sin\eta} \tag{3.13}$$

In the test of Units 1, 2 and 3 the change in length of the diagonal strut relative to the column face was not measured by the diagonal gauges because of the space required by the DEMEC gauges (see Fig. 3.28 (a) and (b)). Nevertheless, photographic records were used to measure this change within $\pm$3mm.

3.9.5 Member Deformations in Terms of Column Displacement

Having calculated the local member displacements or deformations it is necessary to transform them into horizontal column displacements. This procedure enables components of displacement to be determined as a percentage of the total displacement and a comparison to be made of the calculated displacement with that imposed during the test.

Figs. 3.39 and 3.40 show the main source of displacements considered in the test specimens. Displacements occurring in the beams or in the beam-column joint region can be transformed to an equivalent interstorey or column displacement as:

$$\begin{aligned}
\delta_{c,j} &= \frac{\ell_c}{\ell_b}\,\delta_{b,j} \\
\delta_{c,fe} &= \frac{\ell_c}{\ell_b}\,\delta_{b,fe} \\
\delta_{c,f\ell} &= \frac{\ell_c}{\ell_b}\,\delta_{b,f\ell} \\
\delta_{c,s} &= \frac{\ell_c}{\ell_b}\,(\delta_{b,sf} + \delta_{b,ss})
\end{aligned} \tag{3.14}$$

where $\delta_{c,j}$, $\delta_{c,fe}$, $\delta_{c,f\ell}$ and $\delta_{c,s}$ are the equivalent column displacements due to the shear distortion at the beam-column joint region, the fixed-end rotation in the beams, the flexural deformations in the beams and the shear displacements occurring in the beams near the column face respectively, ℓ_c is the distance between the column pins and ℓ_b is the horizontal distance between column centrelines in Units 1 to 4 or between beam pins in Units 5 and 6.

The total column displacement, δ_c, calculated from the deformations components is :

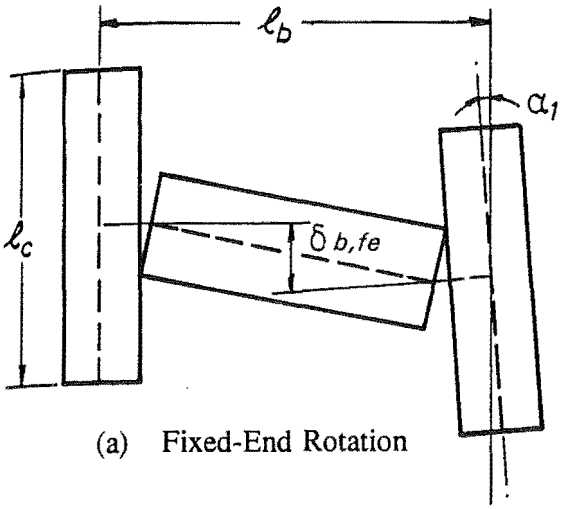

(a) Fixed-End Rotation

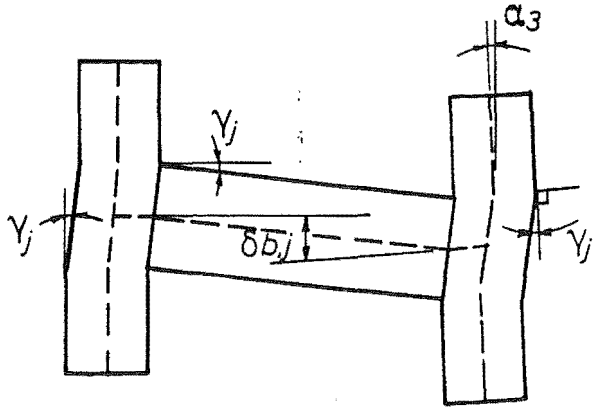

(d) Beam-Column Joint Shear

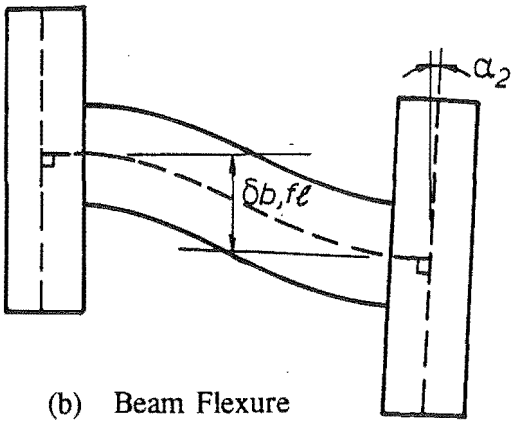

(b) Beam Flexure

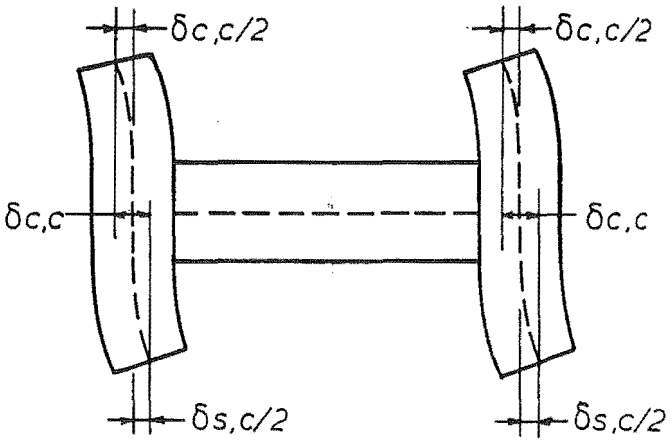

(e) Column Deformations

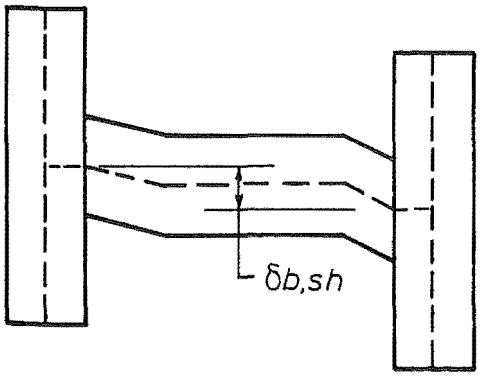

(c) Beam Shear in End Regions

Fig. 3.39 - Mode of Deformation of the H-Shaped Units 1, 2, 3 and 4.

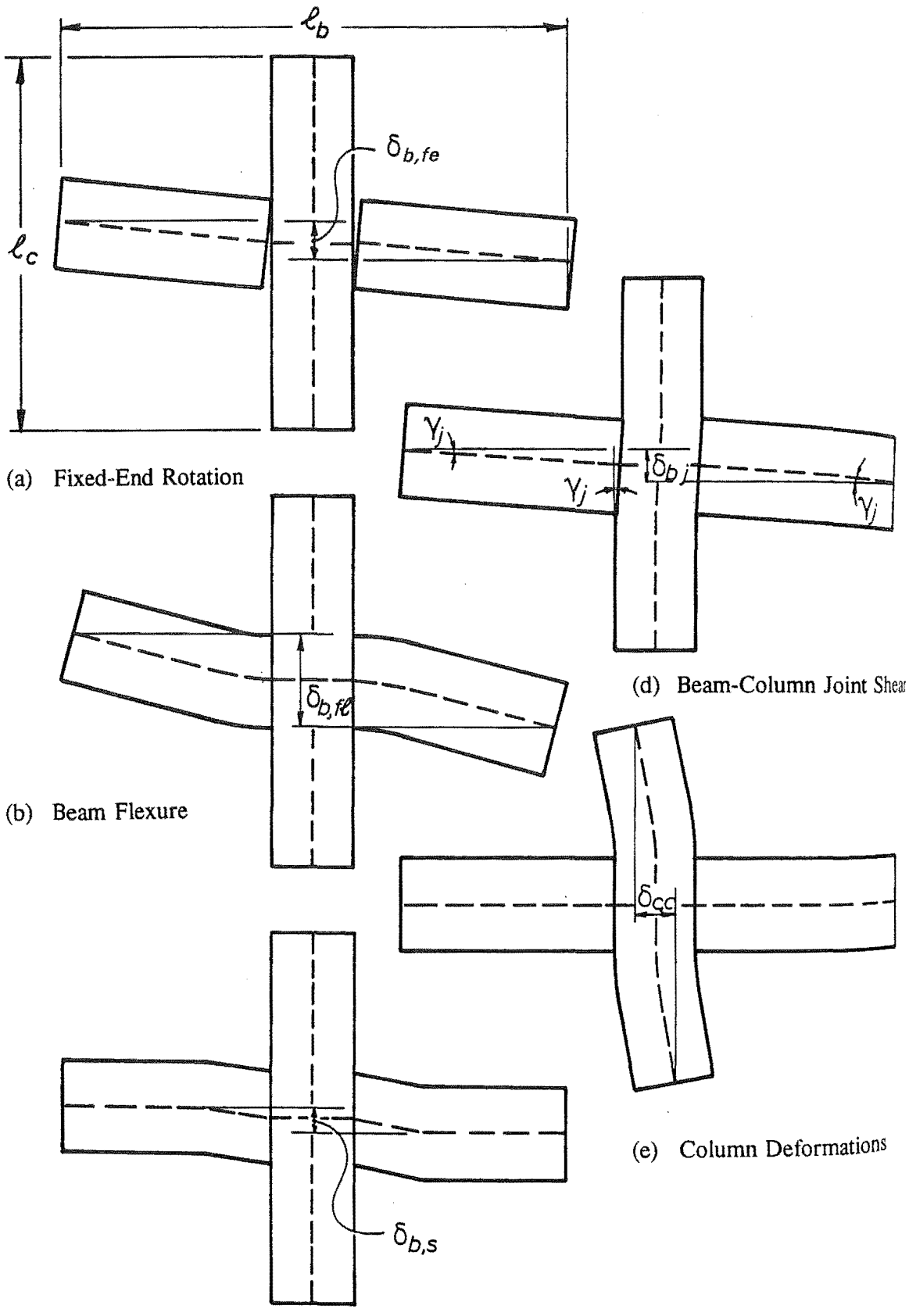

Fig. 3.40 - Modes of Deformation of Cruciform Units 5 and 6.

$$\delta_{co} = \delta_{c,c} + \delta_{c,j} + \delta_{c,fe} + \delta_{c,fl} + \delta_{c,s} \quad (3.15)$$

where $\delta_{c,c}$ is the estimated displacement from deformations within the columns.

With regard to Fig. 3.39, the angles α_1 to α_3 of the slaved column to the vertical do not need to be zero. In theory, however, the sum of these angles should be zero, providing that the displacement occurring in both columns is the same.

3.10 CONCLUSIONS

1. This chapter describes the construction and testing of the six beam-column subassemblages incorporating precast concrete. The test programme was divided into two parts. The first series of tests was conducted to evaluate the cyclic load performance of different connection details located the midspan region of beams. The second series of tests was conducted to evaluate the performance of different connection details located at the beam-column joint.

2. Test results on high strength low viscosity grouts indicated that high compressive strengths are easily attainable. However, one of the main factors in the use of these type of grouts is to ensure the fluidness avoiding excessive segregation and bleeding. Tests on the mechanical properties showed that the ratio of the splitting strength to the compressive strength and the enhancement of the compressive strength due to a lateral confining pressure is similar to that to concrete. However, the Young's modulus is significantly lower.

3. An alternative to the grouting procedure conducted in this programme could be the use of pre-packed aggregates inside the metallic ducting in which a water-cement grout is easily pumped through an orifice in the bottom joint between the lower column and the precast member.

4. The welding of reinforcing bars to steel plates showed an ineffective underfill region under the bars. It is recommended that, in lieu of more data, the welding commence at the midheight of the reinforcing bar be at a slope not greater than 60°.

CHAPTER 4

TEST RESULTS OF UNITS 1, 2 AND 3

4.1 INTRODUCTION

This chapter presents test results from the three H-shaped conventionally reinforced precast concrete units, connected at the midspan of the beam, with short member sizes typical of moment resisting perimeter frames. The main aim of this series of tests was to observe the behaviour of different short connection details at the midspan of the beam and the effect of their proximity to the critical regions where plastic hinges were expected to develop. Units 1, 2 and 3 were designed to induce in the beam the maximum allowed shear stress $v^\circ = V^\circ/bd = 0.30\sqrt{f'_c}$ permitted by the Concrete Design Code [NZS 3101 (1982)] when plastic hinges are expected to form in conventionally reinforced beams with symmetrical reinforcement.

Complete reinforcing details and the test regime were presented in Sections 3.2.2.1 and 3.7 respectively. Test results are presented in terms of the load run number (see the run numbers marked on Figs. 4.2 and 4.3) instead of the displacement ductility factor. The mapping between these systems can be found in Fig. 3.25 where the load sequence was shown.

4.2 UNIT 1

4.2.1 General Behaviour

The first unit to be tested, Unit 1, was designed following an existing connection detail of a building already constructed. The longitudinal beam reinforcement was overlapped at midspan using 180° hooks and transverse rods in contact with the concave side of the hooks to improve the anchorage conditions (see Fig. 3.17). The splice of the bars commenced at a distance of 1.46d from the column faces, where d is effective depth of the beam.

The test took four weeks to complete and attained load cycles in the inelastic range up to a displacement ductility factor of $\mu_\Delta = \pm 5.36$, at an interstorey drift of 2.3%, before losing its lateral load capacity by more than 20% of the maximum recorded. The cumulative displacement ductility factor attained by the test unit was $\sum \mu_\Delta = 59$ which leads to an available displacement ductility factor of $\mu_a = 7.4$ according to the method discussed in Section 3.7 to establish the available ductility of test subassemblages. The overall performance of the test and the connection at midspan was satisfactory in terms of strength and available ductility. However, severe pinching of the hysteresis loops occurred during the final stages of the test.

In the initial cycles in the elastic range, a small error occurred because the unit was loaded to 75% of the ideal lateral load capacity calculated using the nominal properties of the materials instead of the actual lateral load capacity, H_a, estimated from the measured properties. In terms of H_a, the lateral load imposed was 67% at the peak of the load controlled runs 1 to 4. Therefore the displacement history applied to the unit was 67/75 of that if this error had not occurred, that is, the actual displacement ductility factors applied to the unit are smaller than the nominal displacement ductility factors intended to be initially imposed. It is believed that this small error did not bear any significance in the test results.

Other sources of error during the test occurred with the instrumentation used to determine the net lateral displacement of the columns of the unit. Secondary stands required for fixing the linear potentiometers **A**, **B**, **C** and **C'** in Fig. 3.26 were fixed to the test floor. Unfortunately the forces applied to the edge of the floor during the tests were of such magnitude that the floor itself flexed upwards under the column in tension, causing an extra rigid body displacement that was not recorded by the displacement transducers. Independent measurements taken with a theodolite and a high precision level at the peak of each load run confirmed these movements. The unrecorded rigid body movement resulted in an extra lateral displacement in the load controlled cycles in the elastic range that affected the magnitude of the first yield displacement. A further problem that developed in the test of this unit was caused by the high friction forces in the free-to-slide mechanism of the test frame that had been designed to permit for the expected elongation of the beam. As a result, some axial load had to be transmitted through the beam enhancing its flexural capacity and hence the lateral load capacity of the unit itself. These friction forces caused a redistribution of the forces applied by the hydraulic actuators.

Fig. 4.1 illustrates visible cracking of the beam of Unit 1 at different stages during the test. Some very fine randomly arranged cracks developed in the sides of the beam in the cast in place concrete joint at midspan before the commencement of the test. Their pattern suggest they were caused by shrinkage of the concrete.

In the cycles in the elastic range, load runs 1 to 4, several cracks formed regularly in the end of the beams extending to about 600mm from the columns faces. The cracks commencing in the top generally extended further than the cracks commencing in the bottom of the beam. Two main cracks propagated through the web of the beam. The first one was a crack at the interface between the beam and the column and the other one was a diagonal crack appearing between 400 and 600mm from the column and heading towards the compression region in the beam at the column face. Cracks in the beam that opened in one load run nearly closed in the next. In the second in the elastic range, only propagation of the existing cracks was noticed. Cracks in the beam-column joint regions opened only in the loading runs where the column was subjected to axial load in tension and closed in the opposite runs.

In load runs 5 to 8 to $\mu_\Delta = \pm 1.78$ the beams showed signs of the initial yielding of the longitudinal reinforcement. Many cracks propagated in the web of the beam near the column faces with a typical fanned pattern. The main cracks at this stage were observed in the beam at the column face where crack widths of 2.5 and 3.5mm were observed. Previously open cracks at the level of the beam longitudinal

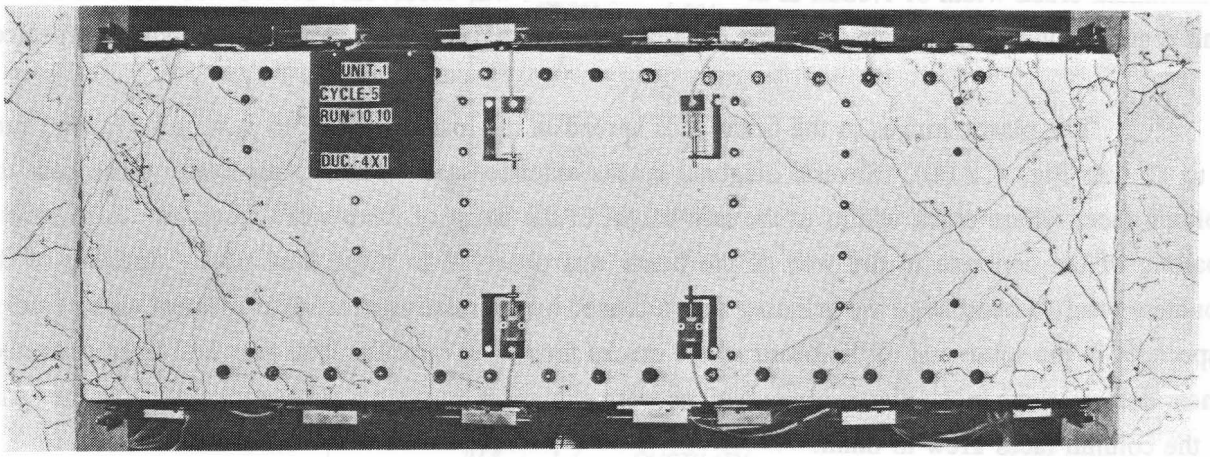

(a) At μ_Δ = -3.57x1

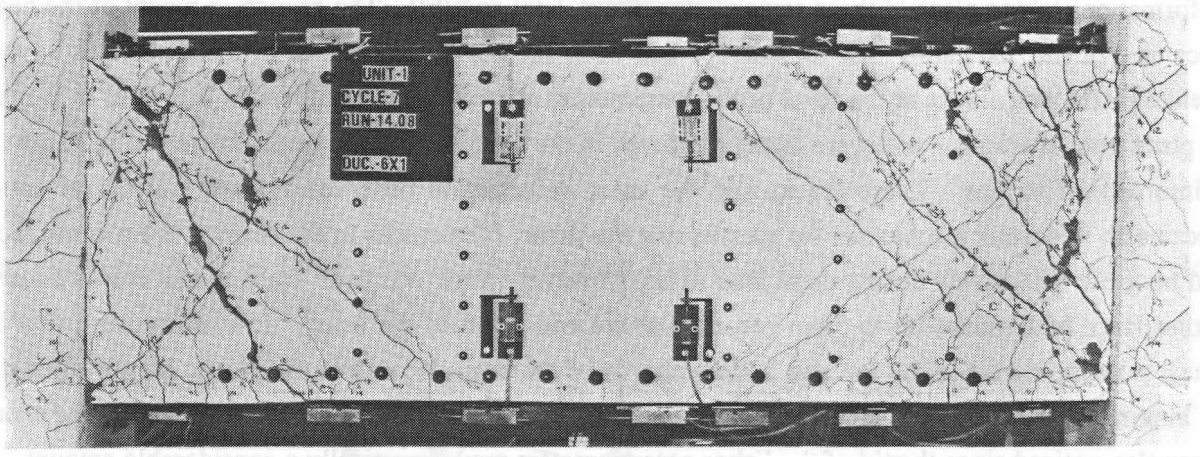

(b) At μ_Δ = -5.36x1

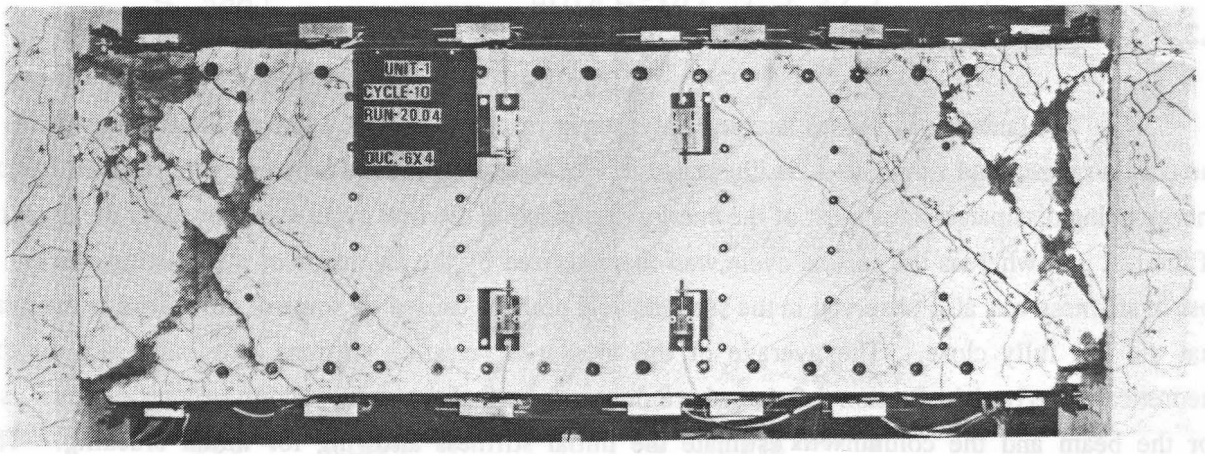

(c) At μ_Δ = -5.36x4

Fig. 4.1 - Cracking of Beam of Unit 1 at Different Stages During Testing.

reinforcement in tension did not close in the opposite load run. Hence lengthening of the beam occurred. Diagonal cracks in the web of the beam commenced to show an increase in their width and a maximum crack width of 1.0mm at the beam mid-height was observed. Cracks elsewhere in the test unit remained very small suggesting that plastic hinges were developing at the beam ends as expected.

The plastic hinges in the beam ends spread in the loading cycles to $\mu_\Delta = \pm 3.57$, load runs 9 to 12 (see Fig. 4.1 (a)). Several diagonal cracks extended and widened, especially those near the column faces where crack widths at the mid-height of the beam of 2mm were recorded. Also, initial spalling of the concrete in the web of the beam was observed in these load runs. Spalling of the concrete resulted because of the grinding action caused by the relative shear displacement along cracks, especially in the south end of the beam where cracks formed in opposite load runs had interconnected. Shear deformations in the plastic hinge regions were evident at this stage. The crack widths in the beam at the column faces grew to 6mm.

The final loading cycles to $\mu_\Delta = \pm 5.36$, load runs 13 to 20, were characterized by the grinding action between the cracks in the plastic hinge regions of the beams because of the sliding shear deformations taking place in these regions (see Fig. 4.1 (a) and (b)). The growth in height of the beam became evident, indicating that the stirrups had been subjected to rather large tensile strains beyond yield. Horizontal cracks at the level of the longitudinal reinforcement in the beam extended to the cast in place joint at midspan and were usually initiated in the spaces provided for the targets to measure the reinforcement strains. These cracks and the shear deformation observed suggest that dowel action became an important mechanism for transferring the shear. The cracks in the beam at the column faces did no grow extensively during these load runs. However, crack widths in the diagonal cracks became rather large with values up to 5mm recorded at the mid-depth of the beam. It was also seen that the linear potentiometers in the top and bottom chords of the beam located in the plastic hinges tilted due to kinking of the steel rods embedded in the diagonally cracked concrete. Large shear displacements were also noticed since the tip of the linear potentiometers moved vertically a considerable amount. In load run 17 a hairline crack crossed one corner of the cast in place concrete at the midspan connection. This crack did not propagate nor increase its width in the subsequent loading cycle.

4.2.2 Load Displacement Response

The lateral load versus lateral displacement response of Unit 1 during the loading cycles in the elastic range, load runs 1 to 4, is illustrated in Fig. 4.2. The second loading cycle resulted in little energy being dissipated since most of the energy dissipated in the first cycle was caused by the cracking of the test unit whereas the second cycle was characterized by the extension of the existing cracks. A loss of stiffness was also observed in the second cycle perhaps caused by some of the cracks in the beam that did not fully close. The average of the measured "elastic" stiffness was only 34% of that theoretically derived in Section 3.2.1, where only one-half of the gross section properties were used for the beam and the columns to estimate the initial stiffness allowing for initial cracking. This measured value of stiffness was probably underestimated, because of the rigid body rotation of the beam which was only partly measured. Nonetheless, it is believed that the unrecorded rigid body rotation would not account for the large difference. This difference is instead largely due to the strain

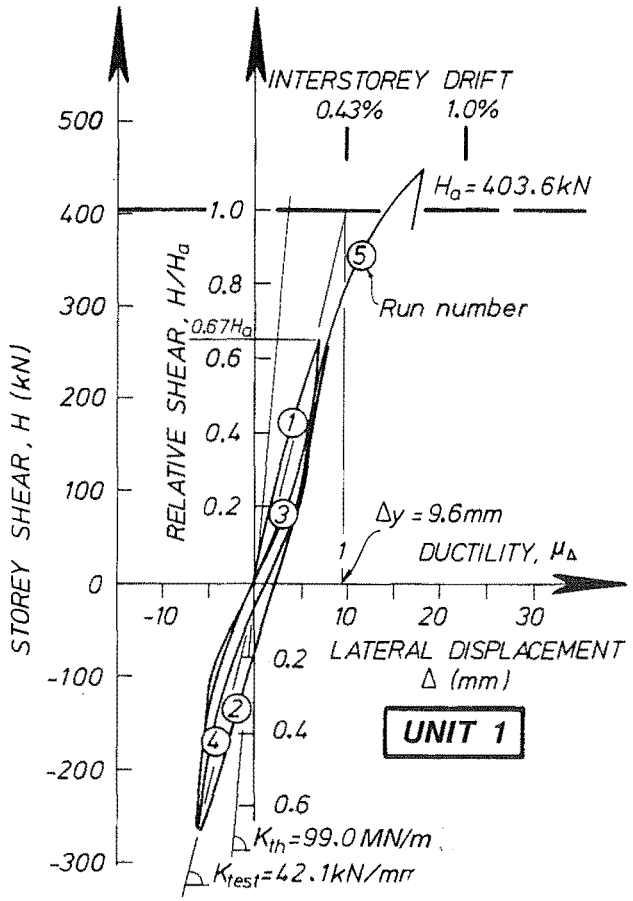

Fig. 4.2 - Lateral Load-Lateral Displacement Response of Unit 1 During Loading Cycles in the Elastic Range.

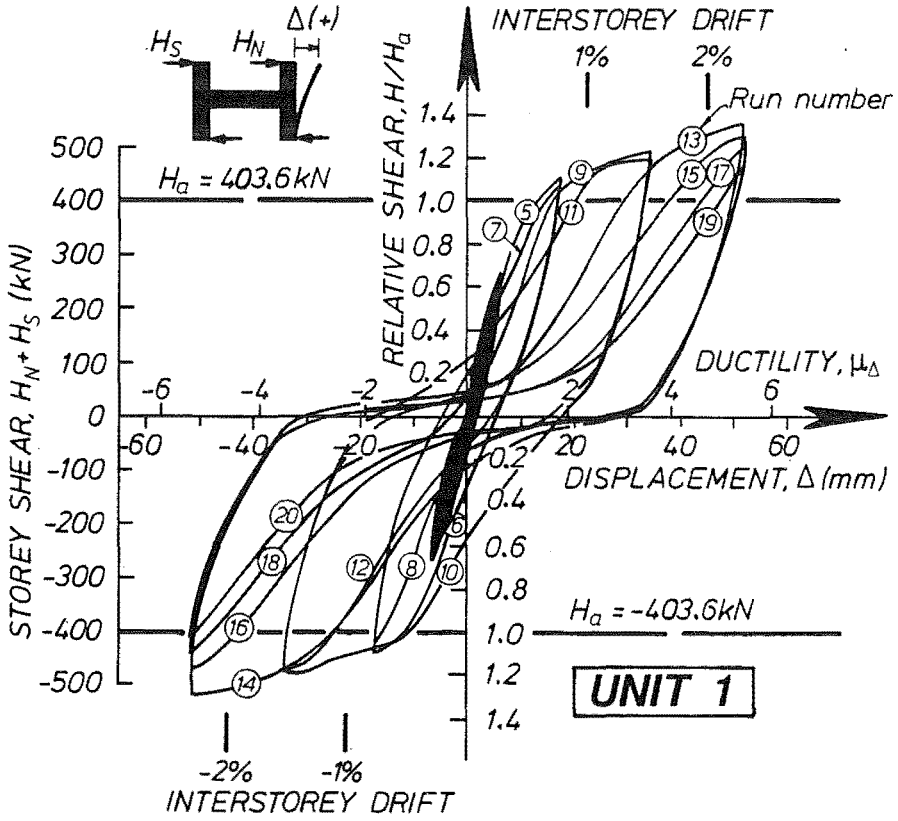

Fig. 4.3 - Lateral Load-Lateral Displacement Response of Unit 1.

penetration of the longitudinal reinforcement in the beam and the column into the beam-column region, which causes a discrete fixed-end rotation at the interfaces of the beam-column joints, to the curvature distribution in the short beam and columns which does not precisely follow the bending moment in the member because of the influence of the tension shift effect caused by diagonal tension cracking, and, to a lesser extent, to the flexibility of the beam-column joints.

Fig. 4.3 shows the complete lateral load versus lateral displacement response of Unit 1. The post-elastic slope of the envelope of the hysteretic response, estimated as the slope of the line passing between the theoretical point at first yield and the point at the maximum load in runs 13 and 14, was 7.8 and 6.2% of the initial "elastic" slope respectively. The measured energy dissipated in each cycle as well the cumulative energy absorbed was normalized using the energy dissipated by an ideal structure responding bi-linearly and having the same elastic and average post-elastic slopes.

In the first post-elastic load run, load run 5 to $\mu_\Delta = +1.78$ the measured lateral load exceeded the theoretical lateral theoretical load, H_a by 11.5%. The measured lateral load in the reverse load run 6 was slightly smaller. This trend was observed during the whole experiment and is believed to be linked to softening of the unit in the previous load run. In load runs 7 and 8 to the same displacement factor the lateral load attained was slightly below that attained in the first cycle. The energy dissipated in these cycles was only 68 and 40%, respectively, of that of the ideal bi-linear loops. The lower energy dissipated in the second cycle was probably caused by the closing of the previous diagonal cracking as well as by the smaller of extension of cracks that was observed.

In the subsequent load runs 9 to 12 to $\mu_\Delta = \pm 3.57$ the measured lateral load increased up to $1.19H_a$ and only a small drop in the measured load was recorded in the second loop to the same displacement ductility factor. The shape of the hysteresis loops became pinched, implying a loss in energy dissipation capacity caused by the closing of the diagonal cracks in the plastic hinge regions of the beam. The energy dissipated in these cycles was 63 and 42% of that of the ideal bi-linear loops.

The maximum overstrengths of $1.35H_a$ and $1.28H_a$ were recorded during load runs 13 and 14 to $\mu_\Delta = \pm 5.76$. In terms of the nominal shear stresses the maximum overstrength recorded in the beam plastic hinges was $v^\circ = 0.37\sqrt{f'_c}$. At this stage it became obvious that the friction developed in the free-to-slide mechanism at the support at the bottom of the south column was causing an enhancement of the flexural strength of the beam, which combined with strain hardening of the longitudinal reinforcement in the plastic hinges accounted for the relatively high measured overstrengths. The subsequent load runs 15 to 20 showed a gradual deterioration of the stiffness and energy dissipation capacity. In fact, the energy absorbed in these cycles was only 46, 27, 19, 15% of the ideal bi-linear loops. This considerable loss of stiffness and energy dissipation was associated with the gradual reduction in length due to grinding of the diagonal strut carrying most of the shear in the plastic hinge regions of the beam. Dowel action, then, became an important mechanism for transferring the shear in the plastic hinge regions. By observing the shape of the hysteresis loops in Fig. 4.3, it can be estimated that approximately 20 to 30% of the beam shear in load runs 13 to 20 could have been carried by this mechanism. A loss of lateral load capacity of 20% of the maximum capacity was recorded in run 19 accompanied by very significant stiffness degradation. However it is believed that had the unit

been displaced further it would probably had attained a lateral load capacity comparable to the maximum recorded. Nonetheless, the test was stopped at this stage because the redistribution of forces implied by the friction at the free-to slide pin caused the loading frame to reach its service load capacity at one end.

The cumulative post-elastic energy dissipated by the test unit up to load run 20 was only 33% of the ideal cumulative energy of the ideal bi-linear loops.

4.2.3 Decomposition of Lateral Displacements

The components of the lateral displacement at the peak of each load run are shown in Fig. 4.4. These components were estimated following the method described in Section 3.9. Calculated displacements in Fig. 4.4 are shown as a percentage of the measured lateral displacement. The top part of this figure displays the results of the load runs to a positive displacement while the bottom part shows the components of the load runs to a negative displacement.

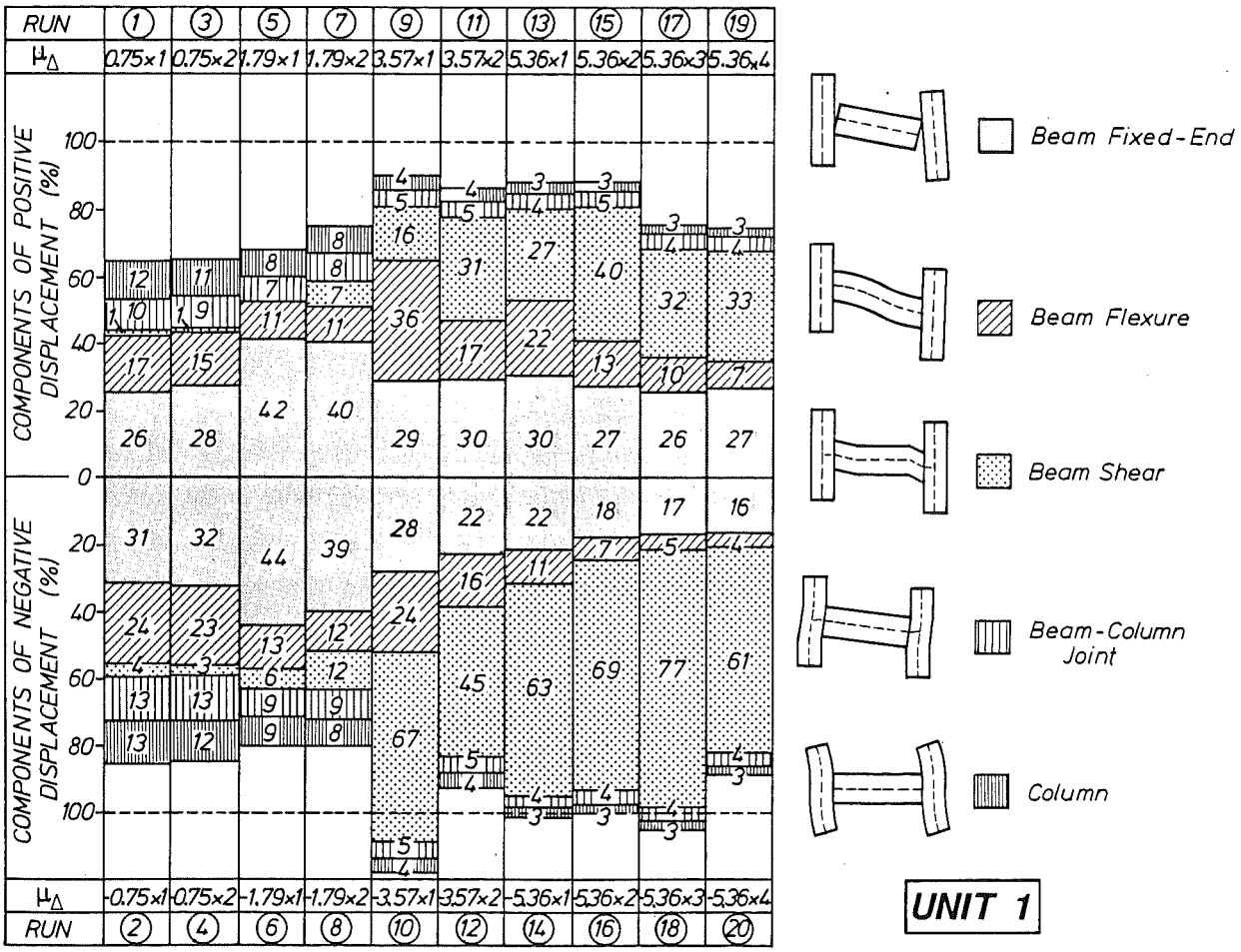

Fig. 4.4 - Components of Lateral Displacement of Unit 1 at Peaks of Load Runs.

In the cycles in the elastic range, the total estimated lateral displacement was on average 74% of that measured. The difference is probably due to the underestimation of the rigid body rotation of the test unit leading to an overestimate of the lateral displacements.

The fixed-end rotation of the beam, due mainly to strain penetration of longitudinal bars (see Section 4.2.1), was the major source of displacement in the initial load runs and its contribution remained important throughout the test, especially in the first cycle to each particular displacement ductility factor. The flexural deformations of the beam had a major contribution to the total displacement of the test unit in the cycles in the elastic range but their contribution to the total displacement gradually diminished as the test progressed. However, the shear displacements in the beam made a small contribution initially, even smaller than what an elastic analysis would indicate, but became the dominant contribution to the total deformation in the final loading cycles of the test. The large shear deformations in the plastic hinge regions of the beam were also associated with the longitudinal extension of these regions, since cracks that were open in a previous load run did not close in the next, increasing the tendency for sliding shear action.

4.2.4 Beam Curvature and Rotational Ductility Factors

Figs. 4.5 and 4.6 show the measured curvature and rotational ductility factors of the beam of Unit 1 estimated from the second set of linear potentiometers placed in the beam chords, commencing at 25mm away from the column faces, where the effect of diagonal cracking and the crack at the interface would be less important. The gauge length for calculating the curvature was 145mm. Both, the curvature and rotation at first yield were extrapolated using the average of the estimated curvatures and rotations at the north and south ends of the beam and following the same method outlined in Section 3.7 for determining the displacement ductility factors . The calculated curvature at first yield, ϕ_y, was 0.0027 radians/m and the rotation at first yield, θ_y, was 0.0033 radians. The estimated curvature ductility factors, μ_ϕ, in load runs 6 to 8 were rather small because yield of the reinforcement was mainly confined to the first segments of the beam next to the column faces. Beyond these load runs, the estimated curvature ductility factors show no definite trends. One reason is that the estimated curvatures are very sensitive to the position and width of the cracks forming in the concrete at and around the gauged region. In addition, at the end of the test it would be expected that some errors could be induced in the readings from the linear potentiometers caused by the large shear distortion at each end of the beam.

The rotational ductility factors, μ_θ, shown in Fig. 4.6 include the measured rotations of the north and south ends of the beam and the fixed-end rotations at the face of the columns. Also presented in Fig. 4.6 are the predicted rotational ductility factors estimated from a plastic analysis assuming that all deformations were due to rotations at the beam ends. The predicted values always overestimate those measured by a rather large margin. There are two main reasons for the disagreement observed. The first and main reason is the difference between the estimated net lateral displacement and the actual one. A second reason is the shear deformations which occurred in the second cycles to a displacement ductility factor meant that not so much flexural rotation was required of the beam. This effect is more

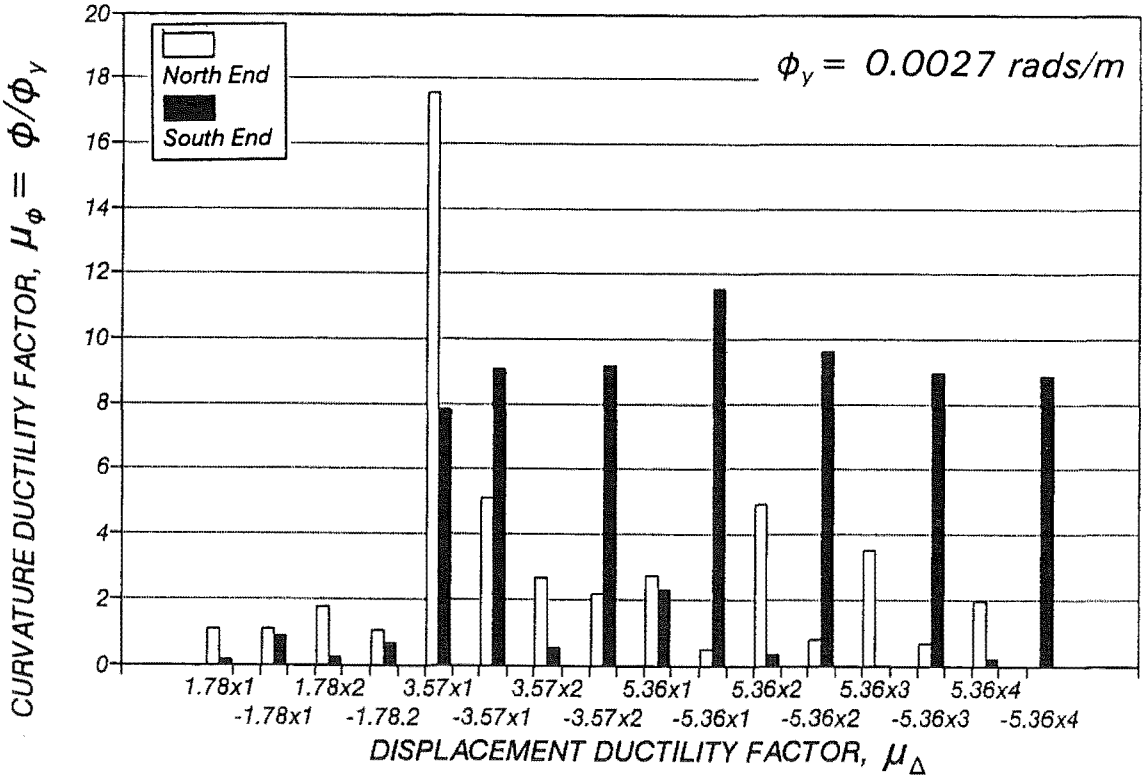

Fig. 4.5 - Beam Curvature Ductility Factors of Unit 1.

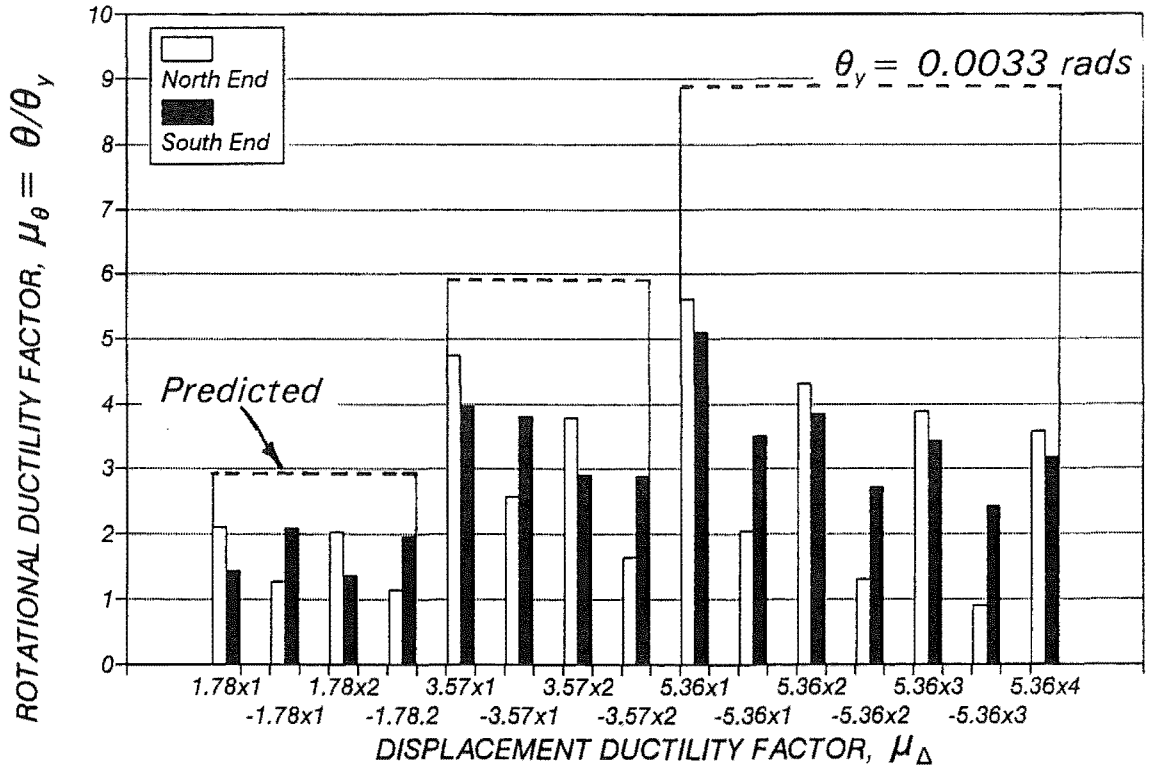

Fig. 4.6 - Beam Rotational Ductility Factors of Unit 1.

pronounced in the cycles near the end of the test when the shear deformations were the main source of lateral deformation.

4.2.5 Beam Longitudinal Bar Strains and Forces

Average strains of the east and west beam longitudinal bars of the beams are shown in Fig. 4.7. These strains were measured using a manual DEMEC gauge with a gauge length of 102mm. In addition, Fig. 4.8 illustrates member strains at the level of the longitudinal reinforcement estimated from the top and bottom linear potentiometers using the procedure discussed in Section 3.8.3.2. Both figures show the gradual increase of tensile strains in the plastic hinge regions at the beam ends. Both measuring systems show similar trends although the member strains near the beam ends in Fig. 4.8 are more erratic, perhaps due to the main cracks passing through the orifices in the cover concrete of the beam provided around the steel rods present for fixing the linear potentiometers. It is important to stress that the differences between the strains in Figs. 4.7 and 4.8 will depend on the quality of the bond between the reinforcing bars and the concrete, which will deteriorate in the plastic hinge regions of the beams as the test progresses.

From load runs 9 to 10 to $\mu_\Delta = \pm 4$ large residual tensile strains were detected in the beam in the plastic hinge regions up to a distance of 335mm from the column faces. The residual tensile strains in the plastic hinges led to a cumulative horizontal lengthening of the beam.

Fig. 4.9 displays the forces in the top and bottom longitudinal reinforcement of the beam of Unit 1 calculated from the measured bar strains shown in Fig. 4.7. The following procedure was carried out to estimate these forces:

a) Estimate the east and west bar stresses from measured data using the steel stress-strain model discussed in Chapter 2 and the mechanical properties of the reinforcement presented in Table 3.8.

b) Average east and west bar stresses.

c) Estimate the force in each section by multiplying the average stress by the nominal steel area.

The extent of yielding shown in Fig. 4.7 is apparently in disagreement with that shown in Fig. 4.9, especially with regard to the top bars in the north side of the beam. In Fig. 4.7 it appears that yielding spread over a distance d from the north column face, where d is the effective depth of the beam, while Fig. 4.9 shows a more limited length of yielding. The reason for this apparent discrepancy is that the kinked east bar yielded a significant amount while the straight west bar remained elastic. The east bars were kinked to create the offset required for overlapping the bars in the connection region at midspan. Their average strain then shows a value larger than the yield strain. However, the average stress shows a value below yield. At these sections in general, the measured strains on east and west

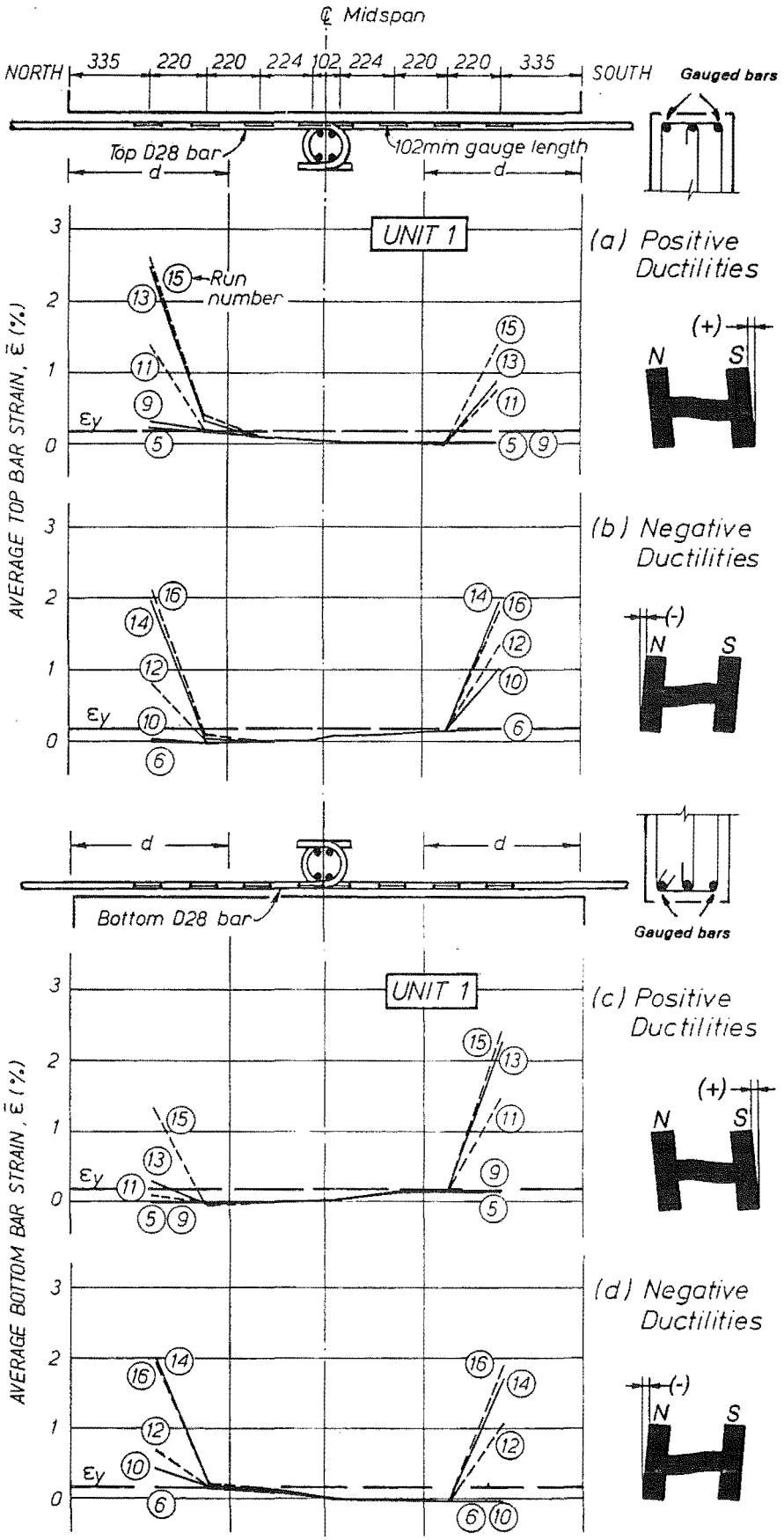

Fig. 4.7 - Average Beam Longitudinal Bar Strains of Unit 1.

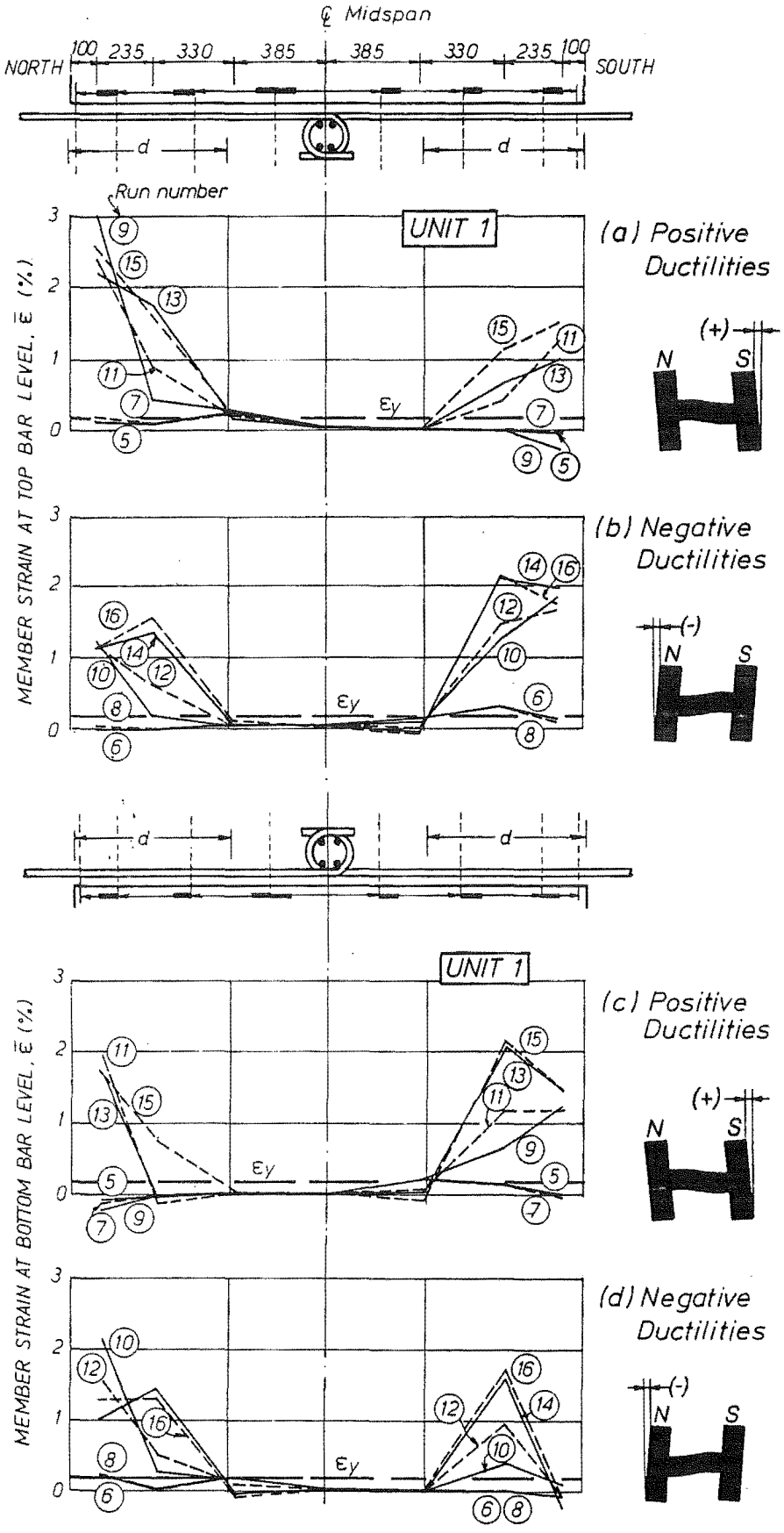

Fig. 4.8 - Member Strains at the Level of Longitudinal Reinforcement of Unit 1.

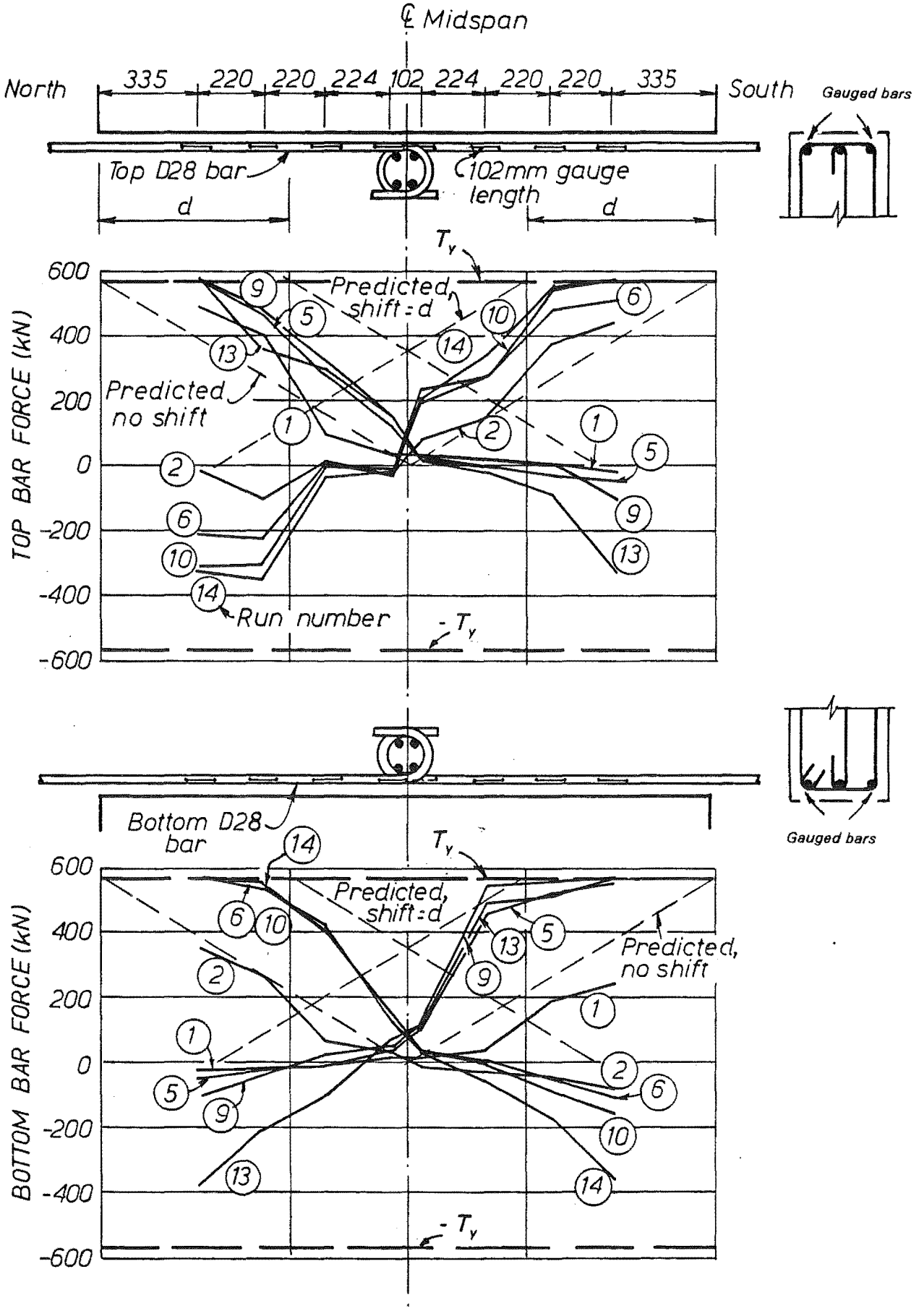

Fig. 4.9 - Longitudinal Bar Forces in the Beam of Unit 1.

bars exhibited rather different strain levels with the kinked bar consistently showing larger tensile strains, beyond yield in the cycles in the inelastic range, than the straight bar.

In the elastic cycles the forces in the top bars were larger than in the bottom bars, as shown in load runs 1 and 2 in Fig. 4.9. A reason for this behaviour is that there was a different moment demand, because for the same applied lateral displacement the lateral load in the column in compression was larger than that for the column in tension.

With the exception of the bottom bars when the test unit was subjected to positive displacements, the plastic hinge regions in the beams were confined to within a distance d from the column face. The tension shift at the beam ends was, on average, approximately equal to d, but rapidly decreased to almost zero at the midspan of the beam.

The forces in the compression bars near the beam ends were initially very small, implying that the concrete was transferring most of the compression, but they increased to approximately two thirds of the force in the tension bars in the final cycles of the test.

4.2.6 Longitudinal Bar Stresses at Midspan

Fig. 4.10 illustrates the stress profile of the beam longitudinal reinforcement in the connection region. The most remarkable feature observed was that there is no lapping action between the overlapping bars. The tension bars are acting as if they were anchored in this region.

The maximum relative longitudinal movement of the bars, measured also with DEMEC gauges, was only 0.1mm. This shows the adequate anchorage conditions of the bars. The transverse rods played an important role in distributing the bearing stresses of the bar in tension and avoiding splitting of the concrete due to the radial nature of the stresses around the longitudinal bars.

4.2.7 Stresses in the Transverse Reinforcement at Midspan

The transverse reinforcement in the connection region at the midspan of the beam was instrumented with 8 electrical resistance foil strain gauges. Recorded strains indicate that the level of the stresses in the vertical and horizontal sides of the stirrups was very low, of the order of $0.1f_y$. This level of stresses agrees with the observed behaviour of the cast in place joint where no significant cracks were detected.

4.2.8 Elongation of the Beam

The measured total elongation of the beam span of Unit 1 plotted against the measured lateral load is illustrated in Fig. 4.11. A small residual elongation was recorded at the end of the cycles in the elastic range, implying that some cracks did not fully close. A feature of the elongation of the beam is that most of it occurred in the first cycle to a new value of displacement ductility factor when the flexural capacity of the test unit was attained. Also, some elastic recovery was observed when

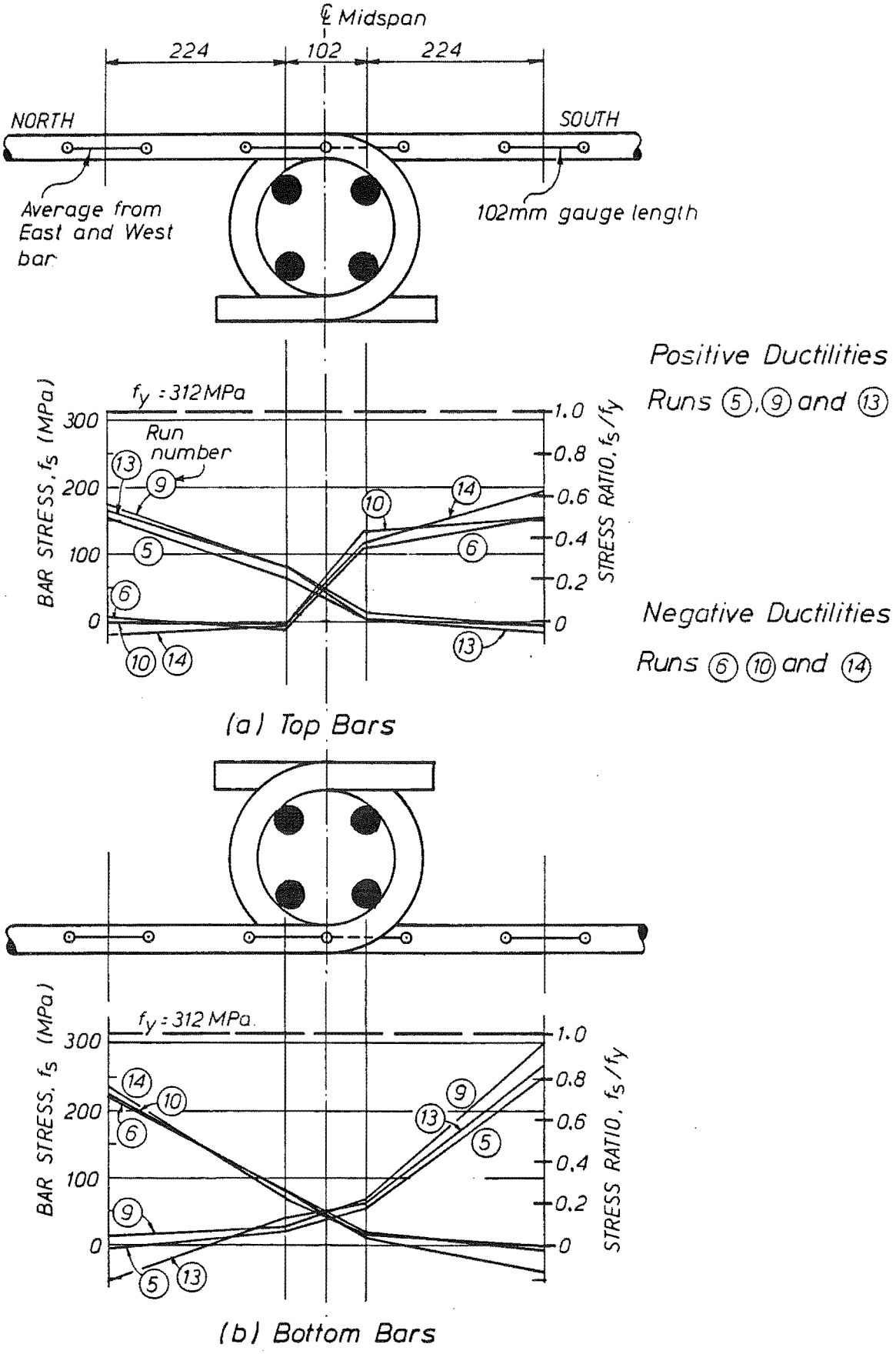

Fig. 4.10 - Bar Stresses at the Midspan of the Beam of Unit 1.

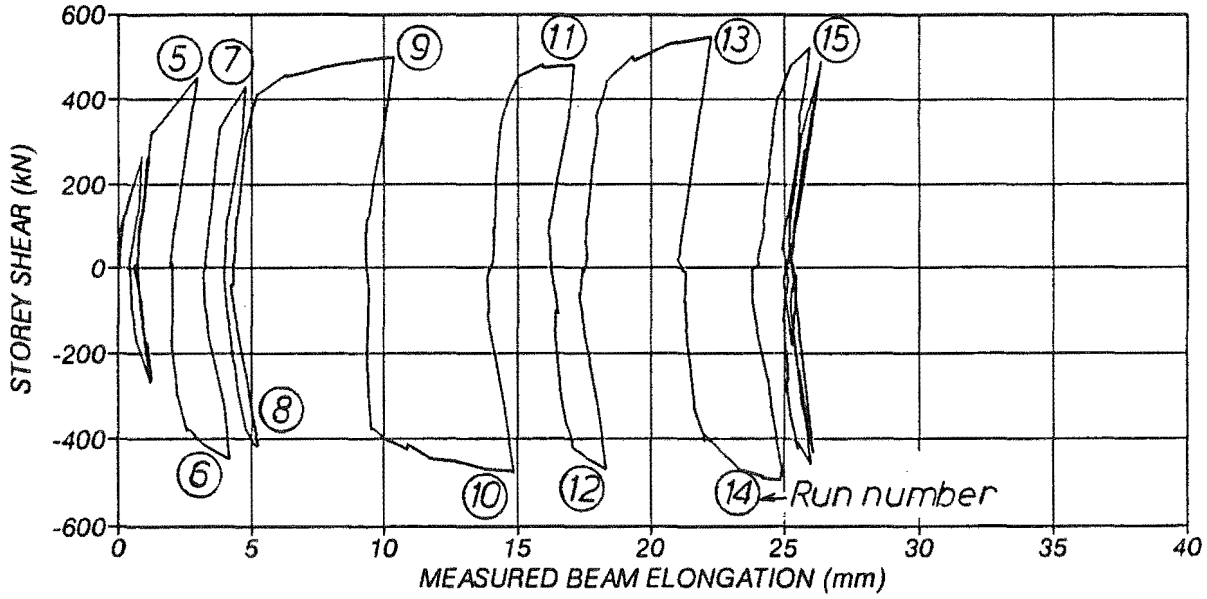

Fig. 4.11 - Total Measured Beam Elongation of Unit 1.

unloading upon reversal. The elongation accumulated in the load runs because of the residual tensile strains in the top and bottom longitudinal bars. No important elongations were recorded in the third and fourth cycles to $\mu_\Delta = \pm 5.36$ since the unit did not develop its flexural capacity in those cycles. The maximum measured total elongation was 26mm recorded at the peak of load run 19 to $\mu_\Delta = 5.36$.

4.3 UNIT 2

4.3.1 General Behaviour

The midspan connection detail used in Unit 2 consisted of 90° double hooked "drop in" bars which lapped two thirds of the longitudinal beam reinforcement. Transverse rods were placed in contact with the concave side of the hooks to improve the bearing conditions (see Fig. 3.18). The connection at the midspan of the beam commenced at a distance of 1.23d from the column faces.

The free-to-slide mechanism at the support at the end of the south column was modified to reduce the friction forces which had developed during the first test (see Section 3.3). Also the instrumentation used to determine the net lateral displacement of the test unit was attached to steel frames fixed outside the test floor area, to avoid the errors due to the flexibility of the concrete floor.

The test of Unit 2 was conducted over a period of two weeks. A decrease of more than 20% of the maximum measured lateral load occurred in fourth cycle to $\mu_\Delta = -6$ at a drift of 2.1%, due to stiffness degradation. The cumulative displacement ductility factor attained before failure was $\Sigma\mu_\Delta = 60$ equivalent to an available displacement ductility factor of $\mu_a = 7.5$ (see Section 3.7). Further cycles to $\mu_\Delta = \pm 8$ showed some reserve of strength since the lateral load measured in this cycle was comparable

with the maximum lateral load measured in the test. Shear deformations in the beam plastic hinge regions caused severe pinching of the measured hysteresis loops, especially near the end of the test. The overall performance of the connection detail was very satisfactory. Also, its relatively close proximity to the critical regions of the beam apparently did not influence the overall response of the test unit.

The visible cracking of the beam of Unit 2 at different stages during the test is shown in Fig. 4.12. In the cycles in the elastic range, the cracks spread in the beam from the column faces to the cold joint between the precast concrete members and the cast in place concrete at midspan. The main cracks in these load runs were the vertical cracks at the column faces, which opened as a result of the strain penetration of the beam longitudinal bars into the beam-column joint region. Cracks at the cold joints near midspan propagated beyond the mid-depth of the beam but they were rather fine. Cracks also appeared in load run 3 around the 90° hook in the top north and bottom south bars in the connection region at midspan. The width of these cracks was only 0.02mm.

In load runs 5 to 8 to $\mu_\Delta = \pm 2$, many cracks extended and widened in the expected plastic hinge regions at the beam ends. The cracks at the faces of the columns were 2.5 to 3mm wide at the tension side. Although their width decreased towards the compression side, they remained open over the full depth of the beam. The maximum width of the diagonal shear-flexure cracks at the mid-depth of the beam was 0.3mm. The vertical cracks at the cold joint between the precast members and the cast in place concrete opened to a width of 0.6mm at the mid-depth of the beam. Diagonal cracks commenced from these cracks and headed towards the compression region in the beam at the column faces. The cracks around the hooked bars also widened and extended. However their maximum width was only 0.2mm.

In the cycles to $\mu_\Delta = \pm 4$, load runs 9 to 12, some diagonal cracks in the plastic hinge regions of the beam became rather wide (see Fig. 4.12 (b)). Crack widths in this region, measured at the mid-depth of the beam, were as large as 3mm. The width of the cracks suggested that plastic hinge regions had commenced to extend from the column faces and that yielding of the stirrups in the beam ends was likely to have occurred. In addition, relative shear displacements of 1mm between the sides of the cracks were observed. The cracks at the cold joint in the midspan region also widened, as if the reinforcing steel in this region had yielded. Relative shear displacements of 1mm along these cracks were observed. In load run 9 two splitting cracks running parallel to the reinforcing bars protruding from the precast members were observed in the cast in place concrete at the bottom south side of the beam. In load runs 11 and 12 several small diagonal cracks formed in the web of the beam in the cast in place concrete.

The vertical elongation of the beams in the plastic hinge regions became evident in the first cycle to $\mu_\Delta = \pm 6$ when the measured expansion at a distance of 280mm from the column faces was 11 and 8mm at the north and south ends, respectively. Spalling of the concrete at the beam ends was also observed at this stage due to the grinding action caused by the sliding shear displacements along the cracks. Many fine cracks formed in the cast in place concrete during these loading cycles, as is seen in Fig. 4.12 (c). The height of the beam in the plastic hinge regions increased with further cycles to

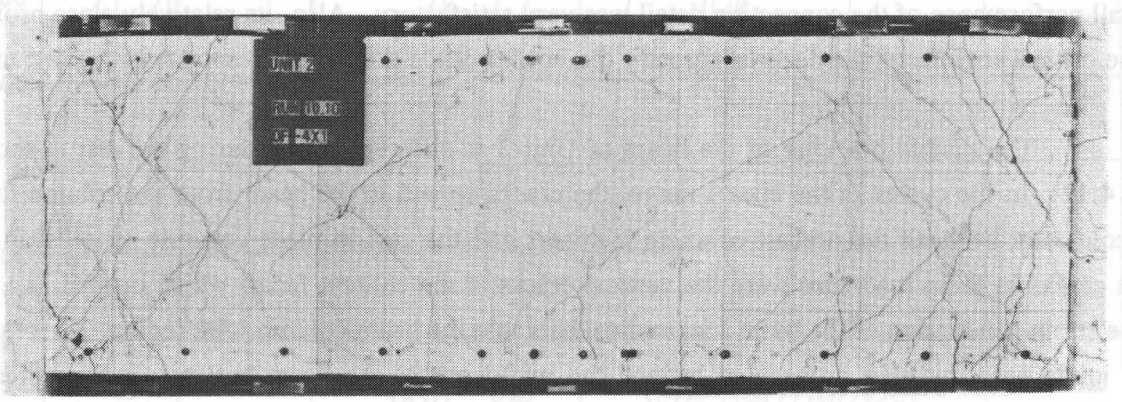

(a) At μ_Δ = -4x1

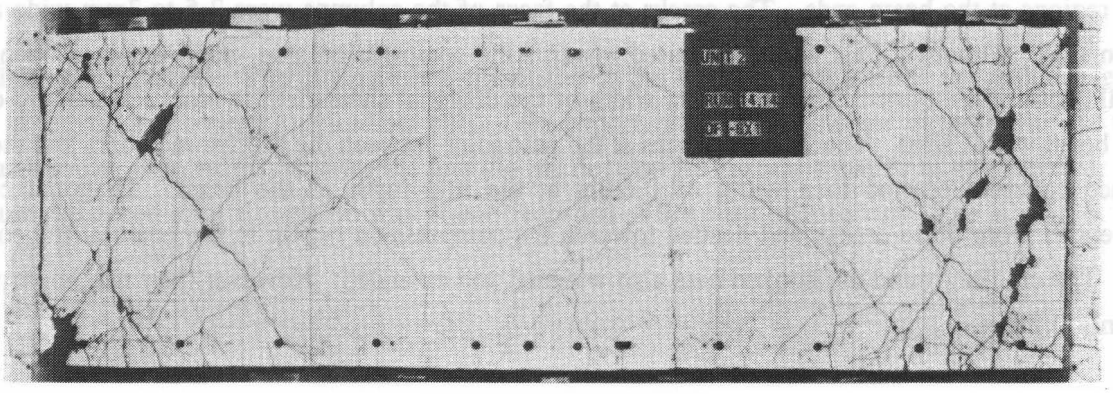

(b) At μ_Δ = -6x1

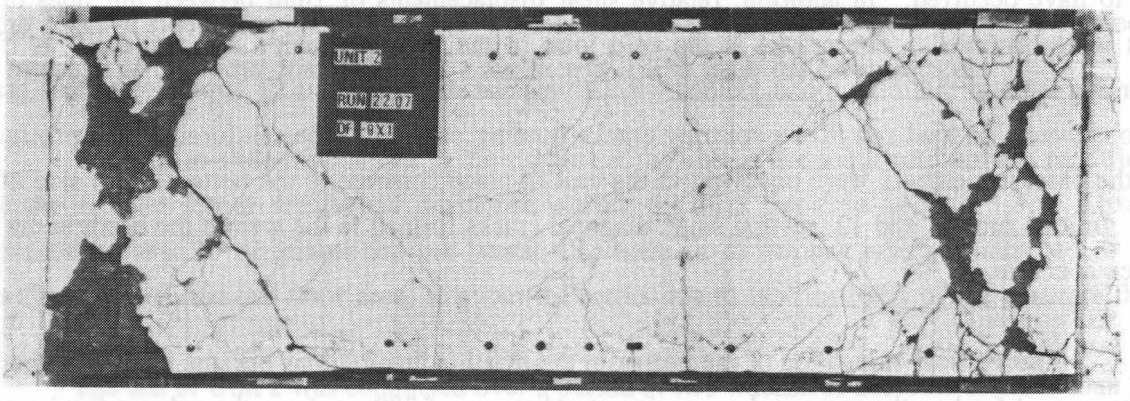

(c) At μ_Δ = -8x1

Fig. 4.12 - Cracking of Beam of Unit 2 at Different Stages During Testing.

the same displacement ductility factor due to yielding of the stirrups. The stiffness of the unit degraded to a point that the measured lateral load in run 19 was below the 80% of the maximum previously attained load. In load run 19 the increase in height of the beams in the plastic hinge regions was 20 and 12mm in the north and south end, respectively. In this load run the relative shear displacement along the cold joint was 2mm and the maximum width of the cracks in the cast in place region at midspan had increased to 0.5mm.

The test unit was taken to $\mu_\Delta = \pm 8$ in load runs 20 and 21 to observe on whether the capacity of the unit had been reduced. In this cycle the plastic hinge regions of the beam appeared severely damaged, but they were still able to transfer shear forces of similar magnitude to the maximum ones recorded in the first loading cycle to $\mu_\Delta = \pm 6$.

4.3.2 Load Displacement Response

Fig. 4.13 shows the lateral load versus the lateral displacement of Unit 2 in the cycles in the elastic range. In the first cycle more energy was dissipated that in the second cycle, since most of the cracking took place in load runs 1 and 2. The measured "elastic" stiffness of Unit 2 was only 42% of the stiffness predicted in Section 3.2.1. The causes for this large difference were the same of Unit 1 (see Section 4.2.2). The interstorey drift at the experimental first yield displacement was 0.35%, and was 0.31% at the theoretical dependable lateral load capacity of the Unit.

Fig. 4.14 illustrates the complete lateral load versus lateral displacement response of Unit 2. The post-elastic stiffnesses estimated as the slopes of the lines passing through the point at first yield and the point at maximum overstrength in runs 13 and 14 were 3.9 and 2.5% of the "elastic" stiffness for the positive and negative loading runs, respectively. An average stiffness of 3.2% of the "elastic" stiffness was used for defining the properties of the ideal bi-linear loops used to normalize the energy dissipated in each cycle.

In load run 5 to $\mu_\Delta = \pm 2$ the measured lateral load was 5% above the theoretical load H_a. In the reverse load run the lateral load did not reach the theoretical value but was only 4% below it. The lateral loads measured in the load runs to a negative displacement were always below those previously attained in the positive load runs, a phenomena that was consistent with the behaviour of the Unit 1. The second cycle to the same ductility factor showed very little strength degradation but the energy dissipated was much smaller, being 77% and only 47% of the ideal bi-linear loops for the first and second loading cycles, respectively.

The load runs 9 to 12 to $\mu_\Delta = \pm 4$ showed the same trends as the previous cycles. However, pinching was more severe in those load runs due to the large diagonal cracks that had to be closed and, perhaps, due to some initial yielding of the stirrups in the plastic hinge regions at the beam ends. The energy dissipated in these cycles was 63 and 36% of the ideal bi-linear loops, respectively.

The maximum measured loads of $1.19H_a$ and $1.12H_a$ were attained in load runs 13 and 14 in the first cycle to $\mu_\Delta = \pm 6$. The maximum measured load in terms of the nominal shear stress in the

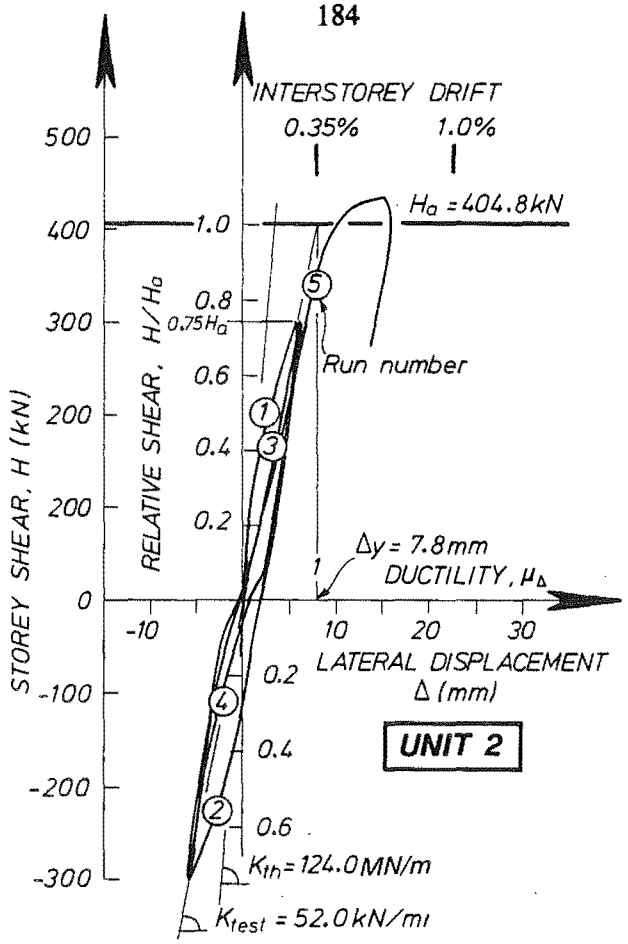

Fig. 4.13 - Lateral Load-Lateral Displacement Response of Unit 2 During Loading Cycles in the Elastic Range.

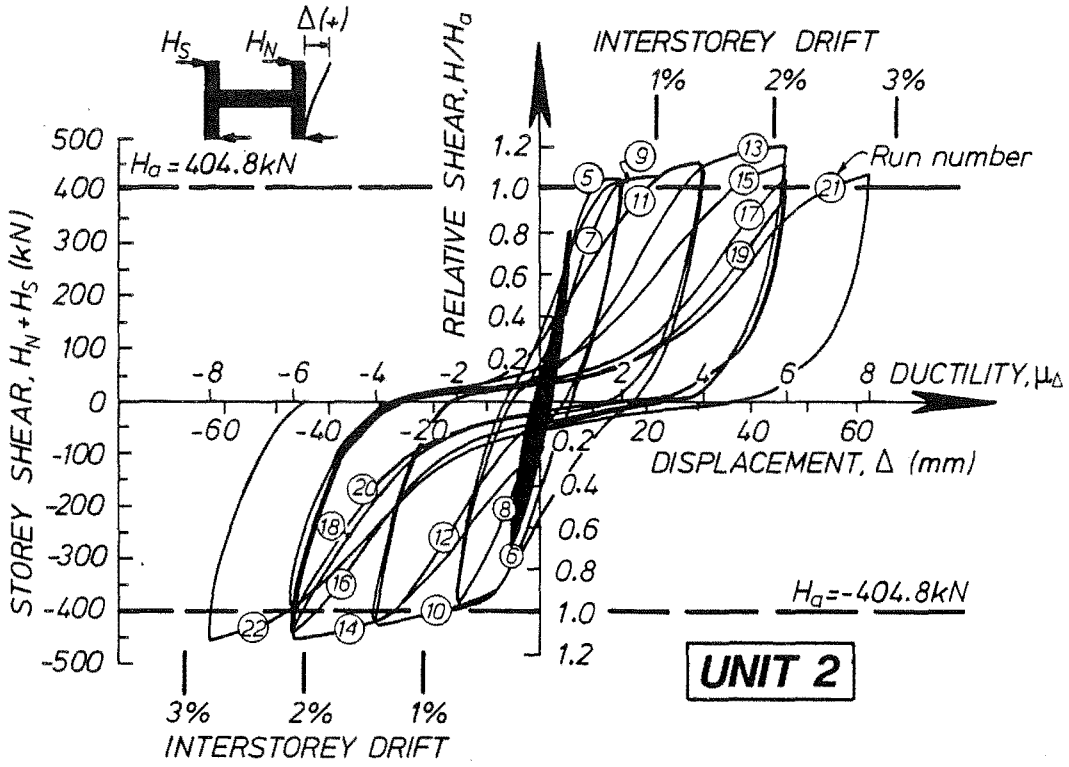

Fig. 4.14 - Lateral Load-Lateral Displacement Response of Unit 2.

plastic hinges of the beam was $v^\circ = 0.31\sqrt{f'_c}$. The measured hysteresis loops of the further loading cycles were severely pinched because of the large shear deformations in the plastic hinge regions of the beam, as can be seen in Fig. 4.14. The shear in the beam at low levels of lateral load was evidently carried by dowel action. By observing the shape of the loops it is believed that 20 to 30% of the beam shear was carried by this mechanism. Associated with the pinching of the loops was the degradation of the stiffness that caused the lateral load capacity in load run 19 to drop by more than 20% of the maximum measured load. The energy dissipated in these cycles was 44, 27, 21 and 15% of the ideal bi-linear loops, respectively. The maximum relative longitudinal displacement between the overlapped hooks was 1.4mm and was measured in load run 19.

The test unit was subjected to a final cycle to $\mu_\Delta = \pm 8$ to observe whether the theoretical lateral load capacity was still attainable. In load runs 21 and 22 the measured lateral load was comparable with the maximum previously measured lateral load indicating that at this level of interstorey drift of 2.8% the unit had some reserve of strength.

The cumulative post-elastic energy dissipated by the test unit up to load run 20 was 33% of the energy dissipated by the ideal bi-linear loops, which was about the same as the energy dissipated by Unit 1.

4.3.3 Decomposition of Lateral Displacements

Depicted in Fig. 4.15 are the components of the lateral displacement at the peak of the load runs of the test of Unit 2. In the first stages of the test the fixed-end rotation of the beam, due mainly to strain penetration of the longitudinal bars, accounted for an important part of the lateral displacement imposed. Flexural displacements within the beam were also important. On the other hand, shear displacements in the beam plastic hinge regions did not account for a large percentage of the lateral displacement in the first stages of the test, but they became the dominant mode of deformation from load run 10 at the first cycle to $\mu_\Delta = -4$.

4.3.4 Beam Curvature and Rotational Ductility Factors

The curvature ductility factors of the second set of linear potentiometers in the beam commencing at 10mm from the column faces are shown in Fig. 4.16. The gauge length covered by the displacement transducers was 170mm and, in theory, they should not include the effects of the strain penetration of the longitudinal beam bars. The calculated initial curvature at first yield, ϕ_y, was equal to 0.0045 radians/m, a rather large value that was probably influenced by the interface crack at the beam ends. The curvature at first yield determined from the first set of strains measured in the longitudinal reinforcing steel was equal to 0.0027 radians/m, which appears to confirm the above hypothesis. Curvatures in this gauged length were erratic since the distribution of cracking was not uniform in the region. The first set of linear potentiometers was placed at 10mm away from the column face and hence the cracks in the beams at the column faces passed through the orifices where the steel rods protruded from the beam and shared their width between the first and second set of displacement transducers.

This effect is clearly seen in Fig. 4.16 in the positive displacement runs beyond load run 9 in the south end of the beam.

The rotational ductility factors are depicted in Fig. 4.17. The initial rotation at first yield including the fixed-end rotations, θ_y, was found in a similar way to the curvature at first yield and its value was equal to 0.0036 radians. The rotation at the loading cycles to $\mu_\Delta = \pm 2$ and at the first cycle to $\mu_\Delta = \pm 4$ and $\mu_\Delta = \pm 6$ compare very well with the rotations estimated by the simple plastic analysis as discussed in Section 4.2.4. In the second cycles to $\mu_\Delta = \pm 4$ and $\mu_\Delta = \pm 6$, the rotational ductility demand decreased due to the shear deformations in the beam dominating the mode of deformation.

4.3.5 Beam Longitudinal Bar Strains and Forces

The strains in the longitudinal bars of the beam of Unit 2 were measured using manual DEMEC gauges in one side and clip gauges incorporating electrical resistance foil strain gauges on the other side. The gauge length was 204mm for both measuring devices. The strains in the reinforcement of both sides of the beam were of similar magnitude and therefore the average of east and west readings is presented in Fig. 4.18.

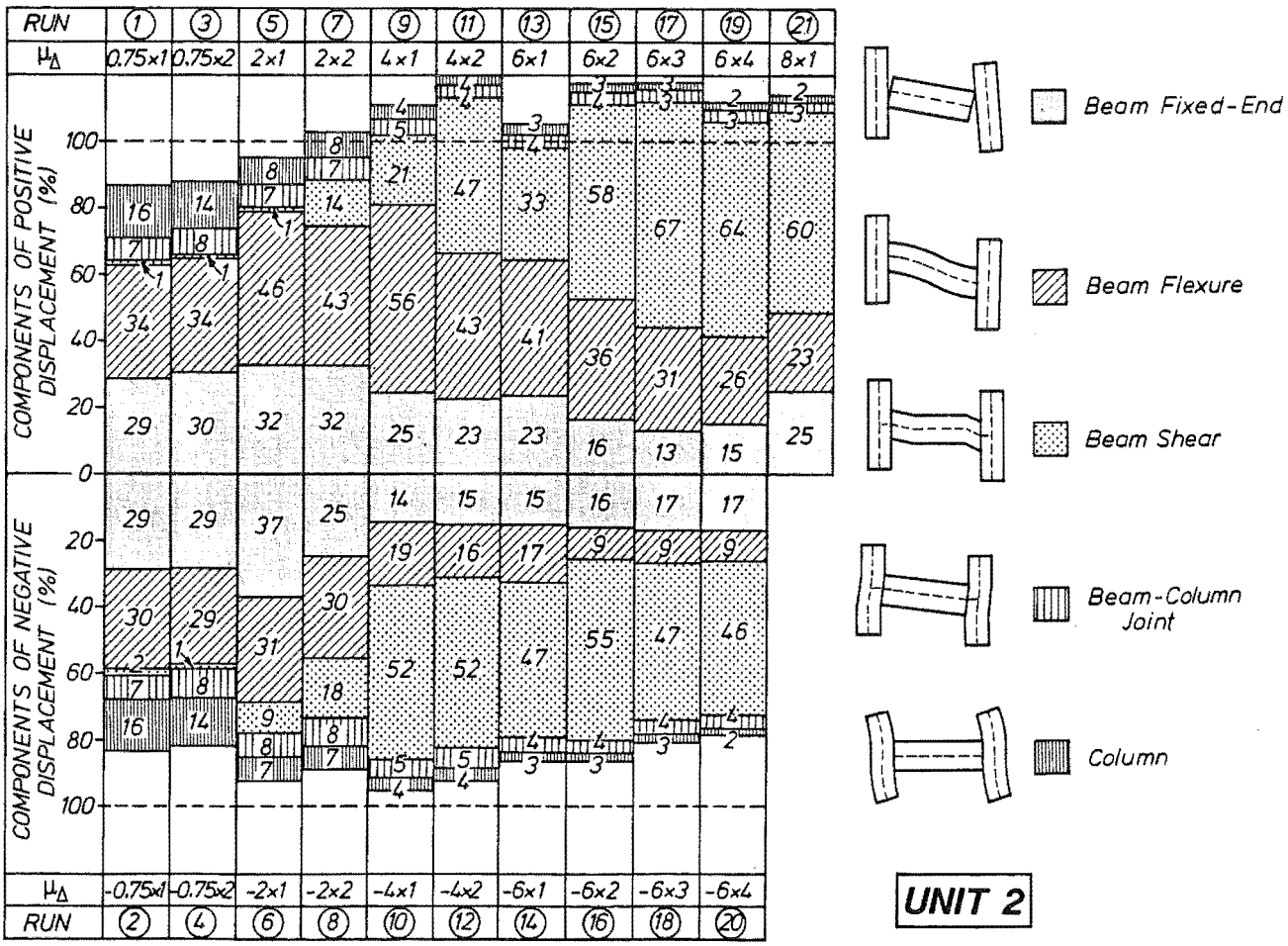

Fig. 4.15 - Components of Lateral Displacement of Unit 2 at Peaks of Load Runs.

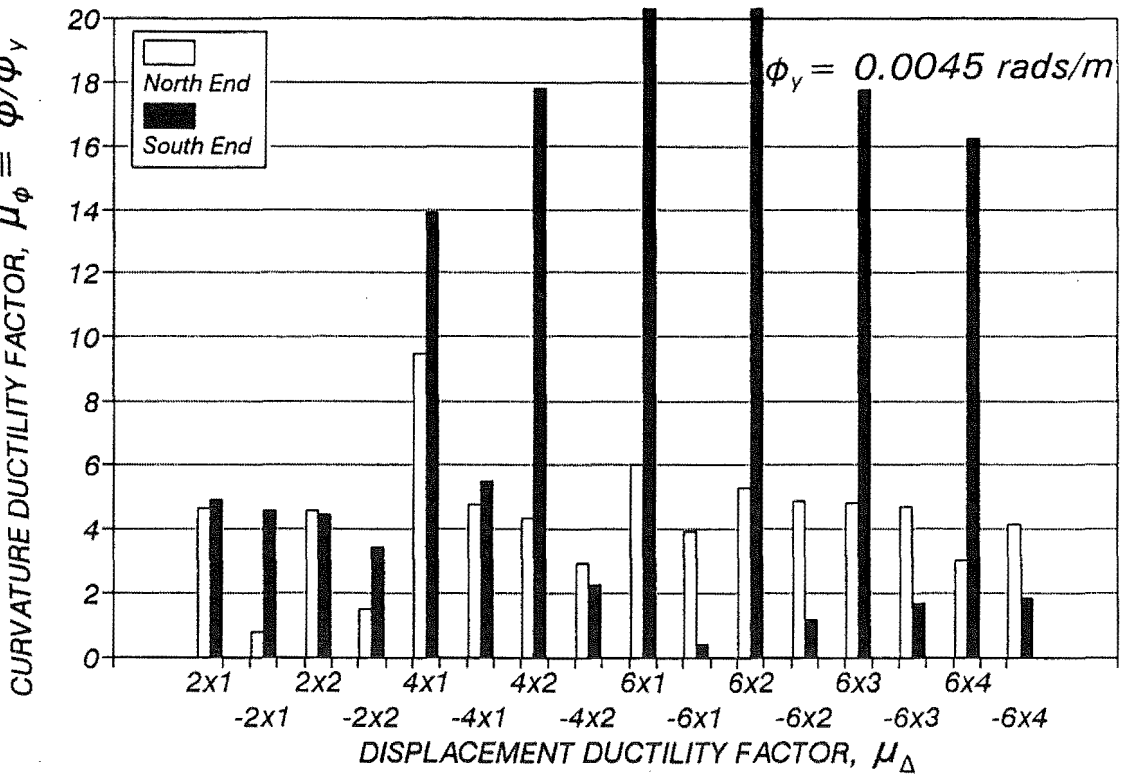

Fig. 4.16 Beam Curvature Ductility Factors of Unit 2.

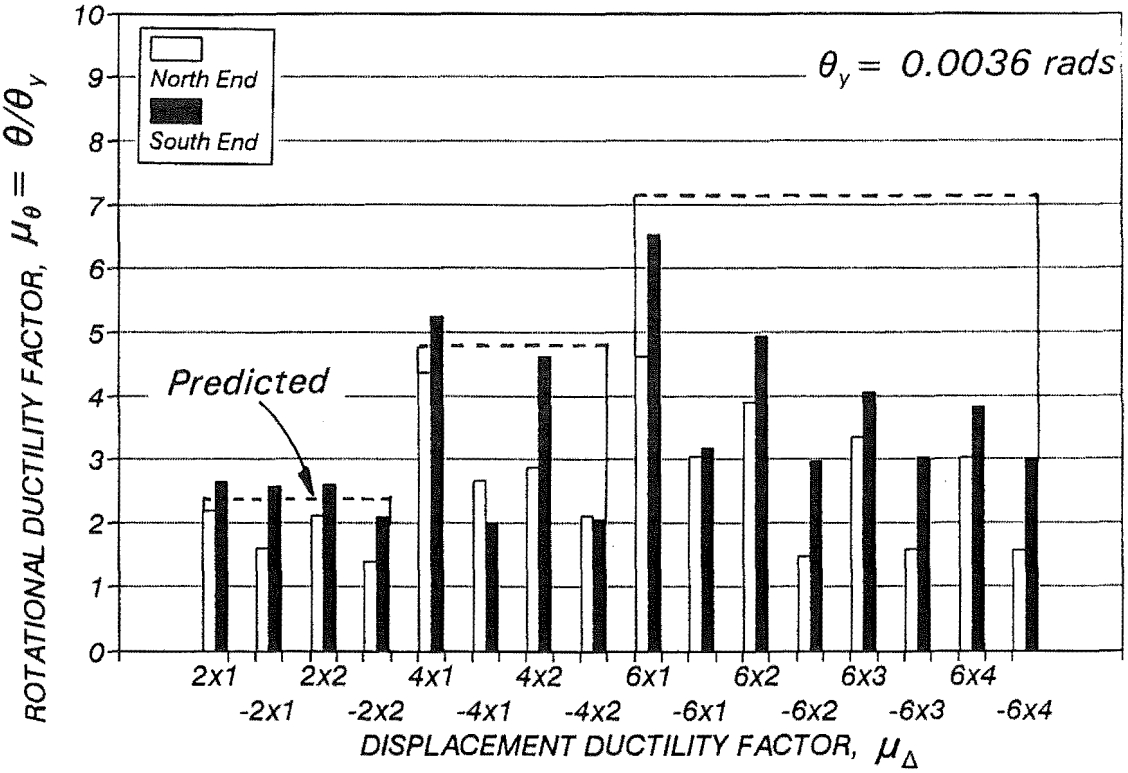

Fig. 4.17 - Beam Rotational Ductility Factors of Unit 2.

The longitudinal bar strain profiles recorded at the peaks of the elastic cycles show clearly the tension shift effect near the ends of the beams. The strains tend to a zero tension shift near the midspan of the beam. The larger elastic strains recorded in the top bars reflect the influence of the different stiffness of the tension and compression columns during the test.

Yielding of the bars gradually spread in the beams from the column faces, as seen in Fig. 4.18. For comparison, Fig. 4.19 depicts the member average strains at the level of the reinforcing steel. It can be observed that the strains near the column face become erratic in the final loading runs because of the effect of the crack distribution in the beam, resulting in the member strain being overestimated in one gauge length and underestimated in the next. Fig. 4.20 shows the bar forces estimated from the measured strains using the procedure described in Section 4.2.6. The trends are very similar to those observed in Unit 1. In the cycles in the elastic range, load runs 5 and 6 in Fig. 4.20, the top reinforcement of the beam was subjected to larger forces than the bottom reinforcement. Plastic hinges regions extended a distance from the column faces equal to almost the effective depth of the beam, d. As in the beam of Unit 1, the tension shift effect rapidly decreased as the midspan of the beam was approached.

4.3.6 Longitudinal Bar Stresses at Midspan

Fig. 4.21 illustrates the level of stresses in the longitudinal bars in the region of the connection at the midspan of the beam. Some transfer of forces by the laps occurred between the bars in tension protruding from the precast concrete member and the "drop in" bars placed at the midspan of the beams. However, it appears that there was no such action between the "drop in" bars and the longitudinal bars at the other side of the beam.

4.3.7 Stresses in the Transverse Reinforcement at Midspan

The stresses in the vertical and horizontal legs of the stirrups surrounding the connection at midspan are shown in Figs. 4.22 and 4.23, respectively. These stresses were estimated from strains measured by double electrical resistance foil strain gauges opposite sides of the diameter of the stirrup. The stresses so calculated at the top and bottom vertical parts of the stirrups, shown in Fig. 4.22, were rather similar for the stirrups surrounding the overlapping bars but they were dissimilar for the stirrups located away from the connection region. The level of stresses in the stirrups in the connection region was well within the elastic range with the central stirrup consistently showing larger stresses.

Fig. 4.23 shows the stress distribution in the top horizontal portions of the stirrups. The higher values recorded in the stirrup outside the connection region were due to the transverse forces generated by the curtailment of the longitudinal bar near this section. The stresses in the connection region were very small and tended to increase in the final stages of the test.

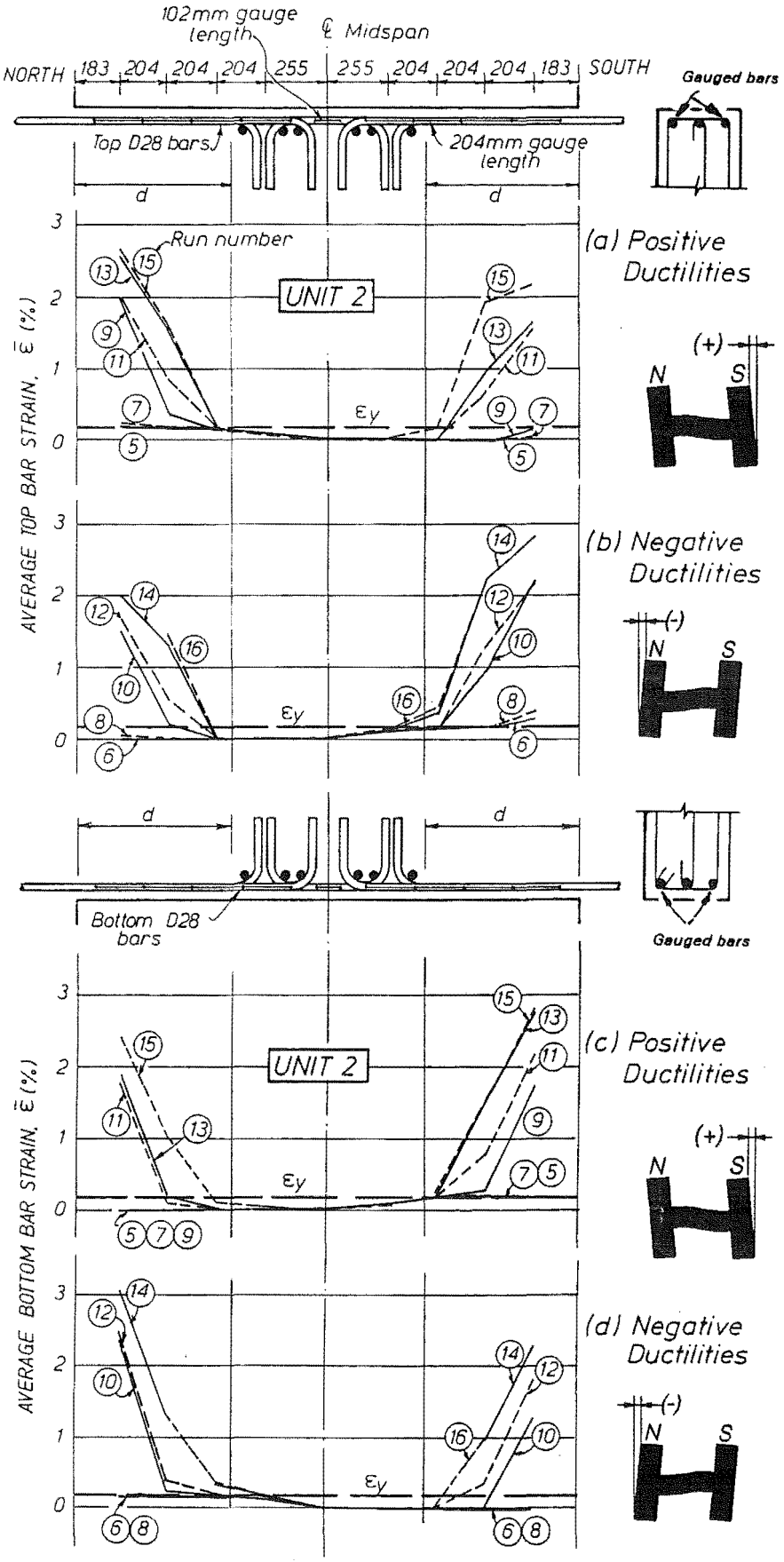

Fig. 4.18 - Average Beam Longitudinal Bar Strains of Unit 2.

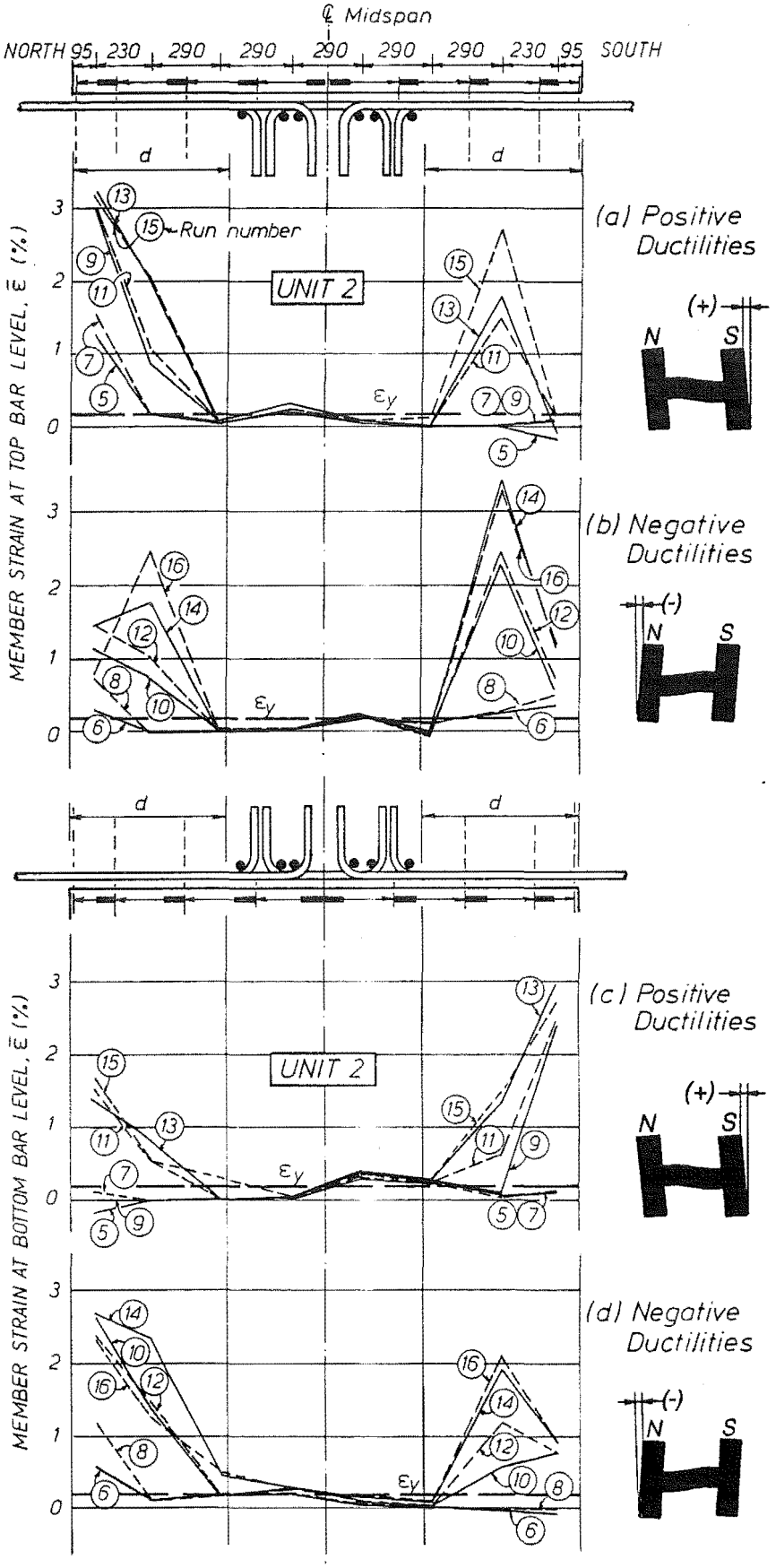

Fig. 4.19 - Member Strains at the Level of the Longitudinal Reinforcement of Unit 2.

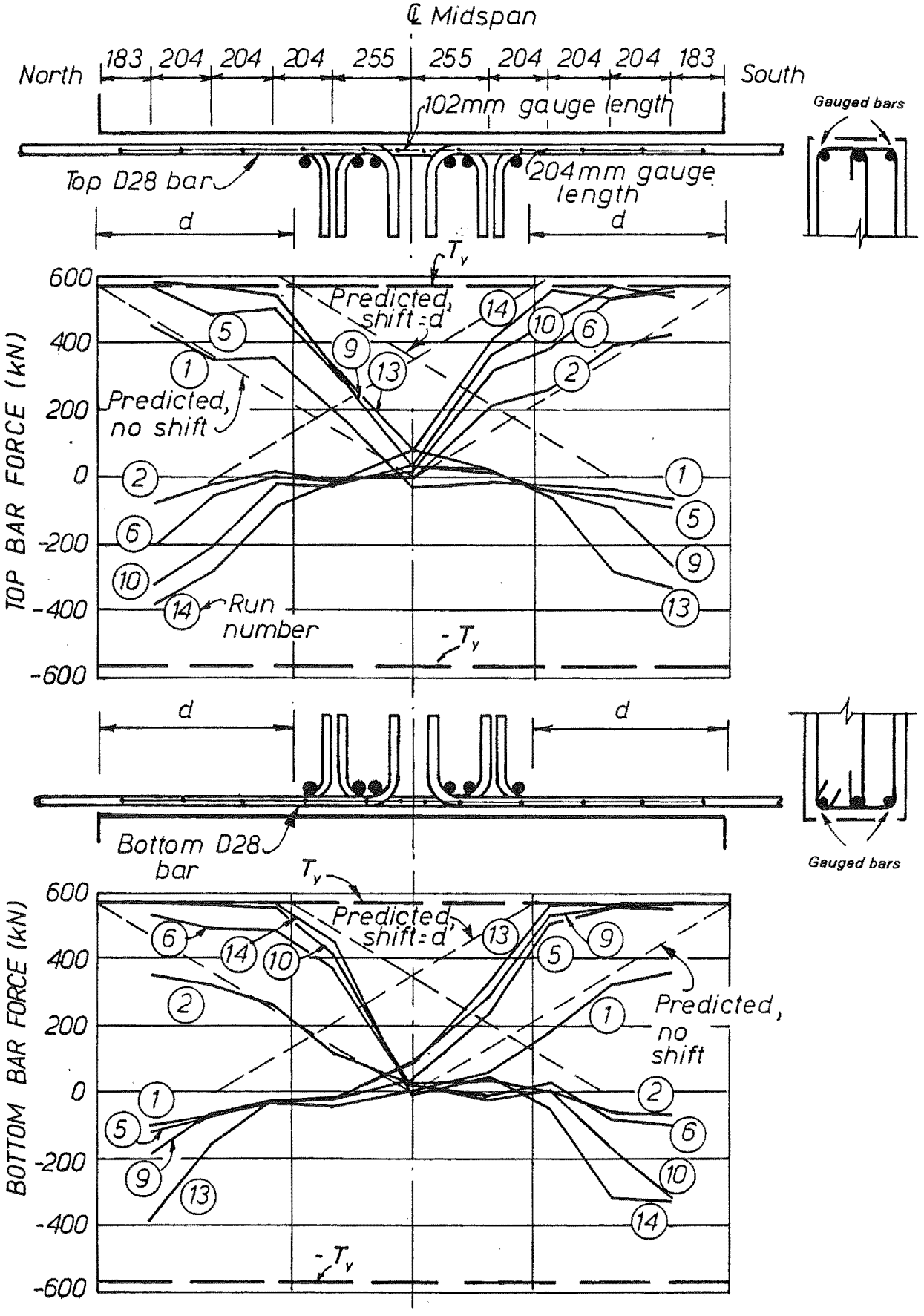

Fig. 4.20 - Longitudinal Bar Forces in the Beam of Unit 2.

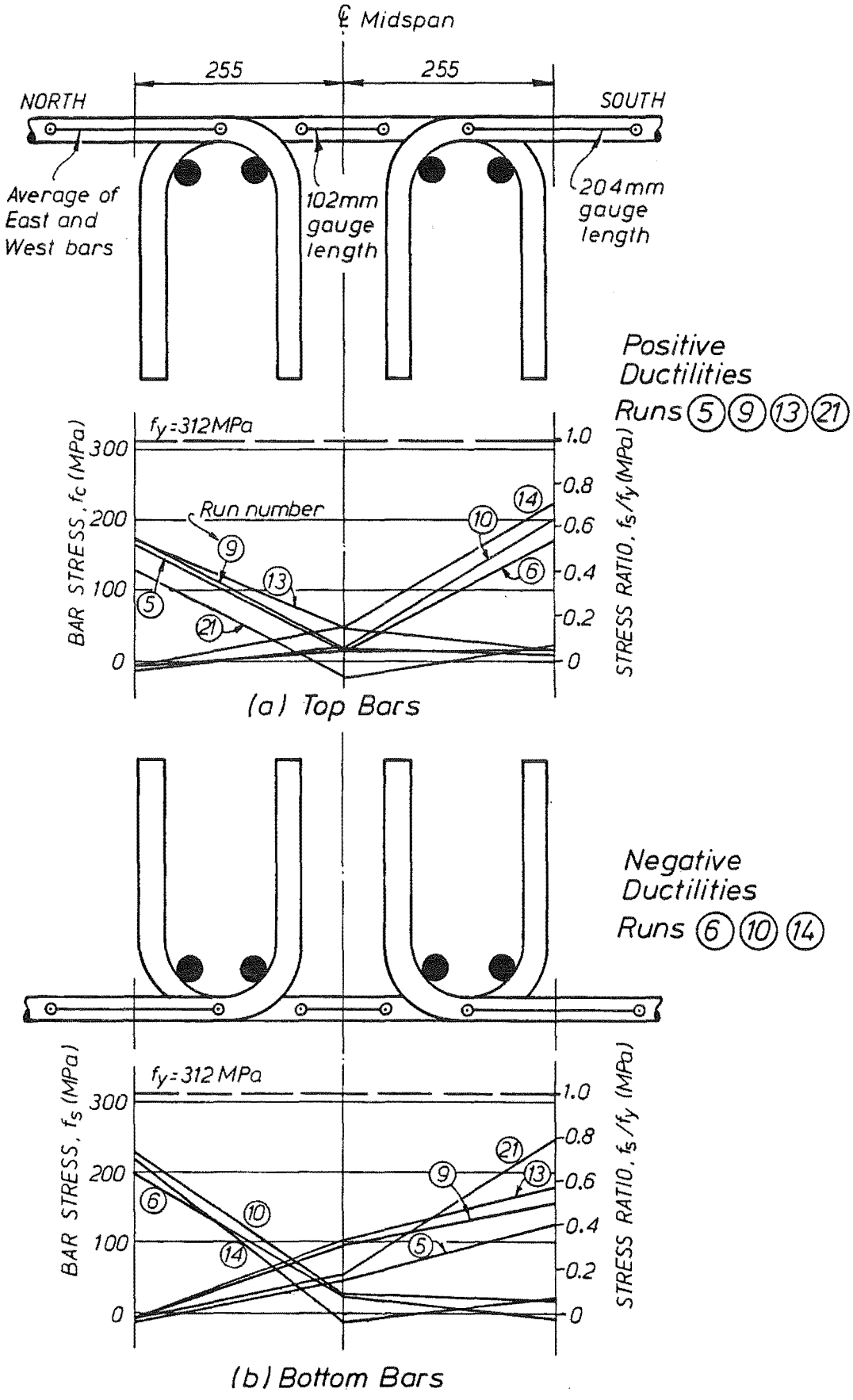

Fig. 4.21 - Stresses of the Beam Longitudinal Bars at the Connection at Midspan.

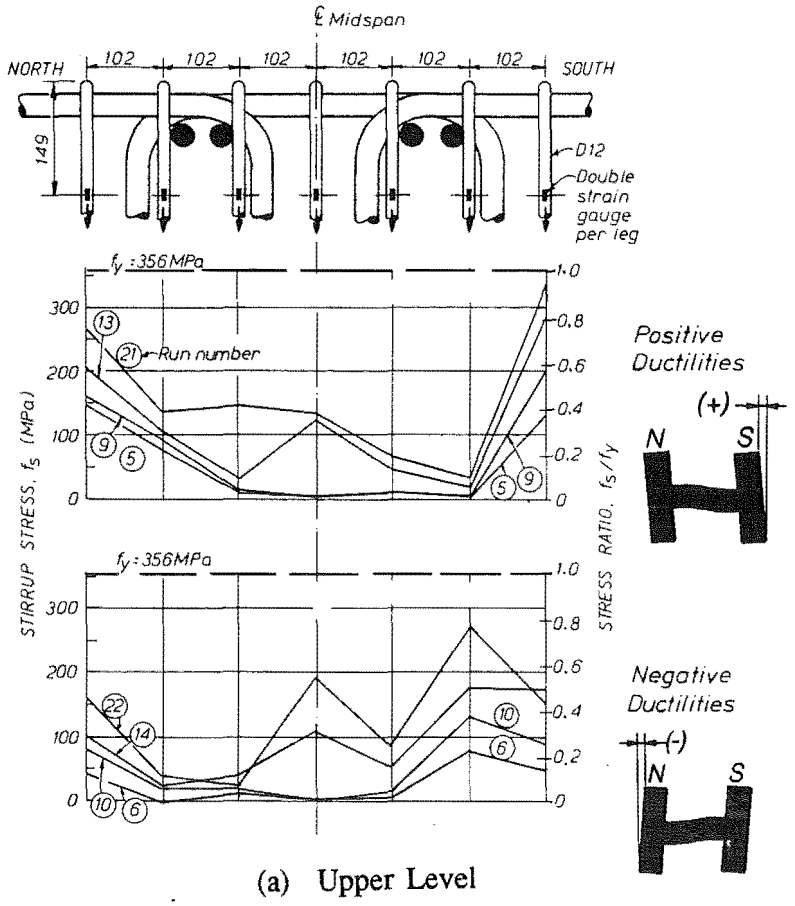

(a) Upper Level

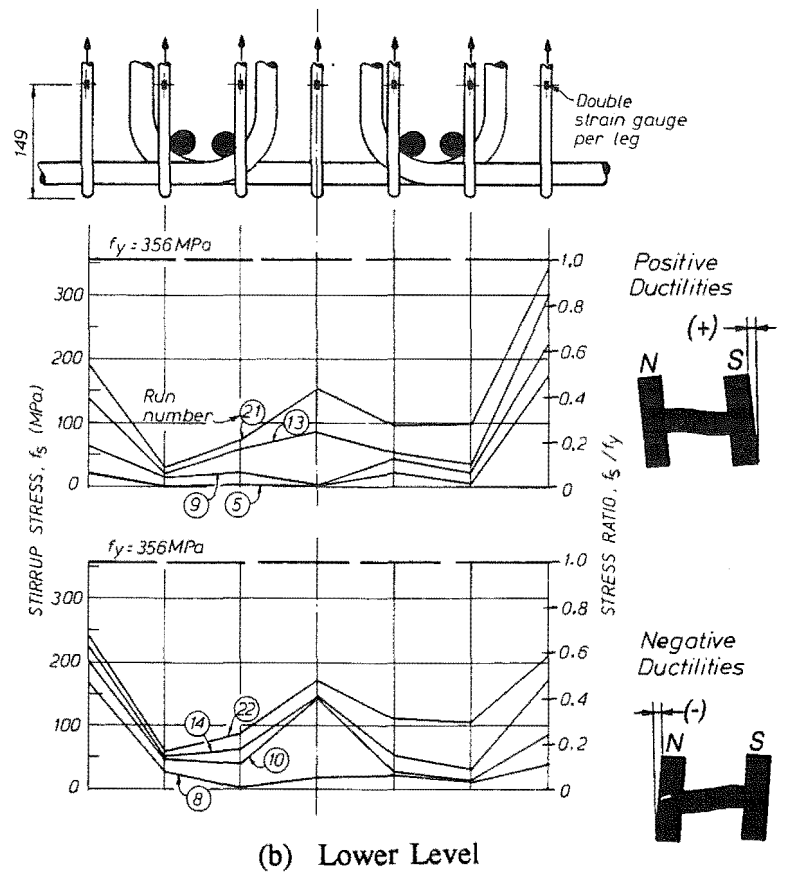

(b) Lower Level

Fig. 4.22 - Stresses in the Vertical Transverse Reinforcement at Midspan of Unit 2.

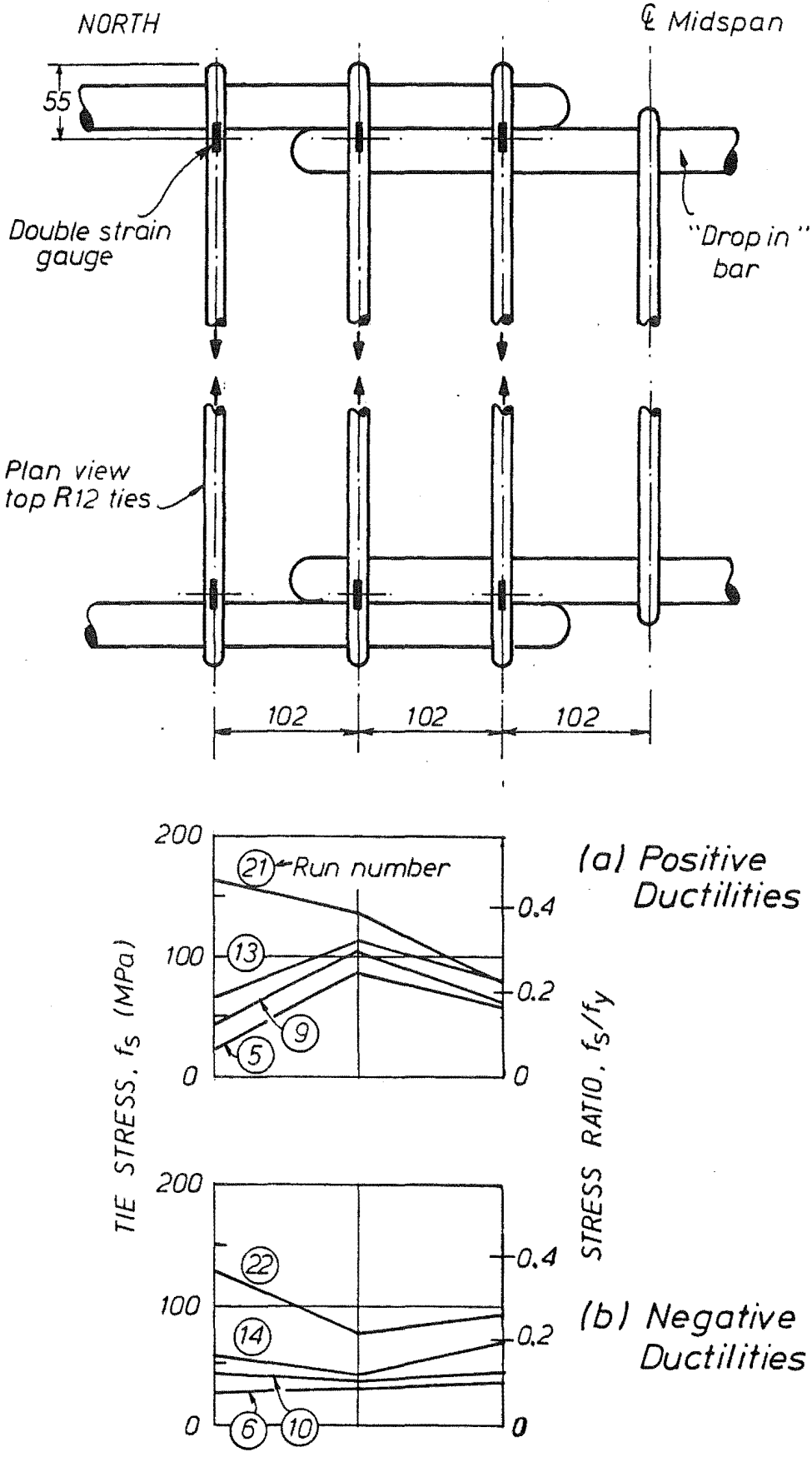

Fig. 4.23 - Stresses in the Horizontal Transverse Reinforcement at Midspan - Top North Stirrups of Unit 2.

4.3.8 Elongation of the Beam

The total elongation of the beam of Unit 2 plotted against the lateral load can be seen in Fig. 4.24. The maximum elongation reached 32mm in load run 22 and in general it followed a similar pattern of the lengthening of the beam of Unit 1.

4.4 UNIT 3

4.4.1 General Behaviour

Unit 3 was connected at midspan by straight non-contact lap splices with two thirds of the longitudinal reinforcement in the beam lapped in this region (see Fig. 3.19). The lap length was equal to $23d_b$ and commenced at a distance of 1.27d from the column faces. Further details are presented in Section 3.2.2.1.

The test of this unit was carried out over a period of two weeks. The test was ended after completing two full cycles to $\mu_\Delta = \pm 8$ at an interstorey drift of 2.7% when the lateral load capacity of the unit dropped to below 20% of the maximum recorded. The cumulative displacement ductility factor at failure was $\Sigma\mu_\Delta = 96$ implying an available displacement ductility factor of $\mu_a = 8$. The overall hysteretic response of the unit was slightly better that the response of the previous two units, since the stiffness degradation was less pronounced and the energy dissipation was greater. It is believed that this improvement was caused by the additional transverse reinforcement provided at the beam ends, which was governed by the requirements to control bar buckling. Nevertheless, the amount of transverse steel provided did not prevent the large shear deformations in the plastic hinge regions of the beam becoming the principal mode of deformation in the final stages of the test.

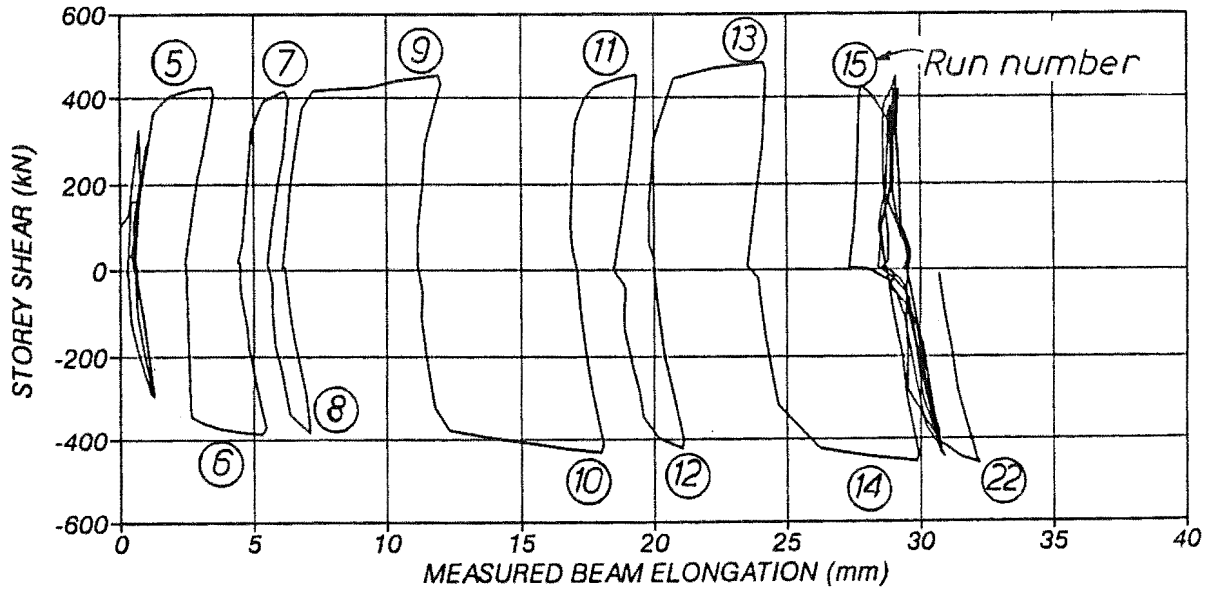

Fig. 4.24 - Total Measured Beam Elongation of Unit 2.

Fig. 4.25 depicts the visible cracking of the beam of Unit 3 at different stages in the test. The cracking of the beam in the cycles in the elastic range extended to the cold joint between the precast members and the cast in place concrete at midspan. Several cracks became inclined and headed towards the compression region of the beam at the column face. Their width remained small with a maximum observed value of 0.2mm at the mid-depth of the beam. Additionally, some splitting cracks running parallel to the reinforcement being lapped formed in the top south side of the beam.

In the load runs 5 to 8 to $\mu_\Delta = \pm 2$ the cracks in the beam at the column faces opened to between 2.5 and 3mm, suggesting that yield had commenced in the longitudinal bars in these regions and had probably penetrated inside the beam-column joints. These cracks remained open for the rest of the test. The diagonal cracks at the beam ends also opened but remained small. The maximum width measured at the mid-depth of the beam reached 0.4mm. New hairline fine cracks formed in the top north and bottom south sides of the beam in the spliced region.

The crack pattern observed in the beam in the cycles to $\mu_\Delta = \pm 4$ showed the growth of the vertical cracks at the face of the column and the steeper diagonal cracks close to the beam ends (see Fig. 4.25 (a)). Some of these diagonal cracks became interconnected and the full depth open cracks resulted in some sliding shear displacements, especially in the south end where some spalling of the concrete cover also occurred.

The critical cracks in the plastic hinge regions of the beam were steeper than the cracks of the previous two units because of the larger amount of transverse reinforcement provided in these regions. However the number of stirrup-legs crossed by the critical cracks was approximately the same in all cases. Yielding of the stirrups in the plastic hinge regions of the beam probably also occurred in this test, since the observed vertical expansion of the north and south ends of the beam was 9 and 8mm in load run 17 and 12 and 23mm in load run 22, respectively.

Sliding shear concentrated in the south plastic hinge region in the final cycles of the test. The loss of the load capacity of 20% of the maximum lateral load recorded was caused by stiffness degradation. A sliding shear failure was observed when the test unit was pushed to an interstorey drift of 5%.

The crack pattern observed on the top and bottom surfaces of the beam at the midspan connection is shown in Fig. 4.26. Crack widths remained small on these surfaces and their inclination indicates that a diagonal compression field in the horizontal plane in the connecting region at midspan developed and formed a mechanism for transferring the forces between the lapped bars.

4.4.2 Load Displacement Response

The hysteresis loops in the loading cycles in the elastic range of the test of Unit 3 are shown in Fig. 4.27. The same behaviour as observed in Units 1 and 2 was typical of Unit 3. The second loop showed less energy being dissipated and was slightly softer. The measured "elastic" stiffness was only

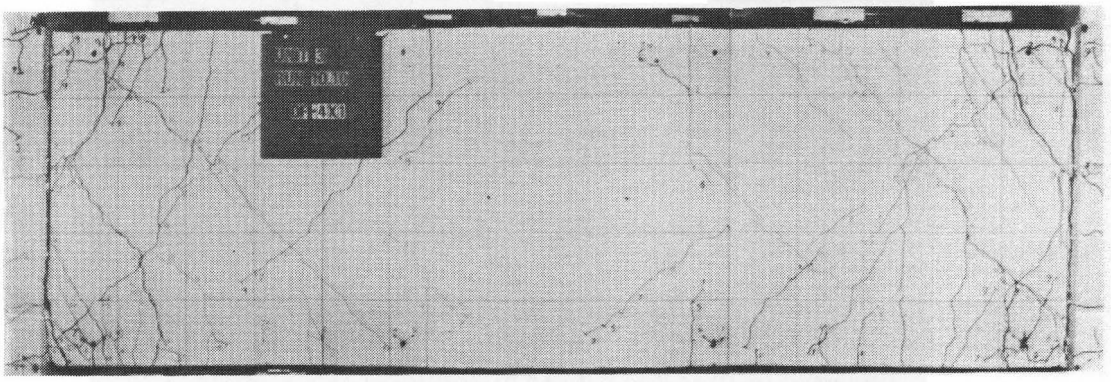

(a) At μ_Δ = -4x1

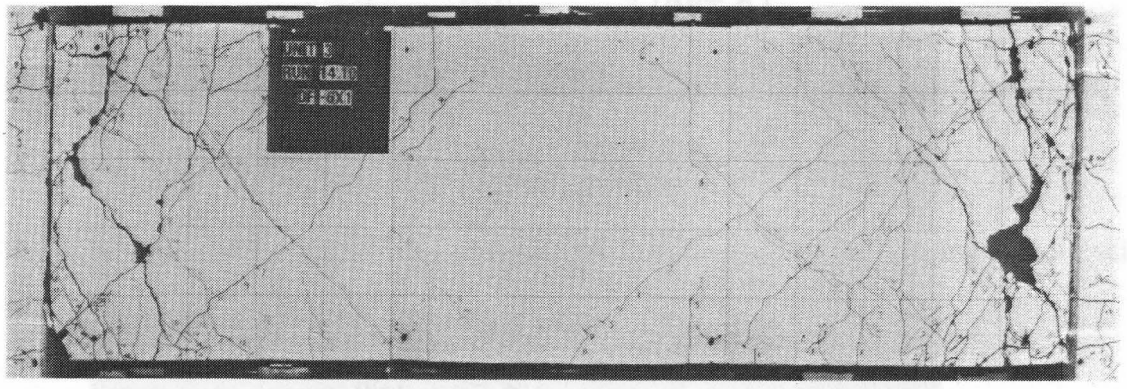

(b) At μ_Δ = -6x1

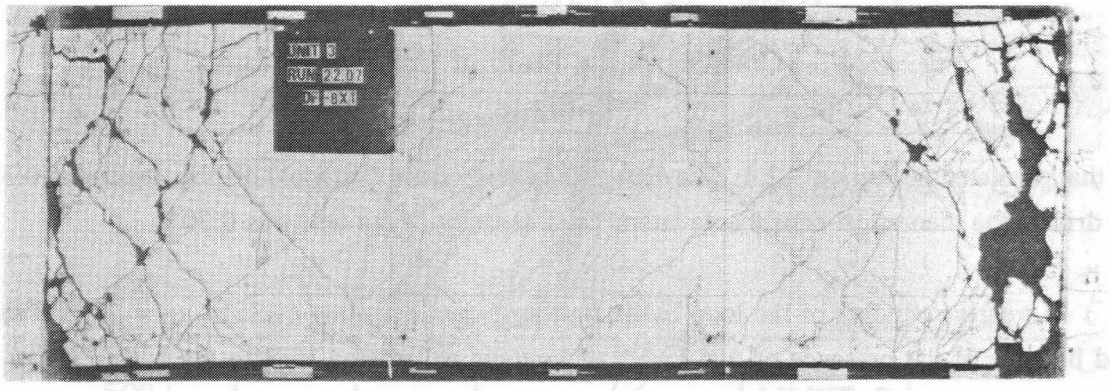

(c) At μ_Δ = -8x1

Fig. 4.25 - Cracking of Beam of Unit 3 at Different Stages During Testing.

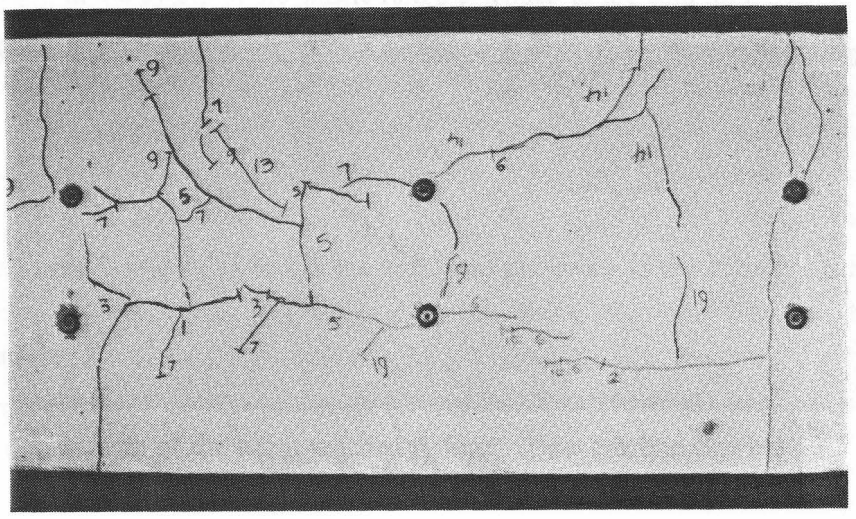

a) Top Surface

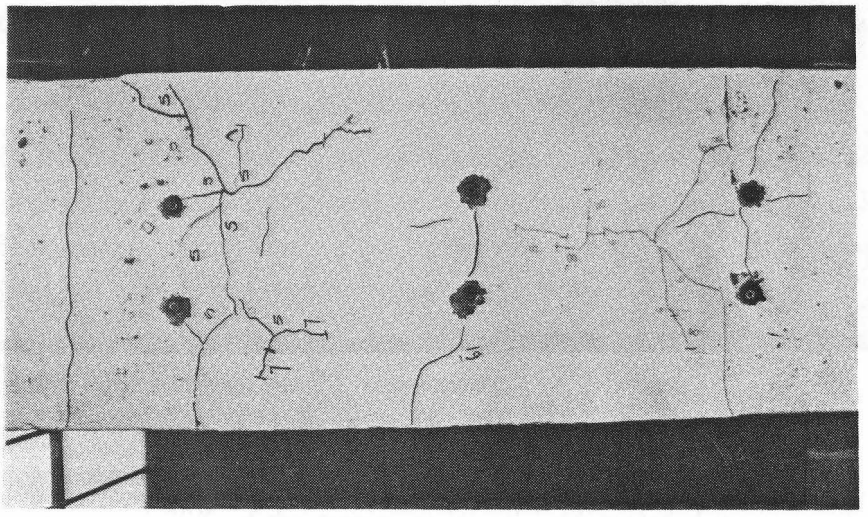

b) Bottom Surface

Fig. 4.26 - Cracking of the Beam of Unit 3 at Midspan.

42% of that predicted in Section 3.2.1. The drift at the extrapolated first yield displacement was 0.34%, and the drift at the theoretical dependable lateral load capacity of the unit was 0.30%.

An early rounding of the loop in the first post-elastic loading cycle to $\mu_\Delta = 2$, load run 5, occurred because of the presence of two layers of longitudinal tension steel in the beams where first yield took place. The lateral load capacity in this load run exceeded by 2.5% the predicted theoretical load H_a. Further post-elastic hysteresis loops are illustrated in Fig. 4.28. In load run 6 the lateral load attained was 5.1% below the theoretical load H_a.

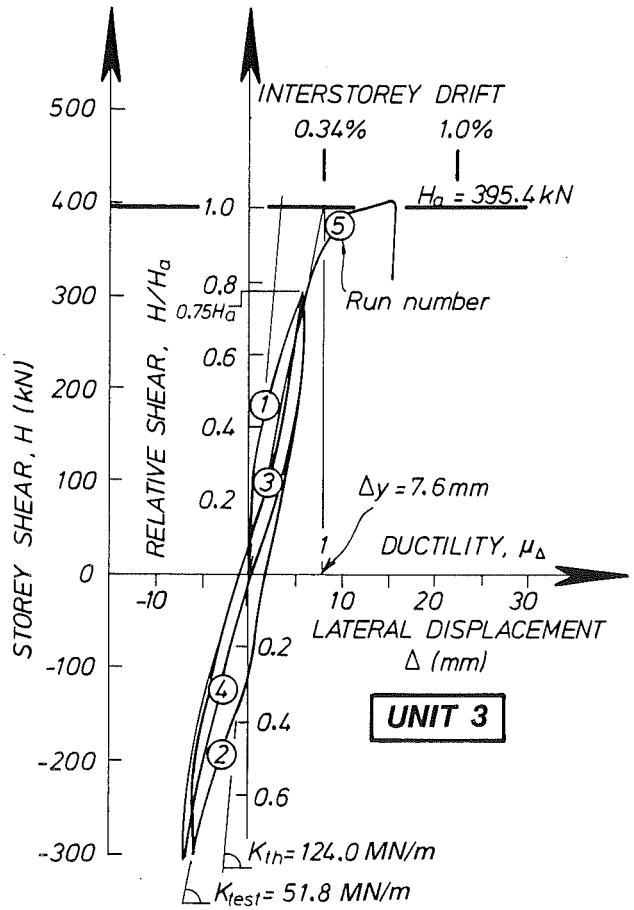

Fig. 4.27 - Lateral Load-Lateral Displacement Response of Unit 3 During Load Cycles in the Elastic Range.

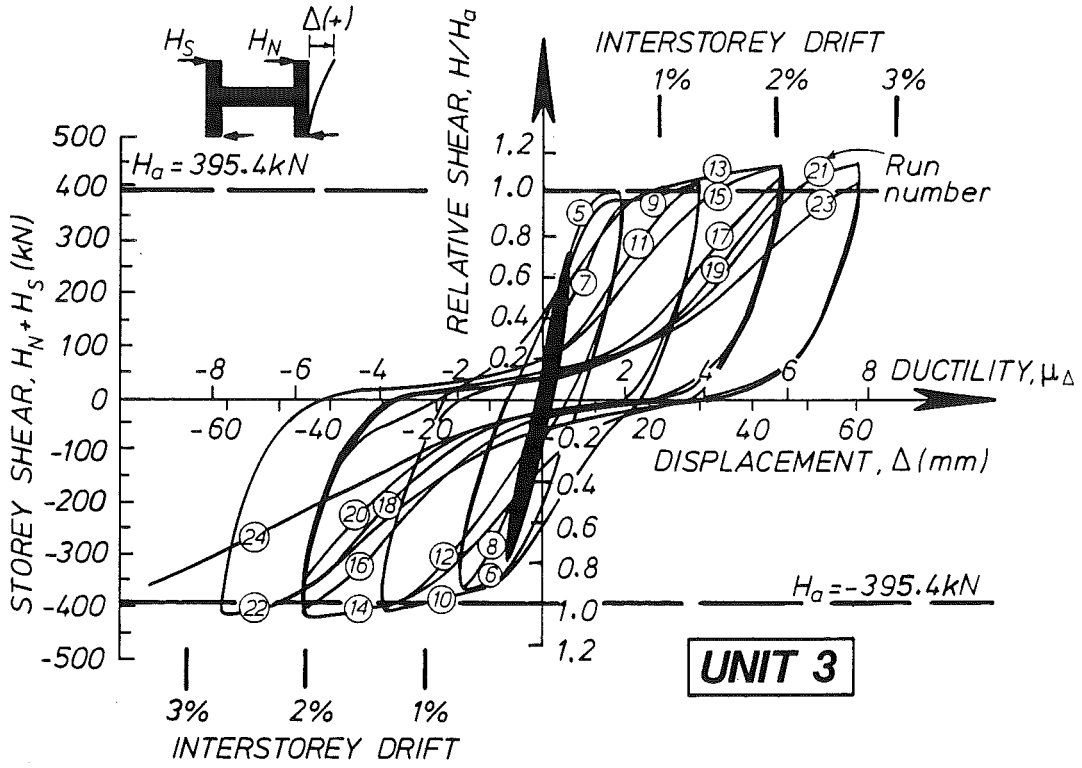

Fig. 4.28 - Lateral Load-Lateral Displacement Response of Unit 3.

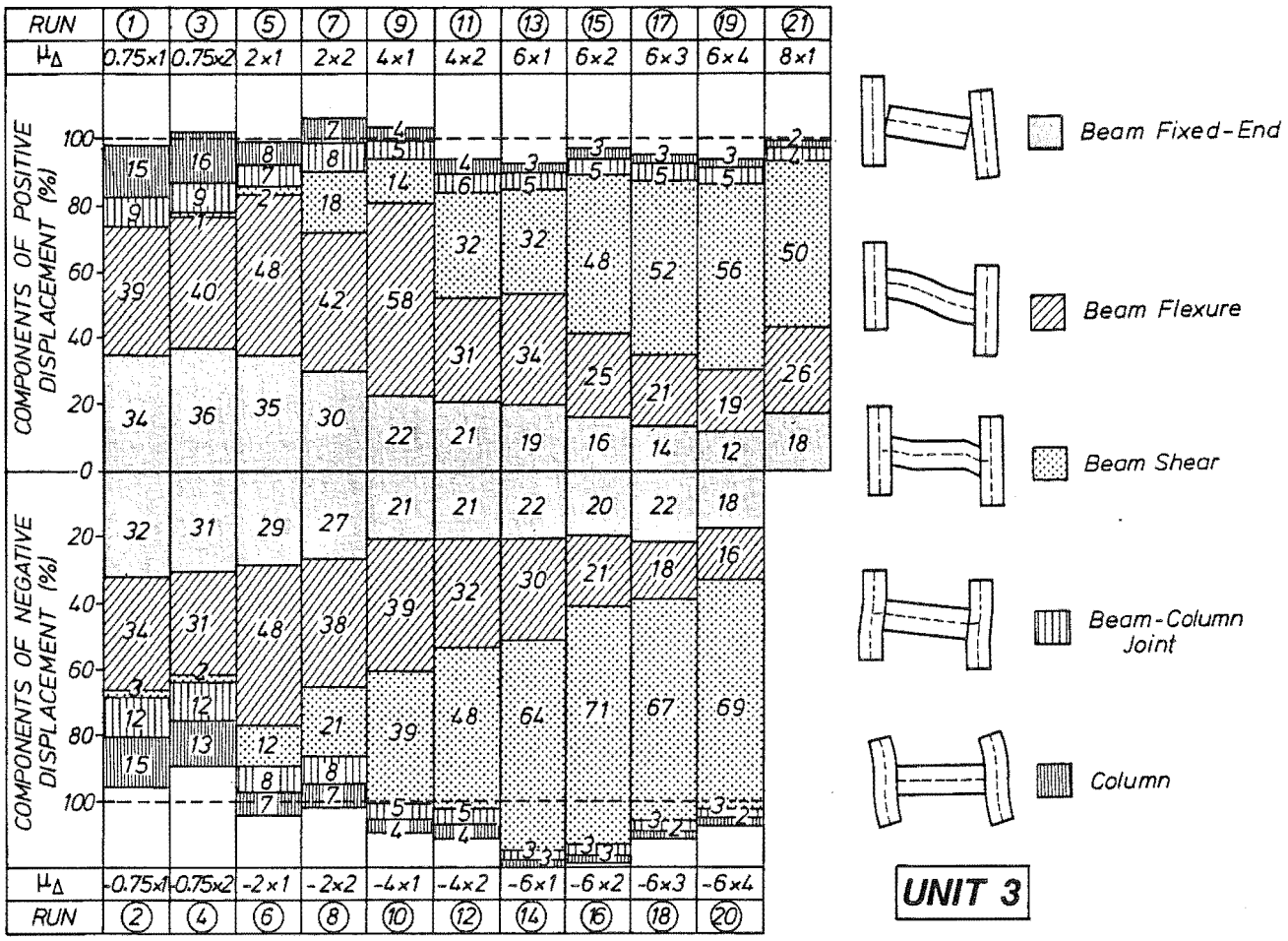

Fig. 4.29 - Components of Lateral Displacement of Unit 3 at Peak Load Runs.

The post-elastic stiffnesses estimated as the slopes of the lines passing through the point at first yield and the point at maximum overstrength in load runs 13 and 14 were 3.3 and 1.7% of the initial stiffness, respectively. These are smaller values than those obtained in the previous two tests, probably because of the second layer of the reinforcement in the beam being subjected to less strain hardening. Using the elastic and average post-elastic stiffness as the basis for evaluating the energy dissipation of the ideal bi-linear loops, the first and second loading cycle to $\mu_\Delta = \pm 2$ showed a normalized energy dissipation of 87 and 55%, respectively.

The response of Unit 3 in load runs 9 to 12 to $\mu_\Delta = \pm 4$ showed a steady increase in lateral load capacity and very little strength degradation. Pinching of the loops was first noticed in load run 12. The normalized energy dissipated in these cycles was 66 and 45%, respectively.

In the four loading cycles to $\mu_\Delta = \pm 6$, load runs 13 to 20, the hysteretic response was very pinched since large shear deformations dominated the response of the unit in these cycles. However, the stiffness did not degrade as in the previous units and the strength reduction was never more than 20% of the maximum lateral load capacity during the test. On the other hand, the energy dissipated during these cycles was rather similar to the other units, being 49, 33, 22 and 18% of the ideal bi-linear loops. The cumulative energy dissipation at the end of load run 20 amounted 38% of the ideal bi-linear

loops. The maximum measured strengths of $1.17H_a$ and $1.09H_a$ occurred in load runs 13 and 14 in the first loading cycle to $\mu_\Delta = \pm 6$, respectively. The maximum nominal shear stress in the beam plastic hinges was $v^\circ = 0.28\sqrt{f'_c}$.

The first cycle to $\mu_\Delta = \pm 8$ in load runs 21 and 22 showed no reduction in the load carrying capacity. In fact, in load run 21 the lateral load attained was very similar to the load observed in load run 13 where the maximum lateral load strength was attained. In the second cycle the diagonal strut carrying the shear in the south end of the beam disintegrated and shortened and consequently a large degradation of stiffness was observed in load run 24. Further displacements to $\mu_\Delta = -10$ indicated that some reserve of strength was still available despite large sliding shear displacements concentrating at the south end of the beam.

4.4.3 Decomposition of Lateral Displacements

The components of the lateral displacement estimated following the procedure described in Section 3.9 are depicted in Fig. 4.29. The component caused by the fixed-end rotation of the beam ends accounted, on average, for 33% of the lateral displacement in the cycles in the elastic range and gradually decreased as the displacement ductility increased. The flexural response of the beam was also an important source of displacement in those cycles and in the cycles in the inelastic range to a new displacement ductility factor. In the second cycles in the inelastic range the flexural response decreased, being replaced by the displacements due to shear deformations in the plastic hinge regions. This was because the open cracks which formed after a new drift had been imposed increased the tendency of the plastic hinge regions to slide along the interconnected vertical cracks. Shear deformations became the dominant source of deformation from the load run 11 onwards. The columns and the beam-column joints made little further contribution to the deformations during the cycles in the inelastic range because they remained essentially elastic.

4.4.4 Beam Curvature and Rotational Ductility Factors

Shown in Figs. 4.30 and 4.31 are the beam curvature and rotational ductility factors. The beam curvature was measured over a gauge length of 170mm using the second set of linear potentiometers from the column faces, which were assumed to be unaffected by the strain penetration of the longitudinal bars inside the beam column joint region. As for previous two tests, the curvature and rotation at first yield were estimated from measured data. The curvature at first yield, ϕ_y, was estimated to be 0.0045 radians/m, a value larger than that predicted by a conventional moment-curvature analysis. It is believed that the main reason for this high initial curvature is the influence of the crack at the column face penetrating into the end regions of the beam as discussed in Section 4.3.4. The curvature ductility factors depicted in Fig. 4.30 exhibit a rather erratic distribution, but in general it can be seen that the curvature ductility demand decreases in the final stages of the test. This would have been because the large shear deformations contributed to a high percentage of the total displacement of the unit.

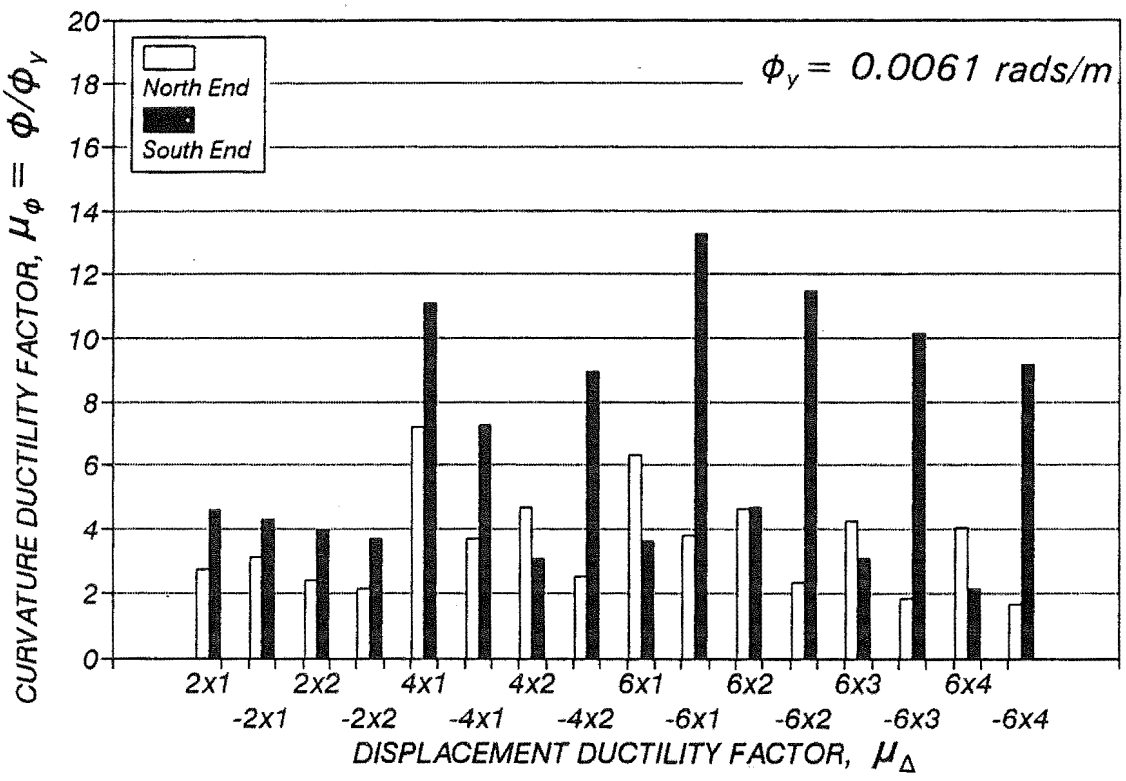

Fig. 4.30 - Beam Curvature Ductility Factors of Unit 3.

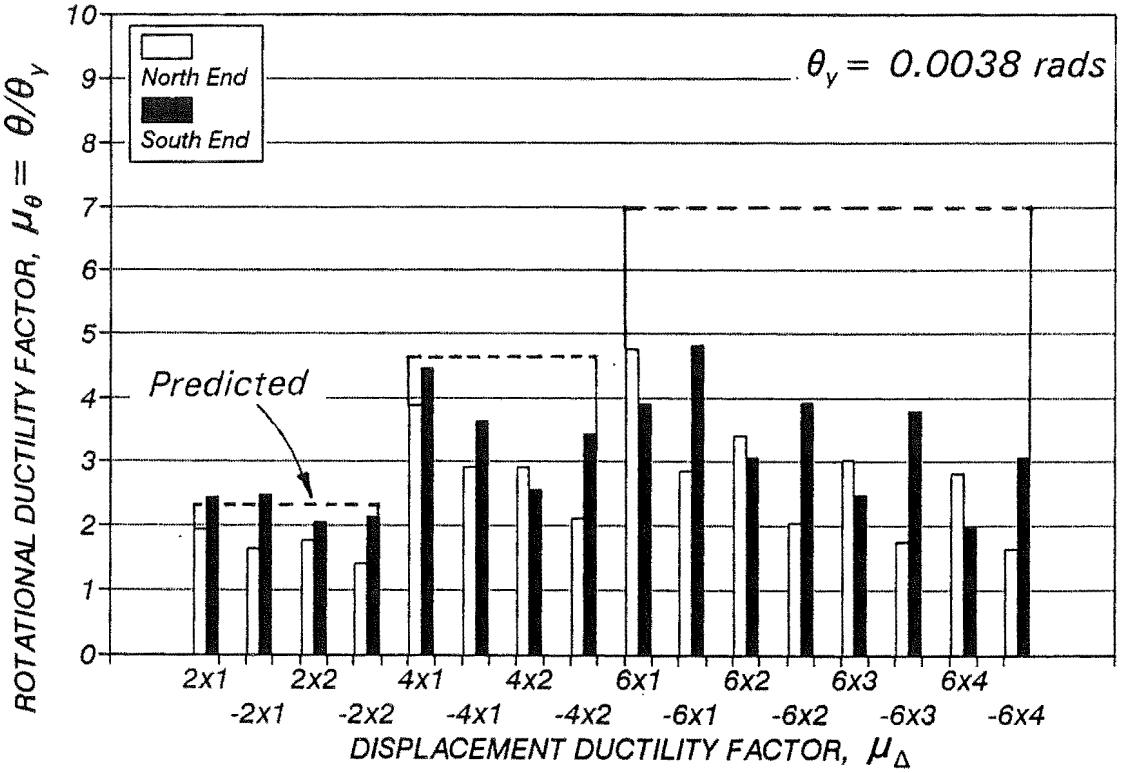

Fig. 4.31 - Beam Rotational Ductility Factors of Unit 3.

The computed rotation at first yield, θ_y, was 0.0038 radians. The rotational ductility factors in Fig. 4.31 show that the rotation demand decreased in the second cycles to the same ductility factor, because of the influence of the shear deformations in the plastic hinge regions of the beams. There is a very good agreement between the rotation estimated from the simple plastic analysis and the measured rotation in the cycles to $\mu_\Delta = \pm 2$ and the first cycle to $\mu_\Delta = \pm 4$. The rotational ductility factor demand was of the same order as the displacement ductility factor imposed on the unit, following the trends of the tests on the other two units.

4.4.5 Beam Longitudinal Bar Strains and Forces

The strain in the longitudinal bars at the beam of Unit 3 were measured using electrical resistance foil strain gauges. Unfortunately these measuring devices failed to provide data when the tensile strains in the reinforcement exceeded 1.0 to 1.5%. That is, in the first runs into the inelastic range the strain gauges near the faces of the column failed and as the test progressed, and the plastic hinges spread along the beams, the set of strain gauges in these regions debonded. Hence in this section only member strains are showed. Fig. 4.32 shows the gradual spreading of the plastic hinge regions and the residual tensile strains which accounted for the elongation of the beam.

Fig. 4.33 illustrates the bar forces in the outer layers of the longitudinal reinforcement of the beam, estimated from the strains measured before failure of the strain gauges. Unlike the two previous tests, the distribution of stresses in the top and bottom outer bars at the beam ends in the cycles in the elastic range was very similar, despite the lateral load carried by the compression column, being higher than the lateral load carried by the tension column. As in previous tests, yielding due to the spreading of the plastic hinge regions was confined to a distance from the column faces within the effective depth of the beam. In the top layer some yielding of the bars was also detected in the region of curtailment of the reinforcement. The tension shift effect of d, suggested by the Concrete Design Code [NZS 3101 (1982)], formed a conservative envelope. Finally, large compression strains appear to have occurred in the reinforcement near the column faces. In this case the second layer of compression steel might not contribute much to carrying the compression force in the reinforcement because it is close to the neutral axis of the beam at the faces of the columns.

4.4.6 Longitudinal Bar Stresses at Midspan

The bar stresses in the connection region illustrated in Figs. 4.34 to 4.36 show that in most of the strain gauged bars yielding spread from the column faces to the commencement of the lap. The average bond stresses estimated in the intermediate section of the two splices of the reinforcement protruding from the side of the precast member subjected to tension were 5.6MPa in the outer layer of the top bars, 2.3MPa in the inner layer of the top bars and 2.7MPa in the outer layer of the bottom bars. It is of interest to observe that some lapping action actually occurred in this region. Bond forces in the bars in this region were transferred in the vertical plane required to balance the shear forces in the beams and in the horizontal plane to the lapping bars.

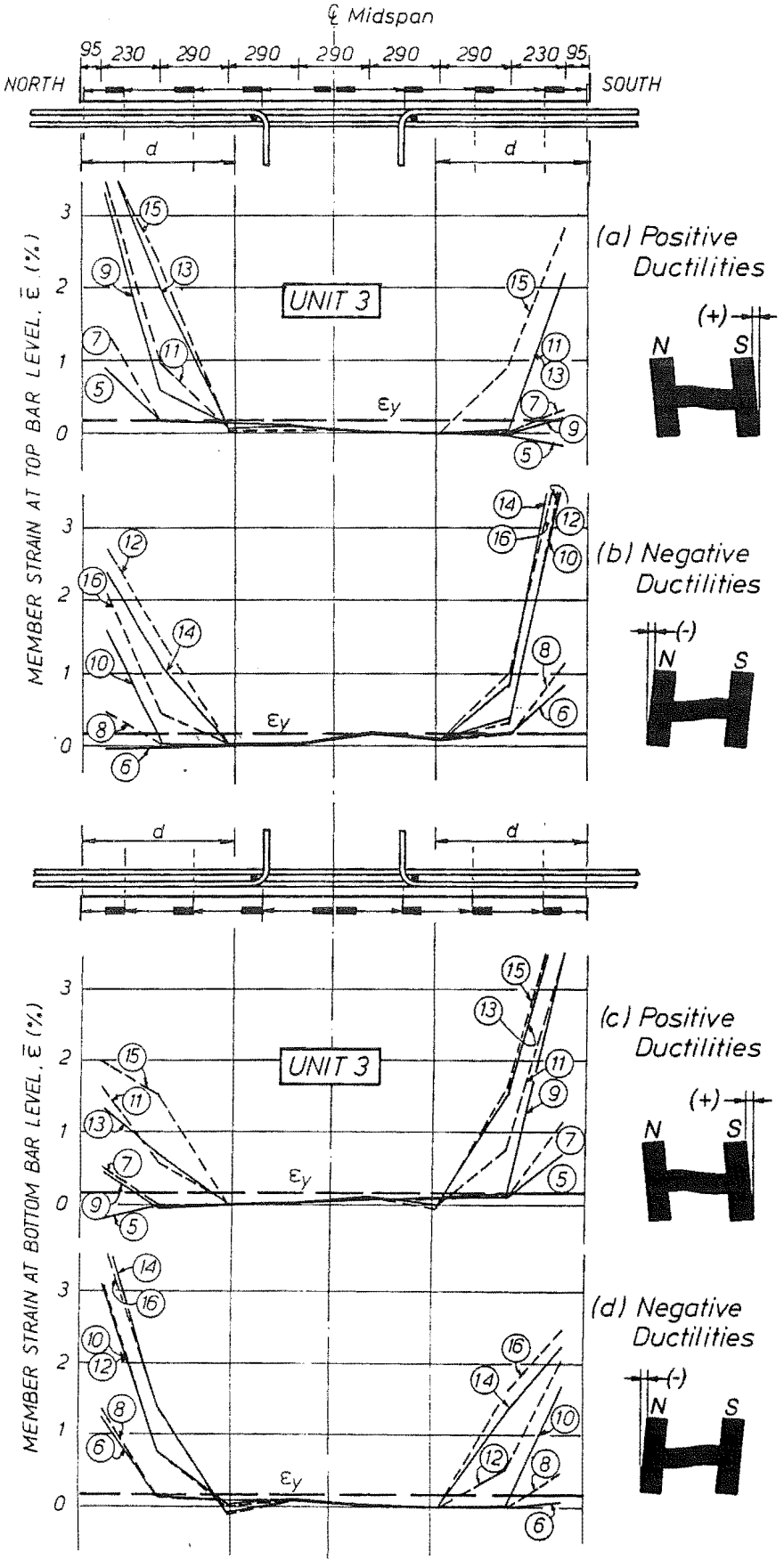

Fig. 4.32 - Member Strains at the Level of the Longitudinal Reinforcement of Unit 3.

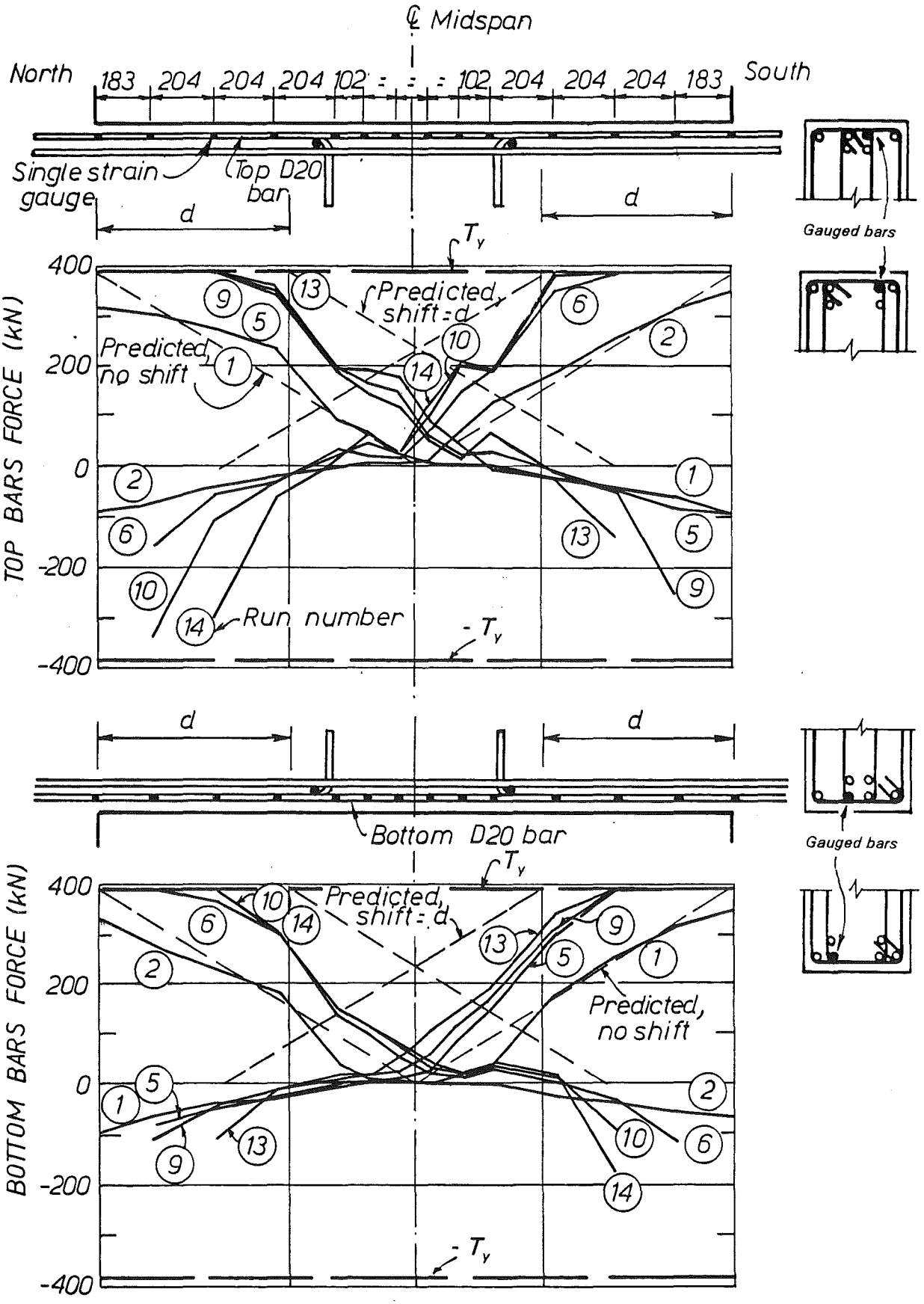

Fig. 4.33 - Longitudinal Bar Forces in the Beam of Unit 3.

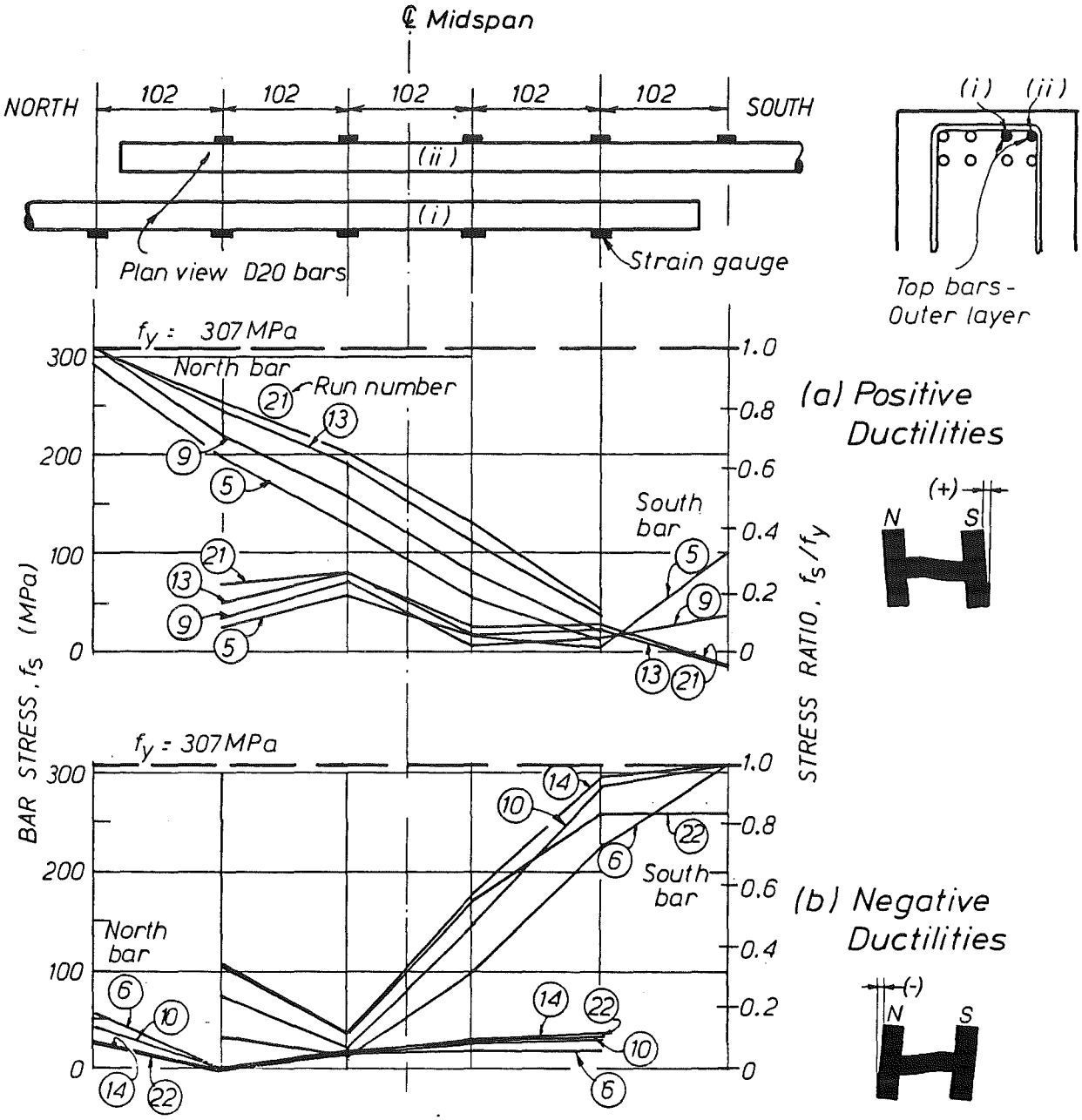

Fig. 4.34 - Longitudinal Bar Stresses in the Lapped Region - First Layer Top Bars of Unit 3.

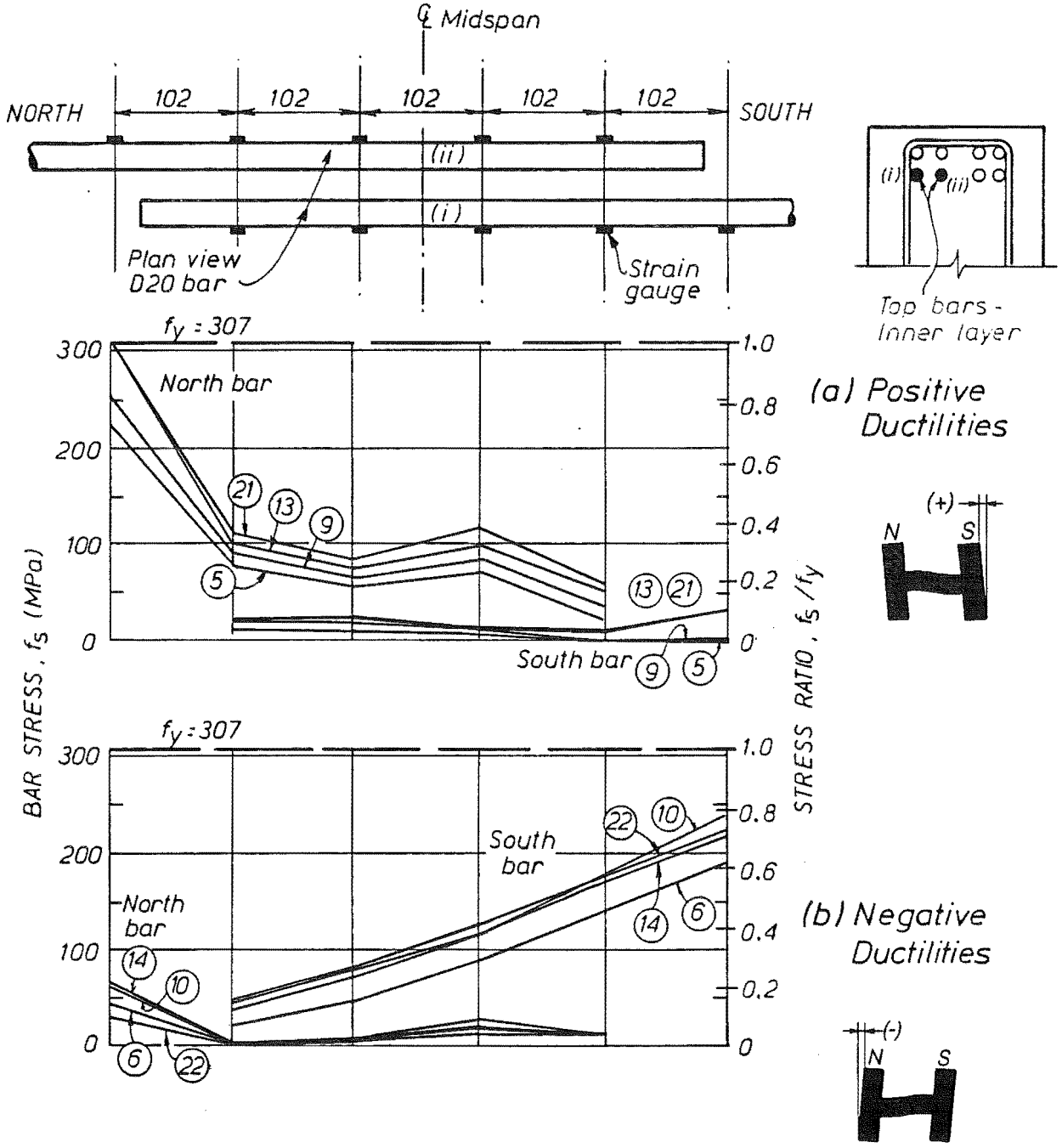

Fig. 4.35 - Longitudinal Bar Stresses in the Lapped Region - Second Layer Top Bars of Unit 3.

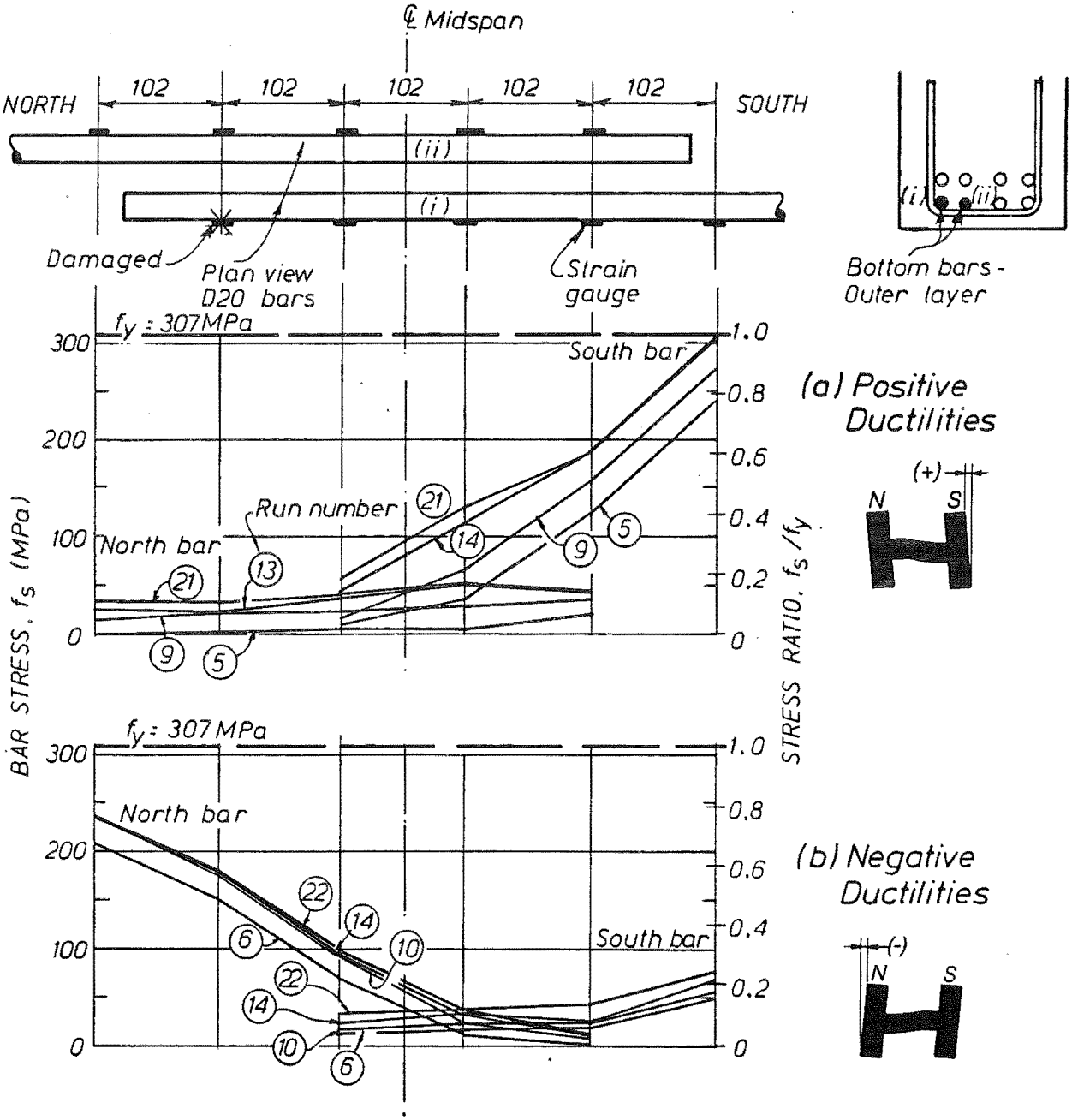

Fig. 4.36 - Longitudinal Bar Stresses in the Lapped Region - First Layer Bottom Bars of Unit 3.

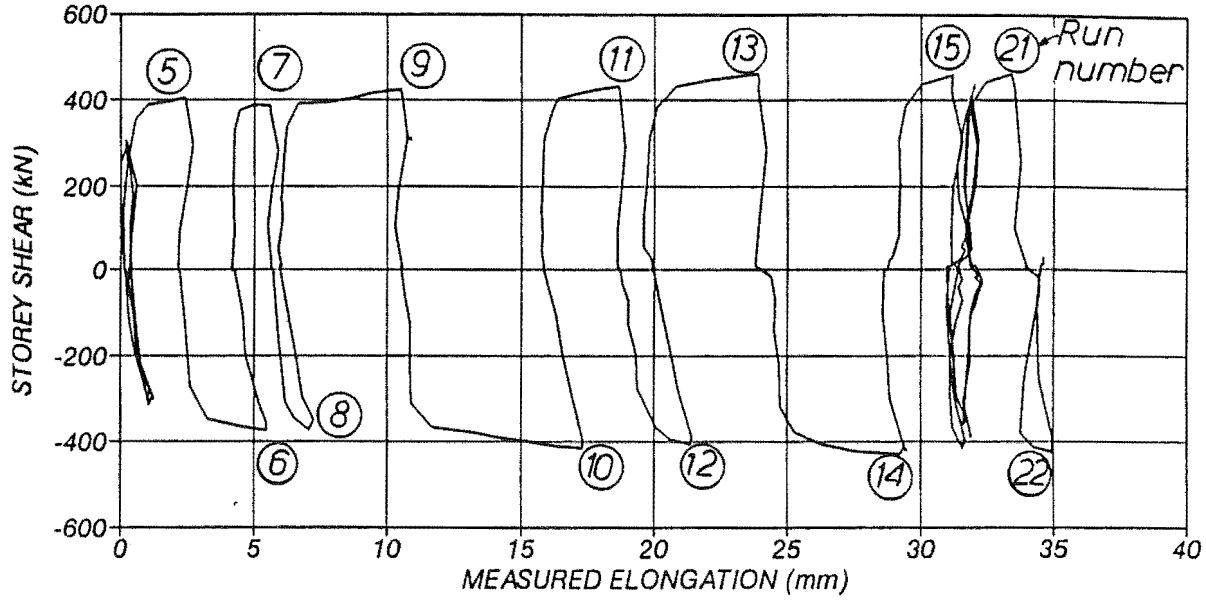

Fig. 4.37 - Total Measured Beam Elongation of Unit 3.

4.4.7 Elongation of the Beam

The total elongation of the beam, depicted in Fig. 4.37, shows almost the same trends as the test of Unit 2. A maximum total elongation of 35mm was recorded in load run 24.

4.5 CONCLUSIONS

1. Units 1, 2 and 3 were beam-column subassemblages with longitudinal reinforcement in the precast beams connected by various splice details in a cast in place joint at midspan. During the seismic load tests the connections behaved very satisfactorily and developed the capacity of the subassemblages. The commencement of the laps at 1.46d, 1.23d and 1.27d from the column faces of the three units did not have a detrimental effect on behaviour of the test units.

2. Observations made during this series of experiments showed the plastic hinge regions of these relatively short beams extended a distance from the column face which was approximately equal to the effective depth of the beam. It is then recommended that splices and other types of connections may commence at a distance as close as d to the column face.

3. The large shear deformations observed in these tests were the result of the small span/depth ratio of the beams and hence of the relatively high shear stress of $0.28\sqrt{f'_c}$ to $0.37\sqrt{f'_c}$ in the plastic hinge regions. These shear deformations affected the energy dissipation characteristics and stiffness, but the theoretical flexural strength of the units was maintained during the tests. The extra amount of transverse reinforcement in the plastic hinge region of Unit 3 resulted in only a slight improvement in performance compared with Units 1 and 2.

4. The estimated tensile forces in the beam longitudinal reinforcement indicate that the recommendations of the Concrete Design Code (1982) of using a tension shift equal to d appear to be too conservative.

5. Significant beam elongations after yielding of the longitudinal reinforcement were observed in these tests. The main reason for beam elongation is the residual plastic tensile strain in the longitudinal reinforcement because in beams with equal amounts of top and bottom steel the steel in compression is subjected to a stress level below of that sustained by the bars in tension.

6. The stiffness of these Units was very low compared with the theoretical predictions using normal design office procedures. The main two reasons are that the curvature diagram does not follow the bending moment diagram and that strain penetration of the beam and column bars occurs in the beam-column joint region resulting in a fixed-end rotation.

CHAPTER 5

TEST RESULTS FROM UNIT 4

5.1 INTRODUCTION

This chapter contains test results from the H-shaped Unit 4, which comprised two precast concrete components with diagonally reinforced beam elements connected by bolts and steel plates at the midspan of the beam. The design of this unit was discussed in Section 3.2.2.2 and complete reinforcing details are illustrated in Fig. 3.6. The reinforcement lay-out for the beams involved strong end regions to relocate the plastic hinges away from the beam ends and to concentrate all inelastic deformations at midspan. This arrangement has occasionally been used in ductile frames of buildings in New Zealand because the Concrete Design Code [NZS 3101 (1982)] requires the use of diagonal reinforcement to carry part of the shear force in the regions expected to respond inelastically during a seismic event when the nominal shear stress at overstrength $v^o = V^o/bd$ exceeds $0.30\sqrt{f'_c}$. Another advantage of this arrangement is that the current Concrete Design Code allows a reduction in the amount of transverse steel required in beam-column joints when plastic hinges are designed to form in a region away from the column faces.

5.2 GENERAL BEHAVIOUR OF UNIT 4

The first test of Unit 4 was completed within one week. After undergoing the loading cycles up to two full cycles to $\mu_\Delta = \pm 4$ the lateral load capacity of the unit dropped to 80% of the maximum recorded load. At this stage it was decided to terminate the test and to evaluate the possibility of retrofitting the damaged regions of the unit to enable it to be capable of a full ductile performance. A cumulative displacement ductility factor of $\Sigma\mu_\Delta = 24$ had been imposed on the unit before ending the first test. The available displacement ductility factor obtained from the cumulative displacement ductility factor was $\mu_a = 3$ (see Section 3.7) that corresponds to a limited ductility performance.

Fig. 5.1 shows the beam of Unit 4 at two stages during the first test. Cracking in the beam was very symmetrical in the loading cycles in the elastic range. Most of the cracks appeared in the strong ends adjacent to the column. These cracks spread at regular intervals and their width did not exceed 0.3mm. Larger cracks, up to 0.6mm wide, were observed to propagate through the vertical construction joints between the precast concrete elements and the cast in place concrete in the midspan region. Only two hairline cracks, with a width of 0.1mm crossed the midspan connection.

In the first loading cycles in the inelastic range up to $\mu_\Delta = \pm 2$, cracks concentrated around the bend of the diagonal bars. These cracks were up to 3mm wide. It was also observed that the concrete at the mid-depth of the beam near the steel straps had become loose and there were some

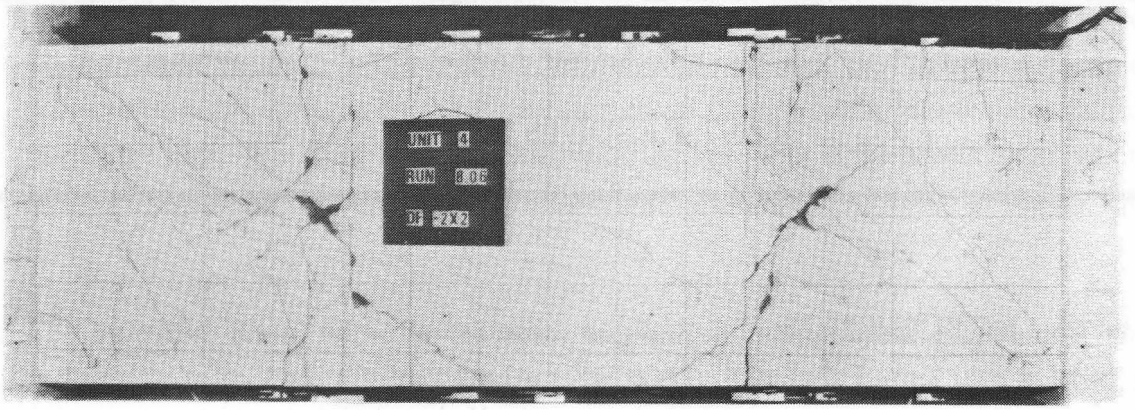

(a) At μ_Δ = -2x2

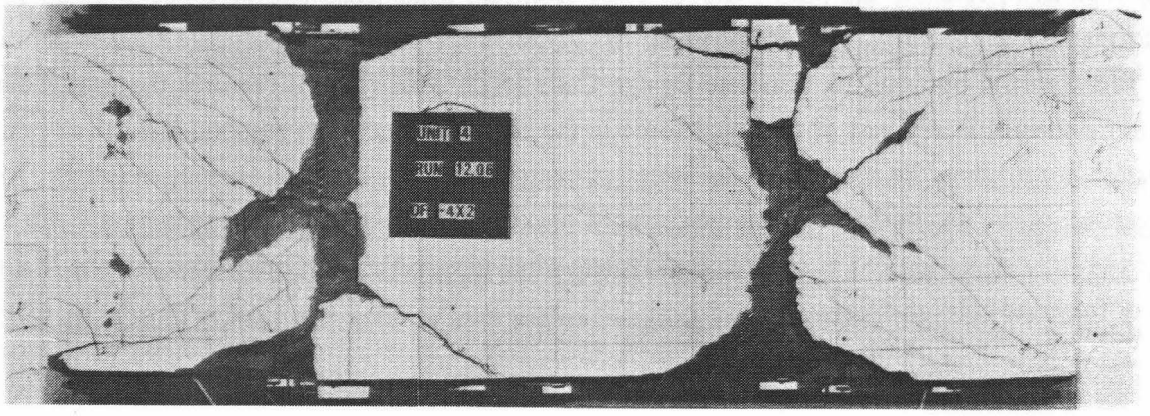

(b) At μ_Δ = -4x2

Fig. 5.1 - Cracking of the Beam of Unit 4 at Different Stages During the First Test.

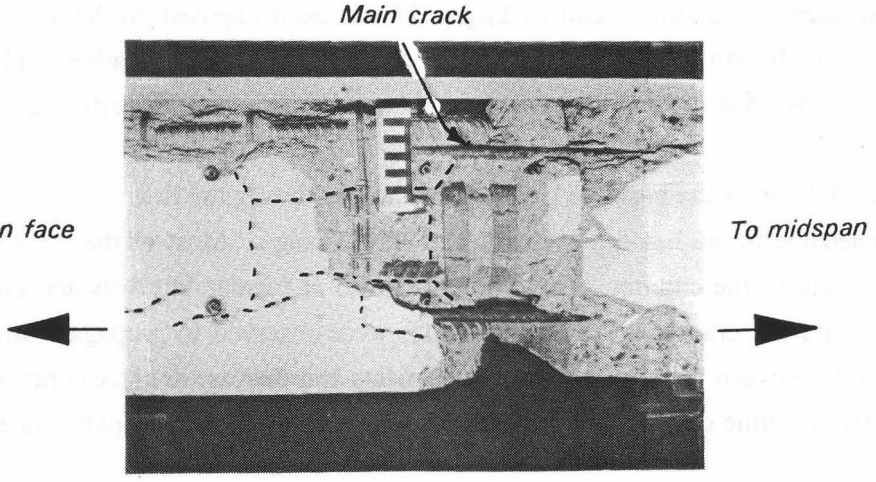

Fig. 5.2 - Plan View of Top South End of the Beam of Unit 4 at the End of the First Test.

incipient signs of spalling of the concrete cover in this region. In further loading runs to $\mu_\Delta = \pm 2$, an out of plane horizontal movement (swelling) of 5mm was noticed in the concrete cover near the bends of the diagonal reinforcement, spalling of the concrete cover was also observed as it can be seen in Fig. 5.1 (a). The main cracks in the beam commenced in the concrete at the bends of the diagonal reinforcement. At the mid-depth of the beam they changed direction and, penetrated with an inclination of 35° into the strong ends, heading towards the compression regions of the beam at the face of the columns. Surprisingly no major cracking occurred in the central region where the inelastic actions were expected to take place.

Extensive damage to the concrete in the strong ends of the beam occurred during the loading cycles to $\mu_\Delta = \pm 4$. At this stage large cracks at the top and bottom sides of the beam running between the D24 and D28 bars in the strong ends were also noticed. It is likely that these cracks had developed in the previous stages. Fig. 5.1 (b) shows the observed damage of the beam of Unit 4 at the end of the test. It is evident that the detailing of the reinforcement in the so called strong ends did not enforce the inelastic deformations to occur at the midspan of the beam as intended in the design, and therefore the simple truss model of Fig. 3.9 cannot be used to explain the behaviour of Unit 4.

Fig. 5.2 shows a close up of the top south end after removing the loose cover at the end of the test. A close inspection of the damaged region showed that the D28 bars in the strong ends had bent outwards as a result of bursting forces in the transverse direction and the lack of adequate reinforcement at the commencement of the anchorage hook (see Fig. 5.2). After removal of the concrete in the damaged regions it was also found that the concrete in the strong ends in contact with the D24 bars beside the 30x10mm steel straps had been completely crushed. There are two main reasons that explain the crushing of the concrete around the D24 bars. The first is associated with the effect of yield penetration of the D24 bars into the strong ends of the beam. The strains in these bars exceeded the yield strain and as a result the D24 bars elongated and slipped relative to the surrounding concrete, shearing it with its deformations. In the design of Unit 4 the current Concrete Design Code [NZS 3101 (1982)] recommendations regarding minimum bend radii for bars had been provided to reduce crushing of the surrounding concrete due to high local bearing stresses. However, these recommendations do not consider the shearing effect due to the local bar slip. The second reason is the high bearing stresses in the concrete around the D24 bars. Since in the test a large vertical crack appeared beside the 30x10mm steel straps, the shear carried by this reinforcement could not be transferred by a direct strut from the node at the bend of the diagonal reinforcement but rather by dowelling of the D24 bars inside the strong ends as depicted in Fig. 5.3. The bearing conditions around the outer diagonal bars were critical because they had to transfer not only the vertical component of the diagonal bar but also the vertical force of the straps. Crushing of the concrete surrounding the outer diagonal bars was seen to extend approximately 145mm or $6d_b$ from the vertical crack (see Fig. 5.3). The average bearing stress, f_b, around one of the outer bars can be estimated as

$$f_b = \frac{\left(\frac{T_V}{4} + \frac{S_T}{2}\right)}{6d_b^2} \qquad (5.1)$$

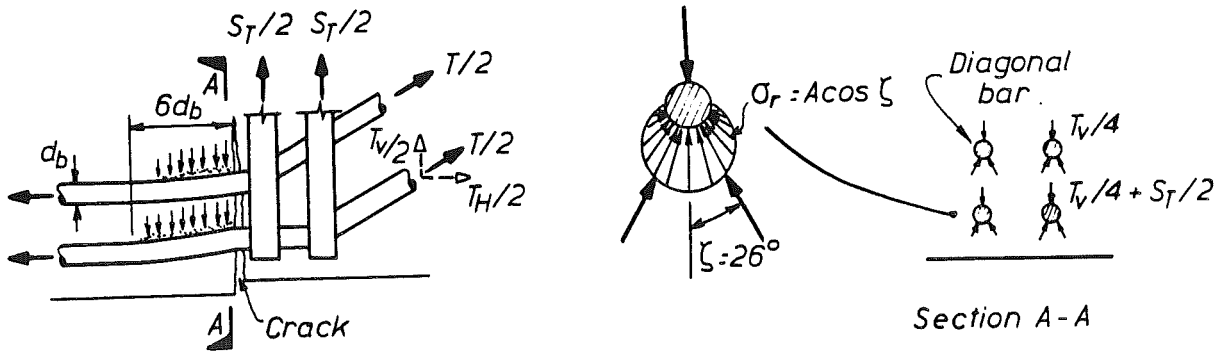

Fig. 5.3 - Transfer of Beam Shear in the Critical Region at the Bend of the D24 Diagonal Bars.

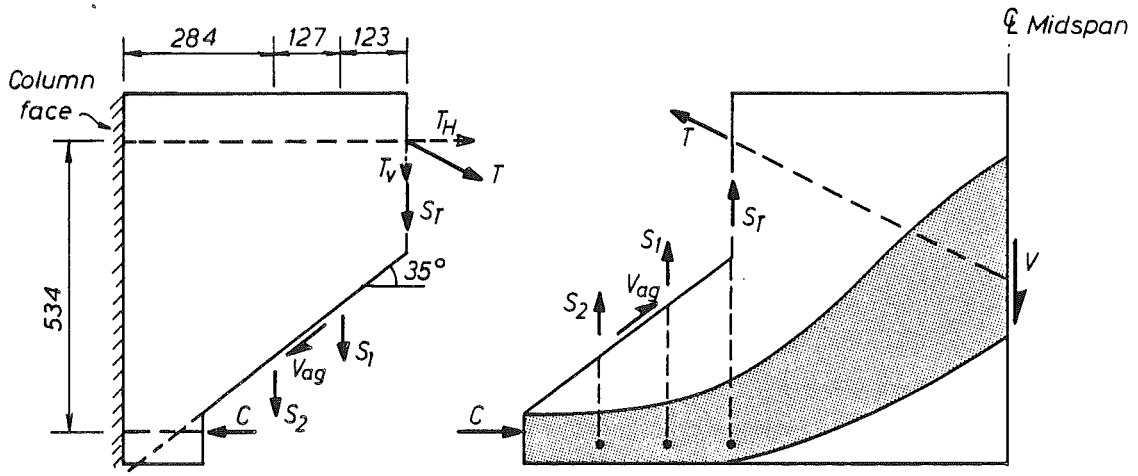

Fig. 5.4 - Free Bodies with Forces Acting upon Unit 4.

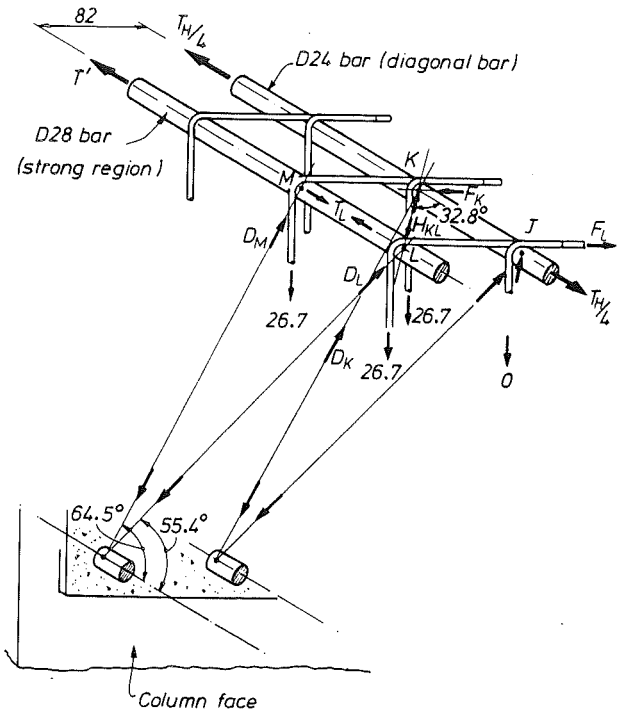

Fig. 5.5 - Refined Three Dimensional Truss Model of Unit 4.

where T_V and S_T are vertical forces in the diagonal bar and in the strap, respectively and d_b is the diameter of the bar as indicated in Fig. 5.3.

As a first approximation, it will be assumed that the truss mechanism of Fig. 3.9 developed at the theoretical lateral load capacity H_a = 636kN. Thus, the bearing stresses around the diagonal bars associated with this mechanism can be readily estimated. Relating the forces T_v and S_v in Eq. 5.1 to H_a and using the nominal bar diameter of the diagonal bars, d_b = 24mm, it can be found that f_b = 58MPa.

It is obvious that such a high bearing stress could not be sustained by the concrete in the strong region of the beam where local crushing was detected, particularly since the concrete was not confined.

A more realistic assessment of the likely bearing stresses acting during the test of Unit 4 can be obtained from the free bodies shown in Fig. 5.4 in conjunction with the refined three dimensional truss model illustrated in Fig. 5.5. The diagonal crack that penetrated into the strong regions of the beam of Unit 4 is modelled as shown in Fig. 5.4. The free bodies in Fig. 5.4 imply that the shear in the beam was transferred in this region not only by the vertical straps and the diagonal bars through a direct strut but also by some of the stirrups in the beam ends.

The truss model in Fig. 5.5 is used to estimate the shear carried by the stirrups. It is assumed, as it will be shown later, that the horizontal portions of the diagonal bars are equally stressed along the strong ends and that the outer bars at the critical region have zero stress. The analysis yields the following results:

Node J: No transverse force can be transferred in the horizontal plane since it is assumed that splitting has already occurred and the outer bars have zero stress.

The force $T_H/4$ in this node does not change and therefore it does not require an equilibrating force at the node. As a result no diagonal compression force in the vertical plane can develop and hence the vertical stirrup at J is rendered ineffective.

Node K: A diagonal force D_K can develop in this node. Its maximum value is limited by the yield force 26.7kN of the stirrup.

$$D_K = \frac{26.7}{\sin 64.5^\circ} = 29.6\,\text{kN}$$

$$H_{KL} = D_K \frac{\cos 64.5^\circ}{\cos 32.8^\circ} = 15.2\,\text{kN}$$

$$F_K = H_{KL} \sin 32.8^\circ = 8.2\,\text{kN}$$

Note that force H_{KL} can be transferred because of the horizontal tie at node L. The force F_K is required to balance the transverse component of the diagonal force H_{KL}.

Node L: As in previous nodes the diagonal force D_L is limited by the yield strength of the vertical stirrup at the horizontal tie. In addition the D28 bar is stressed to balance the longitudinal components of forces D_L and H_{KL}.

$$D_L = \frac{26.7}{\sin 55.4^\circ} = 32.4\,kN$$

$$F_L = H_{KL}\sin 32.8^\circ = 8.2\,kN\ (0.31 f_y)$$

$$T_L = H_{KL}\cos 32.8^\circ + D_L\cos 55.4^\circ = 31.2\,kN\ (0.16 f_y)$$

Node M: Only in-plane forces are necessary for equilibrium in this node. The diagonal force D_M is limited by the yield strength of the stirrup.

$$D_M = \frac{26.7}{\sin 64.5^\circ} = 29.6\,kN$$

$$T_M = T_L + \frac{D_M}{\cos 64.5^\circ} = 99.9\,kN\ (0.52 f_y)$$

The vertical force carried by the 30x10mm straps can be estimated as the difference between the measured shear in the beam and the shear taken by the stirrups as shown in the above calculations. Table 5.1 illustrates this procedure and estimates the difference between the moment predicted with the distribution of forces derived from the analysis and the one obtained from the direct readings of the load cells of the test frame. The symbols in Table 5.1 are illustrated in Fig. 5.4.

The moment calculated using the estimated distribution of forces in the strong ends of Unit 4 gives an accurate value when compared with the measured value except in the semi-cycle of loading to μ_Δ = 2x1 where the straps were not yet activated because the compression force at midspan was mainly carried by the concrete. The difference can be assigned to the moment caused by the shear force carried through aggregate interlock (V_{ag} in Fig. 5.4).

Table 5.2 shows the bearing stresses calculated from Eq.5.1 using the results obtained in Table 5.1. These stresses are more realistic estimates of values which could have been attained during the test.

In the previous analysis it was assumed that splitting of the concrete between the D24 diagonal bars and the D28 outer bars in the strong ends of the beam had already occurred. An analysis to determine that this splitting was predictable is conducted in the following paragraphs.

Table 5.1
Bar Forces Acting on Unit 4

μ_Δ	V_{msrd} (kN)	M_{msrd} [1] (kNm)	T_H (kN)	T_v (kN)	S_1 (kN)	S_2 (kN)	S_T (kN)	M_{calc} [1] (kNm)	$\frac{M_{calc}}{M_{msrd}}$
2x1	522	549	515	267	107	53	-	475	0.87
-2x1	520	546	515	267	107	53	93	525	0.96
4x1	532	558	515	267	107	53	105	531	0.95
-4x1	517	542	515	267	107	53	90	523	0.96

(1) In the beam at the column face

Table 5.2
Bearing Stresses in the Critical Region of Unit 4.

μ_Δ	$\frac{T_V}{4} + \frac{S_T}{2}$ (kN)	f_b (kN)	f_b/f'_c
2x1	67	19	0.54
-2x1	113	33	0.94
4x1	119	35	1.00
-4x1	112	32	0.91

Fig. 5.6 shows the forces required for equilibrium at the node where the diagonal bars are bent and their distribution in the horizontal plane. It is assumed that the diagonal bars are equally stressed after and before the bend. For equilibrium in Fig. 5.6 (a)

$$R_H = \frac{T_V + S_T}{\tan\beta} + T_H - T \qquad (5.2)$$

One half of the force R_H on the outer bars needs, in the absence of any transverse reinforcement, be transferred from the diagonal bars to each side of the beam by pure shear through the concrete (see Fig. 5.6 (b)). The average shear stress, τ_f, associated with this mechanism is

$$\tau_f = \frac{R_H}{2A_\tau} \qquad (5.3\ a)$$

or, substituting Eq. 5.2 in Eq. 5.3 (a)

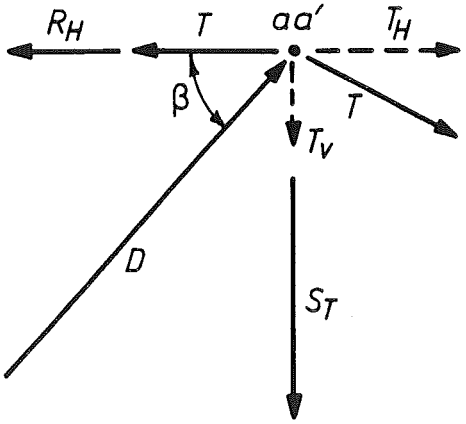

(a) Vertical Plane

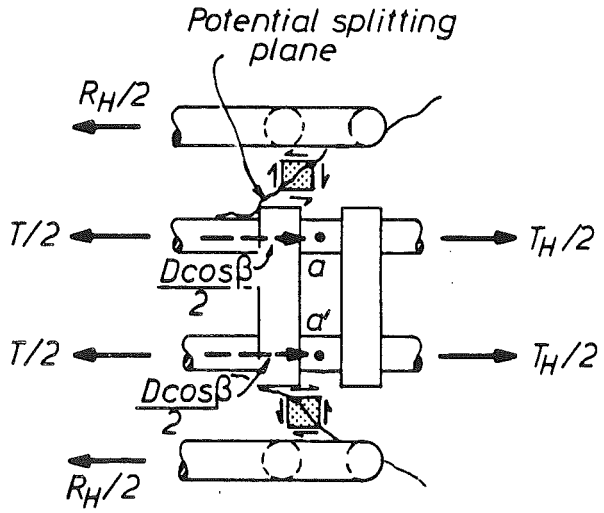

(b) Horizontal Plane

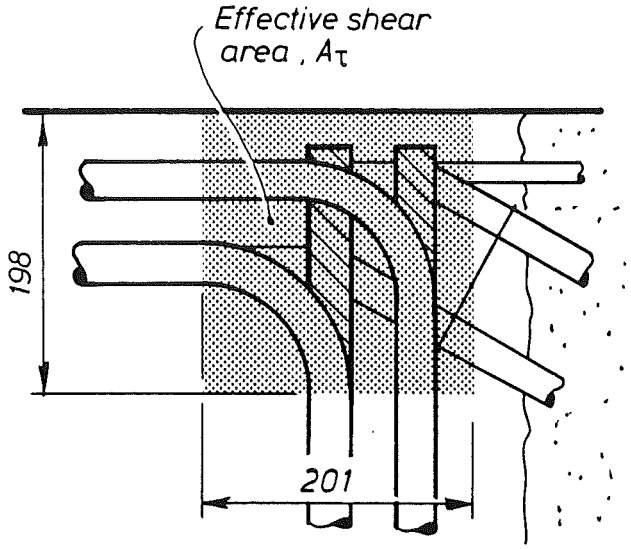

(c) Effective Friction Surface

Fig. 5.6 - Forces in the Bend Region of Diagonal Bars before Longitudinal Splitting of Concrete.

$$\tau_f = \left(\frac{T_V + S_T}{\tan\beta} + T_H - T \right) \frac{1}{2A_\tau} \qquad (5.3\ b)$$

where A_τ is the effective friction area. The area A_τ is difficult to estimate since there is a complex distribution of stresses along the vertical plane between the outer and inner bars. In lieu of a better approach, it will be assumed that this area extends between the lines at the initiation of the bend of the second layer of bars, the concrete surface at the top and the centre line of the extension of the vertical hook of the first layer of bars as shown in Fig. 5.6 (c). That is:

$$A_\tau = 145 \text{x} 214 = 31030 \text{mm}^2 \qquad (5.4)$$

Now substituting $A_\tau = 31030\text{mm}^2$, $\beta = 45^0$ and the values estimated from Table 5.1 for Unit 4 during $\mu_\Delta = 2\text{x}1$, $T_H = 515\text{kN}$, $T_v = 267\text{kN}$, $T = 580\text{kN}$ and $S_T = 93\text{kN}$ in Eq. 5.3 (b) gives

$$\tau_f = 4.8\text{MPa} \qquad (5.5)$$

To rely on the shear transfer mechanism the average shear stress shall be smaller than the diagonal tensile strength of concrete f'_{cr} which can be assumed equal to the uniaxial tensile strength of the concrete, f'_t. The uniaxial and splitting strength of concrete are also related. An expression given by Collins and Mitchell (1991) is

$$f'_{cr} \approx 0.65 f'_t \qquad (5.6)$$

Substituting the measured splitting strength of the concrete of Unit 4, $f'_t = 3.9\text{MPa}$ (see Table 3.2) in Eq. 5.6 results in

$$f'_{cr} = 2.5\text{MPa}$$

which is a significantly smaller value than the estimated value of τ_f. Therefore, the above analysis could have been used to predict a diagonal tension failure between the D24 diagonal bars and D28 outer bars as it was observed in the test of Unit 4.

Consequently, it can be concluded that the refined three dimensional truss model yields acceptable results. The model shows that the diagonal tension failure of the node at the bend of the diagonal bars was caused by the lay-out of longitudinal reinforcement used in the strong regions of the beam. These factors were not taken into account in the initial design.

The refined three dimensional truss model can also be used to explain the excellent behaviour of a diagonally reinforced unit with relocated plastic hinges tested by Bull (1978). In this unit the diagonal bars and the other bars provided for relocating the plastic hinge were in the same vertical plane and therefore no large bursting forces were expected.

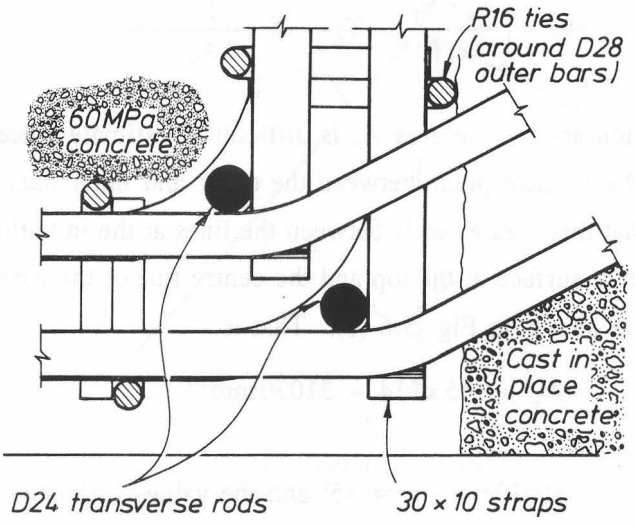

Fig. 5.7 - Reinforcement Detail at the Bend of the Diagonal Reinforcement in Unit 4r.

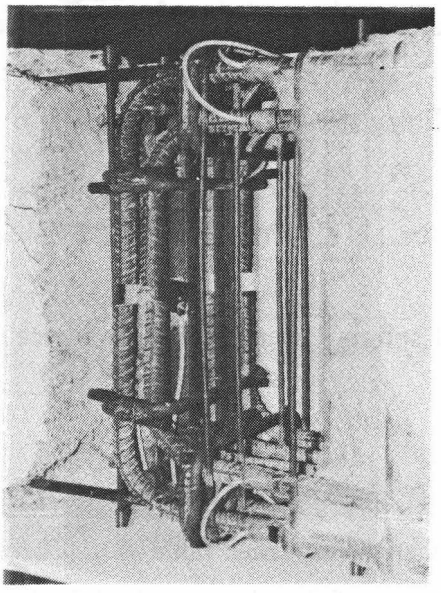

Fig. 5.8 - Close up of Repaired Region of Unit 4r.

5.3 REPAIR OF UNIT 4

Unit 4 was repaired after testing and retested for two purposes:

a) to verify the refined three dimensional truss model described above, and

b) to demonstrate that this type of connection can be designed to give an adequately ductile performance in moment resisting frames resisting earthquake forces.

To repair Unit 4 the damaged concrete was removed, the reinforcement detail appropriately modified and the damaged concrete replaced. Fig. 5.7 shows the reinforcement detail of Unit 4 after repair as it would be seen from a vertical plane passing between the diagonal bars and Fig. 5.8 shows a close up of the reinforcement in one of the repaired ends of the midspan region. The repaired unit is referred to as Unit 4r. Several measures were taken to alleviate the problem of crushing of the concrete surrounding the D24 diagonal bars, namely :

a) one of the 30x10mm steel straps was cut and anchored around the inner diagonal bars to distribute more evenly the bearing stresses between inner and outer bars,

b) transverse D24 rods were placed in contact with the diagonal bars to allow the diagonal bars to pivot in the rods avoiding shearing off the surrounding concrete,

c) higher strength concrete (60MPa) was cast in the repair space, and

d) 4-R16 ties were placed between the hooks of the outer D28 bars. This reinforcement was designed to provide the clamping force required to mobilize a shear friction mechanism to transfer the force $R_H/2$ (see Fig 5.6 (b)) at an overstrength of 1.25 in the diagonal bars. It was assumed that the entire beam shear would be transferred at point aa' in Fig. 5.6 (a) by the force $T_V + S_T$. The hooks of the R16 ties were tack welded to avoid opening.

5.4 GENERAL BEHAVIOUR OF UNIT 4r

Unit 4r was tested 19 weeks after the completion of the test of Unit 4. The test sequence applied to this unit was identical to that of the original subassemblage. The test took a week to conduct and was terminated when the lateral load capacity at the fourth cycle to $\mu_\Delta = +6$ dropped to 72% of the maximum measured load. The cumulative displacement ductility imposed to the third cycle to $\mu_\Delta = -6$ was $\Sigma\mu_\Delta = 60$, which corresponds to an available displacement ductility factor of $\mu_a = 7.5$.

The condition of the beam of Unit 4r at various stages is illustrated in Fig. 5.9. Cracking in the beam in the loading cycles in the elastic range was mainly confined to the strong ends with only one diagonal crack crossing the midspan region. The cracks in the critical region at the ends of the strong region followed the construction joints between the cast in place concrete at midspan and the high strength concrete used in the repaired area. In the top and bottom surfaces of the beam, cracks between the outer D28 bars and the inner D24 bars connections at the bend of the D28 bars were observed. These cracks were of the same shape as the main splitting cracks that penetrated the strong ends in Unit 4 (see Fig. 5.2). The maximum crack width of 0.5mm recorded in these loading cycles was observed in the diagonal cracks at the mid-depth of the beam close to the column faces. All cracks which opened for one direction of loading practically closed when the loading direction was reversed.

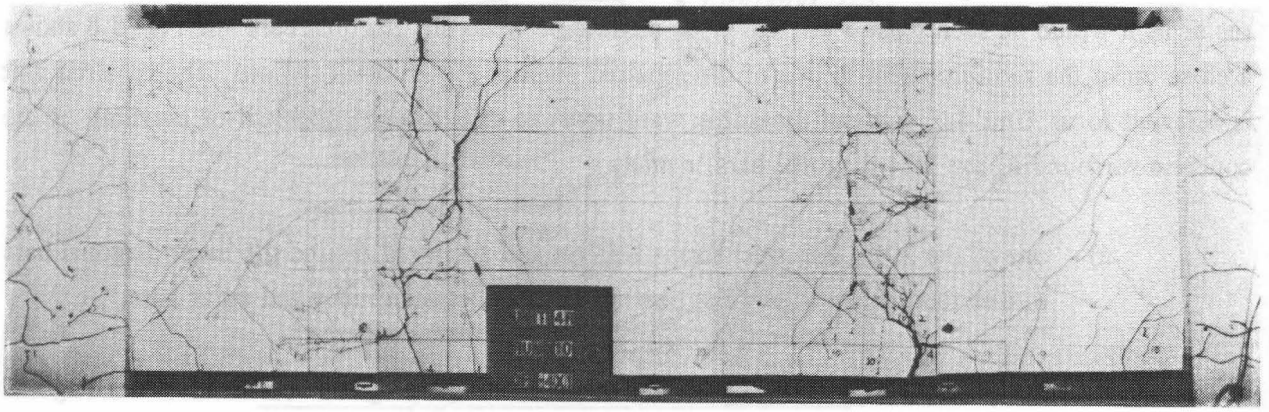

(a) At μ_Δ = -4x1

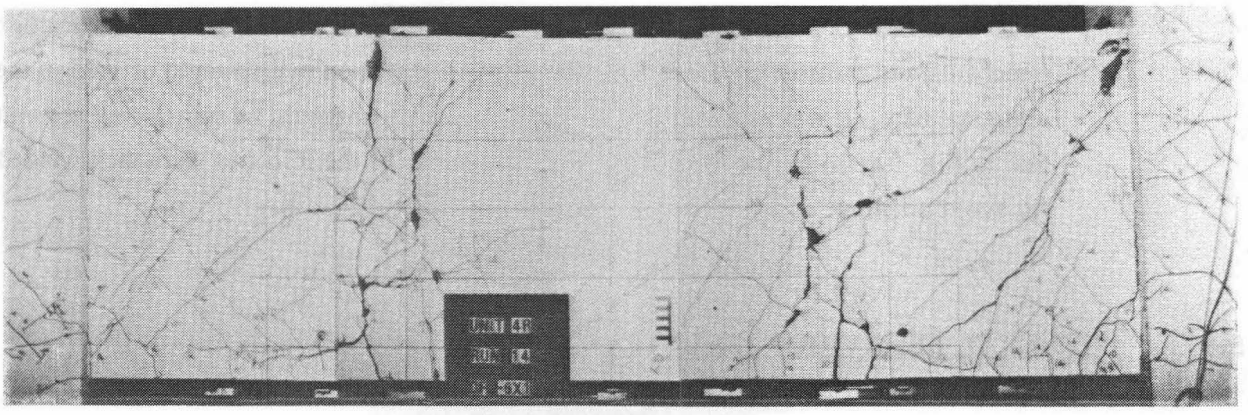

(b) At μ_Δ = -6x1

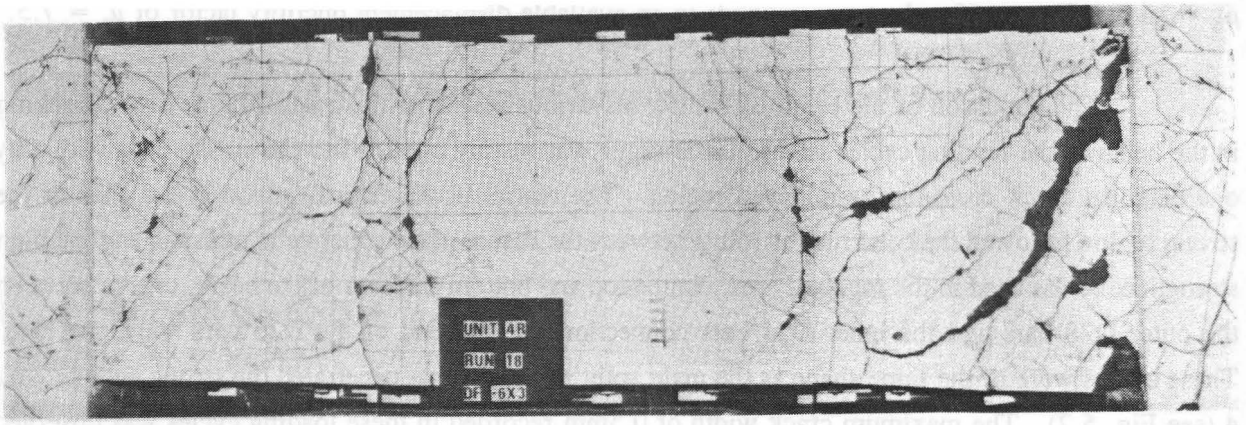

(c) At μ_Δ = -6x3

Fig. 5.9 - Cracking of the Beam of Unit 4r at Different Stages During the Test.

Cracking in the beam concentrated in the critical region in the cycles to $\mu_\Delta = 2$, where crack widths reached 2.6mm in the extreme tension fibre. Crack widths elsewhere remained very small including those crossing the central region of the beam.

In the loading cycles to $\mu_\Delta = 4$ the main cracks in the beam spread from the critical end region towards midspan. These cracks were large with crack widths up to 8mm. It is evident that most of the inelastic deformations had been confined to within the central region of the beam (see Fig. 5.9 (a)). Nevertheless, the cracks in the beam at the column faces grew to 3mm in width in the extreme tension fibres indicating that yield of the beam longitudinal bars had penetrated into the beam-column joints.

In the final cycles to $\mu_\Delta = 6$, wide diagonal cracks developed in the strong ends of the beam, especially in the north end (see Fig. 5.9 (b) and (c)). Associated with this crack pattern was a large sliding shear movement and grinding of the concrete between cracks. It is very likely that the stirrups were subjected to very large strains beyond the elastic range, since a vertical growth of 18mm in the beam depth was recorded in the north end. The repaired Unit displayed a sliding shear failure as a result. No fracture of the reinforcement at the bends of the diagonal bars due to strain age embrittlement occurred during the two tests. However, these results have to be carefully interpreted since the tests were conducted at a temperature of 17°C and embrittlement is very dependent on the temperature conditions.

5.5 LOAD-DISPLACEMENT RESPONSE

The lateral load versus lateral displacement response of the original and repaired unit was significantly different, as can be seen in Fig. 5.10.

The initial elastic stiffness of Unit 4 calculated as the average stiffness at $\pm$ 0.75H_a was 54% of the theoretical stiffness presented in Section 3.2.1. This apparently more flexible behaviour was because the effect of the tension shift on the curvature distribution along the beam, and of the deformations in the beam-column joint region which, amongst others, were not accounted for in the initial theoretical analysis.

In the loading cycles in the inelastic range Unit 4 never attained the theoretical load predicted but the values measured in the first loading cycle were very close to it. Therefore a post-elastic stiffness of 0 was chosen for the ideal bi-linear response in order to normalize the energy absorbed in the measured hysteretic response.

The lateral load measured in load runs 5 and 6 to $\mu_\Delta = \pm 2$ was 98% and 97% of H_a where H_a is the theoretical load capacity calculated using the simple truss analysis assuming that the diagonal reinforcement in the beam yields and the reinforcement elsewhere remains in the elastic range. The second load cycles to the same ductility level showed some decay in load carrying capacity as well as some pinching in the measured response. The normalised energy absorbed by the loops in the first and second cycle was 80% and 43%, respectively.

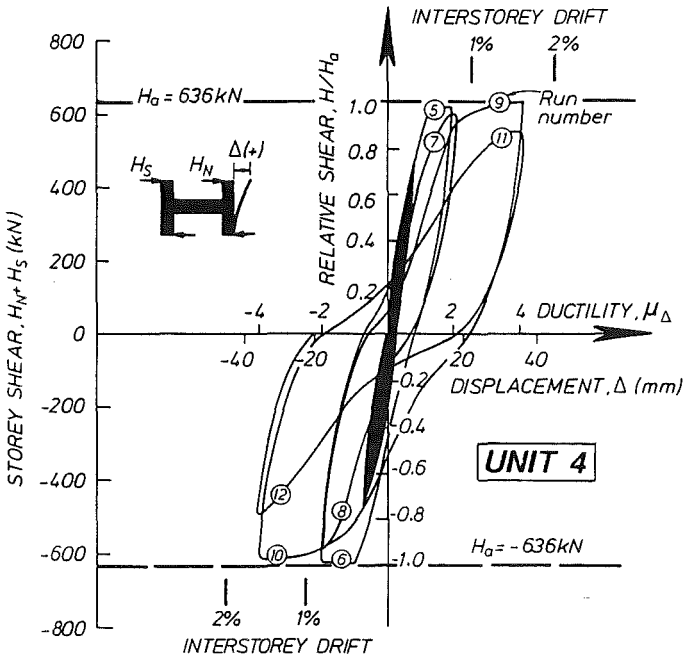

(a) Unit 4

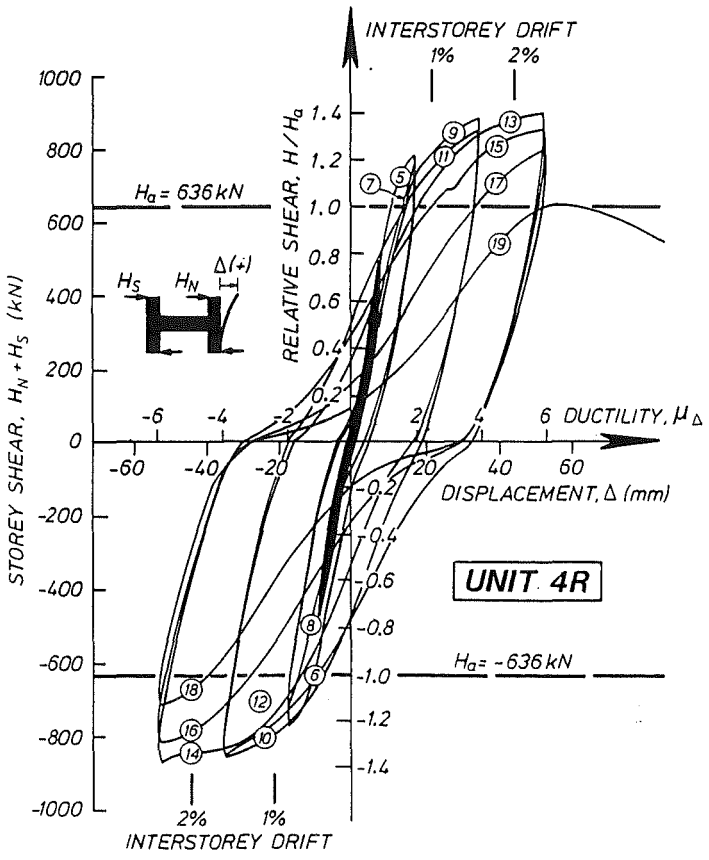

(b) Unit 4r

Fig. 5.10 - Lateral Load-Lateral Displacement Response of Units 4 and 4r.

In load runs 9 and 10 to $\mu_\Delta = \pm 4$ the lateral load attained was $0.99H_a$ and $0.97H_a$, respectively, but the capacity of the unit dropped significantly in the second cycle to the same ductility level. In load run 12 the lateral load measured was 80% of that attained in load run 10. The normalised energy absorbed by the loops in the first and second cycle to $\mu_\Delta = \pm 4$ was 58% and 43%, respectively.

For the repaired unit, Unit 4r, the measured initial stiffness was 79% of the measured stiffness in the elastic range of the original unit. This reduction was caused by the increase in flexibility of the beam-column joints as well as those cracked regions in the beam which were not treated during the retrofitting of the unit. It is likely that, after several loading cycles in the elastic range in the first test, the stiffness of the columns had also diminished.

The measured post-elastic stiffnesses of the positive and negative loading cycles of Unit 4r were rather large because of the significant overstrengths attained. The calculated values were 10.8% and 9.9% of the initial elastic stiffness.

The theoretical lateral capacity H_a was exceeded by 23% and 20% in the first loading cycle in the inelastic range to $\mu_\Delta = \pm 2$. The second loading cycle to the same ductility factor also exceeded the load H_a but there was a slight drop in load carrying capacity. The normalised energy absorbed in these cycles was 81% and 39%, respectively.

The load runs 9 and 10 to $\mu_\Delta = \pm 4$ the unit showed a steady increase in lateral load capacity, reaching overstrengths of $1.37H_a$ and $1.35H_a$. The lateral load attained at the peak of the second loading cycle was slightly smaller than that of the first loading cycle. The normalised energy absorbed in these two cycles was 77% and 63%, respectively. The consequence of reaching such a high strength in the diagonally reinforced midspan region was that the moment capacity of the beams at the column ends was equalled and therefore yielding of the steel commenced at the ends. Yielding of the steel in the strong ends had been discouraged by adding sufficient longitudinal steel there so as to comply with a capacity design philosophy of using a nominal overstrength factor of 1.25 in the diagonally reinforced region.

In the load runs to $\mu_\Delta = \pm 6$, plastic hinges had formed in the beams at the face of the columns. The maximum lateral load of $1.41H_a$ and $1.37H_a$ was measured in load runs 13 and 14 respectively. The large cracks in the strong ends resulted in some loss of aggregate interlock as a manner of transferring the high reversing shear forces of $V/bd = 0.45\sqrt{f'_c}$ based on a concrete compressive strength of $f'_c = 60$MPa. Consequently, there was a gradual degradation of the concrete in one of the strong ends of the beam and with it a loss of stiffness and capacity. In load run 19 the recorded lateral load attained reached 72% of the maximum load measured in load run 13. Further displacements showed that the lateral load capacity had been exhausted, as is seen in Fig. 5.10. A measure of the deterioration of the unit is given by the index of the normalized energy which was 71%

of the ideal bi-linear loops in the first load cycle to $\mu_\Delta = 6$ and 54% and 40% in the subsequent two cycles, respectively. The cumulative energy absorbed including the third cycle to $\mu_\Delta = 6$ was 58%.

It is believed that this high overstrength was caused by a combination of strain hardening following the previous test and by strain ageing of the reinforcement. It is of particular importance to recognise that for diagonally reinforced members an overstrength value of 1.25 might be unconservative. This is because, for the strain history expected in a diagonal reinforcing bar, the concept of the shifted envelop to describe the stress-strain behaviour of New Zealand manufactured steel is not necessarily appropriate (see Section 2.5.2.5). This assumption was used by Andriono and Park (1987) to estimate the overstrength factors of beams using New Zealand steel. Regarding strain ageing it appears that this effect adds an additional overstrength, as indicated by the limited testing already discussed in Chapter 2.

5.6 DECOMPOSITION OF LATERAL DISPLACEMENTS

Fig. 5.11 illustrates the decomposition of the lateral displacements imposed at the peak of each load cycle for Unit 4. The main source of displacement in the loading cycles in the elastic range were the flexural deformations in the strong ends of the beam. These deformations suggest that strong ends in skeletal structures of this type should not be modeled by rigid end blocks. Shear deformations at midspan became gradually more important with the progression of the test. These were caused by crushing of the concrete at the bend of the diagonal reinforcement and were concentrated over a very small length in the beam span, more like sliding shear action. However, flexural deformations in the strong ends contributed a significant percentage of the lateral displacement throughout the test.

Flexural deformations in the strong ends were also the main source of displacement of Unit 4r in the initial loading cycles in the elastic range as illustrated in Fig. 5.12. Shear deformations occurring in the beam and in the beam-column joint panel were much higher than those occurring in the previous test, as a result of the cracked conditions at the beginning of the second test and the effect of the previous loading history. Flexural deformations in the central region of the beam increased in the intermediate stages of the test, owing to the inelastic deformations taking place in this region. However, these deformations became less important in the cycles near the end of the test because of the migration of the plastic hinges towards the beam ends which resulted in large shear and flexural deformations in the strong end regions. Shear deformations, mainly arising from the north end of the beam, governed the displacement response of the unit in the final cycle prior to the end of the test.

5.7 CURVATURE PROFILES ALONG THE BEAM

The curvature distributions along the beams of Units 4 and 4r, obtained from linear potentiometer readings, are shown in Figs. 5.13 and 5.14. These plots are presented in terms of

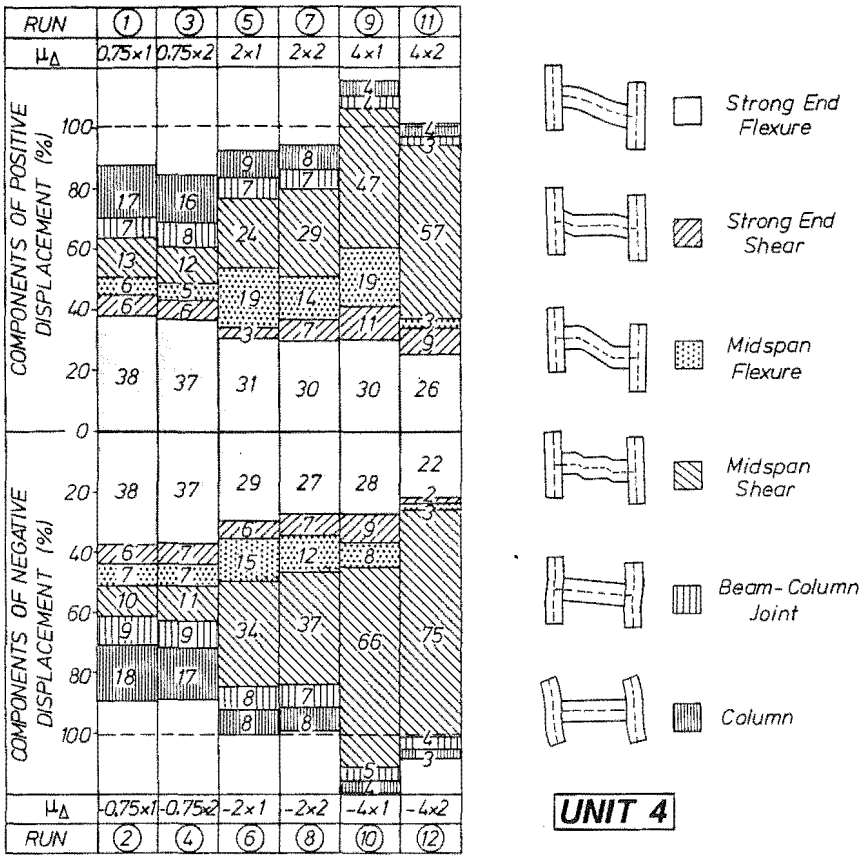

Fig. 5.11 - Decomposition of Lateral Displacements of Unit 4.

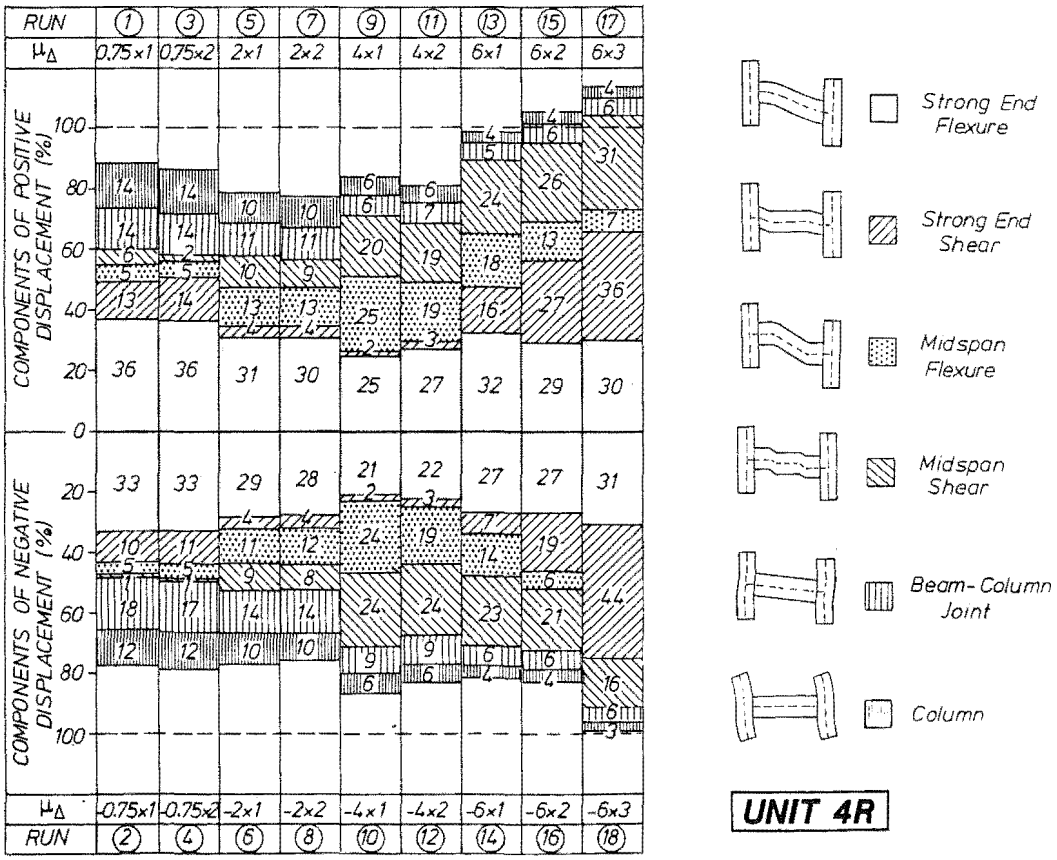

Fig. 5.12 - Decomposition of Lateral Displacements of Unit 4r.

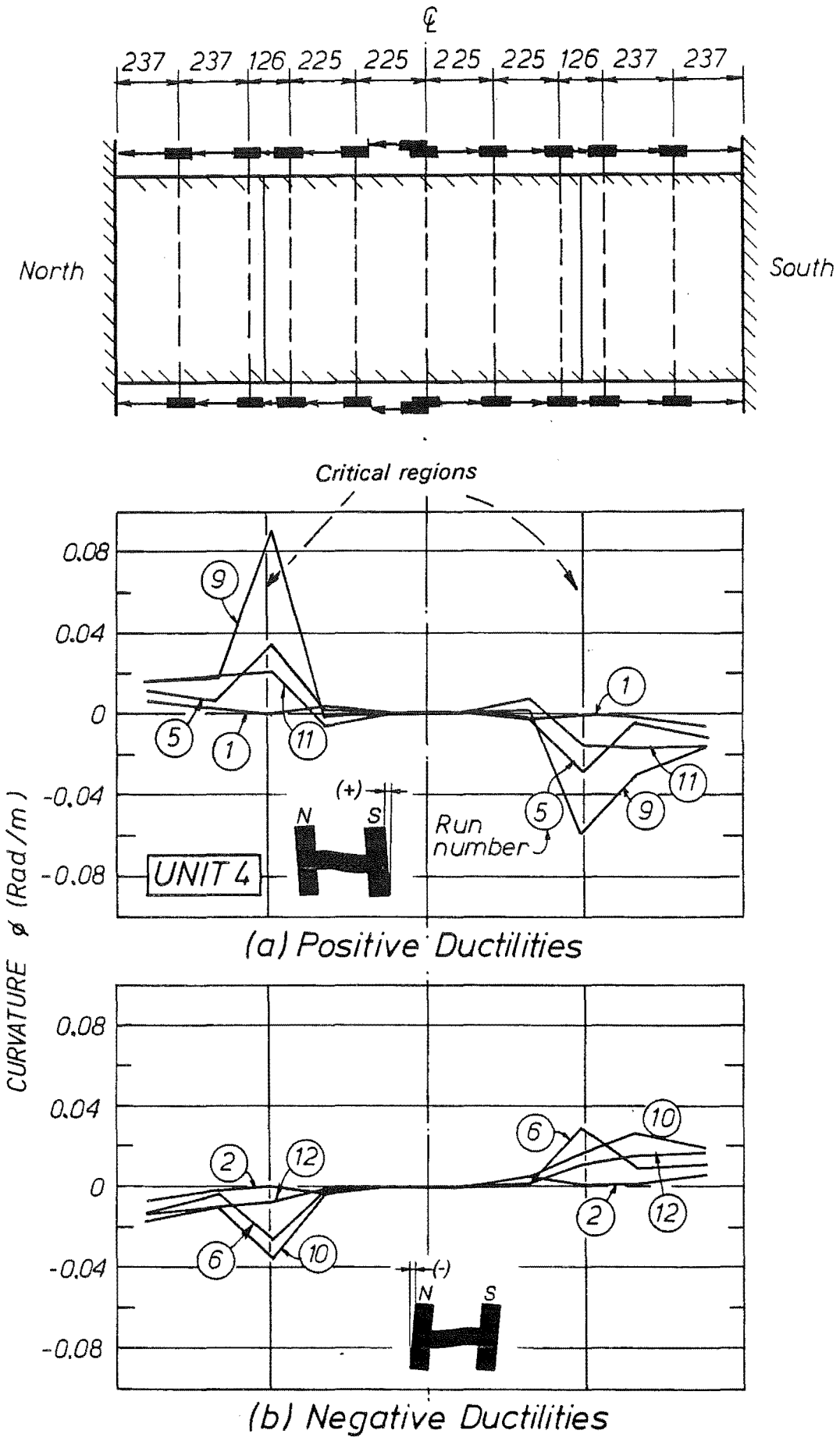

Fig. 5.13 - Curvature Distribution for the Beam of Unit 4.

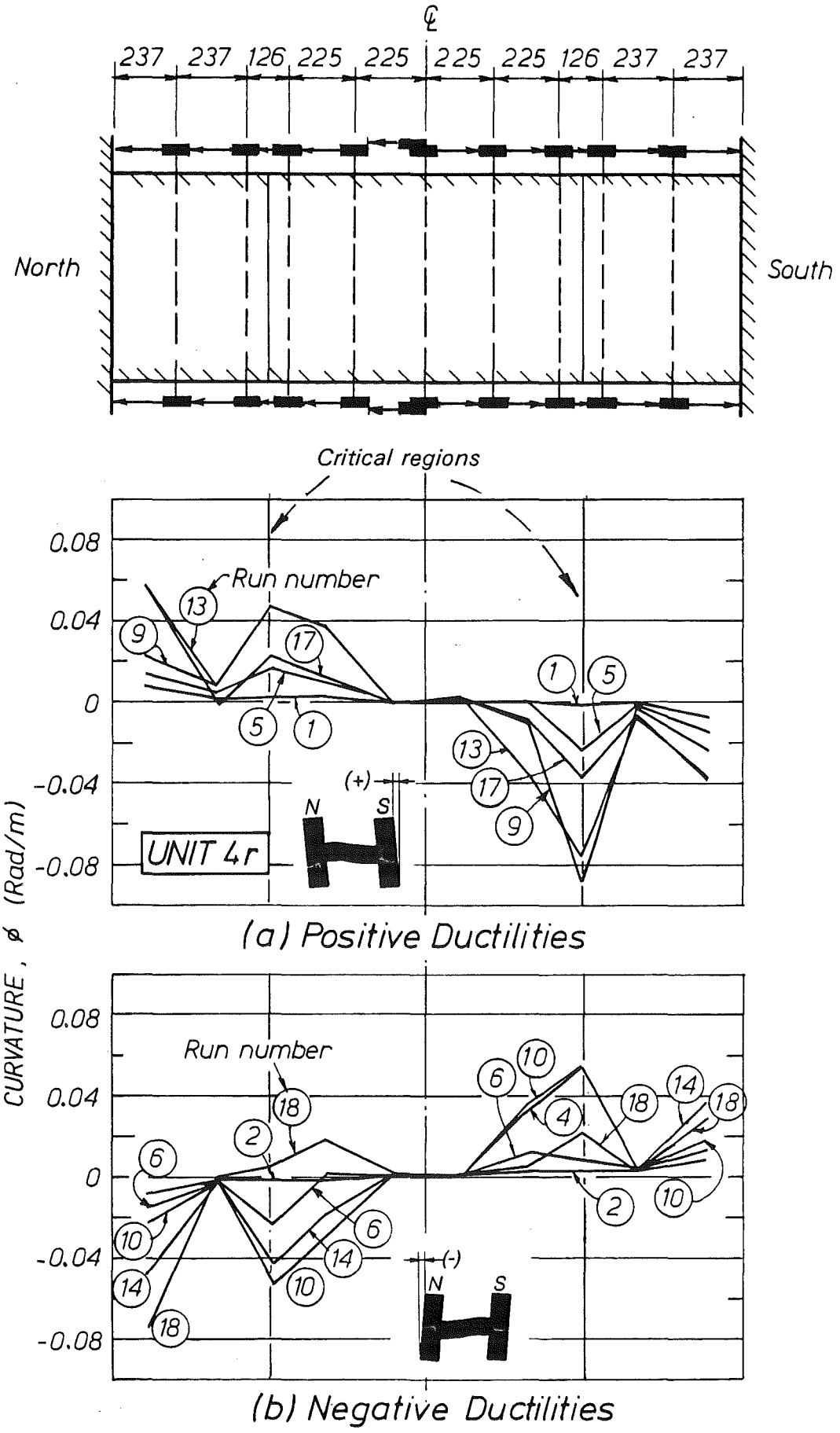

Fig. 5.14 - Curvature Distribution for the Beam of Unit 4r.

curvature rather than curvature ductility factors. This was because an experimentally defined yield curvature was discarded, since it was felt that the readings obtained by the linear potentiometers placed in the critical region at the bend of the diagonal bars would have been largely affected by the strain penetration of the bars inside the strong ends, which led to a fixed-end rotation.

Two distinct trends can be observed in Figs. 5.13 and 5.14. In Unit 4 the large curvatures were concentrated in the critical regions and although penetrating into the strong ends they decreased near the column faces. On the other hand, in Unit 4r large curvatures also concentrated in the critical regions but after the flexural capacity of the strong ends was reached they also spread from the column faces towards midspan. Unlike the curvature distribution in Unit 4, the curvature in the central region of the strong ends of the beam of Unit 4r was very small since yielding of the longitudinal reinforcement in this zone was delayed.

The curvatures in the reversal load runs in Unit 4 were significantly smaller than in the initial or positive load runs, because of the shearing of the beam at the bend of the diagonal bars. The curvatures attained in both tests were moderate and certainly much smaller than expected the response was dominated by flexure in the central region of the beam. Note that the flexural response in the central region was very small in the final cycles of each test (see Figs. 5.11 and 5.12).

5.8 BEAM BAR STRAINS AND STRESSES

5.8.1 Strain Profiles of the Beam Diagonal Bars

The bar strains recorded by the 5mm electrical foil strain gauges on the D24 diagonal bars in Unit 4 are shown plotted in Fig. 5.15. The strain profiles in the loading cycles in the elastic range were very uniform and only decreased in the beam-column joints. The average tensile strain in the D24 bars at the face of the column was 22% larger than that estimated using conventional elastic theory analysis, which assumed a parabolic distribution of stresses for concrete and the measured properties for steel. One reason for this difference can be attributed to the outer D28 bars not fully contributing to the flexural capacity of the unit because of the poor anchorage conditions in the critical region at the bend of the diagonal bars.

Unfortunately many readings in the region where large inelastic strains were taking place became unusable due to early debonding of the strain gauges. Therefore only reliable readings are plotted in Fig. 5.15. It is obvious that yielding of the longitudinal reinforcement was not confined to within the midspan region but it also spread inside the strong ends, reaching the column faces in the load cycles to $\mu_\Delta = \pm 4$.

During the repair of Unit 4 several debonded strain gauges were removed from the bars and were replaced by new ones. This permitted the complete strain profile of the longitudinal bars to be recorded, at least in the initial stages of the test on Unit 4r. The recorded strains of the D24 bars are plotted in Fig. 5.16 for the loading runs in the elastic and inelastic ranges for Unit 4r. In the stages in the elastic range, load runs 1 and 2, the strain profiles in the beam span showed a maximum strain at the column faces. The strain in the bars decreased slightly along the strong ends and peaked again in the central region of the beam. The measured strains at the face of the columns were, on average, 13% smaller than the strains measured in the same load runs in the test of Unit 4 and 6% larger than the theoretical strains predicted from the elastic analysis. Although it is not obvious that this difference was due to the effectiveness of the anchorage conditions of the D28 bars, that anchorage is certainly one of the reasons. As Fig. 5.17 illustrates the D28 bars were moderately stressed at the beginning of the anchorage in these load runs. Another reason could be the influence of the high strength concrete in reducing the lever arm for a given flexural demand. The effects of the high strength concrete are very difficult to quantify since the concrete near the face of the columns was composed of the two different concrete mixes used in the precasting and the repair.

5.8.2 Bar Stresses in the Reinforcement at the Bend of the Diagonal bars

Fig. 5.17 shows the stress level of the reinforcement at the bend of the diagonal bars estimated from measured strains in the test of the repaired unit, Unit 4r. Strain gauges were attached to the reinforcement in this regions in Unit 4r to monitor the transfer of forces in the repaired critical region of the beam.

As shown in Fig. 5.17 (a) the D28 bars were actively working since the beginning of the test. This indicates that it was possible to transfer forces between the diagonal bars and the bars located on the outer planes on the strong ends of the beams. Yielding of these bars finally occurred in the second cycle to $\mu_\Delta = 4$ due to the high lateral load attained during the test at this stage. When Fig. 5.17 (a) is analyzed in combination with Fig. 5.17 (b) it is evident that the transverse ties provided an effective clamping force as required by a shear friction mechanism. Only the stresses estimated from measured strains in the horizontal tie on the bottom side of the bend of the north diagonal bars show an erratic behaviour. It is likely that bending of the ties affected the stress measurements, since only one strain gauge was attached to the side of the reinforcing bars.

The stresses in the vertical steel straps calculated from measure strains indicate that, as expected in the intermediate and final stages of the test of Unit 4r, the shear force carried by this reinforcement was close to half of the beam shear force (see Fig. 5.17 (c)). In the cycle in the inelastic range to $\mu_\Delta = 2$, 34% of the shear was carried by the steel straps. This low value can be explained because the bars in the compression side have not yielded in tension and therefore they do not mobilize the vertical straps at this stage. In the loading runs to $\mu_\Delta = 4x1$ and $\mu_\Delta = 6x1$, the vertical steel straps carried 41% of the beam shear.

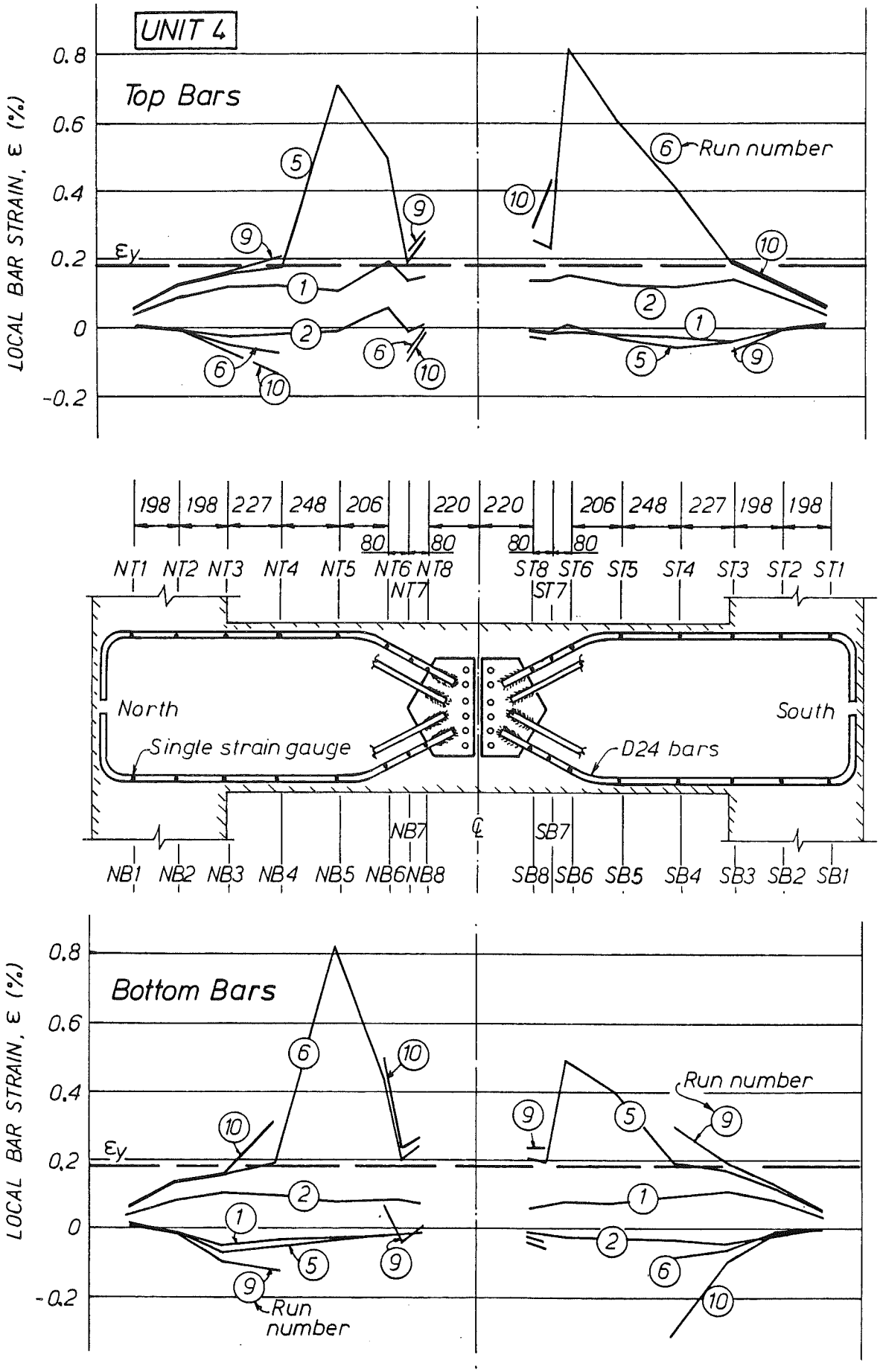

Fig. 5.15 - Strain Profiles for the Longitudinal Beam Bars of Unit 4.

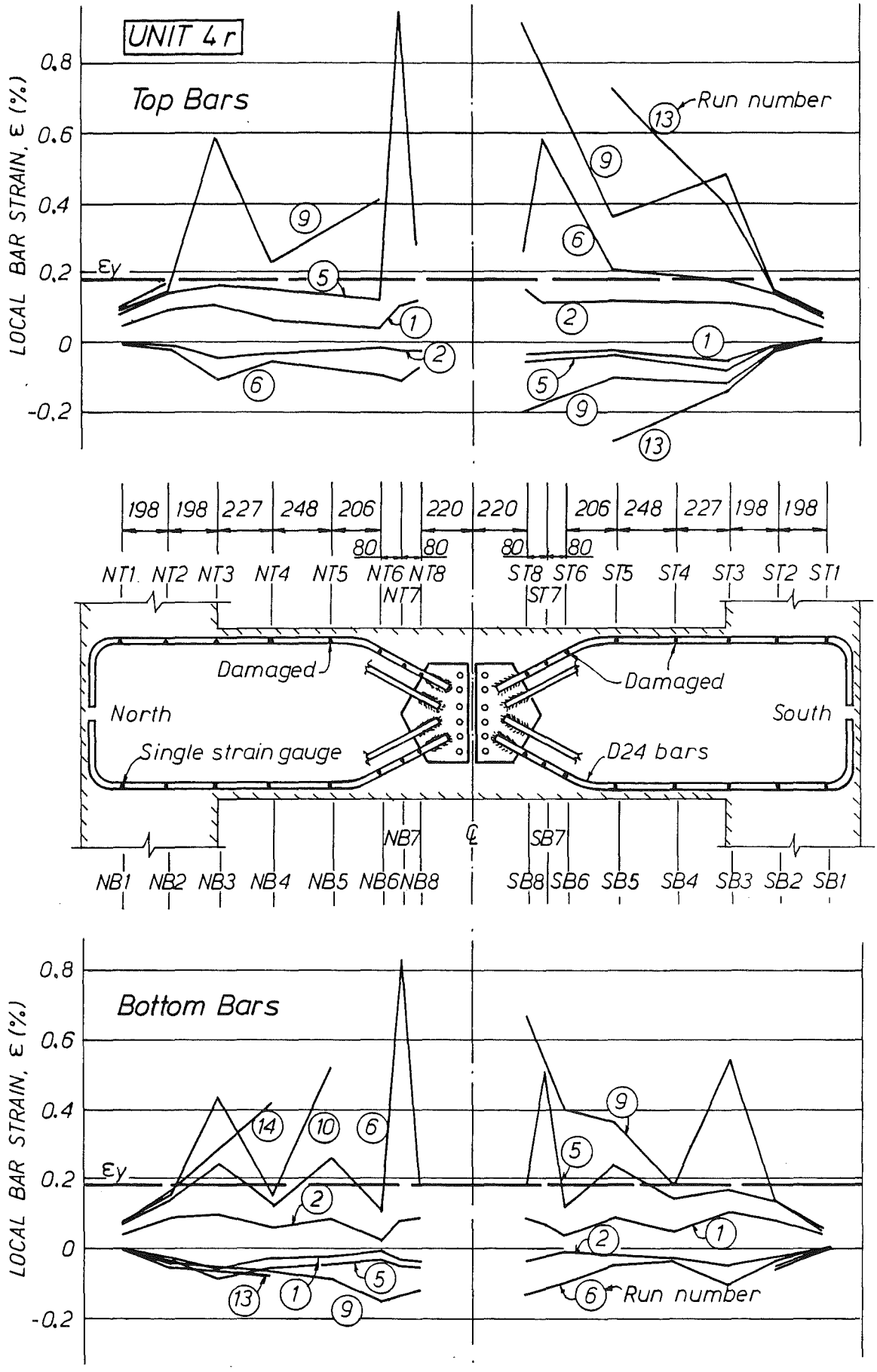

Fig. 5.16 - Strain Profiles for the Longitudinal Beam Bars of Unit 4r.

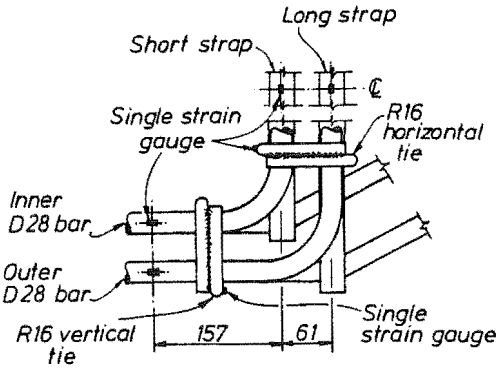

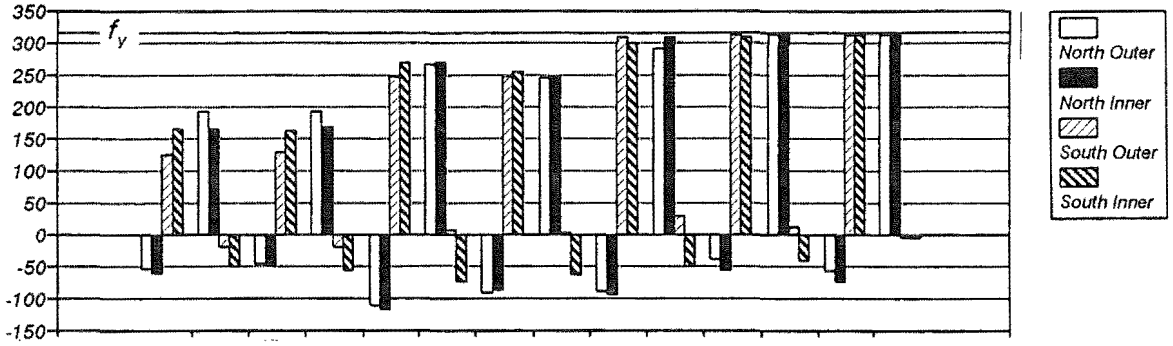

(a) Bottom D28 Bars

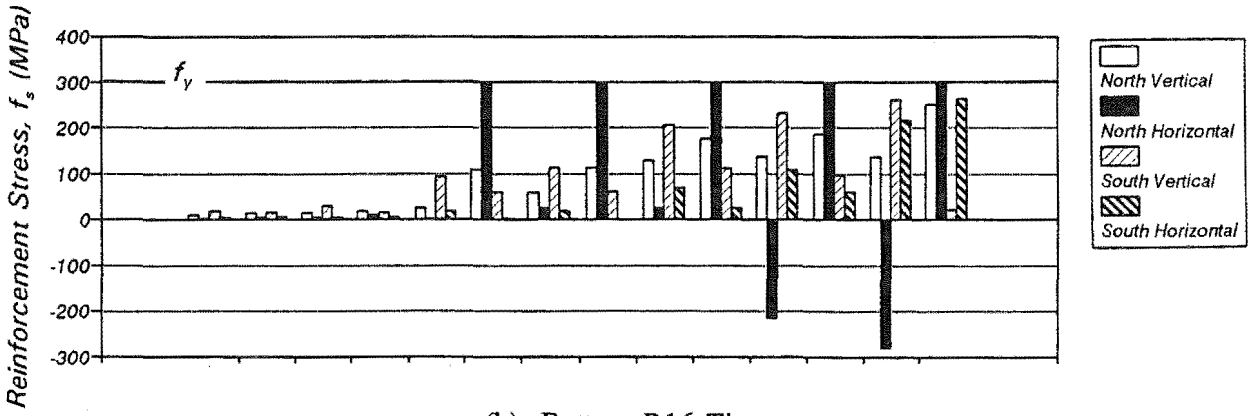

(b) Bottom R16 Ties

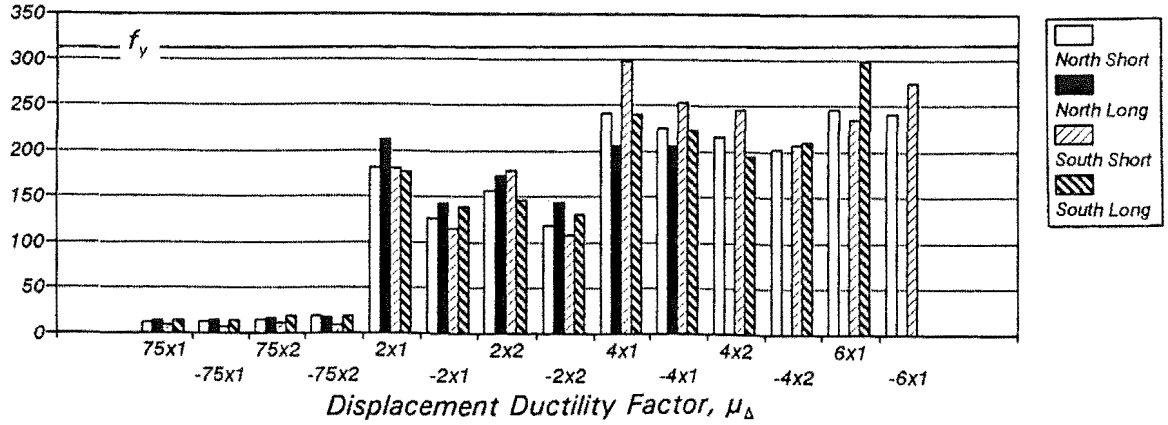

(c) 30x10mm Vertical Steel Straps

Fig. 5.17 - Bar Stresses in Reinforcement at the Critical Region of Unit 4r.

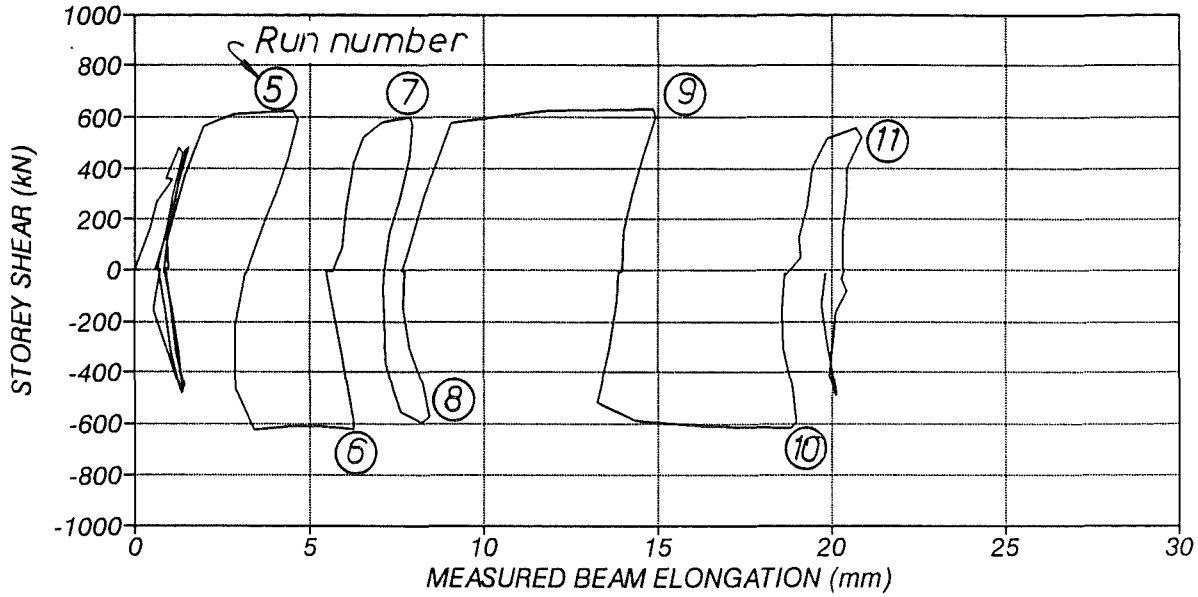

(a) Unit 4

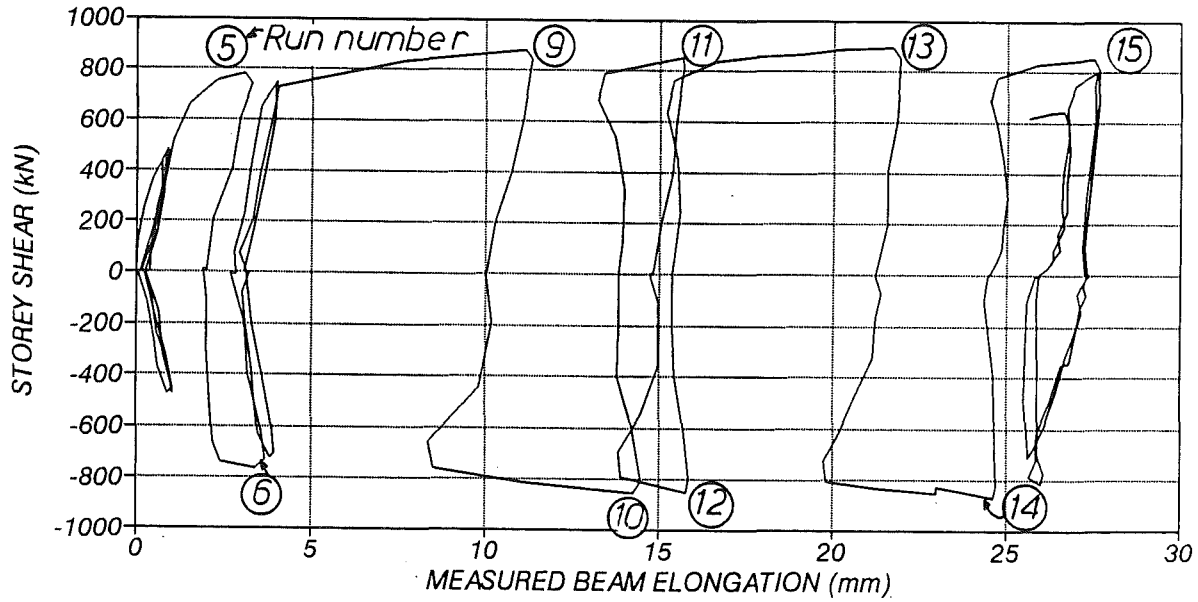

(b) Unit 4r

Fig. 5.18 - Measured Beam Elongation versus Storey Shear.

5.9 BEAM ELONGATION

The measured beam elongation of Units 4 and 4r is plotted in Fig. 5.18 against the storey shear. It is evident that the elongation recorded in the test is significant. However, an even larger elongation would be expected if most of the rotation in the beams had been concentrated at the critical regions. The measured elongation was not so large because in the final stages of the test the main source of rotation in the beam shifted towards the beam ends and also because shear deformations became dominant at this stage.

5.10 CONCLUSIONS

1. The experimental results obtained from the simulated seismic load conducted tests on a diagonally reinforced precast concrete unit, with relocated plastic hinges connected at the midspan at the beam by bolted steel plates, indicated that careful detailing of the regions at the bend of the diagonal bars is required if a full ductile response is to be attained. Two main points need to be considered in the detailing of these regions. First, transverse forces may arise as a result of the lay-out of the longitudinal reinforcement and adequate transverse reinforcement needs to be provided for those forces. Second, a bearing failure caused by crushing and shearing of the concrete in contact with the diagonal bars may occur. In the tests on the repaired unit transverse rods in contact with the inside of the bend of the diagonal bars was shown to be an excellent method for preventing bearing failure. A refined three dimensional truss model can be used to explain the behaviour of the unit in the first test and to design the reinforcement for the repaired unit.

2. Strain age embrittlement of the reinforcing steel at the bends of the diagonal bars was not observed during the test and retest of the unit. Three quarters of the bars had been artificially strain aged to observe this behaviour. However, it cannot be concluded that this phenomena might not be critical since strain age embrittlement is very susceptible to low temperature values and the temperature during the tests was about 17°C.

3. An additional overstrength factor owing to strain hardening and strain ageing of steel should be considered when assessing the post-earthquake capacity of a diagonally reinforced concrete member with relocated plastic hinges. Higher shear forces than normally estimated are expected to develop in a beam of this type, in which the diagonal reinforcement has previously yielded into the strain hardening region. As a result plastic hinges may form in the strong ends of the beam or elsewhere in the structure.

4. The design of the midspan bolted connection using standard procedures for structural steel resulted in satisfactory performance. Several loading cycles where the welded reinforcement

yielded in tension and compression at the connection region were imposed in the tests and no distress was observed in this region.

5. In the initial loading cycles in the elastic range, up to 38% of the imposed lateral deflection was caused by the flexibility of the strong end regions of the beam. It is therefore recommended that allowances for this flexibility be made in structural analysis.

CHAPTER 6

TEST RESULTS OF UNITS 5 AND 6

6.1 INTRODUCTION

Units 5 and 6 were cruciform shaped precast concrete subassemblages typical of the upper storeys of a perimeter frame of a multistorey building, where the absence of high axial compression loads in the columns would cause the most unfavourable conditions in the beam-column joint regions. System 1 of precast concrete construction used in New Zealand, and outlined in Chapter 1 (see Fig. 1.2 (a)) was, incorporated in Unit 5. The precast concrete beams of this subassemblage were partly precast and had the bottom reinforcement anchored in the cast in place beam-column joint region. The precast beams were seated on the cover of the concrete column below and cast in place concrete was placed in the joint region and in the top of the beams after placing and tying the additional beam top bars and the beam-column joint reinforcement (see Fig. 3.7).

Unit 6, on the other hand, had a precast concrete element typical of System 2, outlined in Chapter 1 (see Fig 1.2 (b)), where the beam and the beam-column joint were cast in the same operation. Vertical holes in the beam-column joint region of the beam were preformed using galvanized steel corrugated ducts to allow the vertical column bars protruding from the column below to pass through the precast beam member (see Fig. 3.8). A fluid and rich-in-cement grout was poured by gravity through one of the orifices to make the horizontal joint and to bond the vertical column bars to the beam.

Complete reinforcing details of these two units and the test sequence were presented in Sections 3.2.4 and 3.7 respectively. Both Units were designed for plastic hinging to form in the beams adjacent to the column faces. The shear span/effective depth ratio of the beams was 2.6 for both Units 5 and 6, which corresponds to beams with a clear span/depth ratio equal to 4.5. The beams of Unit 5 had approximately equal top and bottom beam longitudinal reinforcement, while the beams of Unit 6 were symmetrically reinforced. The nominal shear stress in the beams of both Units at an overstrength of 1.25 times the beam flexural strength was $v^\circ = V^\circ/bd = 0.23\sqrt{f'_c}$.

6.2 TEST RESULTS OF UNIT 5

6.2.1 General Behaviour

Unit 5 took a week to be tested. After the completion of loading cycles up to $\mu_\Delta = \pm 6$, at an interstorey drift of 3.6%, its lateral load capacity dropped to 80% of the maximum value recorded. The cumulative displacement ductility attained by Unit 5 was $\Sigma\mu_\Delta = 48$ equivalent to an available

displacement ductility factor $\mu_a = 6$. At the end of the test crushing of the concrete had occurred in the beams surrounding the top bars at the column faces. An earlier bond failure of these bars in the joint region meant that they were anchored in the beam where they would normally be subjected to compression. Neither the construction joints between precast and cast in place concrete, nor the anchorage of the bottom beam bars inside the beam-column joint region, were observed to have a detrimental effect on the general cyclic performance of Unit 5.

The visible cracking in the region of the beam-column joint of Unit 5 at different stages during the test is shown in Fig. 6.1. In the loading cycles in the elastic range, load runs 1 to 4, cracking spread along the top and bottom of the beams at regular intervals to a distance of 970mm from the column faces. The crack pattern in the beam was unsymmetrical. The top regions of the beams showed smaller cracks, with two cracks diagonally propagating towards the compression zone of the beam at the column faces. The bottom regions of the beams showed many fine cracks. The cracks in the beams at the face of the column were wider in the top region than in the bottom region. The maximum crack width recorded at this stage were 0.2mm and 0.3mm in the web and at the column faces, respectively. Some diagonal cracks propagated through the beam-column joint; the maximum width of these cracks was 0.25mm. The crack pattern in the column was very symmetrical and only the cracks at the horizontal construction joint showed a width comparable to the cracks in the beam. The crack widths in these regions of the column were 0.5mm, measured at the extreme fibres of the tension side of the columns.

In the loading cycles to $\mu_\Delta = \pm 2$, load runs 5 to 8, the main cracks concentrated in the beams at the faces of the column, where they reached a width of 5mm in the extreme tension fibres. It was observed that these cracks actually developed in the precast concrete beams rather than in the vertical construction joints. The crack pattern in the joint panel became denser but the width of the cracks there was small, reaching values of 0.8mm. The crack widths at the horizontal construction joint in the extreme tension fibres of the column were up to 1mm wide. Cracks elsewhere remained very fine.

The unsymmetrical behaviour of the top and bottom regions of the beams of Unit 5 became very obvious in the first cycle to $\mu_\Delta = 4$, load run 9. A 7mm crack concentrated in the south beam at the face of the column. Cracks elsewhere in this beam remained very small. On the other hand, the cracks in the bottom region of the north beam extended from the column face, thus spreading the plastic hinge. The main reason for this dissimilar behaviour was that the top beam bars tended to slip through the beam-column joint region.

In the reverse load run 10 to $\mu_\Delta = -4$, a similar crack pattern in the beams was observed. At this stage the top corners of the beam-column joint had been dislodged from the rest of the panel forming a cone around the beam reinforcement. Also, crushing of the concrete was observed in the top region of the south beam, confirming that the top bars were being anchored in the beam on the other side of the joint rather than in the joint itself. The cracks at the column face commencing at the bottom of the beam remained open, mainly because significant slip of these bars did not occur.

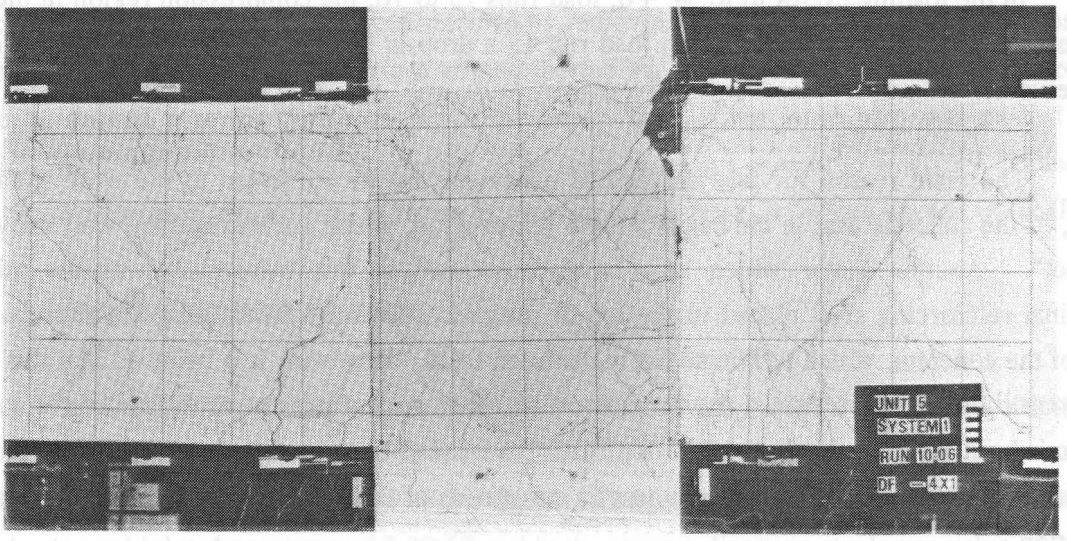

(a) At μ_Δ = -4x1

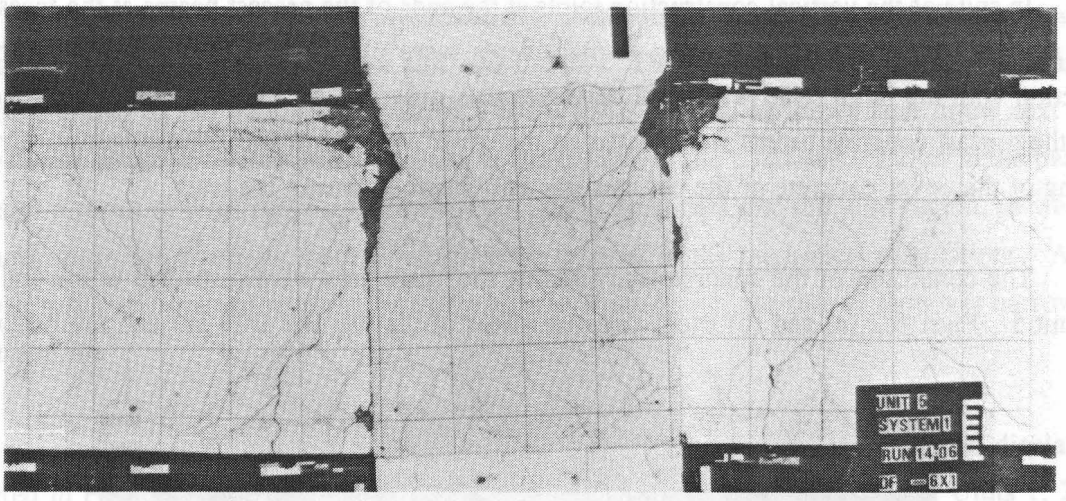

(b) At μ_Δ = -6x1

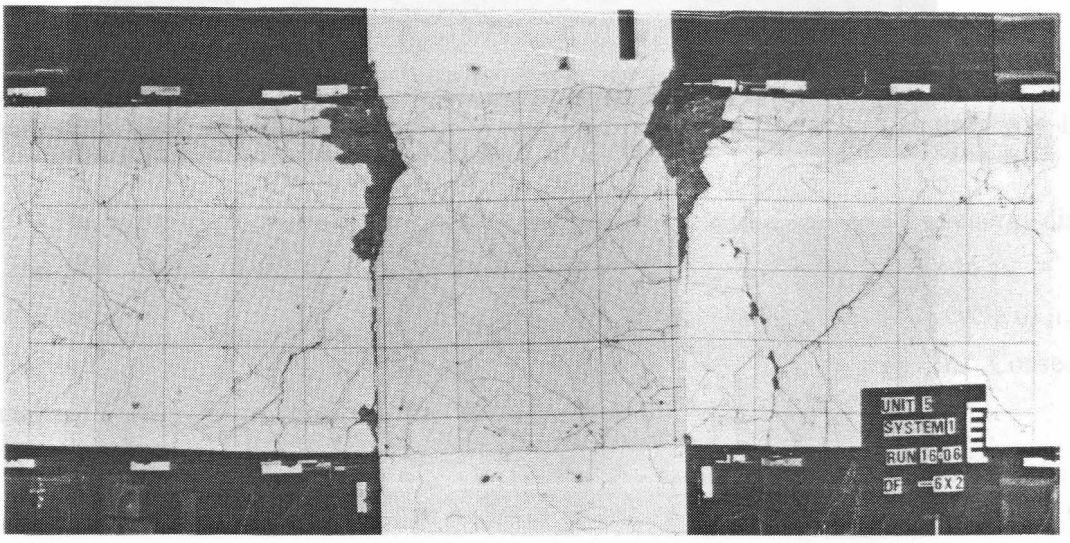

(c) At μ_Δ = -6x2

Fig. 6.1 - Cracking Beam-Column Joint Region of Unit 5 at Different Stages During Testing.

In the loading cycles to $\mu_\Delta = \pm 6$, load runs 13 to 16, the compression region in the top of the beams was gradually crushed until in load run 15 a drop in lateral load carrying capacity of 19% was observed.

The main reason for this unexpected behaviour can be attributed to the poor quality, not strength, of the concrete cast in the beam-column joint region, which accentuated the well known "top bar effect". Another factor which may have contributed to this behaviour, was the minimum longitudinal reinforcing steel placed in the top of the precast beams, for holding the stirrups during casting of the concrete, which terminated at the column faces. However, it is believed that this second factor alone could not have caused the rotation of the beam to concentrate at the face of the columns. Tests carried out by Park and Bull (1986) on filled prestressed U-beams showed the plastic hinges did not concentrate at the face of the column despite the strands of the precast U-beam being terminated at this location.

In spite of the vertical construction joints at the ends of the precast beams at the faces of the column, no large relative vertical sliding displacements were observed in this test. This apparent contradiction with the large relative vertical displacements observed by Beattie (1989) stems from the fact that the precast concrete beams were seated on the cover concrete of the column below. Crushing or spalling of the cover concrete of the column was not observed during the tests.

The conditions of the concrete surrounding the beam bars were inspected at the end of the test of Unit 5. Figs. 6.2 (a) and (b) show close up views of the top east D24 bar and the bottom east

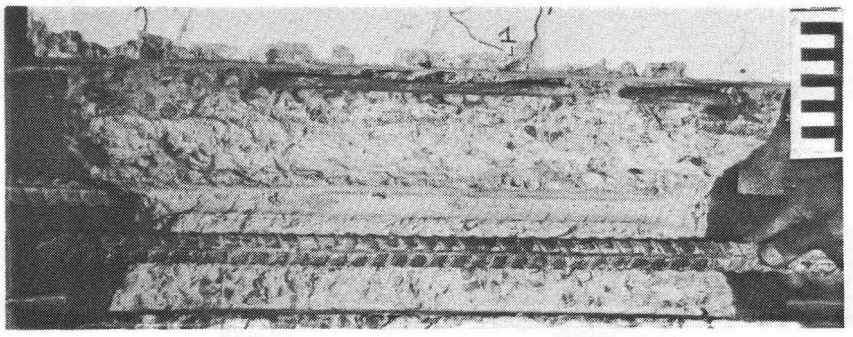

(a) Top East D24 Bar

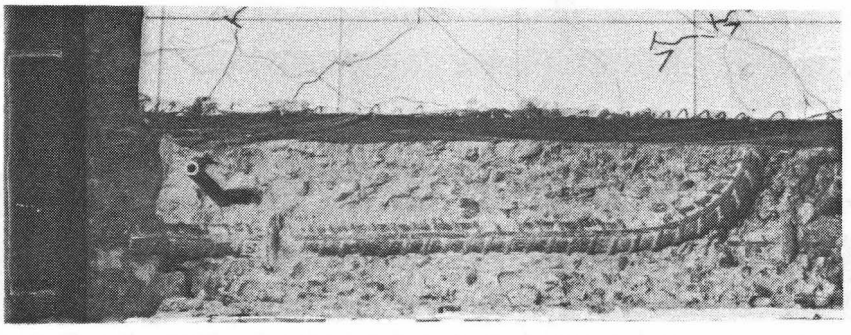

(b) Bottom East D28 Bar

Fig. 6.2 - Beam Bars in the Joint Region of Unit 5 after the End of Test.

D28 bar, respectively. These views were obtained by removing the side cover concrete to expose these beam bars. It can be seen that the surface around the top bar is very smooth. Crushed concrete was found to be packed near the deformations of the bars. One of the inner bars was pushed with a hydraulic jack to measure the residual friction. The frictional force measured was very dependent on the rate of displacement applied but, in terms of average bond stress, it did not exceed 0.18MPa.

6.2.2 Load-Displacement Response

The lateral load versus the lateral displacement response at Unit 5 for the loading cycles in the elastic range is shown in Fig. 6.3. The stage at which first cracking appeared in the beams, columns and beam-column joint is also presented in this figure. The joint cracked in the positive direction at a nominal horizontal joint shear stress of $0.39\sqrt{f'_c}$ and in the reverse direction at a lower value of $0.33\sqrt{f'_c}$. The "elastic" stiffness of this Unit was 17.1kN/mm equivalent to only 42.1% of that predicted in Section 3.2.1. The interstorey drift at the projected first yield displacement was 0.59%, and that at the dependable lateral load capacity of the unit was 0.54%. This value exceeded by a large margin the limitation imposed by the NZS 4203 Loadings Code (1984). As will be shown later in the next section, the large error in the predicted initial stiffness is chiefly due to the fixed-end rotation in the beams and columns as a result of the strain penetration of the longitudinal bars into the joint region, as well as the joint panel shear deformations, both of which were ignored in the theoretical calculations. As it has been observed and discussed with regard to the tests in Units 1 to 3, the second loop was narrower than the first one.

The complete hysteretic response of Unit 5, in terms of the lateral load and displacement, is depicted in Fig. 6.4. The post-elastic stiffnesses defined in the same way that for Units 1, 2 and 3, were 2.3 and 1.3% of the initial "elastic" stiffness for the positive and negative cycles respectively. The positive load runs consistently attained higher loads than the negative load runs.

In the first load run in the inelastic range, the lateral load attained exceeded by 8% the theoretical lateral load, H_a. In the reverse load run, load run 6, the lateral load attained was $1.04H_a$.

The hysteretic loops were very stable until the first cycle to $\mu_\Delta = \pm 4$. The energy dissipated was 79 and 55% of that of the ideal bi-linear loops, respectively, in the two cycles to $\mu_\Delta = \pm 2$ and 57% in the first cycle to $\mu_\Delta = \pm 4$. Pinching of the loops commenced in the second cycle to $\mu_\Delta = \pm 4$ mainly due to the commencement of slip of the top beam bars inside the joint region. Consequently, the normalized energy dissipated dropped to 22% in that load cycle.

In the loading cycles to $\mu_\Delta = \pm 6$, the normalized energy dissipation amounted to only 34 and 23% for the first and second cycle, respectively. The maximum lateral load overstrengths were attained in the first loading cycle to $\mu_\Delta = \pm 6$, load runs 13 and 14, and were $1.14H_a$ and $1.08H_a$. The maximum beam shear, in terms of the nominal shear stress $v^\circ = V^\circ/bd$, was $0.2\sqrt{f'_c}$.

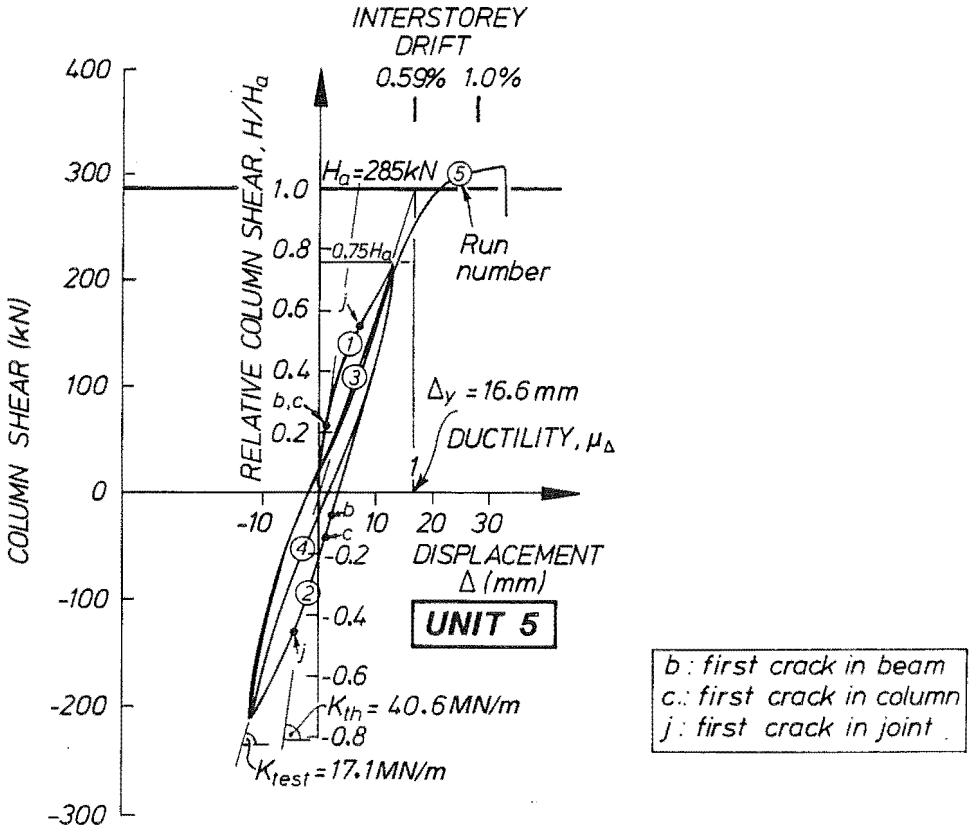

Fig. 6.3 - Lateral Load-Lateral Displacement Response of Unit 5 During the Cycles in the Elastic Range.

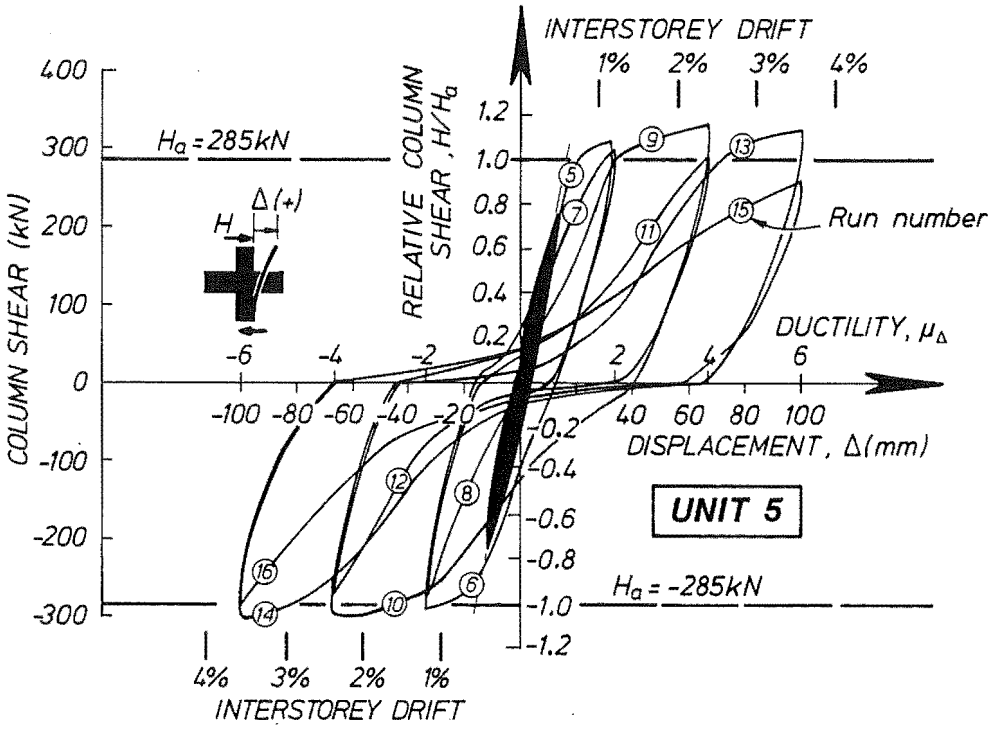

Fig. 6.4 - Lateral Load-Lateral Displacement Response of Unit 5.

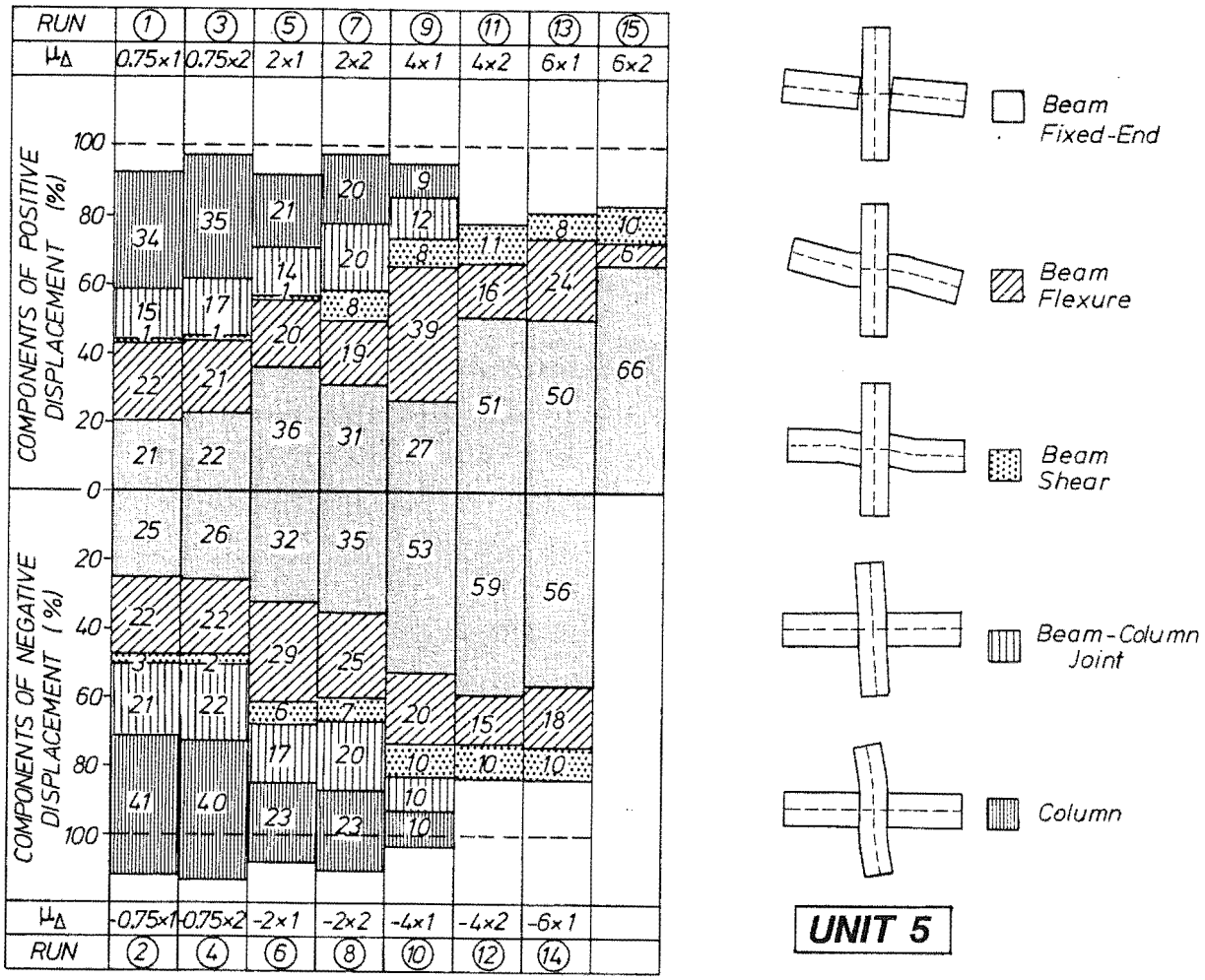

Fig. 6.5 - Components of Lateral Displacement of Unit 5 at Peaks of Load Runs.

The cumulative energy dissipated by the hysteretic response accounting for all the loading cycles in the inelastic range, including that dissipated in load run 16, was 35% of that dissipated by the ideal bi-linear loops.

6.2.3 Decomposition of Lateral Displacements

The components of the total lateral displacement at the peak of each load run is illustrated in Fig. 6.5. In the loading cycles in the elastic range the largest contribution came from the column, which contributed from 34 to 41% of the imposed lateral displacements. However, because the column remained essentially elastic, with minor cracking, its contribution towards the total displacement became less important during the remainder of the test. The fixed-end rotation of the beams made an important contribution to the lateral displacements in the elastic range, and since the top beam bars eventually slipped in the joint this mode of deformation became dominant. Flexure deformations along the beams in the inelastic range arose mainly from the spreading of the plastic hinge regions in the beams during positive bending moment. This flexural contribution was of a similar magnitude to that from the distortion of the joint panel.

Note that the deformations of the column and joint in Fig. 6.5 are not shown beyond the first semi-cycle to μ_Δ = +4x1, because the instrumentation was disturbed by the loss of the corners of the beam-column joint panel.

6.2.4 Joint Behaviour

6.2.4.1 Strains in the Transverse Reinforcement

The transverse reinforcement in the beam-column joint region was designed in accordance with the current Concrete Design Code [NZS 3101 (1984)], which in the absence of axial compression load in the column required the whole horizontal shear at overstrength of the longitudinal reinforcement to be taken by the transverse reinforcement. This approach has been proved to provide an upper bound and therefore no yielding of the joint hoops was expected to occur.

Fig. 6.6 shows the strains in the hoops at different peak load runs, which were monitored by two 5mm electrical strain gauges placed on opposite sides of the perimeter hoops to cancel out the effects of hoop bending. In general, the central hoop showed the larger strains but the strain distribution throughout the set of hoops was rather uniform.

It can also been seen in Fig. 6.6 that beyond load run 9 to $\mu_\Delta = \pm 4$ the strain in the top hoops decreased. On the other hand the strain of the bottom hoops always increased with the test sequence. This effect was due to the bond conditions of the beam bars. The top bars commenced to slip from load run 9 because of bond degradation, and the most of the shear resistance had to come from the diagonal concrete strut mechanism. In contrast, very little slip occurred on the hooked bottom bars and hence part of the bond forces were transferred by the diagonal concrete strut mechanism and the other part mobilized the truss mechanism. These mechanisms of joint shear resistance will be discussed in detail in Chapter 7.

6.2.4.2 Slip of the Beam Bars

The local bar slip of the top D24 beam bars, at three locations in the beam-column joint, are shown in Fig. 6.7. The procedures for determining, and limitations on the definition of local bar slip, were discussed in Section 3.8.4.

The local bar slip at each of the locations shown progressively increased with the test. In load run 10 to μ_Δ = -4x1, the amplitude of the slip at the centre line of the column and in the north side exceeded the clear distance of 11mm between the bar deformations. In the following load run, the local bar slip everywhere else in the joint core exceeded this distance indicating that the concrete surrounding the top bars had been completely sheared off and bond could only be transferred by friction and not by mechanical contact between the bar deformations and the surrounding concrete. This significant slippage resulted in concentration of the rotation of the beam at the column face, where a single large crack developed.

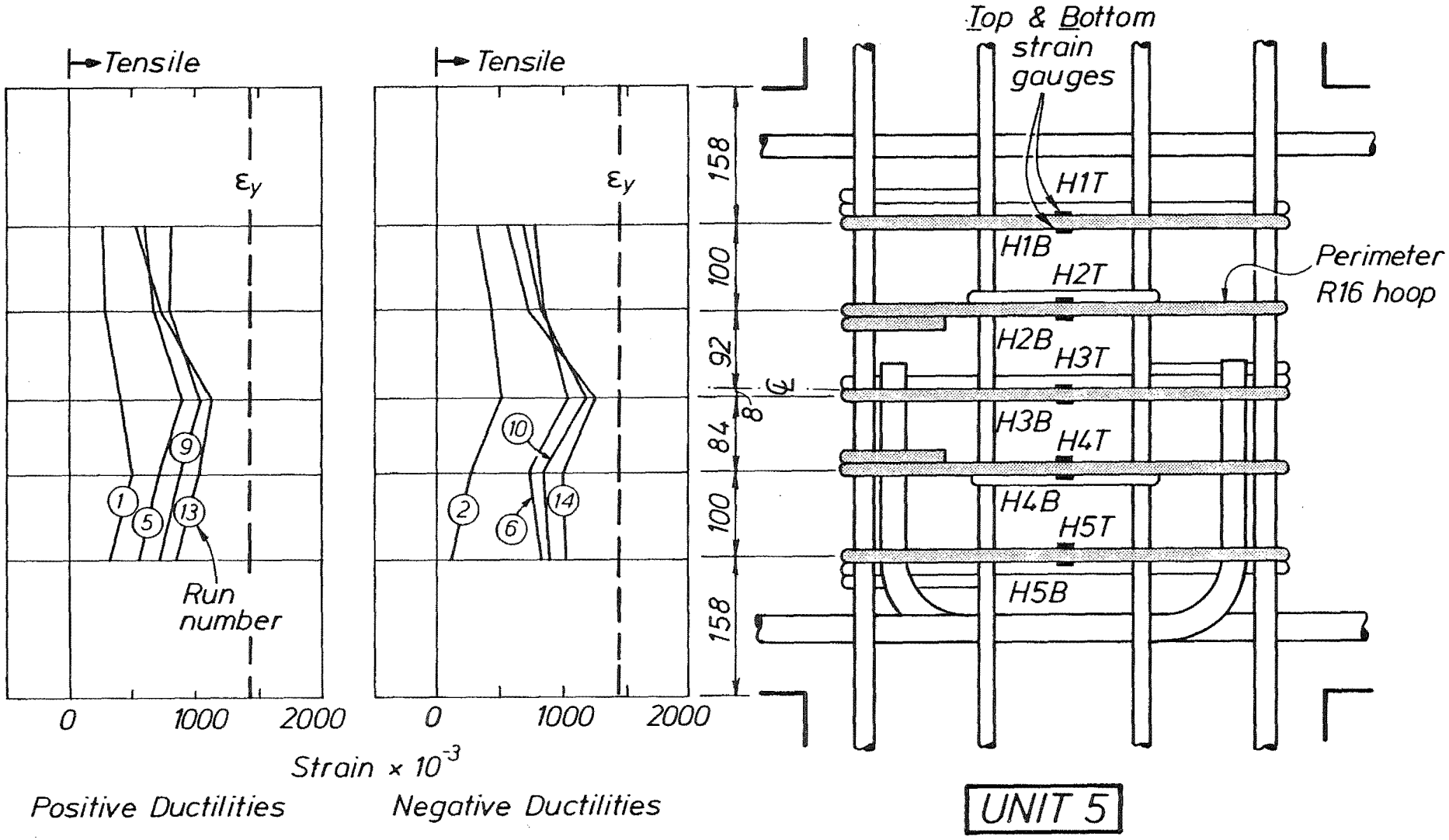

Fig. 6.6 - Measured Strains in Joint Hoops of Unit 5.

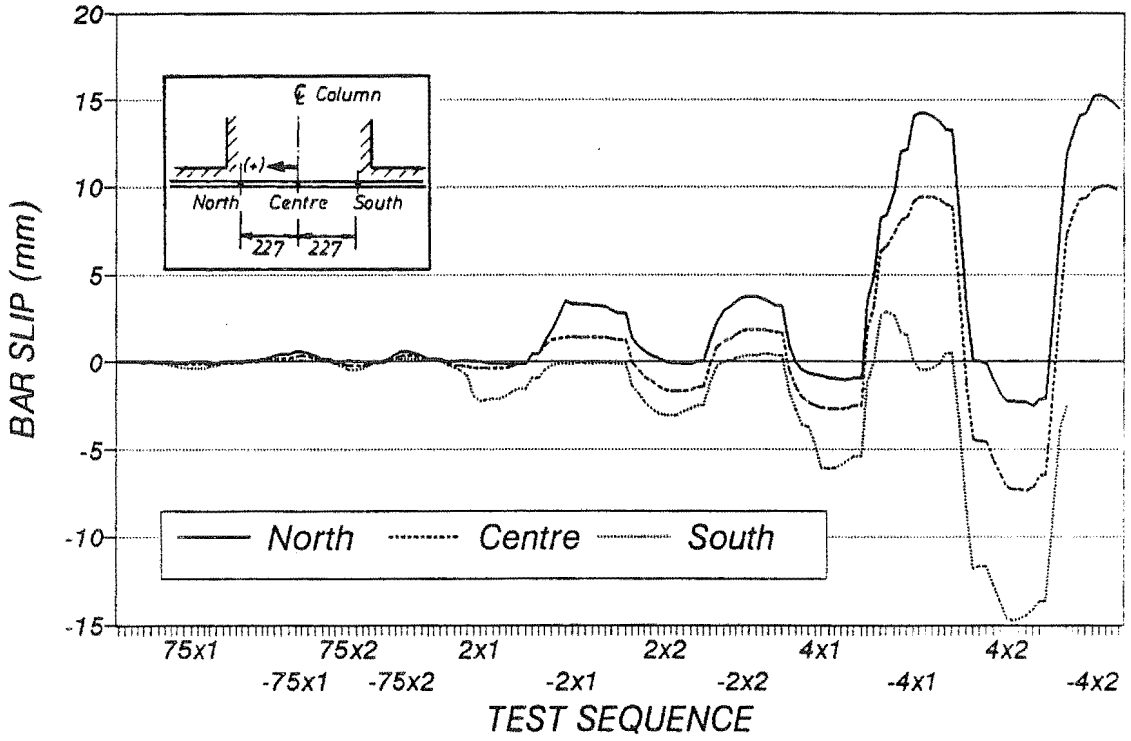

Fig. 6.7 - Measured Slip of Top Beam Bars of Unit 5.

The instrumentation became unreliable beyond load run 12 when the studs welded to the reinforcing bars were bearing against the walls of the hole provided as clearance.

6.2.4.3 Bar and Bond Stresses of the Beam Longitudinal Reinforcement

Figs. 6.8 and 6.9 show the bar and bond stresses for the top and bottom longitudinal bars of the beam anchored in the beam-column joint region.

Bar stresses were estimated using the cyclic strain-stress model for steel discussed in Chapter 2 and the bar strain history collected from the electrical resistance strain gauges attached at regular intervals to the reinforcing steel. In addition the stresses in the reinforcement at each end of the joint during the loading cycles in the inelastic range were calculated from the data collected from the clip gauges. Electrical resistance strain gauges and clip gauges were attached to different bars. In spite of this, it is assumed that the stress is the same in both bars. This assumption is made because the electrical resistance strain gauges located on the bars at the face of the column failed prematurely in the tests. In addition, in Fig. 6.8 and 6.9 is also assumed that the calculated bar stresses at the level of the clip gauges are the same as the bar stresses measured by electrical resistance strain gauges at the column faces. The bond stresses shown in this figures were obtained dividing the difference of stresses between two consecutive gauged points by their distance and by the nominal length of the circumference of the bar.

In the loading cycles, in the elastic range, the load run numbers 1 and 2 in Fig. 6.8, the top bars were in tension all along the joint and hence they were anchored in the compression region of the

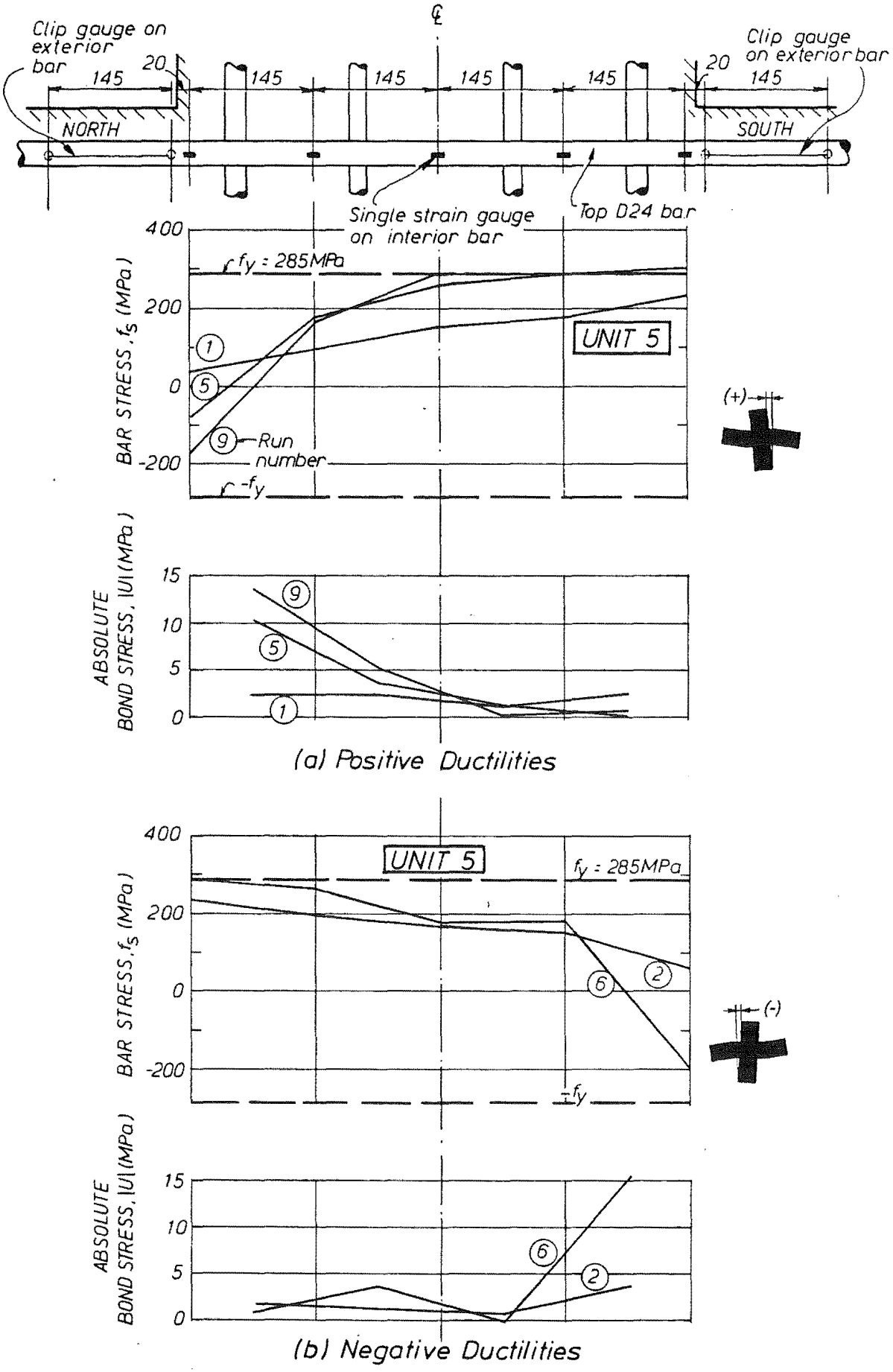

Fig. 6.8 - Bar and Bond Stresses - Top D24 Beam Bar of Unit 5.

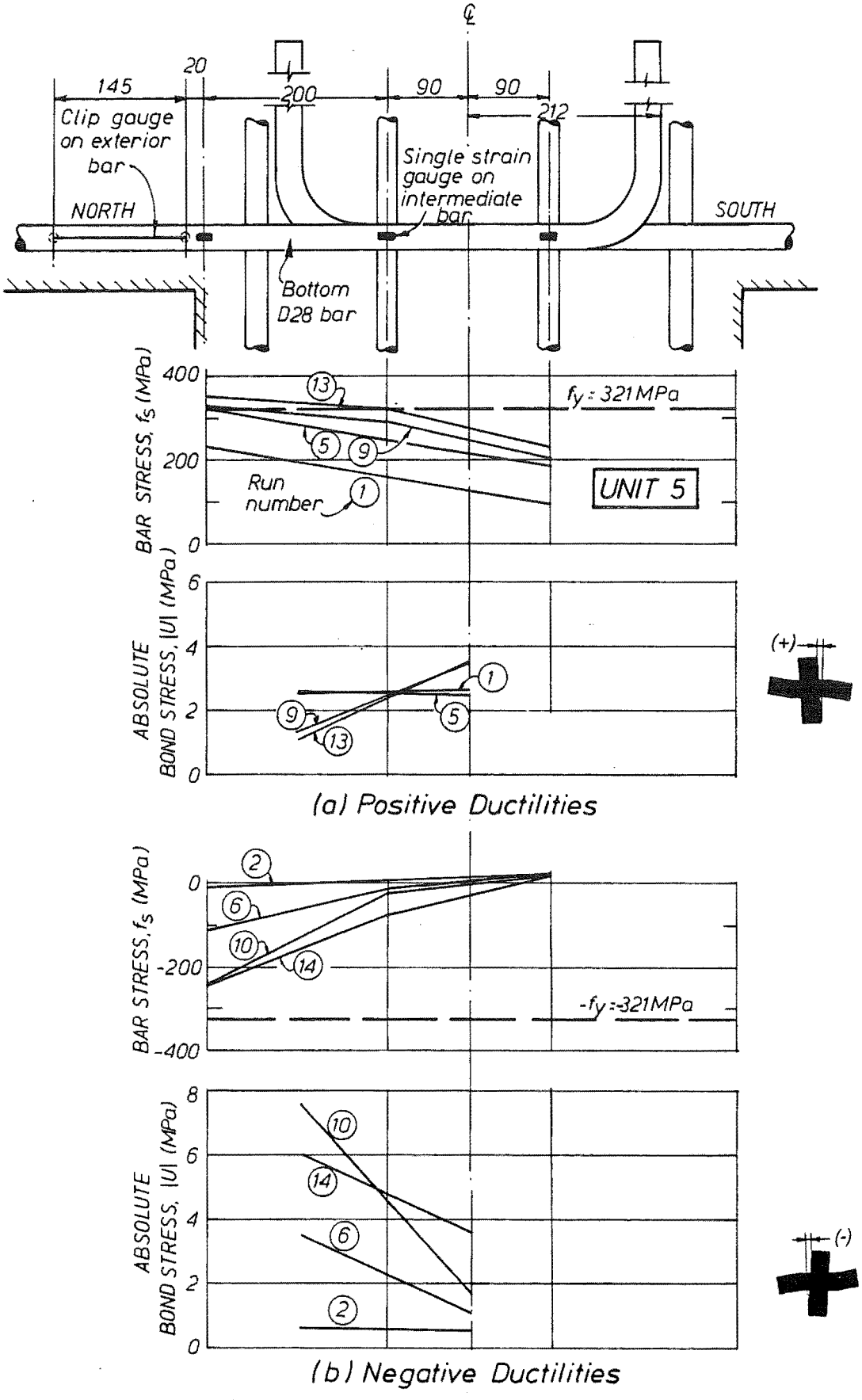

Fig. 6.9 - Bar and Bond Stresses - Bottom D28 Beam Bar Unit 5.

opposite beam, where they would normally be considered to be in compression. The bond stresses at this stage of load were fairly uniform for both directions of loading although there was a trend to increase where the concrete compression stress block from the column acted. This trend was accentuated during the loading cycles in the inelastic range, load runs 5 to 9, when the bond stresses peaked at 15.3MPa. In any case the bond stresses for the top bars at the column centreline did not exceed 5MPa. Yield in the reinforcement penetrated to the column centreline, distance equivalent to $12.5d_b$. Data could not be collected beyond load run 9 at $\mu_\Delta = \pm 4x1$ because all the circuits of the electrical resistance strain gauges were damaged when the top bars slipped.

The bar stress distribution at the bottom north D28 hooked beam bar is also shown in Fig. 6.8. In the positive load cycles, when the bar was subjected to tension, part of the tension force was transferred to the joint core by bond and, in the loading cycles in the inelastic range, a large portion of the force was transferred by the hook of the bar. Yield of the bottom bars penetrated into the joint core to about 210mm from the face of the column. This is equivalent to a distance of $7.5d_b$. It can be observed that the bond stresses at positive ductilities was very uniform at the beginning of the test, but the bond strength deteriorated with the penetration of yield.

A very different behaviour characterized the bar and bond stress distribution of the bottom hooked bars in the load runs at negative ductilities. Most of the bar compressive force was transferred to the joint core near the face of the column where the concrete compression stress block of the column was acting. Bond forces were, then, higher in this region. The stresses in the bar at the beginning of the loading runs were very small, and even were in tension, indicating some internal build up in stresses in the previous loading cycles when the bars were subjected to tension.

The ratio of forces at the beginning and at the end of the hook of the bottom north bar is depicted in Fig. 6.10. This ratio is only shown for load runs to positive ductilities when this bar was in tension. In the loading cycles in the elastic range, when the stress at the beginning of the hook was about 100MPa and the bar behaved elastically throughout its length, the ratio of forces ranged between 1.4 and 1.1. It can be found that the resultant force R in Fig 6.11 forms an angle to the horizontal between 45^0 and 55^0 if the frictional bond resistance along the bend of the hooks is ignored.

In the loading cycles in the inelastic range the ratio of forces at the beginning and at the end of the hook dropped considerably and ranged from 0.4 to 0.5. This low ratio implies a resultant force, R, having an unreasonable angle of inclination to the horizontal of between 22° and 29°, if the bond stress around the hook of the bars is neglected. What appears to happen is that the frictional bond stress around the concave side of the bend plays an important role and cannot be ignored. This effect is depicted in Fig. 6.11.

A common characteristic of the behaviour of top and bottom longitudinal beam reinforcement is that the compressive force carried by the bars at the face of the column was smaller than the tension force at the other face. The compression stress is always below yield, in spite of the beams being approximately equally reinforced. A similar observation was also made in the test of Unit 2 although in that test the recorded strains were not made at the face of the columns but farther away along the span

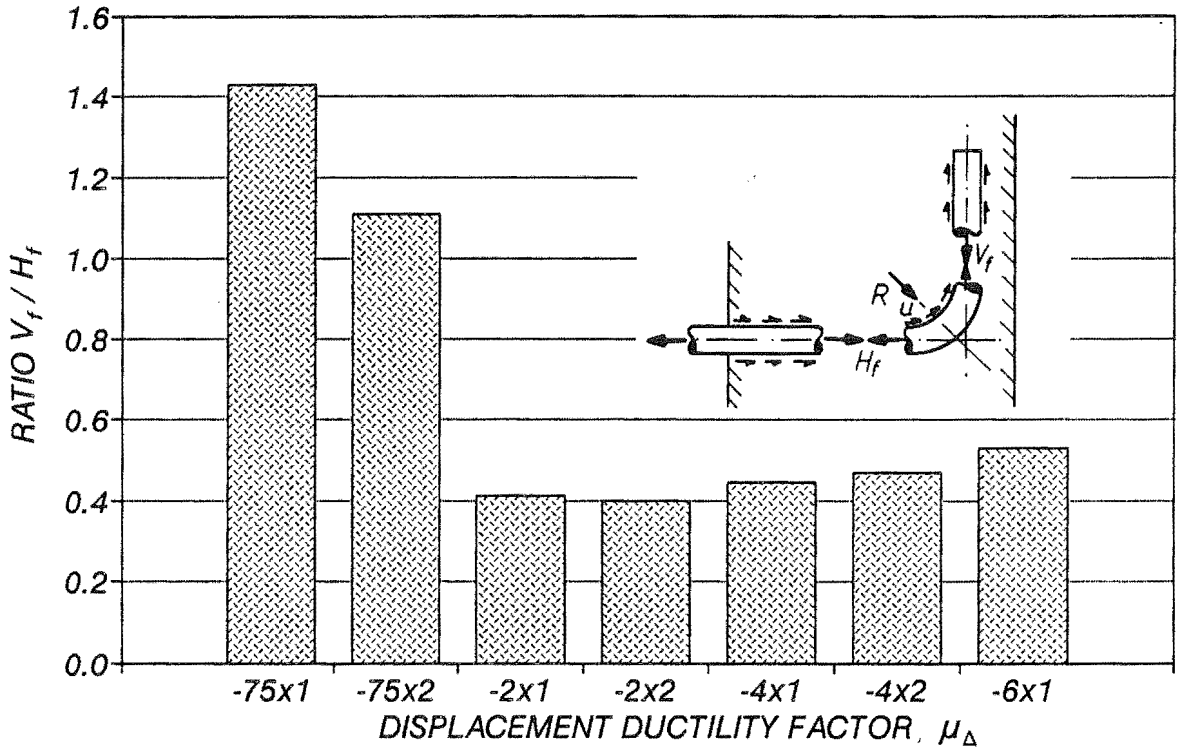

Fig. 6.10 - Ratio Between Forces at the Beginning and End of the Hook in Bottom D28 Beam Bar of Unit 5.

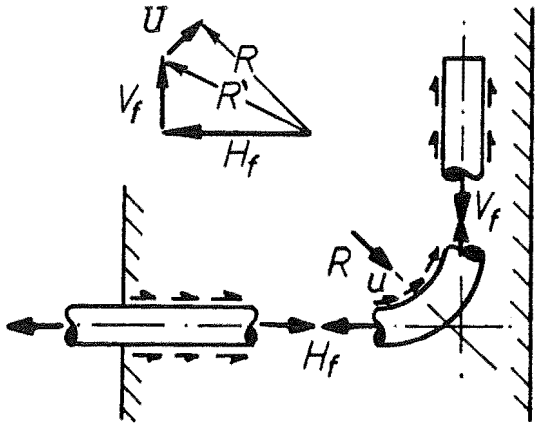

Fig. 6.11 - Effect of Bond Stresses Acting on Hooked Anchorage of Unit 5.

of the beam. Fig. 6.12 plots the predicted bar force in the compression zone of the beam and the estimated total compression force against the measured bar strain. The bar force was determined from the measured bar strain assuming that all the reinforcement was subjected to an equal strain history. The total compression force was found from the shear force in the beams, measured at the beam ends by load cells. It is evident that when the bars go into compression they supply only a fraction of the total compression force with the remainder being provided by compression in the concrete. One question that may arise is: How can the concrete transfer any force if it is widely cracked around the bars? An answer to it is that in this region the hypothesis of plane sections remain plane after bending is not valid. That is, no compatibility of deformations can be assumed on this basis. Instead, a truss model is more applicable. Also, shear deformations and debris cause cracks to transfer compression stresses before they close. A large percentage of the shear in the beam enters the joint region by a diagonal compression strut, which provides the remaining compressive force in the beam. This mechanism of shear transfer in the beam plastic hinges will be discussed in Chapter 7.

6.2.4.4 Bar and Bond Stress of the Column Vertical Reinforcement

Figs. 6.13 and 6.14 show the bar and bond stresses of the strain gauged vertical column bars of Unit 5. Fig. 6.13 plots the results obtained from the south-west corner bar. In the loading cycles in the elastic range, load runs 1 and 2, the bars were in tension over a distance of 24 d_b from the beam faces. This strain penetration led to the wide crack observed to develop at the vertical construction joints. In the loading cycles in the inelastic range the bars yielded in tension. In load run 6 it appears that yield penetrated 270mm into the joint. Unfortunately the strain gauge CE4 at this location failed prematurely after this load run. A simple elastic theory analysis indicates that yield in tension of the vertical column bars at the level of the beam longitudinal reinforcement would commence at a lateral load of $1.12H_a$, a value which was only attained at the final cycles of the test.

Beckingsale (1980) observed a similar effect in the testing of two interior beam-column joint units and postulated the cause to be disturbances resulting from the bond forces of the beam bars. It is believed in the present study that the increase in stress in the outer column bars in tension results of a combination of two different sources. First, the intermediate column bars are required to provide part of the column flexural resistance and the vertical resistance of the inclined truss in the joint panel. When these bars yield due to the combined action, additional flexural resistance cannot be provided and consequently higher tensile stresses are necessary to develop in the outer column bars in tension. Second, it has been observed in this, and other studies, that after few reversal cycles in the inelastic range the column cover along the longitudinal beam bars is dislodged and cannot be fully used to transfer compressive stress in a reduction of the column lever arm and in an increase of the stresses in the tension reinforcement, in order to maintain the equilibrium of the column as a free body with a lateral load directly applied at the end of it.

The bond stresses of the corner bars of the column plotted in Fig. 6.13 indicate that in the loading cycles in the elastic range the bond stresses, as for the beam bars, increased towards the region where the concrete compression stress block of the beams acted. Unfortunately, it was not possible to

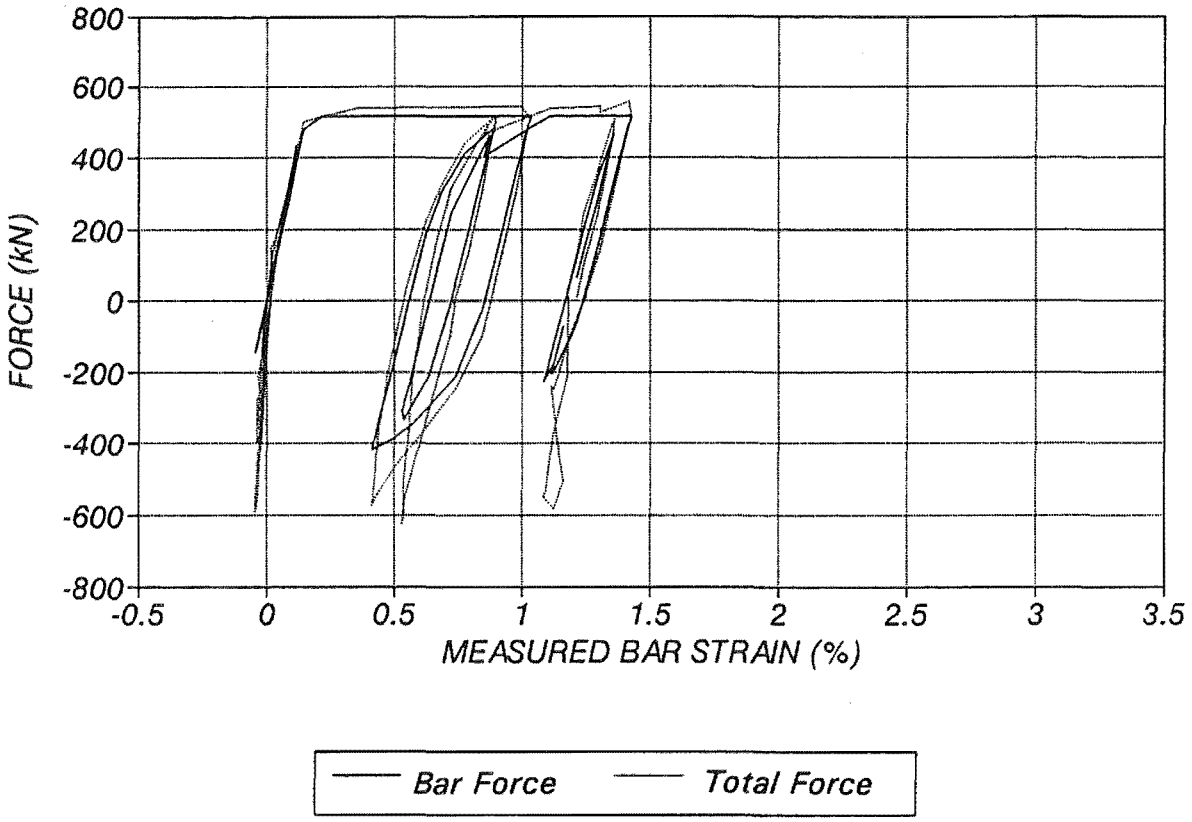

(a) Top North Bars

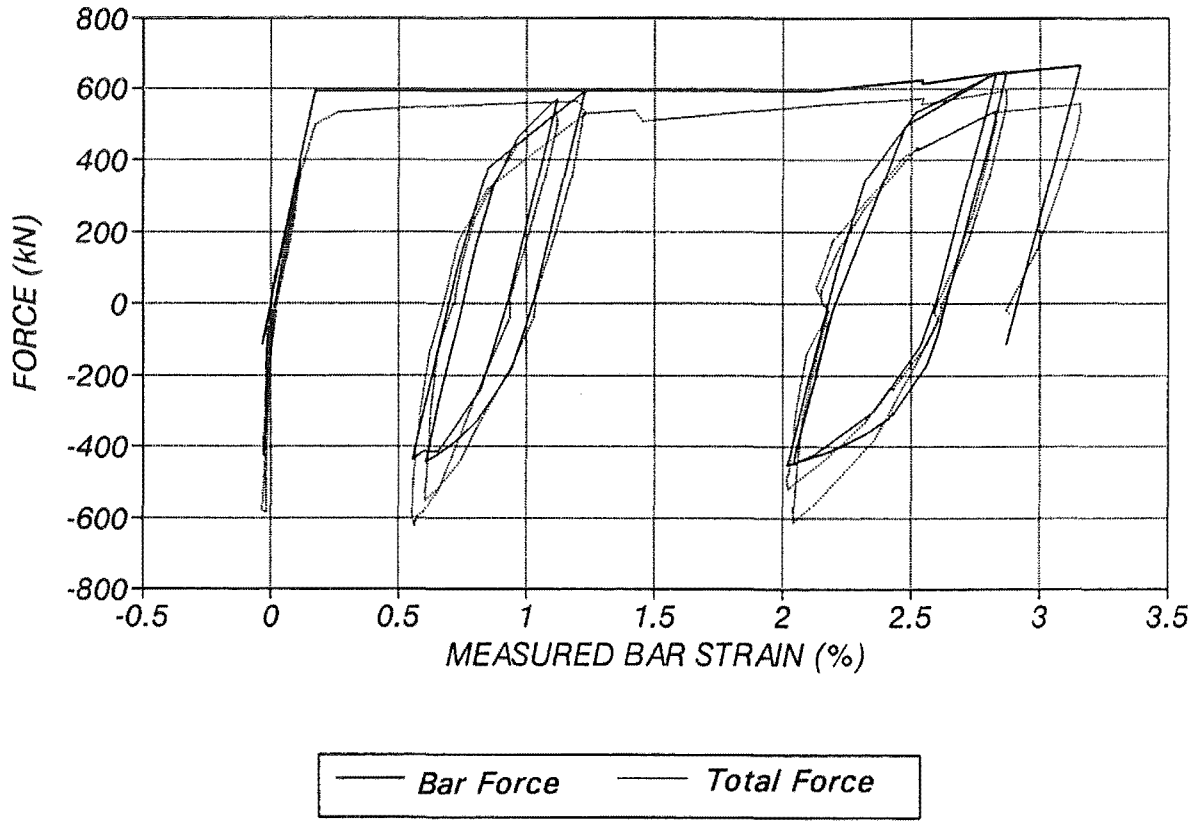

(b) Bottom South Bars

Fig. 6.12 - Predicted Bar Forces versus Measured Total Force in the Beam 78mm from the Column Face of Unit 5.

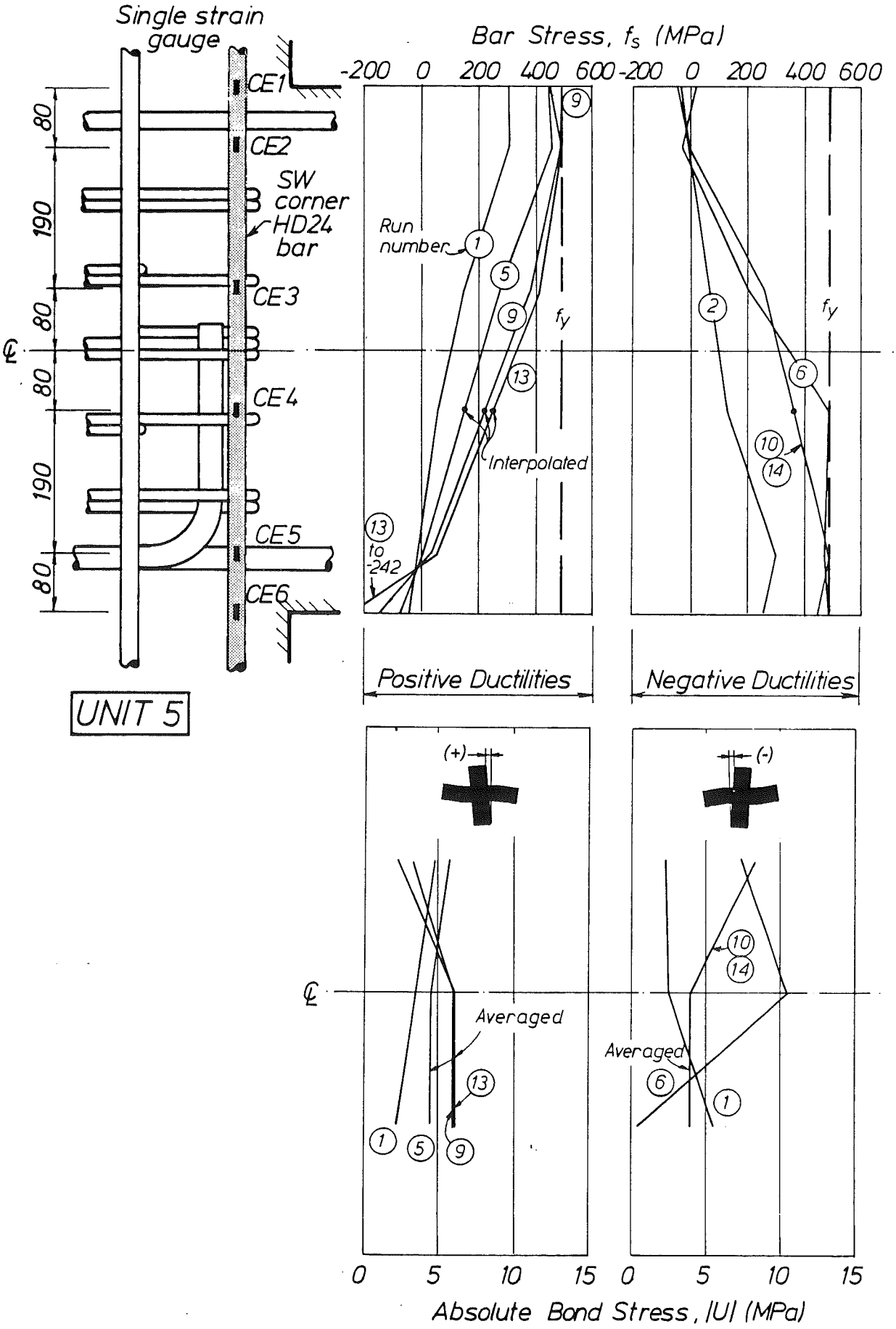

Fig. 6.13 - Bar and Bond Stresses - South-West Corner Column Bar of Unit 5.

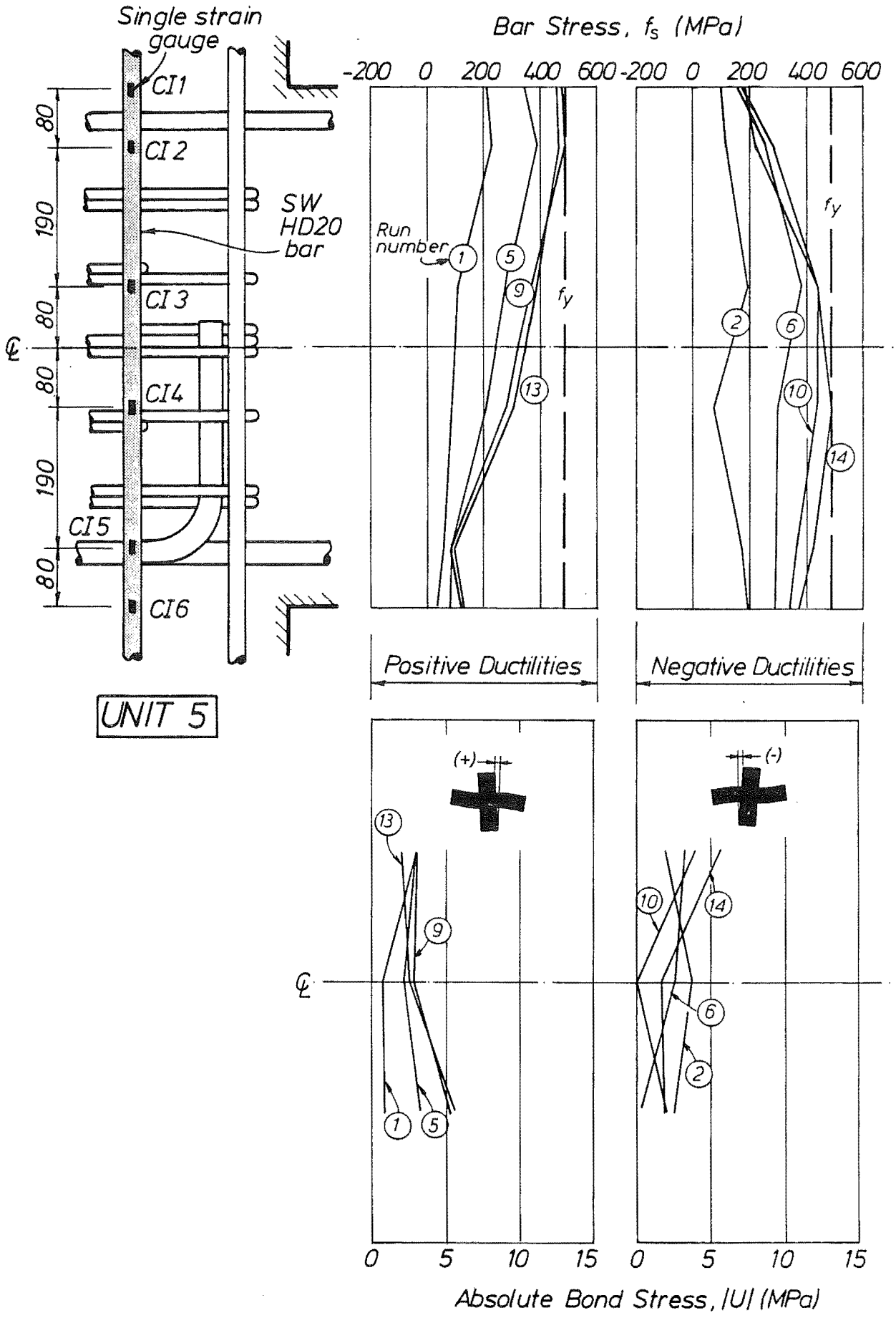

Fig. 6.14 - Bar and Bond Stresses - South-West Interior Column Bar of Unit 5.

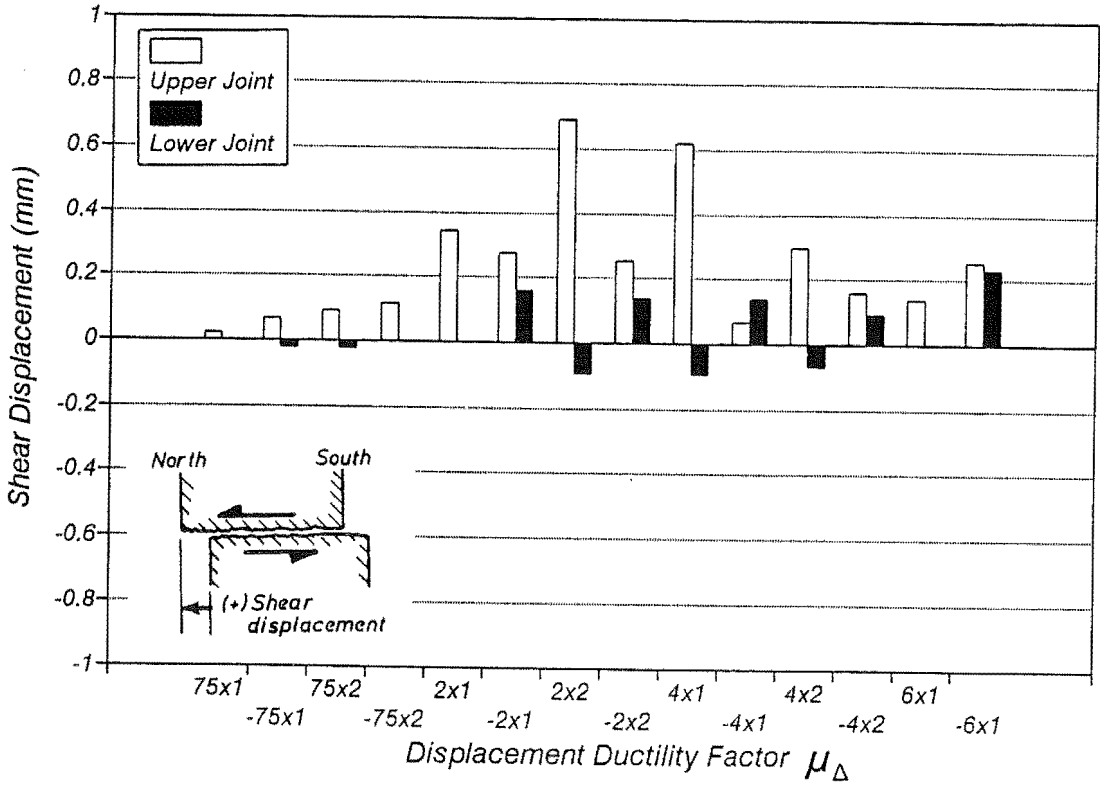

Fig. 6.15 - Shear Displacement along Column Construction Joints of Unit 5.

get conclusive trends of the bond stresses in the loading cycles in the inelastic range because of the failure of the strain gauge CE4 (see Fig. 6.13).

The bar and bond stresses of the inner south-west column vertical bar are plotted in Fig. 6.14. This bar was always subjected to tension at each end of the joint, and, as expected, no large bond forces were recorded.

6.2.5 Column Behaviour

From the visual observations made during the test, the column remained essentially elastic with small cracks distributed at regular intervals up to the end pins. The vertical sliding of the beams along the vertical construction joint at the column faces was very small, as indicated by the chart shown in Fig. 6.15.

6.2.6 Beam Behaviour

6.2.6.1 Curvature and Rotational Ductility Factors

The beam curvature ductility factors shown in Fig. 6.16 were calculated from the second set of linear potentiometers along the north and south beams. The projected curvature at first yield indicated a value lower than that predicted by moment-curvature analysis. The large curvature ductility

factors in the cycles to $\mu_\Delta = \pm 6$ were influenced by the slippage through the beam-column joint of the beam top reinforcement. That reinforcement when anchoring in tension in the beam at the opposite side of the column induce large compressive strains in the compression region of the beam.

Fig. 6.17 illustrates the rotational ductility factors of the north and south beams of Unit 5. Since the components of the total lateral displacement of Unit 5 were controlled by the fixed-end rotation of the beams and the flexural response, the predicted rotational ductility demand was close to that estimated from the test results.

6.2.6.2 Beam Strain Profiles at the Level of the Longitudinal Reinforcement

Figs. 6.18 and 6.19 depict the estimated member strains at the level of the beam top and bottom reinforcement respectively. It is evident in Fig. 6.17 that the slippage of the top reinforcement in load run 9 had a large effect on the distribution of strains along the beam. Beyond this load run the concrete surrounding the top bars in the beam near the column face subjected to compression was subjected to very large compressive strains. As it was mentioned in Section 6.2.1, the loss of the concrete due to crushing in this region was the final cause for the reduction in load carrying capacity of the test unit.

Contrary to the behaviour of the top reinforcement of the beam the strains calculated in the bottom reinforcement of the beam depicted in Fig. 6.19, showed the spreading of the plastic hinges along the north and south beams. From the data reduced it is possible to estimate that the plastic hinges extended a distance close to the effective depth of the beam, d.

6.2.6.3 Beam Elongation

The total measured elongation of the beams of Unit 5 is plotted in Fig. 6.20 against the measured storey shear. The elongation of the beam followed the same pattern as for the other units tested in this programme. However, if Fig. 6.20 is studied together with Figs. 6.18 and 6.19 it is concluded that in Unit 5 the elongation of the beams was caused by the residual tensile strains in the bottom reinforcement of the beams and by the effect of the top bars slipping through the joint, instead by residual tensile strains in the top bars of the beams. The elongation of the beam caused by the slippage of the bars results in a comparatively smaller cumulative elongation of the beam. Hence, it would be expected that the lengthening of the beam of Unit 5 would have been larger had the bond failure in the top bars been precluded.

In the beam of Unit 5 the elongation took place mainly in the first complete loading cycle to a new displacement ductility. The second loading cycles did not increase the elongation of the beam as much as noted in the other units tested in this project, because in the second cycles the Unit did not develop its flexural capacity as a consequence of the loss of stiffness caused by the bond failure of the top reinforcement of the beam.

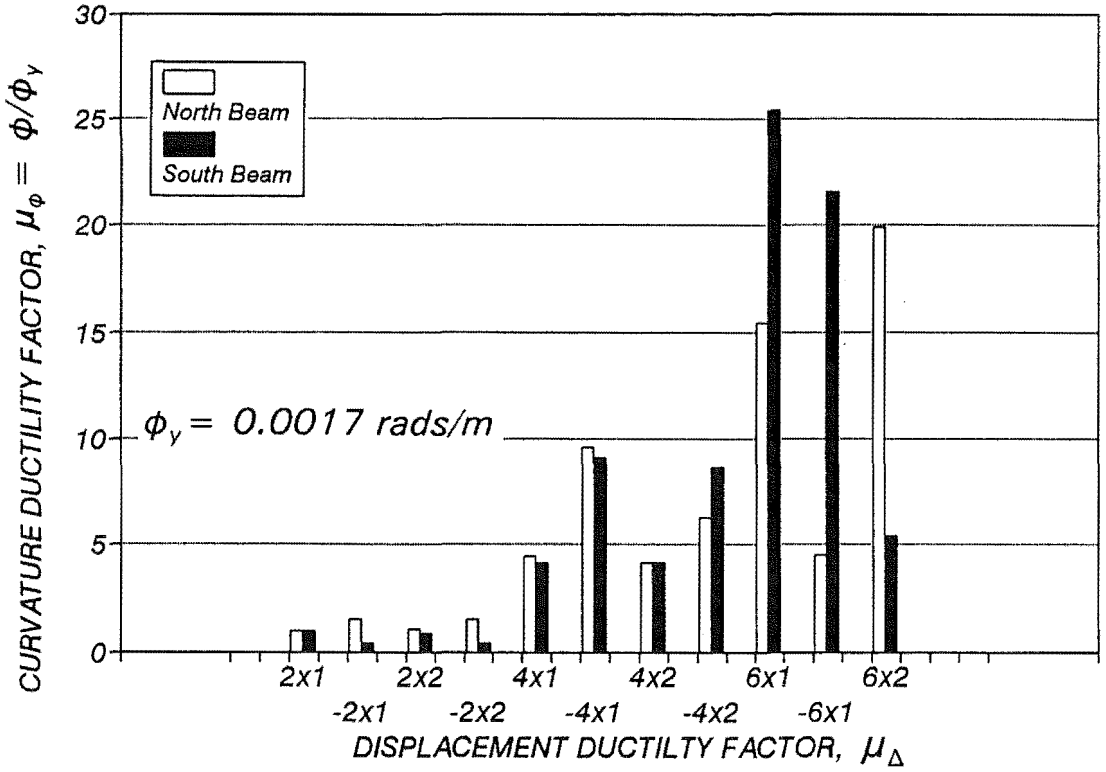

Fig. 6.16 - Beam Curvature Ductility Factors of Unit 5.

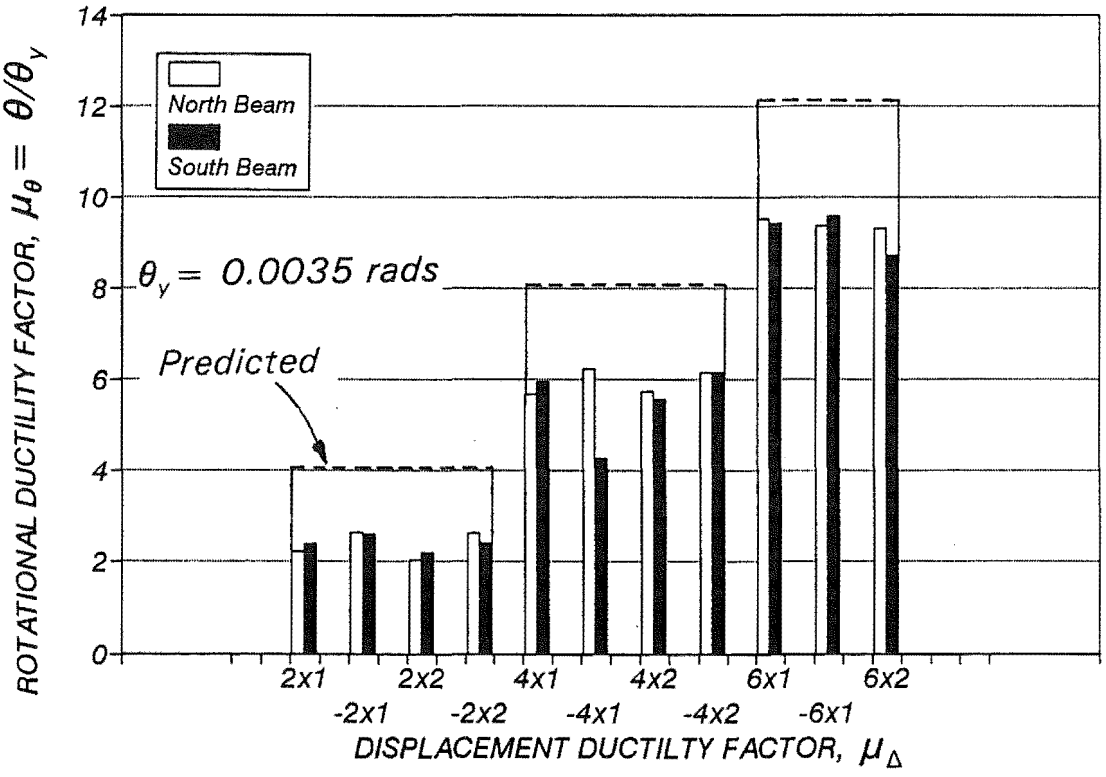

Fig. 6.17 - Beam Rotational Ductility Factors of Unit 5.

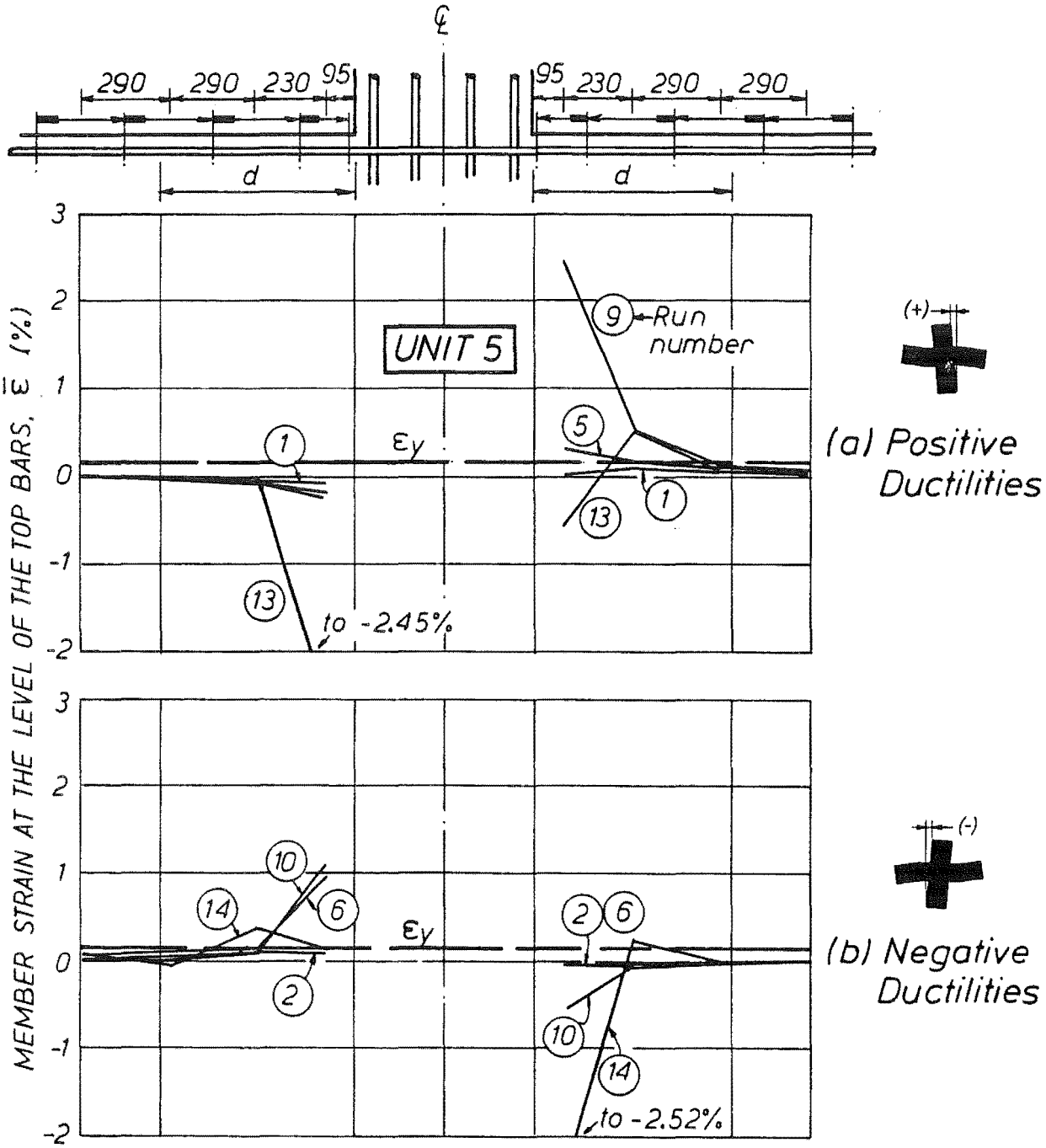

Fig. 6.18 - Beam Strain Profiles at the Level of the Top Reinforcement of Unit 5.

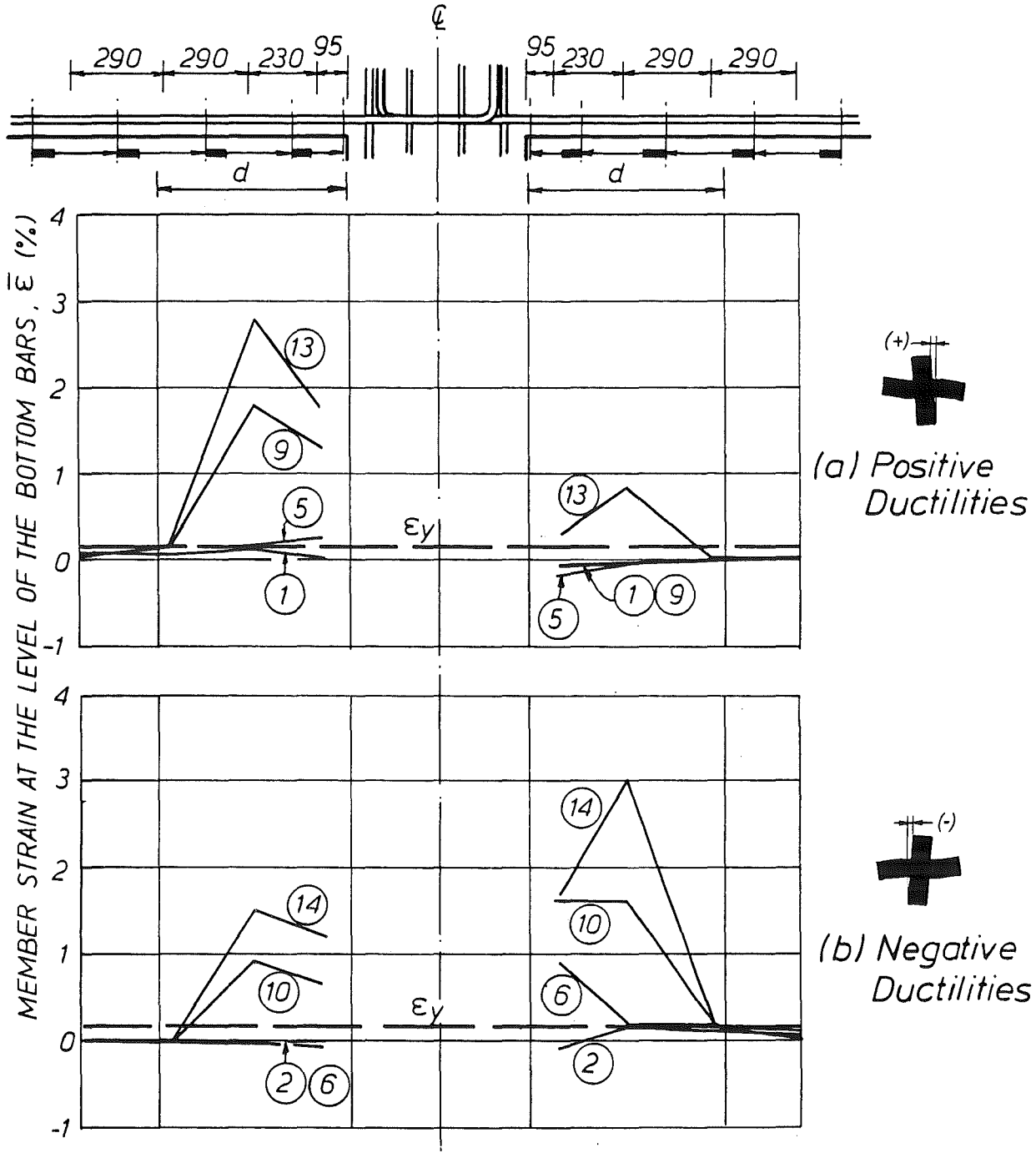

Fig. 6.19 - Beam Strain Profiles at the Level of the Bottom Reinforcement of Unit 5.

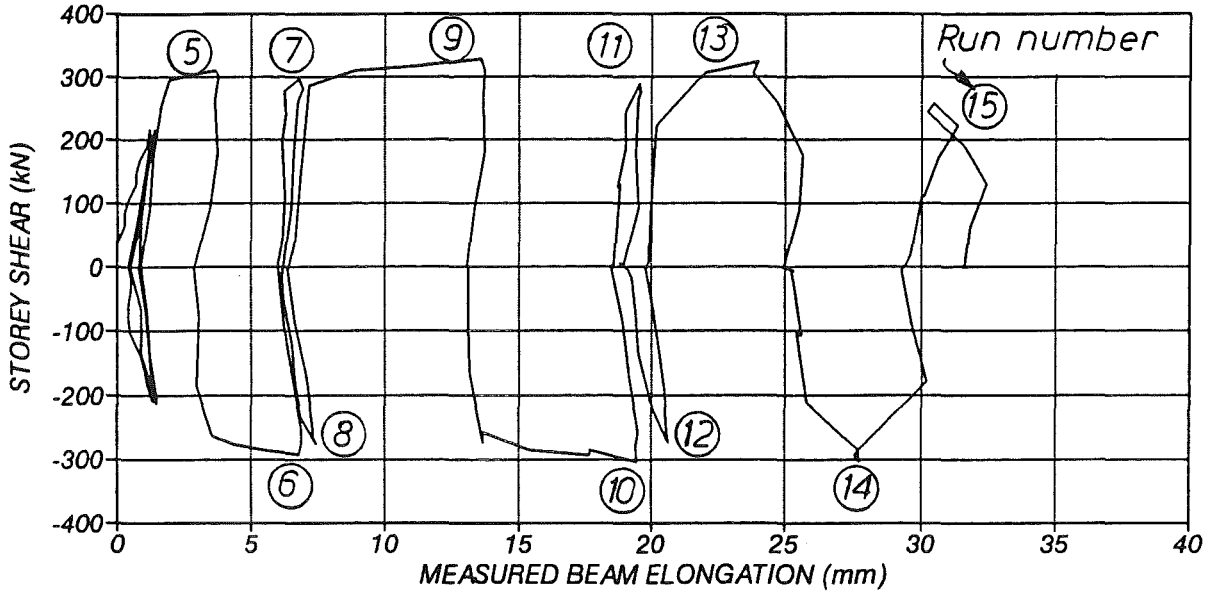

Fig. 6.20 - Total Beam Elongation of Unit 5.

In Fig. 6.20 it can also be observed that after load run 13, the first cycle to $\mu_\Delta = 6$, the measured beam elongation became erratic and lost its typical pattern. It is not known what caused this pattern. The lengthening of the beam calculated from the linear potentiometer measurements along the regions of the beams showed a similar trend, which means that an error was not made in the measurement procedure.

6.3 TEST RESULTS OF UNIT 6

6.3.1 General Behaviour

Fig. 6.21 shows the beam-column joint region of Unit 6 at different stages during the test. Plastic hinges developed in the adjacent beams, as expected, and minor and well distributed cracking was observed to appear elsewhere in the assemblage. The test of Unit 6 took one week to complete and ended after cycles up to a $\mu_\Delta = 7.3$ at an interstorey drift of 3.6% (see Fig. 6.23). The cumulative displacement ductility before losing its lateral capacity by more of 20% of the maximum lateral load measured was $\Sigma\mu_\Delta = 88$ implying, based on the method discussed in Section 3.7, an available displacement ductility factor of $\mu_a = 8$.

At the end of the test the concrete in the plastic hinge regions of both beams appeared damaged as a consequence of the large shear deformations that occurred in these regions. The test unit performed as if of monolithic construction. No adverse effects were observed to occur in the grouted vertical sleeves where the column longitudinal reinforcement was anchored. Some sliding along the

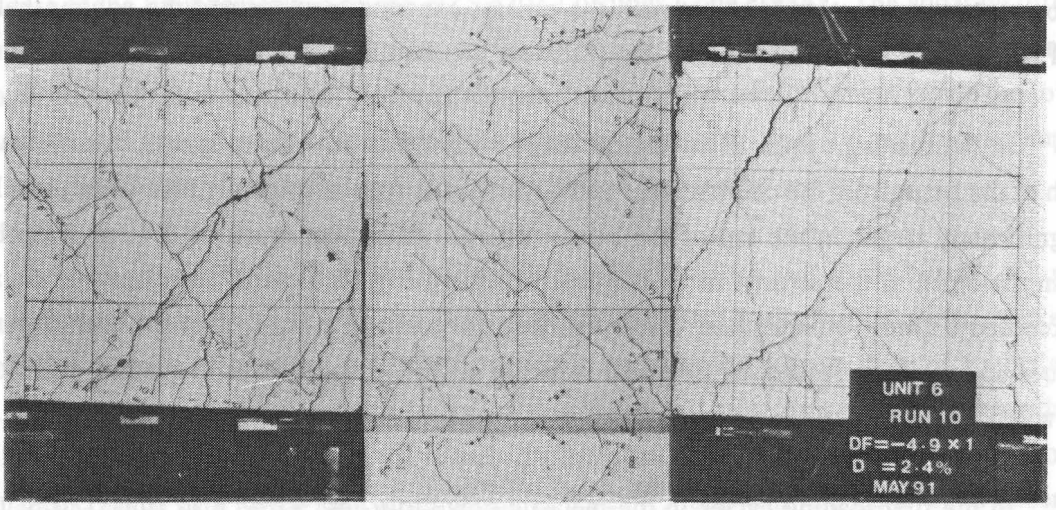

(a) At μ_Δ = -4.9x1

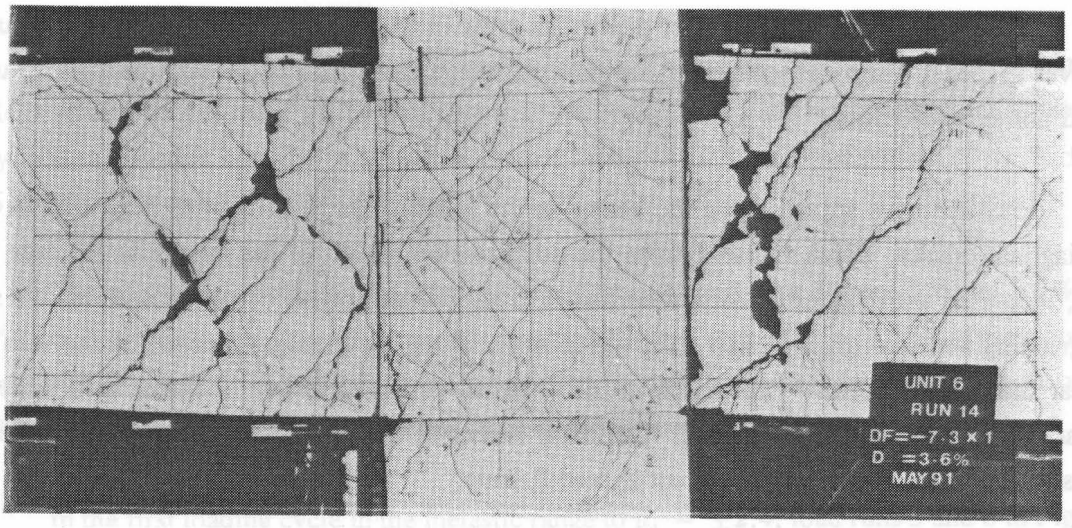

(b) At μ_Δ = -7.3x1

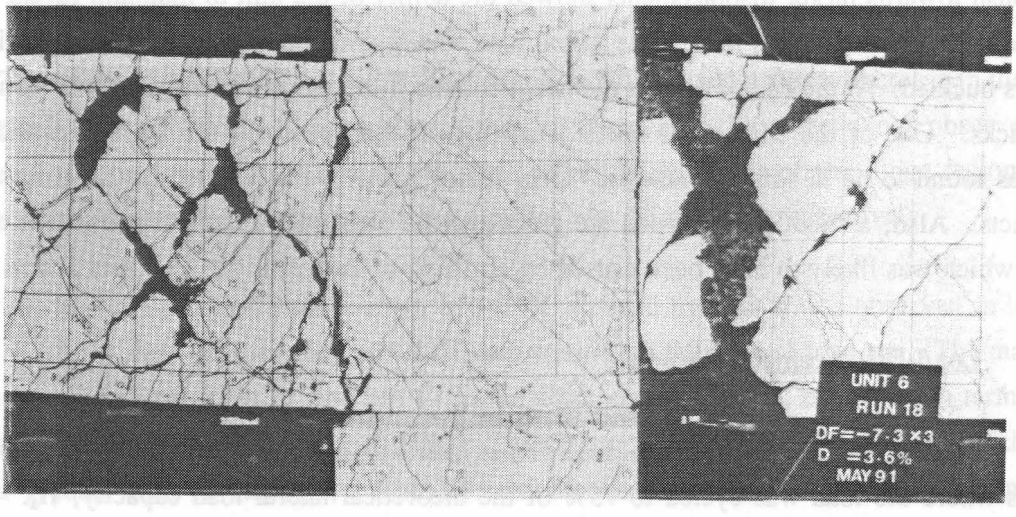

(c) At μ_Δ = -7.3x2

Fig. 6.21 - Cracking of Beam-Column Joint Region of Unit 6 at Different Stages During the Test.

lower horizontal construction joint between the precast concrete member and the column below was recorded but, relative to the total lateral displacement imposed, it was insignificant.

In the loading cycles in the elastic range cracking in the beams spread to a distance equal the depth of the beam from the column faces and developed at regular intervals. However, crack widths were significantly larger in the top of the beams where a maximum crack of 0.4mm was observed. Cracks in the beam at the column faces ran continuously along the column interface but their widths never exceeded 0.2mm. Nonetheless, crack widths in the columns at the face of the beams were larger with values up to 0.4mm recorded. Diagonal cracking in the joint panel was in general well distributed and the width of the cracks did not exceed 0.2mm.

In the first loading cycles in the inelastic range to $\mu_\Delta = \pm 2.4$, load runs 5 to 8, the main cracks developed in the beams at the face of the columns as a result of yielding of the beam longitudinal reinforcement penetrating into the beam-column joint region. These cracks were up to 4mm in width. Some of the diagonal cracks in the web of the beams grew in the second cycle to $\mu_\Delta = \pm 2.4$ but their width never exceeded 1mm. Elsewhere in the subassemblage the crack pattern became denser but their width did not exceed 0.5mm.

Plastic hinges spread along the beams in the loading cycles to $\mu_\Delta = \pm 4.9$. Crack widths of the diagonal cracks, which radiated from the compression region in the beams at the face of the columns, increased with values of 2mm recorded at the mid-depth of the beam. Some relative sliding action, grinding and spalling was also observed to occur along the cracked concrete in the web of the beam near the column faces. The cracks in the columns at the faces of the beams also widened to 1.6mm at the extreme fibres in tension. The main cracks in the joint panel were those crossing the diagonals of the joint. Their width did not exceed 0.6mm.

The concrete in the plastic hinge regions of the beams suffered further deterioration in the loading cycles to $\mu_\Delta = \pm 7.3$, load runs 13 to 20, because of the grinding action caused by sliding shear. A final push towards larger displacements showed the ability of the unit to maintain levels of strength at least equal to the theoretical load. The lateral load finally dropped when the top longitudinal bars of the beams buckled. At the end of the test the beam-column joint region remained in solid condition with small cracks. One of the corrugated ducts was removed and sectioned for inspection and the grout inside was found to be in sound condition. Only radial cracks were detected in the grout at the ends of the ducts. Also, a small gap between the grout and the embedded reinforcing bar was observed at the ends which was likely to have been caused by crushing of the grout due to dowel action of the bar.

6.3.2 Load-Displacement Response

Figure 6.22 depicts the lateral load versus lateral displacement response of Unit 6 in the first load runs where the load was cycled to 75% of the theoretical lateral load capacity, H_a. The initial "elastic" stiffness determined following the procedure discussed in Section 3.7 was only 49% of that predicted based on the assumptions made in Section 3.2.1. The interstorey drift at the projected first yield displacement was 0.49% and that at the dependable lateral load capacity was 0.46%, which was

well in excess of the limit prescribed by the NZS 4203 Loadings Code (1984). The apparent difference between measured and predicted stiffness lies on the additional flexibility due to the fixed-end rotation in the beams and the columns caused by the strain penetration of the reinforcement inside the joint. In contrast with Unit 5, the shear deformations in the beam-column joint panel did not have an important effect on the initial "elastic" stiffness, as it will be explained in the next section.

Also shown in Fig. 6.22 are the load levels at which first cracking in the beams, column and beam-column joint were observed. In the first load run the beam-column joint panel cracked at a nominal horizontal joint shear stress of $0.39\sqrt{f'_c}$, which in terms of the column shear is equivalent at a load of $0.75H_a$. That is, the joint remained uncracked until the last increment before reaching the peak load and hence its contribution towards the lateral displacement was minimal. In the reverse load run the joint panel cracked at a lower joint shear stress of $0.32\sqrt{f'_c}$, following the same trend observed in Unit 5 and which possibly can be related to the notch effect caused the jagged shape of the first diagonal crack.

Fig. 6.23 plots the hysteretic load-displacement response of Unit 6. The displacement controlled cycles followed the displacement sequence applied to Unit 5 and hence the actual displacement ductility factors to which Unit 6 was subjected did not follow the conventional pattern of $\mu_\Delta = \pm 2$, ± 4 and ± 6 but they followed a multiple of them.

The post-elastic stiffnesses of the hysteretic response of Unit 6 were 3.8 and 3.7% of the initial "elastic" stiffness for the positive and negative cycles, respectively. The average of these stiffnesses plus the initial "elastic" stiffness were used to define an ideal bi-linear loop in order to normalize the energy dissipated by the actual hysteresis loops measured for the unit.

In the first loading cycle in the inelastic range to $\mu_\Delta = \pm 2.4$, load runs 5 and 6 in Fig. 6.23, the lateral load attained exceeded the theoretical load H_a by 9% and 2%, respectively. The second cycle to the same ductility level was very stable and the loads attained were only slightly lower. The normalized energy dissipated in these cycles was 76% and 48%, respectively.

The loading cycles to $\mu_\Delta = \pm 4.9$, load runs 9 to 12, showed a steady increase in the lateral load attained and only in load run 12 was some pinching of the measured hysteretic loop observed. The main source of pinching at this stage was due to shear deformations in the plastic hinge regions of the beams. The normalized energy dissipated in these cycles was 65 to 45%, respectively.

The maximum lateral load strength of $1.24H_a$ attained by Unit 6 was observed in load run 13 to $\mu_\Delta = \pm 7.3$. A very similar value of $1.23H_a$ was attained in the reverse load run. The maximum shear in the beams was recorded in load run 13 in the north end. Its value, expressed in terms of the nominal shear stress was $v^\circ = V^\circ/bd = 0.20\sqrt{f'_c}$. The second cycles to $\mu_\Delta = 7.3$ were pinched and there was a gradual loss of stiffness, which affected the lateral load attained at the given lateral displacement. The load attained in load run 20 was 21% below that previously attained in load run 14. The normalized energy dissipated also reflects the gradual degradation of the response at this stage, being 32, 22 and 20% from the first to the fourth cycle to $\mu_\Delta = 7.3$, respectively.

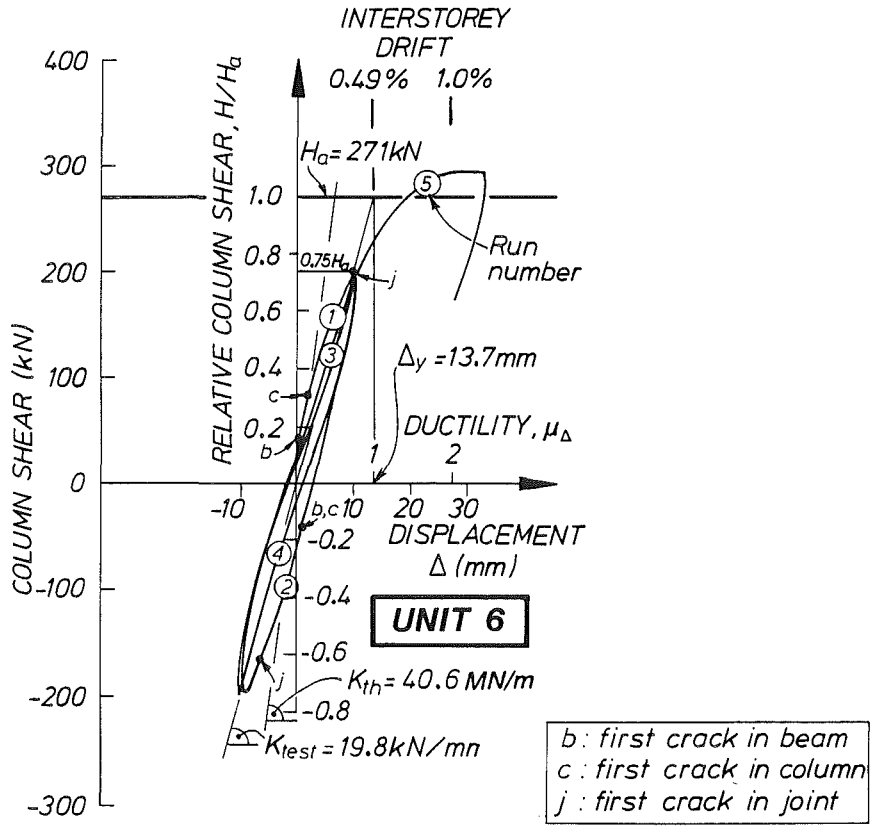

Fig. 6.22 - Lateral Load-Lateral Displacement Response of Unit 6 During the Cycles in the Elastic Region.

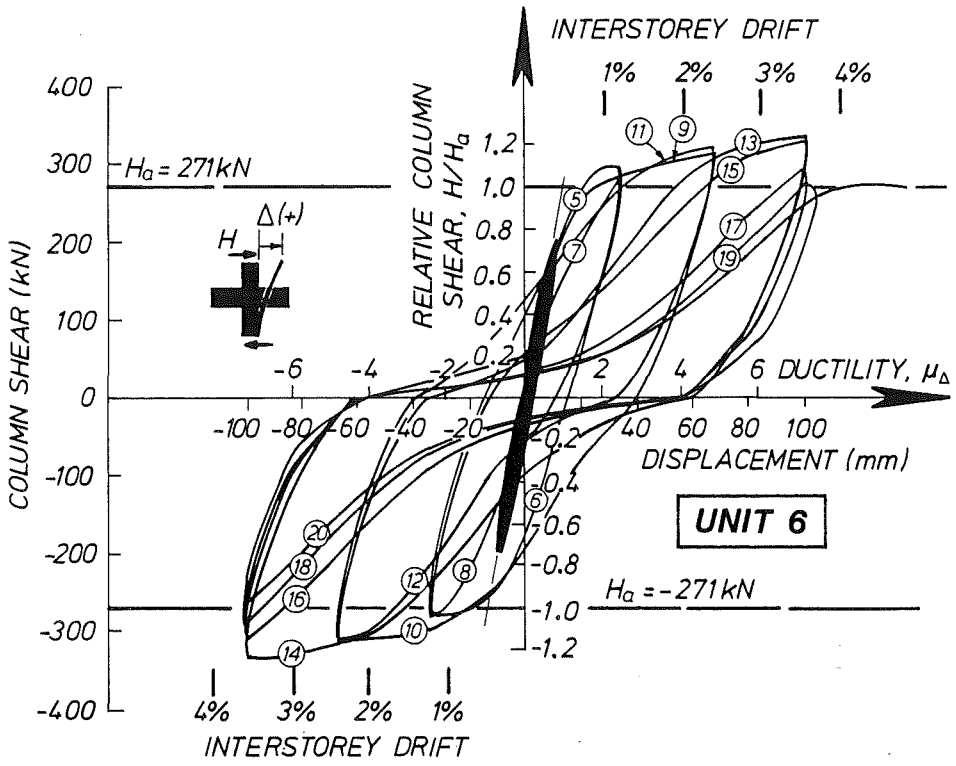

Fig. 6.23 - Lateral Load-Lateral Displacement Response of Unit 6.

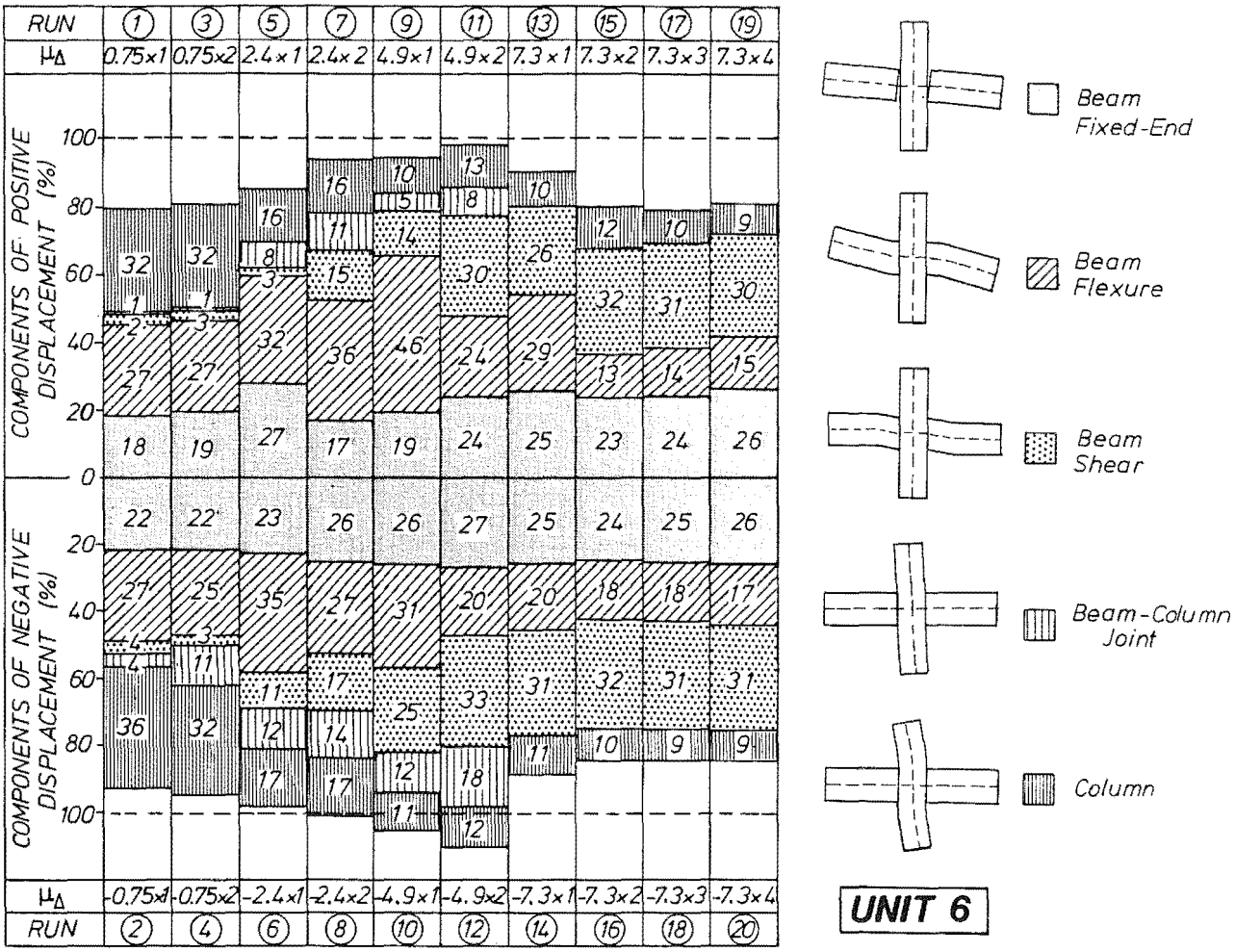

Fig. 6.24 - Components of Lateral Displacement of Unit 6 at Peaks of Load Runs.

The ratio between the cumulative energy dissipated by the loops of Unit 6 and that of the ideal bi-linear loop was 48% at the end of load run 16 and 38% at the end of the test in load run 20. This index indicates that the hysteretic performance of Unit 6 was superior to that of Unit 5.

6.3.3 Decomposition of the Lateral Displacement

The components of the lateral displacement imposed on Unit 6 in the tests are depicted in Fig. 6.24. These components are presented as a percentage of the measured applied lateral displacement.

The deformations of the column during the loading cycles in the elastic range contributed to 32% to 35% of the total lateral displacement and was the largest source. Contrary to the observations made in Unit 5, the distortions of the beam-column joint did not make a large contribution to the deformations in the elastic range. The deformations in the beam, due to flexure, fixed-end rotation and shear, were of similar magnitude to those measured in Unit 5. It appears that the main reason for the difference in stiffness between Unit 5 and 6 was the smaller deformation of the joint region of Unit 6.

In the initial loading cycles in the inelastic range Unit 6 showed a flexural response with most of the displacements being caused by flexure and fixed-end rotation of the beams. However, at the end of the test the flexural response diminished. Instead, shear deformations in the plastic hinge regions became the predominant source of deformation. Unfortunately the devices monitoring the shear displacement of the beam-column joint had to be removed in the first loading cycle to $\mu_\Delta = 7.3$ because the corners of the joint, where they were attached, became dislodged by the longitudinal beam bars. However, if the closure error at the end of the test is assigned to deformations within the joint panel, it is possible to conclude that the joint distortion contributed approximately 20% of the total lateral displacement in the final loading cycles near the end of the test.

6.3.4 Joint Behaviour

6.3.4.1 Strains in the Transverse Reinforcement

The measured hoop strains in the joint recorded during the test of Unit 6 are plotted in Fig. 6.25. Bar strains were measured by double 5mm electrical strain gauges on one leg of the perimeter hoops. The average of the two strain readings is presented in Fig. 6.25, except for the lower hoop where strain gauge H5B failed to work. The strains recorded show in general an increase as the test progressed, implying a gradual transition between a strut and a truss mechanism. They were very small in the loading cycles in the elastic range mainly because cracking was confined to few hairline cracks. The strains were in general very uniform and in the first loading cycle to $\mu_\Delta = \pm 7.3$, load runs 13 and 14, they approached or reached yielding. In the repetitive cycles to $\mu_\Delta = \pm 7.3$ the recorded strains reduced since the lateral load attained by the test specimen diminished.

If it is assumed that the interior and other perimeter legs of the hoops were equally stressed, the force in the transverse reinforcement would be equal to 97% of the total horizontal joint shear in load run 13.

6.3.4.2 Slip of the Beam Bars

The local bar slip of the top and bottom D24 bars in the joint core of Unit 6 are plotted in Fig. 6.26 and 6.27, respectively, for three locations in the joint. The bar slip measured at the centreline of the column was directly monitored by a linear potentiometer mounted on the concrete surface. Strictly, this measurement will be affected by the deformations of the concrete in this region. However, these deformations were considered negligible relative to the magnitude of the local bar slip. The local bar slip at the north and south ends, which correspond to the local bar slip at the level of the outer column bars, were estimated from the measured slip at a target located on the reinforcement at 10mm from the column faces extrapolated assuming that the bar strain was equal to that directly measured on the beam bar at the face of the column.

The local bar slip of the top bars was larger than that of the bottom bars, indicating the influence of the direction of casting of the concrete, commonly referred to as the "top bar effect". This effect is evident when the measurements at the column centreline in Figs. 6.26 and 6.27 are compared.

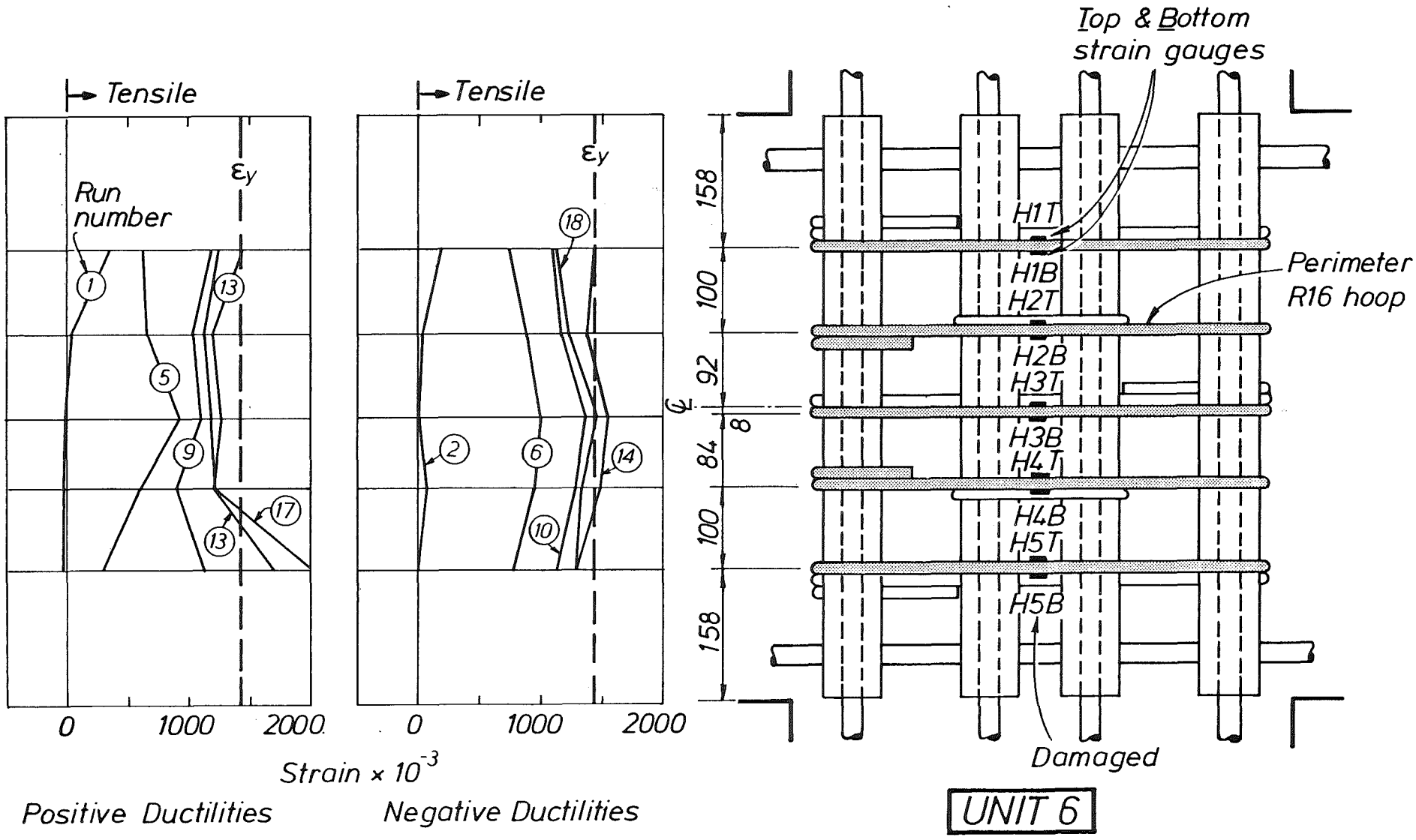

Fig. 6.25 - Measured Strains in Joint Hoops of Unit 6.

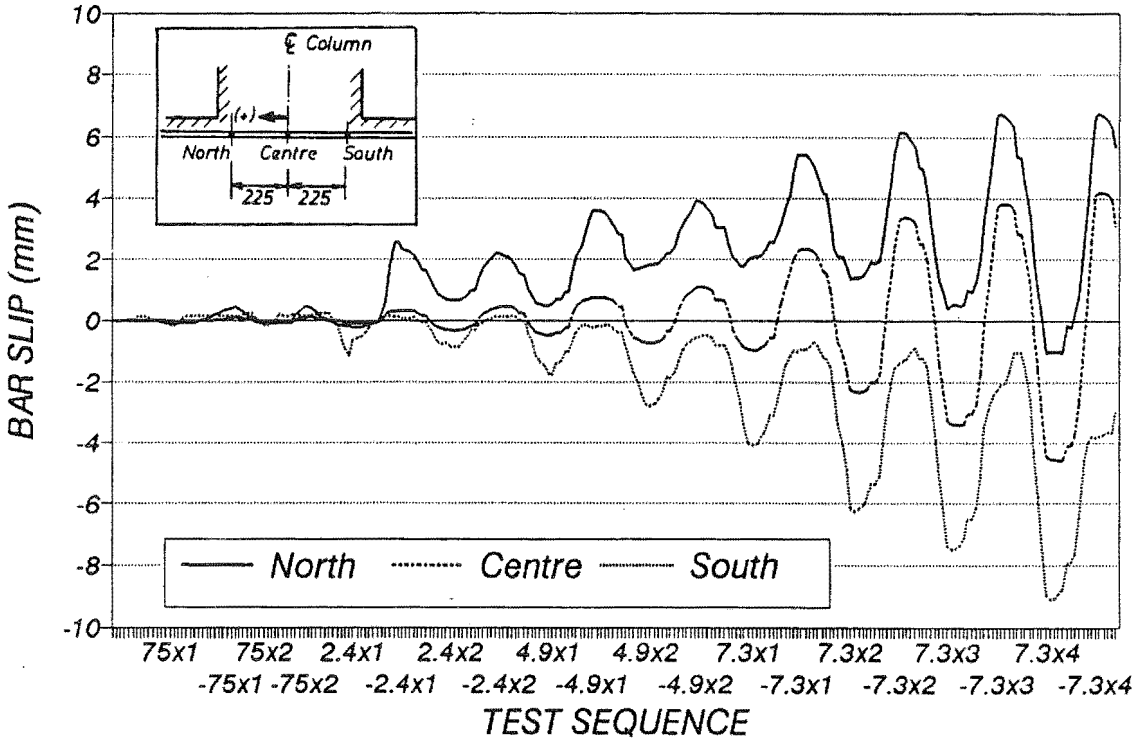

Fig. 6.26 - Measured Slip of Top Beam Bars of Unit 6.

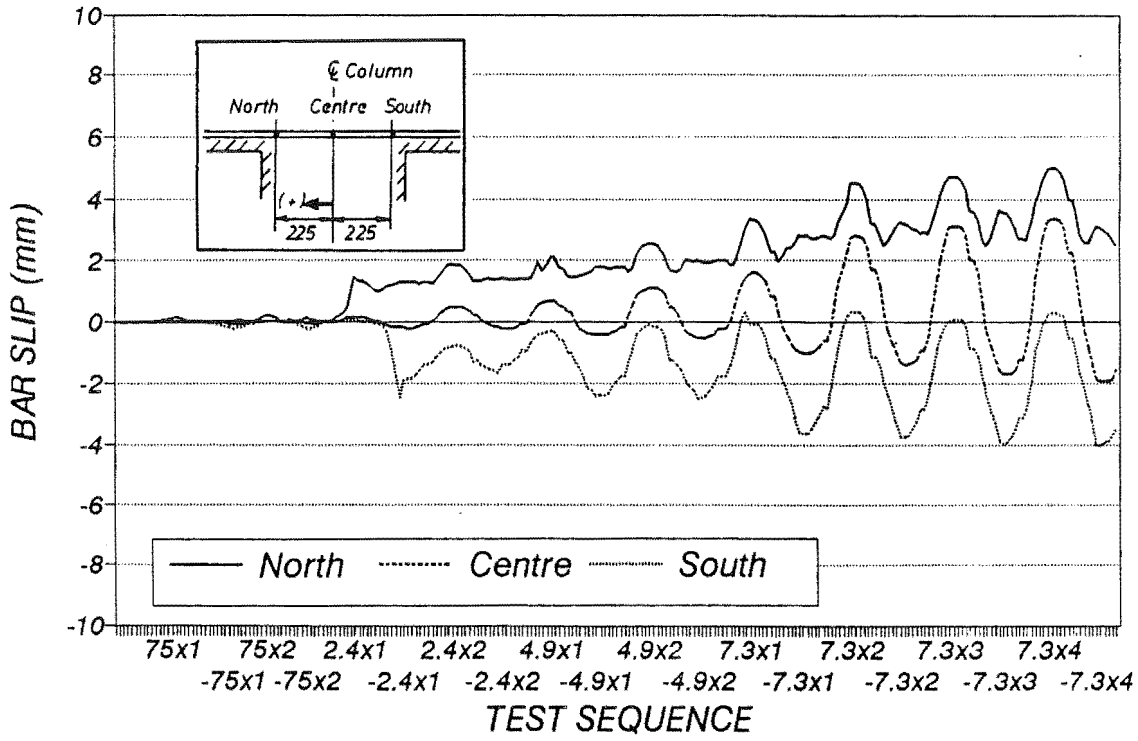

Fig. 6.27 - Measured Slip of Bottom Beam Bars of Unit 6.

For instance, the maximum absolute bar slip of the top D24 bar was 8.3mm and was recorded in the last load cycle to $\mu_\Delta = \pm 7.3$. This value is 51% larger than the maximum absolute local bar slip of 5.5mm recorded in the same cycle at the bottom bar level.

It is obvious that the anchorage conditions for the bars in the beam-column joint core of Unit 6 were significantly better than in Unit 5. However, the better anchorage conditions in Unit 6 implied that the transfer of the joint shear relied more on a truss mechanism while for Unit 5 it relied, in the later stages, on the concrete strut mechanism. The level of strain in the joint hoops in both units, shown in Figs. 6.6 and 6.25, indicate that in the first loading cycles in the inelastic range, when local bar slip was controlled, the hoops were equally stressed down the depth at each load run. Even the hoop stresses in load run 9 were very similar, but beyond this load run, when the top bars of Unit 5 were sliding along the joint core, the hoops were unequally stressed.

6.3.4.3 Bond and Bar Stresses of the Beam Longitudinal Reinforcement

The bar stresses and corresponding bond stresses of the top and bottom beam reinforcement are illustrated in Figs. 6.27 and 6.28, respectively. The method and limitations for obtaining these values have already been discussed in Section 6.2.4.3.

In the loading cycles in the elastic range, load runs 1 to 5, the bond distribution in the top and bottom bars was rather uniform and the stresses in the bars decreased in an almost perfect linear fashion. The top bars were in tension throughout the beam-column joint while the tensile stress in the bottom bars penetrated inside the joint an average distance of 420mm or $17.6d_b$. Eventually, with further loading runs, yield in the reinforcement penetrated into the joint core to a maximum distance of $6.5d_b$ from the face of the column.

The bond stresses in the longitudinal beam bars estimated from measurements show a trend of increasing in the region of the compression zone of the column, which exerted pressure on the bars and clamped them. It is evident that the bond stresses along the length of these bars are far from being uniform. Two different mechanisms can be postulated as to contributing towards the development of bond.

In the first mechanism the bond relies on the mechanical contact between the bar deformations and the surrounding concrete. This is the main source of bond in the region unaffected by the compression zone of the column. The second mechanism is the frictional bond provided by the clamping action caused by the compression region of the column.

It is also evident in Figs. 6.28 and 6.29 that the compressive forces carried by the longitudinal reinforcement were smaller than the tension forces, following the same trend observed in the beam longitudinal reinforcement of Unit 5. This observation disagrees with the concept that for equally reinforced members the reinforcement in compression yields to balance the tension force. The compression force in the beam calculated from the measured shear is shown in Fig. 6.30 compared with the predicted force in the reinforcement at the column face of the top south chord.

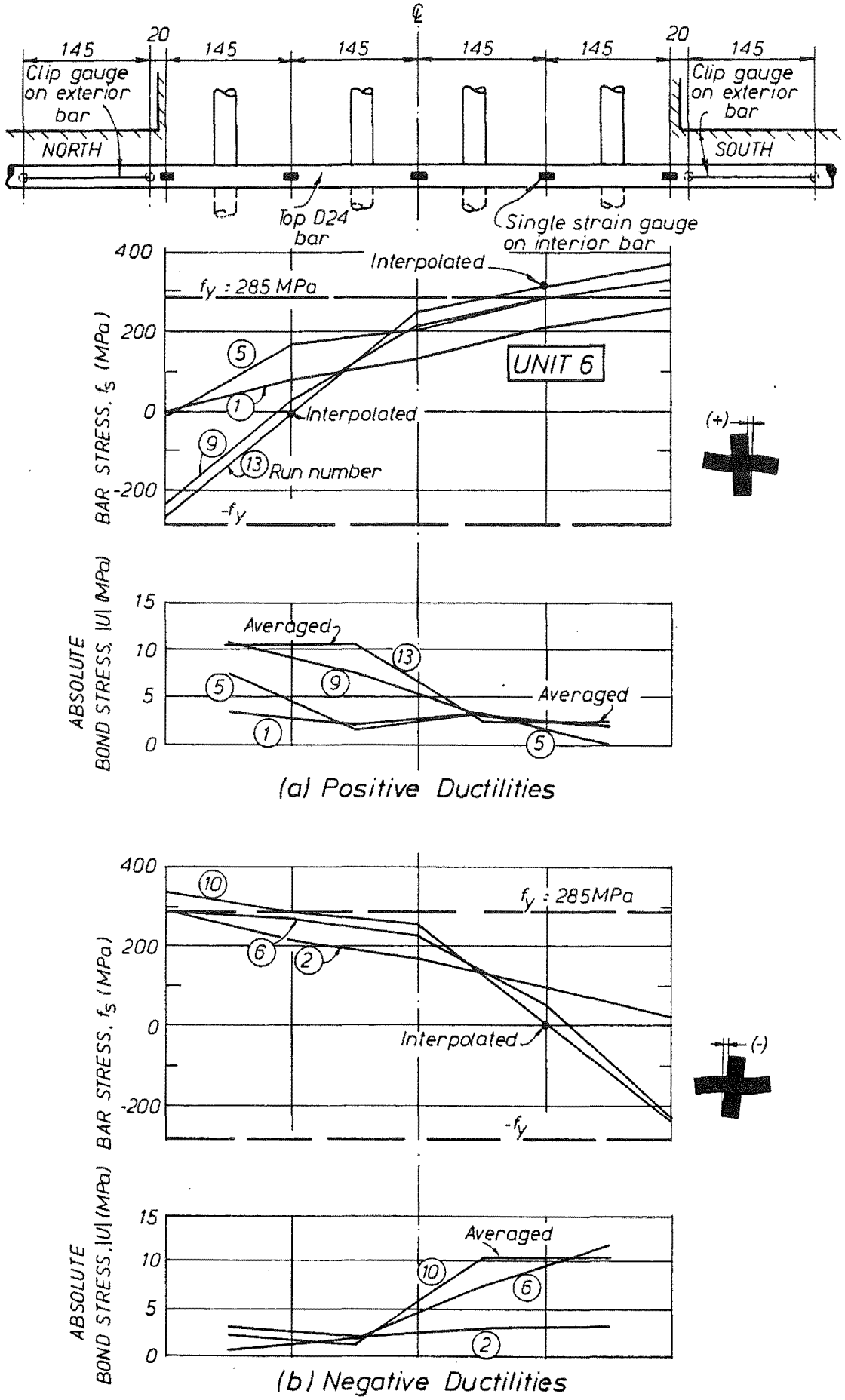

Fig. 6.28 - Bar and Bond Stresses - Top D24 Beam Bar of Unit 6.

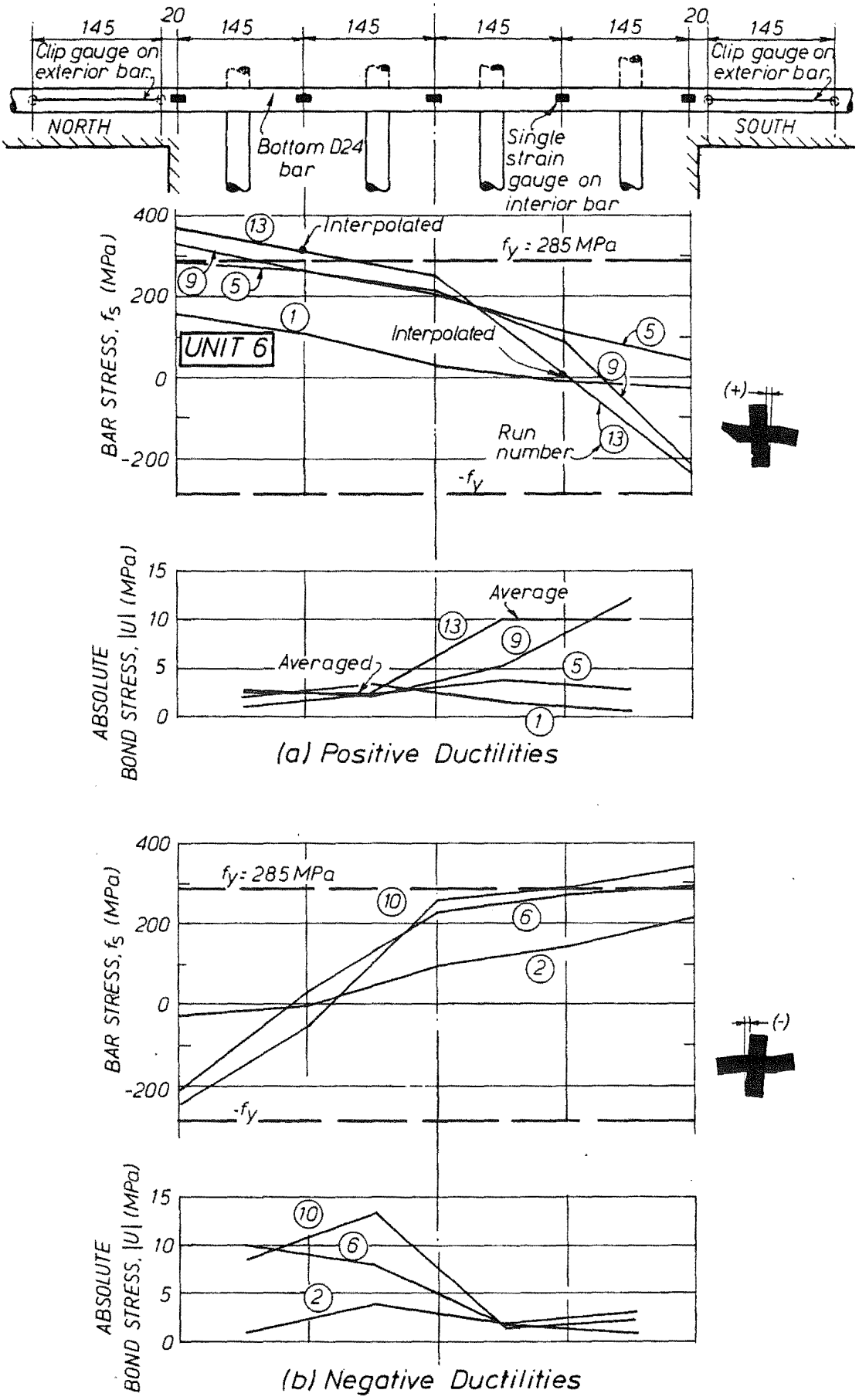

Fig. 6.29 - Bar and Bond Stresses - Bottom D24 Beam Bar of Unit 6.

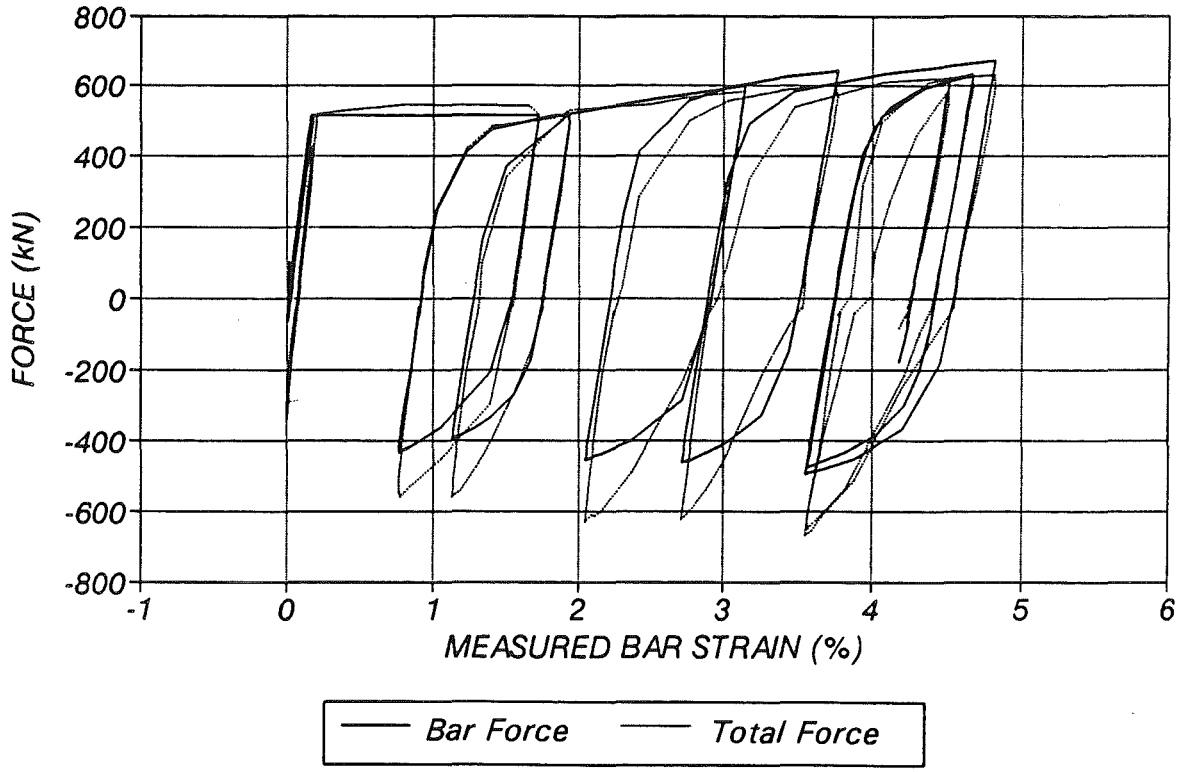

Fig. 6.30 - Predicted Bar Forces versus Measured Total Force in the Beam at 78mm from the Column Face - Top South Bars of Unit 6.

As in Fig. 6.11 the compression force provided by the steel is always smaller than the total compression force estimated from the measured beam shear. The main reasons for this disagreement have already been discussed in Section 6.2.4.3.

6.3.4.4 Bar and Bond Stresses of the Column Vertical Reinforcement

Fig. 6.31 shows the bar stress and bond distribution of the north-west corner bar of the column of Unit 6. In the initial loading cycle in the elastic range, load runs 1 and 2 in Fig. 6.31, the tensile strain penetrated to a distance of $17.7d_b$ from the face of the beams. The level of stresses increased as the test progressed and apparently yielding of the reinforcement occurred at the ends of the corrugated ducting. It is believed that this apparent yielding was caused by a malfunction of the strain gauges there that were probably disrupted by the dowel action of the bars due to sliding shear taking place at the horizontal construction joint.

As in Unit 5, a simple elastic analysis, assuming the critical region in the columns to be at the level of the longitudinal beam reinforcement, predicted that the corner bar would be subjected to a stress of $0.80f_y$ at the maximum recorded load. If the composite action including the duct and grout is accounted for at 80mm from the end of the duct, the maximum stress level in the reinforcement is estimated to be only $0.72f_y$. However, the stress distribution indicates that this may not be the actual case and that it would be appropriate to ignore such composite action.

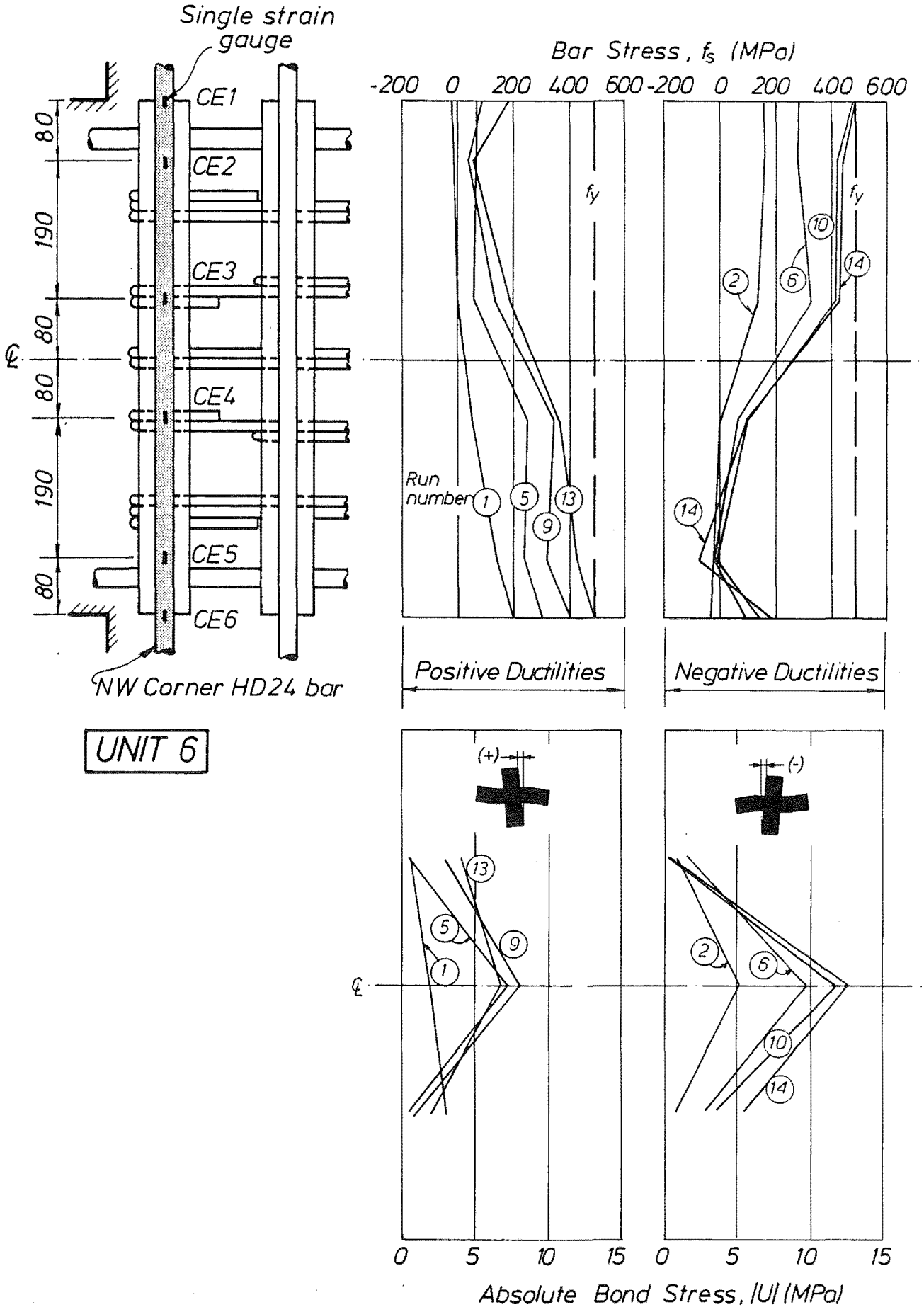

Fig. 6.31 - Bar and Bond Stresses of the North-West Corner Column Bar of Unit 6.

The bond stress distribution along the corner vertical bar in Fig. 6.31 indicates that the bar was mainly anchored in the middle third of the column. This distribution is in full agreement with earlier observations reported by Beckingsale (1980) and Cheung (1991). In addition, no detrimental effects were found to occur because of the lack of steel to steel contact between the longitudinal bar and the transverse hoops bent around the corrugated ducting. The grouted duct appears to act as an effective media through which the tie forces required for equilibrium at the nodes of the truss mechanism can be transferred.

Fig. 6.32 depicts the bar stress and bond distribution of the interior north-west column vertical reinforcement. Again, the apparent yielding at the duct ends was probably caused by the dowel action of the reinforcement due to horizontal sliding shear displacements along the construction joint. The general trend was for the bar stresses to increase with the advancement of the test. This would have been because when the truss mechanism gradually developed the longitudinal reinforcement was required to provide the vertical joint shear resistance in the joint.

The stress distribution in the loading cycles in the elastic range peaked at the ends of the joint, reflecting that the stresses at this stage were due only to flexure of the column, because at this stage the truss mechanism had not developed. In the loading cycles in the inelastic range the combination of both mechanisms (flexure and truss) implied that the bars were subjected to a rather uniform field of stresses along the joint panel. This uniform distribution of bar stress has been observed by other researchers as well.

In summary it can be concluded that the grouted corrugated ducting allowed the development of the truss mechanism, which enabled the transfer of a significant portion of the joint shear through this mechanism.

The bond between the bar and the grout was apparently not degraded at any stage during the testing. Nor was the bond degraded between the corrugated ducting and the concrete of the precast concrete unit.

6.3.5 Column Behaviour

The behaviour of the column during the test was essentially elastic. Cracking developed symmetrically above and below the beams and extended to the end pins. The size of the cracks remained always very small except at the construction joints where the horizontal cracks reached 2.5mm wide at the extreme fibre in tension.

It was also noticed that sliding shear, especially along the lower horizontal construction joint, was one for the main sources of deformation of the column. This displacement was monitored by DEMEC gauges at each construction joint. Fig. 6.33 shows the reduced data. Sliding shear, although small in terms of the overall lateral displacement imposed, accounted for a large proportion of the deformation of the column. The main reason for this source of flexibility was that the surfaces of the construction joints in the precast member were deliberately left smooth. No scrubbing nor water-jetting

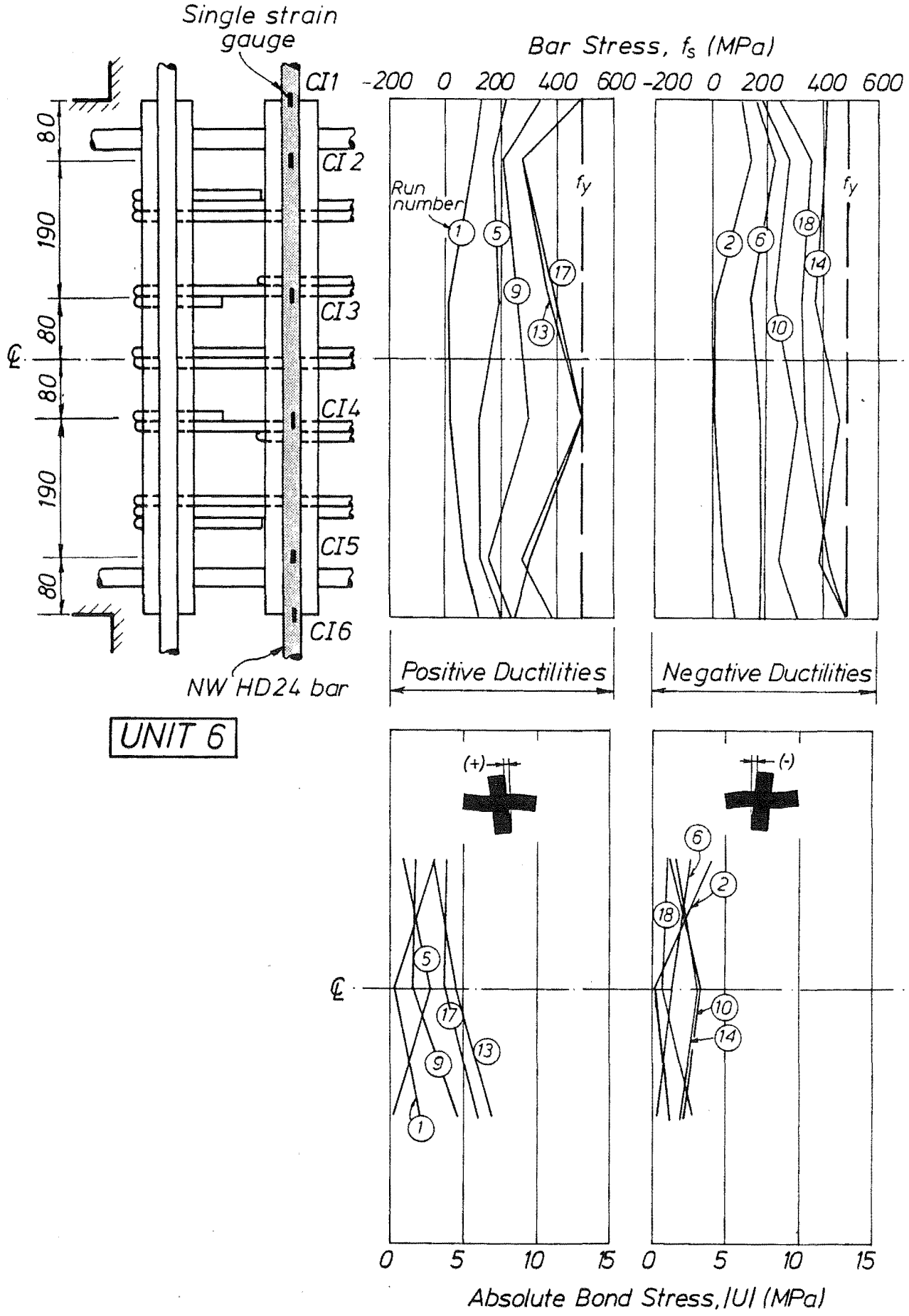

Fig. 6.32 - Bar Bond Stresses of North-West Interior Column Bar of Unit 6.

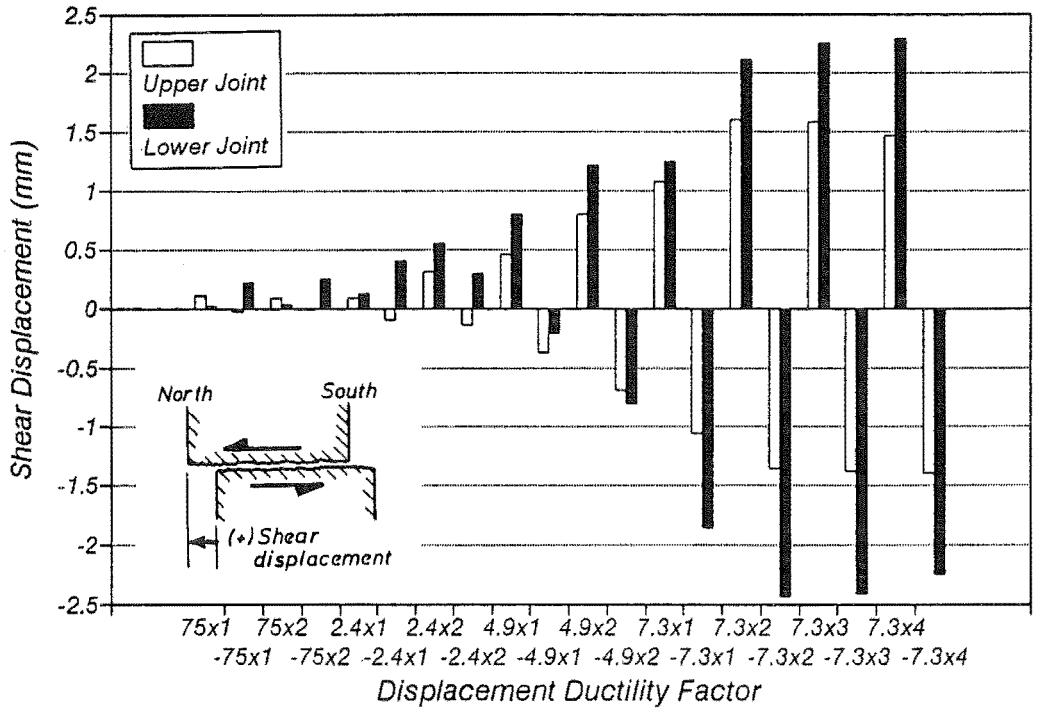

Fig. 6.33 - Shear Displacement along Column Construction Joints of Unit 6.

was applied to roughen the surface. The results of Fig. 6.33 indicate roughening of the interface surfaces should be recommended in practice, particularly since roughness can be achieved by a simple procedure.

6.3.6 Beam Behaviour

6.3.6.1 Curvature and Rotational Ductility Factors

Beam curvature ductility factors obtained over a gauge length of 170mm, using the second set of linear potentiometers along the beam and close to the column faces, are shown in Fig. 6.34. As in all previous results, the beam curvature ductility factors so found have a considerable scatter.

The rotational ductility factors plotted in Fig. 6.35 show a more predictable array. The predicted values always overestimated the measured ones because in the analysis it was assumed that deformations occurred mainly in the beams.

6.3.6.2 Beam Strain Profiles at the Level of the Longitudinal Reinforcement

The strain profiles illustrated in Figs. 6.36 and 6.37 were estimated from the readings taken with linear potentiometers attached to the beam and following the procedure described in Section 3.8.3.2.

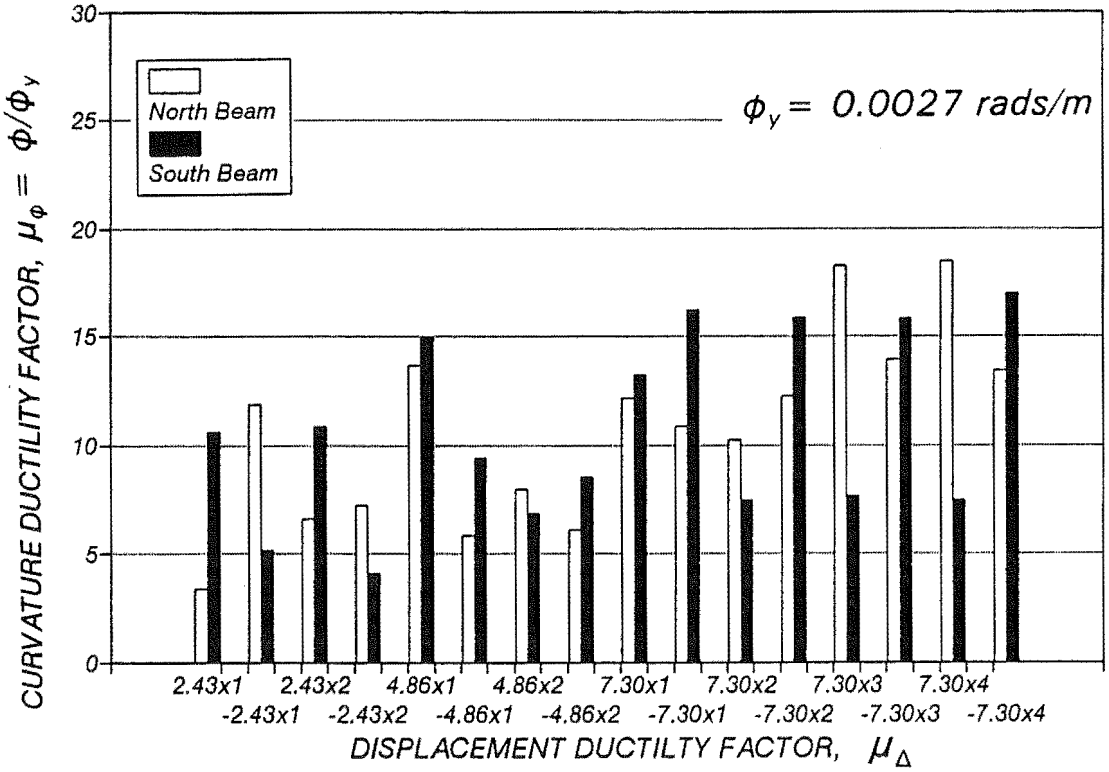

Fig. 6.34 - Beam Curvature Ductility Factors of Unit 6.

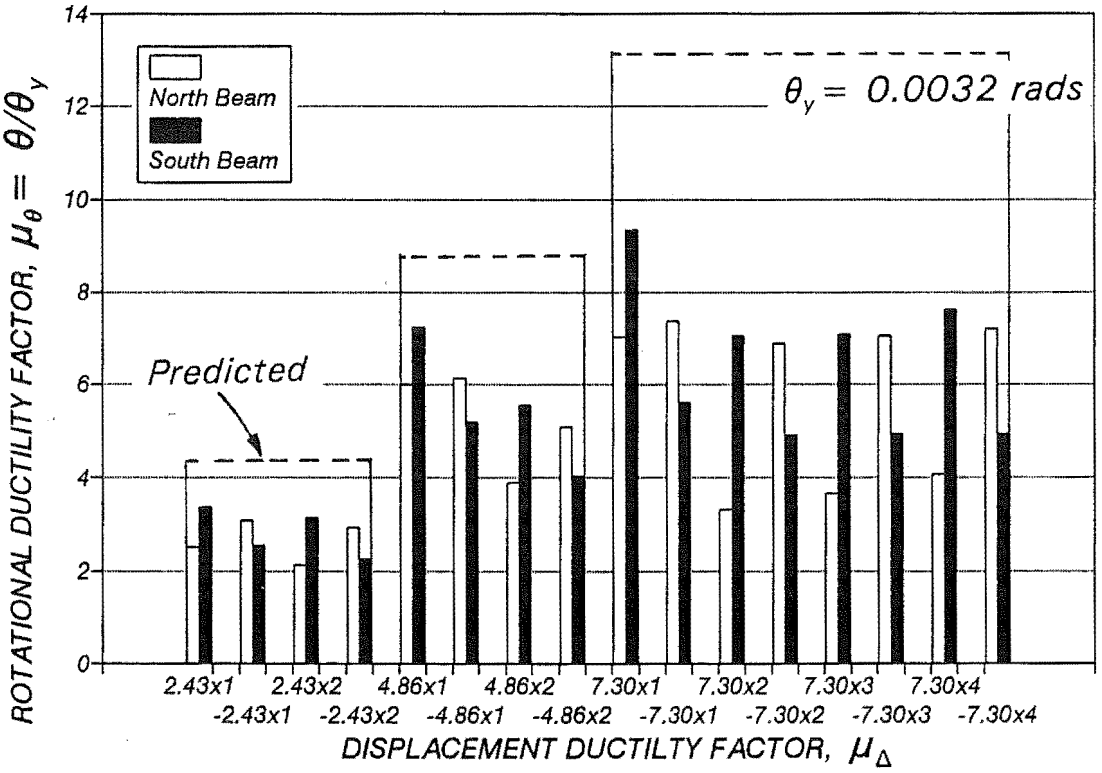

Fig. 6.35 - Beam Rotational Ductility Factors of Unit 6.

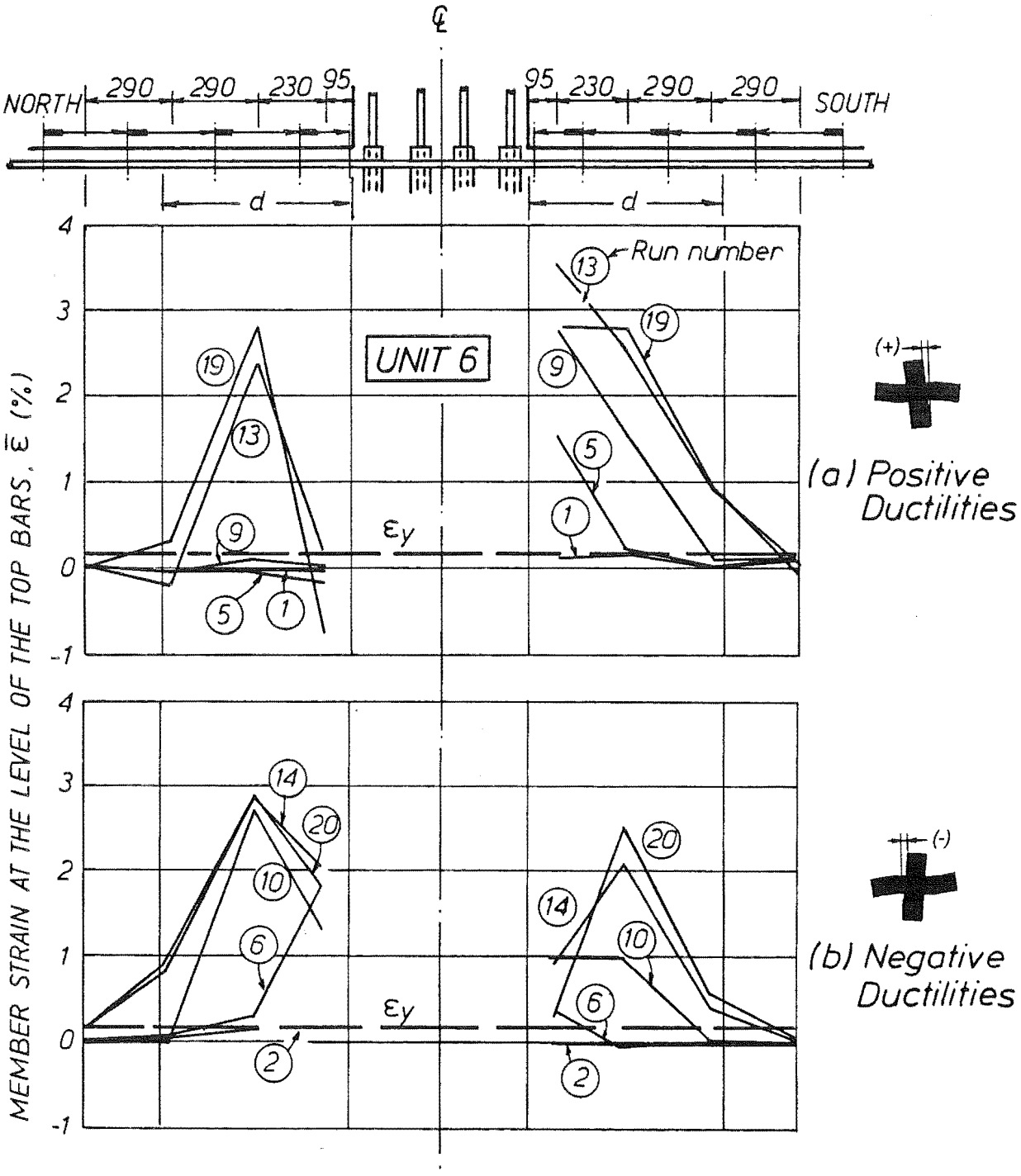

Fig. 6.36 - Beam Strain Profiles at the Level of the Top Reinforcement of Unit 6.

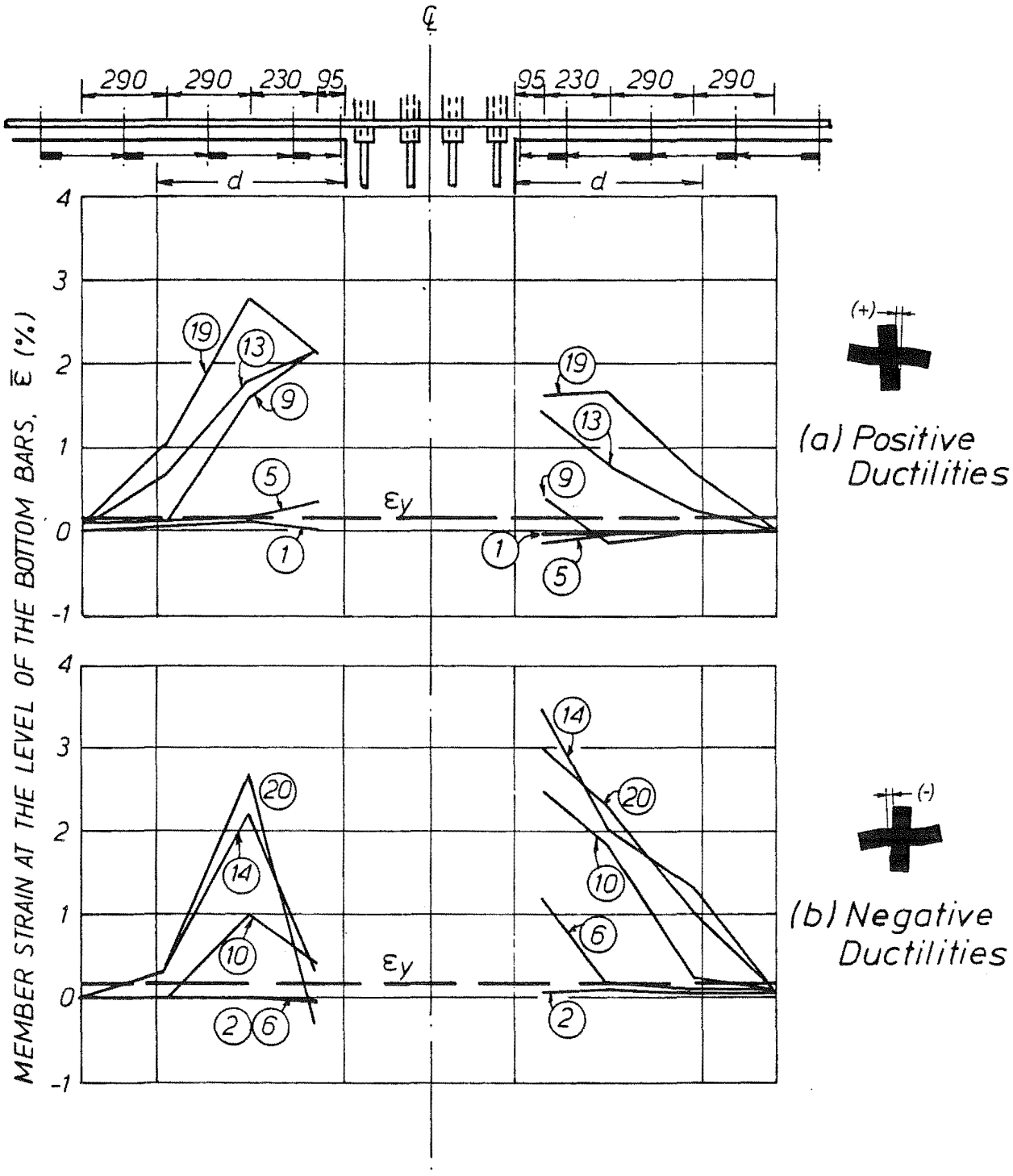

Fig. 6.37 - Beam Strain Profiles at the Level of the Bottom Reinforcement of Unit 6.

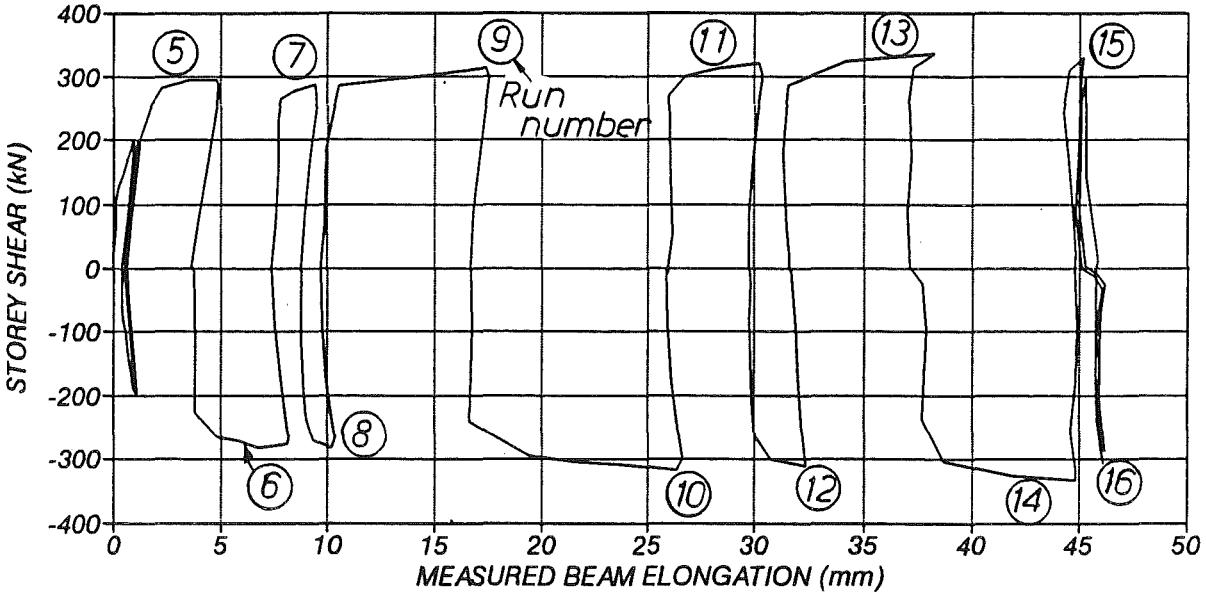

Fig. 6.38 - Total Beam Elongation of Unit 6.

In the initial loading cycles in the inelastic range yielding spread along the beam from the column faces and then gradually extended over a distance larger than d. However, the instrumentation placed did not permit determination with certainty of whether yield of the reinforcement actually occurred beyond a distance d from the column faces.

The strain distribution as estimated from linear potentiometer measurements followed the same trends that those observed in the beams of Units 1, 2 and 3 as well as in the bottom of the beams of Unit 5. That is, the measurements taken near the faces of the columns were very sensitive to the formation of cracks in the beams in that region. Cracks tended to cross the holes provided for clearance around the steel rods embedded in the concrete and used to hold the brackets for fastening the displacement transducers. This is why the strain distributions in the negative displacement ductilities of the north top of the beam (Fig. 6.36) and in the positive displacement ductilities of the north bottom of the beam (Fig. 6.37) did not indicate maximum strain at the faces of the column.

6.3.6.3 Beam Elongation

The total measured elongation of the beams of Unit 6 plotted against the lateral load is depicted in Fig. 6.38. Some residual beam elongation remained after the loading cycles in the elastic range due to the imperfect closure of the initial cracking. In the loading cycles in the inelastic range the cumulative elongation of the beam increased until in load run 15 the flexural capacity of the unit was no longer attainable due to the considerable shear deformations in the plastic hinges. At this stage the total elongation had reached 45mm, a value much larger than that recorded in Unit 5. The main reason for the difference between the two results is the good anchorage conditions in the joint of Unit 6, which permitted the plastic hinges to spread along the beam from the columns faces.

6.4 CONCLUSIONS

1. The overall performance of the units tested was very satisfactory in terms of strength and ductility. The connection details between the precast elements were observed not to have a detrimental effect on the seismic behaviour of the beam-column systems tested. Hence behaviour of the units as if of monolithic constructions was achieved.

2. Unit 5, which had the lower part of the beams precast and the bottom beam bars anchored inside the cast in place concrete beam-column joint core showed that this type of detail can be effectively used in the construction of ductile moment resisting frames. Sliding along the vertical construction joints at the ends of the precast concrete beams at the face of the column was kept to a minimum despite the smooth surface of the construction joints. It appears that by seating the precast concrete beams on the cover of the column below vertical sliding shear is controlled and it is not necessary to provide shear keys along the construction joints. However some surface roughness of the ends of the beams is recommended.

3. From the observation made in Units 5 and 6, it can be concluded that the current recommendations of the Concrete Design Code [NZS 3101 (1982)] for limiting the diameter of the longitudinal bars passing through the joint are adequate but not necessarily conservative. In exceptional cases such as with the quality of the concrete cast in place in the beam-column joint core of Unit 5, bleeding of the concrete may result in bond failure of top bars during severe earthquake loading.

   It is therefore recommended that any revision to the current provisions considers the "top bar effect".

4. In Unit 6 the effect of the grouted vertical ducting for the column bars did not alter the behaviour of the Unit as a whole. The forces developed in the transverse reinforcement in the beam-column joint region were effectively transferred through the grout to provide the node required to mobilise the truss mechanism for shear resistance. The smooth horizontal construction joints at the bottom of the precast concrete beam member allowed some horizontal sliding action to occur, which was not important in terms of the overall lateral displacement imposed but was large in terms of the deformations of the columns. Again some surface roughness at the bottom of the precast beam at the joint is recommended.

5. From the data gathered in this study it is concluded that in short beams typical of perimeter frames with clear span/depth ratios lower than 5, shear deformations will be expected to govern the response of the beam at large displacement ductility factors even if the nominal vertical shear stresses in the plastic hinges of symmetrically reinforced beams are kept as low as $0.20\sqrt{f'_c}$. The main factor determining this behaviour is the aspect ratio of the member.

6. The measured stiffness of the cruciform components tested indicate that the normal design office procedures used to estimate this value need more refinement.

CHAPTER 7

THE DESIGN OF PRECAST CONCRETE MEMBERS OF MOMENT RESISTING FRAMES

7.1 INTRODUCTION

This chapter deals with the design of the connections between precast concrete members using the reinforcement details of the test programme. Truss models and the concept of shear friction are used to explain the distribution of forces and to find the amount of necessary reinforcement. An analysis of the connections at midspan is made in the first part. In the second part the connections at the beam-column joint region are considered. The effects of the elongation of the beam plastic hinges are also discussed in this chapter.

7.2 THE DESIGN OF MIDSPAN CONNECTIONS BETWEEN SHORT BEAMS OF PERIMETER FRAMES

7.2.1 Determination of the Tension Force in the Longitudinal Reinforcement of a Beam

It has long been recognized that in cracked reinforced concrete beams the tension force in the longitudinal reinforcement cannot be directly estimated from the M/jd diagram due to the interaction between flexure and shear [Paulay (1969), Park and Paulay (1975)].

Following experimental work on short coupling beams between walls, Paulay (1969) found that the measured tension force in the longitudinal reinforcement was reasonable parallel to the M/jd diagram but with a permanent shift. He concluded that due to this effect the top and bottom longitudinal reinforcement in a beam will be subjected to equal tension forces in its point of contraflexure and, in extreme circumstances such as very deep beams, all longitudinal reinforcement could eventually be subjected to tension all along the beam.

The effects of the "tension shift" are illustrated in Fig. 7.1, where a typical bending moment diagram for a beam of a perimeter frame of a building is shown. In general in short beams of perimeter frames gravity loading does not have a significant influence and therefore it can be assumed that the point of contraflexure in the beam coincides with its midspan.

The tensile forces in the longitudinal steel of a conventionally reinforced beam can be estimated from Fig. 7.1 (c) by accounting for the "tension shift". If the effect of gravity loading is ignored, the maximum probable tension force T′ at a distance x from the point of contraflexure is

$$T' = V^\circ \left(\frac{x}{jd} + \frac{1}{2\tan\theta}\right) \quad \text{for} \quad \frac{l_b'}{2} - \frac{jd}{2\tan\theta} \geq x \geq -\frac{jd}{2\tan\theta}$$

or

$$T' = V^\circ \frac{l_b'}{2jd} = T^\circ \quad \text{for} \quad \frac{l_b'}{2} \geq x \geq \frac{l_b'}{2} - \frac{jd}{2\tan\theta} \tag{7.1}$$

where V° is the shear at the development of the flexural overstrength of the beam, jd is the internal lever arm, θ is the angle of inclination of the compression field, l_b' is the beam clear span, and T° is the tension force in the longitudinal beam reinforcement at the steel overstrength.

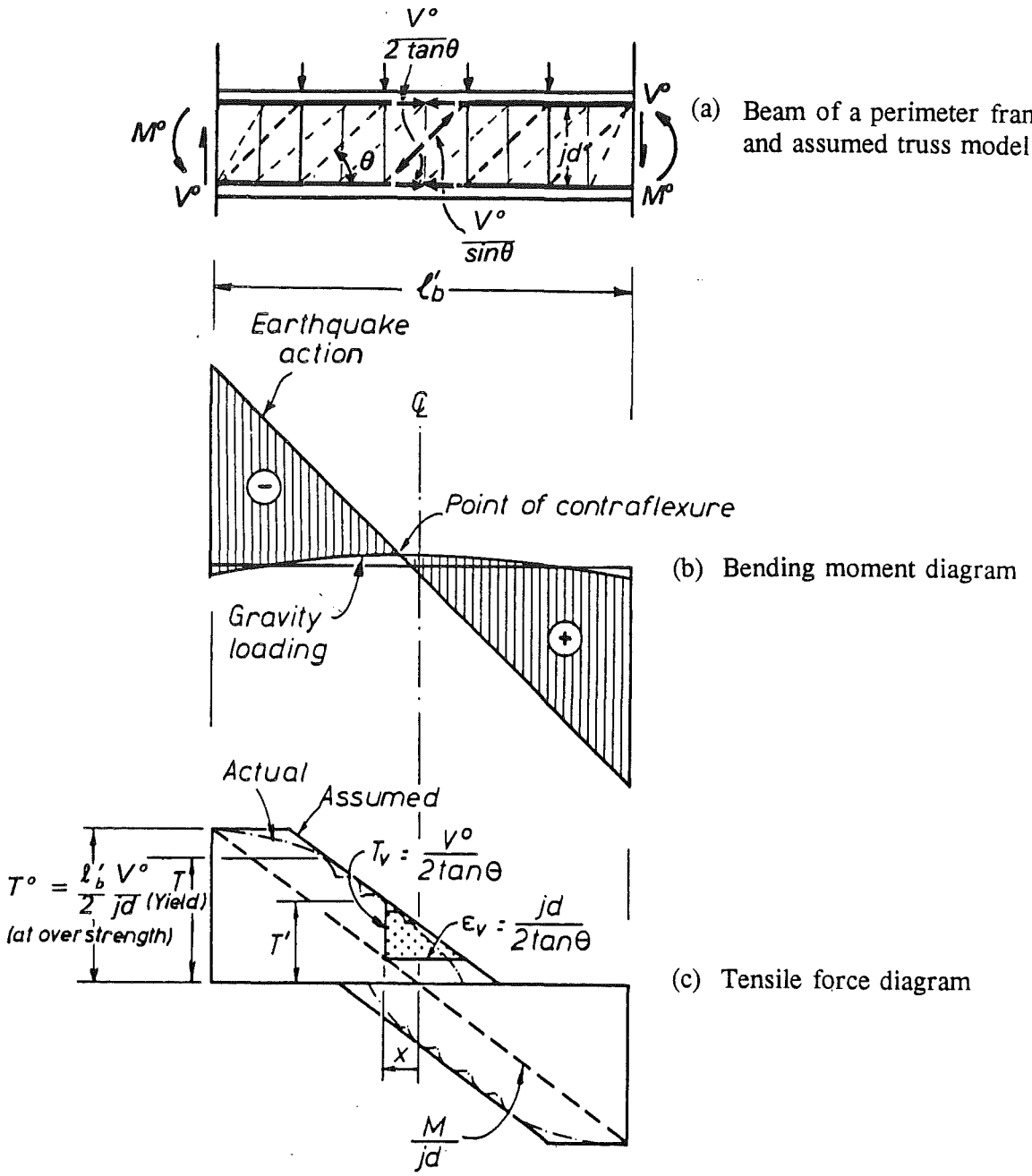

(a) Beam of a perimeter frame and assumed truss model

(b) Bending moment diagram

(c) Tensile force diagram

Fig. 7.1 - A Conventionally Reinforced Concrete Beam of a Perimeter Frame.

The tension force T′ at midspan can be obtained from Eq. 7.1 substituting x = 0,

$$T' = \frac{V^{\circ}}{2\tan\theta} \tag{7.2}$$

It is evident from Eq. 7.2 that any connection located at the point of contraflexure of a short beam will have to resist a moderate set of forces T′ without adversely affecting the capacity nor the ductility of the connecting members. It can also be seen in Eq. 7.2 that larger values of T′ are expected in beams carrying larger shear forces and that the flatter the angle of inclination θ of the diagonal compression field, the larger the effects of the "tension shift".

Park and Paulay (1975) made a theoretical evaluation of the "tension shift" effect based on considerations of equilibrium assuming that the shear in the beam is carried by two different mechanisms, involving the concrete (through aggregate interlock) and the transverse steel. They found a family of solutions for different combinations on the amount of shear carried by aggregate interlock, the inclination of the cracks and the angle of inclination of the stirrups. They recommended that a tension shift e_v = d, where d is the effective depth of the beam, would be a simple value to be used in a design procedure. This value has been implicitly adopted in the ACI-318 Concrete Design Code (1989) and in the NZS 3101 Code (1982) in the curtailment of the flexural reinforcement of beams.

The magnitude of the "tension shift" can also be directly evaluated by modelling the cracked reinforced concrete beam as a truss member with the diagonal compression struts inclined at an angle θ to the horizontal. This is known as the variable angle truss model [Collins and Mitchell (1991)]. In an attempt to quantify the angle of inclination of the struts, the plasticity theory [Nielsen et al (1978), Thürlimann (1978)] assumes that both concrete and steel will reach ultimate conditions at the same time. An effective or reduced concrete strength is accounted for in the equilibrium conditions and some empirical concrete contribution is needed to satisfy the solution for lightly reinforced beams. The variable truss model has been used in the CEB-FIP Concrete Design Code (1978) where the designer chooses an angle of inclination $31^{\circ} \leq \theta \leq 59^{\circ}$. The corresponding "tension shift" is from geometry in Fig. 7.1 (c) $e_v = jd/2\tan\theta$, where jd is the lever arm in the beam. If j is assumed equal to 0.9 the tension shift is limited to $0.27d \leq e_v \leq 0.75d$, which are smaller values than those implicitly adopted by the ACI-318 and the NZS 3101 Concrete Design Codes. In terms of the angle of inclination of the diagonal compression field these two codes assume $\theta = 24^{\circ}$.

A refined procedure to find the values of the angles of inclination of the diagonal struts has been presented by Collins and Mitchell, which considers conditions of equilibrium, compatibility and assuming a stress-strain relationship for the materials. This procedure has been shown to be accurate but can be lengthy for use in practice.

The "tension shift", e_v, measured at the beginning of the hooks in Units 1 and 2 and at midspan in Unit 3 was 0.50d, 0.23d and 0.56d, respectively. These values are closer to the tension shift

predicted by the variable angle truss model than that of e_v = d, implicit in NZS 3101. Note, however, that the above values were determined from calculated stresses in the reinforcement, which in turn were estimated from average strains in the reinforcement. As a result, the total force in the section may be underpredicted because the concrete carries tensile forces between cracks. However, this contribution is unlikely to compensate for the difference observed between e_v = d and that measured.

It is believed that the New Zealand code provisions could be made more realistic. The transverse reinforcement in the critical region of members designed in accordance with NZS 3101 (1982) can be governed either by the shear or by the anti-buckling requirements if the level of axial load is small as it is the case of beams or cantilever structural walls. The design for shear is based on a 45° truss model. The contribution of the concrete in carrying the shear is nil for zero axial load level and increases with the axial compressive load. Outside of the plastic hinge region the contribution of the concrete in carrying the shear is significantly increased in recognition of the shear transfer through aggregate interlock. That is, the resulting diagonal compression field will be flatter in this region. It is estimated that an angle θ = 35° will still provide a conservative envelope in members designed to NZS 3101:1982. This angle of inclination of the diagonal compression field will result in $e_v = 0.7jd \approx 0.65d$, which could have an important effect on the curtailment of the reinforcement of structural concrete and masonry walls and to a lesser extent in the curtailment of the beam reinforcement. This angle will be adopted in the derivation of the design recommendations for the connection between precast concrete members presented in the following sections.

7.2.2 Design of Midspan Connections with Overlapping Hooks

The use of overlapping hooks for connecting precast concrete beams is particularly useful when these beams possess a rather low aspect ratio and have space limitations for the connection. This section deals with the design of the connection details using overlapping hooks at the point of contraflexure such as those that were tested in this study.

In the test of Units 1 and 2 it was indicated that the connection detail at the beam midspan did not fulfil a lapping action since the tension bars were well anchored by the hooked ends.

An equilibrium solution for the connecting detail used in Unit 1 that satisfies the experimental observations is illustrated in Fig. 7.2. Since there is no continuity between the top overlapping bars and the hooked bars protruding from the precast concrete unit to the right in Fig. 7.2 the whole beam shear needs to be locally transferred by a tension tie between the top and bottom connecting details. In the detail using overlapping hooks the compression field will be fanned in a very similar way to that of a simply supported beam. The main difference between this detail and the seating of a simply supported beam is the way how the forces enter the node. With regard to Fig. 7.3, the vertical force in the connecting detail comes from a tie in tension while in the simply supported beam it comes from the compression against the seating.

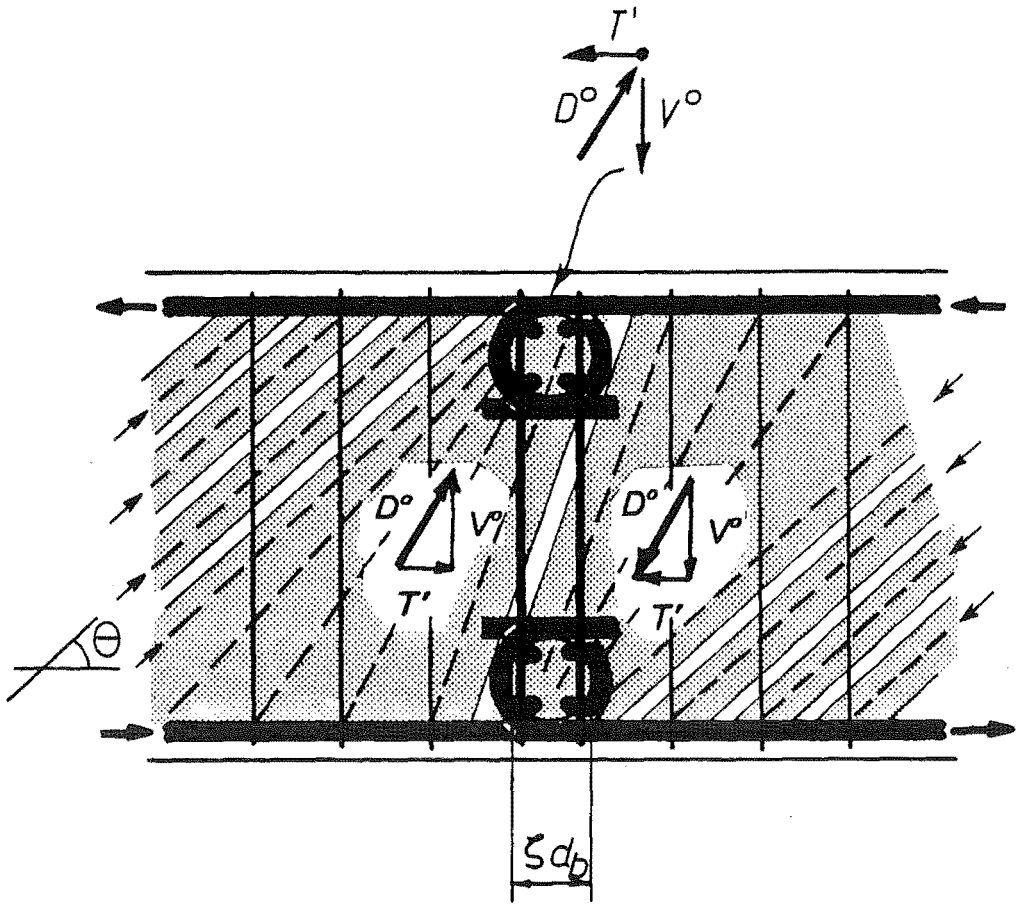

Fig. 7.2 - Truss Model for Midspan Connection with Overlapping Hooks.

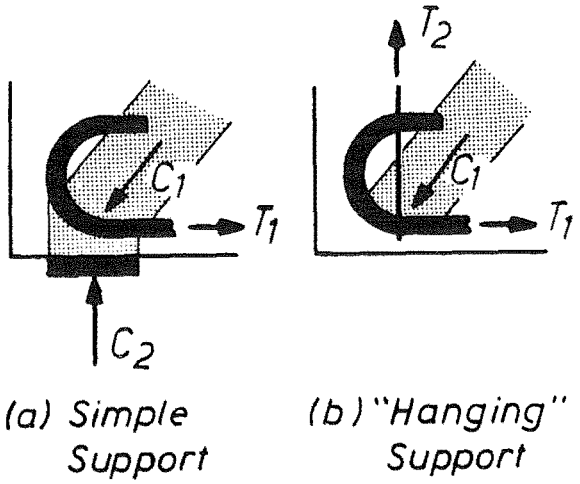

Fig. 7.3 - Comparison of Boundary Conditions between a Simple Supported Beam and a Midspan Connection.

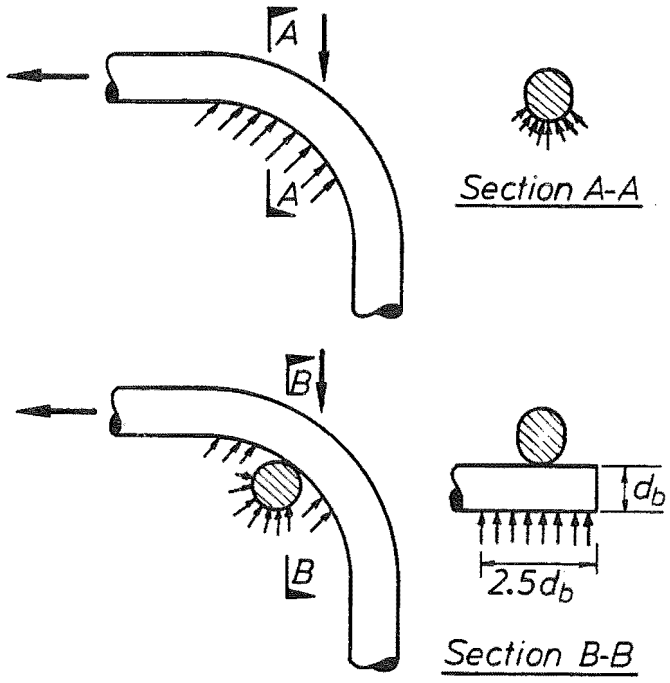

Fig. 7.4 - Role of Transverse Rods in Hooked Connections.

It can be argued that transferring the whole shear at the connection region by a tension steel tie ignores any contribution by tension in the concrete, especially in beams with a nominal shear stress below the diagonal tension cracking stress of about $0.33\sqrt{f'_c}$ as stipulated by the New Zealand Concrete Design Code. However, for this type of short splice a large difference in the amount of tie reinforcement required will not bring large savings to the construction itself.

Splitting of the concrete caused by the radial components of the hooked anchorages can eventually have a detrimental effect on the compressive strength of the concrete strut in the connecting detail. This is why the detailing of the reinforcement in this region is of primary importance. Transverse rods will help in the distribution of the stresses as illustrated in Fig. 7.4. In addition, closed stirrups around the hooked connection will also be required to avoid a premature failure due to splitting.

The bend radii of the hooked bars shall be such to avoid a premature compression failure of the concrete strut at that point. For this, the calculated stresses should be limited to a value related to the unconfined cylinder strength of the concrete, f'_c. From Fig. 7.2

$$D^\circ = \sqrt{V^{\circ 2} + T^2} \tag{7.3}$$

where D° is the diagonal force carrying the beam shear V°. Both forces are associated with the beam flexural overstrength.

Substituting $\theta = 35^\circ$ in Eq. 7.2 gives

$$T' = 0.71V^{\circ} \tag{7.4 a}$$

and substituting T′ from Eq.7.4 (a) into Eq.7.3 gives

$$D^{\circ} = 1.23V^{\circ} \tag{7.4 b}$$

The above force T′ needs to be resisted by the longitudinal reinforcement being overlapped at midspan.

The bearing stresses, f_b, induced by the diagonal strut acting upon the hooked bar (see Fig.7.2) can be estimated as

$$f_b = \frac{D^{\circ}}{\zeta d_b (b_w - 2c_o)} \tag{7.5}$$

where ζ is the ratio between the diameter of the bend and the diameter of the bar d_b, b_w is the width of the beam and c_o is the concrete cover to the reinforcement.

Substituting Eq. 7.4 (b) in Eq. 7.5, assuming $b_w - 2c_o \approx 0.75b_w$ and rearranging for ζ gives

$$\zeta = \frac{1.64V^{\circ}}{d_b b_w f_b} \tag{7.6}$$

According to Schlaich et al (1987) an appropriate value for the maximum bearing stress in a node of the type shown in Fig. 7.3 (b) in terms of the concrete cylinder strength is

$$f_b = 0.6 \times 0.85\, f_c' = 0.51 f_c' \tag{7.7}$$

where a strength reduction factor $\phi = 1$ has been taken for a capacity designed element [NZS 3101 (1982)].

Then substituting Eq. 7.7 in Eq. 7.6 gives the minimum value permitted for ζ

$$\zeta = \frac{3.2V^{\circ}}{d_b b_w f_c'} \tag{7.8}$$

According to the recent amendment to the New Zealand Concrete Design Code, the factor ζ shall not be less than 5 for bars of 6-20mm in diameter or less than 6 for bars of 24-40mm in diameter.

The connection detail using overlapping "drop in" double hooked bars can be considered an extension of the previous case. A truss model based on the experimental evidence is illustrated in

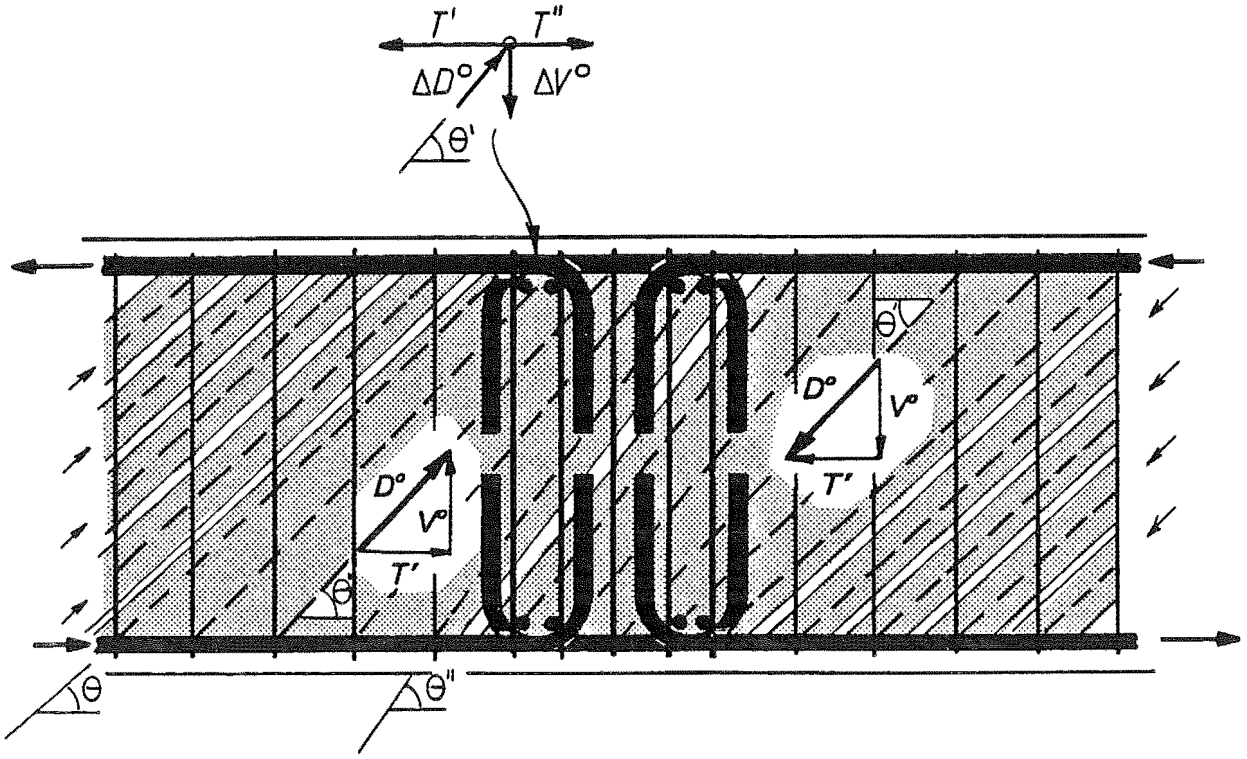

Fig. 7.5 - Truss Model for Midspan Connection Using "Drop In" Double Hooked Bars.

Fig. 7.5. The compression field fan will spread through the splice at an angle varying from θ to θ'' as shown in Fig. 7.5. The resultant diagonal force D° will be at an angle θ' which lies between θ and θ''. For simplicity it can be assumed that the diagonal compression field will spread from the connection at this angle θ'. Therefore the force T" in the "drop in" bars can be estimated from Fig. 7.5 to be

$$T'' = T' - \frac{\Delta V^\circ}{\tan\theta'} \tag{7.9}$$

where $\tan\theta' = V^\circ/T'$ and ΔV° is the fraction of the beam shear force at overstrength transferred by the set of stirrups in the overlapping region.

A practical lay-out of the transverse reinforcement in this region is to have five sets of stirrups arranged as shown in Fig. 7.5. This arrangement implies that $\Delta V^\circ = 2/5 V^\circ$ will be transferred in the overlapping region.

$$T'' = T' - \frac{2}{3}V^\circ \frac{1}{V^\circ/T'} = \frac{3}{5}T' \tag{7.10}$$

The force T' at the beginning of the hooks can be calculated assuming that the offset distance to the point of contraflexure is 0.2jd. This is a reasonable assumption for the dimensions normally used

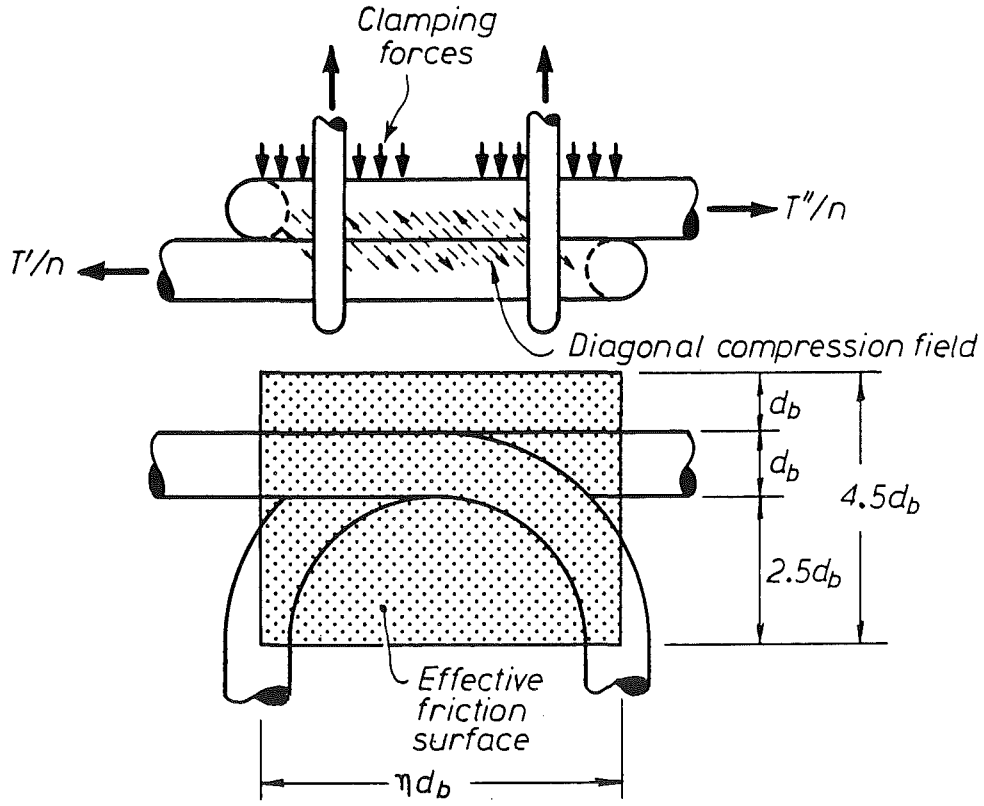

Fig. 7.6 - Transverse Reinforcement Required at the Overlapping of the Hooked Bars in a "Drop In" Connection.

in perimeter beams. Hence, substituting Eq. 7.1 in Eq. 7.10 and x by the approximate value results in

$$\theta = 35°, \tag{7.11 a}$$

$$T' = 0.91\ V°, \tag{7.11 b}$$

and

$$T'' = 0.55\ V°.$$

Enough longitudinal reinforcement should be present in the overlapping region to ensure that the force T′ can actually be developed. Besides, the above force T″ needs to be transferred to the "drop in" bars from the protruding hooked bars through the concrete. The shear transfer mechanism can be designed using the shear friction concept. With reference to Fig. 7.6, the area of transverse reinforcement required, A_{st}, is

$$A_{st} = \frac{T''/n}{\phi \mu_f f_{yt}} \tag{7.12}$$

where f_{yt} is the yield strength of the transverse steel, μ_f is the coefficient of friction taken as 1.4 for monolithic concrete, n is a factor that relates the maximum force to be transferred between the lapped bars estimated as shown in Fig. 7.7, and ϕ is the strength reduction factor taken as 1 for capacity designed members.

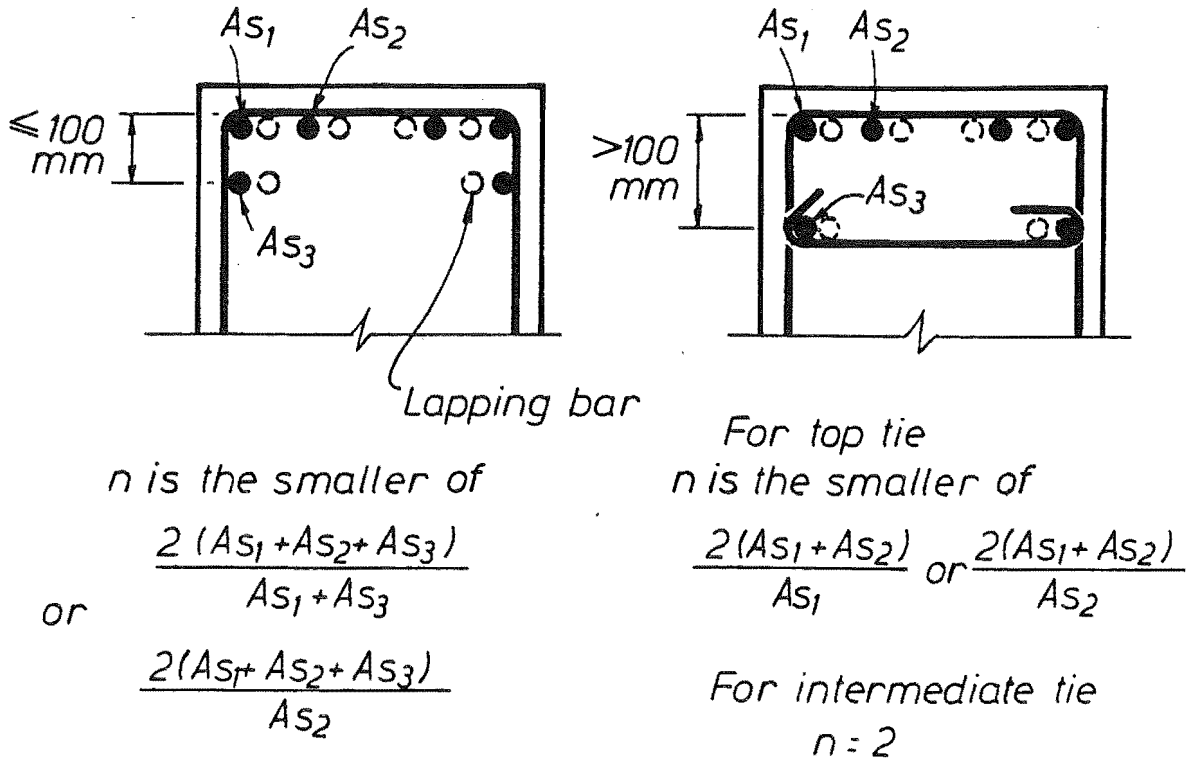

Fig. 7.7 - Criteria for Determining Factor n.

Then combining Eq. 7.11 (b) and Eq. 7.12 gives

$$A_{st} = 0.39 \frac{V^{\circ}}{nf_{yt}} \approx \frac{V^{\circ}}{2.5nf_{yt}} \tag{7.13}$$

It is now necessary to verify that the force T″ can be transferred without premature crushing of concrete. The current New Zealand Concrete Design Code limits the shear stresses in the concrete, τ_f, at the development of the shear friction mechanism to a maximum of $0.2f'_c$ or 6MPa whichever is smaller. The effective friction surface A_τ where the lapping action between the hooks occurs can be estimated as depicted in Fig. 7.6,

$$A_\tau = 4.5\eta d_b^2 \tag{7.14}$$

where ηd_b is the lapping distance measured between the centrelines of the extension lengths of the hooks. In no case will η be less than the minimum diameter of bend plus one bar diameter. That is $\eta \geq 6$ for bars of 6-20mm in diameter and $\eta \geq 7$ for bars between 24-40mm in diameter.

Therefore the average shear stress, τ_f, is equal to the force being transferred, T″/n divided by the area A_τ resulting in

$$\tau_f = \frac{T''/n}{A_\tau} \tag{7.15}$$

Combining Eqs. 7.11 (b) and 7.14 in Eq. 7.15 and rearranging for η gives

$$\eta = \frac{0.12}{n} \frac{V^\circ}{\tau_f d_b^2} \tag{7.16}$$

Now substituting τ_f by the limiting values and summarizing results in

$$\eta \geq \begin{cases} 0.6 \dfrac{V^\circ}{n f_c' d_b^2}, & \text{(7.17 a)} \\ \text{or} \quad \dfrac{V^\circ}{45 n d_b^2}, & \text{(7.17 b)} \\ \text{or} \quad 6 \quad \text{for} \quad 6 \leq d_b \leq 20, & \text{(7.17 c)} \\ \text{or} \quad 7 \quad \text{for} \quad 24 \leq d_b \leq 40. & \text{(7.17 d)} \end{cases}$$

7.2.3 Design of Midspan Connections Using Straight Bar Splices

Straight bar splices offer a very simple and effective way for connecting precast elements together. The straight bars protruding from the precast concrete beams may or may not overlap the bars from the connecting element. In the first case a non-contact lap splice is normally used while in the second case a double straight lap involving additional reinforcement is used.

The design procedure for finding the length of the splice as well as the transverse reinforcement around it can be derived using the recommendations of the New Zealand Concrete Design Code. In evaluating the code required splice length, which is considered equal to the development length, l_d, all modification factors may be considered. This section will present an alternative design procedure to determine the splice length and the transverse reinforcement based on the shear friction concept, which is similar to that presented by Paulay (1982) (see also Paulay and Priestley (1992)).

Fig. 7.8 shows a non-contact horizontal lap splice that is used to connect two precast concrete elements at the beam midspan. Also shown in Fig. 7.8 are two diagonal compression fields, one of them in the vertical plane which is required to balance the shear forces and the force T - T'.

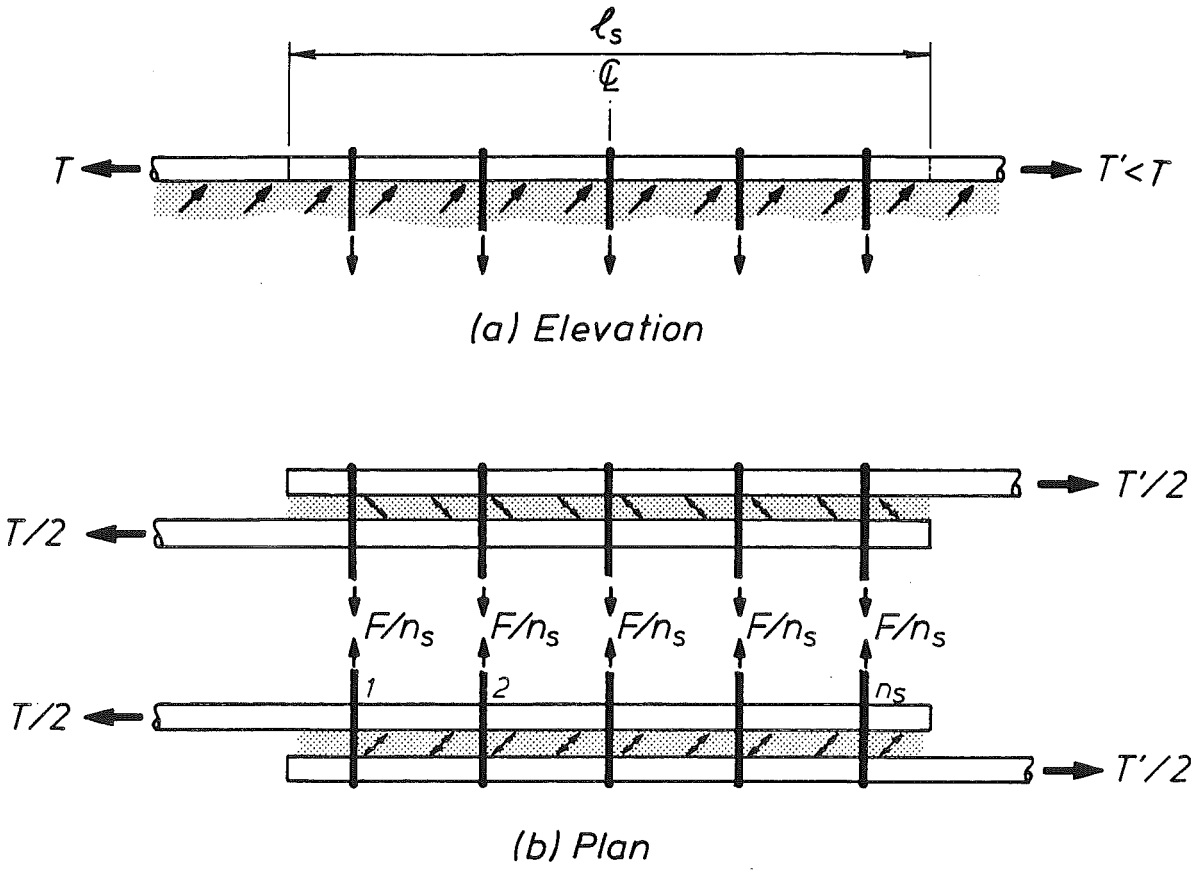

Fig. 7.8 - Diagonal Compression Field around a Midspan Straight Splice.

The other diagonal compression field, acting on the horizontal plane, transfers the force T'/2 between each pair of bars. For a lapped connection symmetrically located at the point of contraflexure it is convenient, and conservative, to assume that the force T' at the end of the splice is equal to that derived from the shifted tension force diagram at midspan T". This assumption has the advantage of uncoupling T' from the length of the splice and also forms the particular solution for a double straight lap.

Therefore, T" is found assuming $\theta = 35°$ in Eq. 7.2.

$$T'' = 0.71\ V° \tag{7.18}$$

The amount of reinforcement required to cross the potential crack along the spliced bars can be estimated using the shear friction concept as in Eq. 7.12. Hence substituting Eq. 7.4 in Eq. 7.12 and replacing $\phi = 1$ and $\mu_f = 1.4$,

$$A_{st} = 0.51\ \frac{V°}{nf_{yt}} \approx \frac{V°}{2nf_{yt}} \tag{7.19}$$

The above expression can also be applied to splices where the shear friction mechanism will develop in the vertical plane.

To enable an efficient use of the transverse reinforcement given by Eq. 7.19, no splicing bars should be at more than 100mm apart from an adjacent tie (see Fig. 7.7).

The force T'/n in each lapping bar will be transferred over the length of the splice, l_s and a width of $3d_b$ as suggested by Paulay (1982). Thus the effective friction surface, A_τ, is given by

$$A_\tau = 3 d_b l_s \tag{7.20}$$

and the average shear stress, τ_f is

$$\tau_f = \frac{T''}{n} \frac{1}{A_\tau} \tag{7.21}$$

Substituting Eqs. 7.18 and 7.20 in Eq. 7.21 and simplifying

$$\tau_f = 0.24 \frac{V^\circ}{n d_b l_s} \tag{7.22}$$

Then the length of the splice shall be such as to satisfy the two limits imposed to avoid a crushing failure at the development of the shear friction mechanisms. That is, substituting 6MPa or $0.2f'_c$ for τ_f Eq. 7.22 and rearranging for l_s gives in summary

$$l_s \geq \begin{cases} \dfrac{1}{25n} \dfrac{V^\circ}{d_b}, \\ \dfrac{1.2}{n} \dfrac{V^\circ}{d_b f_c'}, \\ \text{or} \quad l_{db} \end{cases}$$

7.2.4 The Design of Connections using Diagonal Reinforcement and Bolted Steel Plates

Chapter 5 was concerned with the test of a precast concrete subassemblage with diagonal reinforcement and connected at midspan with bolted steel plates. The test unit had been designed to concentrate all the inelastic deformations within the central part of the beam. Thus, the plastic hinge

regions were relocated from the beam ends using extra reinforcing steel as required by the simple truss model shown in Fig. 3.9 The initial design overlooked the fact that the additional bars used to relocate the beam plastic hinges and the bars that were diagonally bent and welded to the midspan steel plates were in different planes. As a result there were significant out of plane forces that caused splitting cracks between the layers of reinforcement. Consequently the nodes of the simple truss model were destroyed and the test unit displayed a limited ductile response.

The damaged unit was repaired taking into account the three dimensional effects and detailing transverse reinforcement in the critical regions at the bend of the diagonal bars. This test displayed an excellent ductile behaviour.

The experimental results showed an adequate performance of the bolted connection at the midspan of the beams. No further discussion regarding the bolted steel connections is made in this study since the design of these types of connections is found in standard structural steel textbooks. Therefore, the remainder of this section will be limited to the design of the transverse reinforcement around the outer bars in the critical region at the bend of the diagonal bars.

With regard to Fig. 5.6, the force R_H required for equilibrium on the outer bars in the strong ends of the beam was found in Eq. 5.2 in terms of the different forces acting upon the critical region at the bend of the diagonal bars. For a capacity designed member it will be expected that the sum of forces $T_v + S_T$ should be equal to the beam shear. Also, for the inclination of the diagonal reinforcement in normal practice it can be considered that the difference between force T_H and T is sufficiently small that these forces can be ignored. Hence Eq.5.2 can be rewritten in terms of the beam shear force at the flexural overstrength, V°, and the angle of inclination of the diagonal strut, β, as

$$R_H = \frac{V^\circ}{\tan\beta} \tag{7.24}$$

The beam shear force can be found in terms of the force in the diagonal bars as

$$V^\circ = \frac{2A_{sdg}\,\lambda_o\,f_y}{\sqrt{1 + \left(\frac{l_{dg}}{d-d'}\right)^2}} \tag{7.25}$$

where A_{sdg} is the area of reinforcement in each of the diagonals, λ_o is the steel overstrength factor, l_{dg} is the length of the beam between the critical regions and d-d′ is the distance between the centroids of the beam longitudinal reinforcement.

The inclination of the diagonal strut can also be found in terms of the geometry of the beam as shown in Fig. 7.9

$$\tan\beta = \frac{d-d'}{l_{st}} \le 0.75 \tag{7.26}$$

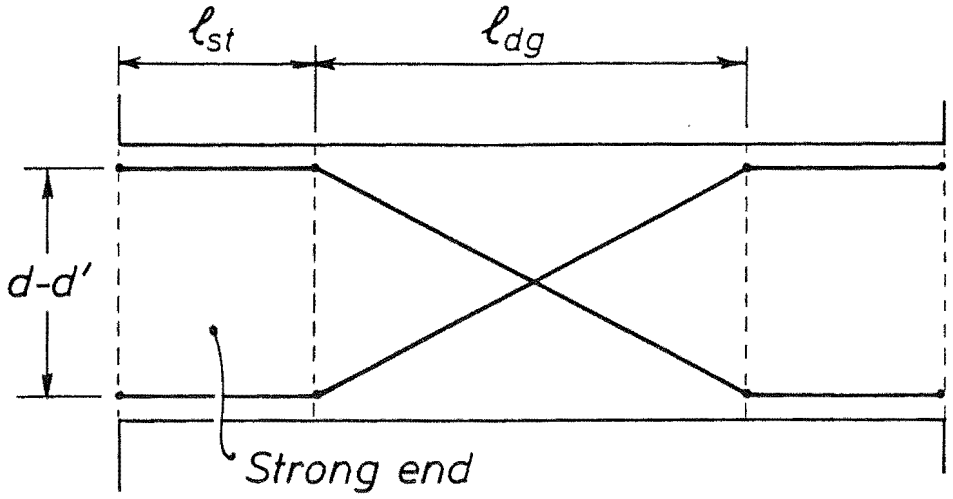

Fig. 7.9 - Diagonally Reinforced Beam with Relocated Plastic Hinges.

where l_{st} is the distance between the face of the column and the critical region at the bend of the diagonal reinforcement. It is suggested that the angle β should not be taken as less than 37° since it is likely that for plastic hinges relocated at a distance larger than 1.33 (d-d') from the column face, the diagonal strut at the bend of the diagonal reinforcement will not converge at the column face.

Thus, substituting Eqs. 7.25 and 7.26 into Eq. 7.24 gives

$$R_H = 2\frac{l_{st}}{d-d'}\frac{A_{sdg}\,\lambda_o\,f_y}{\sqrt{1+\left(\frac{l_{dg}}{d-d'}\right)^2}} \qquad (7.27\text{ a})$$

or

$$R_H = \frac{8}{3}\frac{A_{sdg}\,\lambda_o\,f_y}{\sqrt{1+\left(\frac{l_{dg}}{d-d'}\right)^2}} \qquad (7.27\text{ b})$$

whichever is smaller.

The clamping force required to transfer one half of the force R_H to each side of the beam is found from the shear friction concept

$$A_{st}f_{yt} = \frac{R_H/2}{\phi\,\mu_f} \qquad (7.28)$$

where A_{st} is the area of transverse reinforcement and f_{yt} is its yield strength, ϕ is the strength reduction factor taken equal to 1 for capacity designed elements, and μ_f is the coefficient of friction taken equal to 1.4 for monolithic concrete.

Substituting Eq. 7.27 in Eq. 7.28, assuming $\lambda_o = 1.25$ and rearranging for A_{st} gives

$$A_{st} = 0.9 \frac{l_{st}}{d-d'} \frac{1}{\sqrt{1+\left(\frac{l_{dg}}{d-d'}\right)^2}} \frac{f_y}{f_{yt}} A_{sdg} \qquad (7.29\ a)$$

or

$$A_{st} = 1.2 \frac{1}{\sqrt{1+\left(\frac{l_{dg}}{d-d'}\right)^2}} \frac{f_y}{f_{yt}} A_{sdg} \qquad (7.29\ b)$$

whichever is smaller.

The effective shear friction surface, A_τ, can be approximated to $64d_b^2$ as suggested in Fig. 7.10 where d_b is the diameter of the additional bars placed in the strong ends of the beam. This

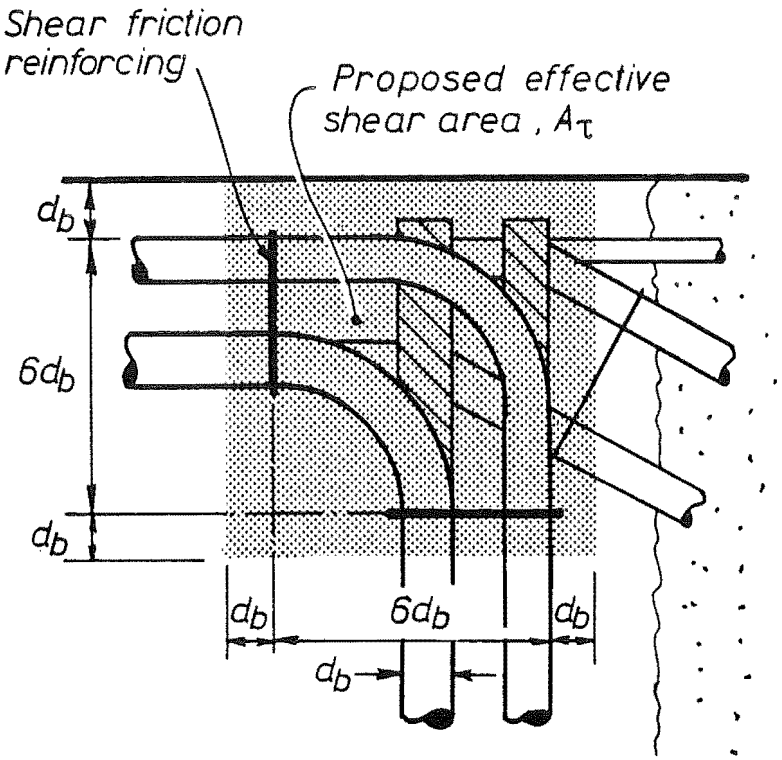

Fig. 7.10 - Effective Shear Area in the Critical Region of a Diagonally Reinforced Beam with Relocated Plastic Hinges.

area is considered to be larger than the unreinforced one shown in Fig. 5.6 (c) due to the extended influence of the clamping forces. Thus the average shear stress is given by

$$\tau_f = \frac{R_H/2}{A_\tau} = \frac{R_H}{128\,d_b^2} \qquad (7.30)$$

where τ_f is to be kept to below the smaller of $0.2f_c'$ or 6MPa.

7.2.5 Example Illustrating the Design of Connections at the Beam Midspan

The precast concrete beams of a perimeter frame are to be connected at midspan in a cast in place concrete joint. Evaluate three different alternatives using the following information,

$A_{ST} = A_{SB} = 6$ HD24
$f_y = 430$MPa
$f_c' = 30$MPa
$d = 900$mm
$b_w = 500$mm
$V^\circ = 605$kN

a) Overlapping Hooks (see Fig. 7.11 (a))

Step 1 - Splice 4 HD24 bars

$$T'_{provided} = 4 \times 452 \times 430 / 1000 = 777\text{kN}$$

Check that the amount of steel provided is greater than that required

$$T'_{required} = 0.71 \times 605 = 777\text{kN} \qquad \text{[Eq. 7.4 (a)]}$$

$$\frac{T'_{required}}{T'_{provided}} = 0.55, \text{ satisfactory}$$

Step 2 - Check the diameter of bend

$$\zeta \geq \begin{cases} 5.4 & \text{[Eq. 7.8]} \\ 6 & \text{[NZS 3101 - Table 5.1]} \end{cases}$$

Use a diameter of bend of at least 150mm ($\zeta = 6.3$).

Use 180° standard hooks and detail HD24 transverse rods in contact with the concave sides of the hooks.

Step 3 - Design the vertical transverse reinforcement in the connection region.

This reinforcement is to carry all the shear force at overstrength.

$$A_{st} = \frac{605{,}000}{430} = 1{,}407mm^2$$

Use 2-4 HD16 closed stirrups (A_{st} = 1,608mm^2)

b) "Drop in" Double Hooked Connection (see Fig. 7.11 (b))

Step 1 - Overlap 4 HD24 bars

$T'_{provided}$ = 777kN
$T'_{required}$ = 0.91 x 605 = 551kN **[Eq. 7.11 (a)]**

$$\frac{T'_{required}}{T'_{provided}} = 0.71, \quad \text{satisfactory}$$

Step 2 Design the vertical reinforcement at the connection to take all the shear force at overstrength

A_{st} = 1,407mm^2
Use 5-4 HD10 closed stirrups (A_{st} = 1,570mm^2)

Step 3 - Design the transverse reinforcement at the overlapping of the hooks to enable the development of the shear friction mechanism.

Only the legs of the outer stirrups are effective for this purpose. There are 2 legs along each splice. Hence

$A_{st\ provided}$ = 2 x 78.5 = 157mm^2
n = 4 (four bars spliced in different vertical planes, see Fig. 7.7)
$A_{st\ required}$ = 141mm^2 **[Eq. 7.13]**

Step 4 - Check the overlapping distance
Overlap the bars a distance of 174mm between centres of the extension lengths (η = 7.25).

$$\eta \geq \begin{cases} 5.3 & \text{[Eq. 7.17 a]} \\ \text{or } 5.3 & \text{[Eq. 7.17 b]} \\ \text{or } 7 & \text{[Eq. 7.17 d]} \end{cases}$$

c) <u>Non-contact splices (see Fig. 7.11 (c))</u>

<u>Step 1</u> - Lap 4 HD24 bars

$T''_{provided} = 777kN$

$T''_{required} = 0.71 \times 605 = 430kN$ [Eq. 7.18]

$$\frac{T''_{required}}{T''_{provided}} = 0.55, \text{ satisfactory}$$

<u>Step 2</u> - Find the length of the splice according to the New Zealand Concrete Design Code.

Basic development length,

$$l_{db} = \frac{380 \times 452}{52 \times \sqrt{30}} = 603mm \qquad \text{[NZS 3101:1982, Eq. 5-6]}$$

Modification factors: [NZS 3101:1982, Eq. 5-6]

Different yield strength factor, $m_1 = \frac{430}{300} = 1.43$

Top bar effect factor, $m_2 = 1.3$

Surplus of reinforcement factor, $m_3 = 0.55$

Transverse reinforcement factor, $m_4 = \frac{62}{62 + 24} = 0.72$

Hence, $l_d = m_1\, m_2\, m_3\, m_4\, l_{db} = 0.74 l_{db} = 446mm$

$l_d \geq 300mm$, satisfactory [NZS 3101:1982, 5.3.7.1]

Find the length of the splice using the alternative procedure from Figs. 7.7 and 7.11 (c),

n = 2

$$l_s \geq \begin{cases} 548\text{mm} & \text{[Eq. 7.23 a]} \\ \text{or } 504\text{mm} & \text{[Eq. 7.23 b]} \\ \text{or } 446\text{mm} & \text{[Eq. 7.23 c]} \end{cases}$$

Use l_s = 600mm ($25d_b$)

Step 3 - Design for shear at midspan

v_i = 1.34 MPa [NZS 3101:1982, Eq. 7-2]

$v_c = 0.11\sqrt{f_c'} = 0.60$ MPa [NZS 3101:1982, Eq. 7-4]

$v_s = 1.34 - 0.60 = 0.74 > 0.35$ [NZS 3101:1982, Eq. 7-12]

$$\frac{A_v}{s} = 0.74 \times \frac{500}{430} = 0.86 \frac{\text{mm}^2}{\text{mm}}$$ [NZS 3101:1982, Eq. 7-14]

Step 4 - Find the transverse reinforcement required to develop the shear friction mechanism along the spliced bars.

$$A_{st} = \frac{605{,}000}{2 \times 2 \times 430} = 352\text{mm}^2$$ [Eq. 7.19]

that is, $$\frac{A_{st}}{l_s} = \frac{352}{600} = 0.59 \frac{\text{mm}^2}{\text{mm}}$$

Therefore the shear friction mechanism controls the design, use 5 HD10 closed stirrups @ 130mm centre to centre,
($A_{v,provided}/l_s$ = 1.21mm²/mm, $A_{st,provided}/l_s$ = 0.6mm²/mm).

7.3 DESIGN OF CONNECTION AT THE BEAM-COLUMN JOINT REGION

7.3.1 General

This section deals with the design of connections between precast concrete members at the beam-column joint region. The experimental programme showed that connections of Systems 1 and 2

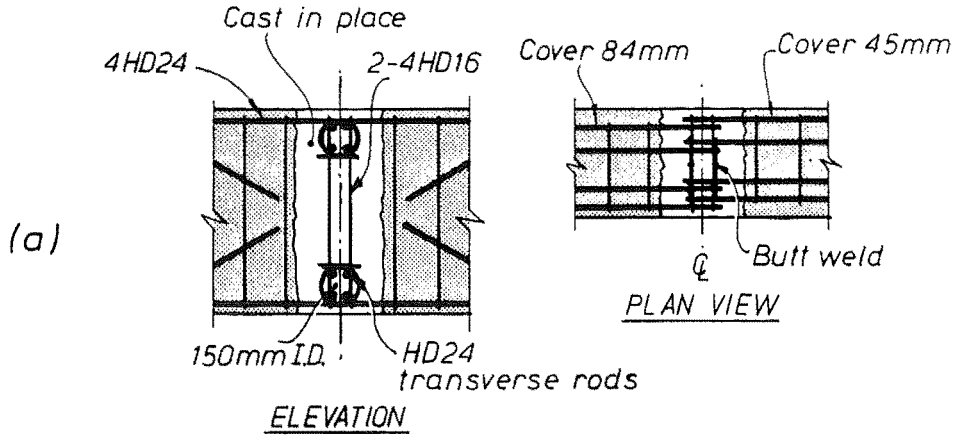

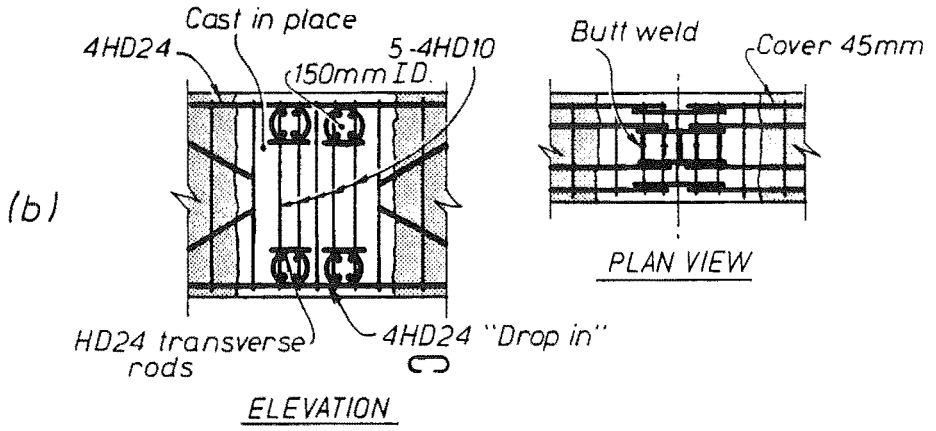

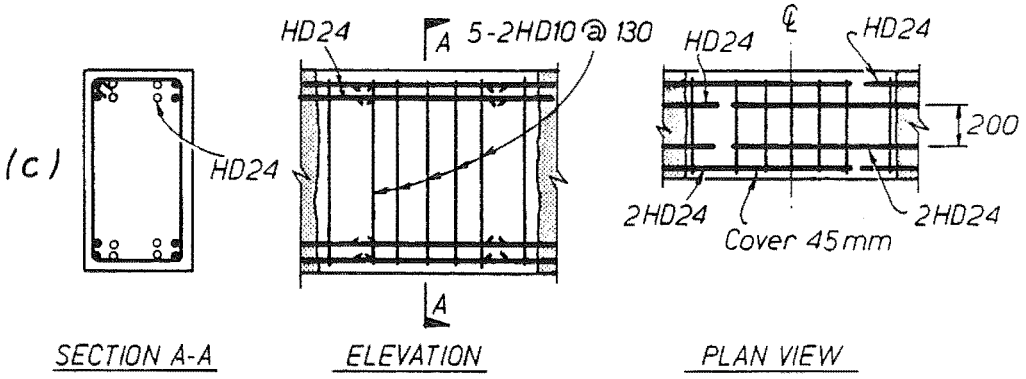

Fig. 7.11 - Design Example of Midspan Connection Details.

behaved as conventional monolithic construction. Hence, the design of interior beam-column joints will be reviewed in relation to the bond and shear transfer mechanisms.

7.3.2 Input Actions in Interior Beam-Column Joints

Fig. 7.12 shows the input forces at an interior beam-column joint once plastic hinges have developed in the beams at the faces of the column.

A reasonable approximation is to assume that the beam shear forces are carried to the boundaries of the joint by a set of diagonal struts with forces D_B and D_T. The inclination of these diagonal struts can be estimated from the fan-shaped crack pattern at the plastic hinges of the beams and assuming that the stirrups in those regions are equally stressed. From Fig. 7.13 where the top plastic hinge of the right beam is analyzed

$$\tan\theta_T = \frac{l_{pf}\,(d - d')}{\int_o^{lpf} x\,dx} = 2\,\frac{(d - d')}{l_{pf}} \qquad (7.31)$$

The length of l_{pf} where the beam shear is transferred through the stirrups is expected to be no more than (d - d') for beams designed according to the New Zealand Concrete Design Code because the transverse reinforcement placed can be governed by the shear requirements, assuming a 45° truss model, or by the need to prevent premature buckling of the longitudinal beam reinforcement. For simplicity it will be assumed

$$l_{pf} = (d - d') \qquad (7.32)$$

therefore the horizontal component of the diagonal force D_T is

$$V_{HT} = D_T \cos\theta_t = \frac{V_T}{\tan\theta_t} \qquad (7.33)$$

now substituting Eqs. 7.31 and 7.32 in Eq. 7.33 gives

$$V_{HT} = \frac{V_T}{2} \qquad (7.34)$$

Equilibrium considerations in the right beam of the column illustrated in Fig. 7.12 require that

$$C_{SB} + C_{CB} = T_T + T_S - D_T \cos\theta_T = T_T + T_S - V_{HT} \qquad (7.35)$$

where T_T is the actual tension force in the top beam longitudinal reinforcement, T_S, is the tension force due to the effective reinforcement in the slab, C_{SB} is the compression force in the bottom longitudinal reinforcement and C_{CB} is the compression force carried through the concrete.

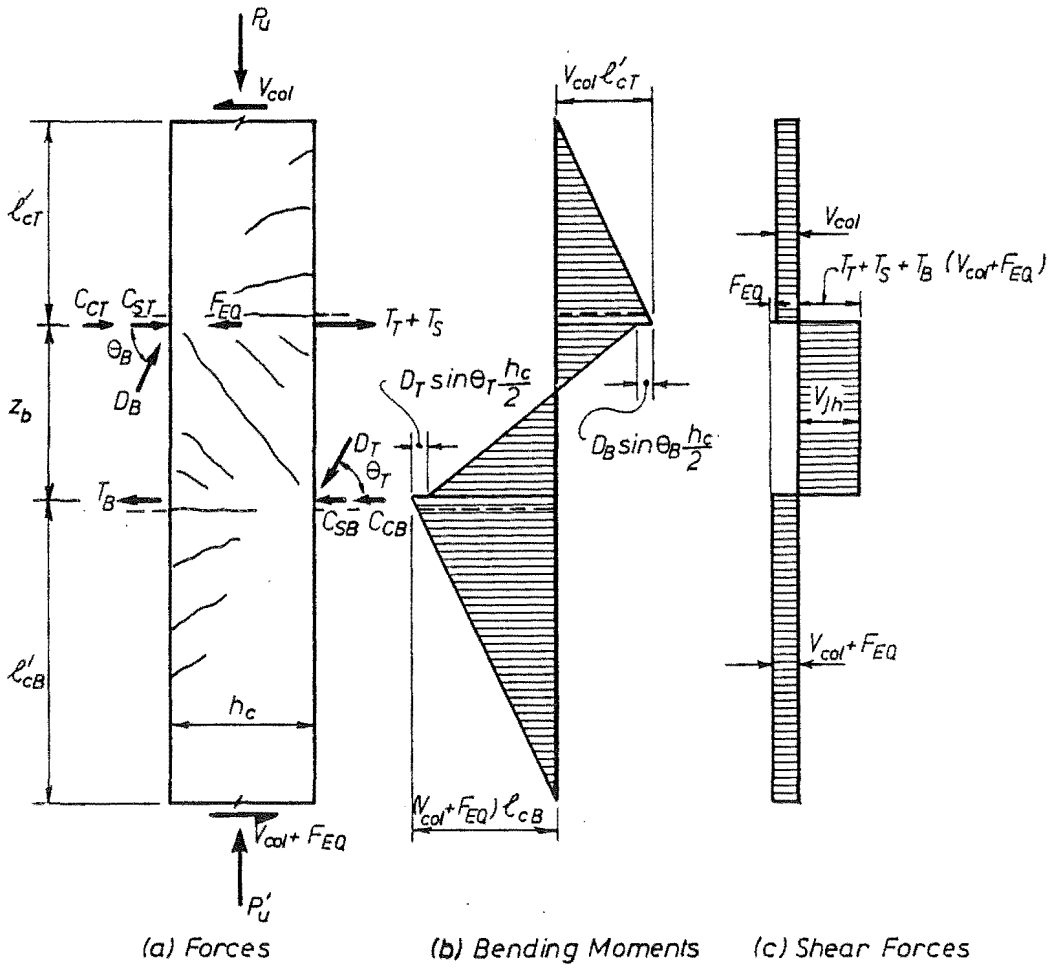

Fig. 7.12 - Forces Acting Upon a Concrete Column.

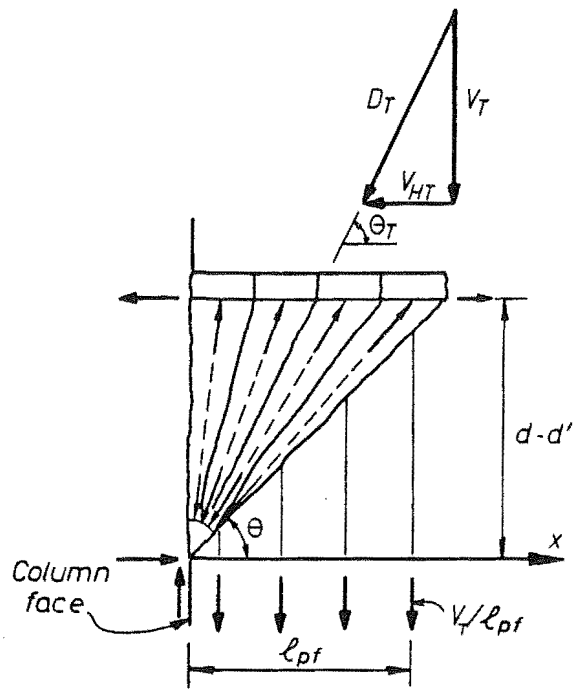

Fig. 7.13 - Shear Transfer in the Plastic Hinge Region of a Beam.

The resultant force $T_T + T_S - V_{HT}$ in Fig. 7.12 is largely carried by the concrete in beams of normal dimensions behaving elastically. Nevertheless, the force C_{CB} will gradually decrease, and eventually become zero, once the longitudinal reinforcement at this point has previously yielded in tension, unless the total compression force is such that the reinforcement yields back in compression, or that the bond in the beam-column joint has deteriorated to an extent where the local slip of the bars is such that this mechanism is unable to provide most of the reaction required, or that the compression bars have buckled. The extreme case of bond deterioration is when a bond failure has occurred and the reinforcement in the compression side is in tension and needs to be anchored in the beam. It is evident that all these cases imply a closure of the crack at the interface between the beam and the column.

Bond deterioration and bar buckling are unlikely to significantly affect the distribution of the resultant $T_T + T_S - V_{HT}$ between forces C_{SB} and C_{CB} in well detailed beams at moderate levels of ductility, since an objective of the design philosophy is to delay these two sources of failure. Hence, these two cases will not be considered in this study.

The compression force in the longitudinal steel after few reversal cycles in the inelastic range can be estimated by combining Eqs. 7.34 and 7.35, rearranging for C_{SB} and assuming $C_{CB} = 0$ results in

$$C_{SB} = T_T + T_S - \frac{V_T}{2} \qquad \text{and} \qquad C_{SB} \leq A_{SB}\,\lambda_o f_y \tag{7.36 a}$$

or in terms of the reinforcement areas and stresses,

$$A_{SB} f_s = (A_{ST} + A_{SS})\lambda_o f_y - \frac{V_T}{2} \qquad \text{and} \qquad f_s \leq \lambda_o f_y \tag{7.36 b}$$

where λ_o is the steel overstrength factor, A_{SB} is the bottom reinforcement in the beam, A_{ST} is the top reinforcement in the beam, A_{SS} is the effective reinforcement in the slab and f_s and f_y are the stresses in the reinforcement.

The beam shear V_T can be estimated as a function of the steel in tension as

$$V_T = (A_{ST} + A_{SS})\lambda_o f_y \frac{jd}{l_c} \tag{7.37}$$

where jd is the internal lever arm and l_c is the distance between the point of contraflexure and the critical region.

Eq. 7.37 can be further simplified assuming a value for $jd/l_c = 0.4$, which is a typical value in beams of perimeter frames and of the negative moment in gravity dominated moment resisting frames. Thus

$$V_T = 0.4(A_{ST} + A_{SS})\lambda_o f_y \tag{7.38}$$

Now combining Eqs. 7.38 and 7.36 (b) gives

$$A_{SB} f_s = 0.8(A_{ST} + A_{SS})\lambda_o f_y \qquad \text{and} \qquad f_s \leq \lambda_o f_y \tag{7.39 a}$$

a similar analysis on the left beam of Fig. 7.12 yields

$$A_{ST} f_s = 0.8 A_{SB} \lambda_o f_y \qquad \text{and} \qquad f_s \leq \lambda_o f_y \tag{7.39 b}$$

Note that in Eq. 7.39 (b) the slab reinforcement has not been taken into account since at the column face this reinforcement will be anchored and cannot participate in transferring the compression forces, as it is evident in the analysis of the free body to the left of Section A-A in Fig. 7.14.

The critical ratios $A_{SB}/(A_{ST} + A_S)$ and A_{ST}/A_{SB} in Eqs. 7.39 (a) and (b) occur when $f_s = \lambda_o fy$, that is,

$$\frac{A_{SB}}{A_{ST} + A_{SS}} = 0.8 \tag{7.40}$$

and

$$\frac{A_{ST}}{A_{SB}} = 0.8$$

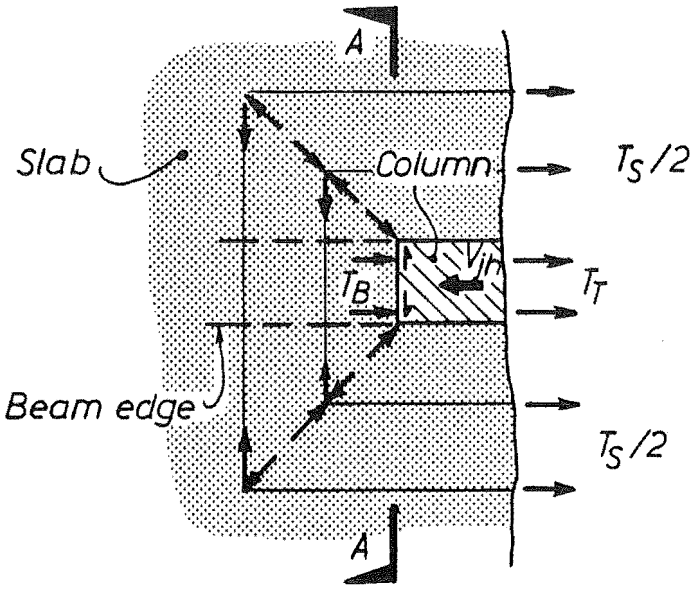

Fig. 7.14 - Transfer of Forces to a Beam-Column Joint in the Horizontal Plane Including the Slab Reinforcement.

These two expressions explain why in symmetrically reinforced beams, without slab, where $A_{SB} = A_{ST}$ the compression steel consistently shows a lower stress level than the reinforcement in tension. This trend was observed in the tests of Units 5 and 6 and discussed in Chapter 6. The level of stress predicted by Eqs. 7.39 (a) and 7.39 (b) agrees with the observed behaviour shown in Figs. 6.12 and 6.30. The stress level of the hooked beam bars anchored in the beam-column joint of Unit 5 and shown in Fig. 6.12 (b) also follows the same trend. Hence, the lower stress level cannot be attributed to bond deterioration as suggested by Cheung (1991) and Paulay and Priestley (1992).

7.3.3 Distribution of Internal Forces in the Joint Panel

The bending moment and shear force diagrams of the column shown in Fig. 7.12 indicate that the shear forces in the joint panel are significantly larger than elsewhere in the column. The horizontal shear force V_{jh} can be estimated from equilibrium of horizontal forces to be

$$V_{jh} = T_T + T_S + C_{ST} + C_{CT} + D_B \cos\theta_B - (V_{col} + F_{EQ}) \qquad (7.41\ a)$$

or similarly

$$V_{jh} = T_B + C_{SB} + C_{CB} + D_T \cos\theta_T - (V_{col} + F_{EQ}) \qquad (7.41\ b)$$

or simply as

$$V_{jh} = T_T + T_S + T_B - (V_{col} + F_{EQ}) \qquad (7.41\ c)$$

where F_{EQ} is the inertial force induced by the earthquake at the level of the slab that is carried by the column.

The consideration of equilibrium of vertical forces in the joint panel will lead to a similar expression for estimating the vertical shear force, V_{jv}. However, a relatively lengthy procedure is often required to find the position of the resultant of the compression force of a column with axial load and the forces on each layer of reinforcement. This calculation often involves a tedious calculation. A simple and quite accurate estimate of V_{jv} can be obtained as

$$V_{jv} = \frac{h_b}{h_c} V_{jh} \qquad (7.42)$$

Now the shear stress in the joint, v_j, which is uniquely defined in both the horizontal and vertical directions, can be found from

$$v_j = \frac{V_{jh}}{b_j h_c} = \frac{V_{jv}}{b_j h_b} \qquad (7.43)$$

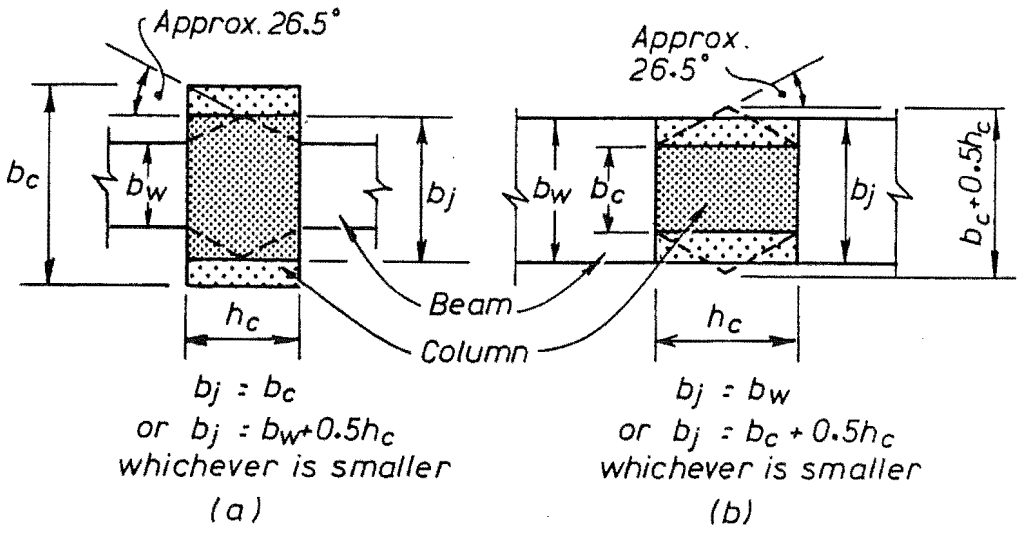

Fig. 7.15 - Definition of the Effective Joint Width.

where b_j is the effective joint width defined as shown in Fig. 7.15 and h_c and h_b are the column and beam depths, respectively.

Uncracked beam-column joints of normal dimensions, where bond of the beam and column bars has not deteriorated due to yield penetration or to excessive bond stresses, can be represented by an elastic body. The first diagonal crack will appear at a joint shear stress v_{jcr} once the diagonal tensile strength of the concrete, f'_{cr}, is exceeded. This value can be found from the Mohr circle of stresses as

$$v_{jcr} = \sqrt{f'_{cr}\left(f'_{cr} + \frac{P_u}{A_g}\right)} \qquad (7.44)$$

where P_u is the axial load acting over the horizontal column gross area A_g. P_u is taken positive in compression.

Table 7.1 illustrates the values of the joint shear stress at which first visible cracking occurred in different tests reported in New Zealand. The mean f'_{cr} obtained from the tests was $0.37\sqrt{f'_c}$. Priestley and Calvi (1991) and Priestley (1992) have suggested that diagonal cracking in beam-column joints can be assumed to occur once the diagonal tension stress exceeds $0.29\sqrt{f'_c}$ and $0.30\sqrt{f'_c}$, respectively.

Before cracking in the joint, the reinforcement in the beam-column joint panel remains nearly unstressed. However, after cracking there is significant redistribution of internal forces and the reinforcement is activated by the mobilization of a diagonal compression field mechanism of shear transfer. A review of the allocation of forces by different researchers in New Zealand in the interior beam-column joints after cracking is presented below.

Table 7.1
Principal Tensile Stress at First Visible Cracking in Beam-Column Joints

Test		P_u/A_g (MPa)	f'_c (Mpa)	v_{cr} (Mpa)	f'_{cr} (MPa)	$\frac{f'_{cr}}{\sqrt{f'_c}}$
Priestley (1975)	Interior	1.32	48.5	1.99	1.43	0.21
Xin (1992)	Unit 1	0	30.9	2.56	2.56	0.46
	Unit 2	0	40.8	2.62	2.62	0.41
	Unit 3	0	42.5	2.67	2.67	0.41
	Unit 4	0	47.2	2.06	2.06	0.30
	Unit 5	0	60.7	2.57	2.57	0.33
	Unit 6	0	59.3	3.23	3.23	0.42
Restrepo-Posada	Unit 5	0	27.0	2.03	2.03	0.39
	Unit 6	0	44.0	2.59	2.59	0.39
					Mean	0.37

The well known concrete strut and truss mechanism proposed by Park and Paulay (1975), based on an admissible state of equilibrium, depends primarily on the bond distribution along the longitudinal reinforcement of the members that may be designed to form plastic hinges and dissipate energy during an earthquake. This shear transfer mechanism is illustrated in Fig. 7.16. Some part of the joint shear forces can be directly transferred by a diagonal concrete strut without the need of any reinforcement. An additive truss mechanism, acting with a compression field parallel to the diagonal concrete strut, transfers the remainder of the shear forces originated by the bond of the outer beam and column reinforcement. Evidently this mechanism requires vertical and horizontal reinforcement.

According to this model the shear forces in a joint panel can be mathematically expressed as the combination of the two mechanisms

$$V_{jh} = V_{ch} + V_{sh} \qquad (7.45\ a)$$

and

$$V_{jv} = V_{cv} + V_{sv} \qquad (7.45\ b)$$

in which V_{ch} and V_{cv} are the contribution of the diagonal concrete strut in the horizontal and vertical directions, respectively and V_{sh} and V_{sv} show the contribution of the truss mechanism.

A lower bound approach was initially presented by Blakeley (1977) for the design of "inelastic" interior beam-column joints where beam plastic hinges were expected to form at the column faces. In this approach the whole horizontal joint shear at the flexural overstrength was to be taken by the truss mechanism if the axial compressive load in the column was below $0.1A_gf'_c$. Some of the joint shear was allowed to be transferred through the concrete strut mechanism for higher axial compressive loads. This approach was justified by Paulay et al (1978) because it was believed that after few reversed cycles of loading in the inelastic range bond forces would concentrate towards the centre of the column due to the effects of yield penetration. Fig. 7.17 (a) shows the bond distribution postulated

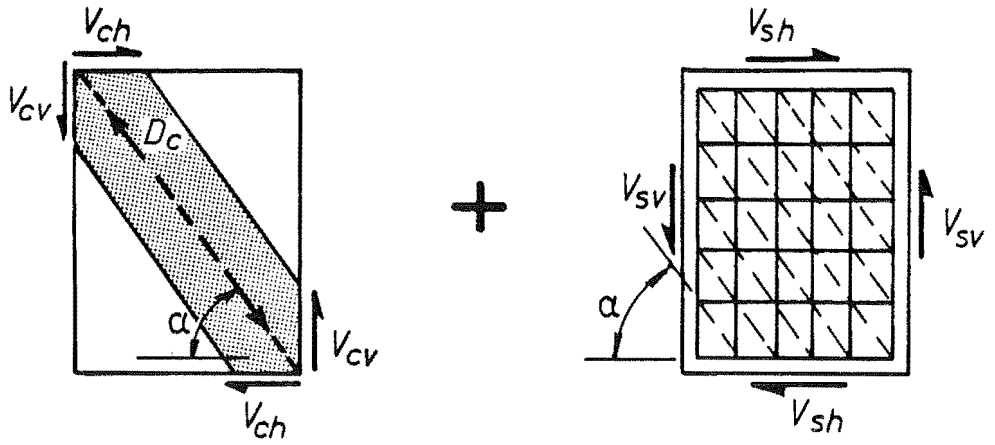

(a) Diagonal strut mechanism (b) Truss mechanism

Fig. 7.16 - Traditional Truss and Diagonal Strut Mechanism for the Transfer of the Joint Shear [Park and Paulay (1975)].

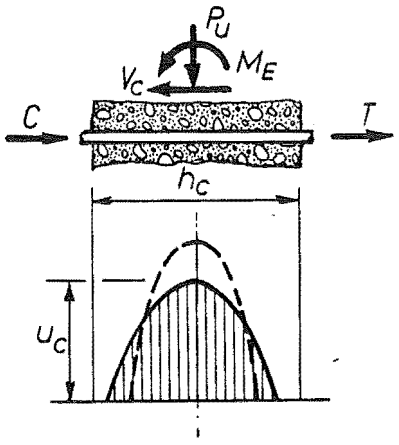

(a) Paulay et al (1978)

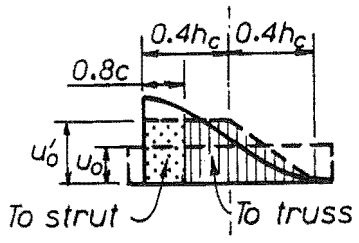

(b) Cheung et al (1991)

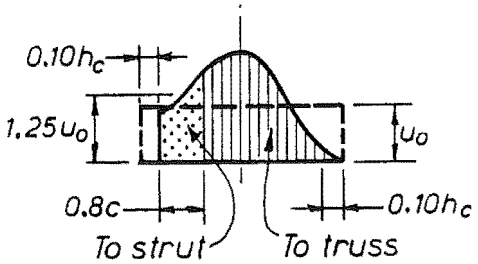

(c) Paulay and Priestley (1992)

Fig. 7.17 - Distribution of Bond Forces along the Beam Bars in Interior Beam-Column Joints after Several Inelastic Reversed Cycles.

by Paulay et al. The requirements for estimating the vertical shear reinforcement were not as severe owing to the expected elastic behaviour of the columns. The proposal presented by Blakeley was incorporated into the New Zealand Concrete Design Code [NZS 3101 (1982)] with slight modifications. In this standard the diameter of the bars passing through the joints was also limited to prevent their premature global slip. It was recommended that the ratio between the column depth h_c and the diameter of the bars yielding at the column faces should not exceed

$$\frac{h_c}{d_b} = \frac{f_y}{11} \tag{7.46}$$

The use of the code recommendations often led to rather congested designs and the placing of the fresh concrete became a very important consideration. An alternative design, utilized to decongest the joint region, was to locate the plastic hinges in the beams in a region away from the column faces to avoid yielding of the beam longitudinal reinforcement penetrating into the joint core. This would eliminate bond deterioration taking place in this region. Such joints were termed "elastic" joints and a large participation of the concrete strut mechanism in carrying the horizontal joint shear was allowed, easing the amount of transverse reinforcement required. Research work conducted by Priestley (1975), Yeoh (1978), Blakeley et al (1979), Fenwick and Nguyen (1981), Beckingsale et al (1980) was used as the basis of the guidelines or as confirmation tests as it was the case of the experimental work carried out by Milburn and Park (1982).

Further experimental work conducted more recently by Park and Dai (1988) showed that the cyclic load performance of interior beam-column joints designed with a fraction of the horizontal and vertical shear reinforcement required by the New Zealand Concrete Design Code was not greatly affected and as a result they concluded that code requirements could be relaxed without reducing the level of seismic performance. They suggested that for axial column load levels below $0.1A_gf'_c$ the concrete strut mechanism could, in "inelastic" interior beam-column joints of structures designed for full ductility, take about 40% of the horizontal joint shear and 70% of the vertical joint shear. It was reasoned that the bond forces at the extremities of the beam bars in the beam-column joint were transferred across the joint by the strut mechanism. For "inelastic" interior beam-column joints of structures designed for limited ductility, they recommended allocating 60% of the horizontal joint shear to the concrete strut mechanism, and place at least one intermediate column bar at each side of the joint.

Park and Dai also observed that the code requirements concerning the limitation of the diameter of the inelastic longitudinal bars passing through the joint should recognize the case of beams with different amounts of top and bottom reinforcement and different concrete compressive strengths f'_c. Based on their experimental work it was proposed that for axial load levels below $0.1A_gf'_c$:

$$\frac{h_c}{d_b} \leq \frac{(1 + \beta)}{5} \frac{f_y}{\sqrt{f'_c}} \tag{7.47}$$

where β is the ratio between the amounts of bottom and top reinforcement and $\beta \leq 1$. The above formulation was made on the assumption that an average bond stress $u_a = 6.88$MPa over the column depth could be sustained in the joint region when f'_c was 20MPa and that the bond strength was a function of $\sqrt{f'_c}$. For structures designed for limited ductility they concluded that no limits were needed.

Cheung et al (1991a) proposed a relaxation to the current code requirements by assuming the trapezoidal bond distribution depicted in Fig. 7.17 (b). They allocated the bond forces within the neutral axis depth of the column to the strut mechanism. They also made an estimate of the possible forces carried by the compression longitudinal beam reinforcement at the column face. The forces carried by the truss mechanism were allocated based on the remaining bond forces and considering the variation of the neutral axis depth of the column with the axial load. The formulation for the vertical shear reinforcement was also reviewed and modified using equilibrium considerations. They also demonstrated that the enhancement of the flexural capacity of the beams due to the reinforcement of the slab induces an extra joint shear force that is carried by the diagonal concrete strut without the need of additional shear reinforcement in the joint panel. Thus, the following expressions were recommended.

$$V_{ch} = 0.3\left(1 + 3.5\frac{P_u}{A_g f'_c}\right) V_{jh} \qquad (7.48\ a)$$

$$\text{and} \quad V_{cv} = 0.5V_{jv} + P_u \qquad (7.48\ b)$$

In a study of the possible maximum bar diameters that could pass across an "inelastic" interior beam-column joint, Cheung et al furthered the work of Park and Dai and presented the following expression

$$\frac{h_c}{d_b} \geq \frac{1}{1.9\xi_m \xi_p \xi_f \xi_t} \frac{f_y}{\sqrt{f'_c}} \qquad (7.49)$$

in which ξ_m is a factor that accounts for the compression forces in the beam bar, ξ_p is a factor to account for the effect of the axial compression load, ξ_f is a factor that accounts for the detrimental effects on the bond strength of joints with beams hinging at the four faces of the joint, and ξ_t is a factor to account for the "top bar" effect where more than 300mm of fresh concrete is cast underneath the bars.

The following values were recommended for the different factors:

ξ_m = 1.3 for top bars,

or ξ_m = $1 + \beta \geq 1.1$ for bottom bars,

ξ_p = 1 if $P_u/A_g f'_c \leq 0.2$,

or $\xi_p = 0.85\ (1 + P_u/A_g f_c') \leq 1.25$ if $P_u/A_g f_c' > 0.2$,

$\xi_f = 1.0$ for two-way frames,

or $\xi_f = 1.2$ for one-way frames,

and $\xi_t = 1.0$ for top bars,

or $\xi_t = 1.1$ for bottom bars.

Paulay and Priestley (1992) followed the same procedure presented by Cheung et al. They used the idealized bond distribution shown in Fig. 7.17 (c) and made some simplifications to derive the following expression for determining the amount of horizontal shear force carried by the truss mechanism in "inelastic" interior beam column joints:

$$V_{sh} = \left(1.15 - 1.3\frac{P_u}{A_g f_c'}\right) T \tag{7.50}$$

where T is the tensile force in the top beam reinforcement at overstrength.

For the vertical joint shear reinforcement they adopted the expression proposed by Cheung et al (see Eq. 7.48(b)).

Paulay and Priestley also presented the following expression for the contribution of the diagonal strut in carrying the joint horizontal shear in "elastic" joints:

$$V_{ch} = 0.5\left(\beta + 1.6\frac{P_u}{A_g f_c'}\right) V_{jh} \tag{7.51}$$

in which β is the ratio between the amounts of bottom and top reinforcement.

They recommended Eq. 7.48(b) for finding the vertical joint shear reinforcement in "elastic" joints.

Concerning the maximum bar diameter passing through an "inelastic" interior beam-column joint they derived the following expression

$$\frac{h_c}{d_b} \geq \frac{\xi_m \lambda_o}{5.4\,\xi_p \xi_t \xi_f}\frac{f_y}{\sqrt{f_c'}} \tag{7.52}$$

where

$\xi_m = 2.55 - \beta \leq 1.8,$

$\xi_p = P_u/(2\, A_g\, f_c')$ and $1 \leq \xi_p \leq 1.25,$

$\xi_t = 0.8$ for top bars with more than 300mm of fresh concrete cast underneath,
or $\xi_t = 1.0$ for bottom bars,

and $\xi_f = 0.9$ if plastic hinges form in all four faces of the interior beam-column joint,
or $\xi_f = 1.0$ in all other cases.

It was also recommended that Eq. 7.52 could be used in the design of elastic joints considering a reduction of the factor ξ_m as follows:

$$\xi_m = \frac{(f_s + f_s')}{\lambda_o f_y} \leq 1.2 \qquad (7.53)$$

where f_s and f_s' are the estimated tensile and compressive stresses in the beam bars at the faces of the column.

An additional formulation to determine the anchorage of beam bars passing through interior beam-column joints with plastic hinges forming in the beams at the face of the columns has been presented by Xin (1992). He based his proposal on the initial formulation postulated by Park and Dai for which he used the results of six interior beam-column joint units. The main variables in this research project were the concrete strength, the ratio top to bottom beam reinforcement and the ratio h_c/d_b. Grade 430 steel was used as main beam and column reinforcement. The columns were not subjected to axial load.

$$\frac{d_b}{h_c} = \frac{3.84\ \xi_t\ k_3}{(1 + 0.56\ \xi_m\ \beta)}\ \frac{\sqrt{f_c'}}{f_y} \qquad (7.54)$$

in which β is the ratio between the amounts of bottom and top reinforcement,

$\xi_t = 1.0$ for top bars,
or $\xi_t =$ 1.1 for bottom bars,

$\xi_m =$ 1.3 for top bars with $\beta \leq 0.75$,
or $\xi_m =$ 1.0 for top bars with $0.75 < \beta \leq 1.0$,

$\xi_m =$ 1.2 for bottom bars with $\beta \leq 0.8$,
or $\xi_m =$ 1.0 for bottom bars with $0.8 < \beta \leq 1$,

and $k_3 =$ 1.0 for top bars,
or $k_3 = \sqrt{\beta}$ for bottom bars.

7.3.4 Alternative Formulation for the Design of Interior Beam-Column Joints

7.3.4.1 Background

A brief review of the evolution of the methods for the design of interior beam-column joints was made in previous section. This section concerns with an alternative formulation of the bond and shear transfer mechanisms.

The design criteria stated by Paulay et al (1978) for the design of beam-column joints is adopted in the formulation:

(a) *The strength of a joint should not be less than the maximum strength of the weakest member it connects, to eliminate the need for repair in a relatively inaccessible region and to prevent the need for energy dissipation by mechanisms that undergo strength and stiffness degradation when subjected to cyclic loading in the inelastic range.*

(b) *The capacity of a column should not be jeopardised by possible strength degradation within the joint.*

(c) *During moderate seismic disturbances a joint should preferably respond within the elastic range.*

7.3.4.2 Mechanisms of Bond Strength

In Chapter 6 it was discussed that perhaps two different mechanisms of bond strength act along the longitudinal bars passing through a beam-column joint. Rather large bond stresses, concentrated towards the corner of the joint panel where the compression forces from the column and the beam meet. By observing Figs. 6.7 and 6.8 as well as Figs. 6.26 to 6.29 it is evident that any additional force in the beam bars entering the joint region after yielding in tension has taken place in the beam longitudinal reinforcement at the column faces is resisted by bond within the corner in compression. This also associated with an initiation of the global bar slip, which can be related to the local bar slip at the centreline of the column.

It is also obvious that the conditions for the development of bond forces are much better towards the corner where the compression forces from the column act than on the other corner at the same level of the beam bars. Two main reasons explain this phenomena. First, the effect of bending in the column inducing tension in one side and compression on the other. In the tension side (see right corner of the section shown in Fig. 7.18) there are splitting cracks along the bar reinforcing. It is quite likely that these cracks propagate from the column interface crack at the beam faces and will not induce a splitting failure due to the presence of the column reinforcement. On the other hand, the splitting cracks will close in the presence of the compressive stresses arising within the column. The second effect is that the intensity of the shear forces entering the joint is likely to be much larger towards the compression region than towards the region in tension. Sections A-A and B-B in Fig. 7.18 depict the probable distribution of the bond forces along the surface of the beam reinforcement.

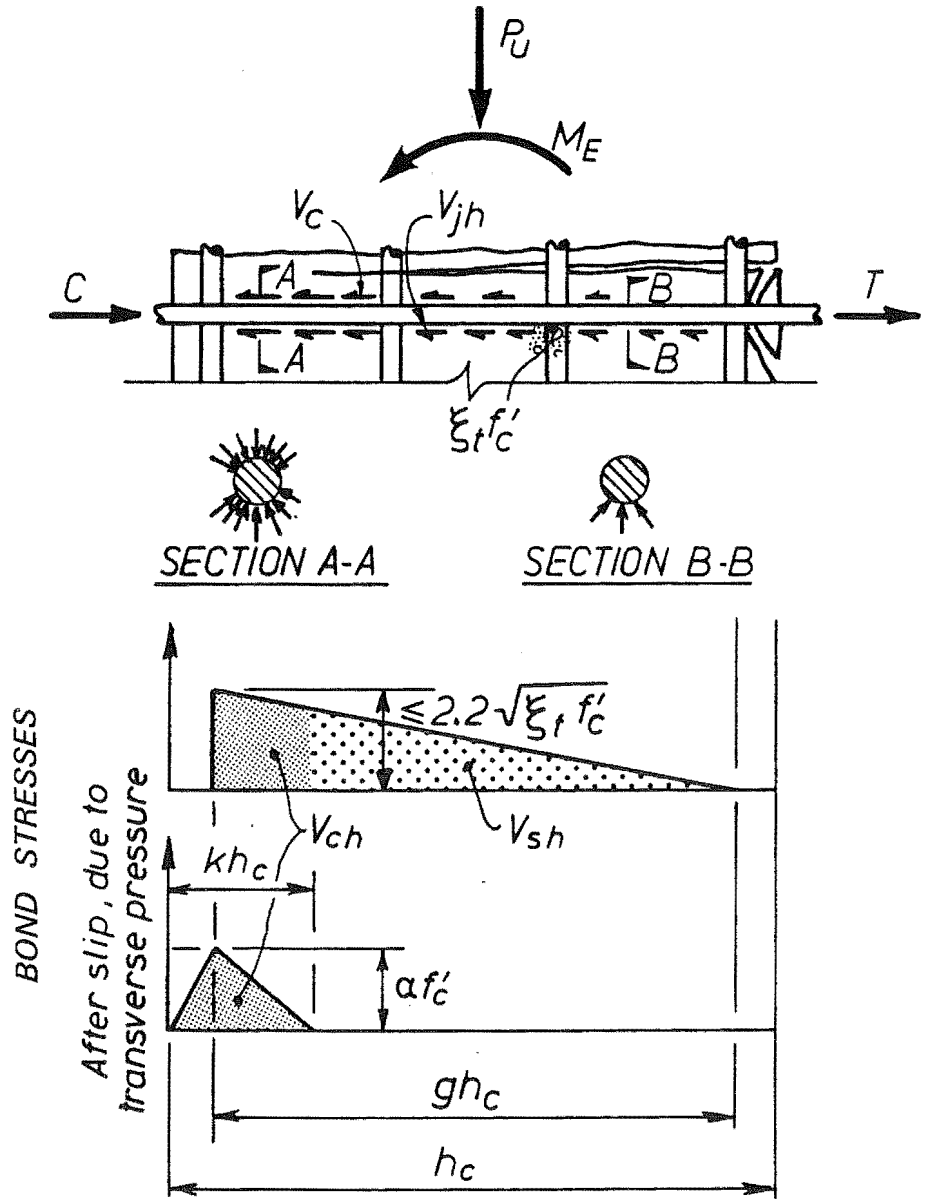

Fig. 7.18 - Proposed Mechanisms of Bond Resistance.

The upper bond mechanism illustrated in Fig. 7.18 acts only within the joint core along the beam longitudinal reinforcement. Its gradient reflects the effects of bending of the column adjacent to the joint. It basically assumes an elasto-plastic cyclic bond-bar slip behaviour, which makes possible simplifications and design guidelines to be proposed, instead of more complex models. An analysis of tests conducted in New Zealand showed that a peak bond of $2.2\sqrt{\xi_t f'_c}$ can be sustained during several excursions in the beam bars in the plastic range without showing signs of significant global bar slip. Factor ξ_t recognizes that in certain circumstances the effects of sedimentation, bleeding and porosity in the local concrete under the bars can significantly make it very different from that tested to determine the concrete compressive strength. A value of $\xi_t = 0.70$ is recommended if 300mm or more of fresh concrete is cast underneath the bars in the same operation. In other cases a value of $\xi_t = 1.00$ is

recommended. Also, this mechanism is associated with the tensile strength of the concrete, as a function of $\sqrt{f'_c}$, based on the results obtained by Eligehausen et al (1983).

Another mechanism will be mobilized when the input forces from the bars are such that the first mechanism can not provide the full bond resistance. Global slip of the bars is likely to commence at this stage without necessarily implying an imminent bond failure. Bond failure in the beam longitudinal bars is defined here as when the local bar slip at the column centreline exceeds the clear distance between bar deformations. This mechanism acts only over the compression zone of the column and it appears to be caused by the crushed concrete around the bar deformations that dilates and permits a frictional mechanism to be developed. Therefore this mechanism is associated with the concrete compressive strength.

The maximum bar diameter that can pass through the beam-column joint can be determined combining these two mechanisms. For this it is necessary to know the frictional factor α. This factor can be related, using the existing data, to the energy dissipated in a similar way as Eligehausen et al (1983) determined the reduced envelope of the cyclic bond-slip relationship for deformed bars. Alternatively, the cumulative displacement ductility factor attained until bond failure was observed can also be used. This second alternative is chosen in this study.

Fig. 7.19 plots the cumulative displacement ductility at which bond failure was reported versus the calculated frictional factor α for all tests that have displayed this type of failure at the University of Canterbury.

Although scattered, this data shows the expected trend for factor α decreasing with the cumulative displacement ductility factor. The "admissible" limit line depicted in Fig. 7.19 demarcates the region where, for a given cumulative displacement ductility factor, α can be attained without

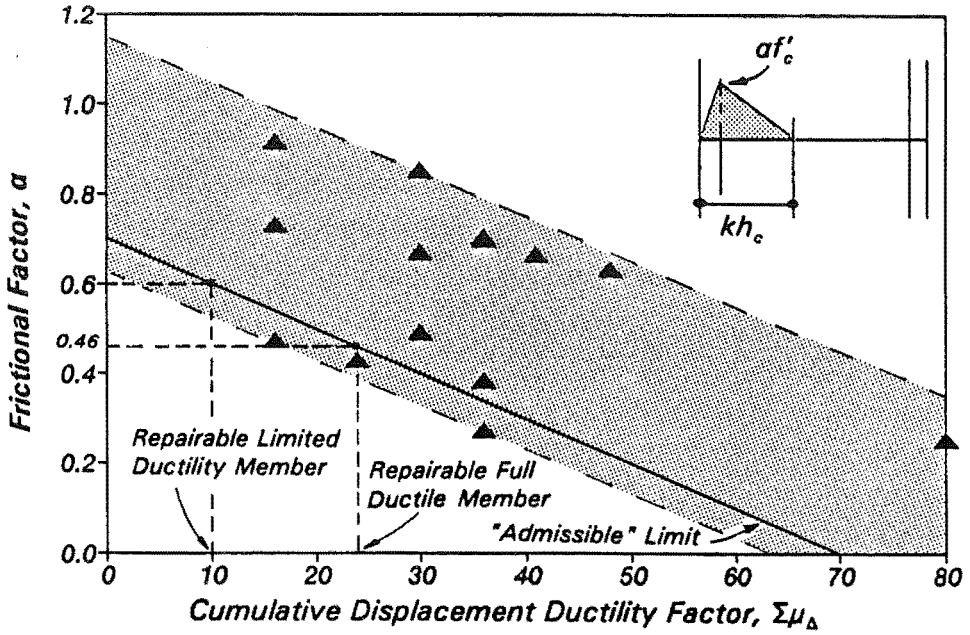

Fig. 7.19 - Tests with Bond Failure Reported at the University of Canterbury.

implying a bond failure. This line has been arbitrarily traced and below it there are three tests that presented this type of failure. One of these tests refers to Unit B11 tested by Beckingsale et al (1980) which had perforations in the concrete cover at 102mm intervals in both sides of the joint, required for instrumentation of the longitudinal bars. It is likely that these perforations could have disrupted the bond of the bars. The other two cases were for Units 1 and 4 tested by Xin (1992) that had no abnormal construction procedures.

The next step consists in quantifying an acceptable performance where bond failure is not necessarily precluded but delayed. It is assumed here that the acceptable performance is attained when bond failure is prevented from occurring before half of the expected available displacement ductility factor is reached. Using the definition of available ductility factor in terms of the cumulative displacement ductility factor given by Park (1989)

$$\mu_a = \frac{\Sigma \mu_\Delta}{8}$$

where for a full ductile member $\mu_a/2 = 3$ and for a member designed for limited ductility $\mu_a/2 = 1.25$, the corresponding cumulative displacement ductility factors are 24 and 10, respectively. According to the criteria of the "admissible" line in Fig. 7.19 the frictional factor α for each case is 0.46 and 0.60.

7.3.4.3 Available Bond Strength in Interior Beam-Column Joints

An assessment of the maximum bond strength in interior beam-column joints is needed to determine the maximum diameter of bars allowed to pass through the joint.

The available bond strength, which is given as addition of the two mechanisms of bond resistance shown in Fig. 7.18 should in every case be larger than the demand of the input forces in the longitudinal bars at the faces of the joint. That is

$$\left(\alpha f_c' kh_c + 2.2 \sqrt{\xi_t f_c'}\ gh_c\right) \frac{\pi}{2} d_b \geq T + C \qquad (7.55)$$

where kh_c is the depth of the neutral axis of the column, gh_c is the distance between the column outer layer of bars, d_b is the diameter of the bar passing through the joint, and T and C are the input tension and compression forces in the bar at the faces of the joint.

Eq. 7.55 is a general formulation that can be used under different conditions. This equation will be first simplified to obtain an expression that permits the evaluation of the minimum ratio h_c/d_b in an interior beam column-joint with hinges at the faces of the joint and then when plastic hinges are, deliberately or not, located away from the faces of the columns.

A simple expression for the neutral axis depth of a column has been given by Paulay and Priestley (1992)

$$kh_c = \left(0.25 + 0.85\,\frac{P_u}{A_g f_c'}\right) h_c \tag{7.56}$$

Combining Eq. 7.55 in Eq. 7.56 and assuming g = 0.8

$$\left[\alpha f_c'\left(0.25 + 0.85\frac{P_u}{A_g f_c'}\right) + 1.76\sqrt{\xi_t f_c'}\right]\frac{\pi}{2}\, d_b\, h_c \geq T + C \tag{7.57}$$

Analyzing the term at the right hand side of Eq. 7.57 when the beam top reinforcement reaches its maximum likely stress,

$$T = T_T = A_{ST}\,\lambda_o f_y \tag{7.58 a}$$

and from Eq. 7.39 (b)

$$C = C_{ST} = 0.8 A_{SB}\,\lambda_o f_y \qquad \text{and} \qquad C_{ST} \leq A_{ST}\,\lambda_o\, f_y \tag{7.58 b}$$

Combining Eqs. 7.58(a) and 7.58(b) gives

$$T_T + C_{ST} = (A_{ST} + 0.8 A_{SB})\lambda_o f_y \leq 2A_{ST}\,\lambda_o\, f_y \tag{7.59}$$

A similar expression can be obtained for the bar forces entering the joint through the bottom reinforcement

$$T = T_B = A_{SB}\,\lambda_o\, f_y \tag{7.60 a}$$

and from Eq. 7.39 (a)

$$C = C_{SB} = 0.8\,(A_{ST} + A_{SS})\lambda_o f_y \qquad \text{and} \qquad C_{SB} \leq A_{SB}\, f_y \tag{7.60 b}$$

Then combining Eqs. 7.60 (a) and 7.60 (b)

$$T_B + C_{SB} = (A_{SB} + 0.8(A_{ST} + A_{SS}))\lambda_o\, f_y \leq 2A_{SB}\,\lambda_o\, f_y \tag{7.61}$$

Eqs. 7.59 and 7.61 can be reduced to one general equation

$$T + C = (1 + 0.8\kappa)T \qquad \text{and} \qquad (1 + 0.8\kappa) \leq 2 \tag{7.62 a}$$

or in terms of the bar diameter and steel stress as

$$T + C = (1 + 0.8\kappa)\,\frac{\pi}{4} d_b^2\, \lambda_o\, f_y \qquad \text{and} \qquad (1 + 0.8\kappa) \leq 2 \tag{7.62 b}$$

where κ is the ratio between the area of steel in compression and the steel in tension. In other words, for top bars, $\kappa = A_{SB}/A_{ST} = T_B/T_T$ and for bottom bars $\kappa = (A_{ST} + A_S)/A_{SB} = (T_T + T_S)/T_B$.

Factor κ is very similar to factor β defined by Park and Dai (1988), Cheung et al (1991, 1991a), Paulay and Priestley (1992), and Xin (1992) (see Section 7.3.3). Nevertheless, the role of the slab bars carrying or not carrying compressive forces is not fully addressed by these researchers. It appears that for the evaluation of the bond condition of the top beam bars the factor β, unlike factor κ, may include both the top beam reinforcement and the effective reinforcement of the slab.

The ratio h_c/d_b can now be obtained by substituting Eq. 7.62 (b) in Eq. 7.57 and rearranging as

$$\frac{h_c}{d_b} \geq \frac{\lambda_o f_y \xi_m \xi_f}{2\left(\alpha f_c' \left(0.25 + 0.85\,\frac{P_u}{A_g f_c'}\right) + 1.76\sqrt{\xi_t f_c'}\right)} \tag{7.63}$$

where $\xi_m = (1 + 0.8\kappa)$ and $\xi_m \leq 2$. The multiplier factor ξ_f has been added in Eq. 7.63 to recognize the detrimental effect of the simultaneous formation of plastic hinges in all four faces of the joint [Cheung (1991)] in which case $\xi_f = 1.1$ is recommended. $\xi_f = 1$ is to be used in all other cases.

Eq. 7.63 has been plotted against Eq. 7.52 in Fig. 7.20 for the top bars of a beam without slab but with equal top and bottom Grade 430 steel and for two cases of ductility: (a) full ductility with $\lambda_o = 1.25$ and $\alpha = 0.46$, and, (b) limited ductility with $\lambda_o = 1.15$ and $\alpha = 0.60$.

The term T + C in Eq. 7.57 can also be simplified if the positive or negative or both plastic hinge regions form in the beam at a distance of at least one effective beam depth from the column faces. This is the case of relocated plastic hinges or when the gravity actions are such that the positive plastic hinge does not form at the column face. In these cases limited yield of the reinforcement may be expected in the beam longitudinal reinforcement at the face of the column and

$$T + C = 1.3T = 1.3\frac{\pi}{4} d_b^2 f_y \tag{7.64}$$

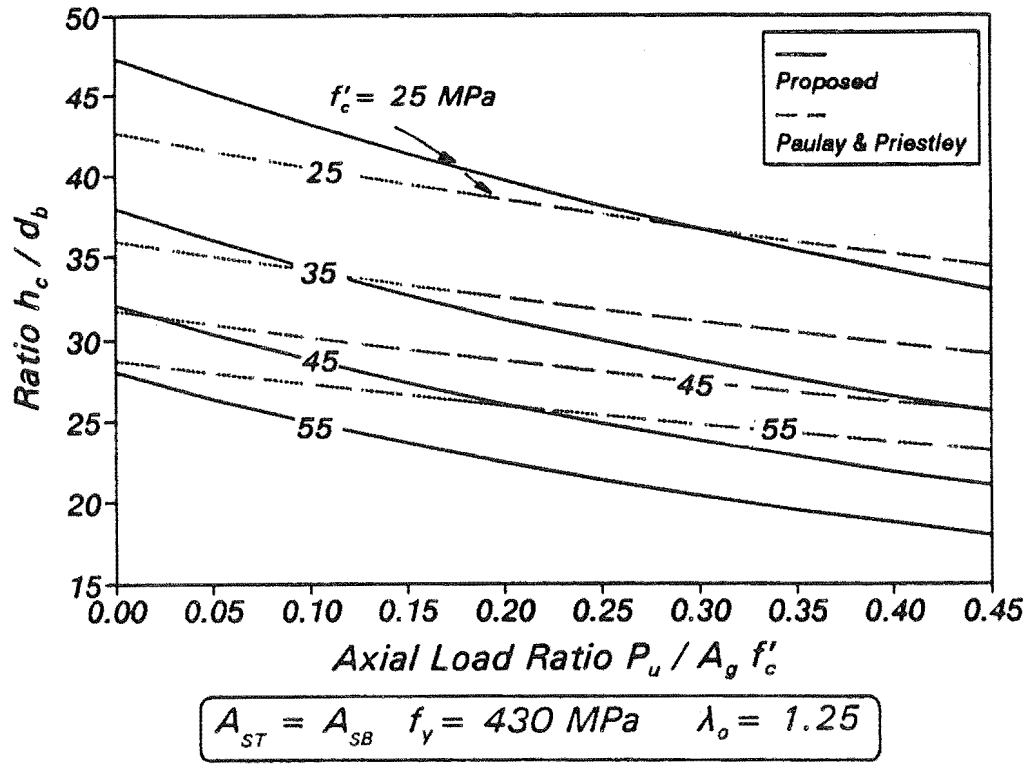

(a) Designed for full ductility

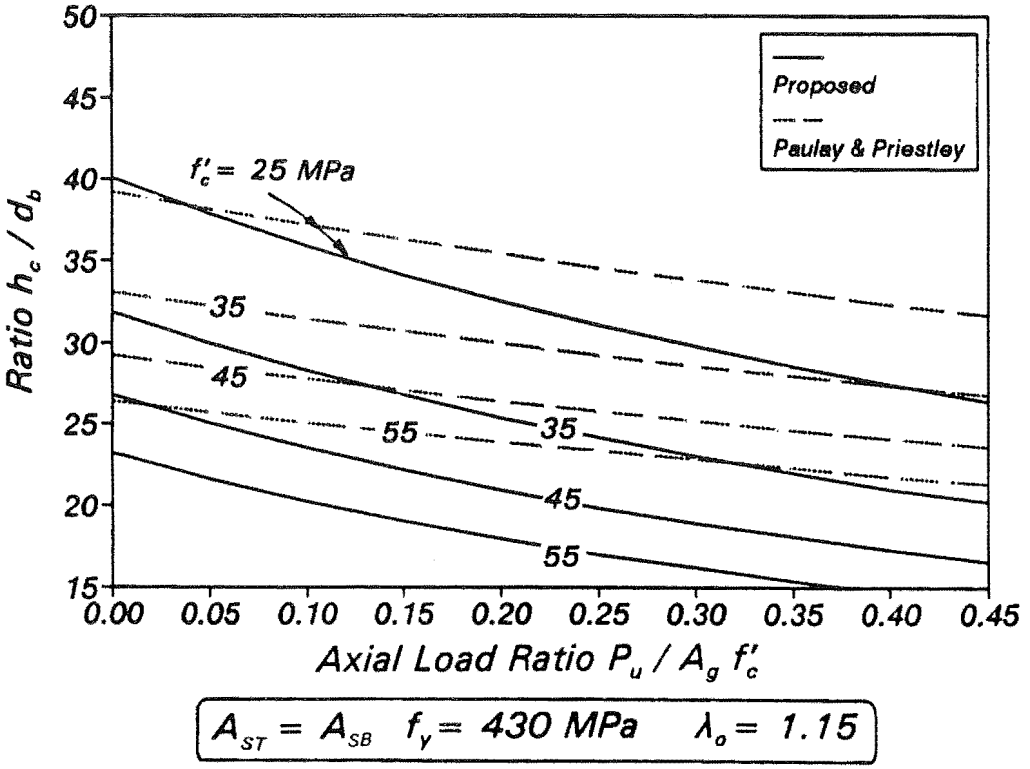

(b) Designed for limited ductility

Fig. 7.20 - Ratio h_c/d_b for Top Bars of Symmetrically Reinforced Beams.

Now the maximum bar diameter for this case is found substituting Eq. 7.64 in Eq. 7.57 and rearranging for h_c/d_b

$$\frac{h_c}{d_b} \geq \frac{0.65 f_y}{\alpha f_c' \left(0.25 + 0.85 \frac{P_u}{A_g f_c'}\right) + 1.76 \sqrt{\xi_t f_c'}} \qquad (7.65)$$

which with $\xi_m = 1.3/\lambda_o$ can be expressed in the same form as Eq. 7.63.

Due to the lack of test data using high axial compressive load in the columns and high strength concrete, it is recommended that in Eqs. 7.63 and 7.65 $Pu/A_g f_c'$ should not be taken larger than 0.45 and f_c' should be limited to 55MPa or less.

7.3.4.4 The Diagonal Strut and Variable Angle Truss Mechanisms of Joint Shear Transfer

The bond mechanisms of bars passing through an interior beam-column joint were already discussed in Section 7.3.4.2, where two different mechanisms were postulated to act. If it is accepted that the horizontal and vertical joint shear forces are carried by a diagonal strut and truss models, the horizontal shear force, V_{sh}, transferred through the truss mechanism by the beam reinforcement can be readily estimated from the first of the bond mechanisms depicted in Fig. 7.18 as

$$V_{sh} = \frac{2.2}{2} \sqrt{\xi_t f_c'} \frac{[((1+g)/2 - k)\, h_c]^2}{g h_c} \pi \Sigma d_b \qquad (7.66\ a)$$

or

$$V_{sh} = (T + C) \frac{[((1+g)/2 - k)\, h_c]^2}{(g h_c)^2} \qquad (7.66\ b)$$

whichever is smaller.

Eq. 7.66 reflects the case when the bond strength is provided by both mechanisms shown in Fig. 7.18 whereas Eq. 7.66(b) applies when the input bar forces are small enough that the frictional bond mechanism needs not to be mobilized.

The above equations can be simplified assuming $g = 0.8$ and substituting Eq. 7.56 into them. Thus V_{sh} is the smaller of

$$V_{sh} = \frac{\sqrt{\xi_t f_c'}}{550} \xi_p h_c \Sigma d_b \qquad (7.67\ a)$$

or

$$V_{sh} = \xi_p \frac{(T + C)}{1.5} \qquad (7.67\ b)$$

where

$$\xi_p = \left(1 - 1.3 \frac{P_u}{A_g f_c'}\right)^2 \qquad (7.67\ c)$$

In Eq. 7.67 (a) V_{sh} is given in kN, f_c' in MPa and h_c and d_b in mm.

Eq. 7.67 (b) can be simplified by relating the force C as a function of T following the same procedure used to find the limiting bar sizes allowed to pass through an interior beam-column joint. First, for plastic hinges forming in the beams at the column faces Eq. 7.62 (a) is substituted into Eq. 7.67 (b). Second, Eq. 7.64 is substituted in Eq. 7.67 (b) for the case when the plastic hinges form in the beams at a distance of at least d away from the column faces

$$V_{sh} = \xi_m \xi_p \frac{T}{1.5} \qquad (7.68)$$

in which $T = A_b \lambda_o f_y$, A_b is the largest area between the top and bottom beam reinforcement passing through the joint, $\xi_m = (1 + 0.8 \kappa)$ for the case of plastic hinges forming at the column faces, and, $\xi_m = 1.3/\xi_o$ for the case when plastic hinges forming at a distance of a least d from the column face.

When Eqs. 7.67 (a) and 7.68 are analyzed, it becomes obvious that the shear force transferred by bond is often different for the top and bottom reinforcement.

The use of Eqs. 7.67 (a) and 7.68 will lead to rather small values of V_{sh} when compared with those currently recommended by the New Zealand Concrete Design Code [NZS 3101 (1982)] and it may, in some cases, be also smaller than those estimated from Eqs. 7.48(a), 7.50 and 7.51 proposed by other researchers.

7.3.4.5 The Joint Horizontal Shear Reinforcement

It appears to be contradictory that most tests carried out in New Zealand in interior beam-column joint subassemblages show that the total horizontal force carried by the hoops is significantly larger than the value of V_{sh} either calculated from test results or from the proposal just discussed. These forces should be of the same order according to the traditional truss mechanism. Take for instance the results from Unit 6. Fig. 6.25 shows that the strains in all hoops in run 13 at μ_Δ = 6x1 are near or past yield and the corresponding force estimated at this stage is 958kN = 0.90 V_{jh}. However, the estimated values of the horizontal shear transferred to the truss mechanism based on the calculated bond forces

in run 13, were 559 and 484kN for the top and bottom bars respectively (see Figs. 6.28 and 6.29). These differences are often too large and cannot be explained using the conventional truss mechanism.

The beam-column joint depicted in Fig. 7.21 (a) is used to explain the above differences noted. In this beam-column joint the area of top reinforcement is larger than that of the bottom reinforcement. The compression field shown in Fig. 7.21 (b) results when the beam-column joint reinforcement has been designed for the "exact" horizontal shear transferred by bond from the top bars, $V_{sh,t}$, arising in the region of the column not subjected to compression. In this example, and following observations made by previous researchers, it can be assumed that after few reversal cycles all the hoops will reach their yield strength and therefore the equivalent transverse pressure from the hoops is constant. On the other hand the horizontal shear transferred by bond by the bottom beam bars, $V_{sh,b}$ is smaller than $V_{sh,t}$ and therefore it cannot balance the total horizontal hoop force as required in the right hand side of the joint of Fig. 7.21 (b). In this approach it is postulated that the remainder of the horizontal force is balance by the compression field marked (b) in Fig. 7.21 (b) that originates in the corner subjected to the column compressive forces. The rest of the horizontal shear is carried by a direct compression strut marked (c) in Fig. 7.21 (b) that runs diagonally through the corners of the joint panel.

The vertical transverse pressure required to equilibrate the compression field is non-linear due to the non-linearity of the bond forces from the beam reinforcement and to the non-uniformity of the compression field marked (a) in Fig. 7.21 (b).

Since there are no external vertical forces acting upon the whole depth of the column, this vertical pressure needs to be provided by vertical reinforcement. The resultant vertical forces from the top and bottom vertical pressure are in most circumstances different in magnitude and generally they are non-collinear. Hence, unlike the horizontal forces, the vertical ones are not self-balanced and require of bond forces on the diagonal compression fields marked (b) and (c) in Fig. 7.21, deviating them from a straight diagonal compression field.

A more general situation arises when the amount of horizontal transverse reinforcement provided exceeds the demand from the bond forces $V_{sh,t}$ and $V_{sh,b}$. This is the case of the interior beam-column joints designed according to the New Zealand Concrete Design Code [NZS 3101 (1982)]. The hoops will reach their yield strength or will be near it unless the amount of transverse reinforcement provided exceeds the horizontal joint shear. In the latter the joint hoops will reach a force smaller than that developed at their yield stress and of similar magnitude to the total horizontal shear force. One example that illustrates the above statement is the interior beam-column joint tested by Priestley (1975). The capacity of the hoops at their yield strength was $2.65V_{jh}$ and at $\mu_\Delta = 6$ the horizontal force in the hoops, determined from averaged strain gauge measurements, was $0.87\ V_{jh}$. This behaviour is explained using the diagonal compression field illustrated in Fig. 7.21 (c). There, the diagonal compression field marked (b), originating in the corners where the compressive forces from the column act, will be required to balance the hoop pressure in conjunction with the horizontal shear forces $V_{sh,t}$ and $V_{sh,b}$. One consequence of placing more horizontal transverse reinforcement in the joint panel is that the angle of

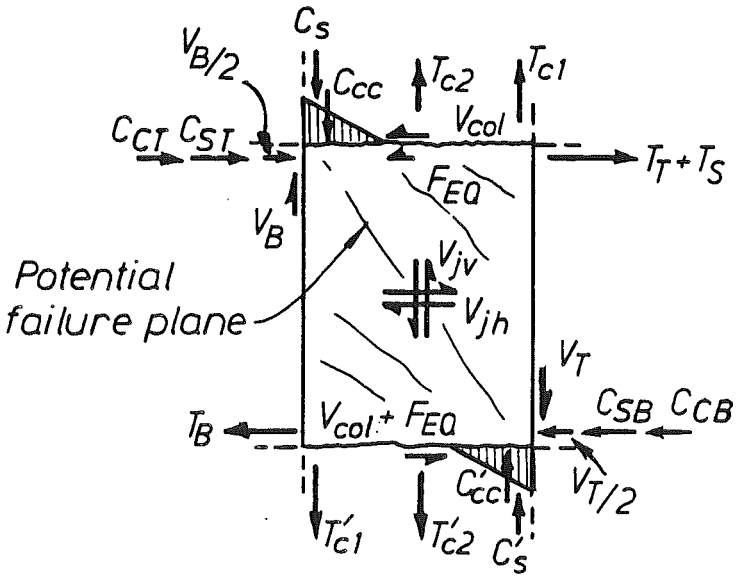

(a) Forces acting

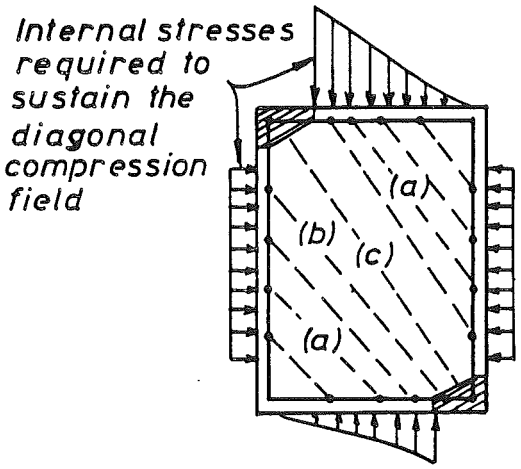

(b) Compression field if joint horizontal reinforcement provided equals V_{sh}

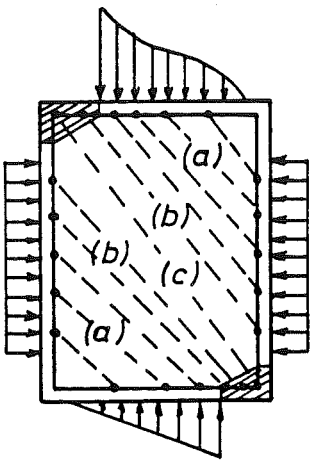

(c) Compression field if joint horizontal reinforcement exceeds V_{sh}

Fig. 7.21 - Forces Acting at the Boundaries of an Interior Beam-Column Joint and Associated Compression Fields.

inclination to the horizontal of the diagonal compression field marked (a) will decrease and as a result the vertical forces necessary to balance this diagonal compression field will also diminish.

Hence the maximum horizontal reinforcement in the joint, $V_{tr,h}$, required to sustain the compression field arising from bond in the bars in the region away from the column compression zone is

$$V_{tr,h} = A_{sh} f_{yh} \geq V_{sh} \tag{7.69}$$

where A_{sh} is the area of horizontal transverse reinforcement of yield strength f_{yh}, V_{sh} is the largest of $V_{sh,t}$ and $V_{sh,b}$, which are calculated independently as the smaller of the values given by Eqs. 7.67 (a) and 7.68.

Only the horizontal transverse steel in the joint in the direction considered that extends beyond $h_c/4$ from the column centreline shall be deemed effective in resisting the horizontal shear. Many tests at the University of Canterbury have also shown that those hoops placed next to the beam longitudinal reinforcement are not effective in resisting the joint horizontal shear. Hence, it is also recommended that this reinforcement be placed within $h_b/4$ from each side of the joint mid-depth. Fig. 7.22 depicts the latter definition.

7.3.4.6 The Joint Vertical Shear Reinforcement

The reinforcement required to balance the vertical component of the diagonal compression field, and the flexural demand due to bending in the column when the joint reinforcement pass the joint and forms part of the column longitudinal reinforcement, can be expressed as

$$V_{tr,v} = V'_{tr,v} + T_{c2} \tag{7.70}$$

where $V'_{tr,v}$ in Eq. 7.55 can be evaluated by lumping the diagonal compression field marked (a) in Figs. 7.21 (a) and (b) in an equivalent strut acting at the centroids of the horizontal and vertical internal field of stresses. For simplicity it will be assumed that the vertical pressure required by the linear bond distribution is linear. With reference to Fig. 7.23.

$$V'_{tr,v} = V_{sh} \frac{y_{tr}}{x_{tr}} \tag{7.71}$$

where

$$x_{tr} = \frac{2}{3}\left(h_c - (1-g)\frac{h_c}{2} - kh_c\right) \tag{7.72}$$

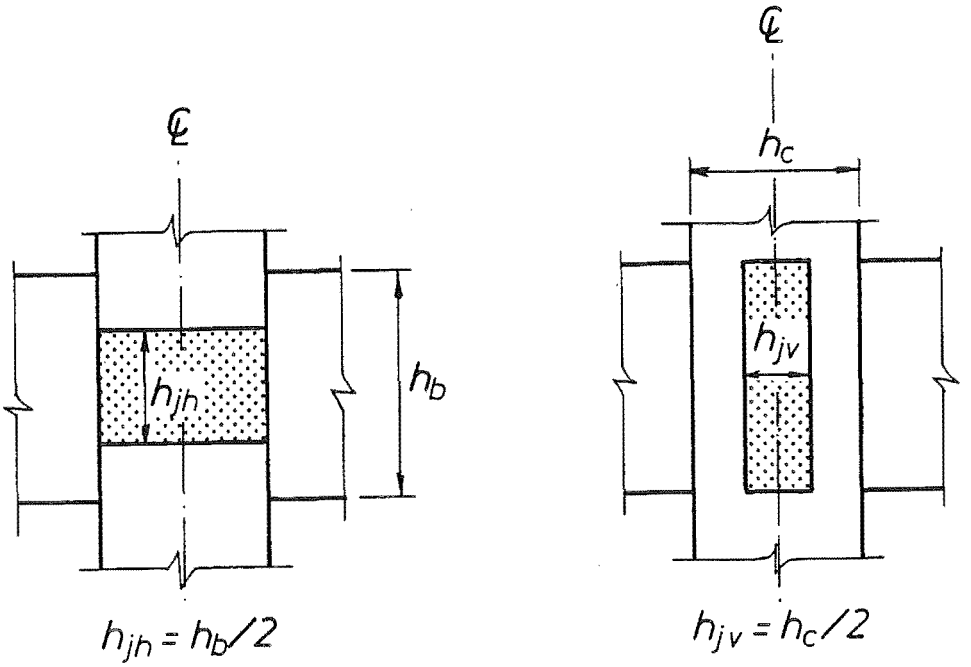

(a) Horizontal reinforcement (b) Vertical reinforcement

Fig. 7.22 - Definition of Joint Effective Reinforcement.

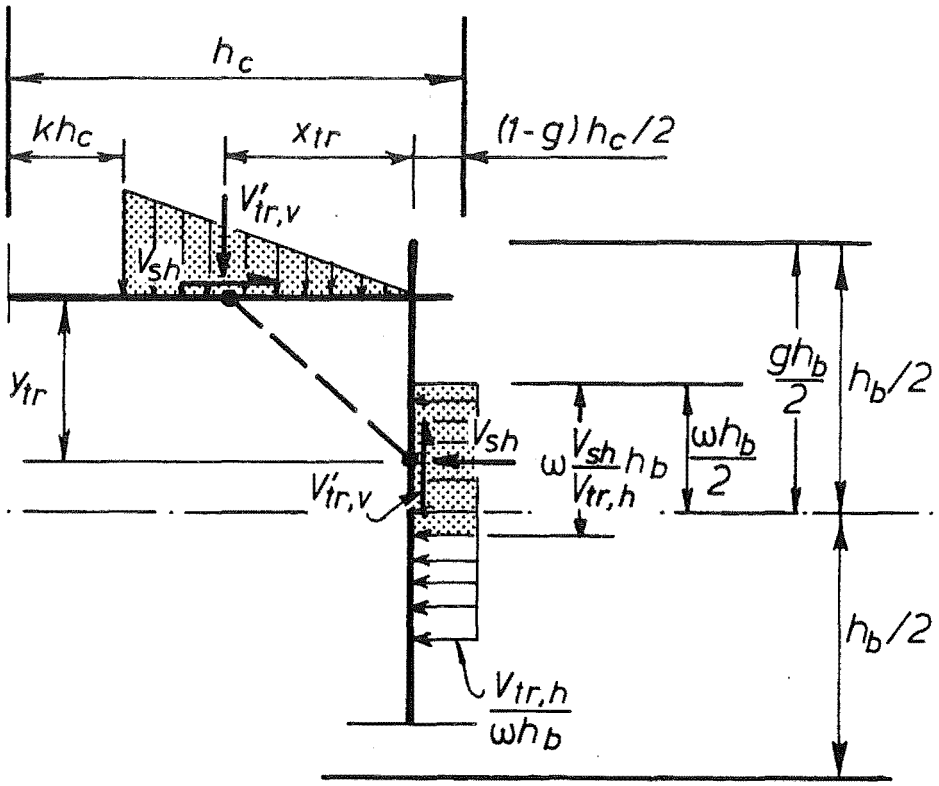

Fig. 7.23 - Vertical Joint Reinforcement Required to Sustain the Diagonal Compression Field Originated by Bond.

and

$$y_{tr} = \left(g - \omega\left(1 - \frac{V_{sh}}{V_{tr,h}}\right)\right)\frac{h_b}{2} \tag{7.73}$$

Now assuming g = 0.8, ω = 2/3 and substituting Eq. 7.43 in Eq. 7.57

$$x_{tr} = \frac{2}{3}\left(0.65 - 0.85\,\frac{P_u}{A_g f_c'}\right) h_c \tag{7.74}$$

and

$$y_{tr} = \left(0.13 + \frac{2}{3}\,\frac{V_{sh}}{V_{tr,h}}\right)\frac{h_b}{2} \tag{7.75}$$

Therefore

$$V'_{tr,v} = \frac{3}{4}\,\frac{(0.13 + 0.67\,V_{sh}/V_{tr,h})}{\left(0.65 - 0.85\,\frac{P_u}{A_g f_c'}\right)}\,\frac{h_b}{h_c}\,V_{sh} \tag{7.76}$$

The actual value of the term T_{c2} in Eq. 7.70 is very difficulty to quantify owing to the influence of parameters such as the amount and arrangement of the longitudinal reinforcement and, most important of all, the deviation from the values determined from the code recommended static loading of the bending moment pattern and axial load on the columns due to the dynamic effects on the structure, which are caused by the higher modes of vibration and plastification of parts of the frame. Fig. 7.24, reproduced from Paulay (1988), shows one of such cases. It can be seen that the column end

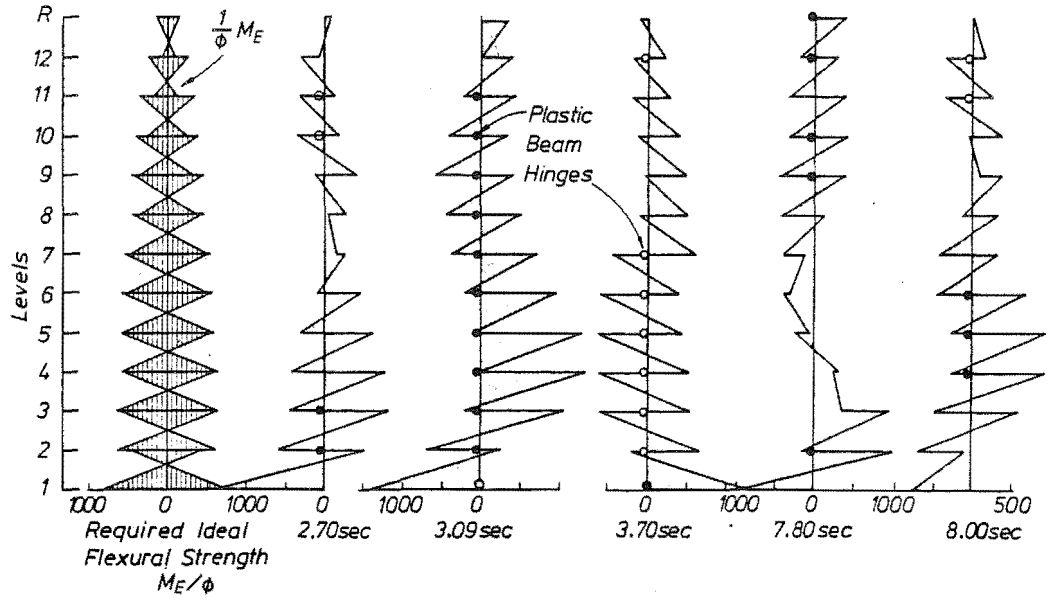

Fig. 7.24 - Dynamic Effects on the Bending Moment of Columns [Paulay (1988)].

moments in the intermediate floors can eventually become much larger than the code calculated moments due to the variation of the point of contraflexure. The New Zealand Concrete Design Code recognizes these dynamic effects and recommends the use of a moment magnification factor. The main aim of the code provisions is to avoid the formation of plastic hinges in the columns located in intermediate floors of the structure and enforce, according to the capacity design philosophy, a weak-beam strong column collapse mechanism. Note, however, that the given provisions do not attempt to avoid yielding of the column longitudinal reinforcement under the worst situation [Paulay and Priestley (1992)].

It is obvious that the critical loading condition for the design of a beam-column joint is in the presence of lower axial compression loads, below the balance point. Under this load condition it could be expected that, due to the dynamic moment demand, the column outer bars will yield in tension and, in the absence of axial load, the intermediate column longitudinal bars will be stressed to about 40% of their yield strength due to flexure. Therefore the remaining 60% can be fully utilized to resist the vertical joint forces generated by the diagonal compression field marked (a) in Figs. 7.21 (b) and (c). It can also be demonstrated that the intermediate column longitudinal bars are not stressed as a result of flexure only at a column compressive axial load between $0.25A_g f'_c$ and $0.30A_g f'_c$. Consequently, the entire intermediate column longitudinal reinforcement can be used to resist the vertical forces of the compression field marked (a) in Figs. 7.21 (a) and (b).

The above rationale can be taken into account by rewriting Eq. 7.70 as

$$V_{tr,v} = \xi_c \, V'_{tr,v} \tag{7.77}$$

where ξ_c is a factor that recognizes the combined flexure and joint vertical forces acting simultaneously in the column intermediate bars. A simple expression for ξ_c is

$$\xi_c = 2.3 \left(0.65 - 0.85 \frac{P_u}{A_g f'_c} \right) \tag{7.78}$$

Substituting Eqs. 7.76 and 7.78 in Eq. 7.77 and simplifying

$$V_{tr,v} = 1.4 \, \xi_v \frac{h_b}{h_c} V_{sh} \tag{7.79}$$

in which ξ_v is a factor that considers the inclination of the compression field between beam and column bars

$$\xi_v = \left(0.17 + 0.83 \frac{V_{sh}}{V_{tr,h}} \right) \geq 0.58 \tag{7.80}$$

The diagonal strut shown in Fig. 7.23 suggests that the required vertical reinforcement, $V_{tr,v}$, be located near the centreline of the column. Hence, it is recommended that this reinforcement be placed within $h_c/4$ from each side of the column centreline as depicted in Fig. 7.22 (b).

7.3.4.7 Strength of the Diagonal Compression Field

At the beginning of Section 7.3.4.1 it was stated that the strength of the joint cannot not be less than the strength of the weakest member. It is very important to recognize that the carrying capacity of a column cannot be jeopardized by a joint failure. Besides, there are great difficulties in repairing a structure in which the damage has concentrated at the beam-column joints.

In an attempt to avoid degradation of the compression field of a beam-column joint, the New Zealand Concrete Design Code [NZS 3101 (1982)] recommends that the shear stresses v_j calculated using Eq. 7.32 should not exceed $1.5\sqrt{f'_c}$, where f'_c is the concrete cylinder compressive strength. The above limit was justified by Paulay and Park (1984) based on an analysis carried out using the compression field theory. Then it was pointed out that no beam-column joints having a shear stress below $0.2f'_c$ had shown a diagonal compression failure. Paulay and Park also recognized the influence of yielding of the transverse reinforcement on decreasing the strength of the compression field as well as the possible detrimental effects of reversed cyclic loading in developing cracks in the joint in two directions.

The effects of yielding of the reinforcement on the strength of a diagonal compression field are now well known [Collins and Mitchell (1991)]. More recently, Stevens et al (1991) have studied the effects of reverse cyclic loading and yielding of the reinforcement in large reinforced concrete panels subjected to pure shear or pure shear combined with biaxial compression. They concluded that the strength of the compression field is further reduced as a result of cyclic reverse loading if the reinforcement is allowed to yield.

The current trends on relaxing the horizontal reinforcement in the joint panel will lead to yielding of the hoops at an earlier stage than for the joints designed with the current code provisions and consequently the strength of the compression field will be expected to decrease more rapidly.

For instance, a recent interior beam-column joint tested by Xin (1992), Unit 1, did not display a full ductile response due to a diagonal compression failure caused by excessive yielding of the joint hoops. The capacity of the joint hoops at their yield strength was 74% of the horizontal joint shear, V_{jh}, calculated at an overstrength of 1.25. The joint shear stresses were expected to be of the order of $0.16f'_c = 0.91\sqrt{f'_c}$, a value well below of the code limiting value. The joint horizontal reinforcement consisted on 5 sets of hoops but the top and bottom hoops were placed next to the beam bars, rendering them ineffective. This means that the effective joint horizontal reinforcement was of the order of $0.44V_{jh}$. Beckingsale (1980) tested a similar interior beam-column joint. The joint shear stress was $0.15f'_c = 0.87\sqrt{f'_c}$. In both tests the beams were symmetrically reinforced and the ratio $A_s f_y/h_c \Sigma d_b \sqrt{f'_c}$ was almost identical. The main difference was that in Beckingsale's test, the effective joint horizontal reinforcement, in which the first and last set of hoops in contact with the beam bars

were disregarded, was able to take up to $0.94V_{jh}$. Other differences in these tests were that a minimum axial compression load in the column of $0.044A_g f'_c$ was present in Beckingsale's test and the ratio h_c/h_b was slightly different. The reinforcement required to sustain the bond forces from the beam bars V_{sh} as given by Eq. 7.69 is $0.52V_{jh}$ for Xin's unit and $0.47V_{jh}$ for Beckingsale's unit. Beckingsale observed no detrimental effects in the concrete in the joint core.

In another series of tests Birss (1978) studied the behaviour of elastic interior beam-column joints. The main variables were the joint shear reinforcement and the column axial load. The first unit was tested under minimum axial compressive load of $0.05A_g f'_c$ and the joint horizontal steel detailed was capable of providing $0.45V_{jh}$. According to Eq. 7.69 a minimum transverse reinforcement equal to $0.40V_{jh}$ will be required. In the second test the axial load was increased to $0.44A_g f'_c$. A minimum joint horizontal reinforcement of $0.14V_{jh}$ was provided, while that required by Eq. 7.69 is $0.12V_{jh}$. Both units failed in the initial cycles of loading in the inelastic range after excessive yielding of the joint hoops. The units attained their theoretical lateral load capacity in the first cycle in the inelastic range but they were unable to maintain it in further cycles. The maximum attained joint shear stress was of the order of $0.2f'_c = 1.12\sqrt{f'_c}$. Both units displayed a diagonal compression failure in the joint region.

The above test results suggest that, in simple terms, the maximum joint shear stress, v_j, that can be sustained without significant degradation of the strength of the compression field may be considered as a function of the ratio between the amount of horizontal reinforcement provided, $V_{tr,h}$, and the joint horizontal shear, V_{jh}. The following expression is recommended for joints of moment resisting frames designed for full ductility

$$v_j \leq \frac{f'_c}{\xi_u} \frac{V_{tr,h}}{V_{jh}} \tag{7.81}$$

where factor ξ_u depends on the level of ductility and v_j is found using Eq. 7.43. In no case shall v_j exceed $0.20f'_c$. It is recommended that $\xi_u = 3.5$ and $\xi_u = 2$ be used for interior beam-column joints of frames designed for full ductility and for frames designed for limited ductility, respectively.

Eq. 7.81 can be arranged for $V_{tr,h}$ as

$$V_{tr,h} \geq \frac{\xi_u}{f'_c} v_j V_{jh} \tag{7.82}$$

Although the terms V_{jh} and v_j are related, Eqs. 7.81 and 7.82 are given in above form to emphasize on the effects of large shear stresses in interior beam-column joints. Therefore the horizontal joint reinforcement required needs to be the largest between that found from Eq. 7.69 and that obtained from Eq. 7.82.

The above formulation differs from the recommended limits given by Cheung et al (1991a) and Paulay and Priestley (1992) who suggested that the joint shear stress should be limited to values smaller than $0.25f'_c$ or 9MPa for joints of one way frames or $0.20f'_c$ or 7MPa for joints of two way frames.

7.3.4.8 Interior Beam-Column Joints in Two-Way Frames

So far, the design of interior beam-column joints has been confined to joints of one-way frames. The same procedure currently included in the New Zealand Concrete Design Code [NZS 3101 (1982)] will be adopted in this study. The provisions for two-way joints are based on judgement and of limited experimental evidence. Only two tests have been carried out on two-way interior beam-column joints in New Zealand. In one test Beckingsale et al (1980) applied an axial compressive load of $0.50A_gf'_c$ to the columns. In another test, Cheung et al (1991) tested a two-way subassemblage including the slab. No axial load was applied to the column.

The code provisions recognize the possibility of plastic hinges occurring simultaneously at each face of the joint and that the critical inclined plane of failure is oriented as a linear combination of the planes of failure in each direction. The design is simplified by enabling the joint reinforcement to be found from independent analysis in perpendicular directions where the beneficial effects of the axial compression load in the column in each of the analysis is apportioned in proportion to the joint horizontal shear force in each direction to avoid superposition. Following the same procedure, the term P_u in Eq. 7.67 (c) can be replaced by C_jP_u where

$$C_j = \frac{V_{jh}}{V_{jx} + V_{jz}} \tag{7.83}$$

in which V_{jh} is the joint horizontal shear force in the direction being considered and V_{jx} and V_{jz} are the horizontal shear forces in each direction.

7.3.4.9 Design Example of an Interior Beam-Column Joint

Determine the horizontal and vertical joint reinforcement of a one-way interior beam-column joint of a moment resisting frame designed (a) for full ductility, and, (b) for limited ductility. The following data is given

$h_b = 650mm$ $\qquad$ $P_u/A_gf'_c = 0.10$

$h_c = 600mm$ $\qquad$ $b_c = 500mm$

$f'_c = 54MPa$ $\qquad$ $f_y = f_{yh} = 430MPa$

The following forces have been estimated from an initial analysis, where no consideration has been given to the probable overstrength.

$$T_T = 735kN \quad T_S = 305kN \quad T_B = 800kN \quad V_{col} = 320kN$$

a) **Design for Full Ductility**

Step 1 - Check for diagonal compression failure

$\lambda_o = 1.25$

$V_{jh} = 1.25\ (735 + 305 + 800 - 320) = 1{,}900kN$ **[Eq. 7.41 (c)]**

$v_j = 1{,}900/(600 \times 500) = 6.3MPa = 0.14f'_c < 0.20\ f'_c$ **[Eq. 7.43]**

$\xi_u = 3.5$

$V_{tr,h} \geq 3.5 \times 0.14 \times 1900 = 931kN$ **[Eq. 7.69]**

Step 2 - Find maximum diameter of bars allowed to pass through the joint

Top bars:

$\kappa = 800/735 = 1.09$

$\xi_m = 1 + 0.8 \times 1.09 = 1.87$

$\xi_t = 0.7$

$\alpha = 0.46$

$d_b \leq 20mm$ **[Eq. 7.63]**

Use 4 HD20 + 2 HD16 ($A_s = 1{,}685mm^2$)

$\Sigma d_b = 112mm$

Bottom bars:

$\kappa = (735 + 305)/800 = 1.30$

$\xi_m = 1 + 0.8 \times 1.30 = 2.04 > 2$, use $\xi_m = 2$

$\xi_t = 1$

$\alpha = 0.46$

$d_b \leq 21mm$ **[Eq. 7.63]**

Use 6 HD20 ($A_s = 1{,}884mm^2$)

$\Sigma d_b = 120mm$

Step 3- Find the horizontal transverse reinforcement, $V_{tr,h}$

Find bond forces required to be transferred by horizontal reinforcement

$\xi_p = (1 - 1.3 \times 0.1)^2 = 0.76$ **[Eq. 7.67 (c)]**

Top bars: $V_{sh,t}$ the smaller of

$$\frac{\sqrt{0.7 \times 45}}{550} \times 0.76 \times 600 \times 112 = 521 \text{ kN} \qquad \text{[Eq.7.53(a)]}$$

$$\text{or} \quad 1.87 \times \frac{0.76}{1.5} \times 1658 \times 1.25 \times 430 = 844\text{kN} \qquad \text{[Eq.7.54]}$$

$\therefore V_{sh,b} = 521\text{kN}$

Bottom bars: $V_{sh,b}$ the smaller of

$$\frac{\sqrt{1.0 \times 45}}{550} \times 0.76 \times 600 \times 120 = 667 \text{ kN} \qquad \text{[Eq. 7.67 (a)]}$$

$$\text{or} \quad 2 \times \frac{0.76}{1.5} \times 1{,}884 \times 1.25 \times 430 = 1{,}026\text{kN} \qquad \text{[Eq. 7.68]}$$

$\therefore V_{sh,b} = 667\text{kN}$

Hence $V_{sh} = 667\text{kN}$. $V_{tr,h}$ is the largest of 667kN and 931kN. Then, horizontal hoops are required to avoid a diagonal compression failure.

Use 5 - 4HD12 hoops, ($A_s = 2{,}260\text{mm}^2$)
Thus, $V_{tr,h} = 972\text{kN}$

Step 4 - Find the vertical joint reinforcement, $V_{tr,v}$

$$\xi_v = \left(0.17 + 0.83 \times \frac{667}{972}\right) = 0.74 > 0.58 \qquad \text{[Eq. 7.80]}$$

$$V_{tr,v} = 1.4 \times 0.74 \times \frac{650}{600} \times 667 = 749\text{kN} \qquad \text{[Eq. 7.79]}$$

$A_s = 749 / 430 \times 1{,}000 = 1{,}740\text{mm}^2$
Use at least 4 HD24 bars in the central part of the column.

b) Design for Limited Ductility

Step 1 - Check for diagonal compression failure

$\lambda_o = 1.15$

$V_{jh} = 1{,}748\text{kN}$ [Eq. 7.41 (c)]

$v_j = 5.8\text{MPa} = 0.13f'_c < 0.20f'_c$ [Eq. 7.43]

$\xi_u = 2$

$V_{tr,h} \geq 2 \times 0.14 \times 1{,}748 = 489\text{kN}$ **[Eq. 7.69]**

Step 2 - Find the maximum bar diameter allowed to pass through the joint

Top bars:
$\xi_m = 1.87$
$\xi_t = 0.7$
$\alpha = 0.6$
$d_b \leq 25\text{mm}$

Use 4 HD24 ($A_s = 1{,}808\text{mm}^2$)
$\Sigma d_b = 96\text{mm}$

Bottom bars:
$\xi_m = 2$
$\xi_t = 1$
$\alpha = 0.6$
$d_b \leq 25\text{mm}$

Use 4 HD24 ($A_s = 1{,}808\text{mm}^2$)
$\Sigma d_b = 96\text{mm}$

Step 3 - Find the horizontal transverse reinforcement, $V_{tr,h}$
$\xi_p = 0.76$ **[Eq. 7.67 (c)]**

Top Bars: $V_{sh,t}$ the smaller of
447kN **[Eq. 7.67 (a)]**
or 906kN **[Eq. 7.68]**
$\therefore V_{sh,t} = 447\text{kN}$

Bottom bars: $V_{sh,b}$, the smaller of
534kN **[Eq. 7.67 (a)]**
or 906kN **[Eq. 7.68]**
$\therefore V_{sh,b} = 534\text{kN}$

Hence, $V_{sh} = 534\text{kN}$
$V_{tr,h}$ the largest of 534kN and 489kN.

Use 4 - 4HD10 hoops ($A_s = 1{,}256\text{mm}^2$)
Thus, $V_{tr,h} = 540\text{kN}$

Step 4 - Find the vertical joint reinforcement, $V_{tr,v}$
$\xi_v = 0.99 > 0.58$ **[Eq. 7.65]**

$V_{tr,v}$ = 802kN [Eq. 7.64]

Use at least 4 HD24 bars in the central part of the column.

7.3.5 Additional Recommendations for the Design of Connections Between Precast Concrete Members Joining at the Beam-Column Joint Region

Stevenson and Beattie (1991) recommended the use of shear keys in the vertical construction joint of beams of System 1 after the performance of a subassemblage of this type showed a pinched hysteretic performance due to sliding of the beams at the column face. However, the test result obtained in Unit 1 indicates that no shear keys are required in the vertical construction joint in the beams at the column faces providing that the beams are properly seated on the concrete cover of the column below. This is because the main crack at the column face will not coincide with the construction joint, making the behaviour similar to that of a monolithic equivalent method of construction.

Based on the above two results it is recommended that the beams possess a series of shear keys along the vertical construction joints unless a minimum seating distance S_d of the beams in the concrete cover of the column below can be guaranteed. A recommended value for S_d is

$$S_d = \frac{V^\circ}{0.85 f_c' b_w} \geq 30\text{mm} \qquad (7.84)$$

where V° is the beam shear associated with the flexural overstrength at negative moment, f_c' is the concrete cylinder compressive strength of the column and b_w is the width of the precast concrete beam seating in the column.

Concerning the anchorage of the hooked bottom bars protruding from the precast concrete beams, it is recommended that the existing code provisions for exterior beam-column joints be used. For obtaining the $V_{sh,b}$ from Eq. 7.67 (a), all the bars in tension and compression being anchored in the joint should be considered in the evaluation of Σd_b.

In relation with the precast concrete System 2 (see Section 1.4.1) no additional requirements are necessary. The existing recommendation [Charleson (1991)] of using a grout with a compressive strength of at least 10MPa larger than the concrete compressive strength of the precast member appears reasonable since, in terms of quality assurance, it is very difficult if not impossible to repair the connection between two precast concrete elements joined using a low strength grout.

7.4 EFFECTS OF THE BEAM ELONGATION

In a series of tests on spandrel beams of shear walls Paulay (1969) observed that, if the beams are unrestrained, longitudinal elongation at the mid-depth occurs due to the offset of the neutral axis depth. However, no large elongation values were recorded mainly because the rotation in the spandrel beams was kept to low values.

Beekhuis (1971), Binney (1972) and Cheung et al (1991) have reported significant elongations recorded during the testing of full scale beams or beam-column joint subassemblages at the University of Canterbury.

Researchers at the University of Auckland have also reported the beam lengthening during the cyclic reverse loading of various series of tests tested to failure [Fenwick and Fong (1979), Fenwick et al (1981), Megget and Fenwick (1988)]. Fenwick (1990) has classified the beam elongation according to two different sources, namely uni-directional hinging and reversed plastic hinging. In the first case, beam elongation occurs because the negative and positive plastic hinges in a beam are offset which is the case of beams of gravity dominated frames. In the second case both directions of plastic hinges form in the same region.

Fig. 7.25 shows the deformed shape of a component of a reinforced concrete frame that has been monotonically displaced well into the plastic range. In this figure it has been assumed that deformations occur only in the beam plastic hinge regions. Evidently an increase in the beam length will occur due to the offset between the beam mid-depth and the neutral axis depth. By assuming that in beams the neutral axis depth coincides with the centroid of the compression reinforcement, the following expression for the lengthening in the span of the bay of a frame, δ_{el}, can be obtained

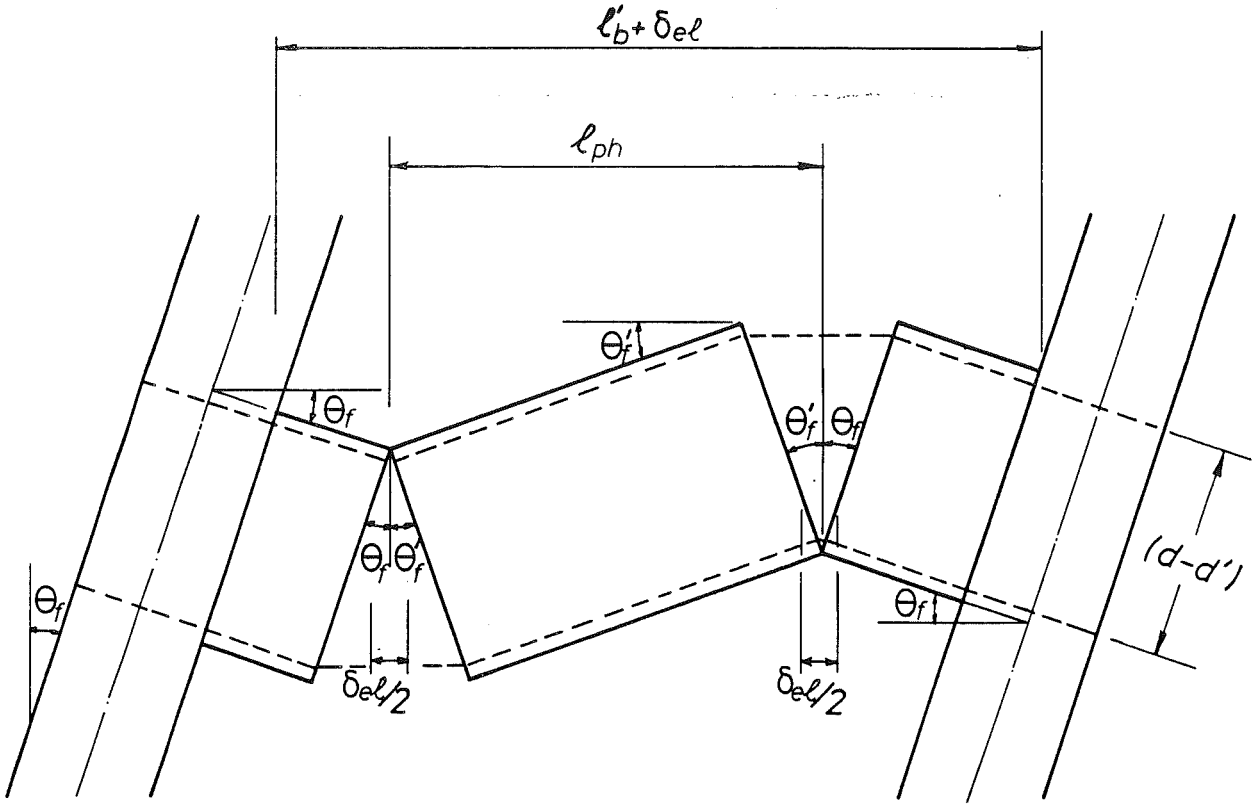

Fig. 7.25 - Deformed Frame Assembly Showing the Beam Elongation.

$$\delta_{el} = \theta_f \frac{l_b'}{l_{ph}} (d - d') \tag{7.85}$$

where θ_f is the angle of drift in each storey, l_b' is the distance between the column centrelines and l_{ph} is the distance between the positive and negative plastic hinges in the beam.

The beam lengthening can even be larger than that calculated using Eq. 7.85 when the member is subjected to post-elastic reversal cycles. This is because either the top or the bottom layer of beam reinforcement or both may not fully yield in compression, as it was demonstrated in Section 7.3.2, and hence the cracks in the compression side will not close. Fenwick (1990) has also stated that the wedging action of the aggregate particles that are dislocated between cracks may also contribute to the non-closure of the cracks. This observation was evident in the tests of Units 1, 2 and 3 where the diagonal strut carrying the shear to the column faces was crossed by several cracks that did not close. That is, the diagonal compression force was transferred by contact between the dislocated particles, which led to grinding of the concrete at advance stages during the test.

An upper bound to envelope the beam elongation is to assume that upon reversal the reinforcement that goes into compression remains with the same residual tensile strain. Thus, the maximum expected lengthening of the beam of a frame subjected to large inelastic reversals can be of the order of

$$\delta_{el} = 2\theta_f \frac{l_b'}{l_{ph}} (d - d') \tag{7.86}$$

Fig. 7.26 illustrates the beam elongations recorded in some different tests in New Zealand. The beam elongation is presented as percentage of the distance between steel centroids d - d'. Also shown are the predicted upper and lower bounds found using Eqs. 7.85 and 7.86. The initial recorded beam elongation at low drift levels is always over-predicted by these equations. This is because being still in the elastic range or just beyond it, the deformations causing the interstorey drift are distributed throughout the test subassemblage. However often Eqs. 7.85 and 7.86 bound quite well the beam elongation recorded because, as assumed, the inelastic deformations concentrated in the plastic hinges.

The recorded elongation of the beams shown in Figs. 7.26 (a) and (b) is very close to the upper bound given by Eq. 7.86. In these units the beam bars were anchored in the beam-column joint region so as to avoid a global bar slip due to bond deterioration. Because of the anchorage characteristics, it would be expected that the elongation of the plastic hinges in a beam at an exterior column display a similar trend. Unit 3, tested in this study, had equal amounts of top and bottom beam

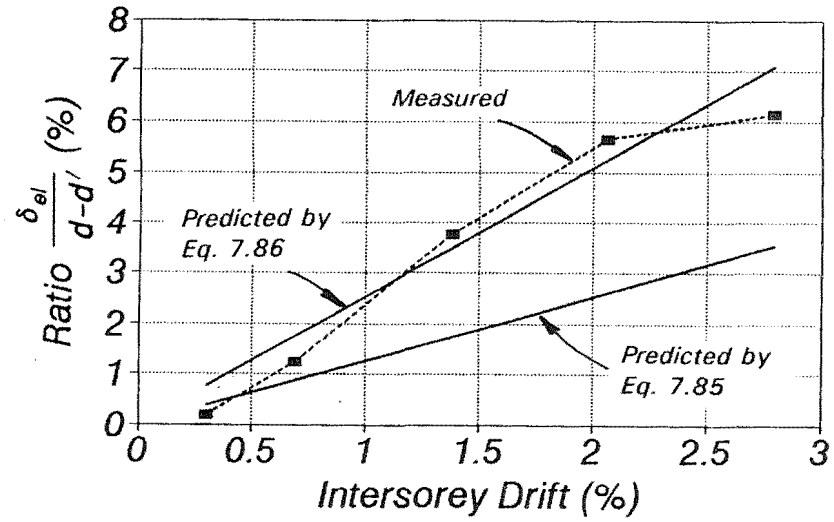

(a) Unit 3

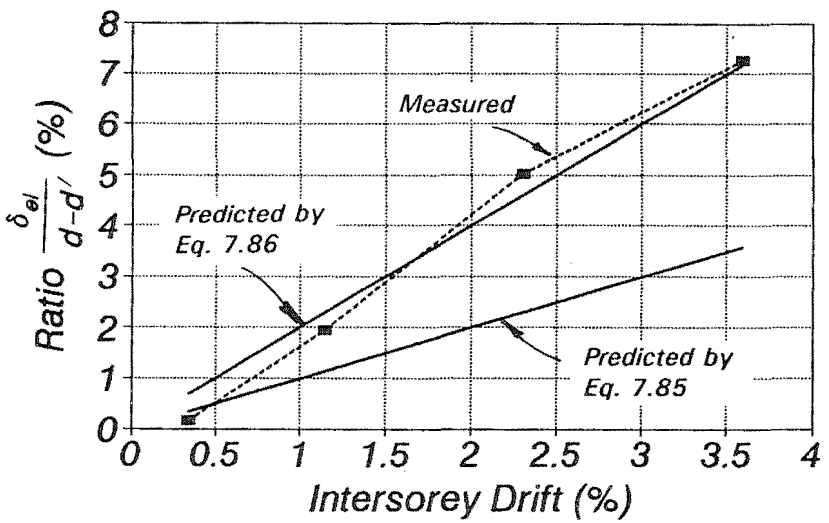

(b) Fenwick et al Unit 2B (1981)

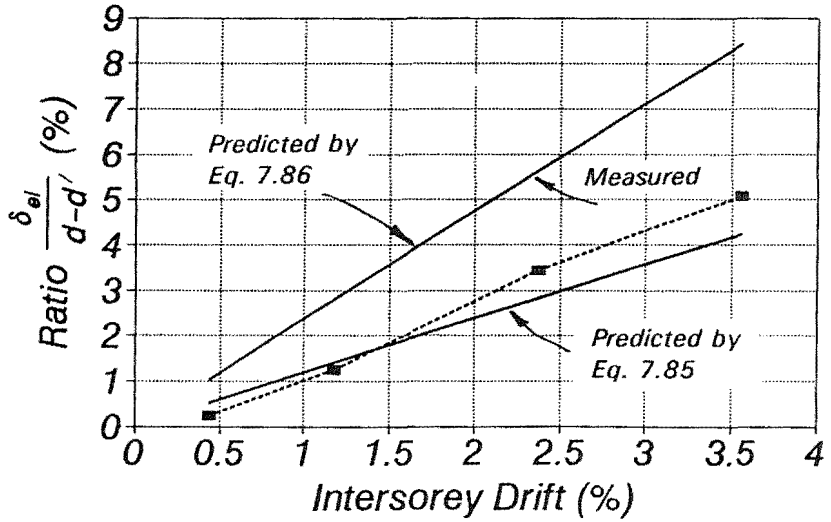

(c) Unit 5

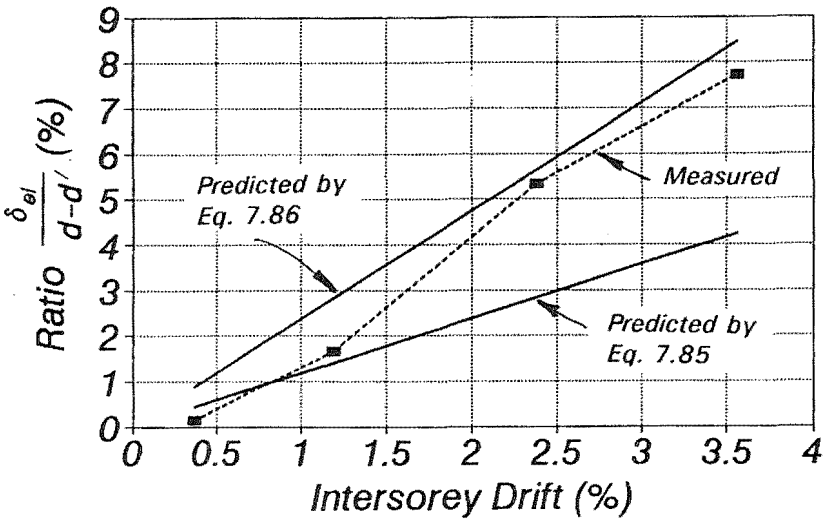

(d) Unit 6

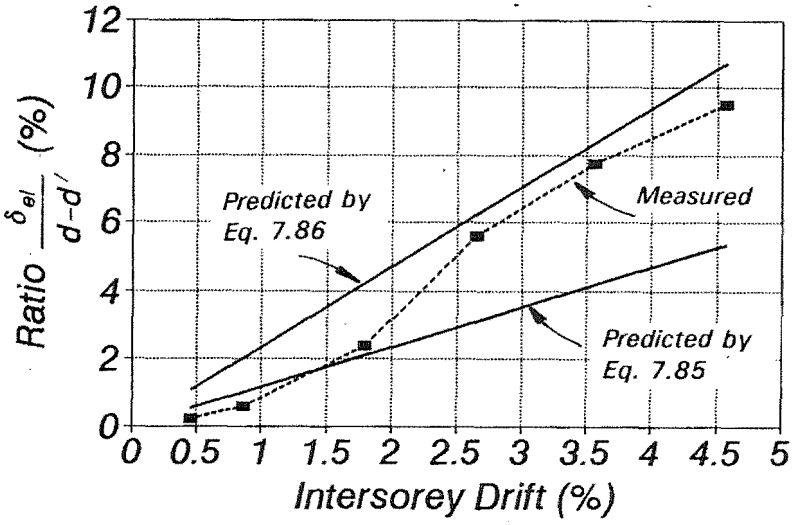

(e) Cheung et al Unit 1D-1 (1991)

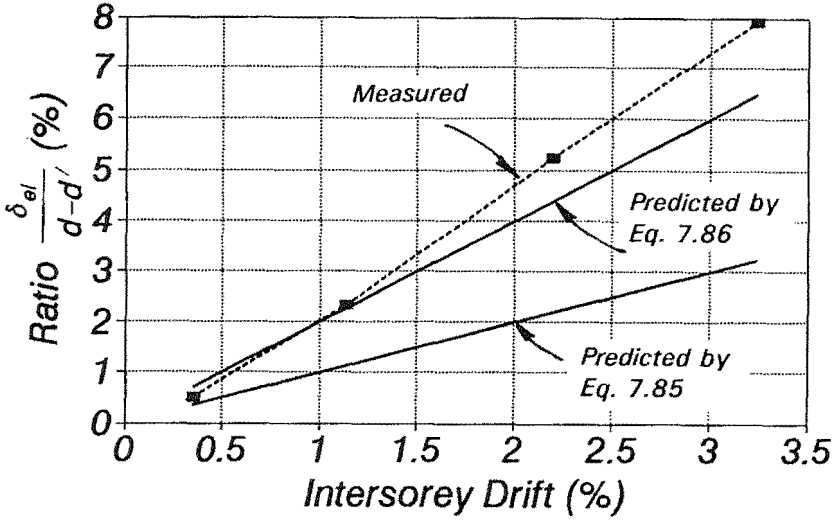

(f) Fenwick et al Unit 4B (1981)

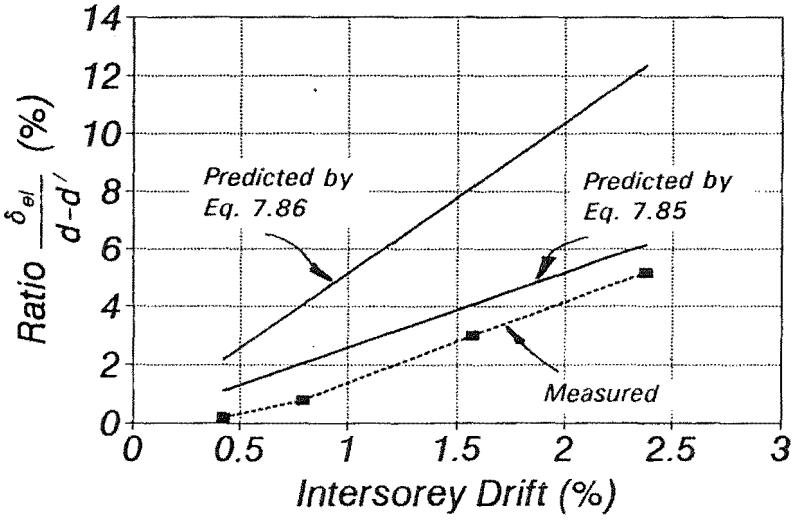

(g) Unit 4r

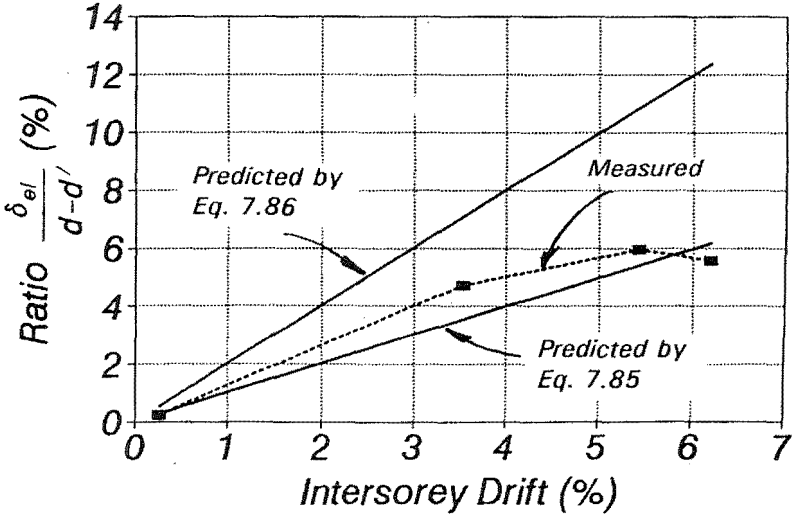

(h) Binney diagonally reinforced Unit 317

Fig. 7.26 - Beam Elongation Recorded in New Zealand Tests.

reinforcement while the beam of Fig. 7.26 (b) had a ratio $\rho'/\rho = 0.8$. It is evident that the elongation is independent of the ratio ρ'/ρ.

Fig. 7.26 (c) and (d) depicts the recorded elongation in two interior beam-column joint units. At moderate and large drift levels, the total beam elongation is enveloped by the predictiongiven by Eqs. 7.85 and 7.86. The elongation is therefore not so large compared with the first two beams due to the effect of global bar slip. For instance Unit 5 showed an early bond failure and its effect is clearly marked in the smaller elongation shown in Fig. 7.26 (d), which is very well defined by the lower bound line.

As Figs. 7.26 (e) and (f) illustrate, the slab does not provide any restraint against the beam elongation. The recorded growth in length along the longitudinal mid-depth axis of the beams is comparatively similar to other tests that did not include a slab.

The only case where Eqs. 7.85 and 7.86 do overpredict the beam elongation is in the recorded growth of Unit 4r. This is because the beam rotations concentrated at the column faces and not at their relocated position as intended.

It is obvious that the effects of beam elongation may be of significant structural and non-structural significance, especially in perimeter frames where the depth of the beams and the number of bays are larger compared with other structural solutions. The elongation of the beams in the upper storeys of a moment resisting is likely to be of the same order of that measured in tests mentioned above because there are no apparent restraints. The magnitude of the elongation is of important concern in the design of the connections of the cladding and glazing systems, as well in proportioning the appropriate seating of the precast concrete floor systems. On the first level of the moment resisting frame or coupled structural walls the effects of beam elongation are more difficult to predict. This is because the columns or the walls may provide some restraining action because of their fixity at ground level. The restraining action will induce an axial compression force in the beams, which will enhance their flexural capacity and reduce the ratio between the beam and column flexural capacities. In the worst case the exterior columns or the interior columns located near the exterior column may eventually form plastic hinges at the beam face as depicted in Fig. 7.27. Yalcin et al (1990) concluded that the restraining action in the test unit caused the redistribution of the shear force in the columns and the decreased of the ratio beam-column capacities.

There are ways to maintain the beam elongation close to the lower bound given by Eq. 7.85. One of them is the use of diagonally reinforced beams. The compression reinforcement will be theoretically subjected to an equal force to the tension reinforcement and therefore the cracks will close or remain rather small. One example is given in Fig. 7.26 (h) of a diagonally reinforced coupling beam tested by Binney (1972). Another alternative is the use of beams with distributed reinforcement. In this type of beam the reinforcement in compression can be easily designed to yield even though if the ratio

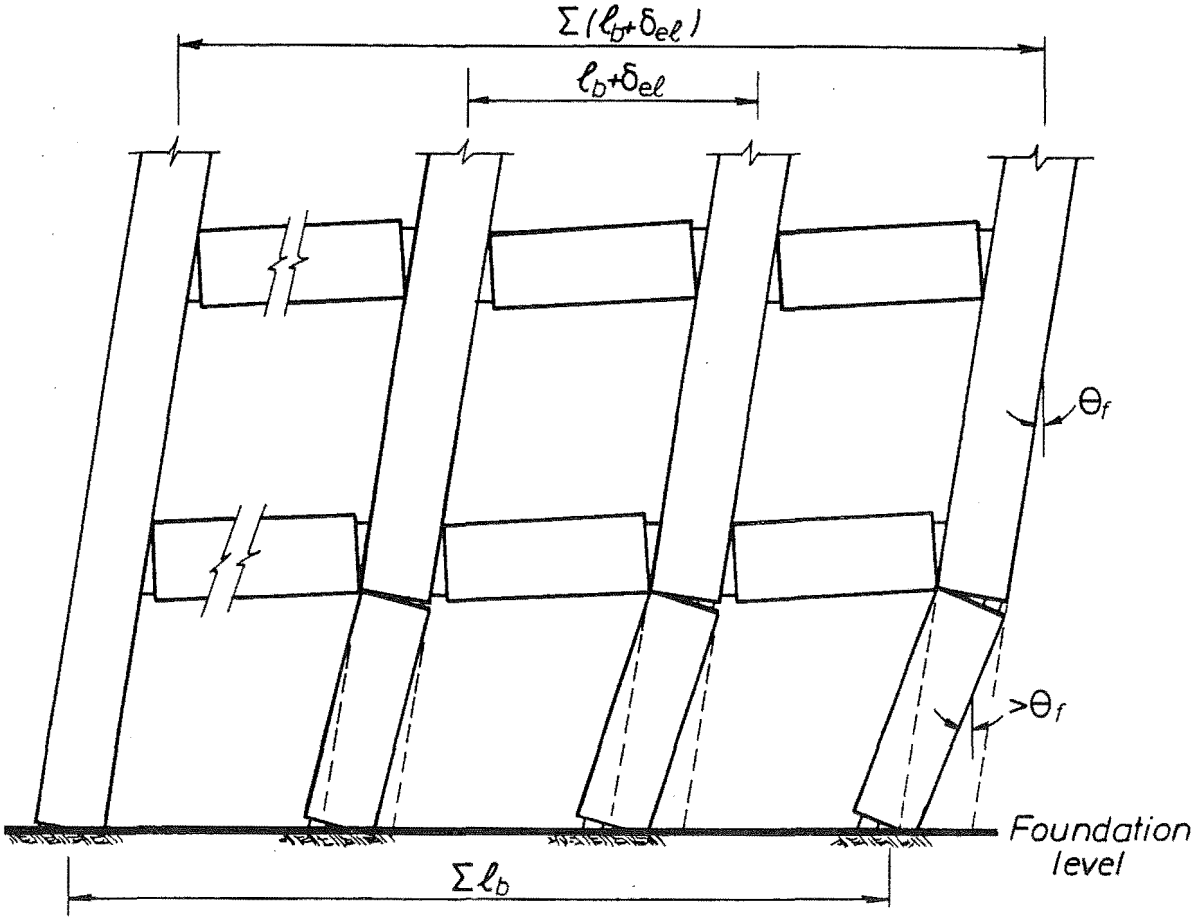

Fig. 7.27 - Effects of Beam Elongation at the Lower Floor Level of a Multi-Bay Frame.

of positive to negative beam moments is unequal. So far there has been very limited testing using this alternative.

The current computer software that is commonly in use for structural analysis of frames does not account for this second order effect. It appears to be appropriate to develop some computer programs that address this effect. An initial step could be the development of a program based on an incremental approach up to the formation of the complete collapse mechanism and where the enhancement of strength caused by the induced axial force in the beams and the probable column hinging at the beam face in the first level could be considered. A model to account for the beam elongation to be used in a time-history analysis is currently under development at Auckland University [Lowe and Fenwick (1992)].

7.5 CONCLUSIONS

The conclusions of this chapter concerning the theoretical background for the design of connections between precast concrete members of moment resisting frames designed for earthquake resistance are:

1. Analytical results and experimental evidence indicate that the tension shift of d implicitly adopted in the New Zealand Concrete Design Code for the curtailment of the beams or walls longitudinal reinforcement is too conservative and could be relaxed. A value of 0.65d is suggested as a more realistic figure.

2. A series of recommendations for the design of midspan connections of precast concrete beams of perimeter frames has been presented. In the derivation of the equations it was assumed that the point of contraflexure coincides with the midspan of the beam. Truss models in combination with the shear friction concept were extensively used. Truss models may be used to derive equations for connections located in a region in the beam span other than at the point of contraflexure.

3. A different approach to the mechanisms of bond resistance of beam longitudinal bars passing through interior beam-column joints is postulated. The model proposed is based on the assumption that there are two bond mechanisms. Data gathered from the experimental programme as well as from test results presented by other researches in New Zealand was used to calibrate the model. Results obtained using the model indicate that, compared with other proposals, smaller values for the ratio h_c/d_b can be used in the presence of axial load or higher concrete strength. The model has also been calibrated to obtain the maximum beam bar diameter permitted in interior beam-column joints of frames designed for limited ductility. The equations so derived are limited to values of $f'_c \leq 55MPa$ and $P_u \leq 0.5A_g f'_c$.

4. An alternative proposal for the design of interior beam-column joints is presented. A new model is suggested that is a modified version of the conventional concrete strut and parallel truss model. The alternative model recognizes that the angle of the compression field can vary according to the amount of horizontal transverse steel provided in the joint region. The alternative model also recognizes that the amount of horizontal transverse reinforcement in the joint panel may be controlled either by the shear forces from bond in the beam bars or by the need to delay early yielding of the hoops, which may cause a premature diagonal compression failure.

5. It is shown that the cumulative elongation of the beams during loading reversal can be large and that this effect can be of important one to both structural and non-structural elements. The effects of beam elongation are not considered in the current office design analytical tools that model members as one-dimensional elements. The beam elongation can be predicted with reasonable accuracy. Available test results show that the slab is unable to provide any significant restraint against beam elongation.

6. A first step towards the understanding of the effects of beam elongation could be the development or adaptation of a computer program that is able to analyze a frame using an incremental load procedure until a collapse mechanism forms. This analysis should consider

the beam growth and the enhancement of strength caused by the induced axial force in the beams and the probable column hinging at the beam face in the first level. This work could be utilized to establish whether the current recommendations of the capacity design procedure need to be modified to allow for this effect. It is expected that the worst conditions will occur in the first storey of columns of multi-bay perimeter frames.

CHAPTER 8

SUMMARY, CONCLUSIONS AND RECOMMENDATIONS

8.1 GENERAL

A study on the seismic behaviour of connections between precast concrete members of moment resisting frames has been conducted in this investigation. The study concentrated on the behaviour of connections at the midspan of beams and at beam-column joints of typical of perimeter frames since data gathered from different consulting engineering firms indicated that this structural solution is widely used in New Zealand in the design of buildings from 9 to 21 storeys high.

The experimental programme comprised the testing of six subassemblages and the repair and retesting of one subassemblage. All units were built with rather smooth construction joints to represent the worst condition found in practice. The dimensions of the test components were almost to full scale. A quasi-static cyclic loading regime with increasing displacements in the inelastic range up to failure was chosen to simulate a severe seismic event.

Further research was undertaken in this study to investigate the cyclic stress-strain behaviour of the two current grades of New Zealand manufactured reinforcing steel.

The main conclusions and recommendations are presented in the remainder of this chapter.

8.2 EXPERIMENTAL EVIDENCE ON THE SEISMIC BEHAVIOUR OF PRECAST CONCRETE MEMBERS OF PERIMETER FRAMES

8.2.1 Tests on Precast Concrete Beams Connected at the Beam Midspan

Four H-shaped precast concrete units were connected in a cast in place joint at the midspan of the beam where during lateral loading the point of contraflexure is expected to occur. They represent the type of connections normally utilized when using Systems 2 or 3 of precast concrete construction in New Zealand (see Section 1.4.1). The beam clear span to overall depth ratio of 3 was deliberately chosen as the smaller value that could normally be used in practice.

Three of the test units, Units 1 to 3, were conventionally reinforced and had different connection details. Another point of interest was the proximity of the connection to the critical region in the beam at the column faces. Unit 1 was connected using 180° hooks with transverse rods in contact with the concave side of the hooks. Unit 2 was spliced using U-shaped "drop in" bars and had transverse rods in contact with the concave side of the hooks. Unit 3 was connected at midspan by non-

contact straight lap splices. The amount of longitudinal reinforcement in the beams was such so as to induce a shear force at the flexural overstrength about equal to the maximum permitted by the New Zealand Concrete Design Code [NZS 3101 (1982)] of $V^o = 0.3\sqrt{f'_c}\,bd$ if diagonal reinforcement in the beams is to be avoided.

The overall behaviour of the conventionally reinforced Units 1 to 3 during quasi-static cyclic lateral loading was very satisfactory. All test units showed an available displacement ductility factor of at least 6. The hysteresis loops were severely pinched, as expected due to the influence of the low aspect ratio and moderate shear, but the flexural strength was maintained to levels of drift beyond 2%. During the load tests the midspan connections displayed an excellent performance, even though the splices were located commencing closer than 2d from the critical region from the faces of the columns. It is recommended that splices can commence at a distance of one effective depth from the critical region.

The beam of the other unit, Unit 4, had beams with strong end regions to relocate the plastic hinges away from the column faces. All inelastic deformations were expected to concentrate at the midspan of the beam where the diagonal reinforcement had been detailed. The connection detail at the beam midspan had the diagonal reinforcing bars mig-welded to mild steel plates, which were interconnected using a sandwich plate and high strength friction grip bolts. Three quarters of the beam diagonal bars were artificially strain aged to check this effect since the bend of the bars was located in the critical region of the beam.

The test of Unit 4 showed only a limited ductile response. This unexpected result was caused by three-dimensional effects originated by the lay-out of the reinforcement in the strong end regions. Splitting of the concrete between the diagonal reinforcement and the additional reinforcement in the critical region at the bend of the diagonal reinforcement as well as the high bearing stresses in the concrete in contact with the diagonal bars were the main causes for the limited ductile performance. These effects were not considered in the initial design. The unit when repaired and retested unit showed that a full ductile behaviour is attainable providing that the three-dimensional effects are considered and a crushing failure in the concrete in contact with the bend of the diagonal bars is avoided. The connection detail at the beam midspan showed a satisfactory performance in both tests. The strain ageing of the diagonal bars did not result in any adverse effects. However, it cannot be concluded that this phenomena might not be critical since strain age embrittlement is very susceptible to low temperature values and the temperature during the tests was about 17°C.

8.2.2 Tests on Precast Concrete Subassemblages Connected at the Beam-Column Joint Region

Two cruciform precast concrete subassemblages, Units 5 and 6, connected at the beam-column joint region were tested as part of the experimental programme.

Unit 5 was typical of a precast concrete method of construction used in New Zealand, System 1 (see Section 1.4.1), where the lower part of the beams is precast and the bottom longitudinal bars protrude from the beams and are anchored in the core of the beam-column joint. The main points

of interest in this type of construction were the influence of the cold joints and the effect of anchoring the bottom beam bars in the core of the beam-column joint, a practice which is not currently allowed by the New Zealand Concrete Design Code.

This unit displayed a satisfactory ductile behaviour. At the end of the test on Unit 5 bond failure of the top beam bars had occurred. These bars had commenced to slip through the beam-column joint at an early stage during the test. The bar diameter of these bars complied with the current New Zealand code recommendations and it is believed that the main cause for the slipping was the "top bar" effect along with the poor quality of the fresh concrete cast.

The construction joints did not adversely affect the behaviour of the unit. Sliding along the vertical construction joints was not observed. This was because the beams were seated on the column cover. A recommendation regarding the minimum width of seating has been given in this study, if shear keys are to be avoided in this region.

The anchorage of the hooked bottom bars, which protruded from the beams into the joint core, had no adverse effect on the performance of the beam-column joint. It is recommended that the New Zealand Concrete Design Code should allow this type of detailing. The existing provisions for anchoring beam longitudinal bars in exterior beam-column joints can be applied for anchoring hooked bars in interior beam-column joints.

Unit 6 was a typical sub-component of System 2 (see Section 1.4.1). The precast member included the beam and the beam-column joint. The longitudinal bars protruding from the lower column passed through preformed vertical holes in the precast concrete member. The joint between the lower part of the precast beam element and the column concrete, and the column bars passing through the preformed holes were grouted in one operation. The principal points of interest were the effects of the grout on the bond of the column bars and the effects of the construction joints.

This study also evaluated the properties of different commercial and self-mixed low viscosity grouts. All grouts showed significant segregation when fed by gravity through a hose. It is suggested that several other alternatives for grouting the preformed holes in this system be evaluated.

Unit 6 displayed excellent overall behaviour during testing. The cold joints and anchorage details had no adverse effects on the performance of the subassemblage. The existing recommendation [Charleson (1991)] of using a grout with a compressive strength of at least 10MPa larger than the concrete compressive strength of the precast concrete member being grouted was satisfactory adequate.

8.2.3 Differences between Monolithic and Precast Concrete Subassemblages

The measurements taken in the experimental programme showed that in that neither the construction joints, nor the connecting details used, had an important influence in the elastic or post-elastic response of the test units. Hence, it is recommended that the precast concrete systems tested can be analyzed as conventional monolithic systems.

8.2.4 Evaluation of the Initial Stiffness

In all tests the measured stiffness of the units was substantially smaller than that predicted using a conventional analysis that took into account only half of the gross section properties to allow for cracking and considered only shear and flexural deformations in the beams and the columns. The large differences observed were mainly due to the "fixed-end rotation" in the beams and the columns at the joint faces. The fixed-end rotation is caused by strain penetration of the longitudinal bars anchored in the joint. This source of flexibility accounted for 20% to 35% of the total elastic displacements in the test subassemblages. Another important source of flexibility was caused by the curvature in the members being affected by the tension shift in the reinforcement (curvature shift). Deformations caused by shear in the beam-column joint panel and in the beams and columns were smaller than initially estimated. In Unit 4 the main source of difference in stiffness was the curvature shift in the beam strong ends.

8.2.5 Beam Elongation

The elongation of the beams which occurred during testing concentrated in the plastic hinge regions. Initially and under monotonic loading some lengthening of the beams can be expected, and was predicted, because of the offset of the neutral axis depth and the mid-depth of the beam. During cyclic load conditions the beam elongation tends to be cumulative because, for conventionally reinforced beams, top and/or bottom reinforcement that yields in tension does not yield back in compression to zero strain when the loading is reversed.

The elongations of the beams tested was quite significant. A maximum elongation of 45mm was recorded in the test on Unit 6.

8.2.6 Influence of the Aspect Ratio of the Beams on the Seismic Performance

The deformations in the final stages of all tests, except for the test on Unit 5, were governed by shear displacements in the plastic hinge regions. Shear deformations led to pinching of the hysteresis loops and a reduction in the energy dissipated. From the test results it can be concluded that symmetrically reinforced beams with a clear span/overall smaller than 4.5 display a pinched hysteretic performance at large displacement ductility values even if the nominal shear stresses are as low as $0.2\sqrt{f'_c}$. The main factor determining this behaviour is the aspect ratio of the member.

8.2.7 The Effects of Short Extension Lengths of the Hooks

An extension of only $8d_b$ was provided to the hooks of the main reinforcement in all units instead of an extension of $12d_b$ recommended by the Concrete Design Code. No adverse effects due to the contravention of this requirement were observed in the test and consequently it is suggested that the extension need not exceed $8d_b$.

8.3 ANALYTICAL CONSIDERATIONS FOR THE DESIGN OF CONNECTIONS BETWEEN PRECAST CONCRETE MEMBERS

An evaluation of the "tension shift" effect shows that the current New Zealand code provisions are unduly conservative and a relaxation for the curtailment rules for the longitudinal reinforcement in walls and beams is possible. For the current design criteria for transverse reinforcement in these elements, it can be demonstrated that a conservative design envelope is still attained when the "tension shift" is reduced from 1.0d to 0.65d.

Truss models and the shear friction concept were effectively used in the development of the design recommendations given in this study.

The recommendations presented for the design of connections at the midspan of beams are only applicable if the connection detail coincides with the point of contraflexure, as it often the case for precast concrete beams of perimeter frames.

The derivation for an alternative approach for the design of interior beam-column joints was also undertaken. This approach is based on a postulate of the bond mechanisms acting on the longitudinal bars passing through the joint region. It was found that the amount of horizontal reinforcement in joints with high shear stresses can be controlled by the need to suppress a premature diagonal compression failure due to excessive yielding of the reinforcement.

8.4 STRESS-STRAIN BEHAVIOUR OF NEW ZEALAND MANUFACTURED REINFORCING STEEL

An experimental programme aimed at studying the influence of different variables on the stress-strain behaviour of New Zealand manufactured reinforcing steel, namely Grade 300 steel and Grade 430 steel, was undertaken in this study. The research was jointly proposed, designed, and carried out by Dr. L. Dodd, a Ph.D graduate, and the author. This chapter is therefore included in Dr. Dodd's Ph.D. thesis (1992).

Approximately 120 test coupons were axially loaded under various conditions. The main variables studied were:

a) The cyclic stress-strain behaviour during various loading histories.

b) The strain rate effects.

c) The strain ageing effects.

d) The effects of bar deformations.

It was found that the stress-strain behaviour of reinforcing steel in the tension and compression regions is identical only if compared using in the true stress-natural strain coordinate system. This is an old finding that has been overlooked in most analytical models.

The shape of the Bauschinger curve is independent of the monotonic stress-strain curve and it is affected by the carbon content of the steel.

The strain rate has a significant effect on the stress-strain behaviour of the steel in the yield plateau region. In the strain hardening region this difference is not so significant. The effect on strain rate is greater for Grade 300 steel than for Grade 430 steel.

The strain ageing effects are not significant for New Zealand manufactured Grade 430 steel because of the presence of vanadium. For Grade 300 steel, the strain ageing effects can be significant in the strain range beyond the yield plateau region where a recovery in stiffness and increase in strength was observed. In the yield plateau region, Grade 300 steel displayed only a recovery in the initial stiffness. It is suggested that the implications of strain ageing should be considered in post-earthquake repair work.

Buckling of longitudinal reinforcing steel can lead to premature fracture due to extremely large local compression strains at the roots of the deformations that cause crack initiation. These cracks may propagate as the bar is straightened when axially tensioned. It is important to consider this phenomenon when using energy or damage models for reinforcing steel.

The cyclic stress-strain behaviour of reinforcing steel of the machined coupons tested under quasi-static conditions was used to calibrate an analytical model based on the recorded data in the true stress-natural strain coordinate system. A computer program, STEEL, was written in Fortran language and is included in Appendix A.

8.5 SUGGESTIONS FOR FUTURE RESEARCH

8.5.1 Tests on Connections between Precast Concrete Beams

It could be valuable to provide information on the seismic behaviour of connections between precast concrete beams joined in a cast in place joint in a region other than at the beam ends and at the point of contraflexure. This information is relevant for the use of precast concrete systems of gravity dominated frames where the connections are required to transfer forces originated by shear and bending.

8.5.2 Beam Elongation

The effects of beam elongation are not considered in the current office design analytical tools that model members as one-dimensional elements. A review of the existing literature has shown that

the phenomena of beam elongation needs to be considered in design. Also, the available results show that the slab is unable to provide any significant restraint against beam elongation.

A first step towards the understanding of the effects of beam elongation could be the development or adaptation of a computer program that is able to analyze a frame using an incremental load procedure until a collapse mechanism forms. This analysis should consider the beam growth and the enhancement of strength caused by the induced axial force in the beams and the probable column hinging at the beam face in the first level. This work could be utilized to establish whether the current recommendations of the capacity design procedure need to be modified to allow for this effect. It is expected that the worst conditions will occur in the first storey of columns of multi-bay perimeter frames.

Experimental work is also required to provide evidence on the possible effects of beam elongation. Tests on multi-bay frames are required to observe the behaviour of the first storey of columns. Besides, more information needs to be given to architects and designers on the effects that the beam elongation might have on the cladding and glazing systems, as well as on the seating and support detailing necessary for precast concrete slab floor systems.

The use of beams with vertically distributed longitudinal reinforcement is a possible solution to reduce the amount of elongation expected to occur in a conventionally reinforced frame. This type of construction offers several other advantages, such as the use of smaller diameter bars of Grade 430 steel passing through the beam-column joint region. It is likely that this system may perform much better in transferring high shear forces in the plastic hinges.

8.5.3 Bond Mechanisms Acting on the Beam Bars on the Beam-Column Joint

Equations which could be used to derive the maximum bar diameter permitted to pass through an interior beam-column joint were calibrated using the existing data. However, there is a lack of information regarding joints subjected to high axial compressive load and joints constructed using high strength concrete.

8.5.4 Evaluation of the Stiffness of Reinforced Concrete Frames

There is extensive literature showing that the current recommendations for calculating the initial "elastic" stiffness of frame components are not sufficiently accurate. The current methods lead to higher design lateral forces because the larger calculated stiffness. Also, the interstorey drifts may actually be much larger than currently estimated.

Analytical work could be conducted to provide simple design recommendations that allows for the effects of fixed-end rotation in beams and columns, for the curvature shift and for the shear deformations in beams, columns and beam-column joints.

8.5.5 Reinforcing Steel

The critical radius of buckling at which the "compression" cracks in deformed bars propagate and cause fracture may be defined in terms of the bar diameter and perhaps the stress-strain history. It is recommended that experimental and analytical work be conducted to endeavour to determine if such a critical buckling radius does exist, and if so, how it can be defined in simple terms.

The existing stress-strain model for reinforcing steel presented in this study can be complemented by adding a subroutine that accounts for the possible buckling in the reinforcing steel under the different boundary conditions provided by the transverse reinforcement in a column.

8.5.6 Experimental Techniques

Alternative experimental techniques to enable the accurate measurement of the inelastic strains in the bars passing through a beam-column joint need to be investigated. These measurements are often hampered by debonding of the strain gauges at moderate levels of strain (1 to 2%) or by local and global bar slipping that causes the break down of the wire connection. One proposed alternative is to split the bar to be instrumented and place spot high elongation strain gages along the diameter of one half bar. The other half bar could have a slot to channel the wires out and could be epoxied to the instrumented half bar.

REFERENCES

"Armenia Earthquake Reconnaissance Report", (1989), Earthquake Spectra, Special Publication, 175 pp.

ACI Committee 439, (1969), "Effect of Steel Strength and of Reinforcement Ratio on the Mode of Failure and Strain Energy Capacity of Reinforced Concrete Beams", ACI Journal, Proceedings Vol. 66, No. 3, pp. 165-173.

ACI Committee 318, (1989), "Building Requirements for Reinforced Concrete (ACI 318-89) and Commentary", American Concrete Institute, Detroit, 353 pp.

Aktan, A.E., Karlsson, B.I. and Sozen, M.A., (1973), "Stress-Strain Relationships of Reinforcing Bars Subjected to Large Strain Reversals", Civil Engineering Studies, Structural Research Series No. 397, University of Illinois at Urbana-Champaign, Urbana, Illinois, 47 pp.

Andriono, T. and Park, R., (1987), "Seismic Design Considerations of the Properties of New Zealand Manufactured Steel Reinforcing Bars", Proceedings of the Pacific Conference on Earthquake Engineering, Wairakei, New Zealand, Vol. 1, pp. 13-24.

Arnold, C., (1991), "The Seismic Response of Nonstructural Elements in Buildings", Proceedings, Pacific Conference on Earthquake Engineering, Auckland, Vol. 1, pp. 335-350.

ASTM, (1972), "1972 Annual Book of ASTM Standards", Part 4, Philadelphia, 803 pp.
(Standards A615-68, A616-68 and A616-68).

ASTM E8M - 90a, (1991), "Standard Test Methods for Tension Testing of Metallic Materials [Metric]", 1991 Annual Book of ASTM Standards, Vol. 1.02, Philadelphia, pp. 535-549.

ASTM Standard C939-87, (1988), "Standard Test Method for Flow of Grout for Preplaced-Aggregate Concrete (Flow Cone Method)", 1988 Annual Book of ASTM Standards, Vol. 04.02, Philadelphia, pp. 457-460.

Bate, P.S. and Wilson, D.V., (1986), "Reversibility in the Work Hardening of Spheroidised Steels", Acta Metallurgica, Vol. 34, No. 6, pp. 1107-1120.

Bauschinger, J., (1886), "On the Change of Elastic Limit and Strength of Iron and Steel, by Drawing Out, by Heating and Cooling, and by Repetition of Loading", (Sumarised translation from

"Mittheilungen aus dem Mechanischen Technischen Laboratorium der k. Hochschule in München"), Minutes of Proceedings of the Institution of Civil Engineers, London, Vol. LXXXVII, pp. 463-465.

Bauschinger J., (1887), "Variations in the Elastic Limit of Iron and Steel", (Sumarised translation from "Mittheilungen aus dem Mechanischen Technischen Laboratorium der k. Hochschule in München"), The Journal of the Iron and Steel Institute, No 1, pp. 442-444.

Beattie, G., (1989), "Recent Testing of Precast Structural Components at Central Laboratories", Proceedings, Silver Jubilee Conference of the New Zealand Concrete Society, Conference Technical Papers TR9, Wairakei, pp. 111-118.

Beckingsale, C.W., Park, R. and Paulay, T., (1980), "Post Elastic Behaviour of Reinforced Concrete Beam-Column Joints", Research Report 80-20, Department of Civil Engineering, University of Canterbury, Christchurch, 359 pp.

Beekhuis W.J., (1971), "An Experimental Study of Squat Shear Walls", M.E. Thesis, Department of Civil Engineering, University of Canterbury, Christchurch, 132 pp.

Berg, G.V. and Stratta, J.L., (1964), "Anchorage and the Alaska Earthquake of March 27, 1964", American Iron and Steel Institute, 63 pp.

Bernstein, M.L. and Zaimovski, V.A., (1983), "Mechanical Properties of Metals", Mir Publishers, Moscow, 413 pp.

Bertero, V.V., (1988), "Ductility Based Structural Design", State of the Art Report in Special Theme Session SG-R2, Proceedings, Ninth World Conference on Earthquake Engineering, Tokyo-Kyoto, Vol. VIII, pp. 673-683.

Bhatt, P. and Kirk, D.W., (1985), "Tests on an Improved Beam-Column Connection for Precast Concrete", ACI Journal, Vol. 82, No. 6, pp. 834-843.

Binney, J.R., (1972), "Diagonally Reinforced Coupling Beams", M.E. Thesis, Department of Civil Engineering, University of Canterbury, Christchurch, 131 pp.

Birss, G.R., Paulay, T. and Park, R., (1978), "The Elastic Behaviour of Earthquake Resistant Reinforced Concrete Interior Beam-Column Joints", Research Report 78-13, Department of Civil Engineering, University of Canterbury, Christchurch, 96 pp.

Blakeley, R.W.C., Megget, L.M., Priestley, M.J.N. and Wood, J.H., (1979), "Cyclic Loading Testing of Two Refined Reinforced Concrete Joints", Bulletin of the New Zealand National Society for Earthquake Engineering, Vol. 12, No. 3, pp. 238-255.

BSI 4449, (1988), "British Standard Specification for Carbon Steel Bars for the Reinforcement of Concrete", British Standard Institution, 13 pp.

Buchanan, A.H., (1979), "Diagonal Beam Reinforcing for Ductile Frames", Bulletin of the New Zealand National Society for Earthquake Engineering, Vol. 12, No. 4, pp. 346-356.

Bull, I.N., (1978), "The Shear Strength of Relocated Plastic Hinges", Research Report 78-11, Department of Civil Engineering, University of Canterbury, Christchurch, 104 p.

Burns, N.H. and Siess, C.P., (1962), "Load-Deformation Characteristics of Beam-Column Connections in Reinforced Concrete", Civil Engineering Studies, Structural Research Series No. 234, University of Illinois, Urbana, Illinois, 261 pp.

Bychenkov, Y., (1978), "Aseismic Structures with Precast Members", Proceedings, FIP 8th Congress, London, pp. 70-90.

Celebi, M. and Penzien, J., (1973), "Experimental Investigation into the Seismic Behaviour of Critical Regions of Reinforced Concrete Components as Influenced by Moment and Shear", Research Report EERC 73-4, Earthquake Engineering Research Center, University of California, Richmond, 185 pp.

Chai, Y.H., Priestley, M.J.N., and Seible, F., (1991), "Seismic Retrofit of Circular Bridge Columns for Enhanced Flexural Resistance", ACI Structural Journal, Vol. 88, No. 5, pp. 572-584.

Charleson, A.W., (editor), (1991), "Guidelines for the Use of Structural Precast Concrete in Buildings", Report of a Study Group of the New Zealand Concrete Society and the New Zealand National Society for Earthquake Engineering, The Printery, University of Canterbury, Christchurch, pp. 174.

Cheung, P.C., Paulay, T. and Park, R., (1991), "Seismic Design of Reinforced Concrete Beam-Column Joints with Floor Slabs", Research Report 91-4, Department of Civil Engineering, University of Canterbury, Christchurch, 328 pp.

Cheung, P.C., Paulay, T. and Park, R., (1991a), "Some Possible Revisions to the Seismic Provisions of the New Zealand Concrete Design Code for Moment Resisting Frames", Proceedings, Pacific Conference on Earthquake Engineering, Auckland, Vol. 2, pp. 79-90.

Coffin, L.F. Jr., (1969), "Introduction", Manual on Low Cycle Fatigue Testing, ASTM STP 465, American Society for Testing Materials, pp. vii-ix.

Collins, M. and Mitchel, D., (1991), "Prestressed Concrete Structures", Prentice Hall, Englewood Clifs, New Jersey, 766 pp.

Comité Euro-International du Béton, (1988), "Concrete Structures Under Impact and Impulsive Loading", Bulletin D'Information No 187, Lausanne.

Comité Euro-International du Béton, (1983), "Response of R.C. Critical Regions Under Large Amplitude Reversed Actions", Bulletin D'Information No. 161, Lausanne, 306 pp.

Constantinescu, D., (1985), "Representative Example of Romania, 9 Storey Framed Structures with Precast Elements", Design and Construction of Prefabricated Reinforced Concrete Systems, United Nations Industrial Development Organization, Vienna, Vol. 2, pp. 199-228.

Cottrell, A.H. and Bilby, B.A., (1949), "Dislocation Theory of Yielding and Strain Ageing of Iron", The Proceedings of the Physical Society, Section A, V. 62, Part 1, No 349 A, pp. 49-61.

Dai R. and Park, R., (1987), "A Comparison of the Behaviour of Reinforced Concrete Beam-Column Joints Designed for Ductility and Limited Ductility", Research Report 87-4, Department of Civil Engineering, University of Canterbury, Christchurch, 65 pp.

Davis, E.A., (1938), "The Effect of Speed of Stretching and the Rate of Loading on the Yielding of Mild Steel", Journal of Applied Mechanics, Vol. 5, No.4, pp. A137-A140.

Dodd, L., (1992), "The Dynamic Behaviour of Reinforced-Concrete Bridge Piers Subjected to New Zealand Seismicity", Ph.D. Thesis, Department of Civil Engineering, University of Canterbury, Christchurch, 460 pp.

Eligehausen, R., Popov, E.P. and Bertero, V.V., (1983), "Local Bond-Stress-Slip Relationships of Deformed Bars Under Generalized Excitation", Report No. EERC 83-23, Earthquake Engineering Research Center, University of California, Berkeley, 178 pp.

Englekirk, R.E., (1979), "Development of a Precast Concrete Ductile Frame", PCI Journal, Vol. 24, No. 6, pp. 46-65.

Englekirk, R.E., (1989), "An Analytical Approach to Establishing the Seismic Resistance Available in Precast Concrete Frame Structures", PCI Journal, Vol. 31, No 1, pp. 92-101.

Erasmus, L.A., (1978), "Safe Bend Radii for Deformed Reinforcing Bar to Avoid Failure by Strain Age Embrittlement", New Zealand Engineering, Vol. 33, No. 8, pp. 170-177.

Erasmus, L.A., (1981), "Cold Straightening of Partially Embedded Reinforcing Bars - A Different View", Concrete International, American Concrete Institute, Vol. 3, No. 6, pp. 47-52.

Erasmus, L.A., (1987), "Strain Ageing in Carbon/Manganese Steels - The Interdependence of Nitrogen, Manganese and Grain Size", Proceedings of the 1987 Australasian Conference on Materials for Industrial Development, Christchurch, pp. 145-149.

Erasmus, L.A. and Pussegoda, N., (1977), "Strain Age Embrittlement of Reinforcing Steels", New Zealand Engineering, Vol. 32, No 8, pp. 178-183.

Fahy, F.W. et al, (1980), "Engineering Metallurgy", 2nd edition, University of Canterbury, Christchurch, 353 pp.

Fattal, S.G., (1977), "Observations on the Behaviour of Buildings in the Romania Earthquake of March 4, 1977", National Bureau of Standards, Washington D.C., 160 pp.

Fenwick, R.C. and Fong, A., (1979), "The Behaviour of Reinforced Concrete Beams under Cyclic Loading", Bulletin of the New Zealand National Society for Earthquake Engineering, Vol. 12, No. 2, pp. 158-167.

Fenwick, R.C. and Nguyen, H.T., (1981), "Reinforced Concrete Beam-Column Joints for Seismic Loading", Research Report No. 220, Department of Civil Engineering, University of Auckland, 62 pp.

Fenwick, R.C., Tankut, A.T. and Thom, C.W., (1981), "The Deformation of Reinforced Concrete Beams Subjected to Inelastic Cyclic Loading - Experimental Results", Report No. 268, School of Engineering, Department of Civil Engineering, University of Auckland, 72 pp.

Fenwick, R.C. and Thom, C.W., (1982), "Shear Deformation in Reinforced Concrete Beams Subjected to Inelastic Cyclic Loading", Report No. 279, Department of Civil Engineering, University of Auckland, Auckland, 51 pp.

French, C.W., Amu, O. and Tarzikhan, C., (1989), "Connections between Precast Elements - Failure Outside Connection Region", Journal of Structural Engineering, ASCE, Vol. 115, No. 2, pp. 316-340.

French, C.W., Hafner, M. and Jayashankar, V., (1989), "Connections between Precast Elements - Failure within Connection Region", Journal of Structural Engineering, ASCE, Vol. 115, No. 12, pp. 3171-3192.

"Guidelines for the Use of Structural Precast Concrete in Buildings", (1991), Report of a Study Group of the New Zealand Concrete Society and the New Zealand National Society for Earthquake Engineering, The Printery, University of Canterbury, Christchurch, 174 pp.

Hirashi, H., (1984), "Evaluation of Shear and Flexural Deformations of Flexural Type of Shear Walls", Bulletin of the New Zealand National Society for Earthquake Engineering, Vol. 17, No. 2, pp. 135-144.

Hollings, J.P., (1969), "Reinforced Concrete Seismic Design", Bulletin of the New Zealand National Society for Earthquake Engineering, Vol. 2, No. 3, pp. 217-250.

Hollings, J.P., (1969a), "A Reinforced Concrete Building in Wellington", Bulletin of the New Zealand National Society for Earthquake Engineering, Vol. 2, No. 4, pp. 420-442.

Housner, G.W., (1956), "Limit Design of Structures to Resist Earthquakes", Proceedings, World Conference on Earthquake Engineering, Berkeley, Vol. 5, pp. 1-11. (Also reprinted in "Selected

Earthquake Engineering Papers of George W. Housner", (1990), Civil Engineering Classics, ASCE, New York, pp. 186-198).

Housner, G.W., (1959), "Behavior of Structures During Earthquakes", Journal of Engineering Mechanics Division, ASCE, EM4, pp. 109-129. (Also reprinted in "Selected Earthquake Engineering Papers of George W. Housner", (1990), Civil Engineering Classics, ASCE, New York,pp. 283-303).

Hundy, B.B., (1954), "The Accelerated Ageing of Mild Steel", Journal of the Iron and Steel Institute, Vol. 178, No. 9, pp. 34-38.

Hutchison, D.L., Andrews, A.L., Butcher, G.W. and Kolston, D., (1986), "Draft Revision of NZS 4203:1984: Seismic Provisions", Bulletin of the New Zealand National Society for Earthquake Engineering, Vol. 19, No. 3, pp. 158-166.

Jago, R.A., (1987), Editorial, Materials Forum, Vol. 10, No. 1, 1st. Quarter, 1987, p. 3.

Kanoh, Y., (1986), "Review of the Japanese Concrete Systems used as Building Structures", Seminar on Precast Concrete Construction on Seismic Zones, Japan Society for the Promotion of Science - United States National Science Foundation, Vol. 2, pp. 35-54.

Kato, B., (1979), "Mechanical Properties of Steel Under Load Cycles Idealizing Seismic Actions", Comité Euro-International du Béton, Bulletin D'Information 131, Paris, pp. 7-27.

Kent, D.C., (1969), "Inelastic Behaviour of Reinforced Concrete Members with Cyclic Loading", PhD Thesis, Department of Civil Engineering, University of Canterbury, Christchurch.

Kent, D.C. and Park, R., (1973), "Cyclic Load Behaviour of Reinforcing Steel", Strain, Vol. 9, No. 3, pp. 98-128.

Leslie, P.D., (1974), "Ductility of Reinforced Concrete Bridge Piers", M.E. Report, Department of Civil Engineering, University of Canterbury, Christchurch, 147 pp.

Lowe, P.G. and Fenwick, R.C., (1992), "Current Concrete Related Research Projects at Auckland University", Conference Technical Papers (TR 13), Concrete'92, New Zealand Concrete Society, Wairakei, pp. 9-11.

Lum, Y., (1981), "Precast Concrete Construction in Zones 1 and 2", Proceedings, Workshop on Design of Prefabricated Concrete Buildings for Earthquake Loads, ATC-8, Applied Technology Council Berkeley, pp. 203-224.

Ma, S., Bertero, V.V. and Popov, E.P., (1976), "Experimental and Analytical Studies on the Hysteretic Behaviour of Reinforced Concrete Rectangular and T-Beams", Report No. EERC 76-2, Earthquake Engineering Research Center, University of California, Berkeley, 241 pp.

Mahin, S.A. and Bertero, V.V., (1972), "Rate of Loading Effects on Uncracked and Repaired Reinforced Concrete Members", Report No. EERC 72-9, Earthquake Engineering Research Center, University of California, Berkeley, 148 pp.

Mahin, S.A. and Bertero, V.V., (1976), "Problems in Establishing and Predicting Ductility in Aseismic Design", Proceedings, International Symposium on Earthquake Structural Engineering, St Louis, Missouri, Vol. I, pp. 613-627.

Mander J.B., Priestley, M.J.N. and Park, R., (1984), "Seismic Design of Bridge Piers", Research Report 84-2, Department of Civil Engineering, University of Canterbury, 442 pp.

Manjoine, M.J., (1944), "Influence of Rate of Strain and Temperature on Yield Stress of Mild Steel", ASME Transactions, Journal of Applied Mechanics, Vol 11, pp. 211-218.

Martin, L.D. and Korkosz, W.J., (1982), "Connections for Precast Prestressed Buildings Including Earthquake Resistance", Technical Report No. 2, Prestressed Concrete Institute, Chicago, 297 pp.

Megget, L.M. and Fenwick, R.C., (1988), "Seismic Behaviour of a Reinforced Concrete Portal Frame Sustaining Gravity Loads", Proceedings of the Pacific Concrete Conference, Auckland, Vol. 1, pp. 41-42.

Menegotto and Pinto, (1973), "Method of Analysis for Cyclically Loaded R.C. Frames Including Changes in Geometry and Non-Elastic Behaviour of Elements under Combined Normal Force and Bending", Symposium on Resistance and Ultimate Deformability of Structures Acted on by Well Defined Repeated Loads, IABSE Reports, Vol. 13, Lisbon, pp. 15-22.

Milburn, J.R. and Park, R., (1982), "Behaviour of Reinforced Concrete Beam-Column Joints Designed to NZS 3101", Research Report 82-7, Department of Civil Engineering, University of Canterbury, Christchurch, 107 pp.

Mughrabi, H., (1987), "Johann Bauschinger, Pioneer of Modern Materials Testing", Materials Forum, Vol.10, No.1, 1st. Quarter, pp. 5-10.

Nádai, A., (1950), "Theory of Flow and Fracture of Solids", 2nd ed., Vol. 1, McGraw-Hill, New York, 572 pp.

Nielsen, M.P., Braestrup, M.W. and Bach, F., (1978), "Rational Analysis of Shear in Reinforced Concrete Beams", International Association for Bridge and Structural Engineering (IABSE) Proceedings, P-15/78, 16 p.

NZS 3101, (1982), "Code of Practice for the Design of Concrete Structures", Parts 1 and 2, Standards Association of New Zealand, Wellington.

NZS 3402P, (1973), "Rolled Steel Bars for the for the Reinforcement of Concrete", Provisional New Zealand Standard, Standards Association of New Zealand, Wellington, 16 pp.

NZS 3402, (1989), "Steel Bars for the Reinforcement of Concrete", Standards Association of New Zealand, Wellington, 15 pp.

NZS 4203, (1984), "Code of Practice for General Structural Design and Design Loadings for Buildings", Standards Association of New Zealand, Wellington, 100 pp.

NZS 4782, (1982), "Metal-Arc Welding of Grade 275 Reinforcing Bar", Standards Association of New Zealand, Wellington, 23 pp.

O'Grady, C.R., (1988), "Precast Cruciform Columns, H Frames and Precast Concrete Shear Wall", Proceedings, Pacific Concrete Conference, Auckland, Vol. 1, pp. 345-354.

O'Leary, A.J., Monastra, D.P. and Mason, J.E., (1988), "A Precast Concrete Moment Resisting Frame System", Proceedings, Pacific Concrete Conference, Auckland, Vol. 1, pp. 287-298.

Pacific Steel Ltd, (1991), Private Communication.

Park, R., (1988), "Ductility Evaluation from Laboratory and Analytical Testing", State of the Art Report in Special Theme Session SG-R1, Proceedings, Ninth World Conference on Earthquake Engineering, Tokio-Kyoto, Vol. VIII, pp. 605-616.

Park, R., (1989), "Evaluation of Ductility of Structures and Structural Assemblages from Laboratory Testing", Bulletin of the New Zealand National Society for Earthquake Engineering, Vol. 22, No. 3, pp. 155-166.

Park, R., (1990), "Precast Concrete in Seismic-Resisting Building Frames in New Zealand", Concrete International, Vol. 12, No. 11, pp. 43-57.

Park, R. and Paulay, T., (1975), "Reinforced Concrete Structures", John Wiley & Sons, New York, 769 pp.

Park, R. and Bull, D., (1986), "Seismic Resistance of Frames Incorporating Precast-Prestressed Concrete Beam Shells", Journal of the Prestressed Concrete Institute, Vol. 31, No. 4, pp. 54-93.

Park, R. and Dai Ruitong, (1988), "A comparison of the Behaviour of reinforced Concrete Beam-Column Joints Designed for Ductility and Limited Ductility", Bulletin of the New Zealand National Society for Earthquake Engineering, Vol. 21, No. 4, pp. 255-278.

Paulay, T., (1969), "The Coupling of Shear Walls", PhD Thesis, Department of Civil Engineering, University of Canterbury, Christchurch, New Zealand, Vol 1, 220 pp. and Vol. 2, 210 pp.

Paulay, T., (1976), "Moment Redistribution in Continuous Beams of Earthquake Resistant Multistorey Reinforced Concrete Frames", Bulletin of the New Zealand National Society for Earthquake Engineering, Vol. 9, No. 4, pp. 205-212.

Paulay, T., (1978), "A Consideration of P-Delta Effects in Ductile Reinforced Concrete Frames", Bulletin of the New Zealand National Society for Earthquake Engineering, Vol. 11, No. 3, pp. 151-160.

Paulay, T., (1982), "Lap Splices in Earthquake-Resisting Columns", ACI Journal, Vol. 79, No. 6, pp. 459-469.

Paulay, T. and Park, R., (1984), "Joints in Reinforced Concrete Frames Designed for Earthquake Resistance", Research Report 84-9, Department of Civil Engineering, University of Canterbury, Christchurch, 71 pp.

Paulay, T. and Priestley, M.J.N., (1992), "Seismic Design of Reinforced Concrete and Masonry Buildings", John Wiley and Sons, 744 pp.

Pillai, S.U. and Kirk, D.W., (1981), "Ductile Beam-Column Connections in Precast Concrete", ACI Journal, Vol. 78, No. 6, pp. 480-487.

Polakowski, N.H., (1951), "Softening of Metals During Cold-Working", Journal of the Iron and Steel Institute, Vol 169, pp. 337-346.

Poole, R.A. and Clendon, J.E., (1988), "An Efficient Precast Concrete Framed Building", Proceedings, Pacific Concrete Conference, Auckland, Vol. 1, pp. 319-332.

Priestley, M.J.N., (1975), "Testing of Two Reinforced Beam Column Assemblies under Simulated Seismic Loading", Report 5-75/1, Ministry of Works and Development, Central Laboratories, Lower Hutt, 114 pp.

Priestley, M.J.N., (1989), "Research Plans for a Coordinated Study on Precast Seismic Structural Systems (PRESSS)", Report No. SSRP - 89/01, Department of Applied Mechanics and Engineering Sciences, University of California, San Diego, 41 pp.

Priestley, M.J.N., (1991), "Overview of PRESSS Research Program", PCI Journal, Vol. 36, No. 4, pp. 50-57.

Pussegoda, N., (1978), "Strain Age Embrittlement in Reinforcing Steels", PhD Thesis, Department of Mechanical Engineering, University of Canterbury, Christchurch, 172 pp.

Raske, D.T., and Morrow, J., (1969), "Mechanics of Materials in Low Fatigue Testing, Manual on Low Cycle Fatigue Testing", ASTM STP 465, American Society for Testing of Materials, pp. 1-25.

Santos, S.P., (1987), "Research on the Structural Behaviour of the Connections in Precast Concrete Structures", Memória No. 697, Laboratório Nacional de Enghenaria Civil, Lisboa, 21 pp.

Schlaich, J., Schäfer, K., and Jennewein, M., (1987), "Towards a Consistent Design of Reinforced Concrete Structures", PCI Journal, Vol. 32, No. 3, pp. 74-150.

Seckin, M. and Fu, H.C., (1990), "Beam Column Connections in Precast Reinforced Concrete", ACI Structural Journal, Vol. 87, No. 3, pp. 252-261.

"Seminar Report - Use of Precast Concrete in Moment Resisting Frames and Floors Designed for Earthquake Resistance", (1988), New Zealand Concrete Society Newsletter, No. 1, pp. 2-12.

Silvester, D.B. and Dickson, A.R., (1988), "Fanshawe Street Building a Precast Concrete Study", Proceedings, Pacific Concrete Conference, Auckland, Vol. 1, pp. 333-344.

Singh, A., Gerstle, K.H. and Tulin, L.G., (1965), "The Behaviour of Reinforcing Steel Under Reversal Loading", Journal ASTM, Materials Research and Standards, Vol 5. No. 1, pp. 12-17.

Sorensen, S., (1981), "Precast Concrete Construction in Zones 3 and 4", Proceedings, Workshop on Design of Prefabricated Concrete Buildings for Earthquake Loads, ATC-8, Applied Technology Council, Berkeley, pp. 183-201.

Spurr, D.D. and Paulay, T., (1984), "Post-Elastic Behaviour of Reinforced Concrete Frame-Wall Components and Assemblages Subjected to Simulated Seismic Loading", Research Report 84-19, Department of Civil Engineering, University of Canterbury, Christchurch, Oct. 1984, 469 pp.

Stanton, J.F. and McNiven, H.D., (1979), "The Development of a Mathematical Model to Predict the Flexural Response of Reinforced Concrete Beams to Cyclic Loads, using System Identification", Report No. EERC 79-02, University of California, Berkeley, 188 pp.

Stanton, J.F., Anderson, R.G., Dolan, C.W. and McCleary, D.E., (1986), "Moment Resistant Connections and Simple Connections", SIRD Research Report No. 1/4, Prestressed Concrete Institute, Chicago.

Steinbrugge, K.V., (1965), "Structural Engineering Aspects of the Alaskan Earthquake of March 27, 1964", Proceedings, Third World Conference on Earthquake Engineering, Vol. III, Auckland, pp. S-50 - S-72.

Stevens, N.J., Uzumeri, S.M. and Collins, M.P., (1991), "Reinforced Concrete Subjected to Reversed Cyclic Shear-Experiments and Constitutive Model", ACI Structural Journal, Vol. 88, No. 2, pp. 135-146.

Stevenson, R.B. and Beattie, G.J., (1988), "Cyclic Load Testing of a Beam-Cruciform Incorporating Precast Beam Elements", Central Laboratories Report 88-B5204/1, Works and Development Services Corporation (N.Z.) Ltd., Lower Hutt, 61 pp.

Stevenson, R.B. and Beattie, G.J., (1989), "Cyclic Load Testing of a Beam-Column Cruciform Incorporating a Precast Joint Zone and Column Bars Grouted in Drossbach Ducts", Central Laboratories Report 89-B5204/2, Work and Development Services Corporation (N.Z.) Ltd., Lower Hutt, 56 pp.

Tanaka,T. and Park, R., (1990), "Effect of Lateral Confining Reinforcement on the Ductile Behaviour of Reinforced Concrete Columns", Research Report 90-2, Department of Civil Engineering, University of Canterbury, 458 pp.

Tasai, A., Otani, S. and Aoyama, H., (1988), "Resistance of Reinforced Concrete Component Repaired with Epoxy Resin", Journal of the Faculty of Engineering, The University of Tokyo (B), Vol. XXXIX, No. 3, pp. 345-359.

The Department of Research of the Beijing Institute of Architectural Design, (Undated), "Research on Monolithic-Precast Concrete Frames", Beijing, 16 pp.

Thomson, E.D., Carr, A.J. and Moss, P.J., (1991), "P-Delta Effects in the Seismic Response of Ductile Reinforced Concrete Frames", Proceedings, Pacific Conference on Earthquake Engineering, Auckland, Vol. 1, pp. 49-60.

Thompson, K.J. and Park, R., (1975), "Ductility of Concrete Frames under Cyclic Loading", Research Report No. 75-14, Department of Civil Engineering, University of Canterbury, Christchurch, 341 pp.

Thompson, K.J. and Park, R., (1978), "Stress-Strain Model for Grade 275 Reinforcing Steel with Cyclic Loading", Bulletin of the New Zealand National Society for Earthquake Engineering, Vol 11, No. 2, pp. 101-109.

Thürlimann, B., (1979), "Reinforced Concrete Members in Torsion and Shear", International Association for Bridge and Structural Engineering (IABSE) Colloquium, Copenhagen, pp. 119-130.

Tjokrodimuljo, K. and Fenwick, R.C., (1985), "Behaviour of Reinforced Concrete under Cyclic Loading", Report No. 374, Department of Civil Engineering, University of Auckland, 151 pp.

Wilson, D.V. and Bate, P.S., (1987), "Bauschinger Effects in Strain Aged Steels", Materials Forum, Vol. 10, No. 1, pp. 33-42.

Wilson, D.V. and Bate, P.S., (1986), "Reversibility in the Work Hardening of Spheroidised Steels", Acta Metallurgica, Vol. 34, No. 6, pp. 1107-1120.

Wood, B.J., (1988), "A review of New Zealand Reinforced Concrete Building Structures", Proceedings, Pacific Concrete Conference, Auckland, Vol. 3, pp. 815-831.

Yalcin, U., Zerbe, H.E. and Durrani A.J., (1990), "Seismic Resistance of Connections with Beams Restrained against Free Elongation", Proceedings of Fourth U.S. National Conference on Earthquake Engineering", Palm Springs, California, Vol. 2, pp. 737-744.

Yap, K.K., (1986), "Strain Aged Steel in Beam-Column Joints", Central Laboratories Report 5-86/5, Ministry of Works and Development, Lower Hutt, 106 pp.

Yeoh, S.K., (1978), "Prestressed Concrete Beam-Column Joints", M.E. Report, Department of Civil Engineering, University of Canterbury, Christchurch, 71 pp.

Zahn, F.A., Park,R., and Priestley, M.J.N., (1986), "Design of Reinforced Concrete Bridge Columns for Strength and Ductility", Research Report No. 86-7, Department of Civil Engineering, University of Canterbury, Christchurch, 330 pp.

Xin, X.Z., (1992), "Behaviour of Reinforced Concrete Interior Beam-Column Joints Designed for Ductility using Grade 430 Steel", M.E. Thesis, Department of Civil Engineering, University of Canterbury, Christchurch, 121 pp.

APPENDIX A

Computer Program:	STEELTEST
Code:	VAX-11 FORTRAN
Computer:	VAX 11/750

```
C
C=======================================================================
C  Written by L.L. Dodd and J. Restrepo  1991
C
C  This program calls Subroutine STEEL to determine the cyclic stress history
C  of reinforcing steel given the tensile skeleton curve properties and the
C  strain history as described by Chapter 2 of this thesis.
C=======================================================================
C
C  The input and output file names are prompted for and an additional input
C  file "Factor.Dat" is required.  All input is in free-format.  Factor.Dat
C  requires the following variables:
C
C    Conversion factor for input strain ---------------------------- Conv
C      (e.g. Conv = 1.0E6 if strain is input as microstrain,
C                   100.  if strain is input as percentage,
C                   1.    if strain is input as as non-dimensional)
C
C    Factor for "Omega", the Bauschinger curve softness term -------- OmegFact
C      (see Section 2.6.1)
C
C    Input File
C    ==========
C
C    Card 1 - Steel Tensile Skeleton Curve Data (in engineering coordinates)
C
C       Yield Strength ------------------------------------------- Fy
C       Stress at peak load -------------------------------------- Fsu
C       Strain at initiation of strain hardening ----------------- ESH
C       Strain at peak load -------------------------------------- ESU
C       Modulus of elasticity ------------------------------------ Youngs
C       Strain for a point on the strain hardening curve --------- ESHI
C       Stress for the point corresponding to ESHI ---------------- FSHI
C
C    Card 2+ - Stress-Strain History (one card per point)
C
C       Engineering Strain Value --------------------------------- Es
C       Measured Engineering Stress Value ------------------------ Fsm
C
C    Output File
C    ===========
C
C    Card 1+
C
C     Strain in percent ---------------------------------------- Es*100.
C     Measured Stress ------------------------------------------ Fsm
C     Calculated Stress ---------------------------------------- Fs
C     Point Number --------------------------------------------- I
C
      Implicit None
      Integer I      ! counter
      Integer IOS    ! input/output status
      Integer LMR   ! Last Major Reversal direction. Value of "s" after reversal
      Integer BFlag(2) ! Strain hardening (0) or Bauschinger (1) curve
C
```

```
      Real C1        ! Temporary constant
      Real Conv      ! strain factor (1 for strain 1.E6 for microstrain)
      Real Epa(2)    ! Strain at end of linear branch (1=tension, 2=compression)
      Real EpaM(2)   ! Major reversal Epa
      Real Epo(2)    ! Maximum "natural" shift (1=compression, 2=tension)
      Real EpoMax    ! The maximum magnitude of Epo(1) and Epo(2)
      Real Eps       ! Natural strain
      Real Epr(2)    ! Reversal strain (1=tension, 2=compression)
      Real EprM(2)   ! Major reversal strain (1=tension, 2=compression)
      Real EpSH      ! Natural coordinate strain hardening strain
      Real EpSHI     ! Intermediate strain hardening curve natural strain
      Real EpsLast   ! Natural strain at last increment
      Real EpsOld    ! Natural strain at second to last increment
      Real Epsu      ! Natural coordinate "ultimate" strain
      Real EpsuSh(2)! Shifted "ultimate" strain value (1=tension, 2=compression)
      Real Epy       ! The yield strain, Fy/Youngs (a positive value)
      Real Es        ! Engineering Strain
      Real ESH       ! Engineering coordinate strain hardening strain
      Real ESHI      ! Intermediate strain hardening curve engineering strain
      Real Esu       ! Engineering coordinate "ultimate" strain
      Real Fpa(2)    ! Stress at end of linear branch (1=tension, 2=compression)
      Real FpaM(2)   ! Major reversal Fpa
      Real Fpr(2)    ! Reversal stress (1=tension, 2=compression)
      Real FprM(2)   ! Major reversal stress (1=tension, 2=compression)
      Real Fps       ! True coordinates stress
      Real FpSH      ! True stress at initiation of strain hardening curve
      Real FpSHI     ! Intermediate strain hardening curve true stress
      Real FpsLast   ! True stress at last increment
      Real FSHI      ! Intermediate strain hardening curve engineering stress
      Real Fsm       ! Engineering coordinate measured stress
      Real Fsu       ! Engineering coordinate "ultimate" stress
      Real Fpsu      ! True coordinate "ultimate" stress (slope at ultimate)
      Real Fs        ! Engineering Stress
      Real Fy        ! Yield Stress
      Real OmegFac   ! Multiplication factor for Omega
      Real Power(2) ! Exponent in normalised Bauschinger eq. (1=tens., 2=comp.)
      Real PowerM(2)! Major reversal Power
      Real SHPower   ! Exponent which governs the strain-hardening curve
      Real Youngs    ! Youngs modulus
      Real YTan      ! Tangential modulus
      Real YpTan     ! True coordinates tangential modulus
      Real YpTanM(2)! Tangential modulus at major reversals (1=tens, 2=comp)
      Real YpTanLast! Tangential modulus at last increment
      Real YoungsUn ! Unloading modulus
      Character*30 InFile,OutFil
C
C Read Input file for factored data
C
      OPEN (UNIT=1,NAME='Factor.dat',STATUS='OLD')
      Read (1,*) Conv,OmegFac
      Write (6,800) Conv,OmegFac
C
C  Required Input ENGINEERING Stress and Strain values
C
   10 Write(6,810)
      Read (5,820) InFile
```

```
      OPEN (UNIT=1,NAME=InFile,STATUS='OLD',Err=10)
      Write(6,830)
      Read (5,820) OutFil
      OPEN (UNIT=7,NAME=OutFil,STATUS='NEW')
      Read (1,*) Fy,Fsu,ESH,ESU,Youngs,ESHI,FSHI
C
C INITIALISE
C
      Epy       = Fy/Youngs
      EpSH      = log(1+ESH/Conv)
      Epsu      = log(1+ESU/Conv)
      Fpsu      = Fsu*(1+ESU/Conv)
      EpsuSh(1) =  Epsu
      EpsuSh(2) = -Epsu
      YoungsUn  = Youngs
      LMR       = 0
      BFlag(1)  = 0
      BFlag(2)  = 0
      Epa(1)    = 0.
      Epa(2)    = 0.
      EpaM(1)   = 0.
      EpaM(2)   = 0.
      Epo(1)    = 0.
      Epo(2)    = 0.
      EpoMax    = 0.
      Epr(1)    = 0.
      Epr(2)    = 0.
      EprM(1)   = 0.
      EprM(2)   = 0.
      I         = 0
C
C  Calculate the power term for the strain hardening branch
C
      EpSHI   = log(1+ESHI/Conv)
      FpSH    = Fy  *(1+ESH/Conv)
      FpSHI   = FSHI*(1+ESHI/Conv)
      C1      = FpSH-Fpsu+Fpsu*(Epsu-EpSH)
      SHPower = log((FpSHI+Fpsu*(Epsu-EpSHI)-Fpsu)/C1)
     +                / log((Epsu-EpSHI)/(Epsu-EpSH))
C
      Read (1,*,IOStat=IOS) Es,fsm
C
      Do While (IOS.EQ.0)
        I = I+1
        Es = Es/Conv
        Call Steel (Es,EpsLast,FpsLast,YpTanLast,EpsOld,Fy,Epy,      ! Input
     *           EpSH,Epsu,Fpsu,Youngs,SHPower,                      ! Input
     *          Epr,Fpr,Epa,Fpa,Epo,EpoMax,EpsuSh,YoungsUn,        ! Changeable
     *         Power,BFlag,LMR,EprM,FprM,EpaM,FpaM,YpTanM,PowerM, ! Changeable
     *           Eps,Fps,Fs,YpTan,YTan,                            ! Output
     *           OmegFac)                          ! Temporary Variable
C        Write (7,840)Eps*1.E6,Fsm*(1+Es),Fps,I
        Write (7,840)Es*1.E2,Fsm,Fs,I
        If (Eps.NE.EpsLast) then
          EpsOld    = EpsLast
          EpsLast   = Eps
```

```
          FpsLast   = Fps
          YpTanLast = YpTan
        End If
        Read (1,*,IOStat=IOS) Es,fsm
      End Do
C
      Stop
C
  800 Format (' Data read from Input file "Factor.Dat"'/
     *        ' Strain Conversion Factor:    ',E12.4/
     *        ' Omega Multiplication Factor: ',E12.4/)
  810 Format (' What is the input file name?')
  820 Format (A)
  830 Format (' What is the output file name?')
  840 Format (3E15.6,I6)
C
      End
C
C
      Subroutine Steel (Es,EpsLast,FpsLast,YpTanLast,EpsOld,Fy,Epy, ! Input
     *           EpSH,Epsu,Fpsu,Youngs,SHPower,                     ! Input
     *          Epr,Fpr,Epa,Fpa,Epo,EpoMax,EpsuSh,YoungsUn,       ! Changeable
     *         Power,BFlag,LMR,EprM,FprM,EpaM,FpaM,YpTanM,PowerM, ! Changeable
     *           Eps,Fps,Fs,YpTan,YTan,                           ! Output
     *           OmegFac)                          ! Temporary Variable
C
C=======================================================================
C  Written by L.L. Dodd and J. Restrepo  1991
C
C  This subroutine determines the cyclic stress history of reinforcing steel
C  given the tensile skeleton curve properties and the strain history as
C  described by Chapter 2 of this thesis.
C=======================================================================
C
C
C PASSED VARIABLES
C
      Implicit None
      Integer LMR   ! Last Major Reversal direction. Value of "s" after reversal
      Integer BFlag(2) ! Strain hardening (0) or Bauschinger (1) curve
C
      Real Epa(2)   ! Strain at end of linear branch (1=tension, 2=compression)
      Real EpaM(2)  ! Major reversal Epa
      Real Epo(2)   ! Maximum "natural" shift (1=compression, 2=tension)
      Real EpoMax   ! The maximum magnitude of Epo(1) and Epo(2)
      Real Eps      ! Natural strain
      Real Epr(2)   ! Reversal strain (1=tension, 2=compression)
      Real EprM(2)  ! Major reversal strain (1=tension, 2=compression)
      Real EpSH     ! Natural coordinate strain hardening strain
      Real EpsLast  ! Natural strain at last increment
      Real EpsOld   ! Natural strain at second to last increment
      Real Epsu     ! Natural coordinate "ultimate" strain
      Real EpsuSh(2)! Shifted "ultimate" strain value (1=tension, 2=compression)
      Real Epy      ! The yield strain, Fy/Youngs (a positive value)
      Real Es       ! Engineering Strain
      Real Fpa(2)   ! Stress at end of linear branch (1=tension, 2=compression)
```

```
      Real FpaM(2)  ! Major reversal Fpa
      Real Fpr(2)   ! Reversal stress (1=tension, 2=compression)
      Real FprM(2)  ! Major reversal stress (1=tension, 2=compression)
      Real Fps      ! True coordinates stress
      Real FpsLast  ! True stress at last increment
      Real Fpsu     ! True coordinate "ultimate" stress (slope at ultimate)
      Real Fs       ! Engineering Stress
      Real Fy       ! Yield Stress
      Real OmegFac  ! Multiplication factor for Omega
      Real Power(2) ! Exponent in normalised Bauschinger eq. (1=tens., 2=comp.)
      Real PowerM(2)! Major reversal Power
      Real SHPower  ! Exponent which governs the strain-hardening curve
      Real Youngs   ! Youngs modulus
      Real YTan     ! Tangential modulus
      Real YpTan    ! True coordinates tangential modulus
      Real YpTanM(2)! Tangential modulus at major reversals (1=tens, 2=comp)
      Real YpTanLast! Tangential modulus at last increment
      Real YoungsUn ! Unloading modulus
C
C INTERNAL VARIABLES
C
      Real a        !
      Real C1       ! Temporary constant
      Real C2       ! Temporary constant
      Real Delta    ! Strain change from previous increment
      Real Epp      ! Abs((Epsush(K) - Epa(M))/Epsu)
      Real FNorm    ! Abs(Fpp/Fpt)
      Real Fpp      ! Fpsu*(s*1.-EpsuSh(K)+Epa(M)) - Fpa(M)
      Real Fpt      ! Fpsu*(2-EpsuSh(1)+EpsuSh(2))
      Real FpSH     ! Strain hardening natural strain (Fy*(1+Epsh))
      Real Omega    ! Percent area term for Bauschinger curve
      Integer MaxFlag ! Flag to tell if reversal point is a new max 0-no,1-yes
      Integer S     ! Straining direction: -1 for compressing, 1 for tensioning
      Integer K     ! Index value          2                  1
      Integer M     ! Index value          1                  2
      Integer L     ! Index value: K for LMR*s.NE.-1,  M otherwise
C
      Eps = log(1+Es)
      Delta = Eps - EpsLast
      If (Delta.Eq.0) Delta = EpsLast - EpsOld
      If (Delta.Gt.0.0) then                        ! tensioning
         M  = 2
         K  = 1
         S  = 1
      Else                                          ! compressing
         M  =  1
         K  =  2
         S  = -1
      End If
      If (Eps*s.Gt.EpsuSH(K)*s) then
         Fps  = 0.
         Fpsu = 0.
         Write (6,800)
                                                    RETURN
      End If
C
```

```
      If (((EpsLast-EpsOld)*Delta).Lt.0.) then     ! Reversal
C
C  =================
C   STRAIN REVERSAL
C  =================
C
        If ((Epo(1).Eq.0.).And.(Epo(2).Eq.0.).And.
     *                          (Abs(EpsLast).Lt.Epy)) then          !Elastic
          Continue
        Else If ((LMR*s.EQ.-1).And.((EpsLast-Epa(K))*s).GE.0.) then !Linear Rng
          Continue
        Else If ((LMR*s.EQ.1).And.(EpsLast-Epr(M))*s.GE.0.) then  !Linear Range
          Continue
        Else
C
          MaxFlag = 0
          If (s*Epo(K).GT.s*(EPsLast-FpsLast/YoungsUn)) then
C
C                                                 ! Max abs strain in direction
C
            MaxFlag  = 1
            Epo(K)     = EpsLast-FpsLast/YoungsUn
            EpsuSh(K) = Epsu*s+Epo(K)
            If (Abs(Epo(K)).Gt.EPoMax) then
              EpoMax   = Abs(Epo(K))                          ! New Max Strain
              YoungsUn = Youngs*(0.82 + 1./(5.55+1000.*EpoMax)) ! Unloading Mod.
            End If
          End If
          LMR     = s
          Epr(M) = EpsLast
          Fpr(M) = FpsLast
          Epa(M) = EpsLast + s*Fy/YoungsUn
          Fpa(M) = FpsLast + s*Fy
          If (((BFlag(K).EQ.0.OR.BFlag(M).EQ.0).And.MaxFlag.EQ.1) .OR.
     +           s*(FprM(K)-Fpr(M)).GT.2*Fy     .OR.
     +       ((Epr(M)-EpaM(K))/(EprM(M)-EpaM(K)).GT.1.0  .And.
     +                  BFlag(K).EQ.1))   then
C
C  ================
C   MAJOR REVERSAL
C  ================
C  Reversal from skeleton curve or more than 2Fy from previous major reversal
C  Reverse to a MAJOR BAUSCHINGER CURVE
C
            EprM(M)   = Epr(M)
            FprM(M)   = Fpr(M)
            EpaM(M)   = Epa(M)
            FpaM(M)   = Fpa(M)
            YpTanM(M) = YpTanLast
            Epr(K)    = Epr(M)
            EprM(K)   = Epr(M)
            If ((Epo(2)-Epo(1)).LT.(EpSh-Epy)) then    ! Between Yield Plateaus
              Power(K) = 0.35
            Else                                        !' Bauschinger Curve
              BFlag(K) = 1
              Fpt      = Fpsu*(2-EpsuSh(1)+EpsuSh(2))
```

```
              Fpp      = Fpsu*(s*1.-EpsuSh(K)+Epa(M)) - Fpa(M)
              Epp      = Abs((Epsush(K) - Epa(M))/Epsu)
              FNorm = Abs(Fpp/Fpt)
              Omega = ((0.001+1.08E-3/(1.043-Epp))/0.18*(FNorm-0.69)
     +                +0.085) * OmegFac
              If (Omega.GT.0.086) Omega = 0.085
              Power(K) = 56.689*(Omega-0.077)**2-4.921*(Omega-0.077)+0.1
            End If
            PowerM(K) = Power(K)
          Else If ((Epr(M)-EprM(M))*s.LT.0) then
C
C  ================
C   MINOR REVERSAL
C  ================
C  Reversal from a major Bauschinger curve less than 2Fy from previous
C  major reversal on
C  Reverse to a MINOR BAUSCHINGER CURVE
C
            EprM(M)    = Epr(M)
            FprM(M)    = Fpr(M)
            YpTanM(M) = YpTanLast
            Power(K)   = 0.35
          Else
C
C  Reversal from a minor Bauschinger curve
C
            Power(K)   = 0.35
          End If
        End If
      End If
C
C  ================================
C   GOVERNING STRESS-STRAIN CURVES
C  ================================
C
      If (LMR*s.NE.-1) Then
        L = M
      Else
        L = K
      End If

      If (BFlag(K).eq.1) then
        If (((LMR*s.Eq.-1).And.(Eps*s.Gt.Epr(K)*s)).Or.
     *      ((LMR*s.Eq.1).And.(Eps*s.Gt.Epa(M)*s))) then
C
C  Post Yield-Plateau Bauschinger Curve
C
          If (s*(Eps-EprM(K)).GT.0.) then
C
C  MAJOR BAUSCHINGER CURVE moving toward ultimate point
C
      Call Bausch (Eps,EpaM(M),FpaM(M),EpsuSh(K),Fpsu*s,YoungsUn,      ! Input
     +             Fpsu,PowerM(K),                                     ! Input
     +             Fps,YpTan)                                         ! Output
          Else
C
```

```
C  MINOR BAUSCHINGER CURVE moving toward previous minor or major peversal point
C
      Call Bausch (Eps,Epa(M),Fpa(M),EprM(K),FprM(K),YoungsUn,         ! Input
     +             YpTanM(K),Power(K),                                 ! Input
     +             Fps,YpTan)                                         ! Output
        End If
      Else
        Fps   = Fpr(L) + (Eps-Epr(L))*YoungsUn
        YpTan = YoungsUn
      End If
C
C  Elastic Branch
C
      Else If ((Epo(1).eq.0.).And.(Epo(2).eq.0.).And.
     *        (Abs(Eps).LE.Epy)) then
        Fps   = Eps*Youngs
        YpTan = Youngs
C
C  Skeleton Curve
C
      Else If (s*(Eps-Epo(M)-s*Fy/YoungsUn).GE.-1.E-5) Then
        If (s*(Eps-Epo(K)-s*Epy).LE.(EpSH-Epy)) then
          Fps   = Fy*s*(1+Es)                          ! Yield Plateau
          YpTan = Fy
        Else
          FpSH  = Fy*(1+Epsh)                            ! Strain Hardening
          C1    = FpSH - Fpsu + Fpsu*(Epsu-EpSH)
          C2    = (Epsu-s*(Eps-Epo(K)))/(Epsu-EpSH)
          Fps   = s*C1*C2**SHPower - Fpsu*(s*Epsu-(Eps-Epo(K))) + s*Fpsu
          YpTan = -SHPower*(C1/(Epsu-EpSH))*C2**(SHPower-1) + FpSU
        End If
C
C Reloading to Strain Hardening
C
      Else If ((EprM(K)-Epo(K))*s.GE.Epsh) then
        If (((LMR*s.Eq.-1).And.(Eps*s.Gt.Epr(K)*s)).Or.
     *      ((LMR*s.Eq.1).And.(Eps*s.Gt.Epa(M)*s))) then

      Call Bausch (Eps,Epa(M),Fpa(M),EprM(K),FprM(K),YoungsUn,         ! Input
     +             YpTanM(K),Power(K),                                 ! Input
     +             Fps,YpTan)                                         ! Output
        Else
          Fps   = Fpr(L) + (Eps-Epr(L))*YoungsUn
          YpTan = YoungsUn
        End If
C
C Between Yield Plateaus
C
      Else
        If (((LMR*s.Eq.-1).And.(Eps*s.Gt.Epr(K)*s)).Or.
     *      ((LMR*s.Eq.1).And.(Eps*s.Gt.Epa(M)*s))) then
          If (s*(Eps-Epr(K)).GT.0.) then
C
C  MAJOR BAUSCHINGER CURVE moving toward yield plateau point
C
      Call Bausch (Eps,Epa(M),Fpa(M),Epo(M)+s*Fy/YoungsUn,Fy*s,YoungsUn,! Input
```

```
     +             Fy,Power(K),                                          ! Input
     +             Fps,YpTan)                                           ! Output
          Else
C
C  MINOR BAUSCHINGER CURVE moving toward previous minor or major peversal point
C
       Call Bausch (Eps,Epa(M),Fpa(M),EprM(K),FprM(K),YoungsUn,          ! Input
     +             YpTanM(K),Power(K),                                   ! Input
     +             Fps,YpTan)                                           ! Output
          End If
        Else
          Fps    = Fpr(L) + (Eps-Epr(L))*YoungsUn
          YpTan = YoungsUn
        End If
       End If
       Fs    = Fps/(1+Es)
       YTan = (YpTan-fps)*exp(-2*Eps)
       Return
  800 Format (/' The peak strain has been exceeded, REBAR FRACTURE!'/)
       End
C
       Subroutine Bausch (Eps,E1,F1,E2,F2,Slope1,Slope2,Power,           ! Input
     +                    Fps,YpTan)                                     ! Output
C
C This subroutine calculates the stress for a given strain on the Bauschinger
C curve
C
       Integer ITest ! Convergence flag
       Integer I     ! Counter

       Real C1       ! (Fpu-Epu*Slope1)/(Fpu-Epu*F2)
       Real C2       ! Eps*(Slope1-F2)/(Fpu-F2*Epu)
       Real C3       ! 1 - Eppn
       Real C4       ! 1 - C3*C3 = 1-(1-Eppn)^2
       Real C5       ! C4**Power-C1*Eppn-C2 (function for which Eppn is a root)
       Real E1       ! Initial strain on Bauschinger curve
       Real Eppn     ! Normalised Strain in the Bauschinger Branch
       Real Eppn2    ! New estimate of Eppn
       Real Eps      ! Natural strain
       Real E2       ! Final strain on Bauschinger curve
       Real Epu      ! Strain from linear branch to ultimate (E2 - E1)
       Real F1       ! Initial stress on Bauschinger curve
       Real Fps      ! True coordinates stress
       Real Fpu      ! Stress from linear branch to ultimate (F2 - F1)
       Real F2       ! Final stress on Bauschinger curve
       Real Power    ! Exponent in the Normalised Bauschinger equation
       Real Slope1   ! Initial Slope
       Real Slope2   ! Final Slope
       Real YpTan    ! Tangential modulus
C
       fpu   = F2 - F1
       Epu   = E2 - E1
       C1    = (Fpu-Epu*Slope1)/(Fpu-Epu*Slope2)
       C2    = (Eps-E1)*(Slope1-Slope2)/(Fpu-Slope2*Epu)
       Eppn = (Eps-E1)/(E2-E1)
       ITest = 1
```

```
      I     = 0
      Do While ((ITest.Eq.1).And.(I.LT.5))
         I     = I+1
         C3    = 1-Eppn
         C4    = 1-C3*C3
         C5    = C4**Power-C1*Eppn-C2
         Eppn2 = Eppn - C5/(2*Power*C4**(Power - 1)*C3-C1) ! Newton-Raphson
         If (Eppn2.GT.0.02) then
            Eppn = Eppn2
            If (Abs(C5).LE.0.001) ITest = 0
         Else
            Call LinInterp(Eppn,C1,C2,Power)
            ITest = 0
         End If
      End Do
      Fps  = Eppn*(FPu-Epu*Slope1)+(Eps-E1)*Slope1+F1
      If (Eppn.LT.0.0001 .OR. (Slope1-Slope2)/slope1.LT.0.01) then
        YpTan = Slope1
      Else
        YpTan=2*Power*(1-(1-Eppn)**2)**(Power-1.)*(1-Eppn) !Normal coordinates
        YpTan =YpTan*(Fpu-Slope2*Epu)/((Epu*Slope1-Fpu)/(Slope1-Slope2))
        YpTan = YpTan*Slope1/(YpTan+Slope1) + Slope2
      End If
      Return
      End
C
      Subroutine LinInterp (Eppn,C1,C2,Power)
C
C  Calculate Eppn using an iterative linear inperpolation
C
      Integer ITest ! Convergence flag

      Real C1       ! (Fpu-Epu*Slope1)/(Fpu-Epu*Slope2)
      Real C2       ! Eps*(Slope1-Slope2)/(Fpu-Slope2*Epu)
      Real C3       ! 1 - Eppn
      Real C4       ! 1 - C3*C3 = 1-(1-Eppn)^2
      Real C5       ! C4**Power-C1*Eppn-C2 (function for which Eppn is a root)
      Real C5L      ! Lower bound of C5
      Real C5U      ! Upper bound of C5
      Real Eppn     ! Normalised Strain in the Bauschinger Branch
      Real EppnL    ! Lower bound of Eppn
      Real EppnU    ! Upper bound of Eppn
      Real Eps      ! Natural strain
      Real Power    ! Exponent in the Normalised Bauschinger equation
       EppnU = Eppn
       C3    = 1-EppnU
       C4    = 1-C3*C3
       C5U   = C4**Power-C1*EppnU-C2
       EppnL = 0
       C5L   = -C2
C       ITest = 1
C       Do While (ITest.Eq.1)
       Do I=1,5
          Eppn = EppnL-C5L*(EppnU-EppnL)/(C5U-C5L)
          C3    = 1-Eppn
          C4    = 1-C3*C3
```

```
          C5     = C4**Power-C1*Eppn-C2
C          If (Abs(C5).LE.0.03) then
C             ITest = 0
C          Else
             If (C5.Gt.0) then
                EppnU = Eppn
                C5U   = C5
             Else
                EppnL = Eppn
                C5L   = C5
             End If
C          End If
       End Do
       Return
       End
```

APPENDIX B

Construction Details of Loading Frames

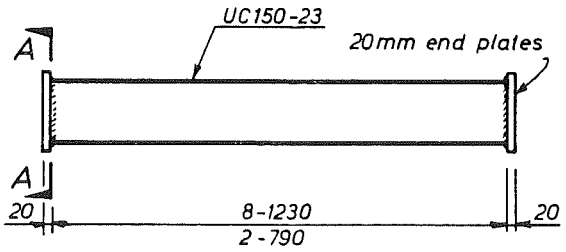

Universal Columns

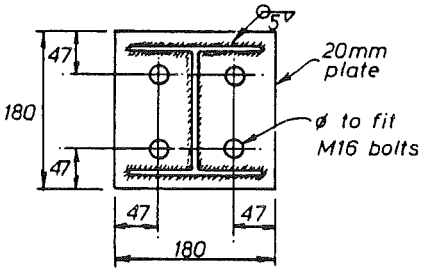

Section A-A

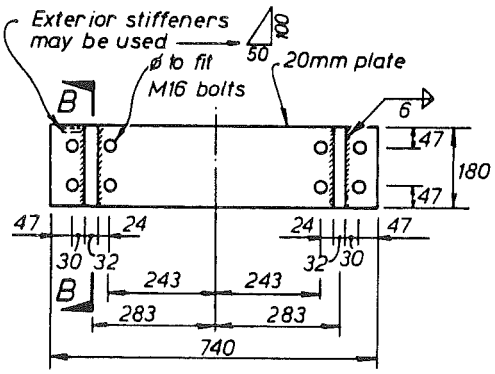

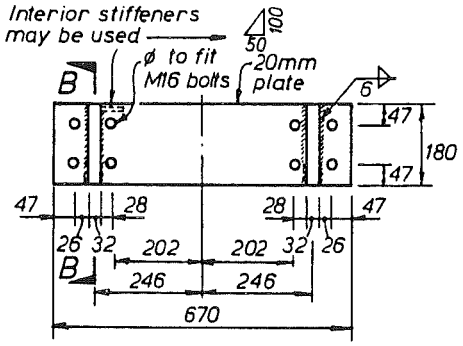

End Brackets

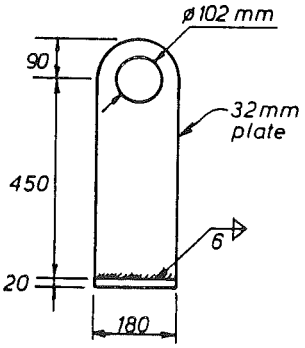

Section B-B

Use 16mm HS bolts
Use 102mm HS pins
Maximum Service Load: 450kN

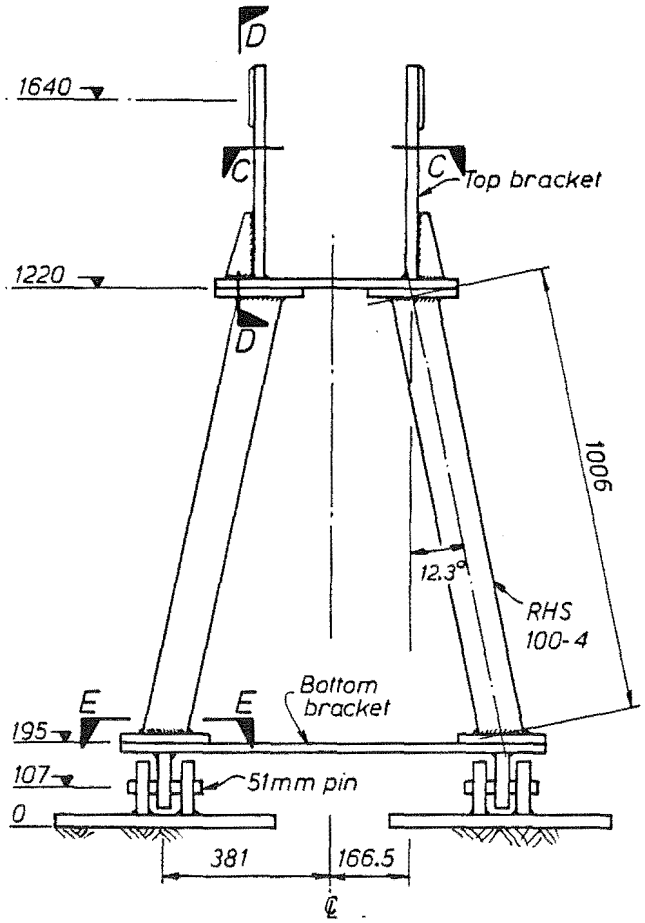

Beam End Supports - LF2

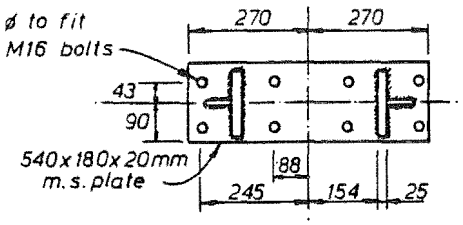

Section C-C

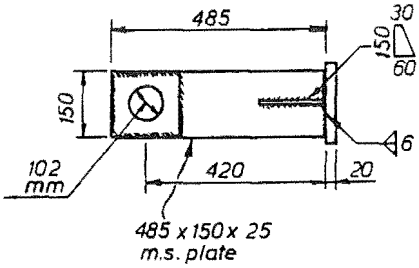

Section D-D

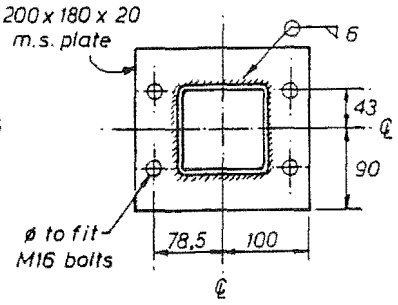

Section E-E

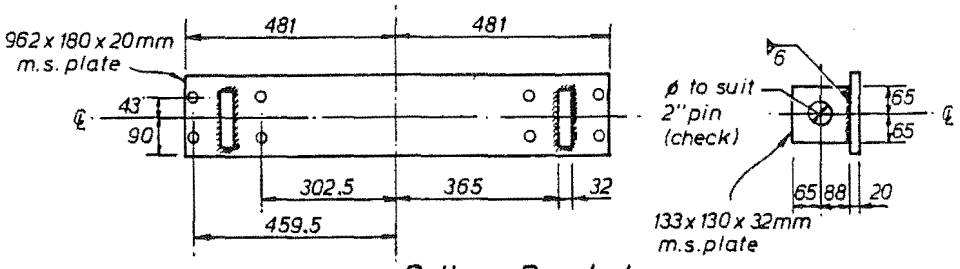

Bottom Bracket

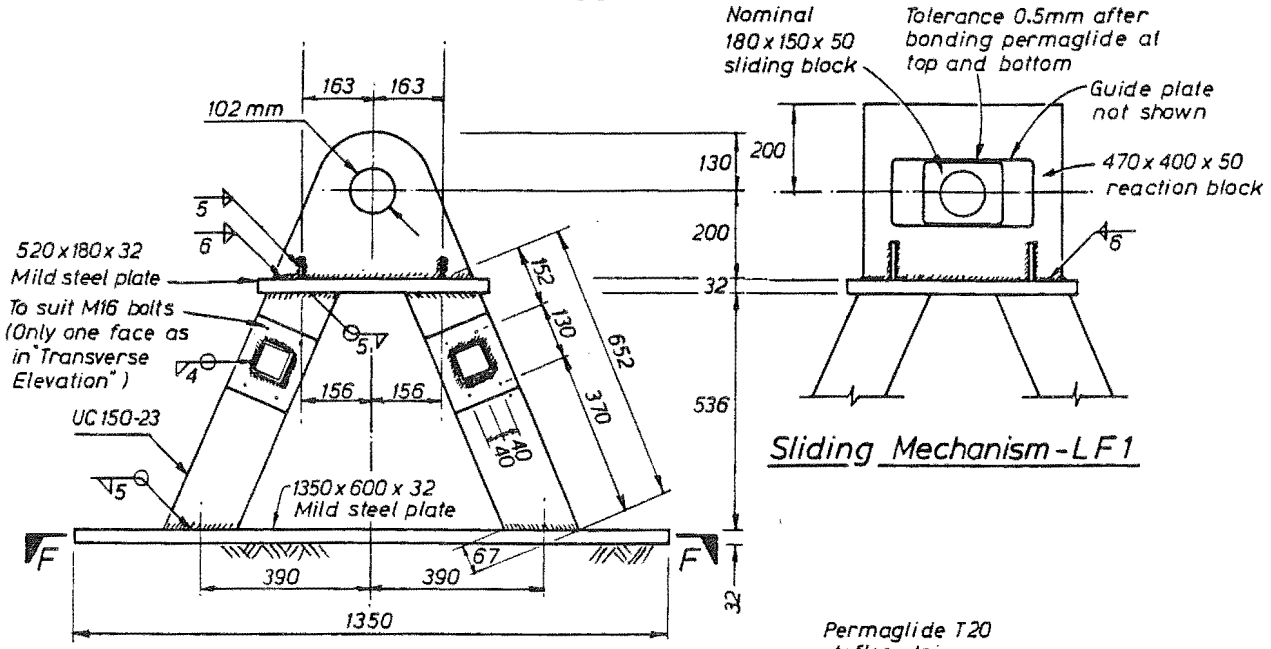

Sliding Mechanism - LF1

Column Base Support

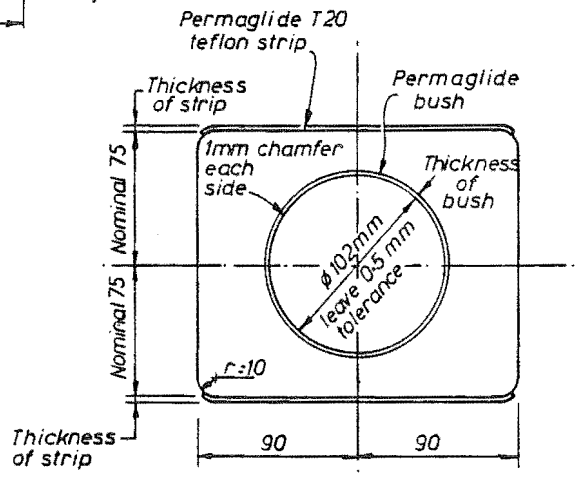

Sliding Block

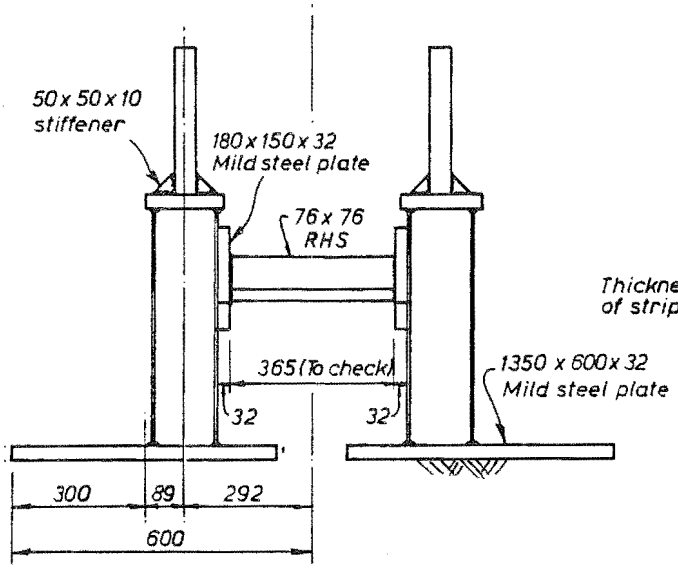

Transverse Elevation Column Base Supports

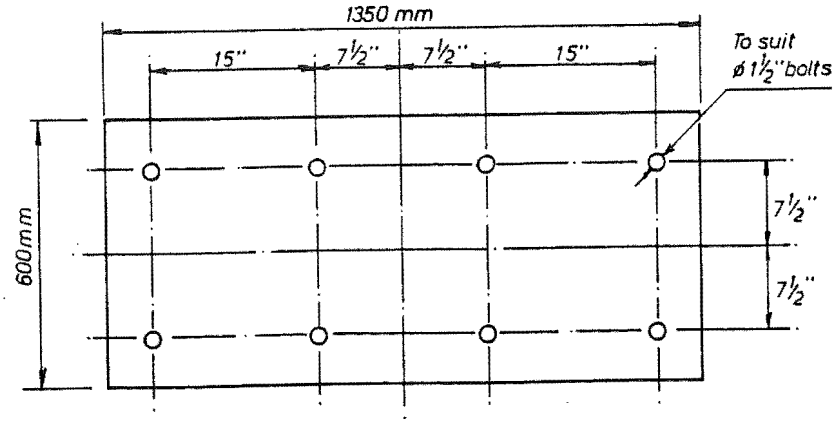

Section F-F

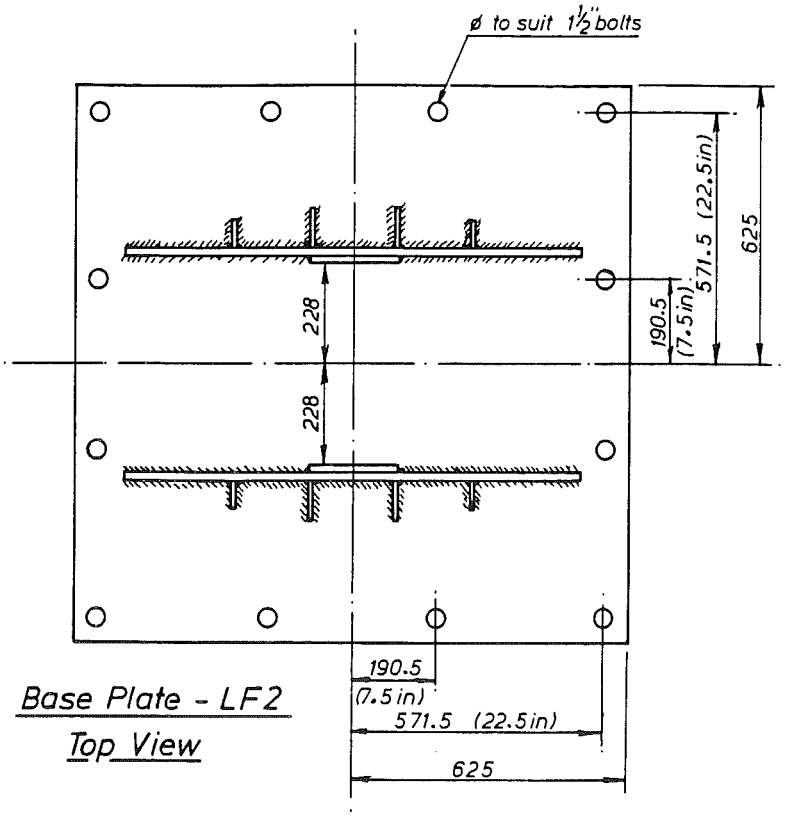

Base Plate - LF2
Top View

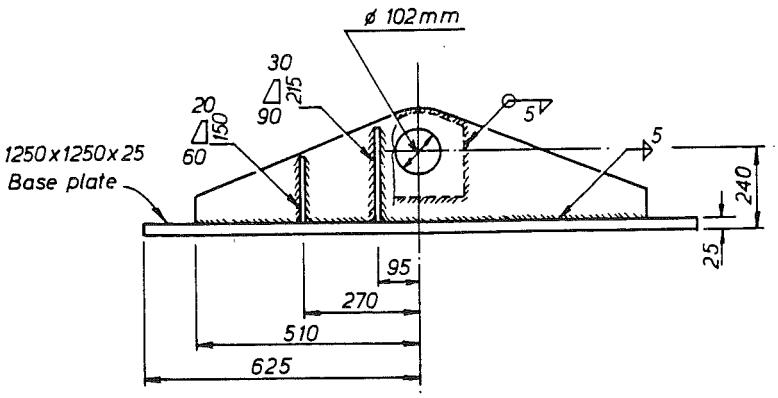

Column Base Plate - LF2

Note: Max. service load 450kN per jack
All M16 bolts are high strength
Maintain dust free sliding mechanism

Classn:

THE SEISMIC BEHAVIOUR OF CONNECTIONS BETWEEN PRECAST CONCRETE ELEMENTS

José I. RESTREPO-POSADA

ABSTRACT: Six full-scale precast concrete subassemblages connected in a cast in place joint were tested under quasi-static reverse cyclic loading conditions. The test specimens were typical of moment resisting perimeter frames and had connection details commonly used in New Zealand. A research on the stress-strain behaviour of the two grades of New Zealand manufactured reinforcing steel was also conducted.

Department of Civil Engineering, University of Canterbury
Doctor of Philosophy Thesis, 1992